Author:
Moore, Stacy R

Title:
A Study of Stress Corrosion Cracking by High-Speed Atomic Force Microscopy

A Study of Stress Corrosion Cracking by High-Speed Atomic Force Microscopy

By

STACY MOORE

School of Physics
UNIVERSITY OF BRISTOL

A dissertation submitted to the University of Bristol in accordance with the requirements of the degree of DOCTOR OF PHILOSOPHY in the Faculty of Science, School of Physics.

MARCH 2021

Word count: 75,790

Abstract

Stainless steels are widely used in the nuclear industry for their well-known behaviour, favourable mechanical properties, and resistance to corrosion. However, under certain conditions stainless steels are susceptible to localised corrosion. Forms of localised corrosion, such as stress corrosion cracking (SCC), are particularly detrimental as they can occur without any obvious visual cues. This can lead to sudden and unexpected failure. The development of accurate prediction methods and technologies for SCC is important for the safe and economical running of nuclear power plants, as well as in various other applications.

Atomic force microscopes (AFMs) are capable of high-resolution mapping of structures and the measurement of mechanical properties at nanometre scales within gaseous and liquid environments. The contact mode high-speed AFM (HS-AFM) invented at the University of Bristol operates at speeds orders of magnitude faster than conventional AFMs and is capable of capturing multiple frames per second. This allows for direct observation of dynamic events in real-time, with nanometre lateral resolution and subatomic height resolution. The enhanced capabilities of HS-AFM make it a viable tool for the in-situ imaging of nanoscale corrosion initiation events, such as metastable pitting, grain boundary dissolution and short crack formation during SCC. Observations of such events could give valuable insight into the processes that take place and the mechanisms behind them.

SCC occurs due to the synergistic interactions of three factors: a susceptible material, a corrosive environment, and sufficient stress. Within this project, SCC and the factors leading to SCC, were analysed using HS-AFM in combination with electron and ion beam microscopy techniques.

Working in collaboration with the National Nuclear Laboratory, sensitised microstructure in nuclear relevant stainless steels was analysed by correlative microscopy. HS-AFM measurements of an irradiated sample of ex-service stainless steel revealed nanometre scale radiation-induced voids identified as plastic voids, helium bubbles, or cavities. present across the sample, previously only observed by transmission electron microscopy. The high throughput of the HS-AFM allowed for statistical analysis across large areas of the sample. This work extended to comparisons between the microstructure and grain boundary chemical compositions of thermally sensitised and irradiated austenitic stainless steels. These comparisons are important when considering thermally treated stainless steels as an analogue to irradiated samples. Further experimental work revealed how such a surface responds to applied stress and corrosive environments.

HS-AFM was used to observe localised dissolution events and pitting corrosion in-situ, both of which can lead to SCC. These measurements were performed by imaging within a custom liquid cell with parallel potentiostatic control. The high resolution of the HS-AFM allowed for observations to be performed at individual reaction sites and accurate measurements of the dimensions of pits formed. Using these measurements, it was possible to calculate, and subsequently model, the volumes of metal reacting with respect to time, and so the current

densities and ionic fluxes at work. In this manner, the local electrochemistry at nanoscale reaction sites may be reconstructed.

Lastly, factors were brought together to study SCC using both in-situ and ex-situ techniques. During in-situ SCC measurements by HS-AFM, uplift of grain boundaries before cracking was observed, indicating a subsurface contribution to the cracking mechanism. Focussed ion beam milling revealed a network of intergranular cracks below the surface lined with a thin oxide, indicating that the SCC process is dominated by local stress at oxide-weakened boundaries. Analysis by atom probe tomography of a crack tip showed a layered oxide composition at the surface of the crack walls. The formation of this oxide is posited to be mechanistically linked to grain boundary uplift. This study shows how in-situ HS-AFM observations in combination with complementary techniques can give important insights into the mechanisms of SCC.

AUTHOR'S DECLARATION

I declare that the work in this dissertation was carried out in accordance with the requirements of the University's Regulations and Code of Practice for Research Degree Programmes and that it has not been submitted for any other academic award. Except where indicated by specific reference in the text, the work is the candidate's own work. Work done in collaboration with, or with the assistance of, others, is indicated as such. Any views expressed in the dissertation are those of the author.

SIGNED: ..... DATE:.....

Dedication and Acknowledgements

First and foremost I would like to thank my supervisors for all of their support throughout this PhD. A big thank you to Oliver Payton and Loren Picco for all their guidance and HS-AFM wisdom. Huge thanks to Tomas Martin for all his advice, seemingly limitless instrumentation know-how, and for helping me become a better writer (notice how I use a comma between every item in a list). Thank you also to Robert Burrows for his sage corrosion advice and corridor conversations where I should have definitely brought several notepads.

I'd also like to thank Xander Warren for our chats and our coffees, Jolene Moon for our walks and our coffees, and Erin Holland for our runs and our coffees. Huge thank you to Office 3.35, the Material Girls, and all those at the IAC. Thank you to Freddie S. Russell-Pavier for always having time to explain confusing things to me, for our endless weird discussions, and his awful jokes. Also, to David Kumar for the never-ending puns.

This thesis is dedicated to all those who stuck by me throughout this PhD. To my family, to my friends, and to all my housemates through the years.

I would like to acknowledge the physics workshop for all their help cutting out samples and producing strain-rigs. Also, Peter Heard for his assistance on the focussed-ion beam (FIB). Xander Warren, Chris Jones, and Peter Martin for their help on the scanning electron microscopes (SEMs). Tomas Martin for performing atom probe tomography analysis, Jean Charles Eloi for performing transmission electron microscopy (TEM) measurements, and Mattia Cattelan for performing NanoESCA measurements. The electron microscopy team at NNL for their assistance at Central Lab. Individual contributions are stated at the beginning of each results chapter where relevant. I would like to thank Outokumpu Stainless AB for the supply of the SAF 2205 duplex stainless steel samples. I would also like to acknowledge COMSOL for providing a trial of COMSOL MP 3.5a with the allowance to publish results produced in the software, and for the provision of technical support throughout the modelling process. Lastly, I would like to acknowledge Robert Burrows for his help performing potentiostat tests, and Freddie Russell-Pavier for assistance in stitching together large-area maps.

"Like most of what I do, it makes up in internal rhyme what it lacks in brevity"

– Tim Minchin, *Mountview Academy of Theatre Arts' 2015 graduation ceremony*

Journal Publications

- **S. Moore**, P.G. Martin, O.D. Payton, L. Picco, R. Burrows, and T. Scott, A Study of Iron Meteorite Microstructure by EBSD and High-Speed AFM - In preparation.

- **S. Moore**, A.D. Warren, R. Burrows, O.D. Payton, L. Picco, F.S. Russell-Pavier, P.G. Martin, T.L Martin, 2021. Sample Preparation Methods for Optimal HS-AFM Analysis: Duplex Stainless Steel. Ultramicroscopy, p.113210.

- **S. Moore**, R. Burrows, D. Kumar, M. B. Kloucek, A. D. Warren, P. E. J. Flewitt, L. Picco, O. D. Payton, and T. L. Martin, 2021. Observation of stress corrosion cracking using real-time in situ high-speed atomic force microscopy and correlative techniques. npj Materials Degradation, 5(1), pp.1-10.

- R.N. Clark, R. Burrows, R. Patel, **S. Moore**, K.R. Hallam, P.E. Flewitt, 2020. Nanometre to micrometre length-scale techniques for characterising environmentally-assisted cracking: An appraisal. Heliyon, 6(3), p.e03448 - *I attended regular meetings, researched and provided input. I aided in writing sections such as the introduction, surface methods, volume methods, reaction sensing, diffraction techniques, and mechanical testing.*

- A.F. Payam, O. Payton, L. Picco, **S. Moore**, T.L. Martin, A.D. Warren, M. Mostafavi and D. Knowles, 2019. Development of a fatigue testing system for in-situ observation of stainless steel 316 by HS-AFM and SEM, International Journal of Fatigue, 127, pp.1-9 - *I assisted in method development and data collection and provided feedback.*

- H. Alzahrani, C. Bentley, R. Burrows, C. Cao, Q. Cai, C. Chikere, R.M. Crooks, J. Dunevall, M. Edwards, A. Ewing, R. Gao, R. Hillman, M. Kahram, F. Kanoufi, C. Kranz, J.F. Lemineur, Y. Long, K. McKelvey, M. Mirkin, **S. Moore**, W. Nogala, H. Ren, W. Schuhmann, P. Unwin, A. Vezzoli, H. White, K. Willets, Z. Yang and Y. Ying, 2018. Dynamics of nanointerfaces: general discussion. Faraday discussions, 210, pp.451-479 - *This paper is a record of the discussion that accompanied the Faraday discussion paper and presentation. I answered a series of questions as part of a panel discussion and my responses were recorded.*

- **S. Moore**, R. Burrows, L. Picco, T. Martin, S. Greenwell, T. Scott, and O. Payton, 2018. A study of dynamic nanoscale corrosion initiation events by HS-AFM. Faraday Discussions, 2018, 210, 409 - 428.

- R. Burrows, A. Baron-Wiechec, C. Harrington, **S. Moore**, D. Chaney, T.L. Martin, J. Likonen, R. Springell, and E. Surrey, 2018. The possible effect of high magnetic fields on the aqueous

corrosion behaviour of Eurofer. Fusion Engineering and Design - *I wrote the literature review section and provided feedback.*

- A. Laferrere, R. Burrows, C. Glover, R.N. Clark, O. Payton, L. Picco, **S. Moore**, and G. Williams, 2017. In situ imaging of corrosion processes in nuclear fuel cladding. Corrosion Engineering, Science and Technology, 52(8), pp.596-604 - *I assisted in editing and provided feedback.*

Conference Publications

- A.F. Payam, O. Payton, M. Mostafavi, L. Picco, **S. Moore**, T.L. Martin, A.D. Warren and D. Knowles, Development of a fatigue testing system for in-situ observation of stainless steel 316 by HS-AFM and SEM, In MATEC Web of Conferences 2019(Vol. 300, p. 14002). EDP Sciences - *I assisted in method development and data collection and provided feedback.*

- R. N. Clark, O. Payton, J. Knapp, L. Picco, A. Laferrere, W. S. Walters, **S. Moore** and R. Burrows, Development of an Adapted Electrochemical Noise Technique for in-situ Corrosion Monitoring of Spent Nuclear Fuel Aqueous Storage Environments, In CORROSION 2018. NACE International - *I collected some of the data and provided feedback.*

- **S. Moore**, R. Burrows, L. Picco, T. Scott, A. Laferrere and O. Payton, Investigating Corrosion Using High-Speed AFM, EUROCORR 2017 PROCEEDINGS.

Internal Reports

- **S. Moore**, R. Burrows, A.D. Warren, O.D. Payton, L. Picco, F.S. Russell-Pavier, High-Speed Atomic Force Microscopy Analysis of AGR Fuel Cladding, 2020.

- **S. Moore**, D. Hambley, S. Dumbill, A. Qaisar, M. Ward, C. Sellars, I. Vatter, E. Cosh, O.D. Payton, R. Burrows, T.L. Martin, and T.B. Scott, Central Lab Industrial Secondment Report: Analysis of the Relationship Between GB Misorientation and GB Segregation in Irradiated Ex-Service AGR Cladding, 2019.

Awards

- International Cooperative Group on Environmentally-Assisted Cracking (ICG-EAC) Student Grant 2019.

- Institute of Corrosion Jack Galloway Award 2017 - Received for my work titled: Investigating Corrosion Using High-Speed AFM, Authors: **S. Moore**, R. Burrows, L. Picco, T.B. Scott, A. Laferrere and O. Payton.

- The UK Surface Analysis Forum (UKSAF) Travel Award 2017.

Talks

- A Study of Stress Corrosion Cracking by HS-AFM (20 minutes), EUROCORR 2020 Taster Session, Online, 30 June 2020.
- A Study of Stress Corrosion Cracking by HS-AFM (20 minutes), EUROCORR 2019, Seville, 9-13 September 2019.
- A Study of Stress Corrosion Cracking by HS-AFM (20 minutes), ICG-EAC Meeting 2019 Tainan, Taiwan, 12-17 May 2019.
- A Study of Dynamic Nanoscale Corrosion Initiation Events by HS-AFM, Electrochemistry at Nano-interfaces: Faraday Discussion, Bath, 26-28 June 2018.
- Internal: A Study of Localised Corrosion Using High-Speed Atomic Force Microscopy (HS-AFM) (10 minutes), University of Bristol Postgraduate Conference, 16 May 2018.
- Development of Fundamental Approaches for Dynamic Study of Nanoscale Corrosion Initiation Events in Irradiated Systems (15 minutes, joint with Reuben Holmes), ICG-EAC Meeting 2018, Knoxville, Tennessee, 15-20 April 2018.
- Investigating Corrosion Using High-Speed AFM (20 minutes), Electrochem 2017 incorporating the 58th Corrosion Science Symposium, University of Birmingham, 10-12 September 2017.
- Investigating Corrosion Using High-Speed AFM (20 minutes), The Joint EUROCORR 2017 and 20th ICC congress, Prague, 3-7 September 2017.
- The Importance of Proper Sample Preparation for High-Speed AFM Analysis (30 minutes), UKSAF Summer Meeting 2017, Teignmouth, 5 July 2017.

Posters

- Internal: Investigating Corrosion Using High-Speed AFM, University of Bristol Postgraduate Conference, 10 May 2017.

Table of Contents

List of Figures

Figure **Page**

List of Tables

CHAPTER 1

INTRODUCTION

Allow me to introduce the topic of this thesis
A destructive process that can crack metals into pieces
A key failure mechanism disrupting industry
Known to those who study it as S.C.C.

Stainless steels are important for structural applications and are widely used within many industries due to their good mechanical properties and tolerance of elevated temperatures [32–34]. However, they remain susceptible to corrosion under certain conditions, such as dilute salt solutions that are ubiquitous in many industrial applications [15, 33]. Corrosion can be affected by several different factors, both internal (e.g. microstructural properties such as grain size and orientation) and external (e.g. environmental conditions, temperature, solute concentration), and as such is considered a highly complex process [35].

Conjoint corrosion and stressing of a metal or alloy can result in the development of cracks which propagate through the material, causing failure due to the reduced fracture resistance [15, 36]. This phenomenon is known as stress corrosion cracking (SCC).

Forms of localised corrosion, such as SCC, can occur without any obvious outward signs of damage accumulation, whilst causing significant deterioration of component structural integrity [35, 36]. Furthermore, subtle changes in environment can lead to considerable differences in SCC behaviour, resulting in its occurrence being difficult to predict. As a result, SCC is often undetected, giving rise to sudden and unexpected failure. This has resulted in a significant number of failure events across numerous structural engineering applications in a range of industries including gas, oil, and nuclear [33, 35, 37–40]. Examples include the collapse of the Silver Bridge in December 1967 [33, 38, 41], or the explosion of the Trans Canada pipeline in

July 1995 [33, 37]. SCC is also responsible for the collapse of some suspended ceilings in indoor swimming pools, as a result of chloride-induced SCC of the high-alloy steel hangers [42].

In September 1969, a steam-turbine disc failed as a result of SCC at Hinkley Point A [33, 39]. Cracks formed by SCC in the semi-circular keyways in the disc bores [33, 39]. This, combined with temper embrittlement [43], resulted in failure by fast fracture [33]. This event caused considerable damage to both the turbine and the turbine hall; it also caused major concern for the many other turbines of the same design across the UK [33]. Indeed, the complicated and unpredictable nature of SCC renders the safe application of stainless steels and other engineering alloys in nuclear power systems a challenge [32, 44]. Further research is required into the mechanisms of corrosion such that the failure of components can be accurately predicted, and maintenance may be performed [35]. This is essential for the improvement of safety of nuclear power plants, as well as the minimisation of the economic impact through the prevention of power outages and the extension of operational lifetime [35, 45].

1.1 Advanced Gas-Cooled Reactors (AGRs)

The majority of the UK's fleet of nuclear power plants is comprised of advanced gas-cooled reactors (AGRs) [2, 46, 47]. These reactors are graphite moderated and use a CO_2 gas coolant [2, 46, 47]. The fuel consists of ceramic UO_2 encased in a stainless steel cladding, as shown in Figure 1.1 [2, 46, 47].

Following its lifetime in-reactor, AGR fuel is discharged and stored pending a decision on the disposition route. Presently, Sellafield store AGR fuel within a caustic dosed pond until future routes, such as geological disposal, may be carried out [2, 46–49]. During storage, the AGR cladding provides the primary containment for the radioactivity within the fuel [2, 46]. Localised corrosion of the fuel cladding does not occur whilst inside the reactor, as it is too hot and dry, however, during storage within aqueous environments intergranular attack (IGA) may occur if chromium depletion is severe enough [2, 30, 48, 50, 51]. Historically, failure has been known to occur within aqueous environments containing Cl^- ions at what would typically be considered as negligible concentrations, as low as around 0.2 mg L^{-1} [30].

As fuel is stored inside the fuel cladding, it is important to understand the localised corrosion behaviours of the cladding material. AGR fuel cladding is made of a niobium stabilised austenitic stainless steel, with 20 wt.% chromium and 25 wt.% nickel, referred to as 20Cr/25Ni-Nb [46–48, 50]. 20Cr/25Ni-Nb is chosen for this application as it is capable of enduring the reactor environment, with temperatures reaching 825°C in a CO_2 atmosphere [46]. This material is resistant to thermal sensitisation that can lead to IGA susceptibility as it is stabilised by niobium additions [2, 46, 50] (discussed further in the following chapter). However, high temperature irradiation can change stainless steel microstructure due to a combination of thermal effects and neutron damage [30, 50]. Of particular significance is a phenomenon known as radiation

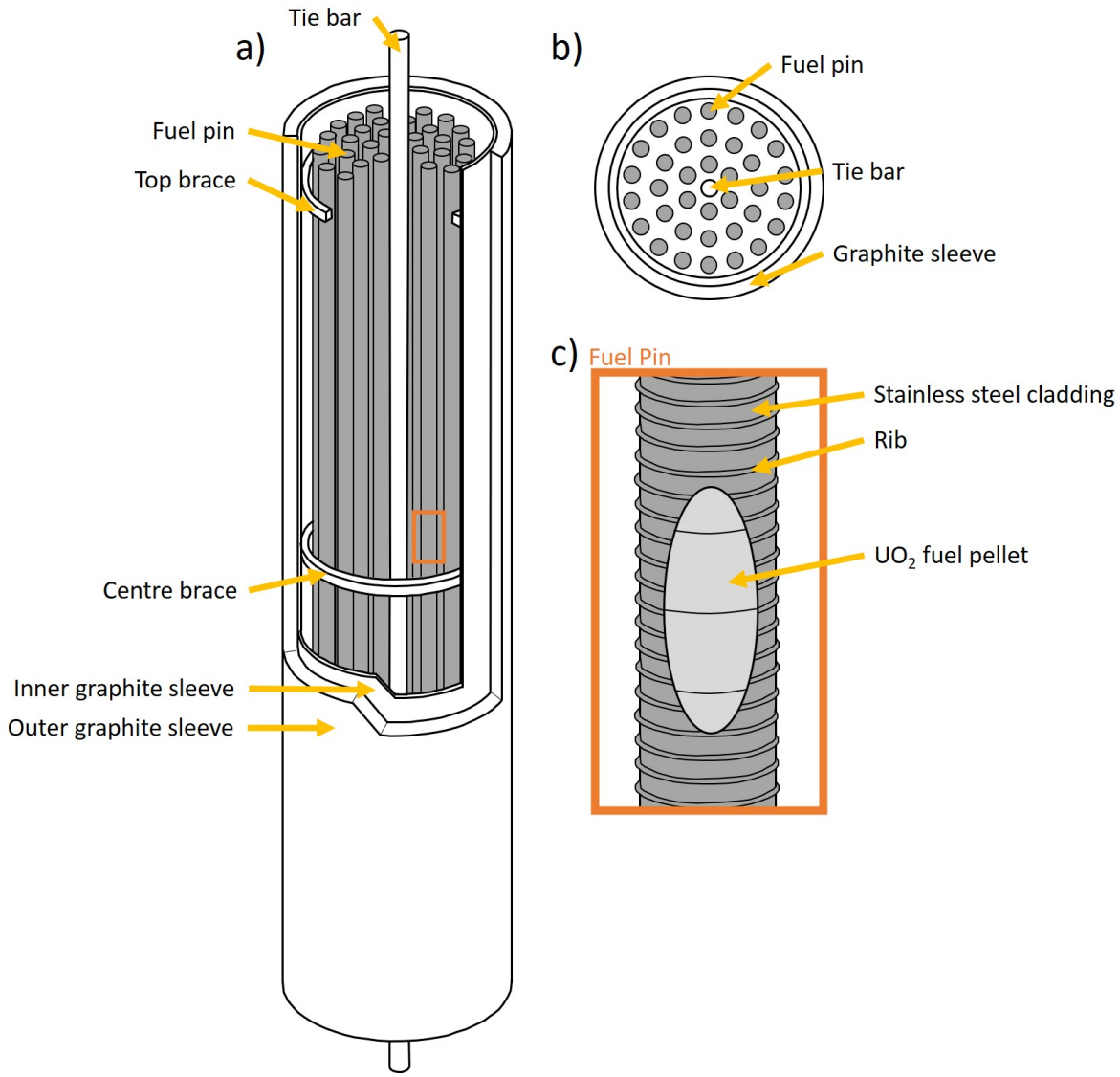

Figure 1.1: Schematic diagrams showing: a) an element from an AGR fuel stringer with view inside showing the fuel pin arrangement, b) a top view cross section of an element from an AGR fuel stringer, and b) a close up image of the region outlined in orange in Figure 1.1a showing a AGR fuel pin with view inside showing the fuel pellet. Adapted from [1] and [2].

induced segregation (RIS), as it results in an increased susceptibility to IGA [2, 30, 48, 50]. RIS is expected to affect the parts of AGR fuel stringers that operate between 350°C and 530°C, with a peak severity at around 420°C [30, 48, 50]. Thus rendering a sub-set of cladding susceptible to IGA [30, 48].

IGA observed within sensitised 20Cr/25Ni-Nb exhibits different morphologies, dependent upon the conditions under which it occurs [30]. In cases where there is a source of tensile stress, IGA can lead to intergranular stress corrosion cracking (IGSCC), which in turn can lead to a

greater depth of corrosion [30]. In severe cases, IGA and IGSCC can lead to failure of the cladding, which could result in significant activity release and fission gas release. As such, it is vital to understand the mechanisms occurring at the microscale and the microstructural characteristics of cladding, such that evaluations can be made into the safety of the system. Current focus of mechanistic work is to underpin the extrapolation of current knowledge and observation of fuel stored for around 25 years, up to anticipated future storage timescales.

1.2 High-Speed Atomic Force Microscopy (HS-AFM)

The unpredictable nature of SCC calls for considerable research in the mechanisms by which it occurs. Direct measurement of localised corrosion initiation and propagation at the nanoscale could give valuable insight into the processes that take place. Such measurements are important for the modelling and prevention of failure events.

Atomic force microscopes (AFMs) are capable of high-resolution topographic mapping of surface structures and the measurement of mechanical properties at nanometre scales within liquid environments, making it an ideal technique for the study of corrosion. The contact mode high-speed AFM (HS-AFM) is capable of capturing multiple frames per second making it orders of magnitude faster than conventional AFMs. This allows for direct observation of dynamic events in real-time. The enhanced capabilities of HS-AFM make it a viable tool for the imaging of nanoscale corrosion initiation, such as IGA and IGSCC, under conditions relevant to industrial applications. Furthermore, due to the high throughput of HS-AFM, large areas may be traversed allowing for surface statistics or large area, high resolution stitched images. These capabilities are explored within this thesis and applied to the study of SCC and the factors leading to SCC.

1.3 Thesis Aims

The main aims of this thesis are summarised as follows:

- To investigate the conditions that lead to localised corrosion and SCC initiation, considering contributions from factors such as material microstructure, corrosive environments and tensile stresses.
- To further understanding of SCC initiation and propagation mechanisms using HS-AFM as part of a novel suite of complementary techniques.
- To explore the capability and potential of HS-AFM for applications in materials and corrosion science.
- To establish new methodologies to optimise HS-AFM for the study of localised corrosion and SCC.

1.4 Thesis Outline

Chapter 2 includes an outline of the theory relevant to the study of SCC and an overview of key literature and previous experiments performed. The analytical techniques applied within this thesis are then described in Chapter 3. Chapter 4 then explores various methods of sample preparation in order to produce sample surfaces optimal for analysis by HS-AFM. This chapter also considers correlative methods such that the sample would not require any unnecessary re-preparation.

Chapters 5, 6, and part of Chapter 8 study sensitised microstructure, corrosive environments, and tensile stress separately to deconvolute their individual contributions to IGSCC. Though it must be noted that these factors are known to act synergistically, and behaviours will differ when isolated. To observe this synergistic behaviour, these three factors are brought together in Chapter 7 and the second part of Chapter 8 in order to initiate and study IGSCC. In addition to HS-AFM analysis, complementary measurements of crack tip chemistry are performed by atom probe tomography (APT) and energy dispersive X-ray spectroscopy (EDX), crystallography is evaluated with electron backscatter diffraction (EBSD), and sub-surface cracking is evaluated by focussed ion beam (FIB) and scanning electron microscopy (SEM). This combination allowed for a more complete characterisation of the IGSCC phenomenon, both in-situ and ex-situ.

The key outcomes of this work are summarised in Chapter 9 and conclusions are drawn from the work performed. This chapter also includes suggestions for relevant further work.

CHAPTER 2

SCC Theory and Techniques Used For The Study of SCC

When planning an experiment it is foolish to ignore
The many years of research that has been performed before
For it is necessary to stand on the shoulders of giants
If we are to push forward the frontiers of science

This chapter provides an outline of the theory applied within this thesis. This includes an overview of the three conditions that synergistically interact to give rise to stress corrosion cracking (SCC): material, stress, and corrosive environment. Also given is a summary of key literature for the specific conditions explored within this thesis: sensitised austenitic stainless steel, the microstructural effects of applied tensile stress, and the effects of thiosulfate or chloride containing solutions. Some of the current techniques used to study SCC are also reviewed, demonstrating how the work performed in this thesis builds upon current and previous research.

2.1 Stainless Steel

Steel is an alloy consisting primarily of iron with up to 2.1 wt.% carbon [52]. Steels can be alloyed with other elements to manipulate and improve various mechanical and chemical properties of the material, such as: strength, hardness, and corrosion resistance [53]. Steels containing more than 12 wt.% chromium are referred to as stainless steels [49, 53]. The chromium in stainless steels forms a passive chromium oxide (Cr_2O_3) film < 5 nm thick on the surface [53–56]. This film is chemically stable, resistant to corrosion in various chemical environments and rapidly regenerated if damaged [49, 52–55]. The corrosion-resistant properties of stainless steels have

resulted in a huge variety of applications. They are widely used for construction in the nuclear, chemical, and petroleum industries [32–34, 57].

2.1.1 Crystals

Stainless steels have crystallographic structures, where a crystal is defined as a repeating arrangement of atoms. This arrangement is known as a unit cell. There are 14 unique unit cells in 3D space referred to as Bravais Lattices. Each unit cell can be described by the relative lengths of the edges and the angle between them. The unit cells most commonly referred to within this thesis are body-centred cubic (BCC) and face-centred cubic (FCC), shown in Figure 2.1. Cubic unit cells have edges of equal length and edge angles of 90°.

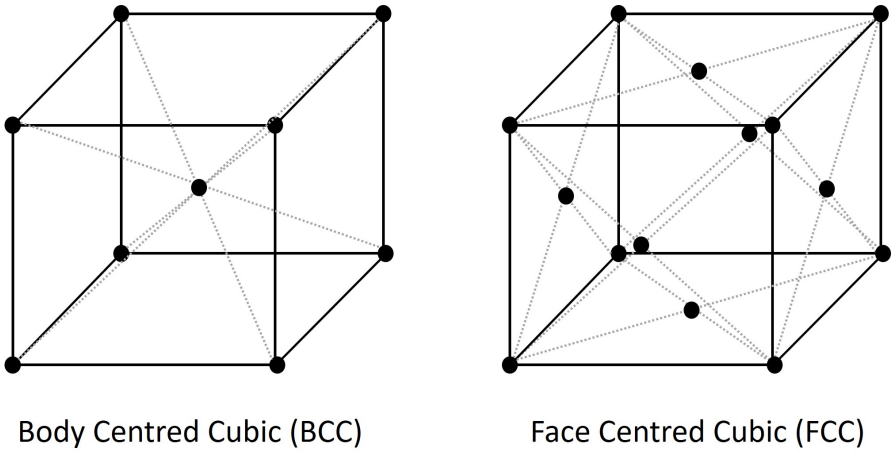

Figure 2.1: Schematics showing: a) a body centred cubic (BCC) unit cell, and b) a face centred cubic (FCC) unit cell.

Iron, the base metal in stainless steels, has a BCC crystal structure, but is allotropic, meaning that it can have different crystallographic structures. This is determined by the alloying elements and processing history.

Within unit cells each plane can be described by a set of co-ordinates known as Miller indices [14]. The Miller indices, (h,k,l), for any plane are equal to the reciprocals of the intercepts the plane makes with the three axes (x, y, and z) [14]. The six faces that make up a cube in a BCC or FCC structure are defined as (100), (010), and (001) (where each plane describes the two faces in that plane, i.e front/back, left/right, top/bottom) [14]. The planes can be referred to collectively as {100} planes, this is a consequence of the symmetry of the lattice structure. Miller indices can also be used to define crystal directions [14]. When describing a direction, the Miller indices, [h,k,l], are equal to the components of a vector that points in that direction, (a,b,c) for example [14]. Considering the direction along the diagonal of a BCC or FCC structure, this can be described by [111] [14]. The family of directions of this type (i.e. along the other diagonals of the cubic structure) are $< 111 >$.

2.1.1.1 Grains and Grain Boundaries (GBs)

If a material consists of one continuous crystal structure it is referred to as a single crystal. Polycrystalline materials however are made up of multiple smaller crystals known as grains. Each grain itself is a single crystal, and adjacent grains have differing crystal orientations [58]. Where two grains meet is termed a grain boundary (GB) [58].

The misorientation between two adjacent grains is defined as the transformation required to rotate the crystal axes of one grain such that they coincide with the other grain, as demonstrated in Figure 2.2a [59]. The simplest description of GB structure is GB misorientation angle, also referred to as disorientation [60–62]. Using this description different GB may be grouped into different GB types that describe how certain GBs behave.

2.1.1.2 GB Types

Different types of GBs can vary significantly in their properties and behaviours, with different GB misorientations leading to a different GB energy, chemistry, and mobility [29]. The different GBs present within a material at the microscale can alter the mechanical and chemical properties on the macroscale.

The possible GB misorientations present within cubic lattices range between 0° and 62.8° [59, 63]. GBs can be categorised within this range as low-angle GBs (LAGBs), if their misorientation is <15°, or high-angle GBs (HAGBs), if their misorientation is between 15° and 62.8° [58, 60, 64–66]. In some cases, referred to as small-angle and large-angle GBs [58]. HAGBs are generally observed to have higher GB energy [66].

In addition to HAGBs and LAGBs, some GBs are termed 'special' GBs due to their unique properties [58]. Such properties include reduced susceptibility to GB segregation, precipitation, localised corrosion, low interfacial energy, and low mobility [64, 66, 67]. The first model developed to describe 'special' GBs was the coincident-site lattice (CSL) model, proposed by Kronberg and Wilson in 1949 [58]. This model uses the assumption that, when the coincidence of two grains is high, the resultant GB energy is low as less bonds are broken across the GB [58]. Specific GB misorientations result in coincident atomic sites either side of the boundary, referred to as coincidence sites [58, 60, 64]. These sites create a lattice known as a CSL [58]. These GBs are known as CSL GBs [64]. LAGBs are considered to be CSL $\Sigma 1$ GBs, because the reciprocal density of common lattice points in the two grains either side of the boundary, Σ, is 1 [60, 64, 65].

The simplest CSL GB is the twin boundary, also known as CSL $\Sigma 3$ GBs [29, 64, 67]. Twin GBs can be coherent or incoherent. Both types of GB have GB misorientation angles of 60°, however coherent twin GBs have a 60° GB misorientation about a $< 111 >$ crystal axis. Within FCC materials, when two {111} planes meet there are two orientations that produce atom matching, one results in a continuous crystal, the other results in a coherent twin GB, as demonstrated in Figure 2.2b. Coherent twin GBs have exceptionally low energy compared to other GBs as a result of the good atomic fit between the two grains [29]. The twinned region separates two regions

of the lattice from one another with varying morphologies depending on sample sectioning as shown in Figure 2.3.

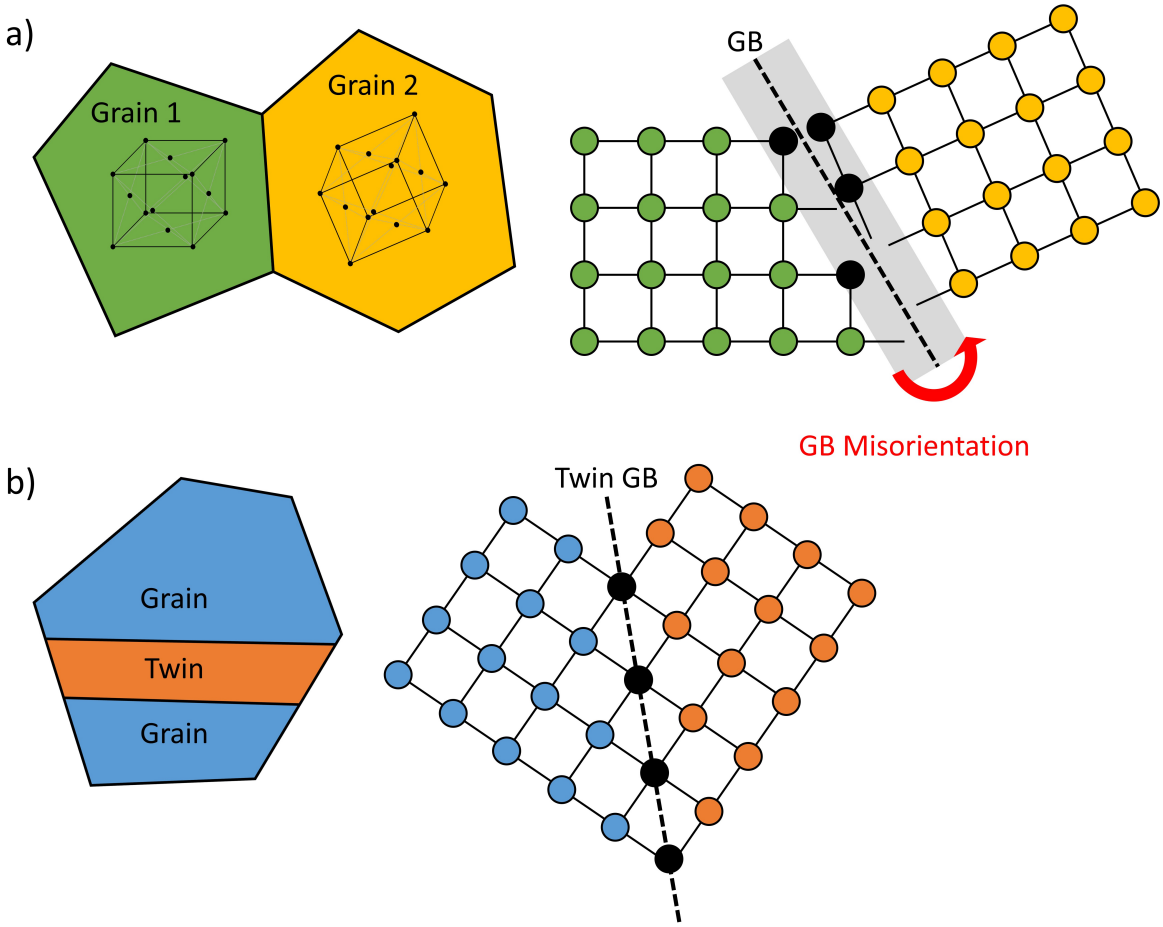

Figure 2.2: Schematic diagrams and ball and stick diagrams showing: a) two randomly orientated grains separated by a GB, and b) a grain with a twin separated by twin GBs. Adapted from [3].

An upper limit for Σ values is often stated as between 29 and 49, where higher values are considered random (i.e. non-special) HAGBs [60]. However, CSL GBs with Σ value greater than 3 are not considered within this thesis. Indeed, some studies have reported higher order CSL GBs to have special properties [68–70], though many works consider the CSL Σ1 and CSL Σ3 GBs to be the only boundaries with special properties [60, 71, 72]. The exclusion of higher order CSL GBs is considered within later analysis.

2.1.2 Phases

Steels can have a number of different crystal structures, known as phases, that can significantly affect their mechanical and chemical properties. Crystallographic materials generally have the crystal structure that is energetically favourable [52]. However, the crystal structure favourable

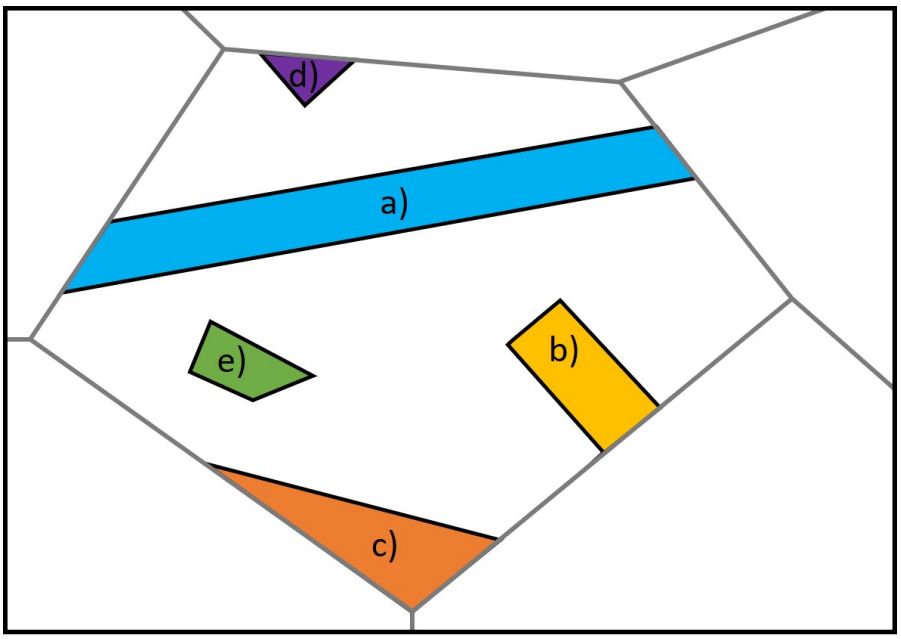

Figure 2.3: A schematic diagram showing the different types of twin morphology: a) complete twin shown in blue, b) incomplete in yellow, c) lamellar in orange, d) corner in purple, and e) tetrahedron in green, adapted from [4].

at one temperature may not be the same as for another temperature. Pure iron has a BCC crystal structure, known as α-Fe or ferrite, at room temperature up to 912°C, at which point it is energetically favourable to transform to an FCC structure known as γ-Fe, or austenite [52, 73]. At even higher temperatures, iron transforms back into a BCC structure, referred to as δ-Fe [52, 73].

When the microstructure of a metal changes it is known as a phase transformation. Phase transformations initiate with the nucleation of the new phase, at this stage the new phase forms as small stable nuclei, these are often formed at defects such as GBs [74]. Once nucleated, the new phase will grow, dominating over the previous phase [74, 75]. Transformations between phases is dependent upon a number of factors: time, temperature, % transformation [74, 75].

The crystal structure of steel stable at room temperature can be manipulated by the addition of different alloying elements. Schaeffler categorised alloying elements as either ferrite stabilisers or austenite stabilisers [74]. If an alloying element promotes a BCC structure, such as chromium, it is referred to as a ferrite stabiliser. On the other hand, if it promotes an FCC structure, such as nickel, it is referred to as an austenite stabiliser. The effects of various alloying elements can therefore be converted into Cr or Ni equivalents, the equations for which vary [76] but typically are of the form [5]:

$$\text{Cr equivalent} = 1.5(\%\text{Si}) + \%\text{Cr} + 0.5(\%\text{Nb}) + (\%\text{Mo}) \tag{2.1}$$

$$\text{Ni equivalent} = 30(\%\text{C} + \%\text{N}) + \%\text{Ni} + 0.5(\%\text{Mn}) \tag{2.2}$$

Using this notation, a Schaeffler-Delong diagram may be constructed to visualise the various phases of stainless steel, as shown in Figure 2.4, where austenite and ferrite have already been defined, and martensite has a body-centred tetragonal (BCT) structure. Each region gives an indication of the microstructure as a result of composition. However, this diagram does not consider additional factors that can affect microstructure such as heat treatments [74].

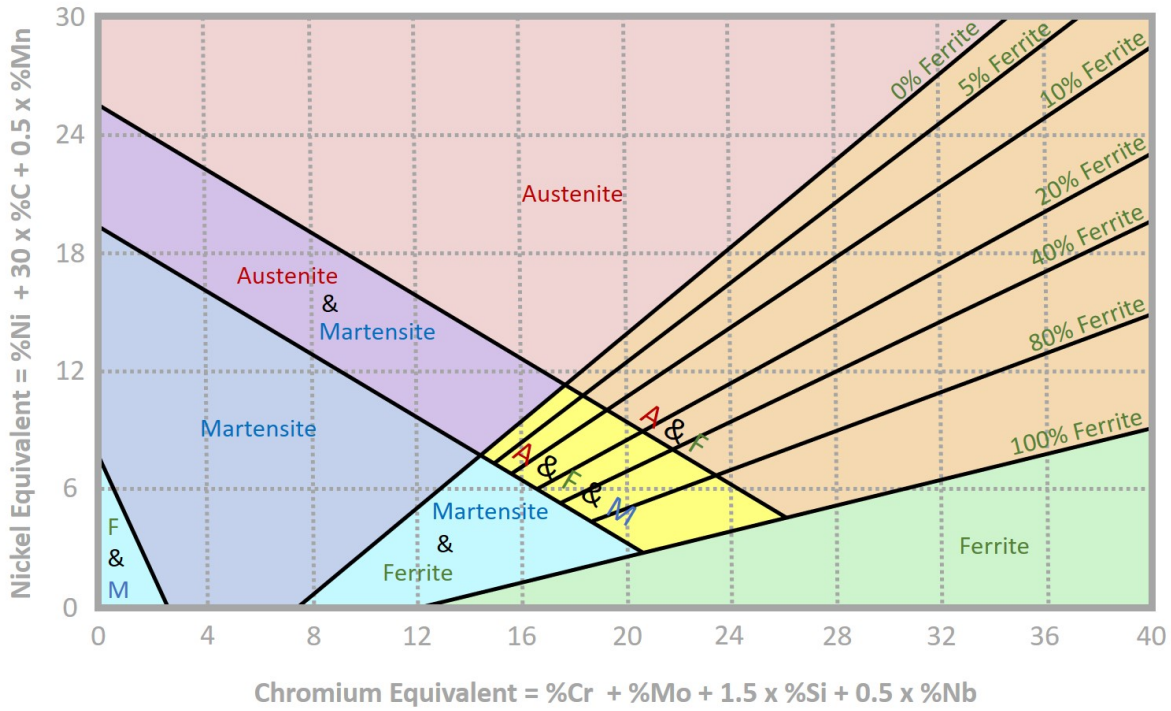

Figure 2.4: A Schaeffler-Delong diagram showing the different phases in steels at varying nickel and chromium equivalences adapted from Schaeffler's final weld composition diagram [5].

2.1.2.1 Classifications of Stainless Steel

There are five main classifications of stainless steel: ferritic, austenitic, duplex (dual phase austenitic-ferritic), martensitic and precipitation hardened [77]. Classifications are primarily determined by the predominant phase of the stainless steel, which is influenced by composition and thermal history. Each classification has differing physical, chemical, and mechanical properties. For example, ferritic stainless steels are ferromagnetic at room temperature, whereas austenitic stainless steels are not [53].

The work presented in this thesis focusses primarily on austenitic stainless steels. Austenitic stainless steels have a primary austenite phase, with small amounts of residual ferrite (typically around 0.1%) dependent on casting conditions and composition (Figure 2.4). The transformation back to ferrite upon cooling is suppressed by the addition of austenite stabilisers, as discussed

previously. Austenitic stainless steels have good corrosion resistance, and excellent mechanical properties, such as formability and toughness over a wide range of temperatures, resulting in their use across a wide range of applications [76]. This type of steel comprises more than two thirds of the worlds stainless steel production [74, 76]. There are two austenitic grades that are the primary focus of this thesis: 20Cr/25Ni-Nb and American Iron and Steel Institute (AISI) Type 304.

20Cr/25Ni-Nb is a niobium-stabilised austenitic stainless steel, with 20 wt.% chromium and 25 wt.% nickel, a typical composition is given in Table 2.1. 20Cr/25Ni-Nb is used as fuel cladding within advanced gas-cooled reactors (AGRs) [50]. Niobium is added to 20Cr/25Ni-Nb as it is a strong carbide former and, following a prior stabilisation heat treatment, results in the formation of NbC precipitates within the matrix [50]. The formation of NbC removes carbon from the metal matrix, impeding the formation of chromium-rich carbides that may result in chromium depletion at GBs and susceptibility to localised corrosion [50]. Despite this, prolonged exposure to high temperatures and neutron fluxes can still result in chromium depletion along GBs as a result of microstructural changes, as discussed further in Section 2.1.5 [29, 50]. The formation of chromium-rich carbides can also occur as a result of carbon pick-up from the reactor coolant [30].

Table 2.1: Example elemental composition of 20Cr/25Ni-Nb, given in weight %, from [30].

C	Si	Mn	P	S	Cr	Nb	Mo	Ni	Fe
0.062	0.58	0.79	0.014	0.019	19.33	0.56	-	24.05	Bal.

AISI Type 304 stainless steel is one of the AISI Type 300 series of austenitic stainless steels. AISI Type 304 stainless steel contains approximately 18-20 wt.% chromium and 8-10.5 wt.% nickel, an approximate composition from AISI is given in Table 2.2. This type of stainless steel is used extensively for a wide range of applications. Common uses include various structural engineering applications and components in nuclear power plants including the primary and secondary (with and without radiation, respectively) sides of boiling water reactors (BWRs) and pressure water reactors (PWRs) [76, 78, 79]. However, as with 20Cr/25Ni-Nb, under certain conditions this material can become susceptible to localised corrosion processes (Section 2.1.5). As a result of this, the application of Type 304 stainless steel has been reduced in newer nuclear plants, though Type 304 remains extensively used in legacy plants [79, 80].

Table 2.2: Elemental composition of AISI Type 304 stainless steel, given in weight %, from [31].

C	Si	Mn	P	S	Cr	Nb	Mo	Ni	Fe
≤0.008	≤1.00	≤2	≤0.045	≤0.03	18-20	-	-	8-10.5	Bal. (66.345-74)

2.1.2.2 Alloying Elements

Key roles of alloying elements most commonly used in stainless steels and most relevant to this thesis are outlined in the following sections.

Carbon Carbon increases solid solution strength in non-stabilised steels [76, 77]. In stabilised steels (i.e. containing niobium, titanium, or vanadium) carbon principally increases strength by precipitation hardening [76]. However, ductility is reduced, and corrosion resistance may be reduced by the formation of chromium-rich carbide precipitates resulting in local chromium depletion [52, 77]. It also acts as an austenite stabiliser [76, 77].

Nitrogen Nitrogen increases the mechanical strength, as well as the resistance to pitting corrosion [76, 77]. It is typically added as an alternative to carbon, with the effect of increasing yield strength without increasing propensity for chromium-rich carbide formation [76, 77]. Nitrogen is also an austenite stabiliser [76].

Silicon Silicon acts as a deoxidiser [77]. The presence of silicon improves the steel's oxidation properties at high temperatures [77]. It also somewhat enhances hardness [77].

Phosphorus and Sulfur Phosphorous or sulfur may be added to steel to increase strength and improve machineability. However, both alloying elements have negative effects of corrosion behaviour. GB segregation of these elements results in increased susceptibility to intergranular corrosion and cracking [81].

Chromium The addition of chromium enhances corrosion and oxidation resistance of steel by forming a surface film of passive oxide [52, 77]. However, it has a high affinity for carbon and is a strong carbide former as a result. This leads to chromium depletion local to these precipitates. Chromium also acts as a ferrite stabiliser.

Manganese Manganese is an austenite stabiliser, and as such can act as a substitute for nickel [76]. It also combines preferentially with sulfur to form MnS [77]. Manganese improves hardenability properties [77]. It also enhances nitrogen solubility which, in turn, strengthens the steel [52, 76].

Nickel Nickel is the principal element added as an austenite stabiliser [52]. It increases high temperature strength, ductility, and toughness [52, 77]. It also improves corrosion resistance [52, 76, 77, 82]. However, it decreases carbon solubility, leading to increased carbide formation [74].

Niobium, Titanium, and Vanadium The presence of stabilising elements such as niobium, titanium or vanadium can improve corrosion resistance by preferentially forming carbide precipitates, thus reducing the formation of chromium-rich carbides [50, 74, 76]. Through precipitation hardening they can also improve strength of the steel.

2.1.3 Secondary Phase Precipitates (SPPs)

When stainless steels are exposed to high temperatures, phase changes can occur, as described previously. These phase changes do not occur instantaneously, and prior to an equilibrium state being achieved, metastable phases can form before evolving or going back into solution [52, 74]. Precipitation is a type of phase change that occurs as a result of temperature change and local chemistry. The crystal structure, or phase, of these precipitates often differs from the phase of the bulk metal, so these are often termed secondary phase precipitates (SPPs). SPPs that commonly appear within austenitic stainless steels as a result of casting or ageing are shown in Figure 2.5 [74].

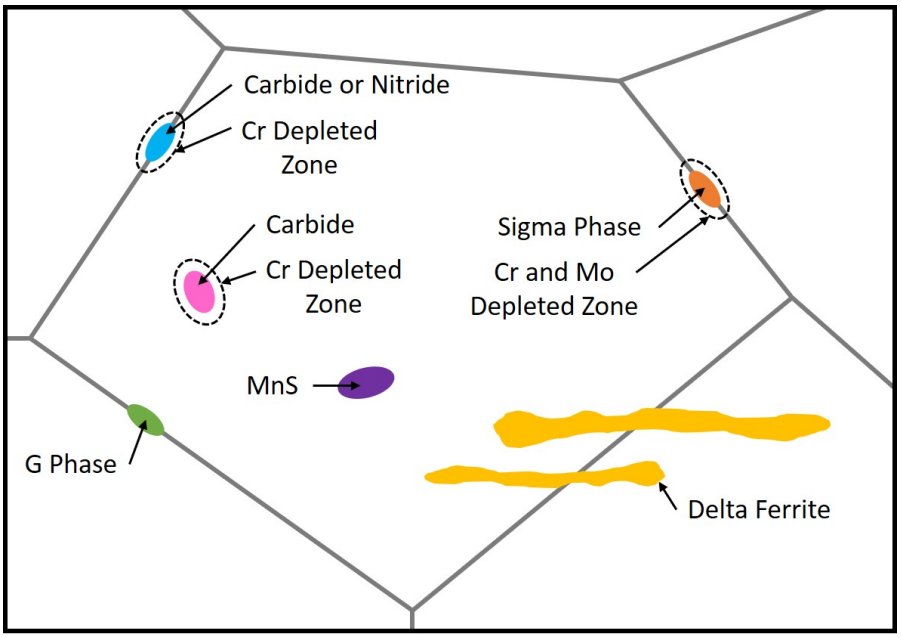

Figure 2.5: A schematic showing some of the common features and SPPs present within austenitic stainless steels, adapted from [6] and [7].

The SPPs that can form are dependent on the composition of the stainless steel, as well as the temperature of the steel and the duration at that temperature. Figure 2.6 shows a time-temperature-precipitation (TTP) diagram for austenitic stainless steels. TTP diagrams act as useful guides to the precipitation expected following heating to a certain temperature for a known time.

There are a large number of SPP types that can occur in stainless steels. These are typically

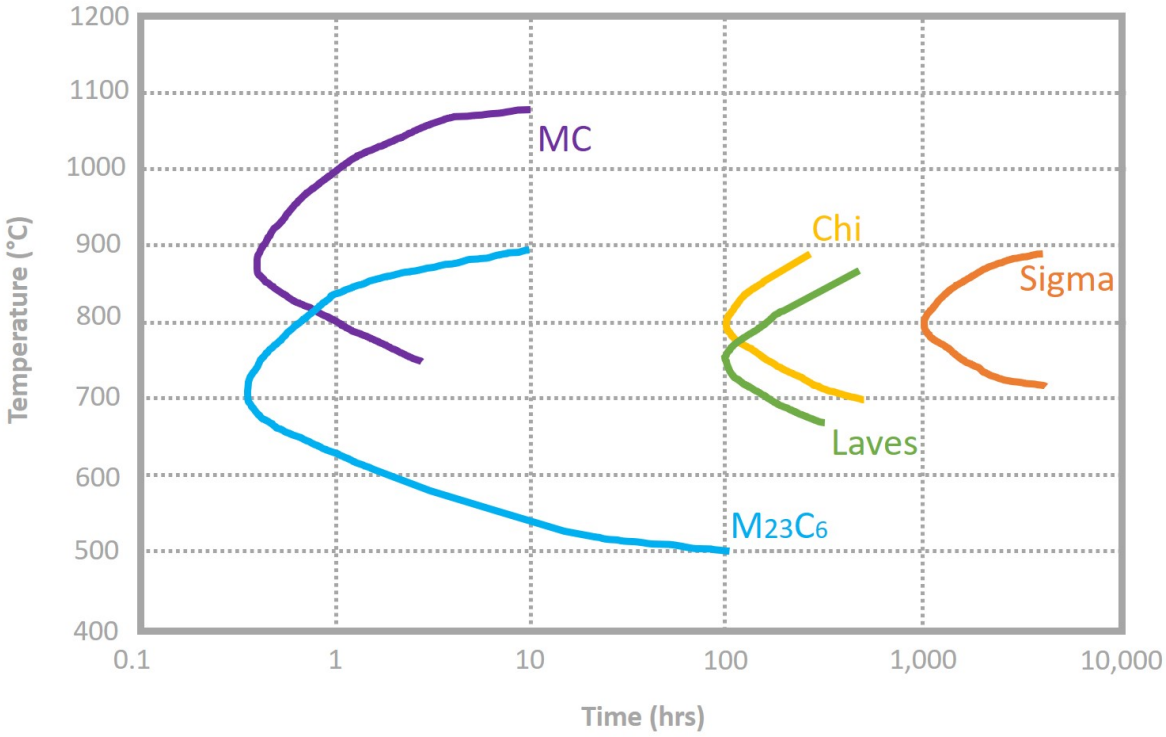

Figure 2.6: A TTP diagram for austenitic stainless steel showing: $M_{23}C_6$ carbide in blue, MC carbide in purple, laves in green, chi in yellow, and sigma phase in orange, adapted from [8].

undesirable as they often adversely affect corrosion or mechanical properties. Some of the important SPPs relevant within this thesis are described in greater detail in the following sections.

2.1.3.1 Carbides

Carbide precipitation in austenitic stainless steels occurs as a result of reduced solubility of carbon at lower temperatures [74, 81]. Carbon solubility is also decreased by their high nickel content [74].

Metal carbides can be present within stainless steels in many different compositions and forms. Typical compositions include MC, M_3C, M_6C, M_7C_3, and $M_{23}C_6$, where M denotes an alloying metal [74].

$M_{23}C_6$ The most common carbide composition in austenitic stainless steels is $M_{23}C_6$ [74]. This type of carbide has a complex FCC type crystal structure known as $Fm\bar{3}m$ and forms primarily at GBs, with a strong dependency on GB type [74, 81]. Intragranular precipitation can also occur, this can be accelerated by cold work [74]. $M_{23}C_6$ can form rapidly at temperatures of 650°C

to 750°C, as illustrated in Figure 2.6 [74]. These SPPs are often the first to form in austenitic stainless steels [74]. Formation is strongly dependent on carbon content [74].

Metal carbides chiefly contain chromium as a result of its high affinity for carbon [76, 83]. As such, the formation and growth of insoluble carbides results in chromium depletion in the regions adjacent to the GB leading to localised corrosion susceptibility [33, 41, 57, 70, 74, 83, 84]. Carbide precipitation can also negatively impact the ductility and toughness of the steel [74]. Within this thesis the term carbide precipitate refers to $M_{23}C_6$ carbides.

MC To delay the formation of deleterious chromium-rich carbide precipitates stabilising elements may be added to the steel, such as titanium, vanadium, or niobium in 20Cr/25Ni-Nb stainless steel [74, 76]. These elements decrease carbon solubility, resulting the precipitation of MC carbides where M is titanium, vanadium, or niobium [74]. These carbides have an $Fm\bar{3}m$ crystal structure and primarily form within the grain, though intergranular formation can occur [74].

2.1.3.2 Sigma Phase

Sigma phase is an intermetallic phase with a tetragonal crystal structure [85, 86]. It has a variable composition though typically contains approximately 50 wt.% chromium and 50 wt.% iron, nickel, or molybdenum [86]. Sigma phase primarily forms on GBs [74]. In particular, it forms at high energy interfaces such as HAGBs, GB triple points (where three GBs meet), intragranular SPPs, or ferritic regions [74, 81, 86, 87]. Typically, sigma phase is only present once the metal has been aged thousands of hours at high temperatures, as shown in Figure 2.6 [74, 81]. Sigma phase is known to form within 20Cr/25Ni-Nb stainless steel following an extended period at elevated temperatures. In this material, sigma phase is typically composed of approximately equal parts iron and chromium [86].

As with chromium-rich carbide precipitates, the formation of sigma phase can result in chromium depletion in the regions adjacent, resulting loss of corrosion protection [74, 86, 87]. Sigma phase is also associated with loss of ductility and toughness [74, 86, 87].

2.1.3.3 G Phase

G phase is an intermetallic silicide with an FCC crystal structure, typically composed of (Ni, Fe, Cr)$_{16}$(Nb, Ti)$_6$Si$_{6 or 7}$ [74, 85]. G phase is typically observed following ageing under irradiation; however, it can form due to thermal ageing [74, 85, 88].

G phase has been reported to form in 20Cr/25Ni-Nb stainless steel [88]. Primarily, G phase forms along GBs but it can also form within the grains at longer ageing times [74, 88]. Previous studies have found that G phase forms from NbC precipitates [88].

The presence of G phase can result in a destabilisation of austenite due to the uptake of Ni [88]. This is not expected to have a significant effect on the corrosion properties [88]. Though

some works report that, following formation from NbC, a local enrichment of carbon and nitrogen can result in the formation of $M_{23}C_6$ carbides [88]. Additionally, due to the destabilisation of the austenite, G phase is associated with sigma phase formation from ferrite [88]. Both sigma phase and $M_{23}C_6$ are known to adversely affect corrosion behaviour [33, 41, 57, 70, 74, 83, 84, 86, 87].

2.1.3.4 Manganese Sulfide (MnS)

Manganese sulfide (MnS) precipitates form during casting [85]. These precipitates are known to adversely affect pitting corrosion resistance [56, 89].

2.1.4 Effects of Irradiation

Neutron irradiation can induce changes in a materials microstructure, as demonstrated in Figure 2.7. This occurs as neutrons displace atoms from their position in the crystal lattice. If these atoms have sufficient kinetic energy, they will go on to displace further atoms leading to a cascade. Each displaced atom results in a vacancy and self-interstitial atom pair [90–92]. Many of these pairs annihilate by recombination, some rearrange into stable configurations including dislocation loops, cavities, or voids [90, 92]. Alternatively, they may migrate towards sinks such as GBs, SPPs, or dislocations [79, 90, 92, 93]. These changes can have significant effects on local corrosion and mechanical properties of the material [90]. Neutrons are uncharged particles, and so can penetrate large distances into materials causing significant structural damage. Irradiation damage is typically measured in displacements per atom (dpa) [79, 90]. Degradation mechanisms and effects include [79, 91–93]:

- Radiation induced segregation (RIS)
- Radiation induced, or enhanced, precipitation
- Radiation hardening
- Helium and hydrogen embrittlement
- Void swelling
- Radiation enhanced creep
- Irradiation-assisted stress corrosion cracking (IASCC)

The severity of these effects varies with irradiation conditions (dose, temperature, etc.) and material composition and thermomechanical history [90]. The key irradiation damage phenomena pertinent to this thesis are discussed in greater detail in the following sections.

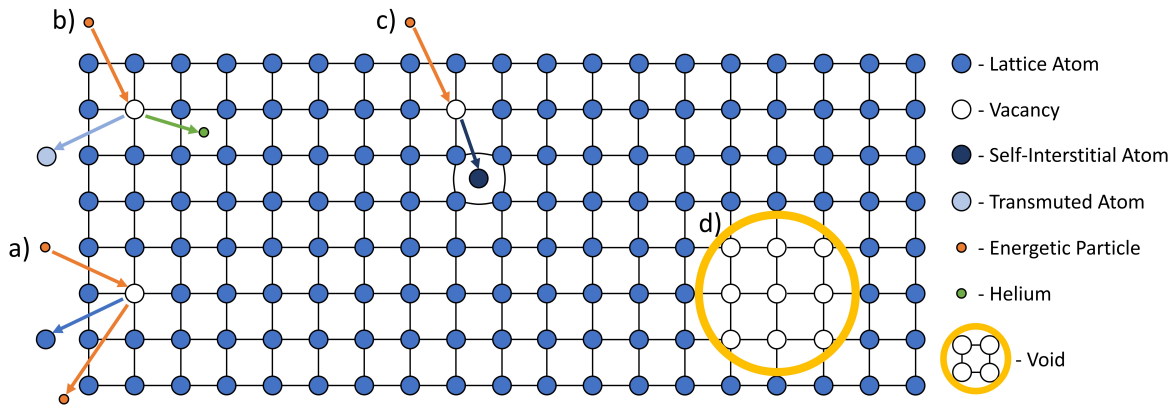

Figure 2.7: A schematic showing some of the defects caused by irradiation: a) an energetic particle (such as a neutron) collides with a lattice atom resulting in its ejection, b) an energetic particle collides with a lattice atom in a transmutation reaction resulting in a transmuted atom, a vacancy, and helium, c) an energetic particle collides with a lattice atom resulting in its displacement forming a vacancy and a self-interstitial, and d) a cluster of vacancies forming a void. Adapted from [9] and [10].

2.1.4.1 Radiation Induced Segregation (RIS)

RIS refers to the segregation of elements at GBs and other sinks. It is caused by the flux of radiation induced point defects (i.e. vacancies and interstitials) to sinks (i.e. GBs), where they exchange positions with other atoms [29, 30, 49, 50, 90, 91]. This is known as the inverse Kirkendall effect [49, 50]. This occurs in combination with different rates of migration for different elements, and solid-state diffusion effects [29, 30, 50, 92]. Species with high diffusion rates become depleted at GBs, whereas species with low diffusion rates become enriched. RIS therefore results in a depletion in chromium, iron, and (to a lesser extent) molybdenum at the GB, and an enrichment in nickel, silicon and phosphorus [30, 50, 51, 90–92, 94, 95]. Minor elements such as boron, carbon, nitrogen, and sulfur can also become enriched [90–92]. If chromium depletion is severe it can lead to increased susceptibility to localised corrosion processes.

RIS typically occurs between 350°C and 530°C, with a peak effect at approximately 420°C [30, 50]. As a result, only a small subset of AGR fuel elements are expected to have an increased susceptibility to localised corrosion [2, 30, 48, 50]. This temperature dependence is due to its effect on rate of diffusion and the equilibrium concentration of point defects [30]. At lower temperatures mobility is reduced, at higher temperatures recombination dominates [90, 91]. At higher temperatures RIS effects are also diminished by chemical back-diffusion, where high diffusivity can no longer support the inverse Kirkendall gradient [90, 91]. A dependency on dose rate is also observed [90, 92].

A characteristic feature of GBs affected by RIS is that the resultant segregation profile is narrow, usually between 5 and 10 nm of the GB for irradiation at round 300°C [91, 92]. Broader, less severe profiles are observed at higher temperatures [92].

2.1.4.2 Radiation Induced/Enhanced Precipitation

Irradiation can induce, or enhance, the precipitation of secondary phases through the migration of alloying elements [50, 79, 85]. These precipitates are described as either: radiation induced, radiation enhanced (or retarded), or radiation modified. As described previously, G phase is typically described as radiation induced, though it can appear following thermal ageing [74, 85, 85, 88, 90]. MC carbides and sigma phase are both radiation enhanced precipitates [85]. Meaning that they can form under irradiation at lower temperatures than without irradiation.

This phenomenon typically occurs at temperatures > 350°C, though some studies have reported radiation induced SPPs forming at temperatures as low as 300°C [79, 90].

2.1.4.3 Radiation Hardening

Point defect clusters (such as dislocation loops or helium bubbles) and SPPs can act as obstacles to dislocation motion [79, 90, 91, 96]. This results in an increase in the material's yield strength (hardening) and a reduction in ductility and fracture toughness [79, 90, 91, 96]. A dose of 4 dpa can increase yield strength up to six times compared to unirradiated material [79, 91].

2.1.4.4 Void Swelling

Voids form at high temperatures (> 300°C) and doses [90]. Void swelling occurs as a result of the nucleation and growth of irradiation induced vacancies [79]. This can lead to a volume increase and result in internal stresses [79]. Void swelling is predicted to peak at around (580°C and decreases in severity at higher temperatures [97].

In this thesis, the term void is used as a general term referring to plastic voids, helium bubbles, or cavities.

2.1.4.5 Helium Embrittlement

Helium is produced from transmutation reactions in which a nucleus transforms from one element to another following an interaction with a neutron [79, 92, 98]. Helium is insoluble in steels, as a result it precipitates in traps, or agglomerates to form helium bubbles [92]. These helium bubbles can result in loss of ductility (embrittlement), they can also diffuse to GBs causing GB weakening [79, 92].

2.1.5 Sensitisation

When a GB becomes sufficiently depleted in chromium (down to approximately 12 wt.%), the protective passive film can no longer form [78, 95, 99]. This is referred to as sensitisation and can result in the GBs local resistance to corrosion being severely reduced [41, 57, 70, 83, 95, 100]. Irradiated stainless steels can become sensitised as a result of neutron damage, in particular

RIS [51, 100]. GBs in stainless steels can also become sensitised after heat treatments, such as post-weld stress relief, or in elevated temperature applications [41, 69, 70, 83, 100].

In this thesis sensitisation is used to refer to GB sensitisation and therefore susceptibility to intergranular localised corrosion.

2.1.5.1 Thermal Sensitisation

Thermal sensitisation occurs as a result of chromium-rich carbide precipitation (typically $M_{23}C_6$) along GBs [41, 51, 57, 70, 74, 78, 101]. This precipitation results in chromium depletion in the regions adjacent to the GB. Chromium depletion occurs as chromium diffusion is much slower than carbon [83, 101]. The region of chromium depletion at the GB forms a depletion profile with characteristic width and minimum chromium concentration [101]. This depletion zone can extend some distance from the GB. The depletion width increases with time following the nucleation of chromium-rich carbides [81]. Minimum chromium concentration also increases as depletion width increases due to desensitisation following chromium diffusion [81].

Thermal sensitisation typically occurs between 500°C to 900°C [78]. This temperature is dependent upon the ageing time and the composition of the alloy, in particular, carbon content [102]. Figure 2.8 shows a time-temperature curve for sensitisation with varying carbon concentrations. This gives an indication of the durations required at various temperatures to result in sensitisation. The extent of sensitisation can also vary by several percent between different GB types and depends upon the distance to the nearest carbide [81, 103, 104].

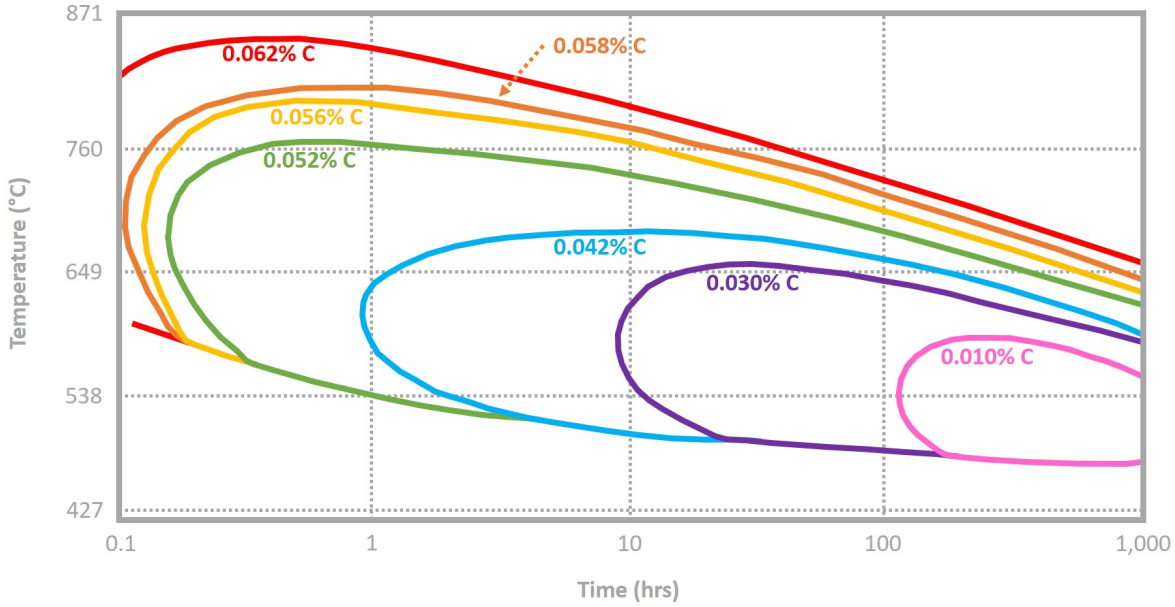

Figure 2.8: A time-temperature curve for sensitisation of 18-8 (i.e. 18 wt.% chromium and 8 wt.% nickel) stainless steels with varying concentrations of carbon, adapted from [11].

Thermal sensitisation is responsible for the reduction in corrosion resistance seen within stainless steels exposed to elevated temperatures such as that encountered within high temperature applications or the heat affected zone associated with welds [78, 82]. The effects of thermal sensitisation may be minimised by reducing the amount of carbon available in solution, such that there is insufficient carbon to result in severe precipitation [84]. This may be achieved by the addition of stabilising elements, such as niobium in the case of 20Cr/25Ni-Nb [51, 84].

2.1.5.2 The Effect of GB Type on Sensitisation

Previous works have considered the variation of the severity of sensitisation by RIS or thermal treatments to be partly due to the geometry of the GB, that is, the dimensions of the GB and the GB misorientation [29, 50, 64, 67, 81, 102, 103, 105, 106].

Variation of thermal sensitisation with GB type is due to the differing morphologies, densities, and distributions of GB carbide precipitates associated with different GB types [74, 81, 102, 107, 108]. This is the result of different ageing times leading to carbide formation (and so, thermal sensitisation). Precipitation occurs first at random GBs, then incoherent twin GBs, then coherent twin GBs, as demonstrated in Figure 2.9 [74, 81, 102, 103]. This variation is often ascribed to variations in GB energies [67, 81, 102, 103, 105]. High energy GBs exhibit early carbide nucleation [67, 81, 107]. This can lead to semi-continuous precipitation along HAGBs before nucleation occurs at lower energy twin GBs, causing heterogeneous sensitisation [67, 81]. Some studies have reported that coherent twin GBs are immune to carbide precipitation as a result of their highly regular atomic structure [67, 102, 108].

In 1991 Laws *et al.* analysed 50 GBs in AISI Type 316 stainless steel with varying misorientation values to determine the relationship between GB structure and chromium depletion [107]. Laws found that the severity of GB chromium depletion was not only dependent on GB type but also misorientation angle, i.e. that HAGBs at higher misorientation angles are more susceptible to sensitisation than lower angle HAGBs [107]. This has also been reported in other works [67, 102].

A similar pattern is observed for samples sensitised through irradiation processes [50]. In particular, RIS has been reported to be dependent on GB type. Twin GBs are more resistant to RIS [29, 50]. Whereas HAGBs are more susceptible to RIS, resulting in more severe chromium depletion and consequent sensitisation [50, 94]. As with thermal sensitisation, this phenomenon may also be explained by differences in energies, though it is often described in terms of efficient or inefficient point sinks. Twin GBs are less susceptible to RIS as they are considered inefficient point-defect sinks [29, 50, 66]. This is the result of a lack of diffusion paths at which point-defects can annihilate within the GB [50]. The opposite case is true for HAGBs. HAGBs are considered as perfect sinks as they contain a high density of dislocations, which act as point-defect annihilation sites [50]. The resultant low concentration of point-defects induces an enhanced flux of point-defects, resulting in further segregation of elements [50].

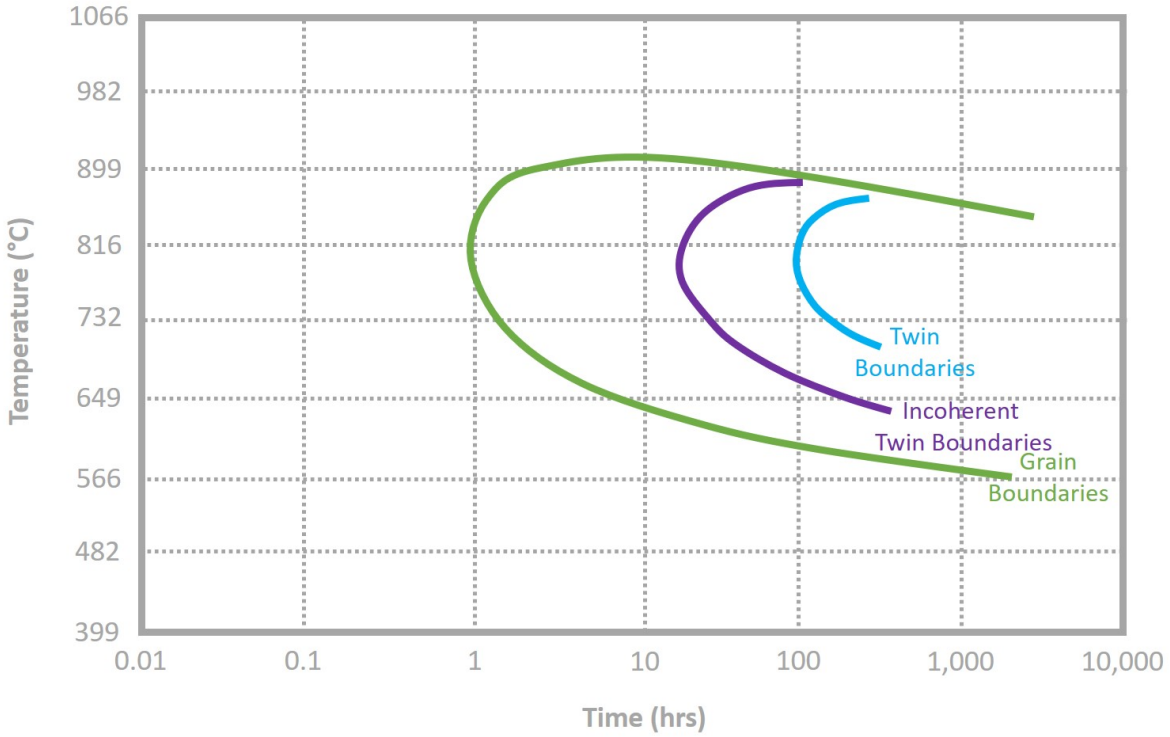

Figure 2.9: A TTP diagram for $M_{23}C_6$ in Type 304 stainless steel, adapted from [12].

2.1.5.3 Proxy Samples

Experimental work performed on irradiated fuel cladding is both technically challenging and expensive [30, 96]. This work is also very time consuming and, due to the high usage of shielded facilities, there is limited availability of suitable workspaces [96]. Given these additional complications that arise for irradiated samples, it is worthwhile to consider the use of surrogate materials that behave similarly to irradiated fuel cladding when exposed to simulated environments [30].

Previous studies have been performed to study the changes to material microstructure as a result of neutron irradiation using proton, electron, or heavy ion irradiated proxy materials [48, 50, 94, 96, 109]. These tests have the advantage that irradiation may be carried out at specific energies, doses, and temperatures for defined durations, and the resultant activity is typically lower than for ex-service specimens so they may be analysed in non-active laboratories [96]. However, key differences are observed, such as the depth of penetration and differing development of radiation-induced defects [30, 94, 96].

Heat treatments intended to purposefully cause thermal sensitisation in unirradiated stainless steel have been used in previous works as a method of simulating the key characteristics of irradiated stainless steel [30, 48]. Thermal sensitisation renders the material susceptible to localised corrosion such that the mechanism by which it occurs may be studied with comparative ease [30]. Such experiments are comparatively safer and would allow for the development of

methodologies and safe lab practices that could subsequently be applied to radioactive samples.

Heat treatments are able to reduce the GB chromium concentration to a similar level as those observed within RIS affected, ex-service AGR clad [30, 48]. However, thermally treated stainless steel has some key differences when compared to irradiated stainless steel. The resulting chromium depletion profile is broader (typically > 30 nm), GB precipitates are dissimilar, and GB concentration of nickel and silicon is higher than that observed within reactor conditions [48, 49]. Additionally, some heat treatments may affect the grain size of the metal, which can affect some material properties. The differences between thermally treated samples and irradiated samples are often inevitable, it is therefore key to consider how this may affect SCC and other localised corrosion processes.

In 2018, Whillock *et al.* explored different heat treatments on samples of 20Cr/25Ni-Nb and Type 304 stainless steel [30]. Resultant GB chromium concentrations were measured, and samples were tested in a simulated storage pond conditions [30]. Whillock found that the Type 304 samples heat treated at 600°C for 72 hrs were a good match to equivalent data yielded from ex-service AGR cladding [30].

2.2 Localised Corrosion

Corrosion is an irreversible process that causes material deterioration as a result of dissolution [110, 111]. It is an electrochemical process in which a potential difference across the material/environment interface results in the flow of ions and electrons through an electrolyte [110, 111]. The process of metallic corrosion is an amalgamation of the oxidation of the metal [112]:

$$M \rightarrow M^{n+} + ne^{-} \tag{2.3}$$

and reduction reactions of the electrolyte:

$$2H_2O + 2e^{-} \rightarrow H_2 + 2OH^{-} \tag{2.4}$$

$$O_2 + 2H_2O + 4e^{-} \rightarrow 4OH^{-} \tag{2.5}$$

$$2H^{+} + 2e^{-} \rightarrow H_2 \tag{2.6}$$

$$O_2 + 4H^{+} + 4e^{-} \rightarrow 2H_2O \tag{2.7}$$

$$M^{n+} + ne^{-} \rightarrow M \tag{2.8}$$

The sites at which oxidation reactions take places are termed anodes, and the sites of reduction reactions are called cathodes [112]. Anodes and cathodes can fluctuate across a materials surface,

or they can be spatially separated at fixed positions [112]. Corrosion of metallic surfaces can thus be classified into two different forms: uniform (if the anode/cathode fluctuate) or localised (if the anode/cathode are spatially separated) [111, 112]. Uniform corrosion takes place over the entire surface and occurs when the surface is in contact with a solution in which it is active [110, 111]. Localised corrosion occurs at specific sites on the metal surface [111].

Considering localised corrosion, corrosion reactions will occur preferentially at anodic zones. Anodic zones are typically distinct from the bulk of the material due to the presence of precipitated phases or segregation and can be intergranular or transgranular [41, 112]. The type and location of anode on the surface determines the form of localised corrosion that occurs [112]. Some forms of localised corrosion are of particular concern as they can occur with little obvious outward signs of damage accumulation, whilst causing significant deterioration of component structural strength [33–35, 42, 113, 114].

2.2.1 Principles of Corrosion

Corrosion is controlled by underlying thermodynamic and kinetic factors [112]. Thermodynamics determines whether the corrosion reactions are energetically favourable. Kinetics determines the rate at which they occur.

Thermodynamically, corrosion will occur if corrosion reactions cause the system to transition from an unstable high energy state to a more stable lower energy state. The associated change in energy, or chemical potential, is known at Gibbs free energy [13]. Consider a reaction with reactants A and B, and products C and D, with respective concentrations a, b, c, and d, i.e.:

$$\mathrm{aA} + \mathrm{bB} \rightarrow \mathrm{cC} + \mathrm{dD}$$

The associated energy change may be expressed as the total energy of formation of the products, $\Sigma\Delta\mathrm{G}_{\mathrm{products}}$, minus the total energy of formation of the reactants, $\Sigma\Delta\mathrm{G}_{\mathrm{reactants}}$, i.e.:

$$\Delta\mathrm{G} = (\mathrm{c}\Delta\mathrm{G}_{\mathrm{C}} + \mathrm{d}\Delta\mathrm{G}_{\mathrm{D}}) - (\mathrm{a}\Delta\mathrm{G}_{\mathrm{A}} + \mathrm{b}\Delta\mathrm{G}_{\mathrm{B}})$$

If the change in energy, ΔG, is negative, the reaction can occur spontaneously as it is energetically favourable. At equilibrium, ΔG is equal to zero, and the specific potential of the system is equal to the reversible potential, E^{rev} [112]. If all reactants and products are in the standard states (at 25°C, 1 atm, and with 1 M concentrations) with an activity of unity, this potential is equal to the standard potential, E_0 [112]. Often conditions under which corrosion occurs are such that reactants/products are not in their standard states, and so, $E^{\mathrm{rev}} \neq E^0$ [112]. Under these conditions specific potential may be calculated from the Nernst equation [112]:

$$\mathrm{E} = \mathrm{E}^0 - \frac{\mathrm{RT}}{\mathrm{zF}} ln \mathrm{Q}_{\mathrm{r}} \tag{2.9}$$

Where E is the potential, R is the universal gas constant, T is the temperature (in K), z is the number of electrons transferred, F is the Faraday constant, and Q_r is the reaction quotient. If

ΔG is positive, the reaction will not occur spontaneously. For such a reaction to occur an external force is required, such as an applied potential. It should be noted that the Gibbs free energy, G, (and so the potential) associated with a reaction is a thermodynamic property of the system. Whilst the Gibbs free energy may determine whether or not a reaction can occur, it cannot give information about the rate at which the reaction will take place [13]. This is determined by the reaction kinetics [13].

The rates at which corrosion reactions take place are influenced by the potential difference across the metal/electrolyte interface [110]. The specific potential of a system in the absence of any applied potential is often referred to as the open circuit potential (OCP), E_{OCP}, or (when considering corrosion reactions) the corrosion potential, E_{corr} [112]. Reactions can therefore be driven, or supressed, by the application of a potential relative to the OCP, referred to as an overpotential or overvoltage.

The effects of applied potential may be described by various laws, dependent upon the conditions of the system [115]. The reaction rate may be limited by two different kinetic phenomena: charge transfer, where the rate is limited by the driving force (i.e. the overpotential), or mass transfer (i.e. diffusion processes) [13]. For example, when a reaction's rate is limited by the overpotential, the reaction rate (which may be expressed as current density, i) and the reaction driving force (i.e. the potential, E) are related by the Butler-Volmer equation [112]. When a reaction is limited by mass transfer, the reactant concentration at the reaction site is not the same as the bulk solution [112]. Under these conditions, the resultant current (referred to as the faradaic current) is related to the material flux at the reaction site by Fick's law [112, 115].

2.2.1.1 Polarisation Curves

Polarisation curves may be produced to characterise the corrosion behaviour of a system. This is achieved by performing a potentiodynamic scan, where the driving force (i.e. the potential) is controlled and the reaction rate (i.e. the current) is measured [13, 112]. For such an experiment a three-electrode set-up is commonly implemented, consisting of a working electrode (WE), counter electrode (CE), and reference electrode (RE) [13, 115]. The WE is the sample whose corrosion characteristics are being interrogated [13]. The CE provides the applied current, and so is made out of inert materials, such as platinum [13]. The RE provides a stable reference potential by which the potential may be measured with respect to [13]. An example is a Ag/AgCl electrode, in which an equilibrium is achieved between silver and silver chloride. A potentiostat adjusts the potential (as measured between the WE and RE) in predefined steps and records the resultant current (as measured between the WE and CE) [13, 112].

An example polarisation curve is shown in Figure 2.10, though it should be noted that polarisation curves can vary considerably. The potential begins at just below the corrosion potential (or OCP), labelled a. As the applied potential increases the measured current decreases until point b. At point b, the cathodic and anodic currents are equal, resulting in a measured

current close to 0 A [112]. This occurs at the corrosion potential (or OCP) [13, 112]. After the corrosion potential, the curve enters the active region, in this region the current increases as metal oxidation reactions occur [13]. The maximum current in the active region occurs at the passivation potential, point d. At potentials above the passivation potential, the surface quickly passivates, from point e to point f, as it enters into the passive region [13]. Passivity is the state in which the corrosion rate of a metal is low due to the presence of a passive layer [112]. For example, stainless steels have a thin chromium oxide layer described previously [53–56]. At point g, the potential reaches the breakaway potential, and the current begins to increase. Passivity breakdown occurs due to an increase in chemical reactions occurring in the system, in stainless steels this occurs following the dissolution of the passive film. For stainless steels in chloride containing solutions, this may indicate the onset of steady pitting corrosion [54, 111]. This is dependent upon the system being analysed.

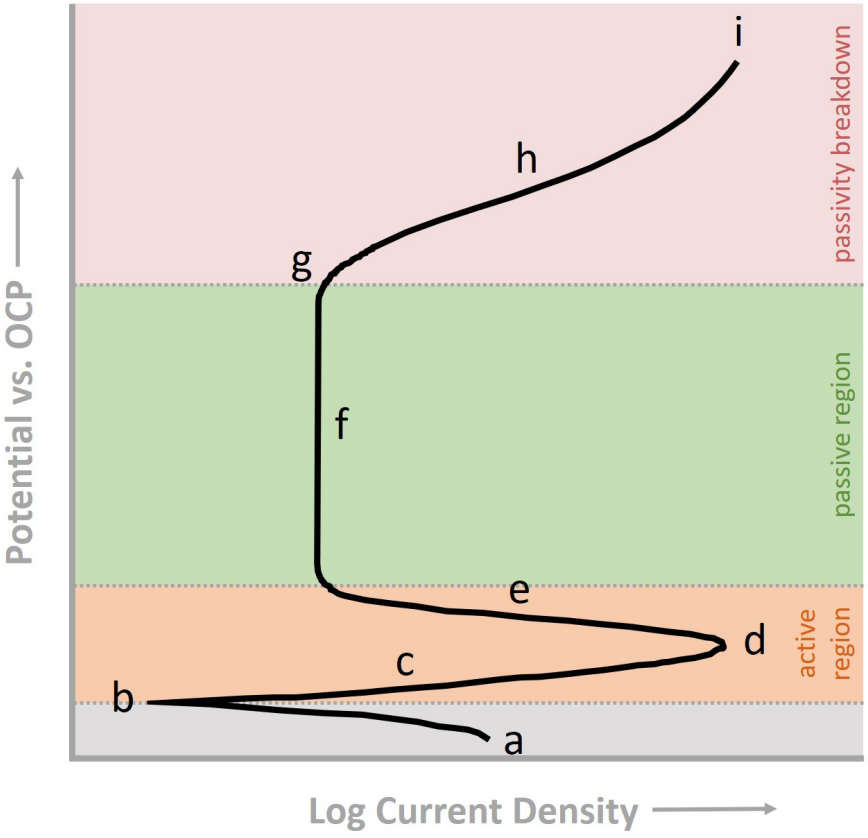

Figure 2.10: An example polarisation curve produced from a potentiodynamic scan, adapted from [13].

2.2.2 Localised Corrosion Forms

There are numerous forms of localised corrosion [112]. The most common forms include:

- Galvanic corrosion
- Crevice corrosion
- Pitting corrosion
- Intergranular corrosion, or intergranular attack (IGA)
- Stress corrosion
- Erosion corrosion

Descriptions of the localised corrosion forms of particular relevance within this thesis are given in the following sections.

2.2.2.1 Galvanic Corrosion

Galvanic corrosion occurs when two dissimilar metals are submerged within a conductive or corrosive solution whilst in contact, due to the potential difference set up between them [41]. The metal with higher/lower resistance becomes cathodic/anodic, respectively, and electrons flow between them [41]. This has the effect of decreasing the rate of corrosion of the cathodic (more resistant) metal and increasing the rate for the anodic (less resistant) metal [41].

2.2.2.2 Crevice Corrosion

Crevice corrosion occurs in occluded regions such as volumes with small apertures or narrow cracks [116]. It is within these occluded regions that comparatively slow diffusion processes as well as lack of fluid convection results in a build-up of aggressive chemistry [116, 117]. The solution in these occluded regions often has a lower pH and is more corrosive than the bulk solution leading to breakdown of passivity and an acceleration of corrosion reactions in these areas [112, 116, 117]. This build-up of aggressive chemistry is similar to that encountered in pitting corrosion [118]. In the presence of stress, crevice corrosion can also act a precursor to SCC.

2.2.2.3 Pitting Corrosion

Pitting corrosion occurs at specific regions on a metal surface leading to the formation of pits on the surface. It is similar to crevice corrosion as the chemistry within the pit is isolated and can vary considerably from the bulk electrolyte [118, 119]. Pitting corrosion can occur in a range of environments, though the most common corrosive ion is the chloride anion [34, 114, 120]. Pits typically initiate at locations where the passive film is thinner or defective, such as at SPPs, GBs, sharp edges, or chromium depleted regions [99, 111, 121].

Pitting corrosion proceeds in three distinct steps: pit nucleation, pit initiation (metastable pitting), and stable pit growth [122]. Nucleation/initiation events are described as potential

dependent [122]. Whereas metastable and stable pit growth have been shown to be diffusion limited, i.e. their corrosion rates are determined by mass transport [122]. This dependency is dependent upon the site geometry being more or less open [122]. Less open pits can propagate at lower potentials as the diffusion barrier is more easily formed [122]. More open pits require higher potentials and so faster reaction rates [122].

Kinetic behaviour can be observed within the resultant polarisation curve. Pitting corrosion may be characterised by the pitting potential. Above the pitting potential pits begin to grow on the surface, below this potential the surface is passive [119]. On the example polarisation curve given in Figure 2.10, this potential is reached at point g. Pitting corrosion can occur at potentials below the pitting potential, forming metastable pits that typically repassivate [119]. Metastable pit formation is therefore characterised by sharp peaks in the measured current as the pit penetrates the passive film [122].

Pitting corrosion is often considered to be a significant, insidious form of localised corrosion as it is difficult to detect and can lead to further damage through SCC [34, 114, 123]. SCC cracks initiate from pits as the pit acts as a stress raiser [124, 125].

2.2.2.4 Intergranular Attack (IGA)

IGA occurs when the GBs are preferentially corroded. It is typically encountered within sensitised microstructures, where chromium depleted GBs are anodic with respect to the bulk grain [33, 38, 41, 101, 105]. Consequently the GB will corrode whilst the surrounding regions remain passive [33, 38].

2.2.2.5 Stress Corrosion Cracking (SCC)

SCC is a localised corrosion phenomenon that results in cracking of a material. It arises due to the synergistic interactions of corrosive species with mechanical loading [33, 41, 44, 70, 113, 126], described in more detail in subsequent sections. The resultant cracks can propagate through the material causing deeper penetration of localised corrosion and ultimately failure.

Tensile stresses can cause rupture of the passive film, resulting in the subsequent formation of an anodic zone, which can then induce further cracking [41]. In turn this can prevent repassivation of the surface around the crack tip area, due to persistent plastic deformation, exposing a clean, reactive metal surface to the corrodent [127]. In addition to this, particular aggressive species can also induce passivity breakdown, such as chloride and bromide ions [35].

SCC cracks can propagate by one of two modes: transgranular SCC (TGSCC), or intergranular SCC (IGSCC) [44, 125, 126]. In TGSCC the cracks propagate through grains within the crystal structure; this is in contrast to IGSCC where cracks develop along the GBs due to the chemical and physical differences across the GB [41, 44, 70, 113, 126]. The path in which SCC occurs (IGSCC or TGSCC) is dependent upon the metal and corrodent under investigation [41]. However, in the majority of instances SCC does not follow one cracking mode exclusively, rather one mode

will be dominant [128]. Transition of cracking mode is dependent upon the metal's microstructural features and composition as well as the specimen's stress state and the environment in which cracking occurs [128].

Intergranular SCC (IGSCC) In sensitised stainless steels, SCC tends to progress along GBs, i.e. intergranularly [95, 100]. IGSCC is a smoother process making it considerably more difficult to detect [44]. It is estimated from percolation theory that around 20-25% of GBs need to be sensitised for IGSCC to propagate [72, 81].

Irradiation-Assisted SCC (IASCC) IASCC is the enhancement of susceptibility to SCC due to irradiation changes to the material microstructure as well as changes to the environmental chemistry [79, 90–92, 96, 129, 130]. Changes to the material due to irradiation that can affect propensity to, and rate of, SCC include: RIS, radiation hardening, embrittlement processes, radiation induced creep, and void swelling [79, 90–92, 129]. IASCC is propagates along GBs and so may be described as a form of IGSCC.

IASCC is a key failure mechanism within nuclear applications [90, 96, 130]. In light water reactors (LWRs) it is the primary cause of failure for stainless steels, as well as nickel based alloys [130]. The factors leading to IASCC are synergistic and irradiation effects are often overlapping making IASCC difficult to untangle and predict [79, 92, 96, 130]. This is further complicated as IASCC accelerates IGSCC processes rather than induces them [91, 129].

RIS is considered to be a significant contributor to IASCC [79, 92, 93, 95, 96]. This is mainly due to the resultant chromium depletion, leading to GB corrosion susceptibility, as discussed previously. However, the segregation of other elements also contributes to the cracking process, such as the enrichment of nickel and silicon [79, 90]. In hot water environments, such as LWRs, silicon oxidises to silicon dioxide (SiO_2) which is highly soluble under these conditions [90].

2.3 Contributing Factors Leading to SCC

SCC occurs due to the combination of three conditions: a susceptible material, sufficient tensile stress (this can be due to applied or residual stresses), and a corrosive environment, as illustrated in Figure 2.11 [33, 41, 44, 70, 113, 126]. In the following sections the separate aspects of SCC are considered, before considering specific models of crack initiation and propagation, and methods for their detection and observation.

2.3.1 Material Susceptibility

Material susceptibility to SCC is determined by many different factors. When considering metals and alloys, the likelihood of occurrence of SCC is influenced considerably by variables such as composition and microstructure [33, 127]. For example, as crystal grain size decreases, often SCC

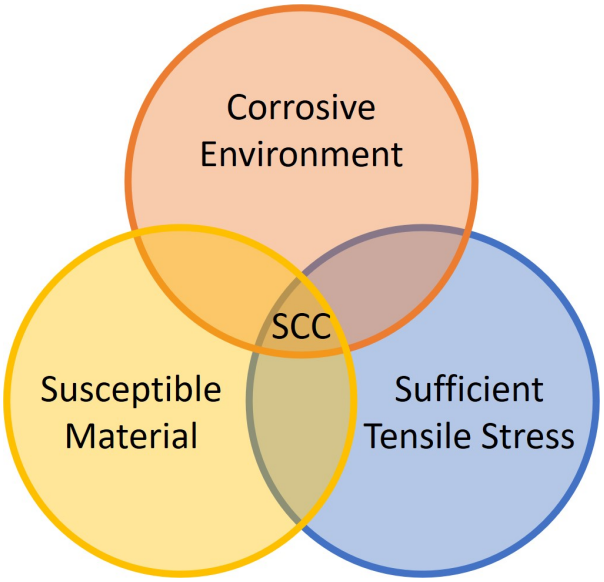

Figure 2.11: A Venn diagram demonstrating the three conditions required for SCC to occur.

susceptibility is also lowered [125, 127]. This is related to various factors. As GBs act as barriers to dislocation movement, smaller grain size leads to strengthening of the material, as well as an increase of ductility (toughness) [131]. Mechanical strength is of particular importance, and its effect can vary dependent on the mechanism considered for SCC [33, 127]. For crack propagation processes that rely on plastic deformation at the tip, it is intuitive that materials with lower mechanical strengths are more susceptible [33]. However, when considering the mechanism of hydrogen embrittlement (discussed further in Section 2.4.2.4), SCC susceptibility increases with mechanical strength [33]. Mechanical strength also has an influence upon the likelihood of fast fracture failure of a material [33]. SCC likelihood is also affected by factors such as heat treatment, or cold work [33, 41, 127].

When considering intergranular cracking, GB chromium depletion is often cited as a determining factor, and that the extent of chromium depletion is a measure of its susceptibility to undergo IGSCC [104]. The extent of chromium depletion is affected by the materials microstructure, such as grain size and material composition [104]. As grain size decreases, so does the chromium diffusion pathway from the interior grain to the GB, therefore aiding in chromium replenishment of depleted zones. In addition, the likelihood of a continuous unbroken network of chromium depleted GBs is much lower [100, 125].

2.3.1.1 The Effect of GB Type on SCC Propensity

In Section 2.1.5.2 the effect of GB type on GB sensitisation through thermal ageing or irradiation was discussed. Factors such as precipitation, GB diffusion, and intergranular corrosion susceptibility are also known to be strongly dependent on GB type [67]. It is little surprise, then, that GB

type is reported to affect propensity to failure by IGSCC [60, 68–72, 100, 108, 125, 132, 133].

As with sensitisation processes, the differences in IGSCC susceptibility observed for different GB classifications is often described in terms of energy. With random HAGBs exhibiting the highest propensity to IGSCC and the highest GB energy [60, 68, 69]. Some works have reported that this dependency varies with GB misorientation angle, i.e. that higher angle HAGBs are more susceptible to cracking than lower angle HAGBs [67, 72, 102, 107, 131]. However other works report that GB misorientation angle alone is insufficient in determining GB energy for HAGBs [62]. This is due to the dependency on boundary planes. A higher angle HAGB may have a lower energy than a lower angle HAGB if it is orientated on a lower energy boundary plane [62].

LAGBs are reported to be resistant to cracking, though cracking immunity is debated [60, 68, 69, 71, 72]. Twin GBs (CSL $\Sigma 3$ GBs) are also reported to be resistant, or possibly immune, to cracking depending on the environmental conditions [50, 60, 65, 66, 68, 69, 71, 71, 125, 132–134]. Some studies state that this resistance is limited to coherent twin GBs (i.e. with GB misorientation about a $< 111 >$ crystal axis) and that incoherent GBs behave similarly to other random HAGBs [60, 69, 72, 100], thus reiterating the importance of boundary plane [62].

Conflicting reports exist about the cracking susceptibility of higher order CSL GBs. Some claim that higher order CSL GBs exhibit the same behaviour as random GBs [60, 68, 71, 72], while other studies consider some or all of these GBs to be crack resistant [70, 125, 133]. However, this is dependent upon the limit imposed on which CSL GBs are 'special'. Some works consider CSL GBs with $\Sigma \leq 29$ to be low CSL GBs and to be crack resistant [100, 108, 125, 133]. In other works, only twin GBs and higher order twin GBs (i.e. $\Sigma 9$ and $\Sigma 27$) are considered crack resistant [68, 69, 100].

In 2001, Gertsman *et al.* studied SCC cracks formed in sensitised austenitic stainless steels (Type 304 and Type 316) in high temperature water environments [71]. Gertsman compared the misorientation distribution of the general GB population to that showing cracked GBs only and found similar distributions, with the exception that significantly less twin GBs had cracked [71]. Gertsman concluded that twin GBs are the only crack resistant GBs (though, not crack immune) and are the only GBs that should be regarded as 'special'. All other GBs, including LAGBs and higher order CSL GBs, cracked with a frequency corresponding to their frequency in the general GB population [71]. Thus, indicating that the Σ parameter is not determinant on a GBs propensity to suffer IGSCC [71].

Indeed, it is difficult to determine the cut-off point between 'special' and non-'special'. This is partly due to the CSL description of the GB being incomplete, in that it does not consider that effect of GB plane [69, 70, 100, 108]. In addition, factors such as GB chemistry and precipitation are key when considering a GBs susceptibility to IGSCC [71].

The notion that some GB types are resistant to cracking forms the basis for GB engineering (GBE), where thermal and mechanical treatments are implemented to maximise the fraction of

resistant GBs in order to decrease IGSCC susceptibility [60, 68–70, 72, 100, 125, 132, 133, 135]. GBE is discussed further in other works [60, 69, 72, 100, 102, 132, 135].

2.3.2 Effect of Environment

There are a number of different environmental parameters that can influence SCC behaviour, these include:

- Temperature
- Electrolyte concentration
- Solution activity and chemical species
- pH
- Electrochemical potential or polarisation
- Stirring/flow rate

Different environments can lead to substantially different SCC behaviours, such as crack propagation rates, cracking mode etc. indicating differing underlying mechanisms. Some of the models for crack initiation and propagation in different environments are discussed further Section 2.4.2.

2.3.2.1 Polarisation

Polarisation of the metal or alloy can have considerable influence over the time to failure due to SCC [33, 35, 41, 127]. Cathodic polarisation typically lengthens the time to failure, and in some cases, can prevent failure by cathodic protection [41, 127]. In contrast, the application of anodic polarisation has the effect of increasing crack density, and accelerating crack propagation velocity, this in turn shortens crack initiation and propagation times [127].

Cracking frequently occurs at potentials in which the surface is within the passive region whilst the tip of the crack is within the active, or passivity breakdown, region [33]. The potential across the surface of the sample is dependent upon the environment, notably, the cathodic reactant content such as oxygen [33].

2.3.3 Mechanical Factors of SCC

2.3.3.1 Stress

Stress, σ, is defined as force, F, per unit area over which that force is applied, A, i.e.: $\sigma = \frac{F}{A}$ [14]. If this force pushes the material, acting to compress it, it is called a compressive stress [14]. If the opposite is true, and this force acts to pull the material at right angle to the face, it is called a

tensile stress [14]. Tensile stresses can be present within a material due to applied stresses, such as deformation, or residual, due to fabrication processes. For forces acting at angles other than 90° to the face, the force may be resolved into tensile/compressive stress and shear stress [14].

The materials response to stress is termed strain. Strain, ϵ, is defined as the change in length of a material, u, divided by the original length, l, i.e.: $\epsilon = \frac{u}{l}$ [14]. For example, a tensile stress will introduce a tensile strain and the length of the material will increase [14]. The relationship between stress and strain is defined by Hooke's law as:

$$\sigma = E\epsilon \tag{2.10}$$

Where E is the Youngs (or elastic) modulus of the material [14]. This is a mechanical property of the material.

Hooke's law applies to materials that are elastically deformed, this means that the material will return to its original shape is the source of stress is removed. However, at higher stresses, the material can become plastically deformed, meaning that it is permanently deformed and will not recover its original shape following the removal of stress sources. The threshold value of stress between these two behaviours is termed the yield stress.

At the atomic level, elastic deformation causes the equilibrium distance between atoms to be shortened or lengthened. Plastic deformation occurs when the modified distance between atoms cannot correct for the change in material length. When this occurs, the atoms are forced to shift, causing material defects, such as dislocations or vacancies.

2.3.3.2 Effect of Load on Austenitic Stainless Steels

At atomic length scales, stainless steels plastically deform most commonly via three modes: slip, twinning, and strain-induced martensite. Slip is the most dominant deformation mode in austenitic stainless steels (FCC crystal structures), particularly at low strain rates [52].

Slip Slip is the mechanism by which dislocations move within crystalline structures [52]. Demonstrated in Figure 2.12. It is a vector quantity with an associated slip direction. The plane in which slip occurs is known as the slip plane. The combination of slip plane and slip direction is known as the slip system [52].

Slip can be planar or cross. This propensity for either slip type is dependent on the materials stacking fault energy (SFE) [95]. Austenitic stainless steels have relatively low SFE, resulting in planar slip [95, 136, 137]. This is characterised by arrays of coplanar dislocations, known as slip bands [127].

In austenitic stainless steel, slip is preferentially produced in the most closely packed {111} planes [138–140]. There are four {111} planes (as illustrated in Figure 2.13) with three possible $< 110 >$ directions [140]. This results in 12 possible slip systems [140]. The slip system activated upon the application of stress is dependent upon the Schmid factor. The Schmid factor is the

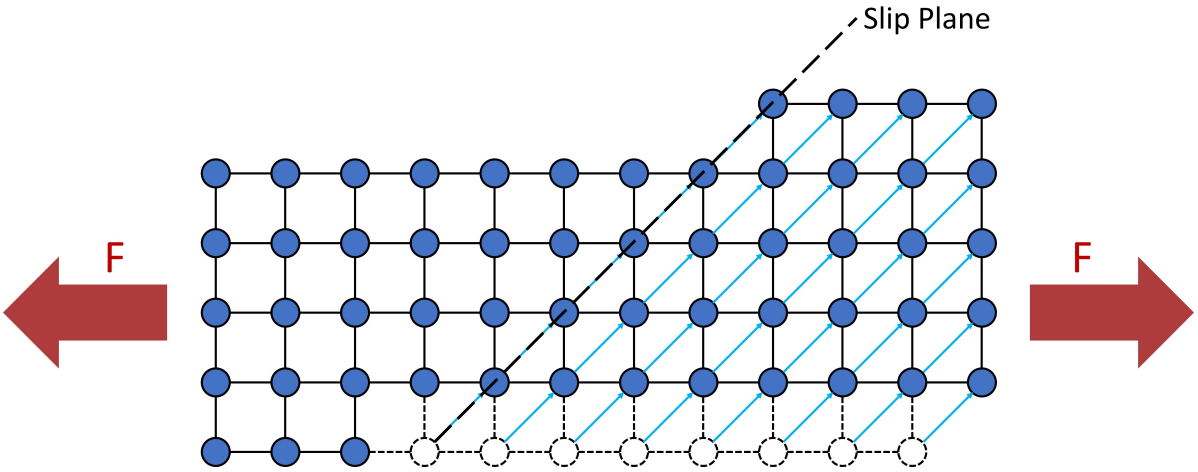

Figure 2.12: A schematic diagram showing the atomic scale effects of plastic deformation in response to an applied force, F, resulting in the formation of a slip band along a slip plane.

maximum resolved shear stress and is a measure of how easily slip occurs when a material is under stress. The slip system with the highest Schmid factor will activate first at lower tensile stresses [140].

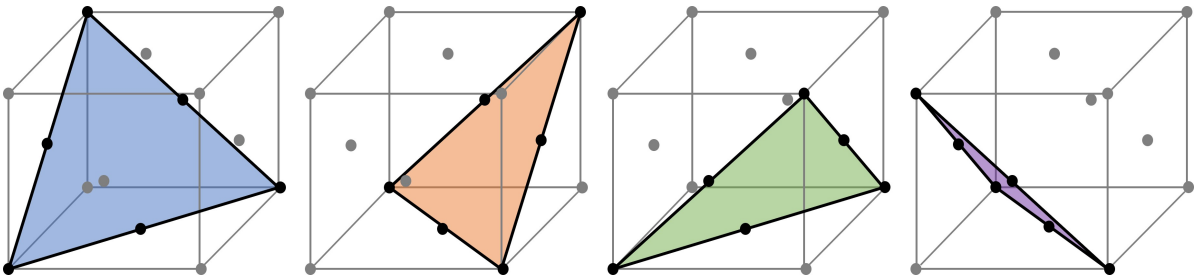

Figure 2.13: Schematic diagrams showing the four {111} slip planes in austenitic stainless steel [14].

It has already been stated that slip is a vector. The magnitude of this vector is equal to number of atomic steps in a given direction, multiplied by the Burgers vector magnitude for that direction. For example, in AISI Type 304 stainless steel, one Burgers vector has a magnitude of 2.58×10^{-10} m [141], as calculated using the following equation:

$$|b| = \frac{a}{2}|<110>| \tag{2.11}$$

$$|b| = \frac{a\sqrt{2}}{2} \tag{2.12}$$

Where b is the Burgers vector, and a is the lattice parameter [136, 142].

Strain-Induced Martensite Martensite can form following sufficient levels of plastic deformation, this is known as strain-induced martensite [81]. The volume of martensite formed is dependent upon the temperature, stress state and strain rate, as well as the composition, SFE, and austenite stability of the stainless steel [81, 143]. For example, with increasing deformation, strain-induced martensite becomes more significant [81].

Martensite is stronger and more brittle than austenite, resulting in changes to the properties of the stainless steel. The crystal structure of α' martensite also enhances hydrogen diffusivity and so is more susceptible to hydrogen induced embrittlement and cracking [105, 144]. Martensite formation reportedly forms at GBs [81, 105], resulting in the promotion of intergranular fracture [81]. Though martensite formation is reported to be less significant than that of chromium depletion in IGSCC initiation and propagation [81].

2.3.3.3 The Effect of GB Type When Under Load

Dislocation generation and slip movement are known to be dependent upon GB type [64]. Slip bands are unable to transfer through HAGBs, including twin GBs, resulting in dislocation pile-up [65, 134, 137]. Whilst improving mechanical strength, dislocation pile-up also leads to a concentration of stress, and ultimately, intergranular fracture [65, 137]. In contrast, slip bands can propagate though LAGBs, resulting in a resistance to fracture [65].

That is not to say, however, that HAGBs will always crack over LAGBs, as it is important to consider other factors including the orientation of the GB plane with respect to the stress axis [60, 71]. It is also important to consider the orientations of the grains either side of the GB, as an incompatibility of Schmid factor can lead to further propensity for crack initiation [108].

2.3.3.4 Stress Accumulation

Features such as holes or notches in the surface of a material can act as stress accumulators. Such features generate high local stresses that can exceed the threshold stress intensity required for SCC to occur, leading to fracture at lower stress values. For example, following pitting corrosion of a surface, SCC often initiates at the base or side of the pit [33, 41, 113].

In a similar fashion, crack initiation can be influenced by the presence of existing cracks on the surface [145]. The rate of crack growth can also be influenced [145]. This is observed when multiple cracks are present on a surface. As the crack tips approach one another, propagation rate increases as a result of the enhanced stress [145]. However, if a crack tip approaches another parallel crack, propagation rates can be suppressed by stress shielding [145].

2.4 Stages of SCC

Fracture mechanics considers both the material properties and the mechanical condition of the crack tip in order to predict whether or not a crack is likely to propagate [33]. When considering

a system in which the material thickness in the direction of the crack and the length of the crack are both large in comparison to the region of plasticity at the crack tip, the stress state at the tip of the crack can be defined by the stress intensity factor, K [33]. Where K is given by:

$$K = Y\sigma\sqrt{\pi a} \tag{2.13}$$

Where Y is a geometrical correction factor, σ is the applied stress, and a is the crack length [33, 127, 146].

In metals and alloys that are not susceptible to SCC, fracture occurs only when $K > K_{Ic}$, where K_{Ic} is the fracture toughness (or critical stress intensity factor) [33, 127, 146]. On the other hand, when SCC susceptible materials are in a corrosive environment, cracks are able to propagate well below K_{Ic}, this is known as subcritical cracking [127]. Subcritical cracking results in an increase in a, which in turn increases K. When the value of K exceeds K_{Ic} fast fracture occurs ultimately leading to the failure of the material [127]. Figure 2.14 shows initial K against crack growth rate, it can be seen that there exists a threshold value of K, below which stress corrosion cracks do not propagate and failure does not occur, often called K_{Iscc} [33, 41, 127]. K_{Iscc} is dependent upon the combination of material and corrodent, and can be determined by time-to-failure testing; it is an important factor to consider when designing SCC resistant systems or predicting failure [33, 41, 127].

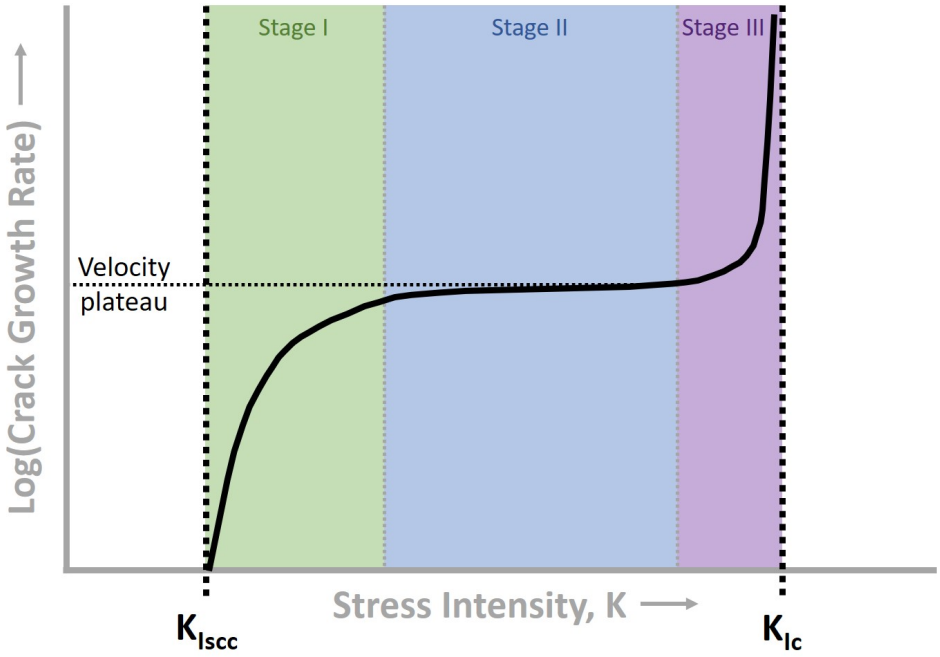

Figure 2.14: A graph showing how crack growth rate varies with stress intensity factor [15–17].

SCC can be divided into three sequential stages: Crack initiation, crack propagation, and failure. The transition between each step is not always clearly defined. The initiation stage can

be separated further into precursor, incubation, and slow crack growth, as illustrated in Figure 2.15 [101, 124]. The initiation stages are much longer than the propagation or failure stages and can last months or even years. At the precursor stage no cracks are visible, instead this stage occurs when the factors required for SCC to occur are present. The first cracks develop during the incubation stage. This leads to slow growth and then rapid growth in which the crack propagates.

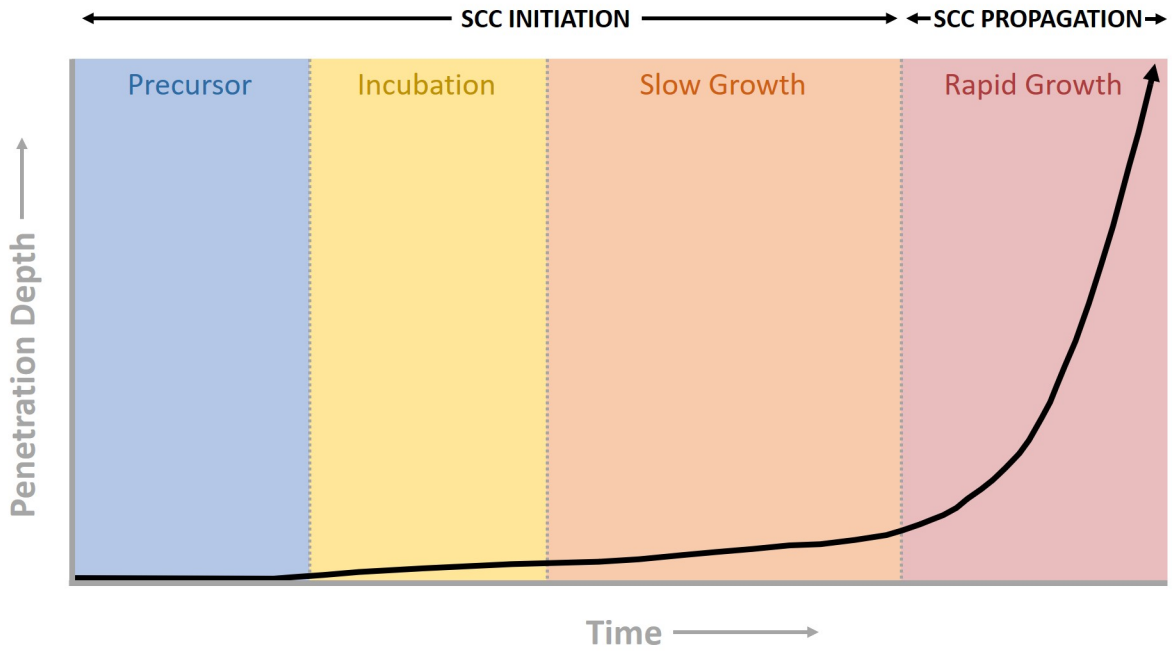

Figure 2.15: A graph demonstrating the change in SCC penetration depth with time at each stage of SCC, adapted from [18].

In fracture mechanics, the transition between each stage is defined in terms of crack velocity. Figure 2.14 shows the relationship between the velocity of SCC propagation and K [127]. Three clear regions can be seen: Stages I, II, and III. In Stage I it can be seen that, once K exceeds K_{Iscc}, the velocity of propagation rapidly increases until the plateau crack growth rate is reached in Stage II [33, 127]. This limiting velocity is controlled by diffusion [127]. In Stage III, as K increases further, as does velocity of crack propagation. This occurs as K approaches K_{Ic}, at which point all materials, susceptible to SCC or not, suffer from fracture [33]. Stage III is not often observed due to fracture often occurring abruptly after Stage II [41].

When considering the current state of SCC research, there has been a significant amount of research at the long crack or rapid growth stage [124]. This includes crack propagation rates for various material-environment conditions. Comparatively little qualitative or quantitative information is available on the initiation stages. This is due to the small length scales and the stochastic nature of these stages.

2.4.1 Crack Initiation

Crack initiation in stainless steels generally occurs at defects on the surface. Such defects may be surface features that can act as stress accumulators, such as polishing lines, pits, or cracks, as described previously and as demonstrated in Figure 2.16. Alternatively, these defects may be regions where the passive film is discontinuous or thin, such as at GBs or SPPs.

When considering TGSCC, initiation events can occur at slip bands, which rupture the protective film [41]. Corrosion processes opt for the path of least resistance, and so it is characteristic in the identification of TGSCC that the crack changes direction from grain to grain as a result of the differing lattice orientations [41].

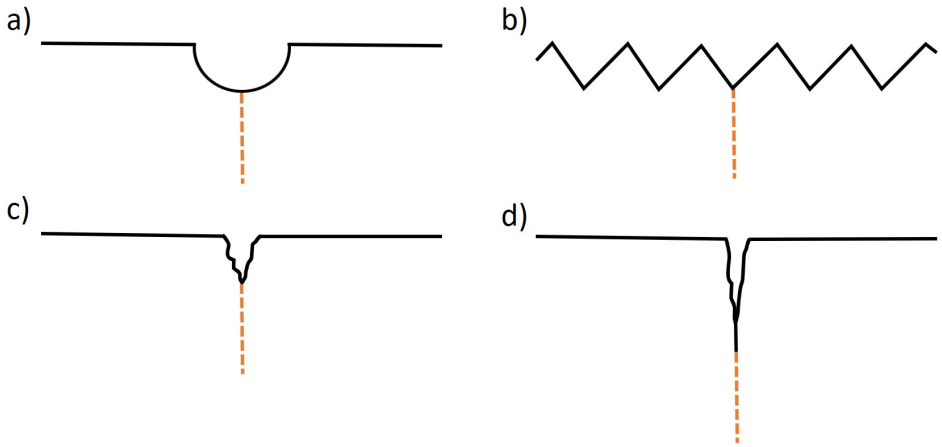

Figure 2.16: Schematics showing examples of crack inhiation events occurring from features that may act as stress accumulators on the surface: a) a pit, b) machining marks, c) IGA, and d) an existing crack. Adapted from [19].

2.4.2 Crack Propagation

There is no singular overarching mechanism by which SCC propagation occurs. Mechanisms are highly dependent upon the combination of material and environment, and often involve multiple processes [38, 41, 57, 126]. At the atomic scale, crack growth can proceed via: the tensile separation of atoms (decohesion), the shear movement of atoms (by dislocation egress/insertion), or atom removal/addition (by dissolution or diffusion) [19, 131].

Despite decades of research it remains uncertain as to which mechanism provides the most accurate model within some environment-material combinations [33, 126]. This is not unexpected given the various mechanical, electrochemical, and metallurgical factors that must be considered. There are several models that attempt to encapsulate the mechanisms under which SCC occurs in various material/environment combinations [33, 38, 41, 57, 126, 127]. These models are able to explain specific experimental results; however, some observations remain unexplained [126]. Some experimental results cannot be modelled by a single mechanism but can be explained

by combinations of existing models. Some of the most commonly described models include [19, 33, 38, 57, 126, 127]:

- Surface Mobility
- Adsorption-Induced Cleavage
- Film Induced Cleavage
- Hydrogen Induced/Assisted Cracking (Hydrogen Embrittlement)
- Localised Surface Plasticity
- Film Rupture or Anodic/Slip Dissolution

Localised surface plasticity and film rupture are dissolution driven mechanisms. These are based on the notion that strain enhances film dissolution at the crack tip. Surface mobility, adsorption induced cleavage, film induced cleavage and hydrogen assisted cracking are mechanical fracture mechanisms. The following sections provide an overview these models. Schematics of these models are shown in Figure 2.17.

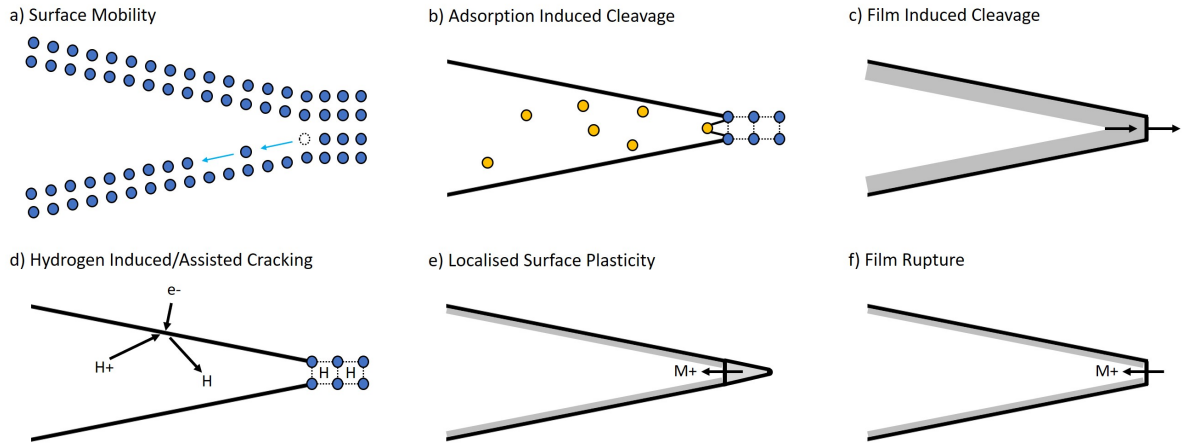

Figure 2.17: Schematics showing crack tip models for crack propagation. Adapted from [19].

2.4.2.1 Surface Mobility

The surface mobility model considers crack propagation as a result of vacancy movement [57, 126]. In this model, stress concentration at the crack tip results in the generation of a vacancy-deficient region [19]. Subsequent capture of vacancies results in the propagation of the crack tip, as illustrated in Figure 2.17a [19]. The surface mobility model further posits that the environment changes the self-diffusivity of the material, that cracking is dependent on temperature with a defined threshold temperature under which SCC can occur, and that only elastic stresses are relevant [19].

In this model, crack propagation is dependent on the surface diffusion coefficient. Therefore, factors such as surface contaminants, which can increase the surface mobility and supply vacancies to the tip, are of particular importance [19]. Using this model, crack growth rates may be approximated if the temperature is known [19].

2.4.2.2 Adsorption-Induced Cleavage

The adsorption-induced cleavage model considers the adsorption of environmental species at the crack tip to result in the weakening of interatomic bonds, this in turns lowers the stress necessary for cleavage, resulting in the propagation of the crack tip [19, 38, 41, 127]. This is illustrated in Figure 2.17b.

A key factor in support of this model is the existence of a potential below which cracking does not take place (cathodic protection) [19]. Cathodic polarisation reduces time to failure, as the rate at which anions are deposited would be reduced [41, 127]. It also interprets the pH sensitivity at the tip of the crack, as adsorption of ions is highly dependent on the pH of the environment [41].

2.4.2.3 Film-Induced Cleavage

When a brittle protective film forms on a normally ductile metal, cracks that are initiated in the film can propagate into the metal for a distance (around 1 μm), exposing the surface to the corrodent before the crack is arrested by ductile blunting, as shown in Figure 2.17c [19, 33, 35, 38]. This is known as film-induced cleavage [33, 38, 57, 126]. This process can be cyclic if the corrodent then causes the brittle film to reform [19]. This model is supported by the observation that crack propagation rate is proportional to dissolution rates [19].

If there are no pre-existing active pathways in a material, the film-induced cleavage model is an alternative mechanism for cracking [19]. This mechanism is often used to explain TGSCC in FCC alloys and copper [33].

2.4.2.4 Hydrogen Induced/Assisted Cracking

Hydrogen induced/assisted cracking occurs as a result of hydrogen entering the metal, resulting in marked loss of ductility (hydrogen embrittlement), and ultimately leading to cracking through a series of brittle failures [33, 38, 41, 57, 127]. Hydrogen is a very small atom with a high mobility, and so diffuses easily through most metals, fitting into interstitial positions in the lattice [19, 33, 38]. It often concentrates in areas of high triaxial stress, such as the tip of a crack, as this is where the metal structure is dilated, as shown in Figure 2.17d [19, 33, 41]. Subsequent failure can occur by IGSCC or TGSCC [19].

Hydrogen can be introduced into a metal or alloy as a result of unavoidable processing steps, acid cleaning, melting and casting, welding, or rolling, for example [33, 38, 41]. Additionally, hydrogen can be released from the corrodent during electrochemical corrosion reactions [41, 147].

Hydrogen atoms are produced via reduction of hydrogen ions, prior to the formation of hydrogen gas [38]:

$$2H^+ + 2e^- \rightarrow 2H_{adsorbed} \tag{2.14}$$

This reaction preferentially occurs at the crack tip due to increased pH of the corrodent in that region [38].

The hydrogen embrittlement process is thought to occur as a result of a number of mechanisms. These include:

- Molecular hydrogen gas released from voids accumulates and gives rise to an **internal pressure** [38, 41].
- **Metal hydrides** are formed at the tip of the crack; these hydrides are brittle and can be fractured resulting in crack propagation [38].
- Hydrogen is absorbed at the crack tip at a faster rate than it is able to diffuse away, resulting in a **reduction of surface free energy** [38, 41, 127]. (A form of adsorption-induced cleavage, with hydrogen as the absorbed species [38, 41, 127].)
- **Plastic deformation** ahead of the crack is promoted by hydrogen diffusion [38].

As discussed previously, an anodic applied potential accelerates cracking by SCC [33]. When considering hydrogen evolution, the opposite is true, the application of a cathodic potential results in the acceleration of hydrogen evolution and so as increase in the concentration of hydrogen at the tip [33, 41]. As such, if an applied cathodic potential gives rise to an increase in the rate of crack propagation, cracking is considered to be due to hydrogen embrittlement [33, 41].

2.4.2.5 Localised Surface Plasticity

In the localised surface plasticity model, SCC propagation occurs as the result of microstructure ahead of the crack tip [19]. The active site at the crack tip and the surrounding passive surfaces result in galvanic corrosion between the two (Figure 2.17e) [19]. The resultant high local anodic current densities cause the formation of a defect structure at the crack tip that becomes a rupture site [19]. The rupture site causes plastic deformation of the region ahead of the crack tip [19]. This event is enhanced by the comparative higher strengths of the passive surfaces surrounding the crack tip [19].

2.4.2.6 Film Rupture or Anodic/Slip Dissolution

The film rupture model (also known as the anodic or slip dissolution model) proposes that crack growth proceeds via localised anodic dissolution, shown in Figure 2.17f [19, 38, 57, 126]. The walls of the crack are passive as they are protected by a passive film such as an oxide [19]. This

film is ruptured at the crack tip by plastic strain [19]. This process can be cyclic resulting in further propagation.

Cracks advance along anodic pathways. These form as a result of heterogeneities within the microstructure of the metal [38]. Anodic paths have a higher susceptibility to corrosion when compared to the bulk, resulting in accelerated corrosion along these pathways [33]. In sensitised materials anodic zones are located along GBs, this leads to preferential corrosive attack in these areas resulting in IGSCC.

2.5 Specific Material-Environment Systems

2.5.1 Austenitic Stainless Steel in Chloride Solutions

Chloride solutions are known to cause pitting corrosion in austenitic stainless steels and, with sufficient stress, SCC. These processes can lead to failure of the material, depending on the application this can lead to significant risk. Localised corrosion occurring in chloride environments is relevant in a huge number of industries and applications. This includes engineering, marine, and nuclear applications, where susceptible materials may be used structurally, in high pressure vessels, or for containment where failure can be catastrophic [148].

2.5.1.1 Chloride Cracking in Austenitic Stainless Steel

Austenitic stainless steels undergo SCC in solutions containing chloride, particularly at elevated temperatures [33, 42]. This can be exacerbated by pitting corrosion, where the chloride becomes concentrated within the pits [33, 42]. Cracks due to chloride cracking can propagate even at low stresses, such as the residual stresses from cold working [33]. SCC cracks can proceed by TGSCC or IGSCC in this system [33, 127]. In the case of TGSCC, the mechanism is thought to be a result of film-induced cleavage [33]. IGSCC occurs when the stainless steel is sensitised, as discussed previously, and is theorised to be due to active path dissolution [33].

2.5.1.2 Localised Corrosion of Austenitic Stainless Steel in Chloride Solutions in the Absence of Stress

It has already been discussed that a key motivation in this thesis is the safe storage of ex-service AGR fuel. It has also been discussed that thermally sensitised stainless steels may act as proxy materials for irradiated stainless steels. In this thesis, localised corrosion events are studied on a thermally sensitised AISI Type 304 stainless steel polarised in a 1% (i.e. 10,000 mg L^{-1} or 0.17 M) sodium chloride solution. It should be noted that the chosen chloride concentration is much higher than that those typically maintained in pond storage, though these concentrations may be encountered in a geological disposal facility (GDF) [47].

2.5.1.3 Pitting

Pitting events on stainless steels have been the focus of considerable research [34, 110, 114, 122, 149–152]. A number of different techniques have been implemented in previous works, these include, but are not limited to: optical monitoring techniques [34, 114, 151], electrochemical noise (EN) [153], electrochemical impedance spectroscopy (EIS) [154], and scanning electron microscopy (SEM) techniques [151, 154].

From this existing body of research, a theory regarding the order of events and the mechanisms that lead to pitting corrosion in chloride solutions has been developed. Some of these events/mechanisms have been discussed more generally in Section 2.2.2.3.

There are two critical steps the give rise to pitting, the first is passive film breakdown, and the second is pit growth stability (from a metastable pit to a stable pit). Chloride ions can interact with the passive layer ultimately resulting in local penetration [42]. Thus far, nucleation sites for localised corrosion events have not been conclusively identified, though they often occur at discontinuities on the surface, such as at GBs or inclusions [110, 111, 121, 149, 155]. This is dependent on the thermal history of the sample.

It is argued that, as the number of metastable pits formed on the surface does not vary with chloride concentration or polarising potential, these pits must initiate at specific microstructural features on the surface [122]. A significant body of literature exists regarding MnS inclusions to be the most significant type of SPP when considering pit initiation, particularly in unsensitised stainless steels [56, 121, 122, 156, 157]. This is supported by the reduction of pit formation following laser-melting of the stainless steel, which reduces MnS inclusion size substantially [122]. The exact mechanism of pit initiation at MnS inclusions is debated, as well as the effects of parameters such as inclusion size/geometry and composition [157]. It is possible that the MnS inclusion is dissolved, alternatively it may act as a crevice corrosion initiation site [121, 156]. Some studies report that adsorption of chloride occurs preferentially at MnS inclusions compared to the bulk, leading to a reduction of the inclusion's activation potential [157]. Dissolution of the MnS inclusion then produces thiosulfate ions [121, 157]. Passivity breakdown can occur as a result of adsorbed sulfur following MnS inclusion dissolution [157].

Whilst the MnS inclusion is clearly significant when considering pit initiation, other SPPs are not ruled out, such as oxides or carbides [56, 155]. Pit initiation/IGA of GB carbide precipitates in thermally sensitised stainless steels are considered in more detail in the following section.

If the pit does not repassivate then it will increase in size and subsequently become anodic with respect to the surrounding areas [42]. The pits tend to undercut the surface [148, 149]. The occluded region inside of the pit leads to a build-up of aggressive chemistry that prevents repassivation [112]. Reactions occurring within the pit result in the electrolyte becoming acidified and concentrated in chloride ions [42, 112]. The pH at the anode (inside the pit) decreases due to metal cation (produced via dissolution of the metal) hydrolysis [112, 119]. As the anode and the cathode are separated by a distance anion will migrate towards the anode, therefore enriching

this region with Cl^- ions [112].

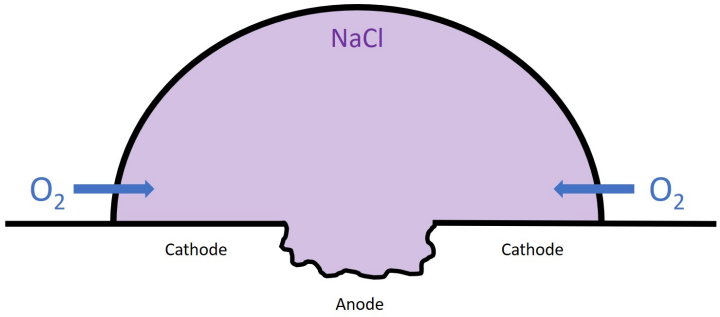

Figure 2.18: Schematic showing pitting in a droplet of NaCl. The passive surface acts as a cathode and the active pit acts as an anode.

The morphology of pits formed in the absence of GB sensitisation stainless steels are often described as lacy pits as they have perforated lace-like covers [122, 149]. These covers exacerbate the build-up of aggressive chemistry allowing for further pit propagation [149]. The mechanism for this morphology in neutral solutions was described by Ernst *et al.* as a result of rapid diffusion at the edges of the pit leading to repassivation [149]. In the deeper central regions of the pit, dissolution continues leading to an undercutting of the repassivated material, eventually rupturing the surface from beneath [149]. This then leads to rapid diffusion at the edge of the pit and subsequent repassivation [149]. This process then repeats [149].

Metastable pit propagation is dependent upon this lacy pit cover [122]. If the pit reaches stability, i.e. its own depth acts a sufficient barrier to diffusion to maintain an aggressive chemistry, the pit cover becomes moot [122]. Whereas, if the loss of this cover occurs prior to stability being reached, the pit will repassivate [122].

2.5.1.4 IGA

Reports state that pitting corrosion has an important relationship with chromium content [86]. In sensitised stainless steels, pitting can therefore occur along chromium depleted GBs: a form of IGA [122]. This has also been related to iron enrichment in these regions [122], as well as the presence of $M_{23}C_6$ precipitates [99]. Indeed, the exact role of sensitisation in pitting corrosion is debated.

Cheng *et al.* performed a wet-dry cycle study on sensitised (700°C for 24 hrs) and unsensitised Type 304 stainless steels in droplets of 50 μL 1.0 M $MgCl_2$ solution in order to isolate the different pitting corrosion mechanisms [99]. Cheng found that in unsensitised Type 304 stainless steel, pitting corrosion initiated at MnS inclusions or oxides [99]. Whereas in the thermally sensitised samples, pitting initiated, and somewhat propagated, along GBs [99]. Cheng posited that this occurred at GB carbides [99]. Pits also formed with a higher probability, a larger average size, and with a more irregular shape than for the unsensitised samples [99].

In another study performed by Burnett *et al.*, thermally sensitised (650°C for 24 hrs) samples of Type 316H stainless steel were pitted in a solution of 0.1 M NaCl [120]. Burnett found that IGA initiated from a pit, however no IGA was observed in regions remote from the pit [120]. This was thought to be the result of the aggressive chemistry generated within the pit [120]. However, following the initiation of IGA, corrosion along GBs was favoured over pit growth [120]. Thus, indicating that pitting and IGA act both synergistically and in competition. Burnett also found that pitting corrosion preferentially occurred at HAGBs, followed by a CSL Σ 11 GB, and finally slip bands [120]. It was noted that this was consistent with the respective boundary surface energies (i.e. high energy boundaries pitted preferentially) [120].

2.5.2 Sensitised Austenitic Stainless Steel in Thiosulfate Solutions

Thiosulfate containing solutions are versatile and are used across numerous industries including nuclear, petroleum, oil and gas, pulp and paper, and chemical [158–160]. However, thiosulfates are also present in a number of other unwanted instances, as a result of contamination for example [158].

Thiosulfates are known to be an aggressive species and can result in a number of forms of corrosion including pitting, crevice corrosion, and SCC [158, 161, 162]. In particular, thiosulfate solutions are known to induce IGSCC within sensitised austenitic stainless steels when under tensile stress at ambient temperatures [101, 103, 126, 147, 158, 160, 161, 163–169]. This is particularly relevant within this thesis and so will be considered in more detail.

2.5.2.1 IGSCC of Sensitised Type 304 Stainless Steels in Thiosulfate Solutions

In this thesis, IGSCC is induced and studied by deforming a sample of thermally sensitised AISI Type 304 austenitic stainless steel in a solution of 395 mg L^{-1} aqueous sodium thiosulfate.

A number of previous studies have been performed analysing the IGSCC behaviour of stainless steels within thiosulfate solutions, largely conducted by reaction sensing techniques [101, 103, 158, 160, 164–166, 168]. These studies have focussed on a variety of factors including mechanisms of crack initiation and propagation, the effect of solution concentration, system electrochemistry, to name a few. An overview of the various mechanisms and key observed features pertinent to this thesis is given in this section.

In 1981, Isaacs *et al.* investigated IGSCC of thermally sensitised Type 304 stainless steel (24 hrs at 600°C) in very low concentration (around 6×10^{-7} M or 0.0006 mM) using constant extension rate tests (or slow strain rate tests (SSRTs)). [163]. Isaacs found that sensitised stainless steels are very susceptible to IGSCC in the presence of thiosulfates, noting that the minimum concentration of sulfur required in the solution was approximately 40 ppb [163]. From this study it was determined that the SCC process is electrochemically controlled [163]. Isaacs suggested a film rupture and anodic dissolution mechanisms whereby film rupture occurred through a salt layer at the crack tip [163]. The precipitation of this salt layer was postulated

to result in a reduction of dissolution rate, whilst subsequent rupture of this layer allowed dissolution to proceed [163].

In 1982, Newman *et al.* performed similar SSRT tests on a thermally sensitised Type 304 stainless steel (24 hrs at 600°C) in 0.6 mM sodium thiosulfate [164]. Newman noted that the formation of sulfur was somehow important in the promotion of cracking, possibly by effecting the entry of hydrogen resulting in embrittlement [164]. However, Newman argued that a dissolution mechanism was determined to be more likely for this particular system, in which sulfur or sulfide ions promote dissolution of iron or nickel [158, 164]. Newman also considered that, in order to be consistent with the electrochemical observations made, the SCC mechanism must include a mechanical cracking step [164]. As this mechanical step was considered unlikely to be due to hydrogen embrittlement, Newman postulated that it was the result of strain-generated martensite at the GBs [164]. This also explained the high crack velocities of up to 8 μm s^{-1} that could not be explained by a dissolution model alone [164].

Newman developed the following model for the cracking process:

1. Cracking initiates due to repeated film rupture and dissolution at GBs. Extending approximately 150 nm with each film rupture event [164].

2. GB martensite formation occurs ahead of the crack tip as a result of localised strain [164].

3. Dissolution results in a sharpening of the crack tip which facilitates GB separation through the martensite region [164].

4. Following crack propagation through the martensite region the crack blunts [164].

5. Dissolution results in a sharpening of the crack tip and the process repeats from point 4) [164].

Also in 1982, Sieradzki concurred that anodic dissolution is likely the principle cause of IGSCC for this particular system [159]. Stating that it is unlikely that SCC caused by thiosulfate will differ in mechanism from cracking caused by polythionic acid [159]. Sieradzki also commented on the role of elemental sulfur in the cracking process, remarking that its role was "undoubtedly to delay or prevent repassivation of the chromium depleted GB material" [159]. SCC then proceeded by anodic dissolution. Though an elemental sulfur layer may assist in hydrogen entry at the crack tip, it was not considered necessary for the SCC process [159]. The rapid crack velocities previously noted by Newman *et al.* were also explained by an intrinsic GB weakness, possibly due to strain-generated martensite or impurities [159, 164].

In 1988, Isaacs *et al.* performed additional measurements using an in-situ scanning vibrating electrode technique (SVET) to investigate crack initiation in a sample of Type 304 stainless steel in 0.06 mM sodium thiosulfate [103]. Isaacs determined that crack initiation must be stress driven, as no indications of initiation event were detected for unstressed specimens [103].

Isaacs postulated that the initiation was more complicated than passive film rupture at the GBs resulting in the exposure of chromium depleted regions [103]. This was demonstrated via scratching tests performed on unstressed specimens in which the passive film was disrupted, and no prolonged dissolution occurred [103]. Though this may have been the result of specific regions on the surface being more prone to initiation events [103]. Isaacs concluded that any mechanism would require a build-up of aggressive chemistry, noting that the GB type was likely a factor in determining whether a particular GB will crack [103].

In 1992, Wells *et al.* detected corrosion pulses associated with microcracking across single GB facets for a similar system of thermally sensitised Type 304 stainless steel (24 hrs at 650°C) in a 0.5 M thiosulfate solution [160]. As previous, these tests implemented an SSRT method [160]. Wells found that crack initiation occurred due to non-uniform deformation at GBs [160]. Subsequent crack propagation extended a few GB facets before stopping [160]. This was observed on multiple occasions by SEM analysis. Post-SCC analysis of the fracture surface by energy dispersive X-ray spectroscopy (EDX) also revealed deposits of sulfur-rich precipitates [160]. Cracks were commonly found to arrest at GB triple points, where a directional change is required, creating a microstructural barrier [160]. In addition to these results, Wells found that sensitisation is key within the cracking mechanism, as specimens sensitised for a shorter duration of 1-4 hrs did not fail by IGSCC [160].

Furthermore, as strain was increased, Wells found a reduction in the frequency of microcracks [160]. This was explained by strengthening due to formation of strain-induced martensite [160].

Gomez-Duran *et al.* performed a series of measurements in 2003 and 2006 investigating the same SCC system for a sample of Type 304 stainless steel thermally sensitised at 650°C for various durations up to 24 hrs and a sodium thiosulfate concentration of 0.5 M using compact tension (CT) specimens [165, 166]. As with Wells' findings, the cracks were found to grow as discrete microcracks extending a short distance of the order of the grain size [160, 165]. Gomez-Duran determined that crack growth was the result of a hydrogen fracture mechanism, and not due to slip or dissolution, thus disagreeing with Newman's findings [164–166]. This was argued on the basis that the fracture dimension was too large to be explained by a slip or dissolution/repassivation mechanism [165, 166].

Within this work, the role of sulfur within the solution was noted, as with previous works [160, 164–166]. Following SCC tests, yellow sulfur deposits were observed within the cracks, similar to that observed previously by Wells [160, 165]. Gomez-Duran argued that, whilst previous works had indicated crack growth enhancement was related to iron and nickel dissolution promoted by the presence of sulfur, this would not affect stainless steels if the chromium content is sufficiently high [165]. As such this mechanism would only be relevant along sufficiently sensitised GBs [165]. Thus, reinforcing Wells' previous observations [160]. In addition to this process, it was suggested that thiosulfates enhanced crack growth by adsorbed sulfur catalysing the entry of hydrogen into the matrix ahead of the crack tip [165, 166]. This is due to sulfur

at the tip inhibiting the recombination of hydrogen atoms, and thereby promoting hydrogen entry and resulting in embrittlement [158]. This process may occur by a number of mechanisms. Once the hydrogen enters the matrix it is transported by the stress field into the region ahead of the crack tip and recombines with voids present due to creep at chromium depleted GBs [158]. The pressurisation of voids at the crack tip GB can then result in an enhancement of the hydrostatic stress [158, 165]. This can then result in a microfracture event if the stress exceeds the fracture stress [158, 165]. Thus, increasing brittle fracture frequency and therefore crack growth rate [158]. Alternatively, hydrogen causes the embrittlement of strain-induced martensite [158]. This results in a region ahead of the crack tip where the crack will next progress through [158]. Hydrogen can also react with segregated metalloids resulting in a decohesion of the GB, once again causing an increase in crack growth rate [158, 165].

Gomez-Duran also performed tests on unloaded specimens within a 0.5 M sodium thiosulfate solution [166]. It was found that the solution initiated and propagated localised corrosion processes [166]. The effect of stress was therefore theorised to increase the rate at which this occurs [166]. This conflicts with previous findings by Isaacs within a 0.06 mM sodium thiosulfate solution [103].

To contrast the results of Gomez-Duran, Roychowdhury reported that a film rupture/anodic dissolution mechanism [168]. This agrees somewhat with Newman's findings [164]. Roychowdhury *et al.* investigated the electrochemical behaviour of a thermally sensitised Type 304 stainless steel (2 hrs at 650°C) in a 1, 10 and 1000 ppm thiosulfate solutions using an SSRT technique in 2004 [168]. IGSCC was found to occur within solutions with 10 ppm thiosulfate or greater [168]. Electrochemical measurements of crack initiation and propagation were explained by the presence of an active path (sensitised GBs) and an aggressive solution resulting in a film rupture/anodic dissolution process [168]. Roychowdhury also measured the presence of a magnetic phase, thought to be strain-induced martensite, on all fracture surfaces in agreement with Newman [164, 168].

Roychowdhury's conclusions agreed with those drawn by Kovac later in 2010 [126]. Kovac *et al.* monitored IGSCC processes in a system of thermally sensitised Type 304 stainless steel (650°C for 24 hrs) under constant load in a solution of 0.5 M aqueous sodium thiosulfate [126]. Simultaneous EN, acoustic emission (AE) and elongation measurements were performed, these methods are described further in Section 2.6 [126]. Kovac deduced that crack propagation occurred by intergranular dissolution (i.e. active path) following film rupture due to local strain [126]. This occurred in discontinuous steps [126]. In some cases, a ductile fracture mechanism was observed, this was thought to be the result of specific GB types being more or less resistant to SCC processes [126]. Ductile facture was more frequent at higher stresses leading to the conclusion that crack velocity also played a role in GB susceptibility [126].

To further previous studies in which the ability of thiosulfate to initiate localised corrosion in the absence of stress, in work performed by Choudhary in 2016, it was found that thiosulfate ions

alone could not initiate breakdown of the passive film [161]. Potentiodynamic tests were performed on samples of Type 316L stainless steel in sodium thiosulfate solutions with concentrations up to 0.5 M. It was noted that the surface following exposure to the thiosulfate solution was "shiny, bright and spotless" [161]. Therefore, whilst the thiosulfate ion may assist in anodic dissolution, it does not assist in the initial passive film breakdown [161]. This is in agreement with Isaacs and Wells but disagrees with the observations of Gomez-Duran [103, 160, 166].

Summary A number of conflicting models have been proposed. Crack initiation and propagation mechanisms are yet to be conclusively identified. The current literature may be coarsely summarised into two main theories: film rupture and anodic dissolution, and hydrogen embrittlement. The key conclusions from the literature can summarised as follows:

- **Film rupture and anodic dissolution** - This model for cracking was suggested by Newman *et al.* with strain-induced martensite causing an embrittlement of the GBs ahead of the crack tip. The processes behind the initial rupture event are not clear. This model has been partially or fully accepted by some authors [126, 158, 159, 163, 164, 168].

- **Hydrogen induced fracture** - This model for cracking was initially suggested by Gomez-Duran to explain brittle microcrack occurring along multiple GB facets and has also been accepted by a number of authors [158, 165, 166].

- **The effect of sulfur at the crack tip resulting in resistance to passivation has been generally accepted** - The metastable thiosulfate anion is known to form elemental sulfur at the crack tip. Adsorbed sulfur then prevents repassivation. The exact mechanism for this is still under some debate. The acceleration of SCC may be due to enhanced dissolution of iron and nickel at sensitised GBs [147, 158, 160, 164] and/or acting as a catalyst to hydrogen entry into the matrix ahead of the crack tip possibly resulting in embrittlement [147, 158, 165, 166].

- **Strain-induced martensite is also generally accepted to form at the crack tip** - Martensitic transformation due to strain is dependent upon the stability of austenite [144]. Strain-induced martensite at GBs has implications for the initiation and propagation of SCC, as its mechanical and corrosion properties differ from austenite [160, 168]. Martensite is more resistant to deformation than austenite, leading to a reduced crack velocity [160, 168]. However, martensite is more susceptible to hydrogen induced cracking than austenite [144]. Martensite formation at the crack tip will therefore promote hydrogen diffusion and accumulation ahead of the crack tip [144].

- **The degree of sensitisation is key in susceptibility to IGSCC in thiosulfate solutions** - Sensitised GBs give rise to GB dissolution processes and therefore plays a key role

within this system [103, 160, 167, 168]. Works have also noted a possible influence from GB type, due to variations in degree of sensitisation [103, 126].

- **The effect of thiosulfate in the absence of stress is unclear** - It is clear that the thiosulfate ion results in anodic dissolution, however there are conflicting works regarding its role in the initial breakdown of the passive film. In some works it is accepted that thiosulfate does not result in anodic activity or localised corrosion in the absence of stress [103, 160, 161, 164]. However, in other works thiosulfate was found to initiate and propagate localised corrosion processes in such a way that the role of stress was considered to be secondary [166]. Overall, there has been very few studies that consider such behaviours [158].

- **Acidification can occur at the crack tip** - Localised acidification at the crack tip has been suggested within some works [159, 163]. Such a process would aid sulfur formation from disproportionation reactions and promote hydrogen evolution [147, 158, 164]. However this acidification is limited by partial buffering of the crack tip solution [159, 160].

2.5.2.2 Sensitised Type 304 Stainless Steels in Thiosulfate-Containing Solutions in the Absence of Stress

Comparatively little literature is available on the effect of thiosulfate-containing solutions in the absence of stress. Key studies have already been discussed in the previous section. These studies reported varying effects [161, 166].

Isaacs *at al.* found no indication that corrosion initiation had occurred [103]. This was also found to be the case during scratching tests, where the passive film was damaged, but dissolution was not prolonged [103]. Similar observations were reported by Wells, Newman, and Choudhary in separate works [160, 161, 164]. Noting that thiosulfate alone was not capable of initiating passive film breakdown [161].

Results reported by Gomez-Duran *et al.* conflicted these observations [166]. In this work thiosulfate was reported to initiate and propagate localised corrosion processes [166]. However, precise reaction sites were not reported as experiments were performed by reaction sensing techniques.

Work has also been performed studying systems where both thiosulfate and chloride ions are present. This can result in enhanced pitting corrosion where these ions have been observed to act synergistically [121, 158, 161, 170]. The thiosulfate ion is posited to lower the pitting potential of Type 304 stainless steels [158, 170]. Chloride ions then breakdown the passive film, forming a pit that is further stabilised by thiosulfate through enhanced dissolution by adsorption of sulfur [121, 158, 161, 170, 171]. This synergy is also relevant following the dissolution of MnS inclusions as thiosulfate can be produced [158].

SCC can also occur under these conditions in sensitised or unsensitised stainless steels following the application of stress [158, 172]. These studies are described in greater detail in other works[158, 172].

2.6 Techniques For The Detection and Observation of SCC

A plethora of physical and electrochemical methods have been developed for SCC testing and observation such that various parameters may be ascertained [126]. These include surface and volume measurements such as optical microscopy [108, 173], electron microscopy techniques [174] and atom probe tomography (APT) [175], and reaction sensing techniques such as EN and SVET [19, 176]. Techniques may be separated further into indirect (ex-situ) and direct (in-situ) methods. Some of the commonly implemented ex-situ and in-situ techniques are shown in Figures 2.19 and 2.20, respectively. These techniques are described in detail in other works [19], a brief description in the context of SCC analysis is given here.

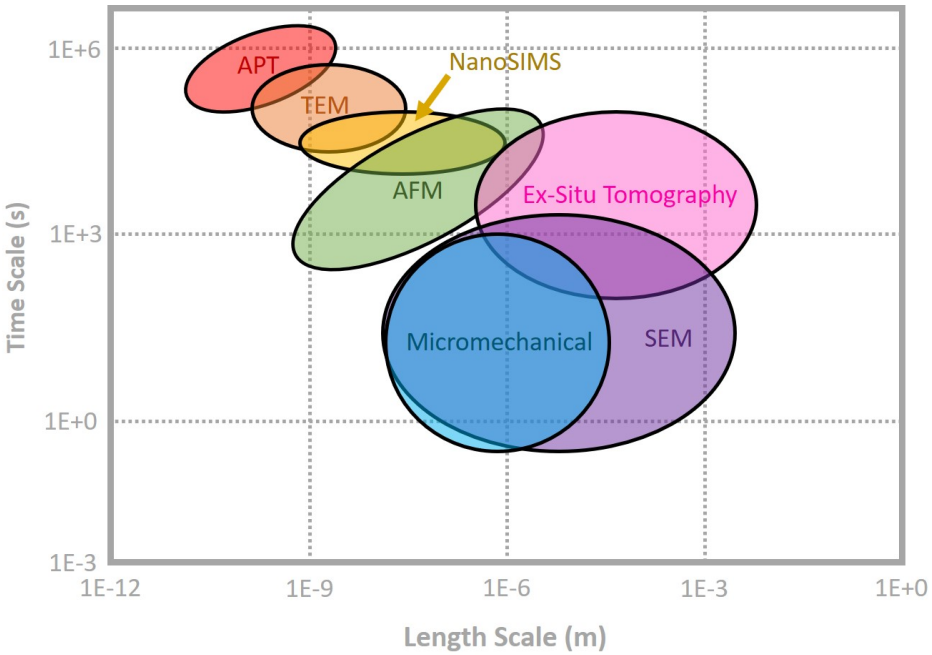

Figure 2.19: A graph indicating the approximate time- and length-scales of commonly implemented indirect (ex-situ) techniques: APT, TEM, atomic force microscopy (AFM), ex-situ tomography (focussed ion beam (FIB) tomography or electron tomography), micromechanical techniques, and SEM. Adapted from [19].

The majority of high-resolution SCC characterisation techniques are indirect techniques. These techniques are capable of producing detailed analysis of chemistry (such as APT), crystallography (such as SEM and TEM techniques) and morphology/topography (such as atomic force microscopy (AFM)). However, these techniques are limited by long timescales or require

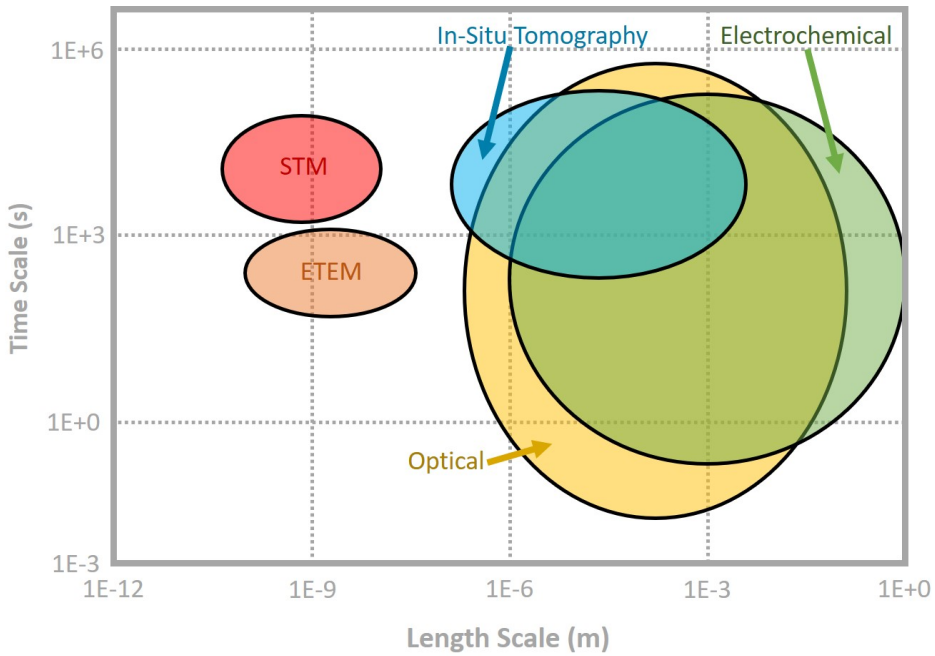

Figure 2.20: A graph indicating the approximate time- and length-scales of commonly implemented direct (in-situ) techniques. Scanning tunnelling microscopy (STM), electrochemical TEM (ETEM), in-situ tomography (X-ray tomography), electrochemical techniques, and optical techniques. Adapted from [19].

environments that are incompatible with corrosion studies (such as a vacuum). These analytical methods are described in more detail in Chapter 3. Whilst these techniques can offer valuable information about the system, the order of events that give rise to the final state has to be inferred.

Many of the methods for the in-situ monitoring of corrosion events are electrochemical [32, 101]. Corrosion processes can be monitored relatively simply by employing direct current (DC) experiments, or potentiodynamic experiments, providing some insight into the electrochemical behaviour of the system under investigation [168, 177]. However, in order to establish a more detailed understanding of the complex mechanisms occurring, alternating current (AC) techniques (such as EIS [178] or EN [32, 101]) may be performed and have previously been used to interpret the processes occurring during corrosion [177]. However, these methods are severely limited by their spatial resolution [177]. As a result, considerable effort and research over the past few decades have produced improved techniques with increased spatial resolution capabilities [177]. These include: Localised EIS (LEIS), scanning Kelvin probe (SKP) [178], and SVET [157], among others [177, 179]. These techniques are described further in other works [19]. Whilst these techniques can reveal the order of events occurring during SCC processes, they are often limited by their resolution if applied to the earlier stages of SCC, in terms of spatial as well as temporal in some cases. Furthermore, it should be kept in mind that SCC is both mechanical and

electrochemical in nature. As a result, electrochemical techniques often do not provide the whole picture.

Techniques that offer complementary information, i.e. chemistry, structural, sub-surface etc. can be implemented to study the same system, this is termed correlative microscopy. The combination of techniques, particularly electrochemical alongside non-electrochemical, could provide considerable insight into the mechanisms that result in SCC by offering a multifaceted analysis [180].

2.7 Contact Mode High-Speed Atomic Force Microscopy (HS-AFM)

The techniques described in the previous section operate over a range of length- and time-scales, however, techniques that offer the highest resolution seldom facilitate the conditions necessary for in-situ measurements. The work presented in this thesis uses a newly developed high-speed AFM (HS-AFM) to obtain the high temporal and spatial resolution necessary for such measurements. An indicated in Figure 2.21.

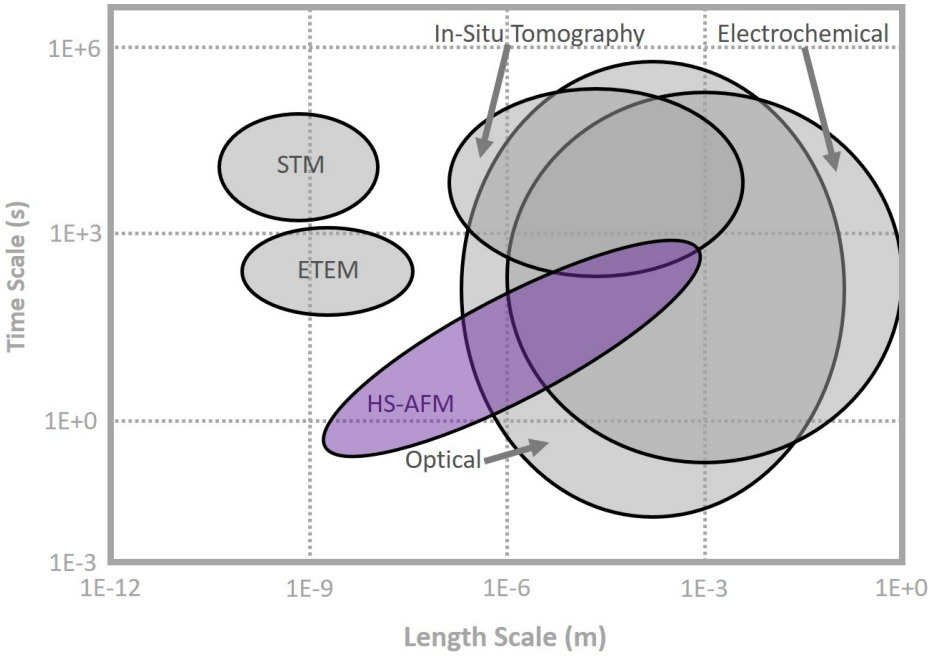

Figure 2.21: A graph indicating the approximate time- and length-scales of commonly implemented direct (in-situ) techniques as shown in 2.20 with the addition of HS-AFM. Adapted from [19].

2.7.1 Atomic Force Microscopy (AFM)

AFM is one of a group of techniques known collectively as scanning probe microscopy (SPM) [181]. AFM was invented by Binnig, Quate, and Gerber in 1986 [182] and has since revolutionised the field of nanoscience, enabling surface characterisation with exceptional resolution in a range of environments [181, 183].

Integral to an AFM is a cantilever with a sharp tip at its end that probes the surface of the sample [184–186]. This tip is raster scanned across the surface and the mechanical response of the microcantilever is monitored as shown in Figure 2.22. The three main imaging modes most commonly implemented are: non-contact mode, intermittent contact mode and contact mode [181]. The cantilevers mechanical response is fed into a feedback loop that moves the sample stage such that an initial condition (a specified deflection angle or cantilever displacement) is recovered [187]. This step is often quite time consuming as a result of the slow response times of the mechanical components [187]. This information is used to build a 3D image of the topography of the sample surface [184, 188].

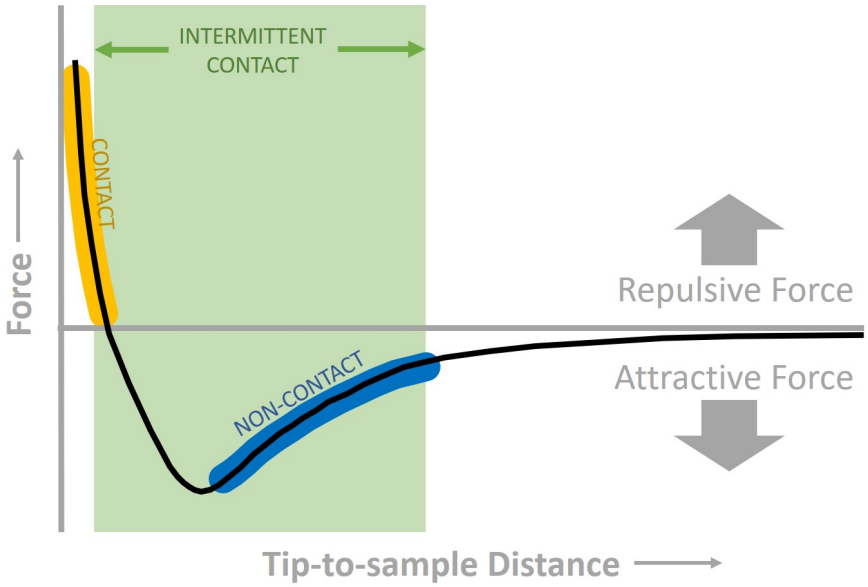

Figure 2.22: A graph indicating the relative forces between tip and sample for each AFM imaging mode. Adapted from [20].

In comparison to other visualisation techniques, AFM offers a multitude of advantages [188]. AFM has the capability for high-resolution imaging of structures and the measuring mechanical properties at nanometre scales in varying gaseous, liquid and vacuum environments [181, 183–185, 189, 189, 190]. AFM is not limited to low pressure or vacuum environments making it a valuable tool for studying solid-liquid interfaces, offering an edge over other techniques such as SEM [181]. As such, it offers a multitude of applications in materials, surface and biological sciences, and is considered one of the most versatile and significant tools in nanoscience [184, 189].

Furthermore, sample preparation for AFM analysis is quick and non-destructive [181], and does not require staining or labelling of the sample [188, 189], nor is it required that the sample be electrically conductive [183, 191].

AFM quickly became a popular technique within the biological sciences due to its unique ability to image molecular systems in-situ [181]. However, a typical image is collected over a period of 10-100 seconds, rendering it unsuitable for measurements of dynamic processes or macro-sized samples; limiting it to static snapshots [181, 183, 184, 186–188]. The clear potential of AFM quickly gave rise to considerable effort to enhance the image rate and address its other limitations, ultimately resulting in the development of HS-AFM [181, 192].

2.7.2 Contact Mode HS-AFM

Contact mode HS-AFM was developed at the University of Bristol in 2004. It is capable of sub-second temporal resolution [181, 189]. This allows for the observation of dynamic processes in real-time with nanoscale lateral resolution and sub-nanometre height resolution [181, 189]. This capability extends to gaseous, liquid or near-vacuum environments [189], making it a valuable tool for in-situ studies of dynamic processes. In addition to this, the high pixel rate means it is capable of mapping macro-sized areas with nanoscale resolution [193].

Contact mode is the simplest of the three main imaging modes, and was implemented as the imaging mode for the original AFM [181, 183]. In this mode, the tip of the cantilever is in constant contact with the sample surface [181]. Unlike non-contact mode or intermittent contact mode, contact mode is not limited by the resonant frequency of the cantilever, thereby removing a major constraint on imaging speed [189].

In contrast to conventional AFM, contact mode HS-AFM does not require a control loop, instead, information about the sample surface is determined directly from the cantilever's response [181, 183]. The probe tip maintains contact with the sample surface, even at high scan velocities [183], with little damage imparted to the sample surface or the sharp tip. The low friction felt between the cantilever tip and the sample surface is a result of a hydrodynamical lubrication force due to a thin layer of semi structured water covering both the sample surface and the tip [183]. In addition to this hydrodynamic lubrication force, a hydrodynamic adhesive force enables continual contact at rapid scanning speeds, this is known as squeeze-film damping [183]. This phenomenon is key to the functionality of contact mode HS-AFM and removes the need for a control loop [183]. As a result, the contact mode HS-AFM is able to successfully image delicate samples with a tip speed in excess of 0.5 mm s^{-1} [183].

2.7.3 Opportunities For Application in Corrosion Science

The nanoscale initiation sites and liquid environment of corrosion are ideal for investigation by AFM, prompting its application in previous studies of localised corrosion phenomena [150, 155, 194, 195]. This includes pitting corrosion and IGA [150, 195], as well as crack propagation

[196–198]. However, with the limited imaging rate capabilities a vast amount of information is lost.

In 2000, Williford *et al.* produced time-lapse images using electrochemical AFM (ECAFM) of the early stages of pitting (in 1000 ppm sodium chloride solution) and IGA (in oxalic acid) of thermally sensitised Type 304 stainless steel [150]. Williford observed that IGA began in the GB between carbides and proposed that this was a result of the carbides being cathodic with respect to the bulk matrix, and thus being partially cathodically protected [150]. Observations were also made of pit growth from an irregular shape into a round pit, with island formations over a period of 6 minutes [150]. However, Williford experienced a number of limitations associated with using AFM. Firstly, time-lapse images were obtained at 3600 second intervals (once every 10-20 cycles of polarisation), this meant that reactions occurring between these intervals must be inferred [150]. Additionally, due to the speed at which images were obtained, in combination with the lateral size of the window, Williford was unable to image localised corrosion events as they occurred as a result of not "being in the right place at the right time" [150].

HS-AFM is uniquely capable of direct imaging of nanoscale dynamic processes in various environmental conditions at sub-second temporal resolution [181, 186–188, 190, 199, 200]. These capabilities make it a viable tool for in-situ observations of corrosion initiation events [84, 181]. This has been demonstrated in previous studies [84, 201]. Laferrere *et al.* have previously performed experiments using the Bristol contact mode HS-AFM to image nanoscale pitting and dissolution events, with parallel electrochemical control [84]. This work demonstrated the ability of HS-AFM to image steels in liquid environments and the potential for new insights into corrosion mechanisms at nanoscales [84]. The work presented within this thesis aims to build upon this previous investigation and further substantiate the potential of HS-AFM within corrosion studies. Though it should be noted that the HS-AFM will not be able to measure later stages of SCC or pitting where the crack/pit is deeper than the height of the tip, as the tip is in constant contact with the surface during imaging. For this reason, it is the initiation and very early propagation stages that are suited to analysis by HS-AFM. These stages are currently not well understood due to the spatial and temporal resolution limitations of current techniques, as well as the environmental requirements for such a measurement, thus offering an exciting opportunity for study.

2.8 Summary

Despite general conditions for SCC being known, it remains difficult to predict due to its non-stationary nature, this renders the safe application of stainless steels and other engineering alloys in nuclear power systems a challenge [32, 44]. The mechanisms involved in SCC remain a source of much ongoing research. The development of accurate prediction methods and technologies for SCC is important for the safe and economical running of nuclear power plants, as well as in

various other applications [32, 35, 45].

It is clear that considerable work is needed in order to ascertain which models are valid for specific metal-environment combinations. Techniques in which SCC processes can be imaged non-destructively and in-situ are of particular importance for the understanding of the physical mechanisms, and the sequence in which they occur [40]. Quantitative analysis also yields valuable data that may be used to test and validate models.

HS-AFM is now an established technique. The application of HS-AFM for the visualisation of localised corrosion of stainless steels is of particular interest. For the study of localised corrosion, in particular the initiation stages, high spatial and temporal resolution are both necessary. The increased speed of HS-AFM not only allows for direct imaging of dynamic nanoscale events, but also for the imaging of macro-sized areas on the sample surface without any drop in resolution. This is particularly important for detailed pre- and post-corrosion comparisons as well as higher throughput allowing for statistically significant data.

Within this thesis, localised corrosion events and SCC initiation are studied in samples of thermally sensitised stainless steel using HS-AFM in combination with other analytical techniques. Following this review of theory and literature, the main aims of this thesis (previously stated in Chapter 1) may be further justified: The main aims of this work are summarised as follows:

- **To investigate the conditions that lead to localised corrosion and SCC initiation, considering contributions from factors such as material microstructure, corrosive environments and tensile stresses** - It has already been stated that the SCC system to be studied in this thesis is the IGSCC of thermally sensitised AISI Type 304 austenitic stainless steel in a solution of 395 mg L^{-1} aqueous sodium thiosulfate. This SCC system is generally well-studied however the SCC mechanisms are still debated. The crack progression observed does not fit neatly into any particular model. Also of interest is the synergy between corrosion and stress. Notably, reports of the corrosion behaviour in the absence of stress are varied, with some stating that no corrosion processes take place. In this thesis, sensitised microstructure, the effect of thiosulfate in the absence of stress, and the effects of stress are studied separately (in Chapters 5, 6, and 8, respectively) and together (in Chapters 7 and 8), with the aim of better understanding this synergy.

- **To further understanding of SCC initiation and propagation mechanisms using HS-AFM as part of a novel suite of complementary techniques** - The determining factors that lead to IGSCC susceptibility along specific GBs are yet to be identified. Factors such as the degree of sensitisation, precipitation, and the effect of GB type are considered. Whilst HS-AFM provides in-situ topographic measurements, more complete understanding may be achieved by using this technique in combination with techniques that analyse crystallography (SEM and TEM techniques), chemistry/composition (APT), and sub-surface contributions (FIB tomography). These techniques are implemented in Chapter 7. Thus far

studies of IGSCC induced by thiosulfate have almost exclusively focussed on electrochemical measurements, rather than visualising the events as they occur. By implementing this suite of techniques reaction sites may be more conclusively identified.

- **To explore the capability and potential of HS-AFM for applications in materials and corrosion science** - It is clear that HS-AFM could be applied to a number of different corrosion systems where in-situ observation and quantification would be valuable for predictive models. In particular, observation of crack initiation at the nanoscale by HS-AFM could give valuable insight into the processes that take place within metals during SCC, this is explored in Chapter 8. In order to produce the highest quality topographic analysis, it is also important to properly prepare the surface being analysed. In order to achieve this, various commonly implemented sample preparation techniques are compared and contrasted in Chapter 4 with the aim of identifying an optimal preparation method.
- **To establish new methodologies to optimise HS-AFM for the study of localised corrosion and SCC** - SCC is particularly difficult to study as it occurs stochastically. This highlights a clear motivation to develop an effective and reproducible methodology for in-situ HS-AFM measurements of SCC. This methodology is developed in Chapter 8.

CHAPTER 3

ANALYTICAL METHODS

How does one study such a stochastic effect?
It is difficult to know which method to select
We can start by considering the information one seeks
When attempting to choose from such a range of techniques

A range of analytical methods were implemented for materials characterisation and in-situ and ex-situ study of stress corrosion cracking (SCC) processes. Such a range is necessary as each method is capable of obtaining complementary information at differing resolutions and timescales. SCC is both a physical and a chemical process. It is therefore important that both aspects are considered when characterising such phenomena.

Within this chapter, an overview is given of each technique applied within this thesis. This includes a description of how the technique works, the information attained, and (where relevant) post-analysis processing.

3.1 High-Speed Atomic Force Microscopy (HS-AFM)

High-speed atomic force microscopy (HS-AFM) is capable of producing high resolution topographic maps of microstructures present on the surface of a sample [181]. The contact mode HS-AFM used within this work was developed at the University of Bristol and Bristol Nano Dynamics Ltd. (UK). The high throughput of this technique allowed for large area maps to be collected with nanometre lateral resolution and subatomic height resolution. Data collected over large areas may then be stitched to form a composite map of the region or used to build up statistics about

specific features across the surface, such as size or distribution. Further details regarding the capabilities of this instrument are given in Section 2.7.

3.1.1 Instrumentation

HS-AFM consists of three major hardware components: the scanner, the probe, and the detection system. A schematic diagram of contact mode HS-AFM is shown in Figure 3.1.

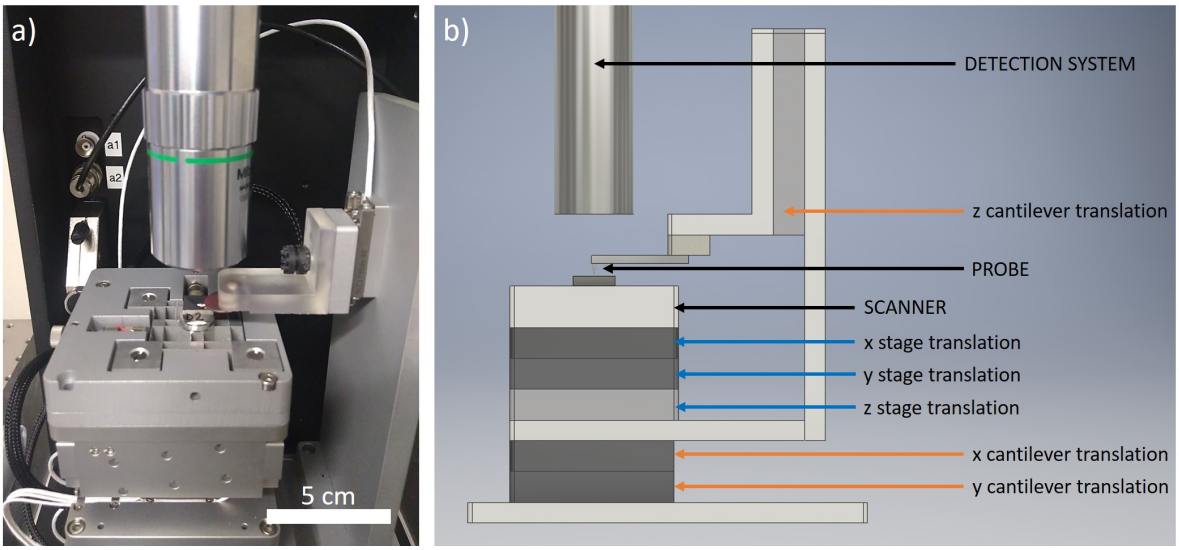

Figure 3.1: a) A photograph showing the contact mode HS-AFM used within this work with inset scale bar, and b) a labelled schematic of the HS-AFM set-up produced in Autodesk Inventor 2019.

The scanner translates the sample beneath the probe. Scans of the sample surface are performed in a sinusoidal raster pattern, as shown in Figure 3.2. This motion is achieved by utilising piezoelectric actuators (piezos) and a flexure mechanism, which allows for independent motion along the x and y axes of motion, whilst maintaining the rigid structure [181, 185]. Piezos have the unique property that their size may be altered by applying a potential, this produces a force that can translate the scanner with nanometre precision [183]. The faster the motion in the fast- and slow-scan directions, indicated in Figure 3.2, the higher the resolution and frame rate, respectively [181]. It should be noted however that topography is currently measured at 2 million pixels per second. This rate is limited by the detection and digitisation systems. It therefore follows that the resolution of any image is dependent upon the frame rate at which it was collected. A frame rate of 2 frames per second is typically implemented such that high resolution images may be collected. However, higher frame rates are possible when necessary. As an example, increasing from 2 to 10 frames per second, will reduce the resolution by a factor of 5, whilst increasing temporal by the same factor.

The probe is a cantilever with a sharp tip that interacts with the sample surface [183]. The

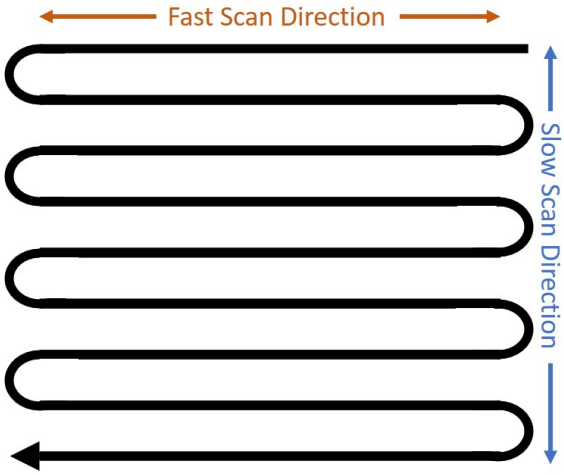

Figure 3.2: A labelled schematic showing a sinusoidal raster pattern.

HS-AFM at the University of Bristol uses MSNL cantilevers manufactured by Bruker from silicon nitride, with a silicon tip. These probes are a type of contact-mode cantilever with a tip radius of 2-12 nm, a tip height of 2-8 μm, and a spring constant of 0.01 N m^{-1}.

As the probe is scanned across the sample surface, interaction forces deflect the cantilever [191]. The detection system measures the displacement of the cantilever such that the topography of the sample surface can be determined. Within the set-up used in this work, cantilever displacement is measured using an interferometric detection system. A frequency modulated laser is scattered off the back of the cantilever and detected by a laser Doppler vibrometer (LDV) that measures the Doppler shift in the scattered light. This allows for the z-displacement of the cantilever to be accurately measured to within ±15 pm. Displacement data is then used to build topographic maps of the surface using bespoke software (Bristol Nano Dynamics Ltd., UK).

3.1.2 Post-Processing and Image Analysis

Topographic data is analysed post-collection using Gwyddion scanning probe microscopy (SPM) data processing software [202] to produce topographic maps, as discussed further in the following sections. The raw data is saved so that reprocessing of the data may be carried out. Statistical analysis of the data may also be performed using bespoke software from Bristol Nano Dynamics Ltd. (UK), which is discussed within the results chapters where relevant.

3.1.2.1 Image Artefacts

Within this section an outline of the most common image artefacts encountered within this thesis is given. Images generated by AFM can suffer from artefacts as a result of the shape of the features on the surface of the sample and the geometry of the probe [21]. These artefacts are typically the result of five primary sources [21]:

- The probe/tip
- The scanner
- Post-processing
- Vibrations
- Other (surface contamination, faulty electronics etc.)

Probe/tip Artefacts Images produced by HS-AFM, as with any tip scanning technique, are a convolution of the probe geometry and the geometry of the features being imaged [21]. Tip convolution can result in inaccurate imaging when the tip is particularly blunt, contaminated with debris, or damaged. The resultant image is a convolution of the actual surface and the shape of the tip, as illustrated in Figure 3.3a. This can be identified by a change in imaging quality or blurred edges of objects on the surface.

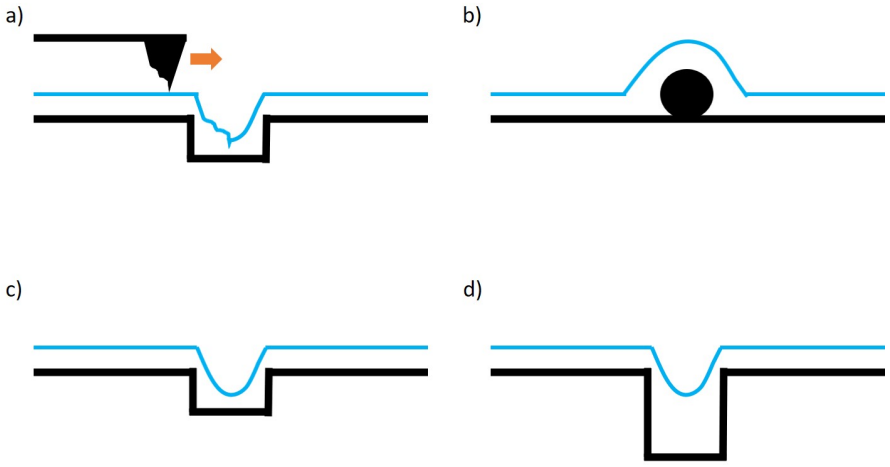

Figure 3.3: A schematic illustrating common artefacts introduced by the probe tip shape: a) damaged or contaminated tip imaging a negative feature, b) blunt tip imaging a positive feature, c) blunt tip imaging a negative feature, d) tip imaging a negative feature with depth greater than tip height. Adapted from [20] and [21].

However, even when imaging with a sharp tip, positive features can appear broadened, as illustrated in Figure 3.3b, and negative features can appear laterally smaller, as in Figure 3.3c [20, 21]. In addition, if a negative feature has a depth greater than the height of the tip, or a width smaller than the tip width, the full extent of the feature will not be imaged and will appear shallower, Figure 3.3d [20, 21].

The effects of probe artefacts can be largely overcome by selecting the optimal probe for the application. Typically, the sharper the tip is, the more accurately the edges of an object may be traced [20, 21]. However, this is also dependent upon the feature being imaged. For example, as

the surface is imaged from one direction (perpendicular to the surface), AFM is unable to image features such as overhangs or edges of vertical features [21, 181, 199].

Scanner Artefacts Artefacts may be introduced into an image as a result of the scanner geometry, such as intrinsic non-linearity (resulting in distorted images), or piezoelectric hysteresis [20, 21].

The scanner artefact most commonly encountered within this thesis is background tilt and bow. Background tilt is introduced as a result of the sample surface not being perpendicular to the probe tip. Background bow is the result of the curved motion of the scanner [20, 21]. The scanner follows an arc as it moves due to one end being fixed (i.e. to the body of the microscope) and one end being free to move [20]. The source of background bow in the HS-AFM used within this work is the trampoline mode of the intrinsic coupled resonant frequencies of the sample and the stage, as the sample is held in a rigid frame [185].

In some cases, images will be non-square as a result of the weight or height of the sample on the stage. In these cases, the longer edge coincides with the fast scan direction.

Post-Processing Artefacts Artefacts introduced during images can sometimes be easily negated through proper post-processing. However, it is sometimes the case that post-processing introduces new image artefacts.

Image tilt and bow as a result of the scanner can be corrected by levelling the data [21]. However, this can introduce a dark band either side of high features within the image [21]. If levelling is required in the x and y directions this can appear as a dark cross centred at the high feature as a result of flattening bringing the mean row and column to zero.

Vibration Artefacts Image artefacts can also be introduced as a result of vibrations. Though every effort is made to vibrationally isolate the equipment, external vibrations can still result in image artefacts. The vibration can be from contact such as through the floor, or from sound waves [20, 21]. Within images they appear as ripples. The high throughput of the HS-AFM when compared to an AFM means that images containing vibration artefacts can be easily collected again.

Other Artefacts The final type of artefact is typically introduced due to inadequate sample preparation. Residue or debris on the surface can result in streaking across the image and can accumulate at the edges of the scan window due to the action of the tip.

3.1.2.2 Gwyddion Image Analysis

Topographic maps of the sample surface are produced within Gwyddion SPM data processing software using variations of the following protocol:

1. Align rows by median difference: Removal of horizontal lines that appear in the fast scan axis (usually in the x direction) as a result of drift [203]. Median difference offsets the lines such that the median of height differences between horizontally neighbouring pixels is equal to zero [203].

2. Levelling: Within this thesis the plane of the data was flattened by two methods. The first method is plane levelling where the plane of the data is calculated from all the image points before being subtracted from the data [203]. The second is three point levelling where the plane of the data is deduced by three points on the surface determined by the user that should be level with one another [203].

3. Correcting horizontal scars or strokes: Horizontal scars appear within images typically as a result of free debris on the sample surface [203]. These scars are typically in the direction of the fast scan [203]. This function within Gwyddion finds and removes these scars by replacing data with neighbouring lines [203].

4. Removal of any polynomial background: This function performs a polynomial fit of the data and subtracts this polynomial to emphasise the surface texture [203]. The order of the polynomial can be varied in the horizontal and vertical direction by the following equation [203]:

$$\sum_{j=0}^{m}\sum_{k=0}^{n} a_{j,k} x^j y^k \tag{3.1}$$

5. 2D continuous Gaussian wavelet transform over 2 pixels: This is similar to a Fourier transform, and results in a smoothing of the data to remove any additional noise [203, 204].

Between each step it is particularly important to consider the changes occurring within the image. For example, following Step 3, prior to removal of any polynomial background, the polynomial background can be identified by producing a 3D plot of the surface. This can give the user an idea of the polynomial correction necessary to produce a flat image, if indeed a flat image is expected.

Transparency within image processing methods is important as different users may implement different post-processing techniques [205]. The aim is for the final image to be accurate, representative, and reproducible.

3.2 Scanning Electron Microscopy (SEM)

Scanning electron microscope (SEM) is a versatile nanoscale resolution imaging technique that is commonly implemented within materials science. Within SEM techniques, a primary electron beam is raster scanned across the sample surface, the response of the surface to this primary beam can be measured and interpreted to collect information about the surface including

topography and composition [23]. Where optical microscopes are limited by the wavelength of light, electron microscopes are limited by the wavelength of electrons. This is known as the de Broglie wavelength, λ, as defined by:

$$\lambda = \frac{h}{p} \tag{3.2}$$

Where h is the Planck constant and p is the electron's momentum.

SEM has already been utilised in numerous corrosion studies [57, 70, 126]. However, a key limitation within in-situ corrosion studies by SEM is that the SEM operates in a vacuum, as such, samples cannot be imaged within liquid environment without alterations to the equipment. Within this thesis SEM imaging is implemented post-corrosion to image intergranular attack (IGA), pitting, and cracked grain boundaries (GBs), as well as pre-corrosion, such that the surface microstructures may be characterised.

3.2.1 Instrumentation

Instrumentation will vary somewhat between various manufacturers. Data shown within this thesis was collected using the following SEM instruments:

- FEI^{TM} Helios NanoLab^{TM} 600 - a dual beam (DB) instrument with combined SEM and focussed ion beam (FIB) with energy dispersive X-ray spectroscopy (EDX) capabilities at the University of Bristol.
- Zeiss ΣIGMA^{TM} Variable Pressure (VP) Field Emission SEM (Oberkochen, Germany. Serial: 03-72) equipped with a Gemini^{TM} electron source - an SEM with EDX and electron backscatter diffraction (EBSD) capabilities at the University of Bristol.
- FEI^{TM} Helios 600i NanoLab^{TM} - a DB instrument with EDX and transmission Kikuchi diffraction (TKD) capabilities at the National Nuclear Laboratory's (NNL's) Central Laboratory.

A schematic demonstrating the principle of a typical SEM set-up is shown within Figure 3.4. An SEM consists of four main parts: the microscope column (electron gun and optics), the specimen chamber, various electron detectors, and the associated electronics [22].

The electron gun is located at the top of the microscope column. There are two main types of electron gun: thermionic emission, and field emission [22]. Within a thermionic emission gun, electrons are generated from a tungsten filament heated to approximately 2700 K [22]. At this temperature, electrons are able to overcome the filament work function by thermionic excitation [22]. Electrons emitted from the filament are then accelerated towards an anode by an accelerating voltage, generating an electron beam [22]. As an alternative to tungsten, some thermionic emission guns contain a lanthanum hexaboride (LaB_6) filament as it possesses a lower work function and so requires lower temperatures [22].

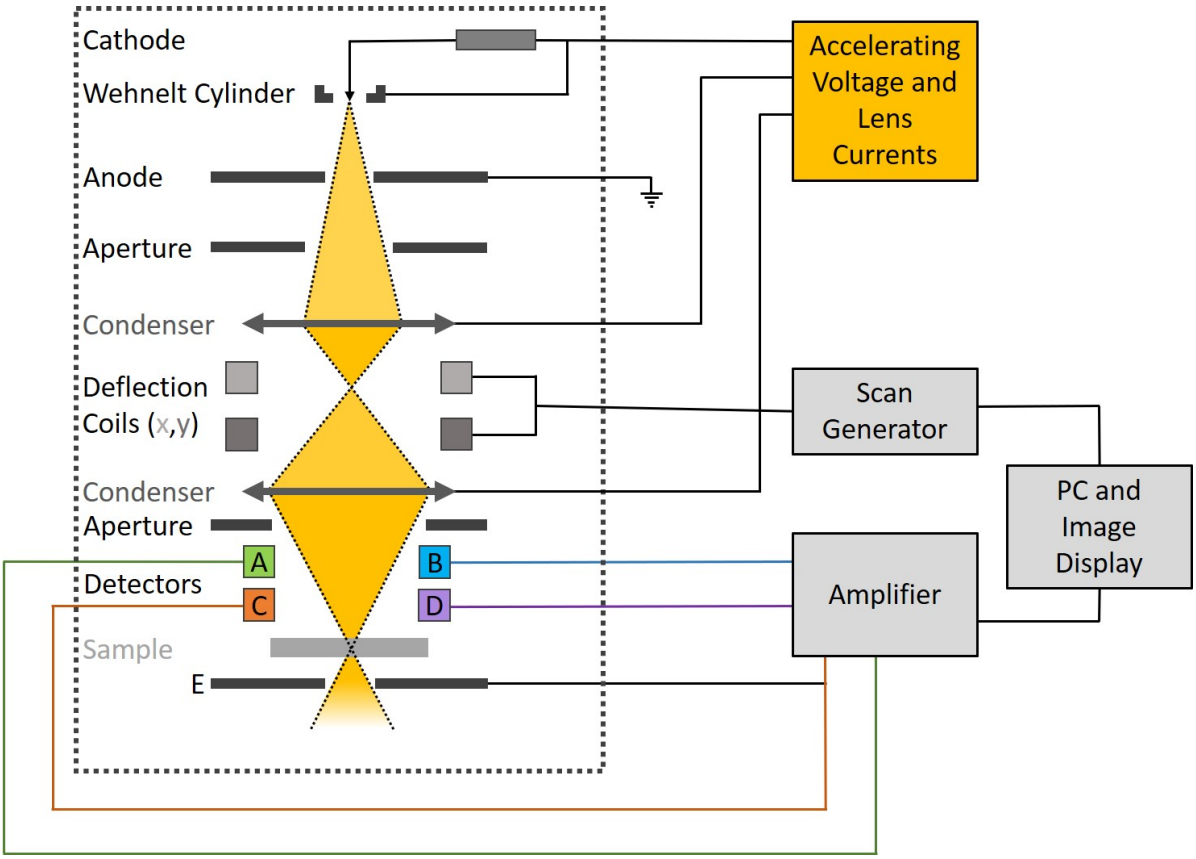

Figure 3.4: A labelled schematic of a typical SEM set-up. Detectors A, B, C, and D indicate the secondary electron detector, backscatter electron detector, X-ray detector, and cathode luminescence, respectively. Transmission electron signal is detected at E. Adapted from [22].

In contrast, field emission guns generate electrons by quantum mechanical tunnelling. By placing a single crystal tungsten needle close to an anode, a strong electric field is generated within its tip [22]. This has the effect of reducing the potential barrier of the electrons within the tungsten, enabling quantum tunnelling and subsequent emission [22]. Following emission, electrons are accelerated towards a second anode, generating an electron beam [22].

The electron beam generated from the electron gun then passes through condenser and objective lenses and apertures to be focussed on the sample surface [22]. The sample is secured to a stage within the evacuated sample chamber. The SEM operates under a vacuum of around 2.5×10^{-5} mbar to allow for minimal interactions as the electron beam travels from the electron gun to the sample [22].

Deflector coils scan the electron beam along the surface in a raster pattern [22, 206]. Electrons then interact with the sample, generating various signals that may be detected and interpreted.

3.2.2 Electron Interactions

As the primary electron beam is scanned across the sample surface, incident electrons interact with the atomic structure within a volume of the sample material to produce various signals, as shown in Figure 3.5. These signals include: secondary electrons (SEs), backscattered electrons (BSEs), auger electrons, X-rays, and visible light. Variations in the detected signals can be interpreted as electron-specimen interaction variations due to topography or composition [22]. Signals may be selectively analysed to determine a number of different specimen properties discussed in the following sections [206].

At high enough electron energies, SEM resolution becomes limited by electron interactions. The volume of interaction varies with which signal is being measured. Approximate respective interaction depths are shown in Figure 3.6. This volume changes with sample material and accelerating voltage [23, 207]. At high accelerating voltages, the volume is much larger, however higher voltages are sometimes required to excite certain emission lines within a spectrum [23, 207]. Whilst lower voltages reduce this volume, they can also result in an increase in electron-optical aberrations, a reduction in signal strength, and a higher sensitivity to surface contaminants [23, 207].

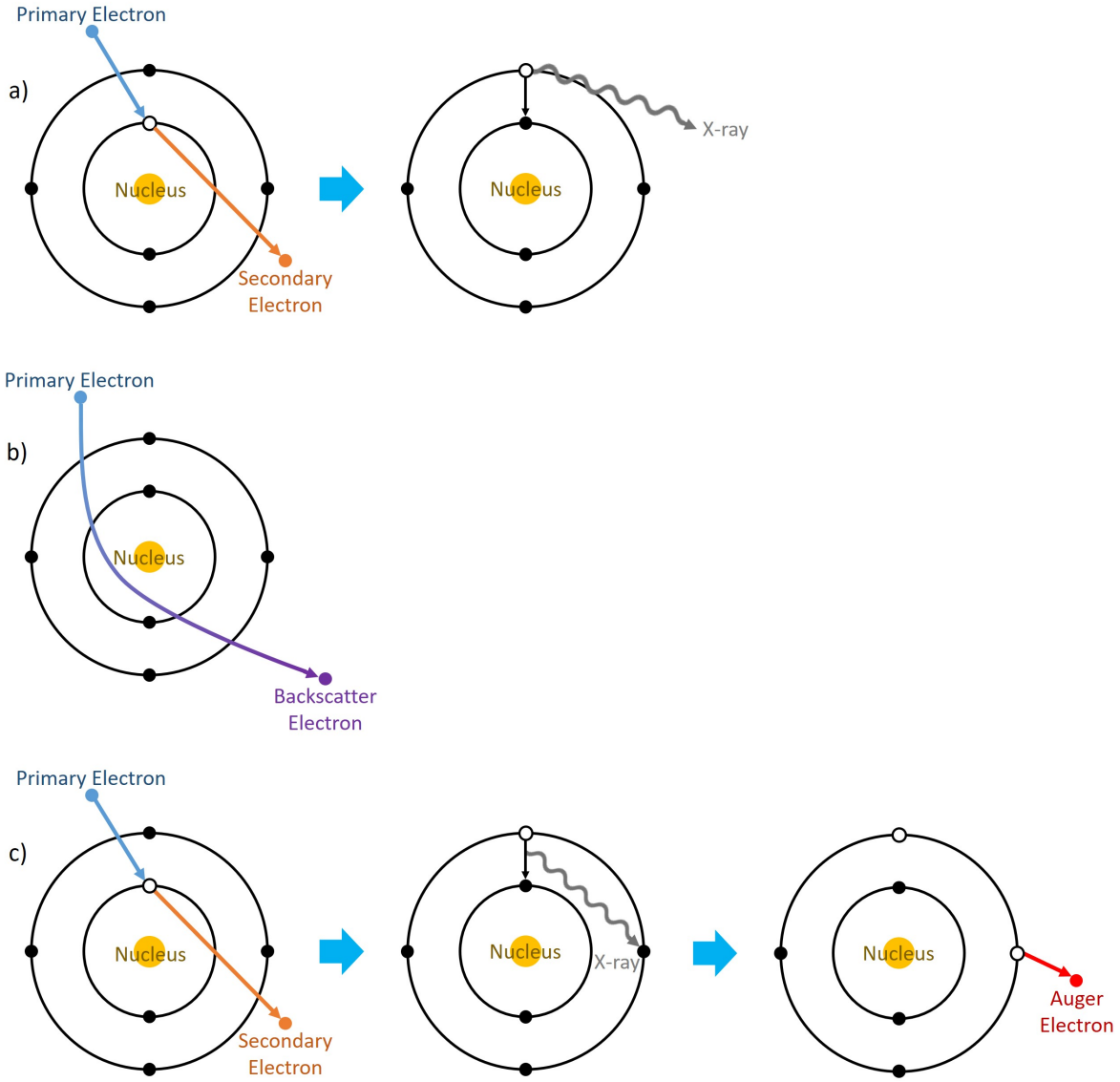

Figure 3.5: A schematic diagram illustrating various electron interactions: a) a primary electron interacting with an atom's orbiting electron resulting in the ejection of an SE, an electron in another orbital then drops into the vacancy resulting in the emission of an X-ray, b) a primary electron becoming deflected by the atom's nucleus resulting in the electron being backscattered, and c) an SE is ejected resulting in the generation of an X-ray which collides with another electron causing the ejection of an Auger electron. Adapted from [23].

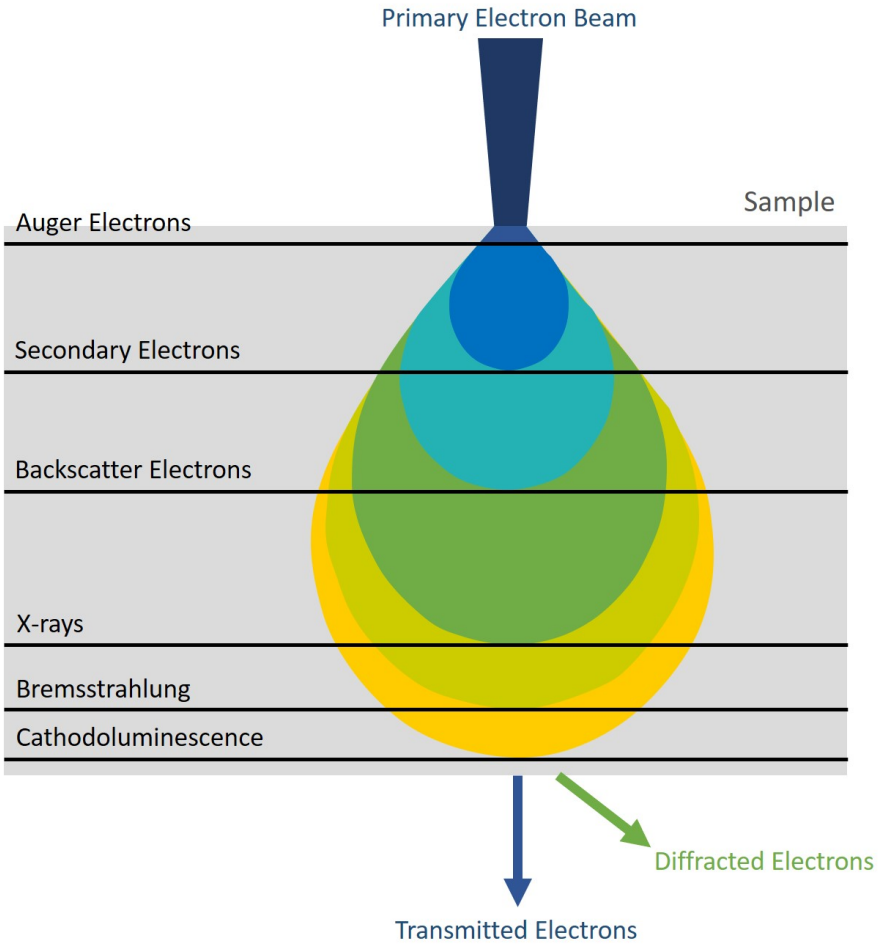

Figure 3.6: A schematic diagram illustrating the respective interaction volumes for each type of electron interaction, adapted from [24].

3.2.3 Secondary Electron (SE) Imaging

When an electron penetrates the sample, it may impart some energy to the electrons bound to the atoms within the material, resulting in the excitation and ejection of an SE, as shown in Figure 3.5 [206].

SEs are then detected by the SE detector within the SEM, labelled A in Figure 3.4 [206]. There are various types of SE detector. Within this thesis SE imaging was performed using an Everhart Thornley detector (ETD). This detector uses a metal coated scintillator with a high applied potential ($\leq$ 10 kV) [23]. When the electrons collide with the detector, they are sufficiently accelerated to cause the scintillator to scintillate, producing photons [23]. These photons are then detected by a photo-multiplier tube and are output as an electrical signal.

SEs are ejected from the top approximately 5 nm of the surface for metals [22, 23]. Due to the small interaction volume the number of SEs detected is highly dependent upon the topography of the sample, and therefore can be used to infer topographical information of the specimen [206].

3.2.4 Electron Backscatter Diffraction (EBSD)

EBSD utilises the BSEs emitted as a result of the incident primary electron beam interacting with an atom nucleus, Figure 3.5b [206, 208]. The number of BSEs increases with the atomic number (Z) of the material, as such the quality of the diffraction pattern improves with increasing Z [206, 209]. BSEs have a larger interaction volume than SEs and are often absorbed by the sample, Figure 3.6. As such, the sample is tilted at 70° to the horizontal, reducing the surface interaction volume to around 4-7 nm [23, 207, 210]. This volume is dependent on the accelerating voltage, sample density, and mean Z [23, 207].

BSEs are produced in all directions when the electron beam interacts with the sample surface. Path differences in the BSEs can produce constructive (when Bragg's law is satisfied) and destructive interference, forming diffraction patterns [208]. These patterns form diffraction cones, known as Kossel cones [60]. The edges of these cones form diffraction lines, referred to as Kikuchi bands, that correspond to specific crystallographic planes and orientations [60, 207]. A small distance from the sample, a phosphor screen placed in the path of the diffracted electrons, converts this signal into light which is then detected by a charge-coupled device (CCD) camera and translated into an electrical signal to the computer [60, 207–209]. Computer software identifies the phase and orientation at each point from the generated diffraction pattern by comparison to a library of known Kikuchi bands [60, 208, 211]. This information can then be compiled to produce a map of the microstructure, which can be used for quantitative analysis of the surface.

EBSD is capable of large area mapping of bulk crystalline samples, as well as the collection of data from regions of interest. It can be used to determine a range of quantitative microstructural data about the specimen, such as GB characterisation, grain size and distribution analysis, phase identification, and surface texture (the average preferred orientation) [23, 60, 207–209, 211–213].

EBSD maps can be used to reveal the locations of GBs, this can be applied to the identification of intergranular SCC (IGSCC) or transgranular SCC (TGSCC) in post-corrosion analysis [60]. EBSD can also be used to reveal the orientation of the crystal lattices of grain either side of a GB, which can influence a material's resistance to sensitisation, as discussed in Section 2.1.5.2. EBSD measurements of SCC cracks and crack tips may offer insight into how GB misorientation influences IGA and crack initiation and propagation [60, 69]. EBSD can also be implemented for the identification of plastic zones and for measurements of determine residual plastic strain in the specimen, this information can then be considered in the analysis of crack formation [207, 208, 212, 214, 215].

The accuracy of EBSD measurements is dependent upon the quality of the produced diffraction pattern. As crystallographic diffraction patterns are generated from only the uppermost region of the sample, the quality of surface preparation is critical [207, 209, 211, 216].

3.2.4.1 Additional Instrumentation

For EBSD analysis performed within this thesis, EBSD instrumentation from EDAX-AMETEK Inc. (Mahwah, NJ, USA) is mounted on the Zeiss ΣIGMA^{TM} VP Field Emission SEM described previously. This consists of a Digiview^{TM} high-speed digital camera alongside the associated OIM^{TM} data collection and analysis software.

3.2.4.2 Data Collection and Post-Processing

The quality of the map is dependent upon the calibration of the equipment, the index pattern quality, and the selected set-up parameters [211]. EBSD analysis performed within this thesis is carried out using a constant beam voltage of 30 kV and aperture of 120 μm. The data points are mapped in a hexagonal grid pattern at 120 points per second (double-clock), using the software's 8×8 pixel binning setting. Any variations to these conditions are stated within the results chapters where applicable.

Diffraction patterns are acquired at each step along the surface, patterns are normalised, and background is subtracted in order to improve signal strength. Specific parameters such as step size were selected based on the size of the area to be studied and the spatial resolution required. The resolution of EBSD maps is dependent upon the step size chosen to collect the data, with each pixel of the final map have dimensions equal to the step size [211]. However, in order to obtain high resolution, high quality EBSD maps, longer acquisition times are required [211].

Following collection, a number of clean-up algorithms are available to improve the map quality. Within this thesis, raw data is cleaned up by filtering points with a confidence index (CI) less than 0.1 and using confidence index standardisation (CIS). By implementing CIS, the fraction of pixels with low CI values but correctly identified orientation are recovered, as demonstrated in Figure 3.7.

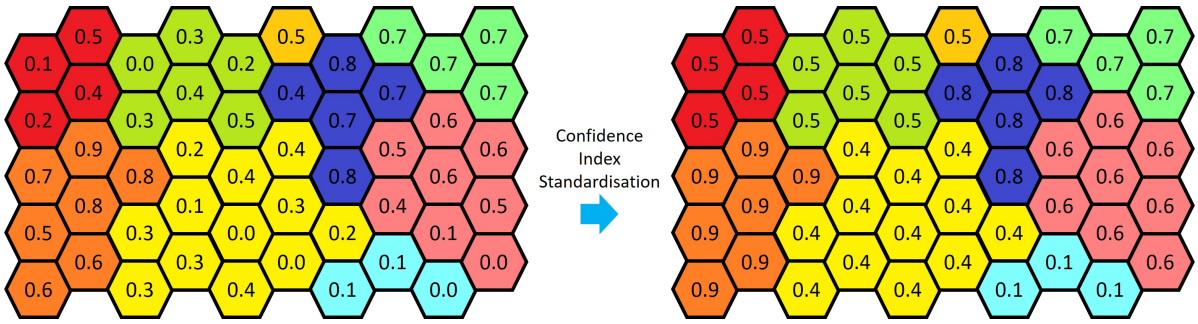

Figure 3.7: A schematic diagram illustrating the confidence index standardisation (CIS) method.

3.2.4.3 Frequently Used Map Types

EBSD software can be used to produce numerous map types and graphs displaying various information about the sample surface. The most commonly used maps within this thesis are shown in Figure 3.8. The first map shown in Figure 3.8a is an inverse pole figure (IPF) map where each grain is coloured based on its grain orientation, as shown in the inset legend. Using maps such as these preferential orientations may be determined, as well as quantitative information such as average grain size or GB misorientation. Preferred orientation may also be evaluated by generating a discrete IPF plot, where the number of grains or pixels with a certain orientation can be observed.

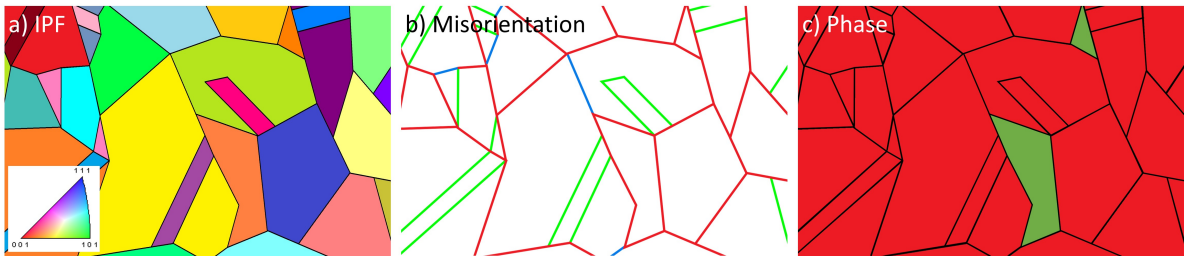

Figure 3.8: A schematic diagram illustrating some of the EBSD maps used commonly within this thesis: a) an IPF map, b) a GB misorientation value map, and c) a phase map.

GB misorientation is an important factor within IGSCC, as discussed within various sections in Chapter 2. Relative GB misorientation values are a standard output from the EBSD software. By manually assigning a colour key for misorientation ranges of interest a GB misorientation map may be generated, as shown in Figure 3.8b. Particularly pertinent to this thesis is the identification of twin GBs. By producing a GB misorientation map coherent and incoherent twin GBs may be identified. Coherent twin GBs may also be identified by visual inspection of the IPF map, as coherent twin GBs are observed as straight lines, often forming a band through all, or part of, a grain.

The final map shown in Figure 3.8c is a phase map. The example map is primarily one colour (red) indicating that it is a single phase material, where red typically denotes austenite. The

majority of the maps collected within this thesis are single phase austenite. Other phases are highlighted as a different colour within the phase map. This can give an indication of phase fraction or allow for identification of large secondary phase precipitates (SPPs).

3.2.5 Energy Dispersive X-Ray Spectroscopy (EDX)

EDX analysis is performed by measuring the characteristic X-rays produced from the sample in response to the primary beam, as illustrated in Figure 3.5a. Each element has a unique atomic structure and so X-rays are produced from a characteristic energy transition, therefore allowing for identification [23]. These X-rays are observed as peaks in the collected EDX spectra [23]. Also present in these spectra is the Bremsstrahlung radiation emitted as a result of the deacceleration of electrons by the atomic nucleus [23].

X-rays produced from the sample following interaction with the primary electron beam are collected on the EDX detector. This is a semiconductor detector in an electric field, where the semiconductor (typically silicon) absorbs the X-ray photon resulting in the ejection of an inner shell electron [23]. This ejected electron inelastically scatters within the semiconductor, resulting in the production of electron-hole pairs [23]. In response to the electric field, the electrons migrate towards the anode where they are collected. This charge is proportional to the incident X-ray photon, allowing for characterisation of the atom from which it originated [23].

EDX analysis provides elemental analysis of a sample surface in order to determine chemical composition. This allows for the identification of surface SPPs and chemical inhomogeneities. However, as this method has a large volume of interaction (Figure 3.6), consideration of the signals excited beneath surface features is important during analysis.

3.2.5.1 Additional Instrumentation

In this thesis EDX analysis was performed using the Zeiss ΣIGMA^{TM} VP Field Emission SEM described previously, this instrument is fitted with a coincident EDAX EDX detector. Measurements were collected at 30 kV with an aperture of 120 μm and processed using TEAM V4.1 (EDAX).

3.3 Focussed Ion Beam (FIB)

FIB microscopy forms an image of the sample surface in a similar way to that formed using SEM, however, instead of a primary electron beam, the FIB uses a primary ion beam generated by an ion source such as liquid metal gallium [23, 217, 218]. It is a versatile method that can be utilised for the fabrication of structures as well as 3D analysis of a material [219].

SCC is a 3D phenomenon that is often studied using 2D techniques. 3D analysis by FIB has been utilised in a number of SCC investigations to study crack profiles and crack development in various materials such as stainless steels and nickel alloys [124, 216, 217, 219]. Using this technique, cracks can be sectioned at specific locations on the surface, without destroying the

whole specimen, or disturbing the rest of the crack or any adjacent cracks that may be present [217]. The crack can then be properly investigated to obtain information such as crack depth [217, 219].

It is a relatively quick method for the analysis of crack tip morphology, crack oxides, and microstructural features along the crack path [124, 219]. FIB is also capable of evaluating cracking mode as FIB images are capable of producing enhanced grain contrast images observations of grains and GBs, without the need for previous etching of the sample surface [217, 219].

It should be noted however that FIB imaging can result in a damaged layer due to ion implantation [23, 218, 220, 221]. For example, Ga^+ ion implantation can lead to a phase change in austenitic stainless steels from face-centred cubic (FCC) to body-centred cubic (BCC) [220]. However, this can be avoided by performing FIB imaging at low voltages and currents [218].

3.3.1 Instrumentation and Principles

In this thesis FIB was performed using the following instruments:

- FEI^{TM} Helios NanoLab^{TM} 600 - a DB instrument with EDX capabilities at the University of Bristol.
- FEI^{TM} FIB-201 - a single beam FIB at the University of Bristol.
- FEI^{TM} Helios 600i NanoLab^{TM} - a DB instrument with EDX and TKD capabilities at NNL's Central Laboratory.

A FIB instrument consists of a FIB gun, an evacuated sample chamber, an ion detector, and associated electronic equipment. A FIB gun typically consists of a tungsten needle and a liquid metal ion source [23, 218]. For all instruments used in this thesis, a gallium ion (Ga^+) source is used for its low melting point, volatility and vapour pressure [218]. The ion beam is generated by applying a large potential between the needle and an extraction electrode [23, 218]. This results in the generation of a strong electric field across the liquid metal ion source, causing Ga^+ ions to be emitted as a result of field ionisation [218, 222]. These ions are then accelerated down the FIB column towards the sample surface [218].

FIB removes the upper layers of the sample surface by sputtering. This is a process that occurs when energetic ions collide with the sample surface. The ion imparts energy to the electrons and atoms present in the sample resulting in the ejection of particles (secondary ions, neutral atoms, and electrons) from the surface [23, 218, 222]. During FIB imaging, the FIB is rastered across the surface and secondary ions are collected by the secondary ion detector to form a FIB image. By increasing or decreasing the beam energy, the amount of material removed can be increased or decreased, respectively.

FIB can also be used to deposit metals onto the sample surface, such as platinum, for protection during FIB trenching (discussed later) or for the fabrication of nanostructures. This is

achieved by a process called chemical vapour deposition [218]. In the case of platinum deposition $C_5H_5Pt(CH_3)_3$ gas is injected into the chamber close to the sample surface, the FIB causes decomposition of this gas into volatile and non-volatile components [218]. The non-volatile components (in this case, platinum) are deposited onto the sample surface.

3.3.2 Applications

FIB can be implemented to provide high resolution images of the sample surface. FIB is also capable of performing analysis of sample microstructure through ion-beam contrast imaging [218]. In this method, a high-energy beam of gallium ions is rastered over the sample surface. This produces a contrast image of the crystallographic structure as a result of the varying hardnesses of different grain orientations.

By increasing the current of the ion beam, the FIB can be used to mill away the surface forming a trench allowing for cross sectional analysis. This milling is stress free with an accuracy up to tens of nanometres [217]. A platinum strip may be deposited prior to milling to protect the sample surface, as shown in Figure 3.9. The trench may then be imaged by tilting the sample and reducing the current in a single beam FIB instrument, or by using the electron beam in a DB instrument [217].

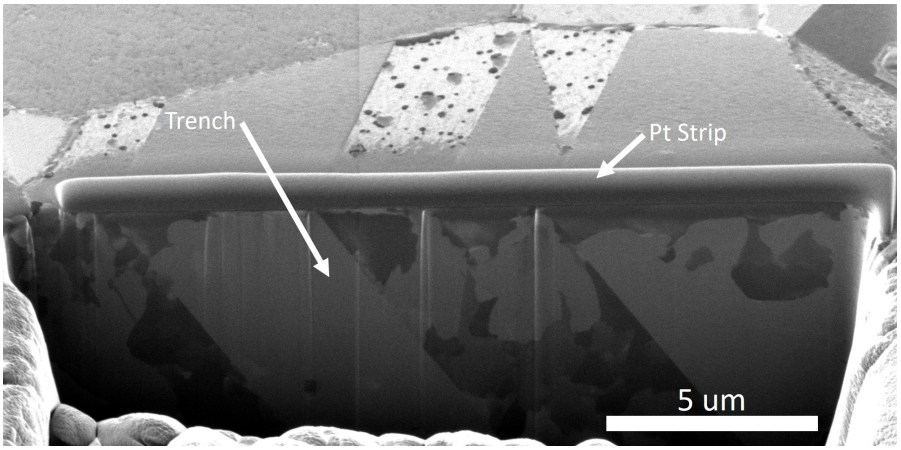

Figure 3.9: A labelled SE image showing a FIB cut trench in an AISI Type 304 stainless steel sample, with protective platinum strip.

By a similar method to cross sectional analysis, specific regions on the surface may be milled away at higher beam currents in specific patterns to fabricate nanostructures or create a fiducial, as demonstrated in Figure 3.10. By marking the surface with a fiducial, specific areas may be revisited in order to observed surface changes or using multiple correlated techniques. The fiducials shown in Figure 3.10 can also be used to identify the rotation of the sample as they are not rotationally symmetric.

FIB may also be used for sample preparation or a surface (discussed in Chapter 4), or sample fabrication such as for transmission electron microscopy (TEM) or atom prob tomography (APT)

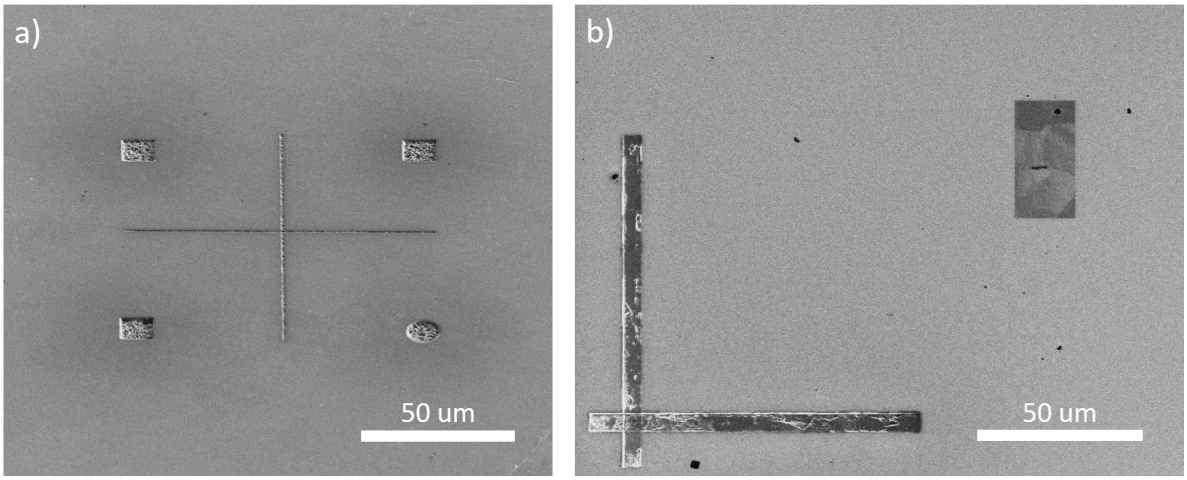

Figure 3.10: SE images showing examples of fiducial markers created using FIB milling: a) a quadrant where sample orientation can be determined by symbol positions, and b) an uneven cross where sample orientation can be determined by cross orientation.

analysis, as discussed in Sections 3.4.4 and 3.5.3, respectively.

3.4 Transmission Electron Microscopy (TEM)

TEM is a similar technique to the SEM techniques discussed previously, however TEM measures the electrons that are transmitted through the sample. The sample is therefore placed between the source and the detector. TEM can be used to attain information about a sample's microstructure with exceptional resolution (from micrometre to angstrom-scale) [223]. This includes measurements of crystallographic parameters (i.e. lattice parameter, phase), crystal defects (i.e. dislocations, stacking faults), small scale elemental segregation, and SPP identification [223–225].

The wide range of information attainable by TEM has prompted its applications in studies of SCC, for investigations into the effects of stress [174], the effects of elemental segregation and SPPs [226, 227], and chemical and crystallographic analysis of crack paths and crack tips [207, 219, 223, 228, 229].

However, TEM is limited by arduous sample preparation requirements. As the electrons are required to transmit though the sample, the sample must be very thin (electron transparent). This process is described in greater detail in Section 3.4.4. In addition, TEM is typically limited by the requirement of a vacuum. Though some studies have developed methodologies where environmental chambers may be used for in-situ corrosion studies, this is discussed in other works [174, 230].

3.4.1 Instrumentation and Principles

In this thesis, TEM analysis was carried out using the following instruments:

- JEOL 2100F TEM - a TEM instrument with scanning TEM (STEM) EDX capabilities at the University of Bristol.
- JEOL 2100 TEM - a TEM instrument fitted with STEM EDX and electron energy loss spectrometry (EELS) capabilities at NNL's Central Laboratory.

A TEM consists of an illumination system (electron gun and condenser lenses), a sample stage/holder, an objective lens system, a magnification system, and an imaging system [231]. A beam of high-energy (typically 100-1000 keV) electrons are generated at the electron source/gun [224, 231]. This is commonly a LaB_6 filament thermionic emission gun or a field emission gun, discussed previously [22, 231]. These electrons travel through the evacuated electron column through a series of electromagnetic lenses [224]. The initial lenses are condenser lenses which focus the electron beam on the sample.

Samples for TEM analysis are thin foils, and so electrons travel through the whole width of the sample. Some electrons pass through the sample without interacting (transmission electrons), whilst some are scattered by a small angle (diffracted electrons), as illustrated in Figure 3.6 [224].

Transmitted electrons then pass through additional lenses, including the objective lens, and apertures in order to form an image or diffraction pattern [231]. This image or pattern is then focussed onto the fluorescent (typically phosphor) viewing screen or transferred into an electrical signal for computational analysis, typically via CCD [224, 231].

3.4.2 Imaging Modes

TEM imaging can be performed using bright field (BF) or dark field (DF) imaging modes. BF images are formed from the undeviated beam, whereas DF images are formed from the diffracted beam [231].

There are three main contributors to contrast in TEM images: absorption (due to variations in sample thickness or atomic mass), diffraction, and phase contrast (from elastic scattering) [224]. In BF imaging mode, the size of the objective aperture determines what information is included in the final image [231]. For a small aperture size, almost all diffracted beams are excluded [231]. The image is largely formed by diffraction contrast along a single diffracted beam by tilting the sample, increasing the sensitivity to crystal distortions such as defects or strain [231]. Larger aperture sizes allow for higher resolution BF images [231]. The sample is titled such that strong Bragg reflected beams are detected [231]. The BF image is then the result of interference between the Bragg reflected beams and central transmitted beam, forming a phase contrast image [225, 231].

In DF imaging mode an annular DF (ADF) detector is implemented. This is larger than the BF detector and can therefore detect electron scattered at larger angles [225]. DF imaging mode involves tilting the incident beam (typically using deflection coils) until a diffracted beam passes through the objective aperture [225, 231]. DF imaging can be applied to study individual atoms, as well as crystals and crystal defects [225].

Within BF images, areas that transmit electrons, such as holes or low-mass materials, appear brighter, whereas areas that absorb or scatter electrons appear darker [225]. Whereas in DF images holes appear dark as the transmitted beam is excluded [225].

3.4.3 Scanning TEM (STEM)

Scanning TEM is largely similar to TEM, however the beam is rastered across the sample by a set of scan coils, as in SEM [225]. Images are then formed by recording electrons collected at each point in the raster scan [225]. By scanning the electron beam, techniques such as EDX and EBSD may be performed at higher resolution to attain further information about the sample's elemental composition or microstructure.

As with TEM, STEM images can also be produced in BF or DF imaging modes. However, by scanning the beam, a high angle ADF (HAADF) detector may be implemented for DF imaging. When imaging using an HAADF detector the signal is approximately proportional to Z^2, producing a Z-contrast.

3.4.3.1 Transmission EBSD (t-EBSD)

By analysing the transmitted BSEs, the sample's microstructure can be evaluated by a technique called transmission EBSD, or t-EBSD (alternatively known as transmission Kikuchi diffraction, or TKD). This technique uses a similar principle to that applied in EBSD analysis. The same hardware is also implemented: an SEM and EBSD detection system, described previously. However, the electron beam is transmitted through the sample where it is detected, as such the specimen position and orientation are altered compared to EBSD [207]. Instead of a 70° grazing angle (as implemented in EBSD), the sample is almost horizontal (< 10°) with respect to the primary electron beam [232].

As the sample is very thin for TEM analysis, the interaction volume is reduced during t-EBSD analysis [232]. This results in an increased lateral resolution compared to EBSD [207, 232].

Within this thesis, t-EBSD was performed using the FEI™ Helios 600i NanoLab™ DB instrument whilst the sample was mounted on an EasyLift probe or TEM grid. To achieve a suitable tilt with respect to the primary beam, samples mounted on TEM grids were then mounted onto a pre-tilted sample holder and secured onto the sample stage. Post-processing was performed using Tango (HKL CHANNEL5).

3.4.3.2 STEM EDX

EDX can be performed within a STEM instrument using an EDX detector, this is referred to as STEM EDX. In the same way as for t-EBSD, as the sample is very thin, the interaction volume is decreased therefore offering higher resolution capabilities. The electron beam can be directed at specific features on the surface such as SPPs or GBs for high resolution elemental analysis [225].

In this thesis, STEM EDX analysis was performed using both TEM instruments described previously, with subsequent quantification of EDX spectra performed using AZtec software (Oxford instruments).

3.4.4 Specimen Preparation for TEM/STEM Analysis

Sample preparation for subsequent analysis by TEM/STEM is typically performed in a DB instrument. The area of interest on the sample surface is identified by SE imaging, and a protective platinum layer (around 2 μm thick, 2 μm wide and 10s of micrometres long) is deposited in order to protect this region during subsequent FIB milling steps. Two large trenches are then FIB milled either side of this platinum strip, as indicated in Figure 3.11. This initial cut is performed at high voltage and current (30 kV and 20 nA). Subsequent steps are performed as gradually decreasing current values (down to 2.7 nA), in a similar manner to reducing grit size during mechanical polishing steps. Each cut progresses further into the platinum strip resulting in a thinning of the sample, forming a TEM lift-out, foil, or lamella.

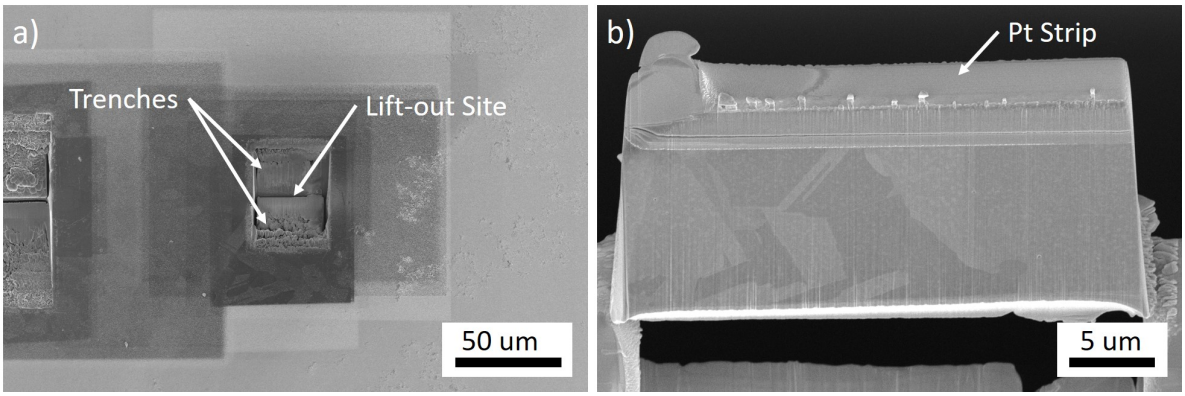

Figure 3.11: SE images showing: a) a sample of ex-service 20Cr/25Ni-Nb with a TEM lift-out site with FIB milled trenches either side, and b) the TEM lift-out collected from the site shown in a) with labelled platinum strip.

The resultant lamella is attached to a needle (via platinum deposition) attached to a micromanipulator and then removed from the bulk. The lamella can then be placed onto a TEM grid before further polishing steps performed by FIB at even lower currents (from 1.4 nA to 0.21 nA). The final FIB polish is performed at a low voltage and current (2 kV and 75 pA) and at a glancing angle in order to reduce ion implantation. The lamella is FIB polished until it is electron transparent (approximately 100 nm) and thus suitable for TEM, as shown in Figure 3.11b [224, 232]. If further thinning of the sample is required, this may be achieved by use of a precision ion polishing system (PIPS). Other similar methods can be performed, described in other works [218, 224].

Within this thesis, TEM sample preparation was performed using two instruments. Work performed at the University of Bristol implemented the FEI^{TM} Helios NanoLab^{TM} 600 DB instrument described previously. This instrument is fitted with an MM3A micromanipulator from Kleindiek Nanotechnik GmbH (Reutlingen, Germany). TEM sample preparation performed at NNL's central lab was performed using the FEI^{TM} Helios 600i NanoLab^{TM} DB fitted with an EasyLift NanoManipulator probe (FEI).

3.5 Atom Probe Tomography (APT)

APT is a mass spectrometry technique that is capable of measurements of chemical composition with excellent spatial resolution (around 0.2 nm) and chemical sensitivity (a few ppm) [233, 234]. Using this technique, individual atoms within a small needle specimen can be identified [175, 235]. Each atom analysed also carries spatial information, allowing for a full compositional reconstruction of the needle [175, 235]. Consequently, APT is a powerful technique with a large range of applications within materials science [175, 233, 235]. Site specific needle preparation has allowed for further studies of regions of interest [175, 223]. This technique has already been

applied to study a range of SCC-related phenomena including: GB segregation, SPP nucleation and growth, oxide composition, and crack tip analysis [175, 223, 233, 234, 236].

3.5.1 Instrumentation and Principles

An APT is a combination of a field ion microscope and a time of flight mass spectrometer [233, 234]. The basic concept of APT is illustrated in Figure 3.12. The key components of this set-up are the sample, the local electrode, and the position sensitive detector (a microchannel plate, or MCP, and detector).

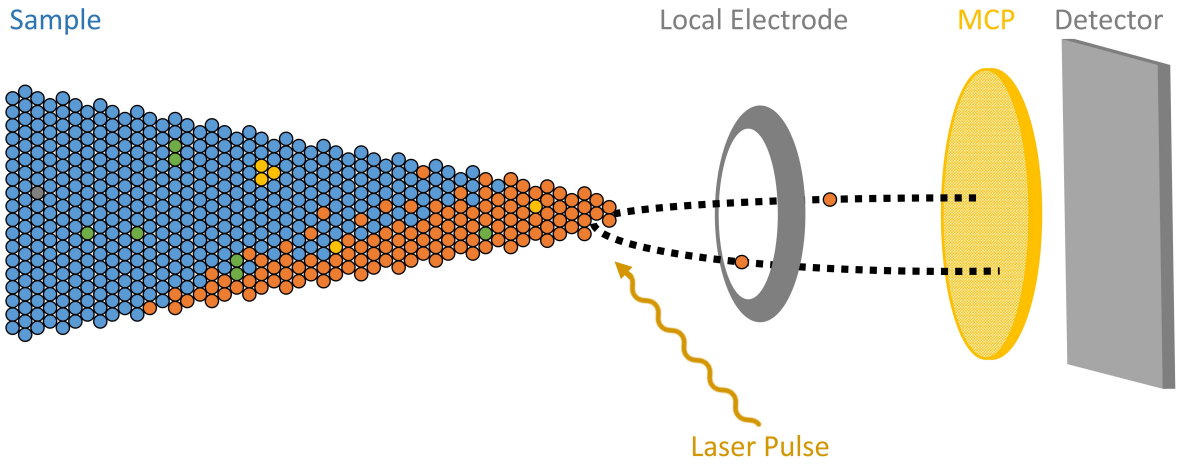

Figure 3.12: A schematic diagram showing the APT concept. Different compositional regions within the needle sample are shown in different colours. Adapted from [25].

The APT specimen is shaped to a needle only a few atoms thick at its tip, prepared using FIB milling (as described in Section 3.5.3). A high voltage is applied between the sample and the local electrode creating an electric field [175, 235]. A laser pulse (or a voltage pulse in some systems) is directed at the tip [175, 235]. This pulse results in the removal of atoms one-by-one from the tip of the needle by thermally-assisted field evaporation (or electric field evaporation in voltage pulsed systems) [175, 223, 233–235]. Atoms are then accelerated towards the detector through the electrode aperture before hitting an MCP coupled with a delay line detector [233, 234].

Time-of-flight (i.e. the time between the laser pulse and detection) is recorded for each atom [223, 233–235]. This corresponds to a mass-to-charge ratio allowing for chemical identification of each atom [175, 234, 235]. The detector also records the x,y position of the atom, and the z position is determined from the order of evaporation [223, 233–235]. This information can then be reconstructed during post-processing to produce a 3D model of the needle where each atom's chemical identity and position within the needle are known [175, 235].

APT experiments within this thesis were carried out using a Cameca Local Electrode Atom

Probe (LEAP) 5000 XR at the University of Oxford. Specimens were run in laser pulsing mode, with a laser pulse energy of 50 pJ and a pulse rate of 200 kHz. The specimen was analysed at a temperature of 50 K, and a detection rate of 0.5% was maintained. Low temperatures are necessary to reduce thermal vibrations of the atoms.

3.5.2 Post-Collection Reconstruction

The APT outputs raw data detailing the x and y coordinates of the ion on the sensor, the time-of-flight, and the order in which ions were detected. This data requires a few calibration steps prior to analysis. This includes correcting for the bias introduced as a result of the laser hitting to one side of the needle sample (x,y calibration), correcting for voltage changes during the experiment, and calibrating the timing window such that mass can be accurately quantified. A time-of-flight correction is also required, introduced by the curved needle tip and the flat detector (bowl correction).

Following these calibration steps, a mass spectrum is produced where ions can be identified by their mass-to-charge ratio [234]. Labelling each peak requires user input, though many ions are relatively straight forward as most elements typically have only a few charge states [234]. In cases where peaks overlap, they may be deconvoluted by considering relative abundances of certain isotopes, however in some instances this process is not straight forward [234].

Lastly, tip geometry can be reconstructed using a number of methods including using the voltage as an approximation for the tip radius, applying a fixed shank angle, or tracing the dimensions of an image of the final needle tip. For reconstructions shown in this thesis this was achieved by tracing an SE image collected following sample preparation steps.

The final tip reconstruction produced gives an atom-by-atom model of the original sample. This model can be manipulated to ascertain specific information about the sample, such as composition, or identification of compositionally varying regions such as sensitised GBs or SPPs. Tip reconstructions included in this thesis were produced using the Integrated Visualization and Analysis Software (IVAS) by Cameca (version 3.8.4).

3.5.3 Specimen Preparation For APT

APT needle specimens were produced using the FEI^{TM} Helios NanoLab^{TM} 600 DB instrument fitted with a micromanipulator described previously. For APT analysis described in this thesis, seven APT needle specimens were produced from a single lift out containing a cracked GB and a region ahead of the crack tip, outlined in yellow in Figure 3.13. A thin line of platinum was initially deposited by electron beam along the visible crack tip on the surface, using a method adapted from Lotharukpong *et al.* [237]. This initial layer acted as a fiducial marker to position the crack within the final APT needle specimen, this layer also protects the feature of interest [238]. Following this, a thicker deposit of platinum was applied using the FIB beam, covering the rectangular region to be extracted.

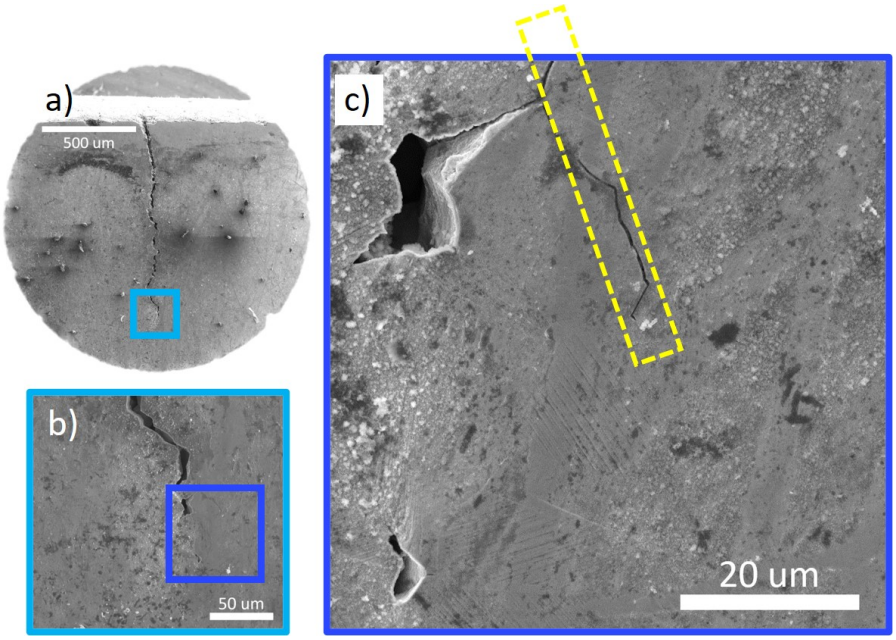

Figure 3.13: SE images showing: a) an arrested crack in a sample following failure by IGSCC, b) a higher magnification image of the region outlined in light blue in Figure 3.13a, c) a higher magnification image of the region outlined in dark blue in Figure 3.13b with the region of APT analysis outlined by a dotted yellow box.

Trenches are milled either side of this protective platinum strip in a similar manner to that performed for TEM sample preparation. However, APT lift-outs are much thicker and milled at such an angle that a triangular wedge of material attached at one edge is formed. This shape is achieved by a implementing a 30° angle between the FIB beam and the specimen and tilting the specimen to 22°. The resultant structure is attached at its free end to a micromanipulator by platinum deposition (Figure 3.14a). The lift-out is then removed from the bulk and a mounted onto a post on a microtip array (Figure 3.14b). This is a prefabricated silicon wafer with an array of posts, each around 100 μm tall [233]. The lift-out is divided into segments and mounted onto separate posts. For APT analysis performed in this thesis, the lift-out was divided into seven segments, an example of a mounted segment is shown in Figure 3.15a. Each segment is then ready to be sharpened.

For the needle specimens in this thesis, sharpening was performed using an annular milling method. With each subsequent sharpening step, the FIB current is decreased. The final step is performed at 5 kV and 0.13 nA to remove FIB damage, such as Ga^+ ion implantation [234, 238]. Similar needle preparation methods are described by other authors [233, 234, 238, 239].

This tip is sharpened until the apex has a radius ≤ 100 nm. The FIB thinning process for one of the APT needle specimens is illustrated in Figures 3.15, where Figure 3.15d shows the final APT needle ready for analysis.

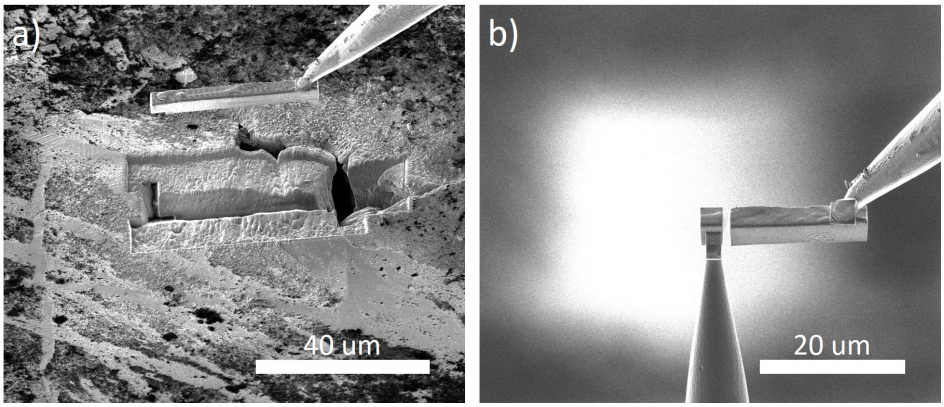

Figure 3.14: FIB images showing: a) a lift-out of the area outlined in yellow in Figure 3.13 mounted onto micromanipulator, b) a segment of the lift-out mounted onto a microtip post.

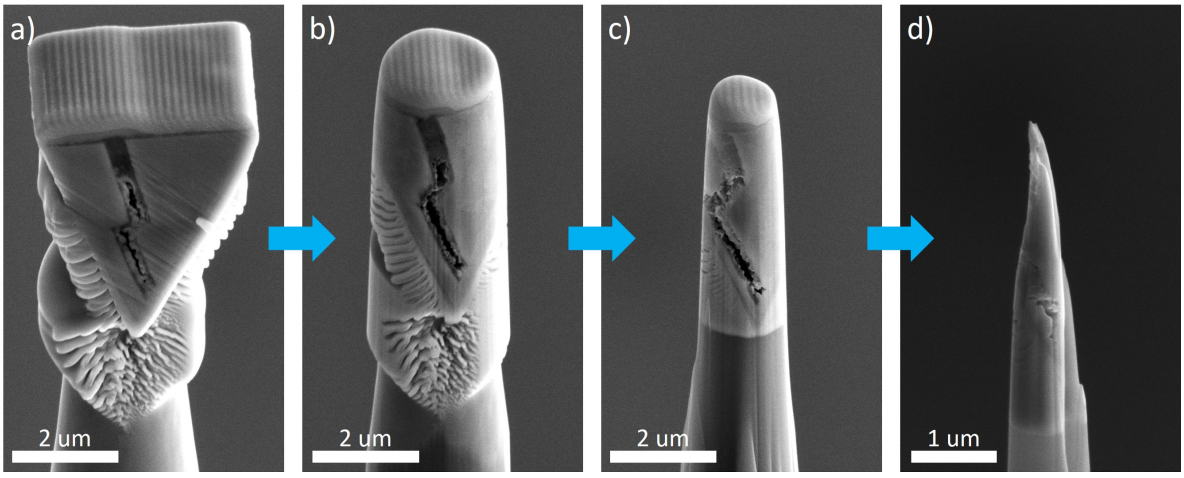

Figure 3.15: SE images showing: a) a segment of the area outlined in yellow in Figure 3.13 mounted onto a microtip post, b) and c) intermediate needles following FIB thinning, and c) a final APT needle.

3.6 Energy-Filtered Photoelectron Emission Spectromicroscopy (EF-PEEM)

Where SEM and TEM use electrons to probe the material, spectroscopy methods use photons. In a similar manner to electrons, when photons hit the sample surface, they can either be absorbed, or elastically or inelastically scattered. This interaction can result in the emission of an electron or the excitation of an electron. By measuring the various resultant signals, information about the surface can be attained.

In this thesis, energy-filtered photoelectron emission spectromicroscopy (EF-PEEM) is used to measure the work function of a surface. This method is part of a suite of methods known

collectively as nano electron spectroscopy for chemical analysis (NanoESCA) [26, 27, 240]. Work function is a measure of the electrons ability to escape the surface. As corrosion takes place by the oxidation of the surface by the liberation of electrons, it stands to reason that by measuring the work function, the propensity of the surface to undergo corrosion processes may also be measured. By mapping the work function variation across the surface, specific areas on the surface that may preferentially corrode are highlighted.

3.6.1 Theory

Photoelectron spectroscopy methods utilise the photoelectric effect [26]. This is the phenomenon where a photon incident on a material releases an electron whose binding energy is less than the energy of the photon [26]. Where the energy of the photon is equal to the product of its frequency, v, and Planck's constant, h [26]. If the kinetic energy imparted to the electron is sufficient, the electron will overcome the work function of the material allowing for it to be detected [26].

By measuring the kinetic energy of this electron at the detector, information about the surface can be determined including: the chemical identity, the work function, and the electronic structure, as well as surface orientation and segregation [241].

3.6.1.1 Photoelectron Emission Microscopy (PEEM)

A photoelectron emission microscopy (PEEM) image is produced by collecting all of the electrons released by incident photons. These electrons have a distribution of energies [26]. This is a combination of valence electrons, core electrons, and SEs [26]. The PEEM image is often dominated by SEs, however these signals can be filtered for energy-selective imaging [26].

Energy-Filtered Photoelectron Emission Spectromicroscopy (EF-PEEM) The energies of the photoelectrons can be filtered by band pass energy filters (e.g. a hemispherical energy analyser) [26]. Thus, allowing for energy-filtered spectroscopic PEEM analysis, or EF-PEEM [26]. This method can be applied for quantitative mapping of the surface work function.

3.6.1.2 X-ray Photoelectron Spectroscopy (XPS)

The chemical composition of the surface can be mapped using X-ray photoelectron spectroscopy (XPS) [240, 241]. In this method, X-ray photons liberate core electrons [27]. The binding energy of these electrons corresponds to the elemental identity of the atom from which it was released [26, 27]. In an XPS spectrum, these energies are observed as peaks that are characteristic to each element. Shifts in the peak positions can also give information about the chemical (i.e. bonding) state of the atom [26].

3.6.2 Instrumentation

NanoESCA II (Omicron Nanotechnology GmbH) at the University of Bristol is an ultra-high vacuum (UHV) PEEM system. It is capable of high-resolution spectroscopy and imaging in both real and momentum space, as well as the quantification of the electronic and chemical properties of the sample under investigation. The NanoESCA system has different modes of operation. UV photons are used for ultraviolet photoelectron spectroscopy (UPS), angle resolved UPS, and PEEM. Soft X-ray photons are used for XPS.

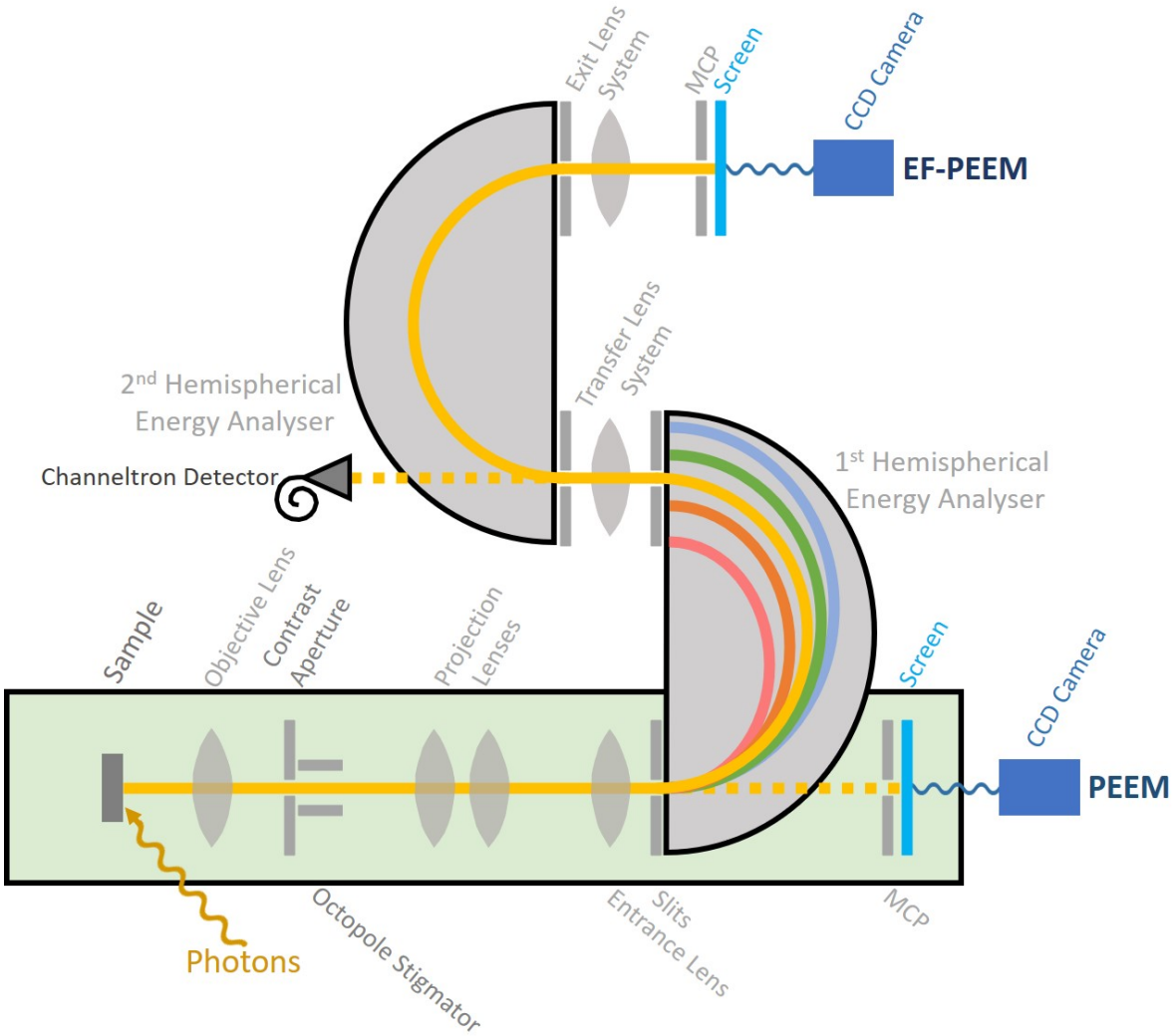

Figure 3.16: A labelled schematic of the NanoESCA system, adapted from [26] and [27].

The key components of the NanoESCA include the sample chamber, the photon sources, a series of lenses and apertures, two hemispherical energy analysers, and detectors, as shown in Figure 3.16.

The photon source emits photons that are incident on the surface of the sample. Different

photon sources are implemented dependent upon the desired photon energy/frequency. Photon sources for UV photons include various discharging lamps: mercury (for photon energies of 4.9 eV), deuterium (for photon energies of 6.2 eV), and helium (for photon energies of 21.2 eV) [26]. X-rays can also be generated using a monochromatic X-ray source delivering Al K radiation (for photon energies of 1486.6 eV) [26].

A high voltage (10-20 kV) is applied between the sample and the extraction anode [26, 27]. This allows collection of electrons from a wide range of emission angles [26]. Electrons liberated from the sample, first pass through the immersion objective lens in the PEEM column, resulting in a deceleration [26, 27]. Electrons then pass through a series of adjustable apertures and an electrostatic octopole stigmator [27]. This stigmator corrects for axial astigmatism [26].

The projection lenses decelerate the electrons further, prior to entrance into the analysers [26, 27]. These lenses also magnify the electrons for direct non-filtered PEEM [26, 27].

For EF-PEEM, electrons pass through two hemispherical energy analysers in an antisymmetric configuration (referred to as an imaging double energy analyser, or IDEA) [26, 27, 240]. The first hemisphere separates the electrons by their kinetic energies. The second hemisphere corrects for spherical aberrations introduced by the first [27]. The electron then collides with the detector.

For both EF-PEEM and non-filtered PEEM, the detectors consist of an MCP and fluorescent screen [26]. This screen is imaged by a CCD camera [26, 240].

3.6.3 Work Function Maps

In this thesis, NanoESCA is applied to measure variations in the surface work function. Prior to imaging the sample surface is sputtered using a 0.5 kV argon ion (Ar^+) beam (at 45° to the sample normal) until the upper oxide layers are removed, as indicated from XPS analysis of the surface. This step is necessary for analysis of the bulk material as only the upper layers (typically only the first three atomic layers) are probed during analysis.

Measurement of the work function of a surface is achieved by measuring the emission threshold energy, i.e. the minimum energy required for the liberation and detection of a photoelectron [26]. This threshold kinetic energy, E_k^0, can be expressed in terms of the work function of the surface, ϕ_S, the voltage applied to the surface, U_s, and the work function of the analyser, ϕ_A, as [26]:

$$E_k^0 = \phi_S - eU - \phi_A \tag{3.3}$$

Where e is the electron charge.

EF-PEEM analysis of the surface produces a series of photoemission intensity images by scanning the sample voltage [26]. These may be combined across a range of energies to form a work function map of the surface.

Table 3.1: A table showing comparisons between the different techniques used within this work.

Technique	Information Attained	Resolution (Spatial and Temporal)	Key Limitations (in the Context of Corrosion Studies)
HS-AFM	Quantified surface topography	Nanometres lateral, ± 15 pm height, sub-second collection time	Flat surface
SE	Surface topography	Nanometres lateral, seconds to minutes collection time	Vacuum
EBSD	Grain structure, misorientation, phase	10s of nanometres lateral corresponding to collection times from minutes to hours	Vacuum, flat surface
t-EBSD	Grain structure, misorientation, phase	Nanometres lateral, corresponding to collection times from minutes to hours	Vacuum, sample preparation
EDX	Chemical composition	Sub-micrometre lateral, minutes to hours collection time	Vacuum, volume interaction
FIB	Grain structure	Nanometres lateral, seconds to minutes collection time	Vacuum, destructive
TEM	Grain structure, misorientation, phase	Approximately 0.2 nm lateral, seconds temporal	Vacuum, sample preparation
STEM EDX	Chemical composition	Nanometres lateral with collection times from minutes to hours	Vacuum, sample preparation
APT	Chemical composition with associated location information	0.2 nm spatial, hours temporal	Destructive, vacuum, sample preparation
EF-PEEM	Surface work function	10s of nanometres lateral, collection times up to hours	Vacuum, high surface sensitivity

3.7 Summary

Within this chapter the various methods of analysis were discussed and placed in context of corrosion studies. Table 3.1 gives a brief overview of the techniques used within this work and the information each attains.

CHAPTER 4

SAMPLE PREPARATION METHODS FOR OPTIMAL HS-AFM ANALYSIS

Now you may find yourself seeking a solution
How can I make the most of nanoscale resolution?
What better way than an exploration
Into the various methods of sample preparation

High-speed atomic force microscopy (HS-AFM) has considerable potential for materials science applications. However, the quality of the surface analysis obtained by HS-AFM is highly dependent upon the standard of sample preparation and the resultant final surface finish. As with many atomic force microscopes (AFMs), it is important that the sample surface is relatively flat, thus to avoid loss of imaging due to sudden troughs in the sample surface, or damaging the sample/probe due to sudden peaks [21, 84, 181, 183, 199]. Samples are required to be pristinely polished (free of scratches) to reveal any microstructures present, and free of loose matter such that resolution quality is maintained, and image artefacts are avoided [242]. In 2016, Warren *et al.* described a methodology for the preparation of American Iron and Steel Institute (AISI) Type 300 series austenitic and Sandvik Austenite Ferrite (SAF) 2205 duplex stainless steels for optimised scanning probe microscopy (SPM) analysis [242]. The investigation presented here follows on from this previous work by exploring the effects of additional sample preparation steps.

Within this chapter, various sample preparation methods are compared with the aim of identifying an optimal method for HS-AFM analysis. This may be determined by whether high quality topographic images (with discernible microstructure and clear of surface debris

or imaging artefacts) are produced from the prepared surface. Samples of SAF 2205 stainless steel were prepared by mechanical polishing and etching in an oxide polishing suspension (OPS) before undergoing one of three treatments: acid etching, electrolytic etching, or focussed ion beam (FIB) etching. Samples were then imaged by HS-AFM and compared for signs of surface deformation and damage, preferential etching, and inhomogeneities. To give the most effective comparison between the behaviours of different phases under surface preparation techniques, a duplex stainless steel was utilised - SAF 2205 stainless steel comprises an approximate 1:1 ratio of austenite to δ-ferrite in a banded structure. The selected sample preparation methods are commonly implemented in metallurgy studies as well as for other analytical techniques, such as electron backscatter diffraction (EBSD) [207]. By testing a selection of methods used within other disciplines and techniques, a sample preparation method may be identified that is versatile and suitable across a range of analytical methods without the requirement for re-preparation.

This chapter includes figures and large sections of text taken directly from the following publications:

- **S. Moore**, A.D. Warren, R. Burrows, O.D. Payton, L. Picco, F.S. Russell-Pavier, P.G. Martin, T.L Martin, 2021. Sample Preparation Methods for Optimal HS-AFM Analysis: Duplex Stainless Steel. Ultramicroscopy, p.113210.

- **S. Moore**, R. Burrows, L. Picco, T. Martin, S. Greenwell, T. Scott, and O. Payton, 2018. A study of dynamic nanoscale corrosion initiation events by HS-AFM. Faraday Discussions, 2018, 210, 409 - 428.

- **S. Moore**, R. Burrows, L. Picco, T. Scott, A. Laferrere and O. Payton, Investigating Corrosion Using High-Speed AFM, EUROCORR 2017 PROCEEDINGS.

4.1 Duplex Stainless Steel Sample Composition

Samples of SAF 2205 stainless steel ('as received' condition from Outokumpu Stainless AB, composition given in Table 4.1) were cut to size using an automated diamond disc cut-off saw (Struers™Accutom) before being set into a resin (cold set, Struers™Clarocit) mount for polishing, described in the following section (Section 4.2).

Table 4.1: Elemental composition of SAF 2205 duplex stainless steel, as stated by the manufacturer.

C	Si	Mn	P	S	Cr	Mo	Ni	N	Cu	Ti	Ce	Fe
0.016	0.39	1.43	0.022	0.001	22.39	3.19	5.7	0.178	0.2	0.001	0.002	Bal.

4.2 Mechanical and OPS Polishing

The upper layers of the sample surface were removed by progressively finer silicon carbide (SiC) papers, from P180 (Federation of European Producers of Abrasives (FEPA) grit) up to P4000, using water as lubricant. The surface was then polished to a mirror finish using 1 μm, 0.25 μm, and finally 0.1 μm diamond pastes (Kemet International Ltd., KD Diamond Pastes) on a nylon cloth lubricated with Struers^{TM} DP-Lubricant (Brown). For each step, the sample was orientated in such a way that it was 90° rotated to the previous polishing direction. Polishing was performed for the time required to remove all polishing lines from the previous steps, when necessary this was confirmed by optical microscope (Figure 4.1). The sample was washed thoroughly with detergent and deionised water between each step to avoid cross contamination.

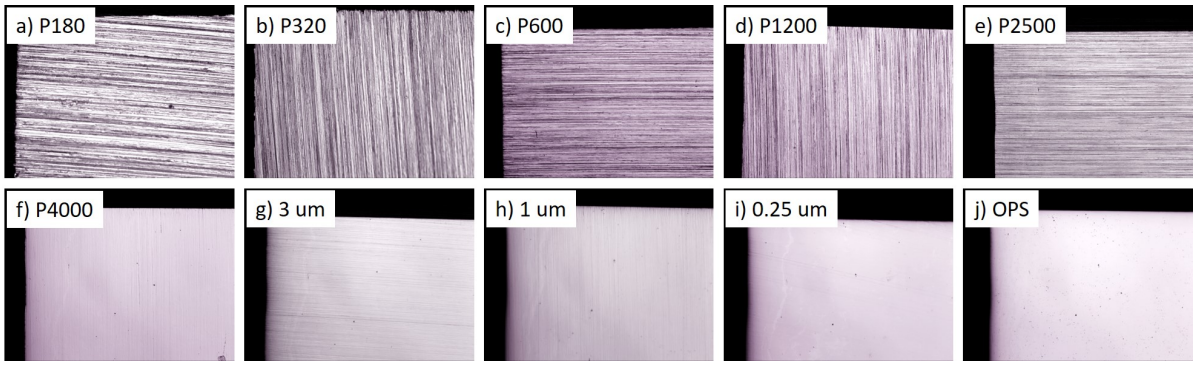

Figure 4.1: Optical images of example surface finishes following progressively finer polishing steps for a sample of AISI Type 304 stainless steel. Images taken following polishing with: a) P180 SiC paper, b) P320 SiC paper, c) P600 SiC paper, d) P1200 SiC paper, e) P2500 SiC paper, f) P4000 SiC paper, g) 3 um diamond paste, h) 1 um diamond paste, i) 0.25 um diamond paste, and j) OPS. Images were collected using a ×10 optical objective.

Following polishing steps, each sample was placed onto a vibrational polisher (VibroMet^{TM}, Buehler) with colloidal silica (MasterMet^{TM}, Buehler), an OPS, for a duration of 12 hrs to provide a deformation free surface [243]. This step may be extended to longer durations, such as 24 hrs as suggested by Warren *et al.* [242]. Longer durations may result in greater preferential etching across the surface. Once removed from the vibrational polisher the sample was rinsed thoroughly with detergent and deionised water.

Once these steps were completed, the samples were removed from the resin mount and cleaned. Each sample was sonicated for two minutes in several organic solvents a total of six times - twice with acetone, twice with ethanol and finally twice with isopropanol, changing for a fresh solution each time. The sample was then thoroughly rinsed with deionised water and dried with dry air to avoid drying marks or salt growth [242].

The surface was then marked with a razor blade to create a fiducial such that specific areas on each sample could be revisited. Imaging was performed by HS-AFM as well as by EBSD. Samples

were stored on pin stubs secured within sample boxes to prevent any contact with the sample surface, as this can result in surface residue.

4.2.1 HS-AFM Measurements of the Resultant Surface

HS-AFM maps were collected in the area adjacent to a fiducial on the sample surface, seen in Figure 4.2. Optically the austenite and δ-ferrite phases could only be faintly differentiated, with one appearing somewhat lighter than the other. By correlating EBSD measurements with optical images it was possible to determine that the darker phase was ferrite, and the lighter austenite.

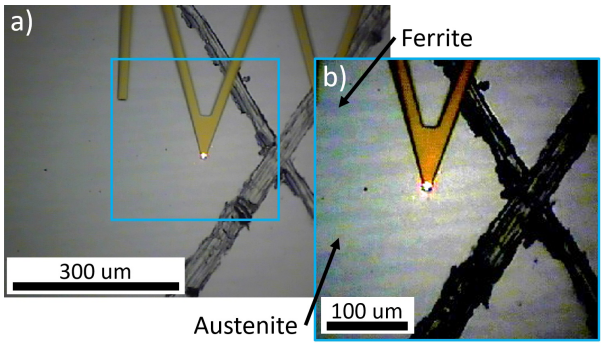

Figure 4.2: a) and b) show optical images of the SAF 2205 stainless steel surface following mechanical and OPS polishing steps during HS-AFM measurements, where b) is an enhanced contrast version of the image outlined in blue in a), with labels indicating areas of austenite and ferrite phases. The fiducial is seen to the right of the cantilever beam.

Topographic maps of the sample surface are shown in Figure 4.3. The high throughput of the HS-AFM allowed for measurements to be performed in several different areas on the sample for higher confidence in phase identification. Within these images darker features are lower topographically, and lighter features are higher. Topographic maps were compared to optical images where it was found that the higher phase (lighter in Figure 4.3) is ferrite and the lower phase (darker in Figure 4.3) is austenite. The step height between the two phases was measured during post processing as between 1.4 nm and 2.4 nm, with a mean step height of 1.9 nm (calculated from 15 measurements). Figure 4.3 also shows a grain boundary (GB) in austenite, highlighted in Figure 4.3a.

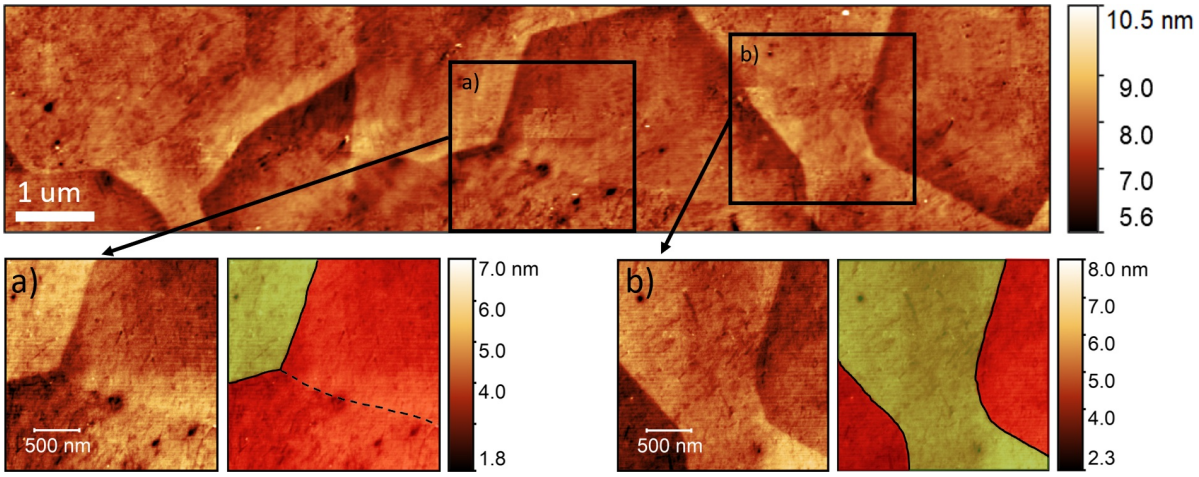

Figure 4.3: A composite topographic map of the SAF 2205 stainless steel sample surface following mechanical polishing steps with two frames, a) and b), selected, with coloured versions highlighting ferrite in green and austenite in red. Frame a) shows austenite and ferrite phases with an orientation change within the austenite phase, as indicated by a dotted line. Frame b) shows austenite and ferrite phases. This data was collected from the region adjacent to the fiducial, shown in Figure 4.2.

4.3 Wet Etching

Acid etching and electrolytic etching are both common wet etching procedures for the examination of stainless steel microstructure. There are a multitude of recipes for both techniques; etchants are selected dependant on the chosen material as well as the purpose of study, such as revealing GBs, phases, or precipitates [243–250]. This is achieved by preferential or selective etching, producing a contrast between certain microstructural features, such as different colours or etch patterns [244, 245, 248–250]. As such, these preparation techniques are typically implemented within optical studies of microstructure [244, 247] and will likely produce surfaces that are considerably rougher than those typically prepared for analysis by HS-AFM.

4.3.1 Acid Etching in Carpenter's Reagent

The duplex sample initially prepared by the step described in Section 4.2. The sample was then acid-etched by immersion in a Carpenter's reagent (a mixture of ethanol and hydrochloric acid) [247, 249, 251]. This technique is reported to reveal grain and phase boundaries in duplex stainless steels [247, 251]. The etchant was prepared by mixing 85 mL of ethanol with 15 mL of 35% hydrochloric acid, and the sample was immersed for a duration of 35 minutes [247, 251]. Experimental work was performed in ambient conditions (room temperature and pressure).

4.3.1.1 HS-AFM Measurements of the Resultant Surface

Etching the surface using Carpenter's reagent clearly revealed austenite and ferrite regions, visible by optical microscope, as seen in Figure 4.4. This result is expected as Carpenter's reagent is known to identify grain and phase boundaries in duplex stainless steels [247, 251]. Following comparison with EBSD results, the lighter, smoother looking areas were identified as austenitic, and the darker areas as ferritic.

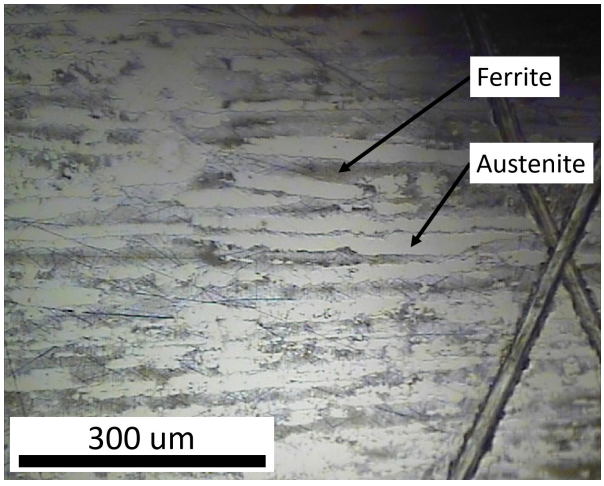

Figure 4.4: An optical image of the SAF 2205 stainless steel surface following acid etching with Carpenter's reagent, with fiducial. With labels indicating regions of austenite and ferrite phases.

Topographic maps collected by HS-AFM in the region adjacent to the fiducial are shown in Figure 4.5. Within these images two different phases are distinct from one another, as each phase has been affected differently by the etch. The flatter, lower (darker) phase was identified as austenite, and the higher (lighter) phase as ferrite. The step height between the two phases was measured to be between 22 nm and 47 nm, with a mean step height of 35 nm (calculated from 15 measurements).

HS-AFM topographic maps show that areas of ferrite contain deep pits (Figure 4.5a). These regions exhibit some variation in pit size and distribution. There are no obvious boundaries between different orientations due to etching within the ferritic areas, nor in the austenitic areas.

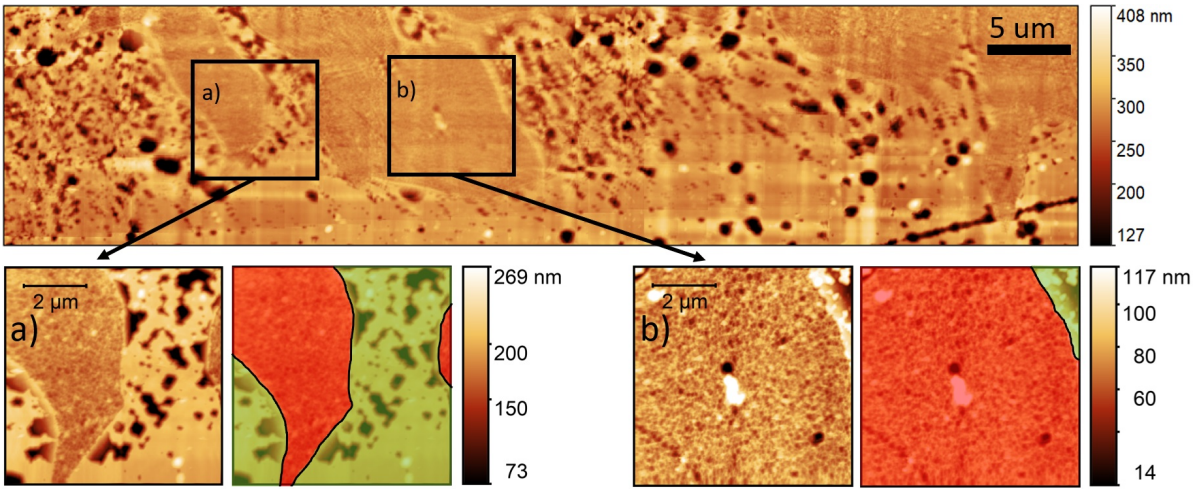

Figure 4.5: A composite topographic map of the SAF 2205 stainless steel sample surface following acid etching with two frames, a) and b), selected, with coloured versions highlighting ferrite in green and austenite in red. Frame a) shows austenite and ferrite phases. Frame b) shows an area with majority austenite phase. This data was collected from the region adjacent to the fiducial, shown in Figure 4.4.

4.3.2 Electrolytic Etching in an Oxalic Acid Solution

Electrolytic etching offers a number of advantages over other etching techniques. It is capable of uniform polishing and deburring of samples without direction lines and without the requirement of a flat surface [252–254]. In particular, when compared to acid etching, electrolytic etching is easier to control and produces more reproducible results [243, 253, 255]. This method implements a two electrode electrolytic cell for etching, where the sample acts as the anode (positive electrode) and the etchant solution acts as the electrolyte [252–254, 256]. By supplying a direct current (DC) voltage across the cell, oxidation reactions are driven at the anode and metal ions from the sample are conducted away, entering into the etchant solution [252–254, 256].

Following initial sample preparation steps given in Section 4.2, the sample was electrolytically etched with an etchant solution of 10 g of oxalic acid ($C_2H_2O_4$) dissolved in 100 mL of water (H_2O) [246]. This etch is reported to reveal grain structure in austenite and outline δ-ferrite [248]. The sample acted as the anode, with 0.87 cm^2 of surface exposed to the solution facing towards the cathode, separated by approximately 1 cm. The cathode consisted of a stainless steel wire (3.5 cm immersed). A DC voltage of 6 V was applied across the cell using a TENMA®72-10480 Digital-Control DC power supply for a duration of 1 minute [246]. During electrolytic etching a current of 0.4 A was measured. Experimental work was carried out in ambient conditions.

4.3.2.1 HS-AFM Measurements of the Resultant Surface

Optical images were collected of the sample surface in the region of the fiducial following electrolytic etching within an oxalic acid solution, Figure 4.6a. The surface appeared very rough,

with some areas appearing more etched than others. It was evident that a large portion of top surface had been removed by electrolytic etching, and a shadowing effect was observed within EBSD maps due to the uneven surface. As such, phase identification by EBSD in the region of the fiducial was not conclusive. However, for these particular etch conditions, the rougher, darker-looking areas are expected to be austenite, with the grain structure outlined, and the smoother areas δ-ferrite [248].

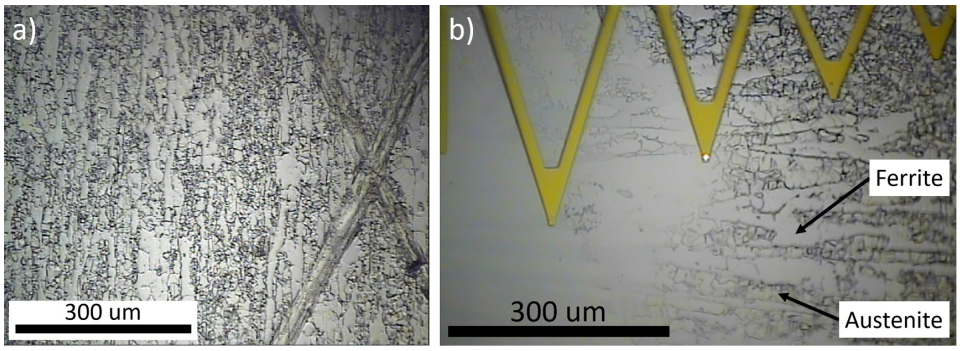

Figure 4.6: Optical images of the SAF 2205 stainless steel surface following electrolytic etching in an oxalic acid solution showing: a) an area adjacent to fiducial mark, and b) an area next to the partially covered section.

Analysis by HS-AFM was performed in the area adjacent to the fiducial, shown in Figure 4.6a. The uneven surface within the austenite regions resulted in challenging imaging conditions; this was particularly evident while traversing large areas. Figures 4.7a-c were collected from regions of austenite. By tracking the cantilever optically during imaging, it was deduced that the large pit structures occurred around the visibly etched regions on the surface. Figures 4.7d and 4.7e were collected from a region on the surface identified as ferrite. In contrast to the austenite regions, the ferrite regions on the surface were much flatter. This was evident in the reduced height range.

Measurements were collected while traversing areas on the surface identified as ferrite into regions identified as austenite. Figure 4.7f contains pitted structures on the left hand side and a smooth region on the right hand side. This may be an example of a boundary between ferrite and austenite; however, this is purely speculative.

Due to the high aspect ratio of some of the pit structures within the austenite regions, it is possible that tip convolution artefacts are present in the resultant HS-AFM data [257]. Additionally, in some cases the depth of the pit structure exceeded 4 μm, and as such were deeper than the height of the probe tip [258]. To accurately measure the full extent of the pit would require another technique such as FIB cross-sectioning, or alternatively a higher aspect ratio cantilever may be used. However, in the context of gauging suitability of the etched surface for HS-AFM analysis it is deduced that these conditions are not suitable.

An area on the surface was identified where the surface was etched to a lesser degree, shown

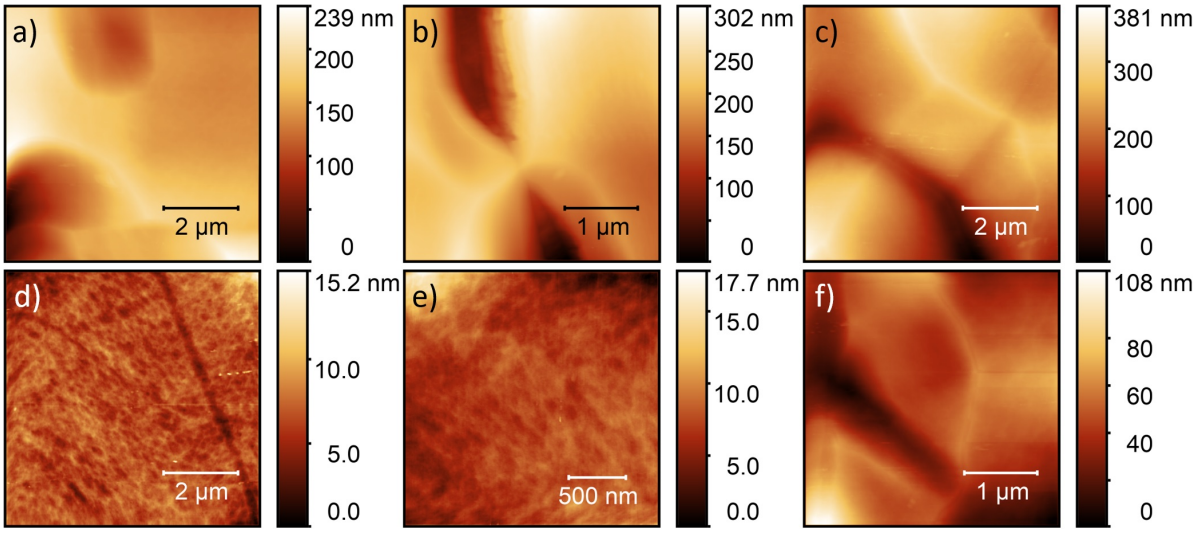

Figure 4.7: Topographic maps of each phase identified on the SAF 2205 stainless steel surface following electrolytic etching in an oxalic acid solution collected in the region adjacent to fiducial mark (shown in Figure 4.6), where a), b) and c) show austenite regions, and d) and e) show ferrite regions. f) Shows a region possibly containing a phase boundary, with austenite on the left hand side and ferrite on the right.

in Figure 4.6b. This area was not fully submerged during the etching process as it was partially covered. By comparing images collected from this region to the phases identified previously in Figure 4.2, the smoother areas were confirmed as ferrite, and the rougher areas as austenite.

HS-AFM topography measurements performed in the area in Figure 4.6b are shown in Figure 4.8. This region was markedly more suitable for HS-AFM analysis. Figure 4.8 shows two distinct phases. Areas identified as ferrite were generally uniformly etched, whereas austenite had irregular clusters of pits. In contrast to the results from the previous sample preparation methods (Sections 4.2.1 and 4.3.1.1) the austenite phase was topographically higher than the ferrite phase. The step edge between the two different phases in this area was measured as between 11 nm and 54 nm, with an average step height of 25 nm (calculated from 10 measurements). This is a much larger range than that measured on the acid-etched or mechanically polished samples, this is likely the result of sampling in the partially covered area, where the etch conditions vary. The step height between each phase varied considerably and was dependent upon the location at which measurements were collected.

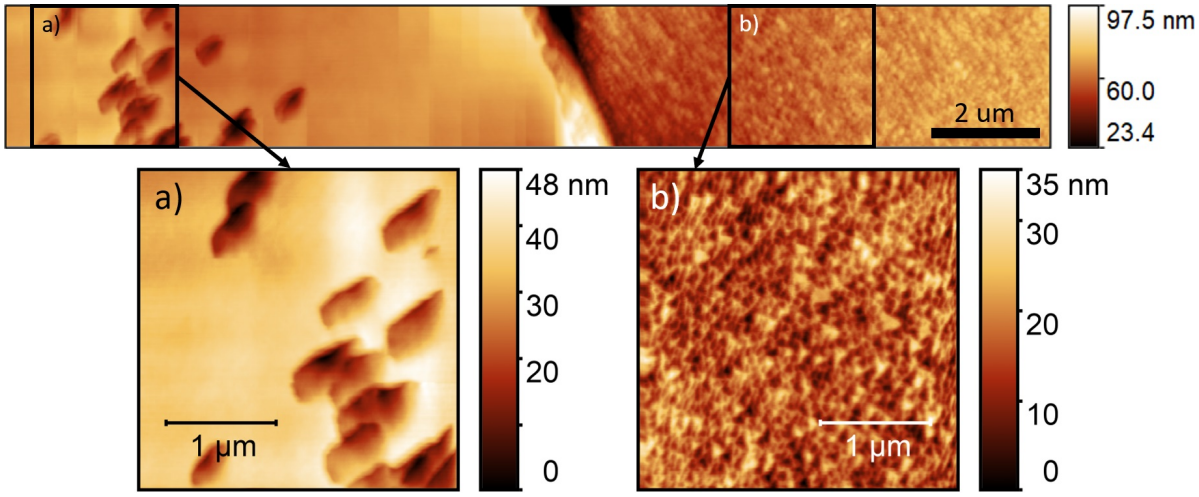

Figure 4.8: A composite topographic map of the SAF 2205 stainless steel sample surface following electrolytic etching collected in the area adjacent to the covered area with two frames, a) and b), selected. Frame a) shows an area identified as austenite. Frame b) shows an area identified as ferrite.

4.4 Dry Etching

4.4.1 FIB Etching

FIB etching (or milling) is a dry etching method in which an ion beam (typically Ga^+ ions) is scanned over the sample surface, where upon material in the upper layers of the specimen are sputtered away [222]. Different grain orientations are etched at slightly differing rates, resulting in the crystallographic structure being revealed [259]. However, it is not known whether the grain contrast observed within the FIB microscope will be reflected within the small-scale topography measured across the resultant sample surface by HS-AFM. Previous studies by scanning electron microscopy (SEM) and EBSD have found that FIB etching can result in damage to the upper layers of the surface [212, 220, 221, 260]. This damage can be observed as ripples or dots that appear periodically across a surface [260]. Furthermore, ion-implantation can result in a reconfiguration of sample structure, resulting in a localised phase change [220, 221]. These factors must be considered when interpreting the microstructures observed on the resultant surface.

FIB etching was undertaken using a Ga^+ ion beam at 30 kV and 11 nA for a duration of 20 seconds over an area of 120 μm × 100 μm at 0° from flat. Material was removed at a rate of approximately 0.5 μm^3 nC^{-1}, this corresponds to 5.5 μm^3 s^{-1} for a beam current of 11 nA. The beam was scanned over an area of 12,000 μm^2, thus giving an etch rate of 0.46 nm s^{-1}, which, for a 20 second period, translates to the removal of approximately 9.2 nm of the upper material.

4.4.1.1 HS-AFM Measurements of the Resultant Surface

The final sample preparation method was FIB etching of the surface. The area adjacent to the fiducial was etched, as outlined by a blue box in Figure 4.9a. Following FIB etching, the surface appeared somewhat darker in the region of the etch, making phase identification difficult optically. FIB images of the etched region before and after 20 seconds of etching are shown in Figures 4.9b and 4.9c, respectively. Figure 4.9c shows grain contrast, where different orientations of grain are etched at different rates [259]. This was confirmed by comparing this image with EBSD maps collected from the same region. It was found that, generally, the lighter grains within the FIB image were austenitic, and the darker grains were ferritic.

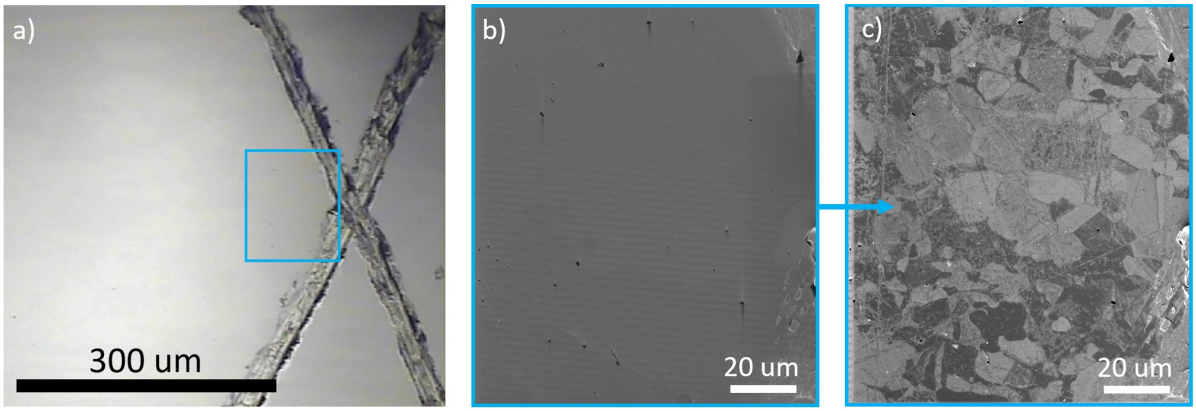

Figure 4.9: a) An optical image of the SAF 2205 stainless steel surface following FIB etching, with the etch area outlined in blue, also FIB images showing the area outlined in blue after etching for: b) 0 seconds, and c) 20 seconds.

Topographic maps were collected in the etched region, as shown in Figure 4.10. By comparing these maps with those collected by FIB and EBSD it was found that ferritic areas had higher topography, whereas austenitic areas were generally lower. However, phase boundaries were not obvious or consistent. A step height between the two phases was not measured as it varied depending on which orientations were adjacent to one another.

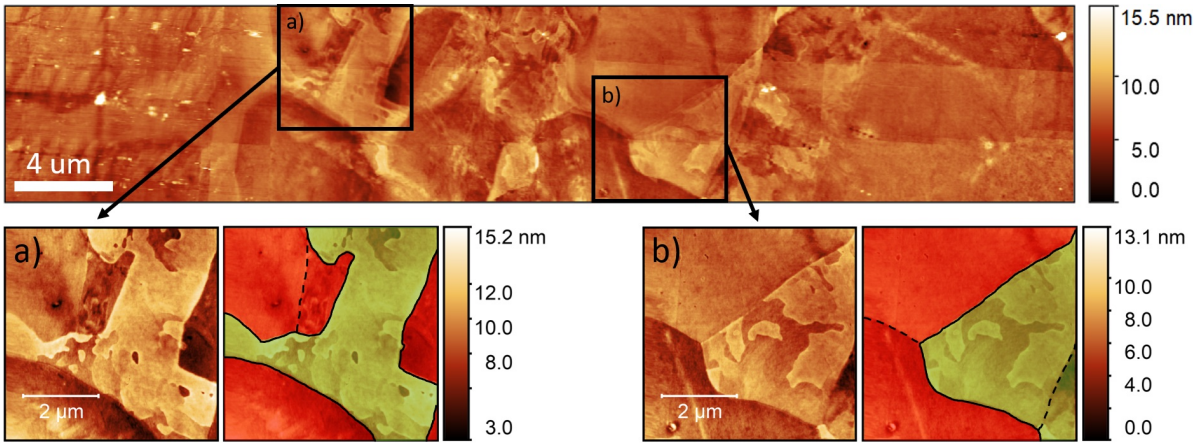

Figure 4.10: A composite HS-AFM topographic map of the SAF 2205 stainless steel sample surface following FIB etching with two frames, a) and b), selected, with coloured versions highlighting ferrite in green and austenite in red. a) and b) both show areas containing both austenite and ferrite phases. This data was collected from the region adjacent to the fiducial, shown in Figure 4.9.

4.5 Discussion: Optimal Sample Preparation Method for HS-AFM Analysis

Within this study, four commonly implemented sample preparation techniques were performed on a duplex stainless steel and compared: mechanical and OPS polishing, acid etching, electrolytic etching, and FIB etching. A summary for each sample preparation method is given within Table 4.2 and discussed in the following sections.

The importance of sample preparation in the process of acquiring high quality topographic data cannot be understated and must be considered carefully for accurate analysis. When considering sample preparation techniques, it is important to first consider what features on the surface are of interest and what imaging technique will be used to perform the analysis. This is particularly important when drawing conclusions from this study.

It is also important to note that sample surface condition can affect the samples corrosion behaviour. Surface defects such as machine marks or scratches may act as a preferential site for localise corrosion, or as a stress accumulator following the application of tensile stress [122, 124, 155]. This is particularly relevant in later chapters in which corrosion behaviours are studied.

4.5.1 Wet Etching Techniques

As stated previously, acid etching and electrolytic etching are commonly implemented for optical studies of microstructure as they preferentially etch or colour specific features of interest [243–250]. This can result in a rough surface that may be unsuitable for AFM studies, however this is

highly dependent upon the etch conditions. In the work presented here it was found that acid etching and electrolytic etching of the surface allowed for optical identification of the austenite and ferrite phases. This was reflected within HS-AFM measurements where each phase was etched differently. However, topographic measurements had much larger height ranges than those measured following initial sample preparation steps. This can result in finer microstructural information being more difficult to identify.

4.5.1.1 Acid Etching in Carpenter's Reagent

In optical images of the surface acid etched with Carpenter's reagent the two phases could be distinguished as the austenite appeared lighter and smoother whereas the ferrite appeared darker and rough (Figure 4.4). HS-AFM measurements performed on the surface were considered to be of good quality as images were clean and free of debris, with consistent and clear differences between phases allowing for confident phase identification. The austenite phase was lower topographically, whereas the ferrite phase was higher and pitted. These microscale pits are likely the cause of the rough looking texture on the macroscale.

The pits within ferrite varied in pit size and distribution, the cause of this is unknown, though may be due to changes in orientation. Alternatively, these pits may coincide with precipitates. However, precipitates such as sigma phase are not expected to be present as the specimen was not aged [261]. It has been found in other works that ferrite is preferentially attacked by acidic-chloride solutions [249, 250, 262]. In particular, preferential pitting of the ferrite phase has been observed in other works [263]. It is possible that this is due to differences in chemical composition between the two phases [263], however this is beyond the scope of this study.

4.5.1.2 Electrolytic Etching in an Oxalic Acid Solution

HS-AFM data collected from the surface electrolytically etched in an oxalic acid solution (Figure 4.7) contained deep pit structures within areas identified as austenite. These pits likely occur at austenite GBs and gave rise to the structures seen optically on the macroscale, as in Figure 4.6 [244, 248]. However, these large pits caused imaging artefacts during HS-AFM analysis. Furthermore, due to the lack of supporting EBSD data it is also of concern that electrolytic etching may have altered the phase fraction.

Comparing the data collected in the region of the fiducial to that collected in the partially covered region (shown in Figure 4.6b) may give an indication of how the surface changed as the etch progressed (Figure 4.8). The pits present within the austenite regions became much larger and deeper, as indicated by the large change in height values, from 48.2 nm (Figure 4.8a) up to 381 nm (Figure 4.7c). In contrast to this, the ferrite region became flatter and smoother as the etch progressed. The surface in this region was much flatter and more suited to analysis by HS-AFM.

Reflecting upon these results, the conditions explored within this work for electrolytic etching are not recommended for optimal analysis by HS-AFM. It is suggested that performing electrolytic etching for a reduced time, or at a lower etchant concentration, may result in better surface conditions for HS-AFM imaging. It must be stressed that these results are that of a specific etch recipe and is not true of all electrolytic etching. There are a wide range of recipes available, and other recipes have been successful in previous studies [264, 265]. In studies of duplex stainless steels by scanning Kelvin probe force microscope - a different type of SPM method - electrolytic etches have produced suitable surface finishes. For example, electrolytically etching in potassium hydroxide [264], which results in stained ferrite, or a nitric acid solution [265].

In Chapter 5 a sample of ex-service 20Cr/25Ni-Nb is prepared by an electrolytic etching procedure often used to produce samples suitable for TEM studies, known as the disc technique [266]. The etch recipe implemented was found to be suitable for both HS-AFM and SEM analysis. This sample was etched in a solution of 5% perchloric acid in methanol at -50°C. Previous works have reported that this recipe, and similar variations of this recipe, can produce well-polished surfaces of various metals including stainless steels and titanium [267–269]. The resultant surface is suitable for medical applications, optical analysis, and TEM analysis [267, 268]. The resultant surface as analysed by HS-AFM and SEM techniques is shown in Section 5.2.1.

4.5.2 FIB Etching

FIB images of the surface following FIB etching revealed the grain structure on the surface, due to different grain orientations within each phase being etched at varying rates (Figure 4.2c). Optical images of the surface were relatively featureless (Figure 4.2a). HS-AFM analysis revealed a topographic contrast from grain to grain allowing for clear observations of grain structure, as seen in Figure 4.10. However, as a result of this contrast, it was difficult to discern between different phases. The grains also appeared distorted, making microstructural characterisation particularly challenging.

Differences in topography are due to differences in the interaction with the Ga^+ ion beam, resulting in varying etch rates. The variation in topography observed between different grain orientations within each phase may be due to local chemical inhomogeneities. Alternatively, this topography may be the result of micro-alloying of the near surface which can occur as a result of ion implantation [220, 221]. In austenitic steels, Ga^+ implantation can lead to a phase change from face-centred cubic (FCC) to body-centred cubic (BCC) [220]. This may be the cause of the distorted microstructure observed by HS-AFM, however no clear phase change was measured by EBSD.

Due to the difficulty of identification of features present on the sample surface, this method of sample preparation was found to be unsuitable for observations of microstructure by HS-AFM. However, this may not be the case for different materials or etch conditions. In other works, it has been found that lower acceleration voltage and shorter imaging times can reduce the effects

of ion implantation [212, 221].

4.5.3 Mechanical and OPS Polishing

Following mechanical and OPS polishing little detail could be discerned optically, with phases only differentiated following enhanced contrast (Figure 4.2). However, HS-AFM analysis performed of the surface following produced high quality topographic maps with a consistent step height between the two phases, allowing for phase identification (Figure 4.3). However, each phase had a similar surface texture and so phase identification would require measurement of the step edge. The height difference between the two phases is a result of preferential mechanical polishing combined with the effects of colloidal silica on each phase. In previous work colloidal silica has been found to preferentially etch austenite in comparison to ferrite, resulting in the ferrite grain appearing higher topographically [54, 140]. This agrees with the observations made in this study. Topographic maps may be collected before polishing with colloidal silica; however, this step is required for a scratch free finish on the nanoscale which is vital for acquiring good quality HS-AFM maps.

Within Figure 4.3a the austenite phase contains two areas that appear to have polished anisotropically: this is likely due to differences in the orientation between grains in austenite [270]. This effect was less clear within the ferrite phase, though it may be the case that no ferrite GBs were present in the areas analysed by HS-AFM. Mechanical and OPS polishing was the only sample preparation method that allowed for clear observations of GBs within austenite. While GBs were observed within the FIB etched surface, phase identification was considerably more challenging.

This sample preparation method has been successfully implemented in other AFM studies of stainless steels [54, 140, 242], as well as for high resolution characterisation by EBSD [140, 207, 212].

HS-AFM excels at imaging topography changes measured against an otherwise flat surface. This allows for observations of fine microstructure, such as small-scale precipitates, or subtle changes in surface texture. Sample preparation methods that result in the flattest surface possible, free of imaging artefacts or surface debris, will allow for the identification of these finer microstructures. It is on this basis that conclusions were drawn. Therefore, mechanical polishing followed by colloidal silica etching is recommended as an optimal surface preparation method for HS-AFM. This method is relatively fast and allows for initial observations of fine microstructure across the surface. Following these measurements further etches may be appropriate for observations of specific features. This may be applicable where surface chemistry may be of interest. Mechanical polishing alone produces a hardness induced topography, whereas various etchants provide information about the reactivity of the surface microstructures within specific environments. Iterative application of various etches may provide substantial information about the microstructures present and their properties.

Table 4.2: Summary of sample preparation techniques studied within this work. Example surfaces as measured by HS-AFM are given as 3D topographic maps. Identified phases are indicated within each image. *Please note that these phases were identified by optical and HS-AFM analysis and were not confirmed by EBSD analysis.

Method	Example Surface	Summary
Mechanical and OPS Polish	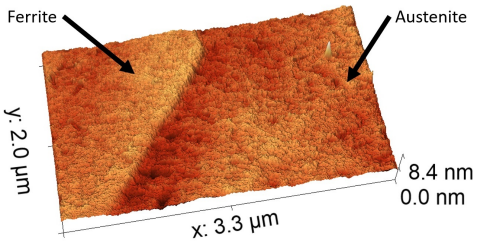	• **Optical**: Smooth, mirror-like surface. Phases could only faintly be differentiated. • **HS-AFM**: High quality topographic images with discernible phases with an average step height of 1.9 nm. Different grain orientations within austenite were also thought to be observed.
Acid Etch in Carpenter's Reagent	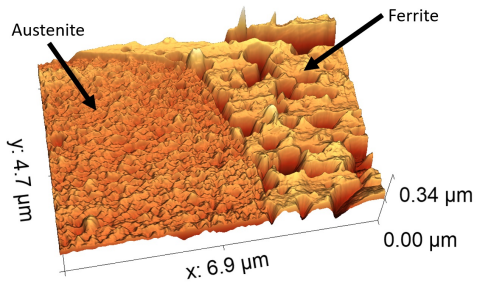	• **Optical**: Ferrite appeared darker than austenite allowing for identification. • **HS-AFM**: Clear topographic images, with discernible phases with an average step height of 35 nm. Austenite was flatter and smoother, whereas ferrite contained large pits likely giving rise to the macroscale appearance of the surface. Different grain orientations were not obviously distinguishable.
Electrolytic Etch in an Oxalic Acid Solution	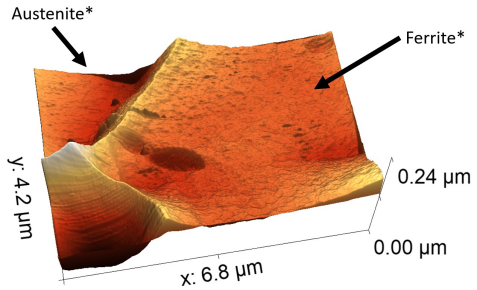	• **Optical**: Etching of the grain and phase boundaries within austenite regions allowed for tenuous optical identification of the phases. • **HS-AFM**: The rough surface was not optimal for analysis by HS-AFM. Each phase was etched differently, with austenite containing deep pit structures, and ferrite appearing largely flat. There was no consistent step height between phases. • **EBSD**: Due to uneven surface, phase identification was not achieved.
FIB Etch	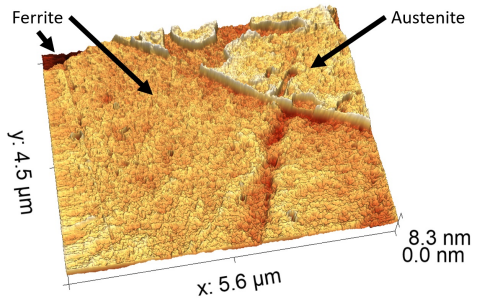	• **Optical**: Identification of the phases or microstructural features was not possible. • **HS-AFM**: Grains within ferrite and austenite observed, however difficult to identify each phase and no consistent step height between phases. Distorted grain appearance thought to be the result of ion implantation.

4.6 Conclusions

Within the work presented here, different surface preparation techniques that are commonly implemented within metallurgical studies were compared for samples of SAF 2205 duplex stainless steel using HS-AFM. The results of this study are also applicable to conventional AFM. The following conclusions were found:

- Mechanical and OPS polishing provided a gentle etch that allowed for high quality topographic measurements to be collected. Phase identification was possible by measuring the height change at the phase boundary. Grain structure in austenite was also discernible.
- Acid etching in Carpenter's reagent led to smooth austenite and pitting in ferrite allowing for phase identification.
- Electrolytic etching in an oxalic acid solution resulted in deep pits in austenite causing imaging artefacts during HS-AFM analysis. A shorter etch time or different etch solution is recommended.
- Acid etching and electrolytic etching recipes performed in this work were optimal for the low resolution of optical microscopy, but less suited for analysis by high resolution HS-AFM. This was due to the large height changes across the surface, which may distort or hide any finer microstructures present.
- During FIB etching of the surface the different orientations within each phase were etched at varying rates, allowing for observations of grain structure but conversely making phase identification somewhat challenging. A distorted microstructure was observed by HS-AFM, possibly due to Ga^+ ion implantation.
- It is suggested that initial study of the sample surface should be performed following mechanical polishing and vibropolishing with colloidal silica. Initial measurements may then be used to inform additional sample preparation methods that may be undertaken if appropriate.

Following the conclusions of this chapter, samples in future chapters will be prepared by the mechanical and OPS polishing steps outlined in Section 4.2 unless specified otherwise.

CHAPTER 5

CHARACTERISATION OF SENSITISED MICROSTRUCTURE

We must be careful not to jump to a hundred from none
Let's start by considering factors one by one
We can begin with a process called sensitisation
Which can occur with heat treatments or irradiation

Extensive research was performed in the 70's, 80's and 90's on the microstructure and physical and corrosion properties of advanced gas-cooled reactor (AGR) cladding. However, since these studies, AGR reactor conditions have changed considerably, operating at higher burn-up as a result of longer dwell times. There is a need for additional research to highlight any differences in chemical composition and the microstructures observed as a result of the current operating conditions. This is particularly important when identifying safe disposal routes and avoiding localised corrosion processes such as stress corrosion cracking (SCC).

Within this chapter, a series of measurements are performed on ex-service AGR cladding samples in order to evaluate the microstructural changes caused by irradiation and heating. Comparisons are made between the measurements performed on ex-service samples and those performed on thermally sensitised stainless steel samples. Such analysis is important when considering thermally treated samples as an analogue to irradiated samples.

Measurements of grain boundary (GB) elemental segregation due to thermal treatments and irradiation are performed. The relationship between these measurements and GB misorientation angle is evaluated. These results may be used to inform future inspection of ex-service AGR fuel cladding. Presently, analysis of ex-service AGR fuel cladding by scanning transmission electron microscopy (STEM) energy dispersive X-ray spectroscopy (EDX) to evaluate GB sensitisation is performed on two or three GBs. It is envisioned that the work presented here will inform on

whether this is adequate to determine the extent of sensitisation across different samples.

Scanning electron microscopy (SEM) and transmission electron microscopy (TEM) (including STEM EDX and transmission electron backscatter diffraction (t-EBSD)) sample preparation and measurements of ex-service AGR fuel cladding included in this chapter were performed at the National Nuclear Laboratory's (NNL's) Central Lab with the assistance of the Electron Microscopy Team. Sample preparation was carried out by Christian Sellars and Ellen Cosh, and measurements were performed with the assistance of Adam Qaisar, Ian Vatter, Michael Ward and Simon Dumbill. NNL also provided the cladding samples for analysis at the University of Bristol. TEM measurements of thermally sensitised American Iron and Steel Institute (AISI) Type 304 stainless steel were performed by Jean-Charles Eloi in the Chemistry Department at the University of Bristol. This chapter includes figures and large sections of text taken directly from the following reports and papers:

- Internal Report: **S. Moore**, R. Burrows, A.D. Warren, O.D. Payton, L. Picco, F.S. Russell-Pavier, High-Speed Atomic Force Microscopy Analysis of AGR Fuel Cladding, 2020.
- Internal Report: **S. Moore**, D. Hambley, S. Dumbill, A. Qaisar, M. Ward, C. Sellars, I. Vatter, E. Cosh, O.D. Payton, R. Burrows, T.L. Martin, and T.B. Scott, Central Lab Industrial Secondment Report: Analysis of the Relationship Between GB Misorientation and GB Segregation in Irradiated Ex-Service AGR Cladding, 2019.
- **S. Moore**, R. Burrows, D. Kumar, M. B. Kloucek, A. D. Warren, P. E. J. Flewitt, L. Picco, O. D. Payton, and T. L. Martin, Observation of Stress Corrosion Cracking of Stainless Steel Using Real-Time In-Situ High-Speed Atomic Force Microscopy and Correlative Techniques. Npj Materials Degradation, 2021, 5(3).

5.1 Sample Compositions and Histories

5.1.1 Ex-Service AGR Fuel Cladding

Samples of ex-service AGR fuel cladding (20Cr/25Ni-Nb) had an approximate composition given in Table 5.1 [30]. Samples 1XA, 2YB, and 2YC were prepared by NNL at Central Lab. Sample names indicate the stringer they were collected from, 1 or 2, the element position, X or Y, and the pin number, A, B, or C. This allows for samples from the same positions or stringer to be identified. Respective pin sections were defueled, mounted, and mechanically polished. The final polish was performed with an oxide polishing suspension (OPS) and H_2O_2 solution for 20 minutes.

Sample 1XA was produced by punching out a 1 mm diameter TEM disc from a pin section. This disc was ground down from both sides to a thickness of approximately 100 μm and mounted in a gold washer before electropolishing in a solution of 5% perchloric acid in methanol at -50°C. This resulted in an electron transparent sample suitable for analysis by TEM and bulk measurements by high-speed atomic force microscopy (HS-AFM) and electron backscatter diffraction (EBSD).

Table 5.1: Elemental composition of AGR fuel cladding, given in weight %, from [30].

C	Si	Mn	P	S	Cr	Nb	Mo	Ni	Fe
0.062	0.58	0.79	0.014	0.019	19.33	0.56	-	24.05	Bal.

Three lamellae, referred to as Lamellae A, B and C were produced from Sample 2YB by the steps outlined in Section 3.4.4. Samples were selected from the central region of cladding, as shown in Figure 5.1.

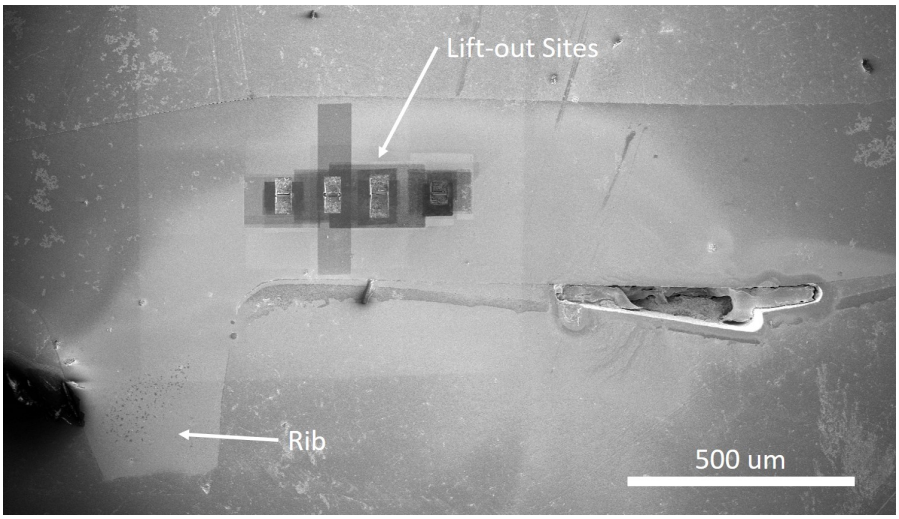

Figure 5.1: A secondary electron (SE) image showing the area from which the TEM lamellae were collected from Sample 2YB.

5.1.1.1 Relevant Previous Work Performed at NNL

Analysis has been previously performed on the samples at NNL by light optical microscopy (LOM), focussed ion beam (FIB), and electron microscopy techniques including SEM and TEM/STEM. Additional measurements by complementary techniques may be combined with previous results and correlated with one another, with the aim of producing a more complete analysis of the microstructure and the effects of irradiation and heating.

Analysis was performed on the same material from which Sample 1XA was collected, including: LOM, SEM/FIB and TEM/STEM. These measurements found:

- $M_{23}C_6$, globular in shape.
- Sigma phase.
- Inter- and intragranular NbC with size ranging from sub-μm to several μm.

- G phase on the majority of GBs across the sample.
- Inter- and intragranular radiation-induced voids with a mean matrix void diameter value of 18.7 nm.
- GB chromium concentration of 19 wt.%, a nickel enrichment of 1 wt.%, and a silicon enrichment of 0.1 wt.%.

Analysis by LOM, SEM/FIB and TEM/STEM was performed on Samples 2YB and 2YC by NNL prior to measurements performed here. These measurements found:

- GB $M_{23}C_6$ and M_6C.
- Intragranular NbC
- G phase.
- Ni_3Si.
- Inter- and intragranular radiation-induced voids with a mean matrix void diameter value of 11.9 nm and 5.6 nm for Samples 2YB and 2YC, respectively.
- EDX analysis of Sample 2YB detected a chromium concentration of 11-12 wt.%, a nickel enrichment up to a maximum of 43 wt.%, and a silicon enrichment up to around 3 wt.%. Similar measurements performed on Sample 2YC detected a depletion of chromium down to 10-11 wt.%, nickel enrichment up to around 42 wt.%, and a silicon enrichment up to a maximum of 2 wt.%. The compositional profile collected for 2YC was asymmetric, indicating GB migration. The misorientations of the GBs from which these measurements were collected were not measured.
- Intergranular SCC (IGSCC) is apparent within Sample 2YC.

5.1.2 Thermally Treated AISI Type 304 Stainless Steel

Samples were produced from a 1 mm thick sheet of AISI Type 304 stainless steel supplied by Goodfellow Cambridge Ltd. (Huntingdon, UK). Material composition was measured by inductively coupled plasma optical emission spectrometry (ICP-OES) and combustion by Element Materials Technology (Sheffield, UK), and is given within Table 5.2. This sheet was thermally treated at 600°C for 70 hours within an oven and allowed to air cool in order to produce a thermally sensitised microstructure [30]. The material and sensitisation conditions were selected to produce samples that may act as a proxy to AGR fuel cladding [30], whilst also being relevant within other industries. Samples were cut from this sheet using an automated diamond disc cut-off saw (Struers™Accutom) into approximately 5 mm × 5 mm squares and set into a resin (cold set,

Table 5.2: Elemental composition of AISI Type 304 stainless steel, given in weight %.

C	Si	Mn	P	S	Cr	Nb	Mo	Ni	Fe
0.059	0.34	1.47	0.022	0.005	18.46	-	0.08	7.93	Bal.

Struers™Clarocit) mount for polishing. The surface was polished following the steps described in Section 4.2.

Three lamellae, referred to as Lamellae 1, 2, and 3 were produced from samples of thermally treated AISI Type 304 stainless steel following the steps outlined in Section 3.4.4.

5.2 Ex-Service AGR Fuel Cladding Analysis

5.2.1 Large Area Surface Measurements of Microstructure by HS-AFM and Correlated Microscopy

The surface of Sample 1XA was first observed optically, as shown in Figure 5.2a. The surface appears largely smooth with no scratches or polishing lines present, however a dent or bend is apparent in the bottom left hand corner. A number of large secondary phase precipitates (SPPs) are observed across the surface as small dark features. Figures 5.2b and 5.2c show SE images of the surface collected at a potential of 30 kV. Numerous SPPs and GBs are observed within Figure 5.2c, these SPPs are primarily observed to be intergranular.

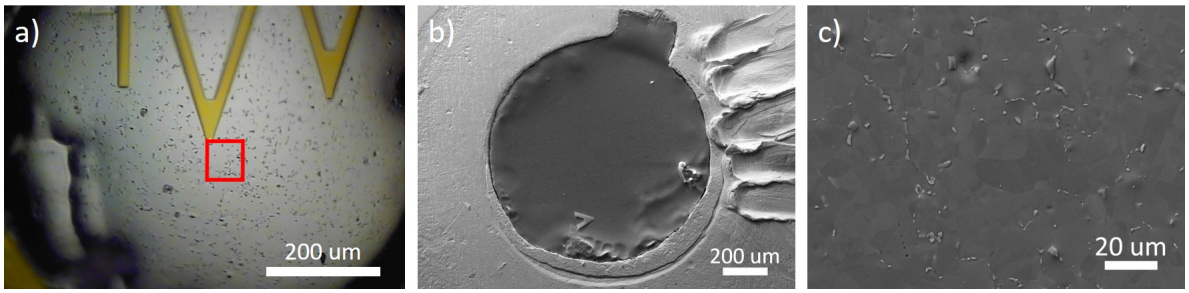

Figure 5.2: Images showing the surface condition of Sample 1XA: a) an optical image of the sample surface, b) an SE image of the sample surface surrounded by the gold washer, and c) an SE image of the sample surface.

Topographic measurements by HS-AFM were collected from the region outlined in red in Figure 5.2a. Individual frames were stitched together to form a composite image, shown in Figure 5.3. Numerous large SPPs are highlighted as white features distributed across the image. These features have a high aspect ratio and result in the immediate surrounding areas to exhibit image artefacts due to flattening post-processing.

A number of GBs are also observed within the region, some appearing as dark regions indicating that they have been preferentially etched during sample preparation. Slip bands are present across the sample surface indicating that the sample has been plastically stressed. This is likely the result of unintentional bending of the sample during sample preparation or handling.

Figures 5.3a and 5.3b show two smaller composite HS-AFM images, from the regions outlined within the larger composite topographic map. Figure 5.3a shows a region containing numerous GBs and a region of a concentration of voids. The voids vary in depth, with more frequent and deeper voids appearing to concentrate at the GBs. Figure 5.3b shows a region containing a number of smaller SPPs and a lower concentration of voids. Smaller SPPs are primarily observed to be intragranular.

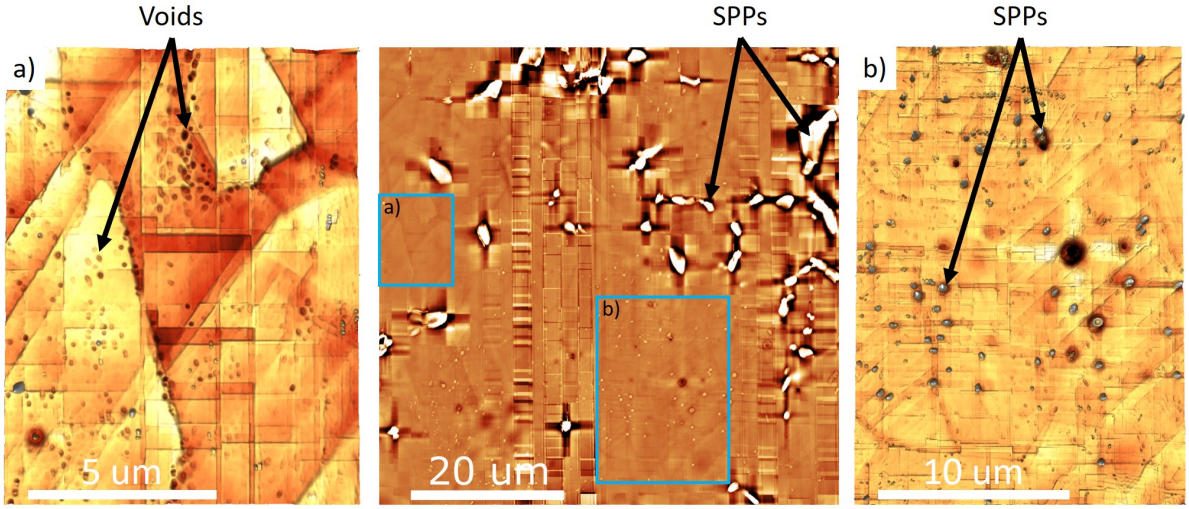

Figure 5.3: A large area composite HS-AFM topographic map collected from Sample 1XA with two smaller composite maps from the regions outlined, where: a) highlights a region of a concentration of voids, and b) highlights a region of smaller SPPs.

Following large area HS-AFM analysis, individual HS-AFM frames were considered. A selection of HS-AFM frames are shown in Figure 5.4. Within Figures 5.4a and 5.4d, the z-scale has been inverted such that voids appear as peaks. This puts emphasis on their location and depth. It is observed that voids concentrated along GBs. The deepest voids are intergranular, whereas intragranular voids tend to be shallower.

Figures 5.4b and 5.4c were collected from the same region as that shown in Figure 5.4a. Figure 5.4c is a HS-AFM map collected at a higher magnification. Within this image a cluster of voids is observed where multiple voids appeared to have either coalesced or formed nearby one another. A large pit is observed in Figure 5.4d, this is likely due to the removal of an SPP.

Large area maps of the surface were also collected by EDX, for information on the chemical composition of the microstructures observed. EDX maps collected from a region on the sample surface containing the area analysed by HS-AFM are shown in Figure 5.5. These maps were

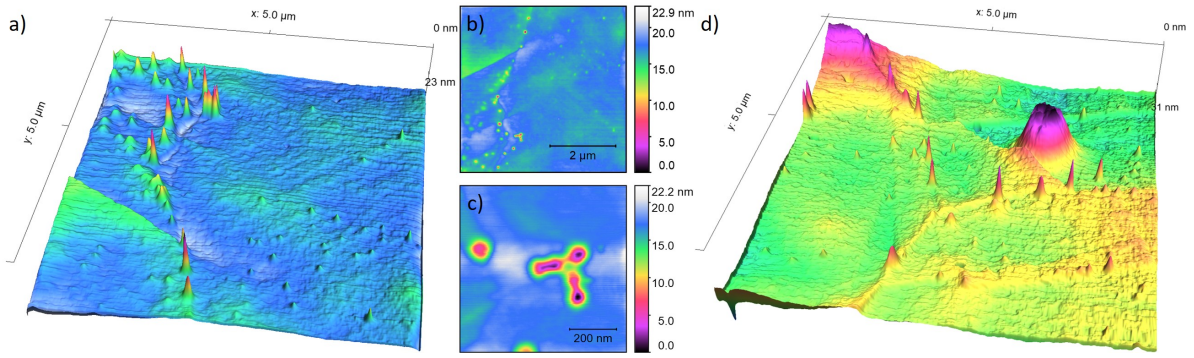

Figure 5.4: A selection of images showing inverted and standard HS-AFM topographic maps of voids observed across the surface of Sample 1XA. a) and d) show 3D topographic maps with an inverted z-scale, b) and c) show topographic images from the same region as that shown in a).

collected at 30 kV with 200 ms dwell time.

Figure 5.5a shows the elemental composition. SPPs across the surface are highlighted as they contain a differing composition to that of the bulk material. Figure 5.5b shows an EDX 'phase' map generated for the region. Where 'phase' is determined compositionally and not by crystallography. Each 'phase' colour is defined within Table 5.3. It is clear that the SPPs present contain differing ratios of elements, with some appearing to have a compositionally different shell, or altered bulk composition immediately adjacent to where they have formed. Figure 5.6 shows the element specific EDX maps for the same region, such that each element may be considered separately.

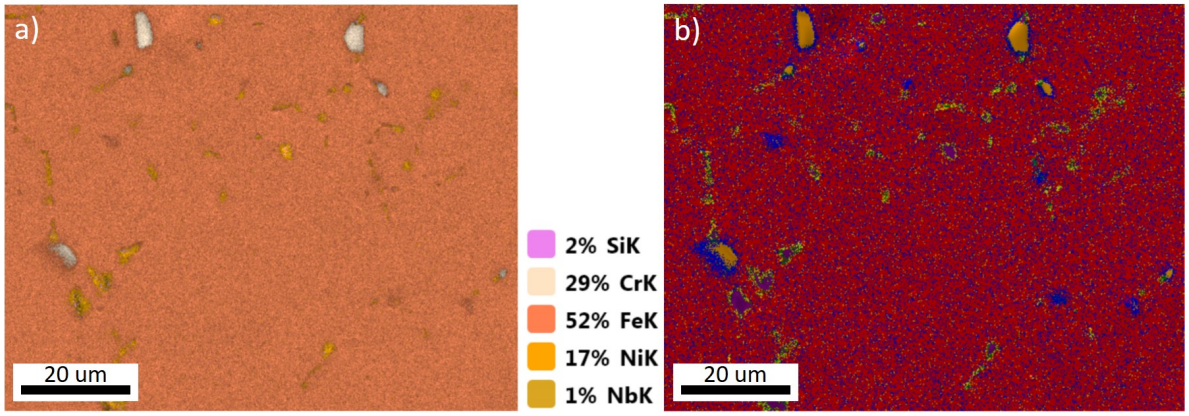

Figure 5.5: EDX maps collected from the surface of Sample 1XA: a) an EDX elemental composition map (individual element maps are given in Figure 5.6), and b) an EDX 'phase' map (each phase composition is given in Table 5.3).

EBSD maps produced from a region containing the area analysed by HS-AFM are shown in Figures 5.7a-d. These maps were collected using a constant beam voltage of 30 kV, an aperture of 120 μm and a step size of 50 nm. Raw data was cleaned up using confidence index standardisation

Table 5.3: A table of weight % as measured by EDX for each 'phase' shown in Figure 5.5b.

	Si	Cr	Fe	Ni	Nb
Orange	0.00	55.87	31.52	11.66	0.96
Blue	0.00	22.61	53.94	23.45	0.00
Purple	7.55	9.81	24.80	31.18	26.66
Green	3.86	20.66	39.53	28.90	7.06
Yellow	1.29	18.07	49.23	29.52	1.89
Red	0.00	17.91	60.94	21.15	0.00

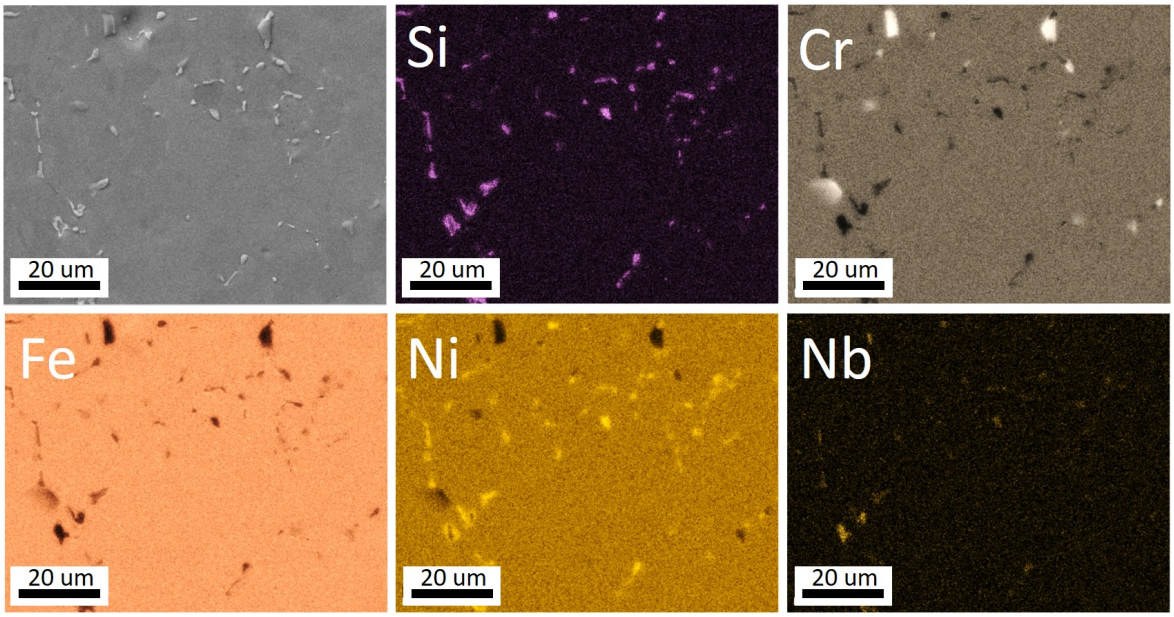

Figure 5.6: The first image shows an SE image of the area analysed on the surface of Sample 1XA for reference, the other images show element specific EDX maps collected from the sample surface, where brighter areas contain a higher concentration of the given element, and dark areas contain a lower concentration. (Individual element maps are overlayed in Figure 5.5a.)

(CIS) and points with a confidence index (CI) less than 0.1 were filtered.

Figure 5.7a is an inverse pole figure (IPF) and image quality (IQ) map showing the orientation of the grains present within the area measured. The grain size (diameter) in this region varied from approximately 0.1 μm to 30.8 μm, with an average diameter of 1.4 μm and a standard deviation of 3.9 μm. This figure confirms the intergranular nature of the larger SPPs. Figure 5.7b and 5.7c are discrete IPF plots, these highlight any preferred orientations observed in Figure 5.7a. Figure 5.7b contains a point for each pixel in Figure 5.7a. Figure 5.7c contains a single point for each grain in Figure 5.7a weighted by size, i.e. the larger points map to the larger grains. These plots give insight into the surface texture. A preferred orientation is observed, with the

largest grains aligning with the {101} planes.

Figure 5.7d shows a phase diagram for the same area shown in Figure 5.7a. EBSD data collected in this region was mapped to 3 phases that were expected to be present within the material: austenite, sigma phase and body-centred cubic (BCC). Areas identified as austenite are shown in red, sigma phase in yellow, and BCC in green. It can be seen that the majority of the material is austenitic. The majority of large SPPs were identified as austenitic, others were identified as BCC or sigma phase. However, measurements performed on SPPs were at a much lower confidence index due to their small size and non-flat surface. Furthermore, the high aspect ratio of the SPPs resulted in a shadowing effect observed as a white (non-indexed) edge in Figure 5.7d.

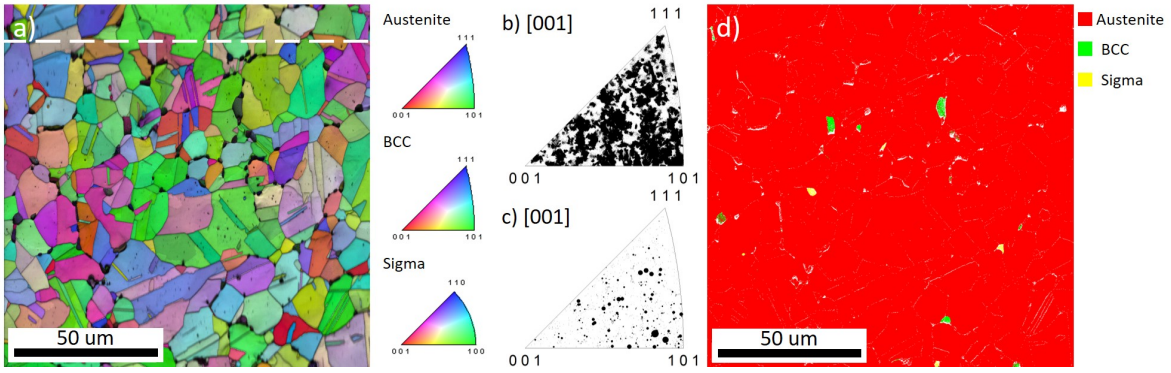

Figure 5.7: EBSD maps collected from Sample 1XA: a) an IPF and IQ map with inset legend and white dotted line marking a collection error, b) a discrete IPF plot where each point represents each pixel collected in the Figure 5.7a, c) a discrete IPF plot where each point represents each grain in the Figure 5.7a weighted by size, and d) a phase map where red is austenite, green is BCC, and yellow is sigma phase.

For direct comparison between each large area map, Figure 5.8 contains rotated and cropped versions of the EDX and EBSD maps presented previously such that they coincide with the composite HS-AFM topographic map shown in Figure 5.3.

By correlating these maps and comparing to previous work performed at NNL described in Section 5.1.1.1, SPPs present across the surface may be tentatively identified. This process is described in detail in Appendix A, where additional spot EDX results are also evaluated. Following the colour key established by the EDX 'phase' map in Figure 5.5b, the following SPPs were identified: orange 'phase' SPPs are $M_{23}C_6$, blue 'phase' is sigma phase, purple 'phase' SPPs are NbC, and green/yellow 'phase' SPPs are G phase. Following identification, further analysis of the surface textures of each SPP type measured by HS-AFM is given in Appendix B.

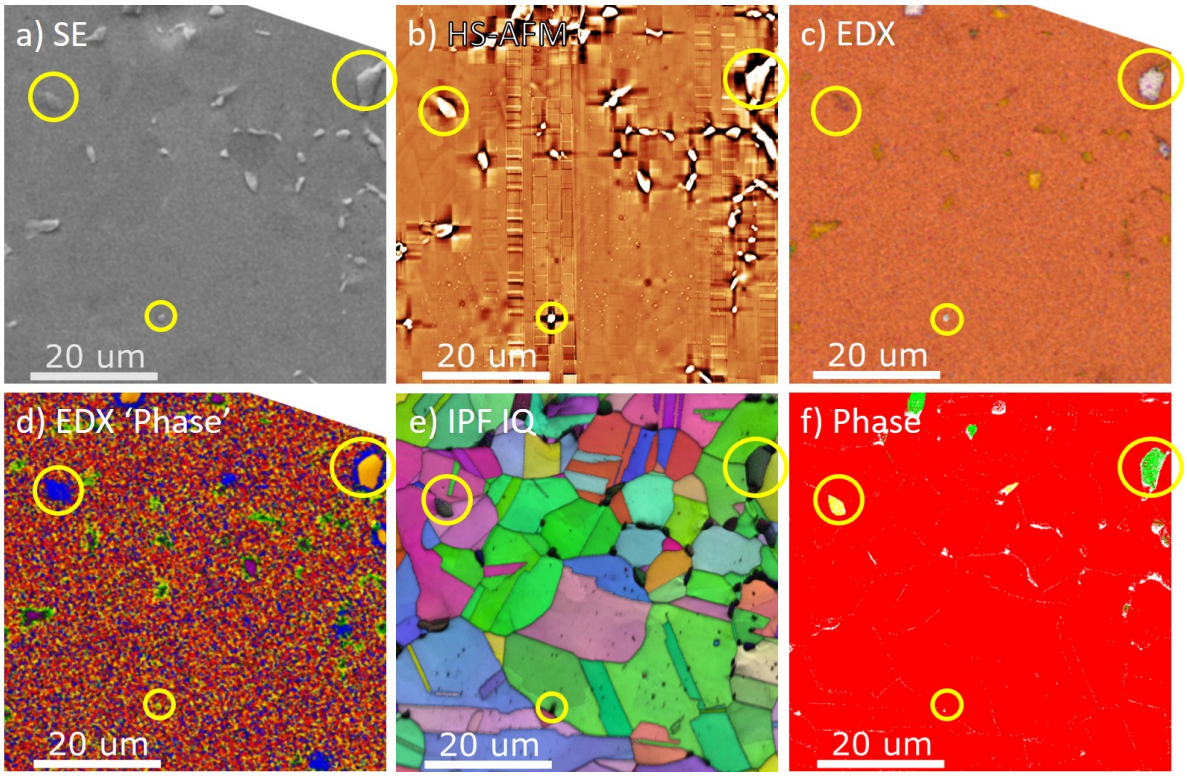

Figure 5.8: Large area maps collected from the surface of Sample 1XA rotated and cropped to coincide with the area analysed by HS-AFM: a) SE image, b) HS-AFM topographic map, c) EDX map, d) EDX 'phase' map, e) IPF IQ map, and f) phase map. This figure is for reference use only, inset legends have not been included but may be referred to within previous figures.

5.2.1.1 Distribution of GB Misorientations

EBSD data was analysed to produce a GB misorientation map of the region, shown in Figure 5.9. During analysis, each GB was classified as either a low-angle GB (LAGB), high-angle GB (HAGB), or a coherent twin GB, dependent upon the measured GB misorientation. Within this map LAGBs (with misorientation value in the range 5°-15°) are indicated in blue, HAGBs (with misorientation value 15°-62.8°) in red, and twin GBs (with misorientation value 60° and misorientation axis $< 111 >$ [29]) in green. GBs with misorientation values $< 5°$ are considered to be sub-GBs (i.e. within a grain). Other types of coincident-site lattice (CSL) GBs were not considered within this work. This map highlights the high proportion of coherent twin GBs.

GB misorientations present were plotted as a histogram, Figure 5.10. 39.4% of the GBs measured were HAGBs, 2.6% were LAGBs, and 45.1% of the GBs were coherent twin GBs. The remaining GBs are sub-GBs. If sub-GBs are negated from analysis, this corresponds to 45.2% HAGBs, 3.0% LAGBs, and 51.8% coherent twin GBs.

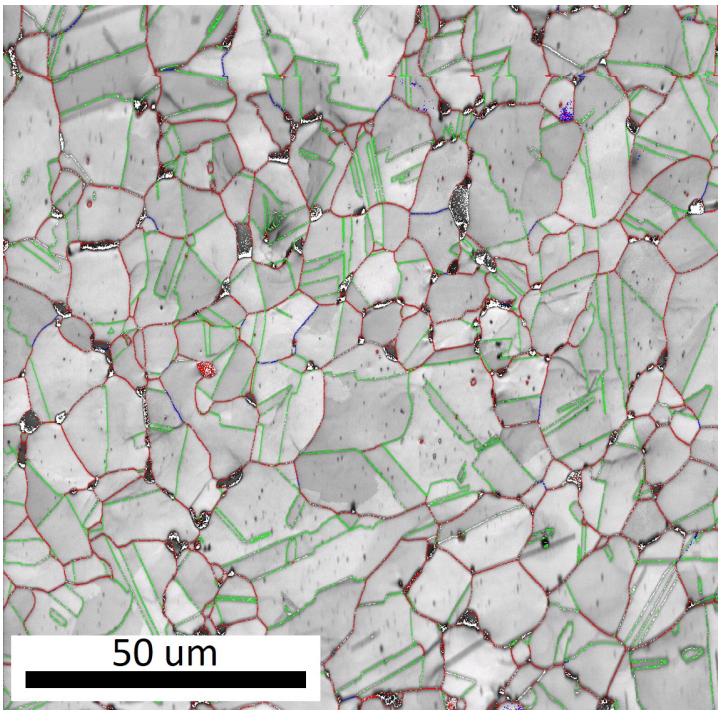

Figure 5.9: A map showing GB misorientation collected from Sample 1XA in the same region shown in Figures 5.7a, where GB misorientation values in the range 5°-15° are indicated in blue, 15°-62.8° in red, and 60° (with misorientation axis < 111 >) in green.

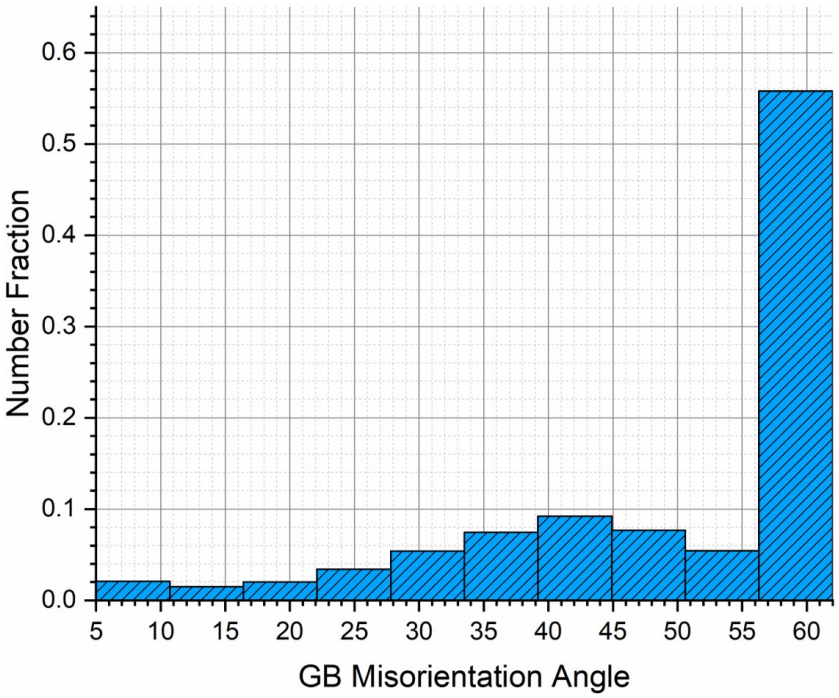

Figure 5.10: A histogram of all GB misorientations measured in the range 5°-62.8° in Figure 5.9 from Sample 1XA.

5.2.1.2 Analysis of Void Patterns

Large Area Statistical Analysis of Void Distribution From initial observations of the surface by HS-AFM, voids were observed to concentrate along or near certain GBs. Analysis of the distribution of voids present across the surface was performed using bespoke software (Nanomapper - Bristol Nano Dynamics Ltd. UK). The data used for this analysis is the same data collected for the large area composite HS-AFM map shown in Figure 5.3. As a result, analysed frames will overlap with one another and features will be counted more than once. Therefore, statistical data produced does not provide an accurate value for the frequency. Instead, this data should be considered as indicative of the patterns and relative frequencies of void size and distribution.

Within this analysis, a feature was identified as a void if it was a negative feature (in the z-direction) with a bounding rectangle width of 1-500 nm and length of 1-500 nm, and a ratio of ellipse axes between 0.5 and 3. HS-AFM data used within this analysis was first processed to allow for clearer images of voids, this is particularly important for regions surrounding high features such as large SPPs. The data was processed through a frequency filter and a relative standard deviation of 2.5 was applied. This resulted in the thresholding of negative features with depth greater than 2.5 relative standard deviation, in order to differentiate between voids and other surface height changes.

This data was used to plot a histogram of the void size, shown in Figure 5.11. The voids were found to have a mean void diameter of 75 nm, with a mode of 66 nm. The distribution was found to follow a long-tailed distribution and so a log-normal fit was performed in Origin software, shown in red in Figure 5.11. The log-normal fit had a peak at 64 nm.

During this analysis, no voids were identified with a diameter less than 32 nm. Analysis of individual frames largely supported this with no voids observed with a diameter less than approximately 30 nm.

Following these observations, void patterns were analysed in relation to GB misorientation and SPP locations. A heat map of features identified as voids is shown in Figure 5.12a. This map indicates an inhomogeneous distribution of voids, with structures of high and low concentrations of voids. The heat map was compared to the grain structure of the material as measured by EBSD (Figure 5.12b), and the locations of the large SPPs (Figure 5.12c). An area sparse in voids is seen in the bottom right hand quarter. This area aligned well with a region of twin GBs and a lack of large SPPs. Generally, areas of high numbers of voids align well with HAGBs.

Analysis of Specific HS-AFM Frames HS-AFM data was analysed frame by frame to build up a database of images containing HAGBs, LAGBs and twin GBs, as identified by EBSD. Example topographic maps are given in Figures 5.13 - 5.18. It can be seen that HAGBs are clearest within HS-AFM topographic maps, with LAGBs appearing much less prominently. This is due to HAGBs appearing darker (i.e. lower topographically). HAGB visibility is also accentuated

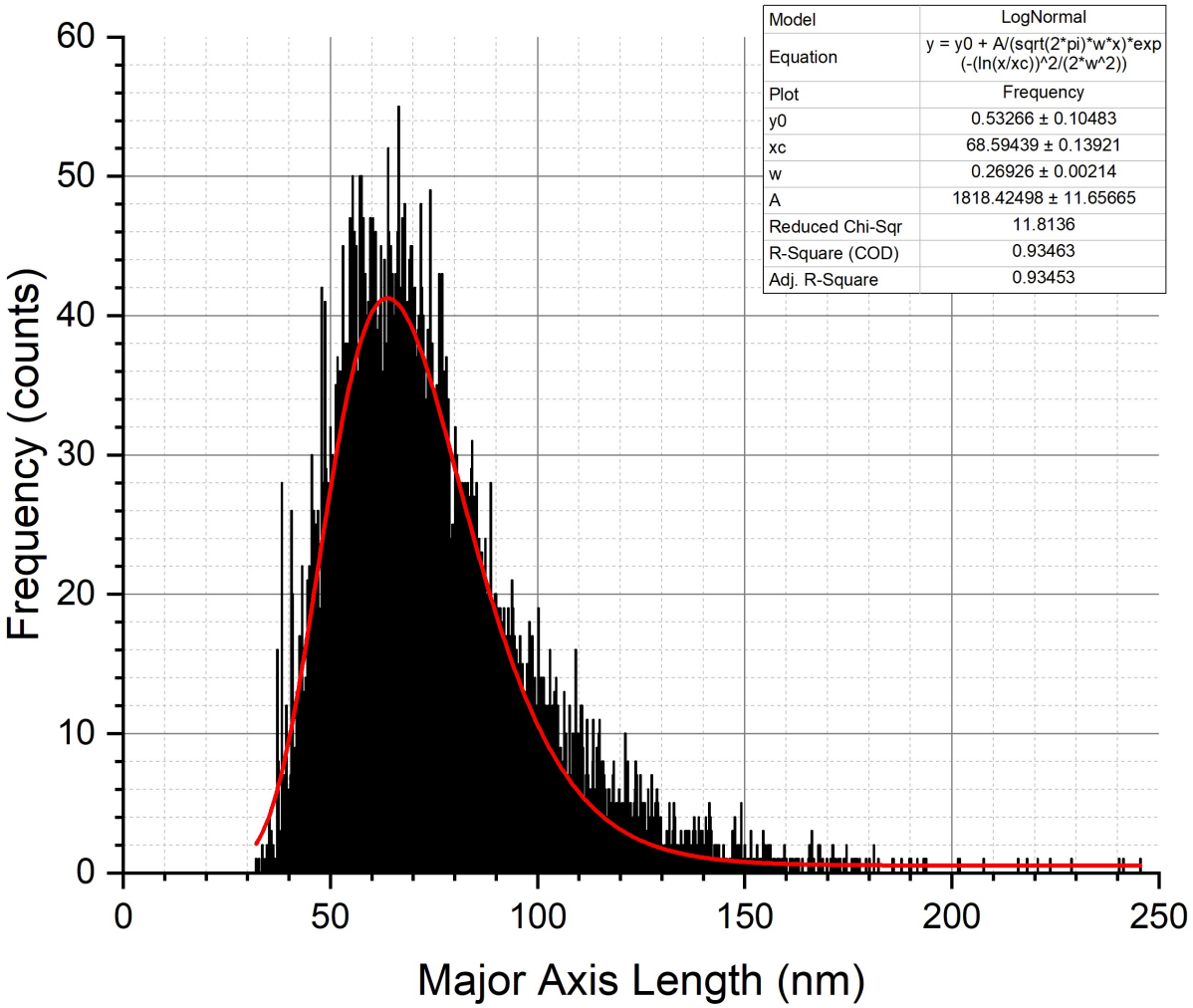

Figure 5.11: A histogram showing the major axis length of the voids measured by HS-AFM on Sample 1XA, with a log-normal fit shown in red.

by the presence of dislocations across the surface, as the dislocation direction varies from grain to grain either side of HAGBs. In contrast, dislocations are able to move through LAGBs, as observed in Figures 5.16 - 5.18.

Figures 5.13 - 5.18 show that voids appear to concentrate along GBs, as previously observed in Figure 5.4. Line scans were performed across numerous voids, these measurements are summarised in Table 5.4. It should be noted that values stated in Table 5.4 were calculated from measurements performed in the regions shown in Figures 5.13 - 5.18 and therefore vary from the values calculated from the large area analysis shown in Figure 5.11. Voids were found to be more frequent, deeper and have a larger diameter at HAGBs compared to LAGBs or coherent twin GBs. Figure 5.18 contains a large concentration of voids that appear to bridge from one HAGB to another. By comparing the known location at which this map was collected with the EBSD maps collected from the region, these two GBs are either side of a thin cross section of a grain.

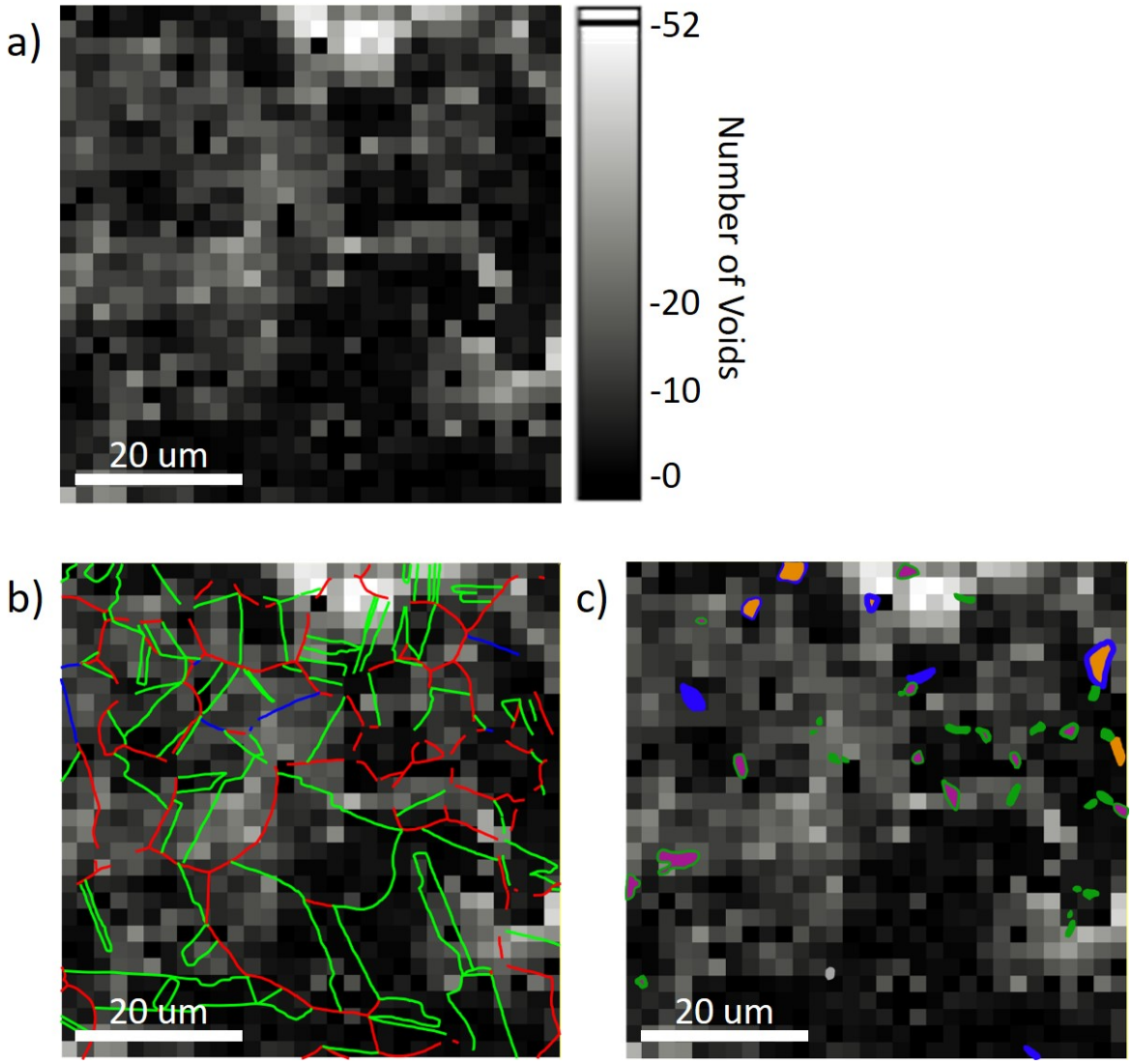

Figure 5.12: a), b) and c) show images of heat maps for the region on Sample 1XA analysed by HS-AFM, where lighter areas have a higher number density of features identified as voids, and darker areas have a lower number density. b) Shows the heat map with the GB misorientations overlaid from Figure 5.9, and c) shows the heat map with an image of the large SPPs overlaid from Figure 5.5b.

Voids measured along coherent twin GBs were varied, but were typically smaller in diameter than for HAGBs, and less frequent, as observed in Figures 5.13 - 5.15 and Figure 5.16. Figure 5.15 contains a twin GB with non-coherent twin steps. In this case, voids were located in such a way that they appeared to pin the GB at the turning point. Figures 5.16-5.18 contain LAGBs. Again, voids were observed to line-up along these GBs, these voids were often shallow.

Voids were also aligned along slip dislocations; in turn these voids must also align along crystallographic planes in the material. Some voids, however, do not appear to follow any clear

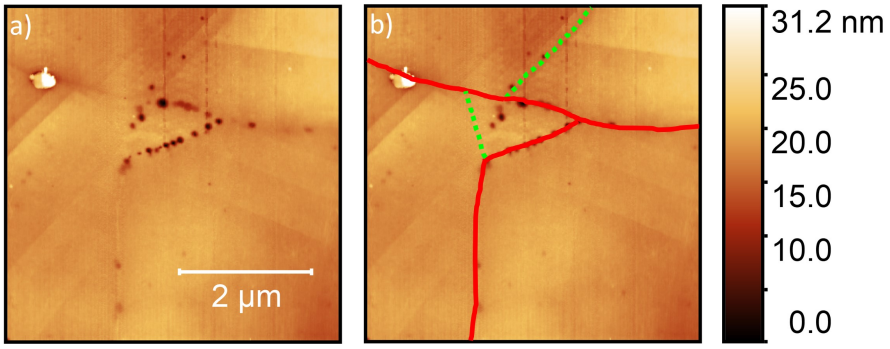

Figure 5.13: HS-AFM topographic maps showing GBs present in Sample 1XA: a) without labels, b) with labelled HAGBs (in red) and coherent twin GBs (dotted in green).

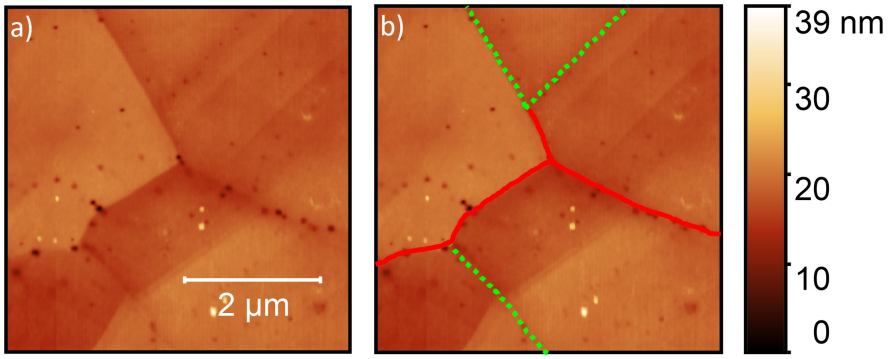

Figure 5.14: HS-AFM topographic maps showing GBs present in Sample 1XA: a) without labels, b) with labelled HAGBs (in red) and coherent twin GBs (dotted in green).

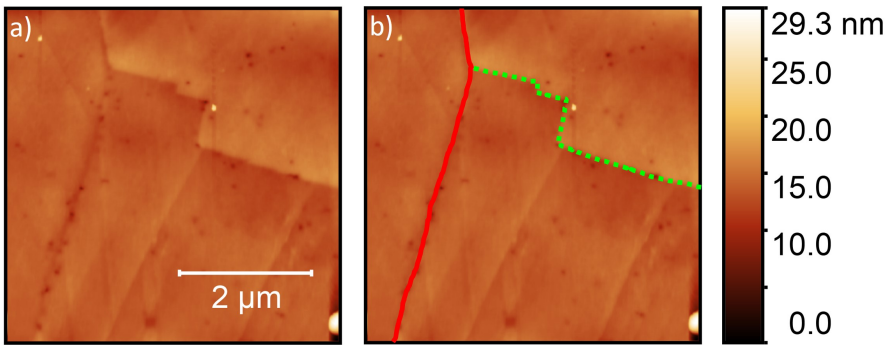

Figure 5.15: HS-AFM topographic maps showing GBs present in Sample 1XA: a) without labels, b) with labelled HAGBs (in red) and coherent twin GB (dotted in green).

pattern.

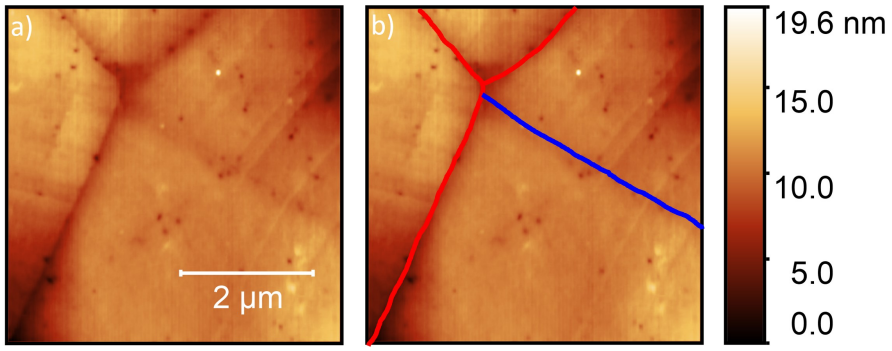

Figure 5.16: HS-AFM topographic maps showing GBs present in Sample 1XA: a) without labels, b) with labelled HAGBs (in red) and LAGB (in blue).

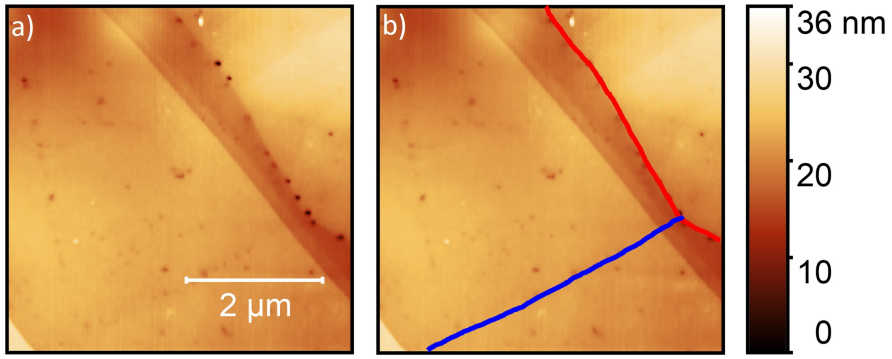

Figure 5.17: HS-AFM topographic maps showing GBs present in Sample 1XA: a) without labels, b) with labelled HAGBs (in red) and LAGB (in blue).

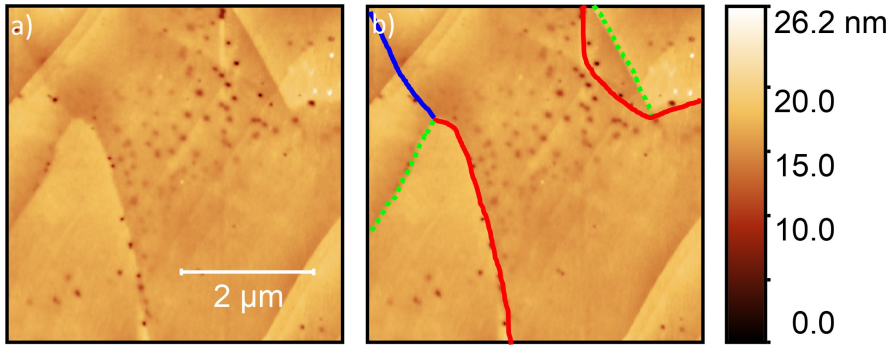

Figure 5.18: HS-AFM topographic maps showing GBs present in Sample 1XA: a) without labels, b) with labelled HAGBs (in red), LAGB (in blue) and coherent twin GBs (dotted in green).

Table 5.4: Measured void diameters and depths for different regions on the surface (bulk and GBs), and different GB types on Sample 1XA. Averages were calculated from measurements performed in the regions shown in Figures 5.13 - 5.18.

Region Type	**Void Diameter (nm)**		**Void Depth (nm)**		**No. of Voids Measured**
	Mean	**Range**	**Mean**	**Range**	
GB	134	60 - 270	6.1	0.9 - 20	102
Bulk	100	50 - 200	2.2	0.4 - 8	85
GB Type	**Void Diameter (nm)**		**Void Depth (nm)**		**No. of Voids Measured**
	Mean	**Range**	**Mean**	**Range**	
HAGB	143	70 - 270	7.2	1 - 20	73
LAGB	108	65 - 200	2.9	0.9 - 10	14
Twin GB	113	60 - 180	3.4	0.9 - 9.5	15

5.2.2 Measurements of GB Depletion Profiles for Irradiation Sensitised GBs

EBSD maps were collected by t-EBSD from Lamellae A, B and C (produced from Sample 2YB), as shown in Figure 5.19. For these datasets, GB misorientation values were determined for each GB present during post-processing. Specific GBs within the lamellae were identified for further measurements of GB segregation by TEM. These GBs were chosen to include a range of GB misorientation values.

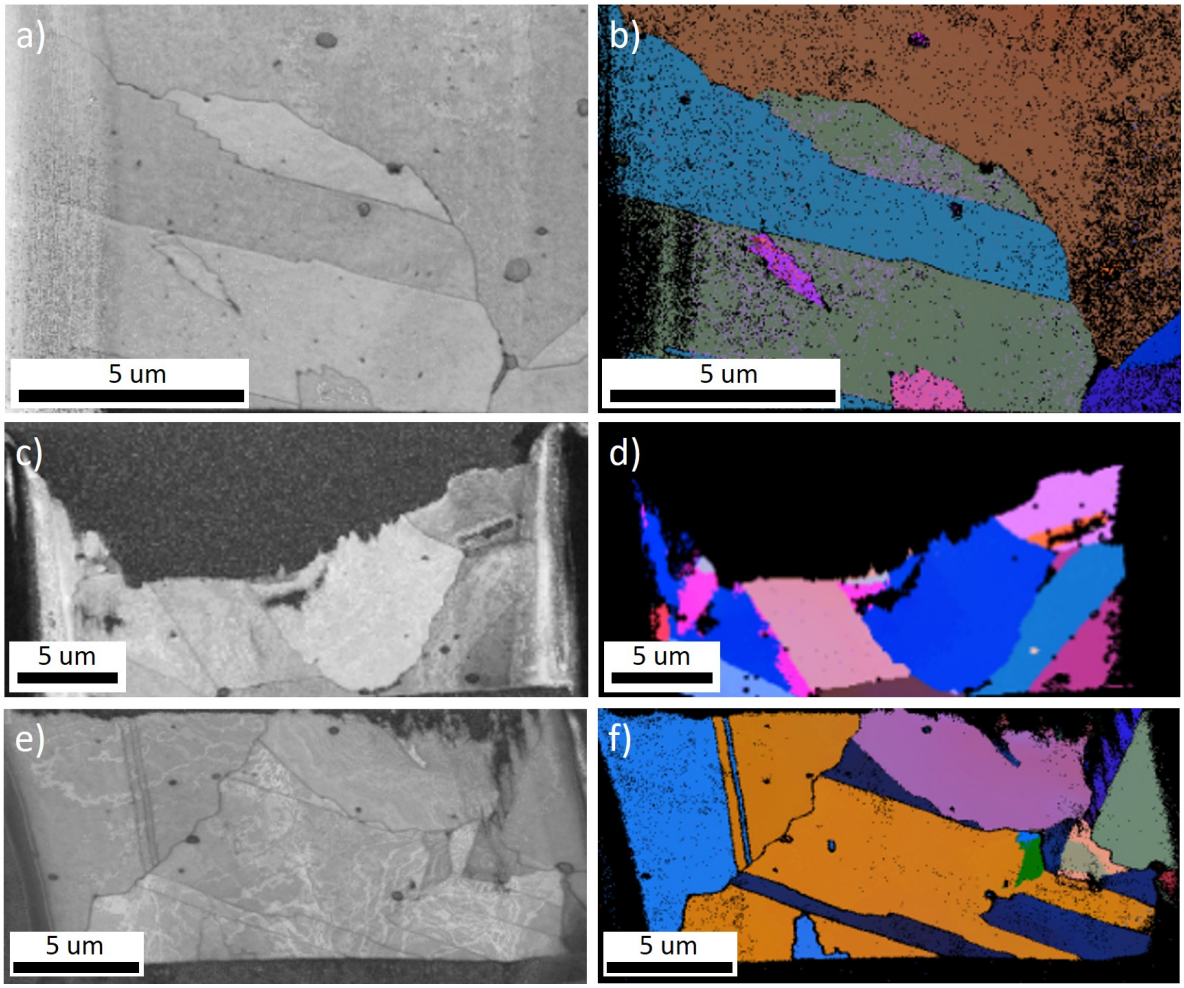

Figure 5.19: a), c) and f) show band contrast images of Lamellae A, B and C (Sample 2YB), respectively. b), d) and f) show EBSD orientation maps of Lamellae A, B and C, respectively, in Euler colours with hit rates of: b) 64.75%, d) 14.52%, f) 69.18%.

STEM EDX line scans were collected across selected GBs. For accurate measurements to be taken across a GB it is important that the GB is aligned to the incident electron beam. Suitable alignment was confirmed when the GB appeared no more than approximately 2.5 nm in projected width. For each GB, 2 nm, 5 nm, and in some cases 10 nm, line scan steps were used. Examples of these measurements are shown in Figures 5.23-5.25. It was found that, for all GBs analysed,

chromium and iron was depleted at the GB, whilst nickel and often silicon was enriched. The extent of this varied for each type of GB measured.

Measurements performed on HAGBs resulted in a range of composition profile shapes with widths between approximately 40 nm and 60 nm. Some profiles appeared symmetric, such as that observed in Figure 5.20, whilst others were asymmetric such as those seen in Figures 5.21 and 5.22. Four of the nine measured HAGBs were found to contain <12 wt.% Cr, with the lowest concentration found to be 10.89 wt.%. The highest minimum chromium concentration was measured at 13.22 wt.%. Nickel was enriched up to 42.61 wt.%, and silicon was enriched up to 4.35 wt.%.

Only one LAGB was analysed, shown in Figure 5.23. This GB was less severely depleted in chromium than measured HAGBs. Measured chromium does not drop below 12 wt.%, with a minimum chromium concentration of 13.42 wt.%. Nickel is enriched up to a value of 38.8 wt.% and silicon is not significantly enriched. The elemental profile collected for this GB has a much larger width than that of other measured GBs: approximately 130 nm. However, as can be seen within the collected STEM bright field (BF) image of the GB, Figure 5.23a, the measured GB has a shadow, which indicates that the TEM beam may not be properly aligned to the GB.

STEM EDX line scans performed across twin GBs were symmetric. In Figure 5.24 the depletion profile has a similar width to that observed for HAGBs. One of the measured GBs produced a double-peaked W-shaped profile (approximately 90 nm wide), seen in Figure 5.25. Twin GBs were less severely depleted in chromium than that measured for HAGBs, with lowest concentration measured at 12.27 wt%. Nickel was enriched up to a value of 48.72 wt.%, and silicon was enriched up to 5.34 wt.%.

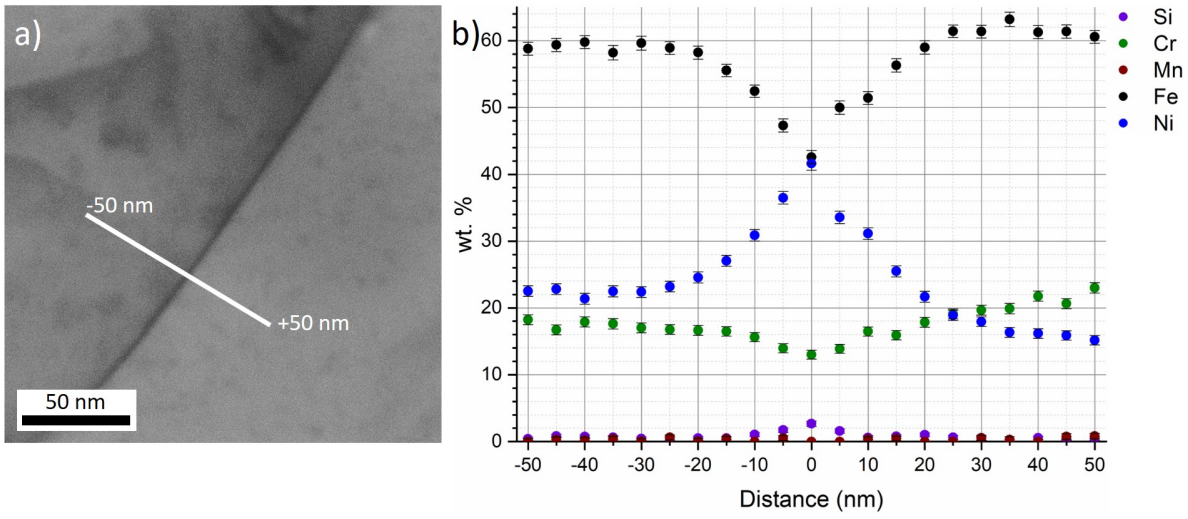

Figure 5.20: Images showing TEM measurements collected for an HAGB with GB misorientation 45.83° (Sample 2YB): a) an STEM BF image showing the GB analysed by STEM EDX, b) an STEM EDX elemental line scan collected across 100 nm with 5 nm steps.

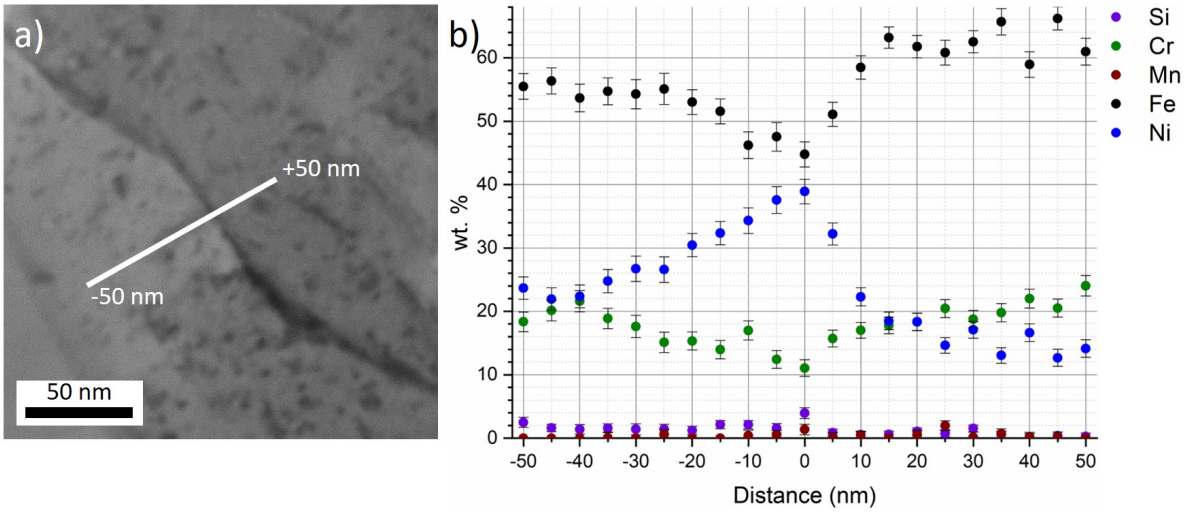

Figure 5.21: Images showing TEM measurements collected for an HAGB with GB misorientation 32.17° (Sample 2YB): a) an STEM BF image showing the GB analysed by STEM EDX, b) an STEM EDX elemental line scan collected across 100 nm with 5 nm steps.

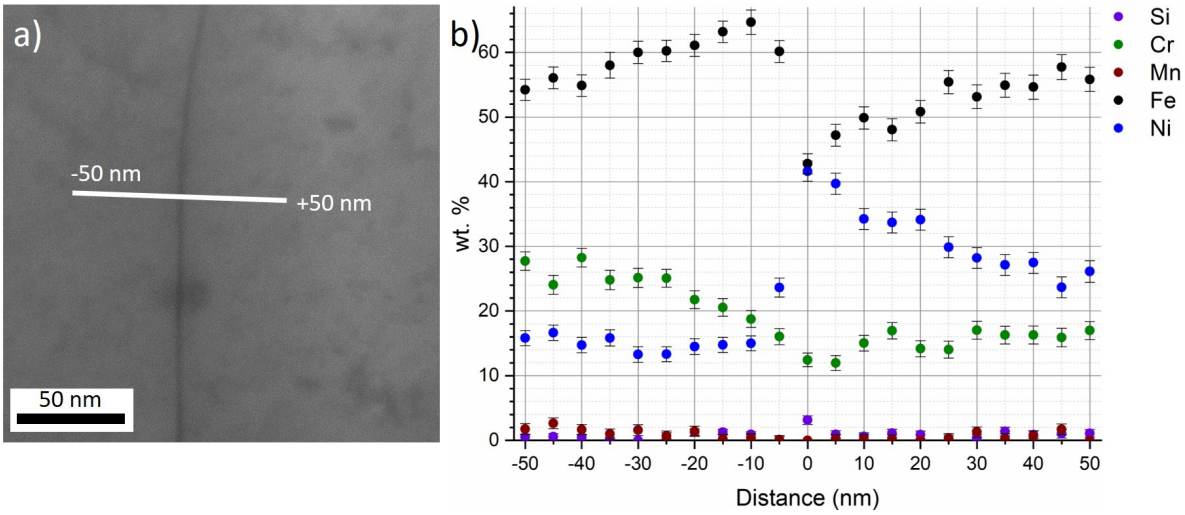

Figure 5.22: Images showing TEM measurements collected for an HAGB with GB misorientation 56.54° (Sample 2YB): a) an STEM BF image showing the GB analysed by STEM EDX, b) an STEM EDX elemental line scan collected across 100 nm with 5 nm steps.

Figure 5.26 shows the relationship between elemental segregation measurements and GB misorientation for chromium, nickel, and silicon. The raw data used to plot these graphs is given in Table 5.5. An indication of the relationship between GB segregation and misorientation can be observed within these graphs. However, these graphs also indicate that more measurements are required to determine a clear relationship. This is particularly evident within Figure 5.26c, where there is no obvious relationship between maximum silicon concentration and GB misorientation.

Minimum chromium concentration was observed to vary with GB misorientation. Higher

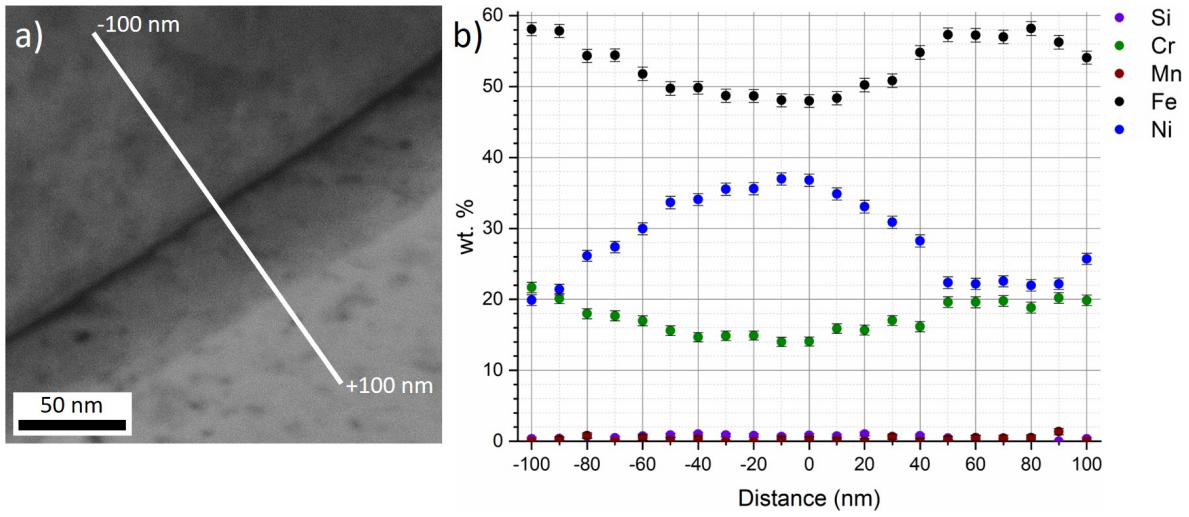

Figure 5.23: Images showing TEM measurements collected for an LAGB with GB misorientation 13.96° (Sample 2YB): a) an STEM BF image showing the GB analysed by STEM EDX, b) an STEM EDX elemental line scan collected across 200 nm with 10 nm steps.

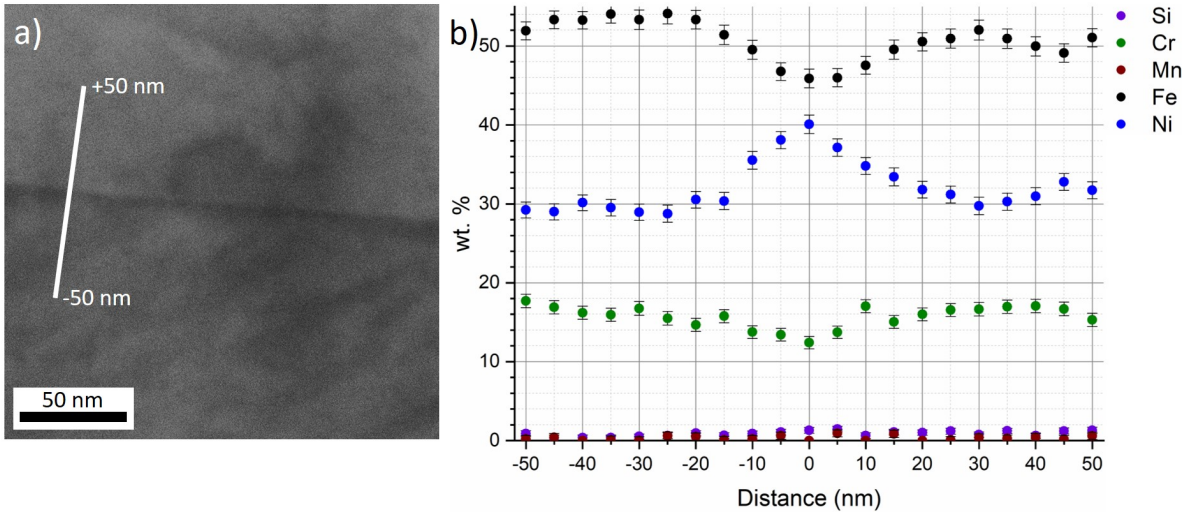

Figure 5.24: Images showing TEM measurements collected for a twin GB with GB misorientation 59.46° (Sample 2YB): a) an STEM BF image showing the GB analysed by STEM EDX, b) an STEM EDX elemental line scan collected across 100 nm with 5 nm steps.

minimum values were measured in LAGBs (13.42 wt.% lowest) and twin GBs (12.27 wt.% lowest), and lower minimum values were measured in HAGBs (10.89 wt.% lowest). Two horizontal lines have been added to Figure 5.26a, indicating the expected bulk chromium concentration at 20 wt.%, and the threshold value for sensitisation at 12 wt.%. Sensitised GBs appeared to be restricted to HAGBs. Chromium measurements collected for twin GBs had a large range, from 12.35 wt.% up to 19.46 wt.%. Figure 5.26a reveals the highest measured chromium concentration to be an

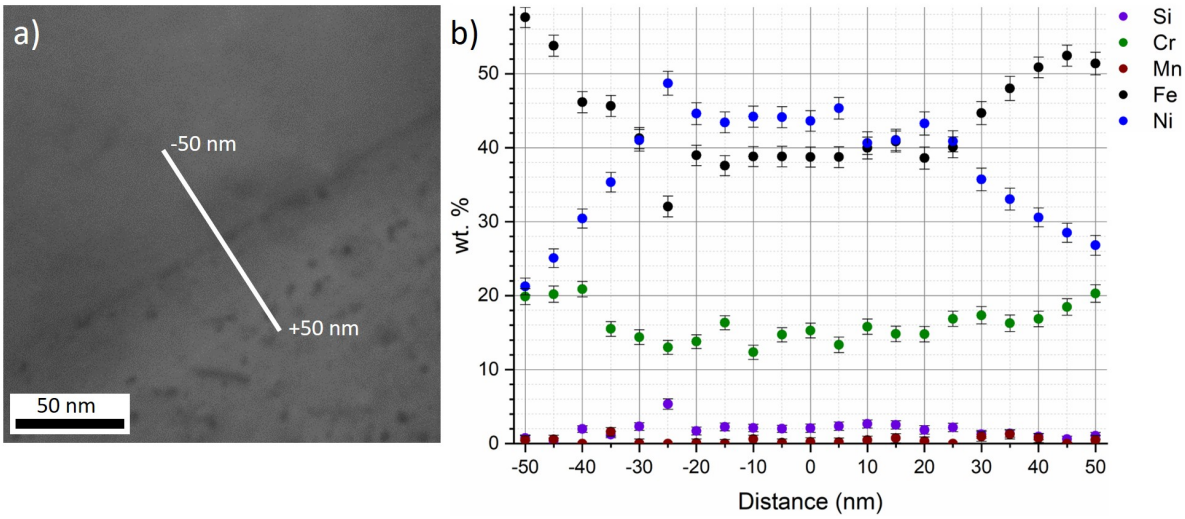

Figure 5.25: Images showing TEM measurements collected for a twin GB with GB misorientation 59.44° (Sample 2YB): a) an STEM BF image showing the GB analysed by STEM EDX, b) an STEM EDX elemental line scan collected across 100 nm with 5 nm steps.

outlying measurement, this is likely a result of poor alignment of the GB to the TEM beam.

Maximum nickel concentration, as shown in Figure 5.26b, followed an opposite trend to that observed for minimum chromium concentration, however this relationship is less well defined. Within this graph a horizontal line was added to indicate expected bulk nickel concentration at 25 wt.%. There was a considerable scatter within measured nickel concentrations, though the lower values were measured for the twin GBs. Again an outlying measurement was observed, this was identified as the same outlier as that observed in Figure 5.26a.

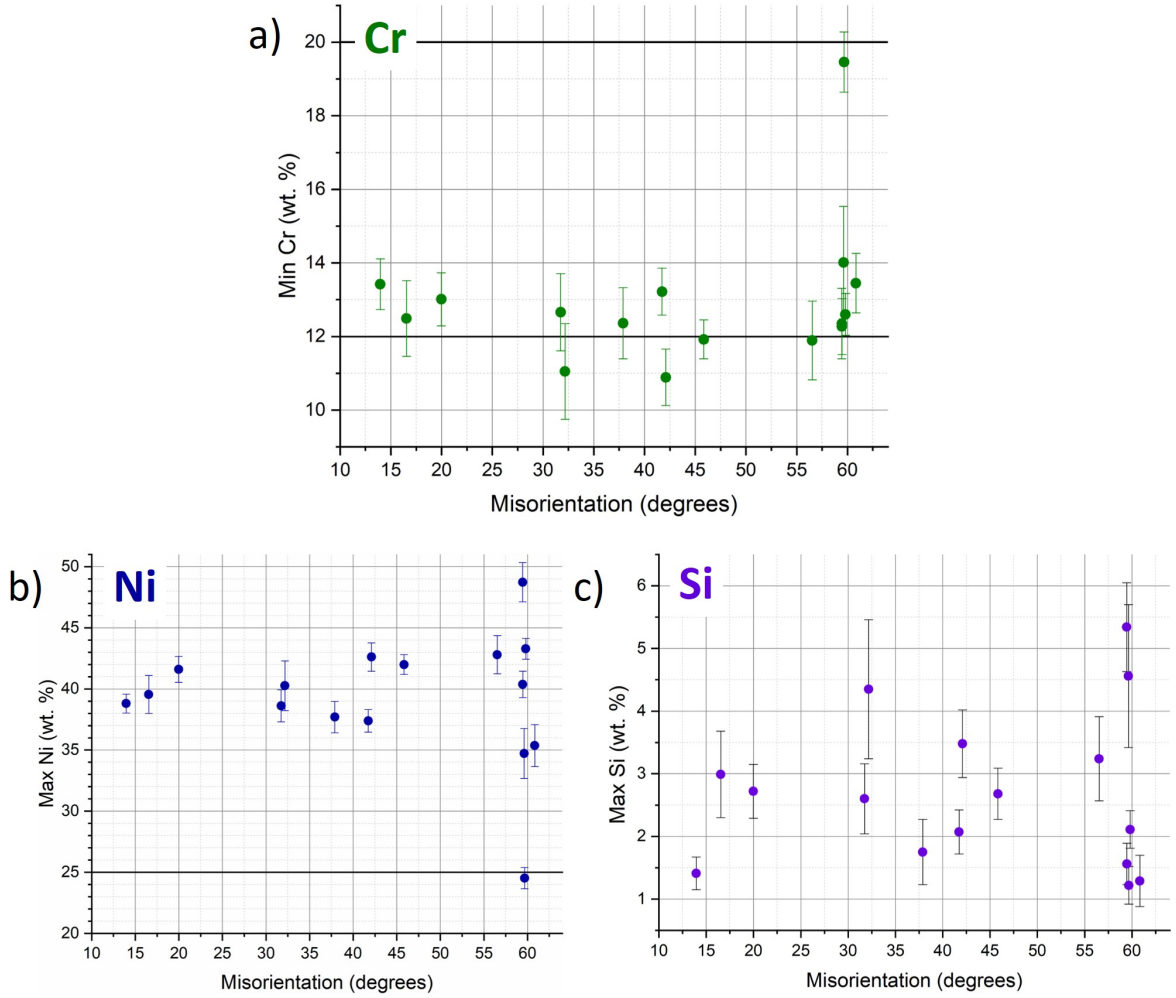

Figure 5.26: a) Minimum chromium wt.% vs. GB misorientation with two horizontal lines indicating approximate initial chromium concentration for AGR fuel cladding (20 wt.%) and the threshold value for sensitisation (12 wt.%), b) maximum nickel wt.% vs. GB misorientation with a horizontal line indicating approximate initial nickel concentration for AGR fuel cladding (25 wt.%), and c) maximum silicon wt.% vs. GB misorientation. (All data points were collected from Sample 2YB.)

Table 5.5: TEM measurements of GB segregation in Sample 2YB lamellae. *This point has been highlighted as an outlying value.

GB Misorientation (degrees)	**Min Cr wt%**	**Max Ni wt%**	**Max Si wt%**
13.96	13.42	38.8	1.41
16.55	12.49	39.55	2.99
19.98	13.01	41.6	2.72
31.74	12.66	38.62	2.6
32.17	11.05	40.26	4.35
37.89	12.36	37.7	1.75
41.74	13.22	37.39	2.07
42.10	10.89	42.61	3.48
45.83	11.92	41.99	2.68
56.54	11.89	42.8	3.24
59.44	12.35	48.72	5.34
59.46	12.27	40.37	1.56
59.62	14.01	34.72	4.56
59.66*	19.46	24.53	1.22
59.80	12.60	43.29	2.11
60.84	13.45	35.37	1.29

5.3 Analysis of SCC Observed Within Ex-Service Fuel Cladding

SCC in Sample 2YC was located at the sintox-cladding interface, with smaller cracks located at the gas facing side. Forward-scatter detector (FSD) images collected by SEM for Sample 2YC are shown in Figure 5.27. Within these images it can be seen that the crack path is intergranular with multiple branches.

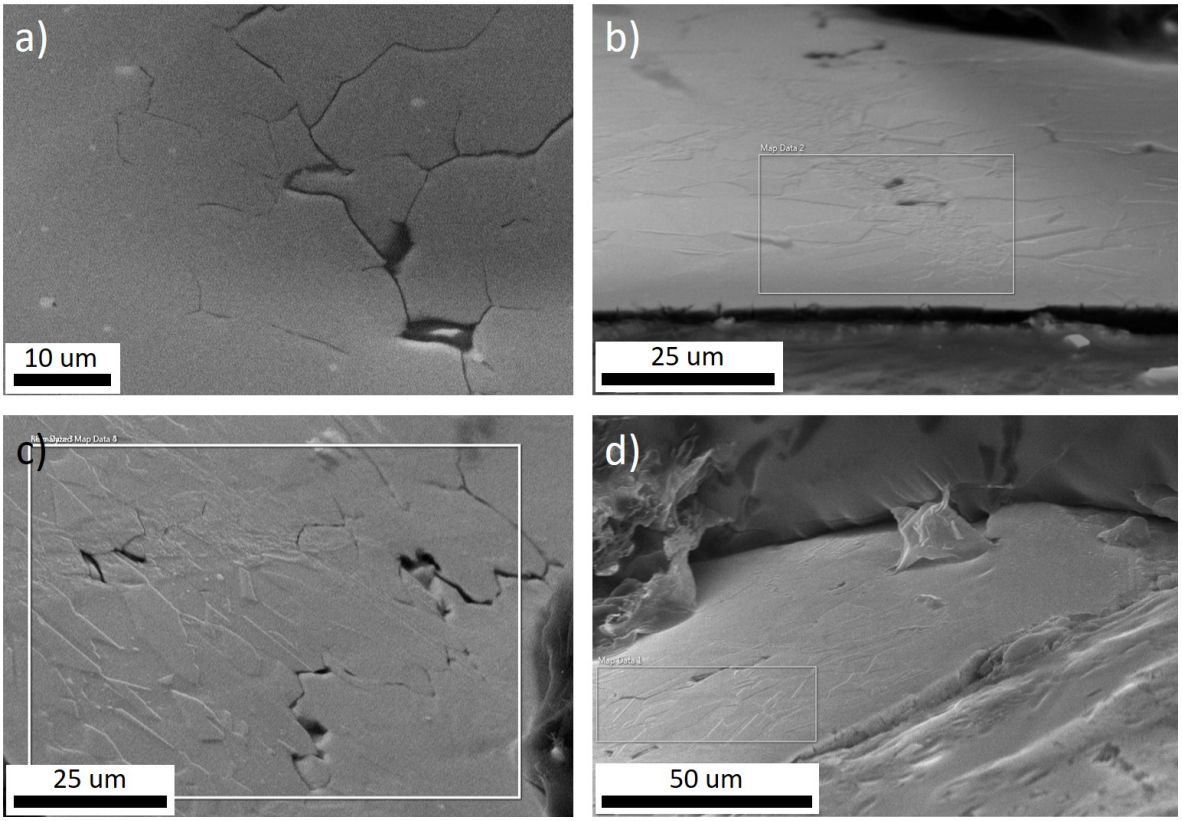

Figure 5.27: a) An SE image and b)-d) FSD images showing cracking within Sample 2YC.

EBSD measurements were performed on the bulk sample, however, the quality of the EBSD maps produced were not optimal as a result of the quality of the surface finish. The surface was affected by preparation damage, debris, and previous coating. The surface was gently ion polished by FIB to produce the EBSD map shown in Figure 5.28a. Dark regions within this map are the result of areas that could not be indexed. These areas draw out thick lines, an indication that this is due to scratches or mechanical polishing. The GBs along, and adjacent to, the crack path were labelled in white and green, respectively. The misorientations of these GBs were measured and recorded in Table 5.6. Histograms showing the measured GB misorientations along the crack path, and non-cracked GBs adjacent to the cracked path are shown in Figures 5.29a and 5.29b, respectively.

GB misorientations present along the crack path, were exclusively categorised as HAGBs,

with no LAGBs or twin GBs being observed. Measured GB misorientations of adjacent GBs, that is, non-cracked GBs located at triple points where the other two GBs have cracked due to IGSCC (Table 5.6), show that higher misorientation GBs crack preferentially, with the exception of twin GBs which did not crack. Unfortunately, few adjacent GB misorientations were measured due to the quality of the EBSD maps collected, and so analysis is not considered as statistically significant.

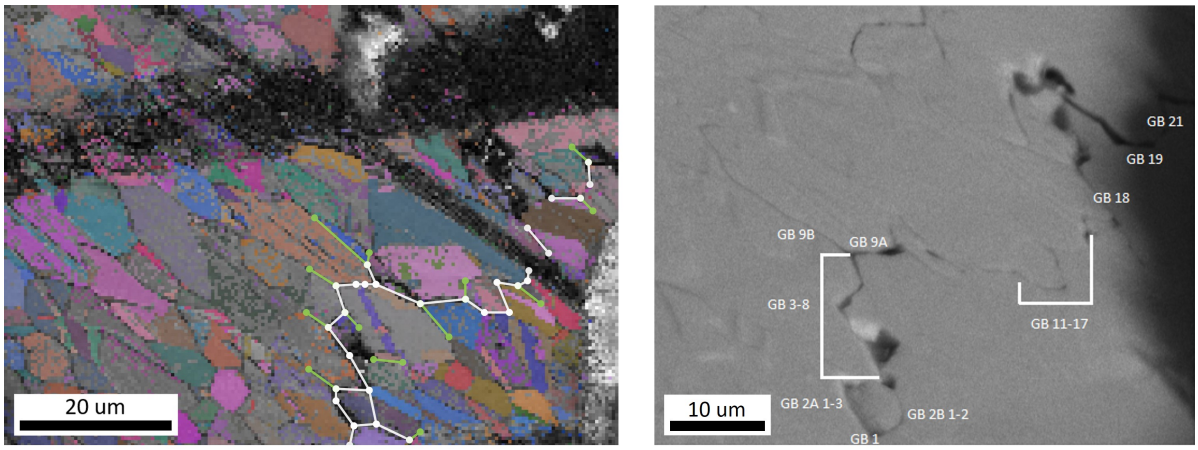

Figure 5.28: a) A band contrast IPF map in Euler colours collected from Sample 2YC with the crack path labelled in white and adjacent non-cracked GBs in green, and b) an SE image of the same area with labels indicating crack path GB names.

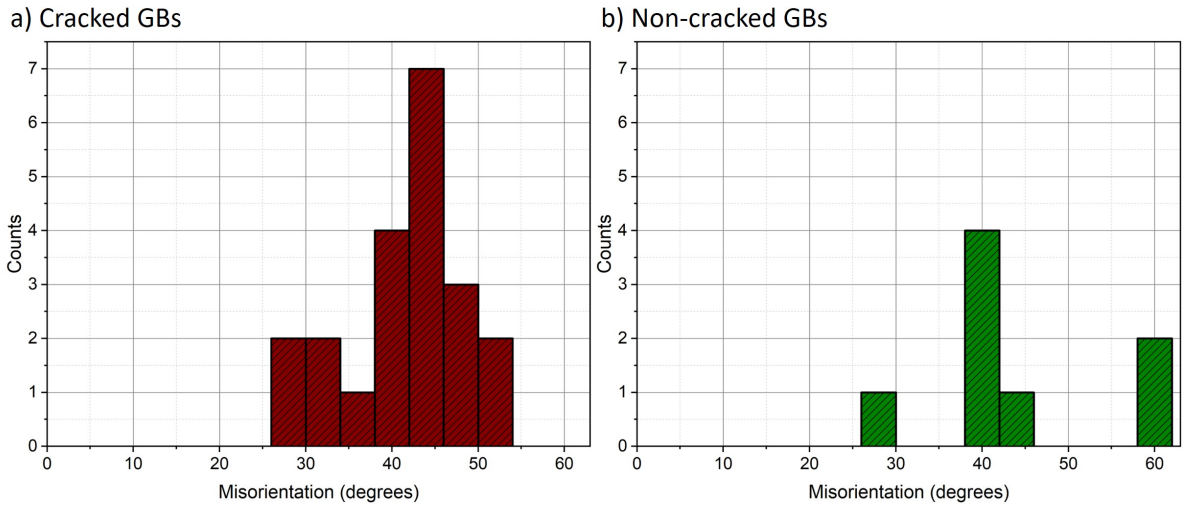

Figure 5.29: a) A histogram of GB misorientation values measured along the crack path in Sample 2YC, b) a histogram of GB misorientation values measured across the non-cracked GBs adjacent to the cracked GBs.

Table 5.6: Measured GB misorientation values along the crack path in Sample 2YC, with GB names as per Figure 5.28.

	GB Misorientation (degrees)	**Adjacent Non-cracked GB Misorientations (degrees)**
GB 1	40.02	-
GB 2A - 1	50.54	29.87
GB 2A - 2	31.08	29.87
GB 2A - 3	-	-
GB 2B - 1	37.51	-
GB 2B - 2	46.34	-
GB 3	-	-
GB 4	42.07	-
GB 5	-	38.58
GB 6	41.21	59.93
GB 7	40.40	59.93, 58.16
GB 8	29.80	58.16
GB 9A	44.26	-
GB 9B	26.10	-
GB 10	47.02	-
GB 11	43.51	-
GB 12	52.31	-
GB 13	47.67	-
GB 14	-	-
GB 15	42.74	39.80
GB 16	42.41	39.80
GB 17	30.02	-
GB 18	43.50	-
GB 19	45.50	41.90
GB 20	-	41.90
GB 21	40.13	40.55
GB 22	-	40.55

5.4 Thermally Treated AISI Type 304 Stainless Steel Analysis

5.4.1 Large Area Surface Measurements of Microstructure by HS-AFM and Correlated Microscopy

HS-AFM measurements were performed across the surface of a sample of thermally treated AISI Type 304 stainless steel, shown in Figure 5.30. GBs are clearly observed within these maps as they are topographically lower (and so appear darker) than the bulk grain. Present within these GBs are numerous 30-300 nm diameter SPPs. A topographic image showing only the bulk grain is shown in Figure 5.30b, this is very flat as a result of sample preparation and largely

featureless. Figures 5.30a, 5.30c and 5.30d contain GB triple points where three GBs meet. The majority of observed GBs appeared as shown in Figure 5.30a or 5.30c. In some cases, GBs were observed to change direction, as if at a triple point, but only two GBs were observed, such as that in Figure 5.30e. Indicating the presence of an unseen GB. A similar phenomenon is observed in Figure 5.30d, where a GB appears to end suddenly. It should be noted that this type of feature could be the result of sample preparation.

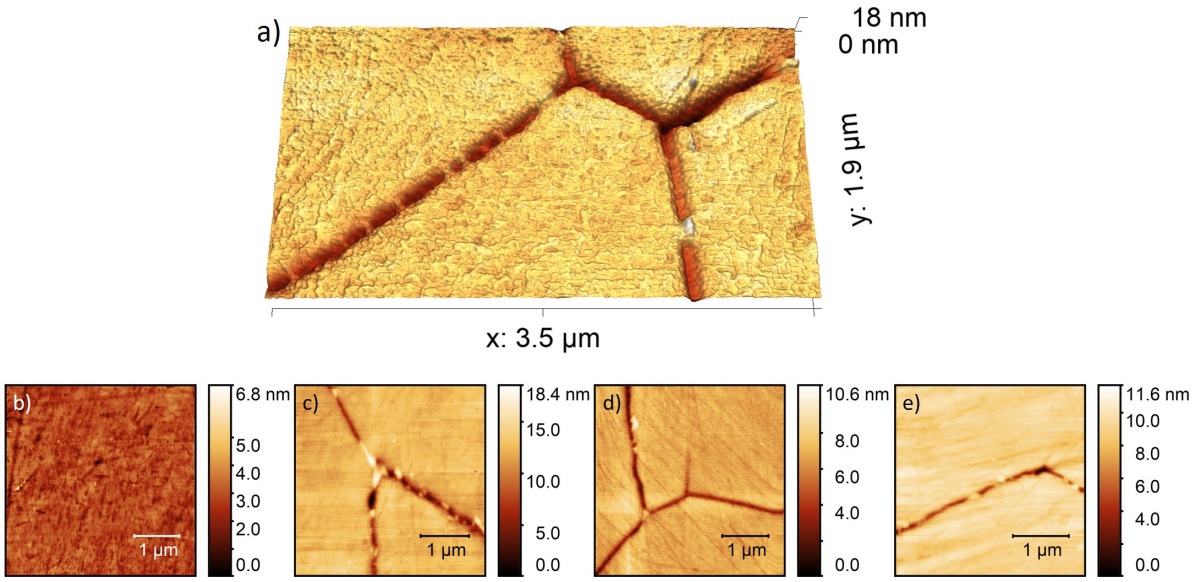

Figure 5.30: a) A 3D topographic image of two GB triple points in thermally treated AISI Type 304 stainless steel. Also, topographic maps showing: b) the bulk material, c) a GB triple point, d) two GB triple points with a discontinuous GB, e) a GB that changes direction.

Figure 5.31 shows line profiles collected across a GB at various points. Figure 5.31b shows the height profile across a GB SPP. This SPP is as wide as the GB and topographically higher than the bulk surface by approximately 5 nm. Figures 5.31c- 5.31e show that GBs, as observed topographically, are approximately 250 nm in width and vary in depth (between -4 nm and -12 nm within these measurements).

A selection of HS-AFM topographic maps showing the various microstructural features observed across a sample of thermally treated AISI Type 304 stainless steel is shown in Figure 5.32. Figures 5.32a - 5.32c show the variations of distributions of GB SPPs. Figure 5.32a contains many small SPPs along the whole length shown. Figure 5.32b contains a GB triple point with a larger SPP, each GB at the triple point has a differing distribution, with the top GB showing very little precipitation. The GB in Figure 5.32c has near continuous precipitation. On occasion, SPPs were observe to spill out of the GB, as shown in Figure 5.32d, it is expected that this is due to a small angle between the GB and the plane in which the surface was polished. Compared to GB SPPs, very few intragranular SPPs were observed across the surface. Figure 5.32e shows a large

Table 5.7: A table of weight % as measured by EDX for each 'phase' shown in Figure 5.33c.

	Si	S	Cr	Mn	Fe	Ni
Red	0.86	0.00	16.86	1.29	73.91	7.08
Blue	1.11	0.00	21.67	1.77	67.71	7.74

square shaped SPP observed that was approximately 3 μm in size.

Figures 5.32f and 5.32g show small round pits. These features were also rarely observed across the surface. These pits may be an imperfection from the casting process, or possibly due to the removal of an intragranular SPP such as that seen in Figure 5.32h.

Compositional analysis of a larger SPP such as that shown in Figure 5.32e was performed by EDX, Figure 5.33. This SPP is compositionally different to the bulk material, as indicated from the EDX composition map in Figure 5.33b and the EDX 'phase' map in Figure 5.33c. Each 'phase' colour is defined within Table 5.7. Element specific EDX maps are given in Figure 5.34. It is clear from these results that the SPP contains increased amounts of chromium and may be identified as a chromium-rich carbide precipitate.

Due to the resolution limits of standard EDX, STEM EDX was required for compositional analysis of the smaller intergranular SPPs. Figure 5.35 shows element specific STEM EDX maps collected at a GB containing GB SPPs such as those observed in Figures 5.32a-d. A STEM EDX line scan collected across a GB and GB SPP is shown in Figure 5.36. Increased concentrations of chromium and carbon were detected at the GB SPPs. Following this analysis, these SPPs may be identified as chromium-rich GB carbide precipitates.

During STEM EDX analysis of Lamella 1, an SPP was identified that had not been observed within previous HS-AFM analysis indicating that it is considerably less common than other observed SPPs, Figure 5.37. This SPP is intragranular, equiaxed, and approximately 300 nm in diameter. The blurred edges in Figure 5.37 are due to a tilt of the sample during measurement. Specific elemental STEM EDX maps show increased concentrations of sulfur and manganese, indicating that this SPP is an MnS inclusion.

EBSD maps collected from a sample of thermally treated AISI Type 304 stainless steel are shown in Figure 5.38. These maps were collected at 30 kV, using an aperture of 120 μm, and a step size of 0.5μm. Raw data was cleaned up using CIS and points with CI > 0.1 were filtered. Figure 5.38a is an IPF IQ map, showing grain size and orientation. At this scale, no SPPs were clearly observed within this sample. The grain size (diameter) in this region varied from approximately 1 μm to 43 μm, with an average diameter of 15 μm and a standard deviation of 9 μm. A slight preferred orientation is observed, as indicated by discrete IPF plots shown in Figures 5.38b and 5.38c. The largest grains align with the {101} planes.

Figure 5.38d is a phase map, where regions mapped to austenite are shown in red and regions mapped to BCC are shown in green. The majority of the surface is observed to map to an austenite

crystal structure. As no SPPs are observed at this scale, regions mapped to BCC indicate residual ferrite. Approximately 0.1% of this region was mapped to ferrite.

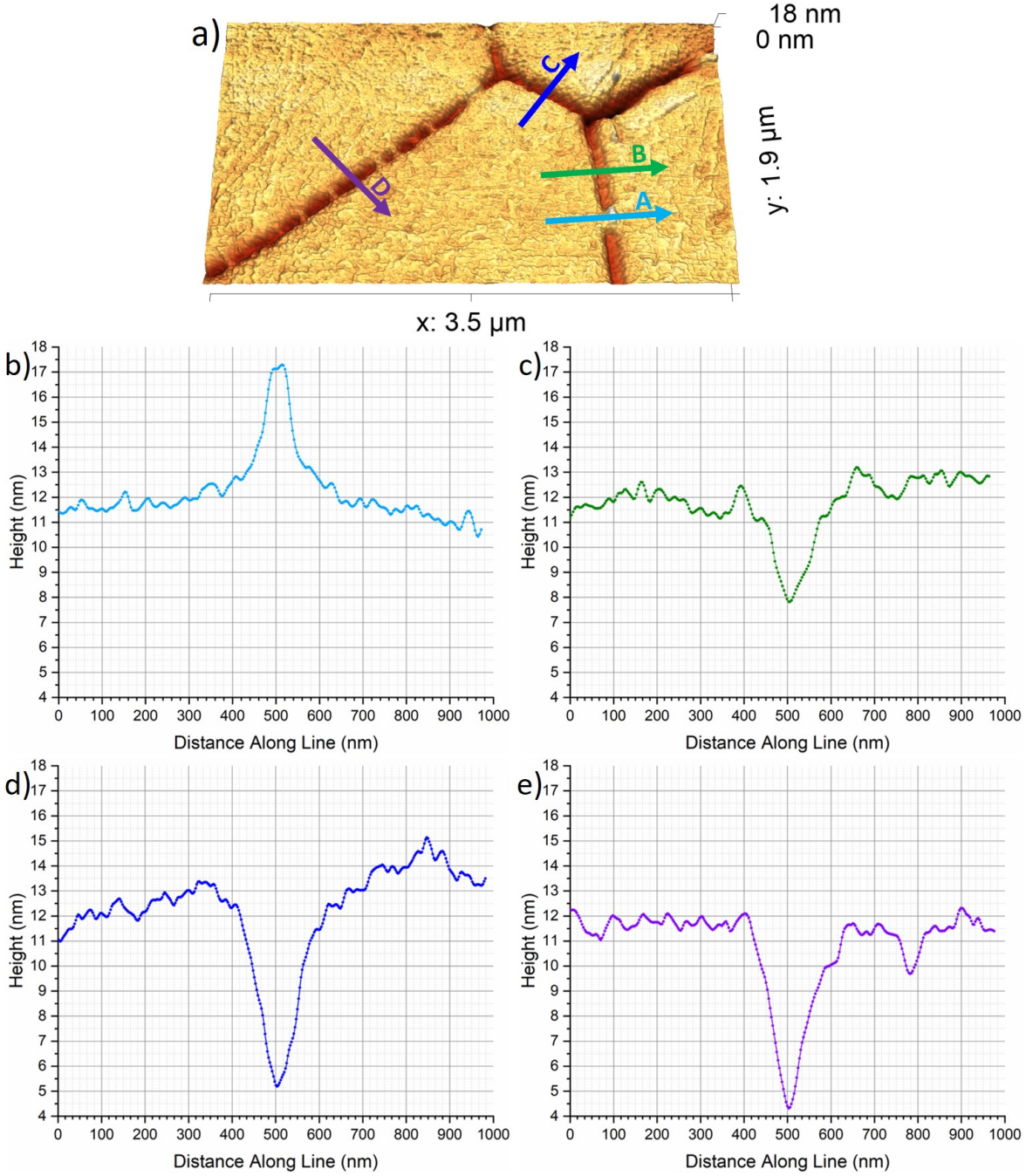

Figure 5.31: a) A 3D topographic image showing two GB triple points in thermally treated AISI Type 304 stainless steel, b) a line profile collected across the blue line labelled A in a), c) a line profile collected across the green line labelled B in a), d) a line profile collected across the dark blue line labelled C a), and e) a line profile collected across the purple line labelled D a).

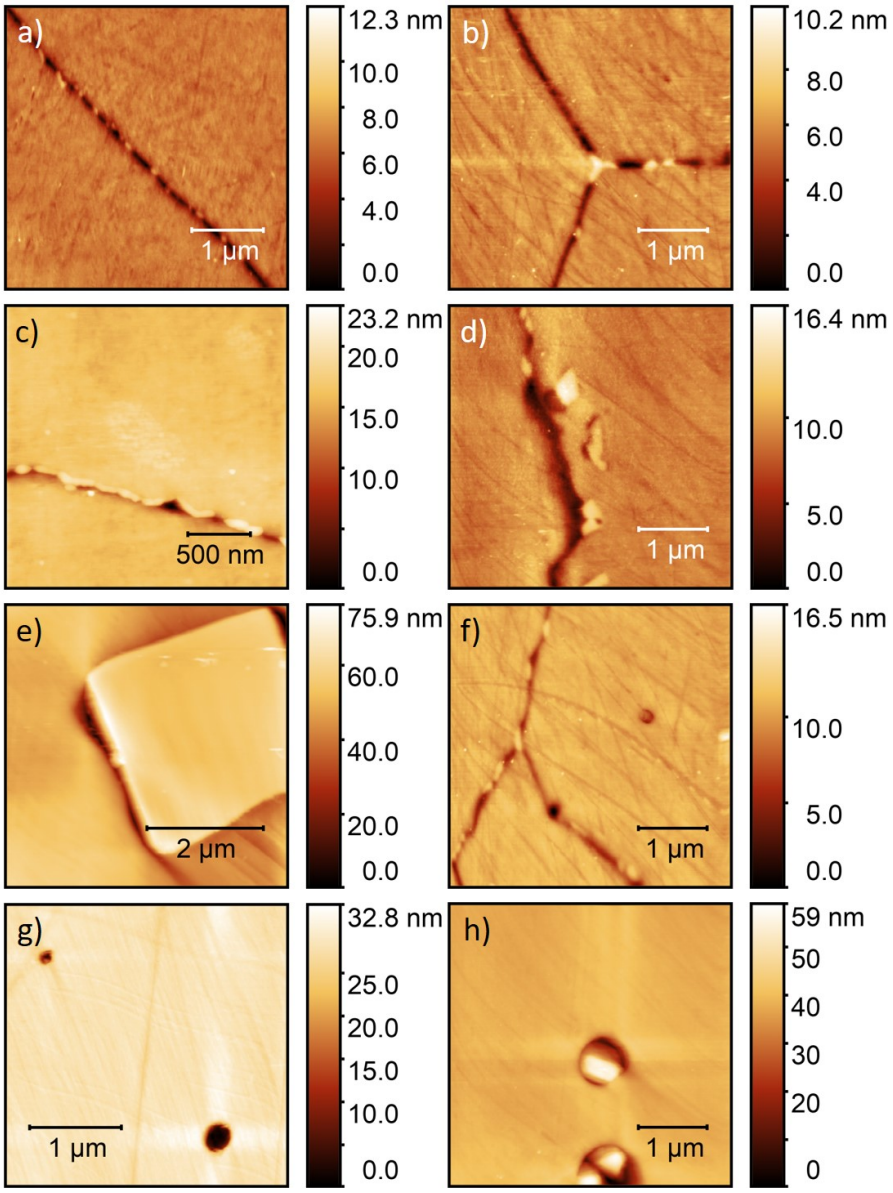

Figure 5.32: HS-AFM topographic maps collected from thermally treated AISI Type 304 stainless steel showing: a) a GB with SPPs, b) a GB triple point with SPPs, c) a GB with near continuous precipitation, d) a GB with SPPs in the adjacent grain, e) an intragranular SPP, f) a GB triple point with an intergranular pit and an intragranular pit, g) intragranular pits, h) intragranular pits around intragranular SPPs.

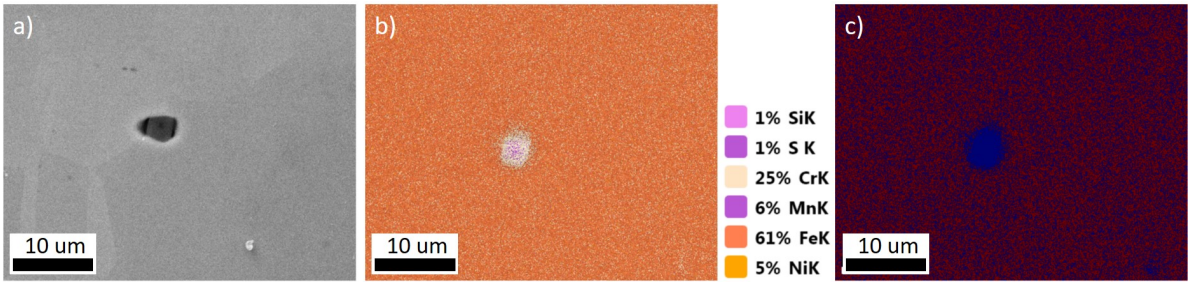

Figure 5.33: a) An SE image of the area on a thermally treated AISI Type 304 stainless steel sample analysed by EDX, a large SPP is present near the centre of the imaged area. Also, EDX maps collected from the sample surface: b) an EDX elemental composition map (individual element maps are given in Figure 5.34), and c) an EDX 'phase' map (each phase composition is given in Table 5.7).

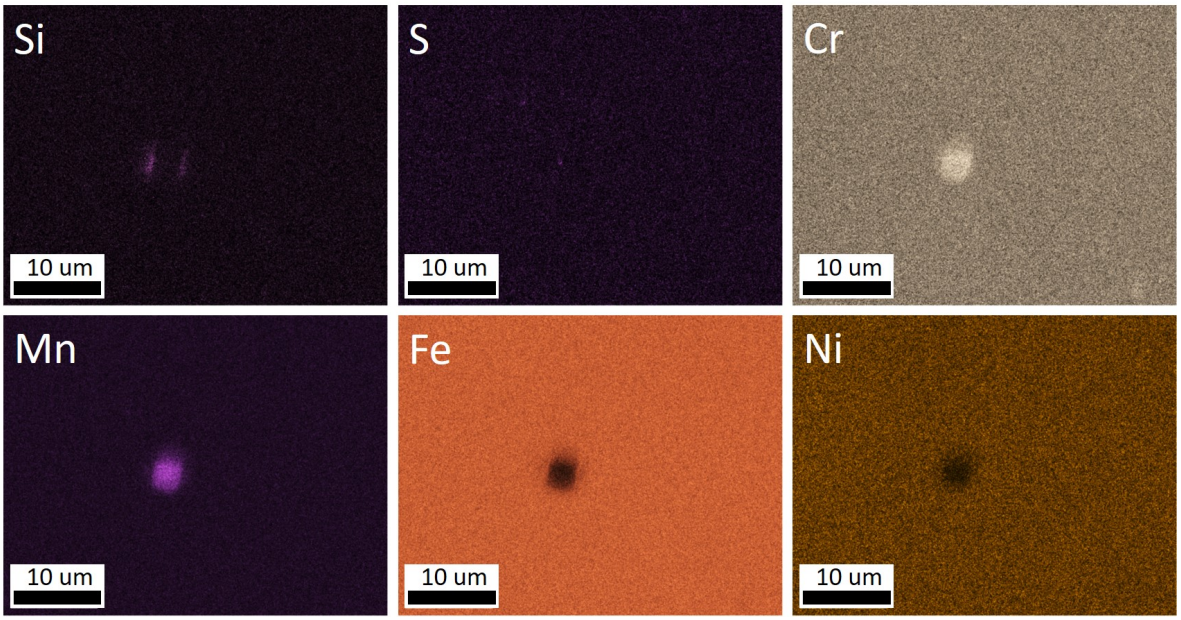

Figure 5.34: Element specific EDX maps (silicon, sulfur, chromium, manganese, iron and nickel, as indicated) collected from a thermally treated AISI Type 304 stainless steel sample in the same area shown in Figure 5.33. Brighter areas contain a higher concentration of the given element, and dark areas contain a lower concentration. (Individual element maps are overlayed in Figure 5.33b.)

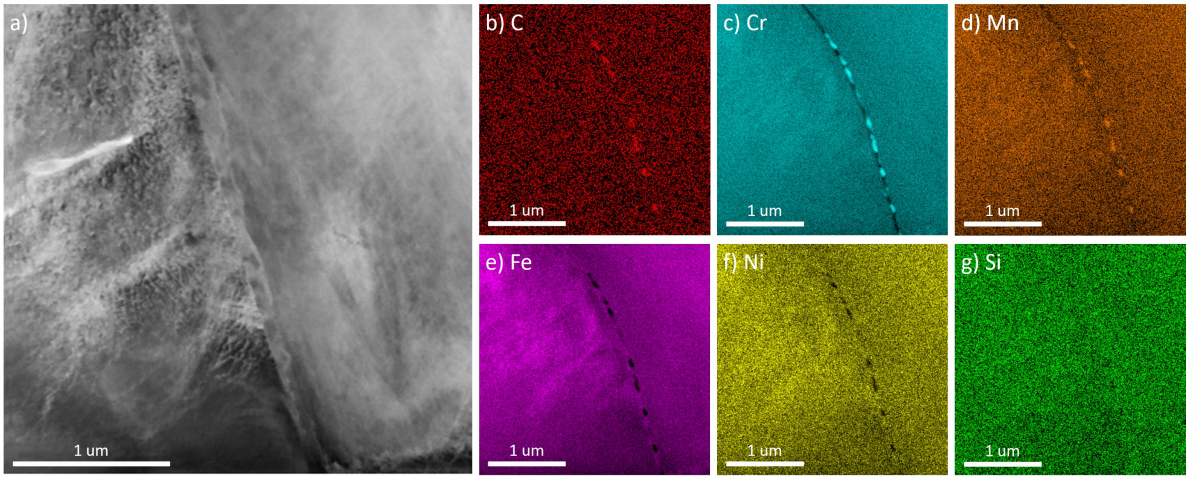

Figure 5.35: a) An STEM dark field (DF) image showing a GB in thermally treated AISI Type 304 stainless steel Lamella 1 containing GB SPPs. Also, element specific STEM EDX maps showing: b) carbon, c) chromium, d) manganese, e) iron, f) nickel, and g) silicon.

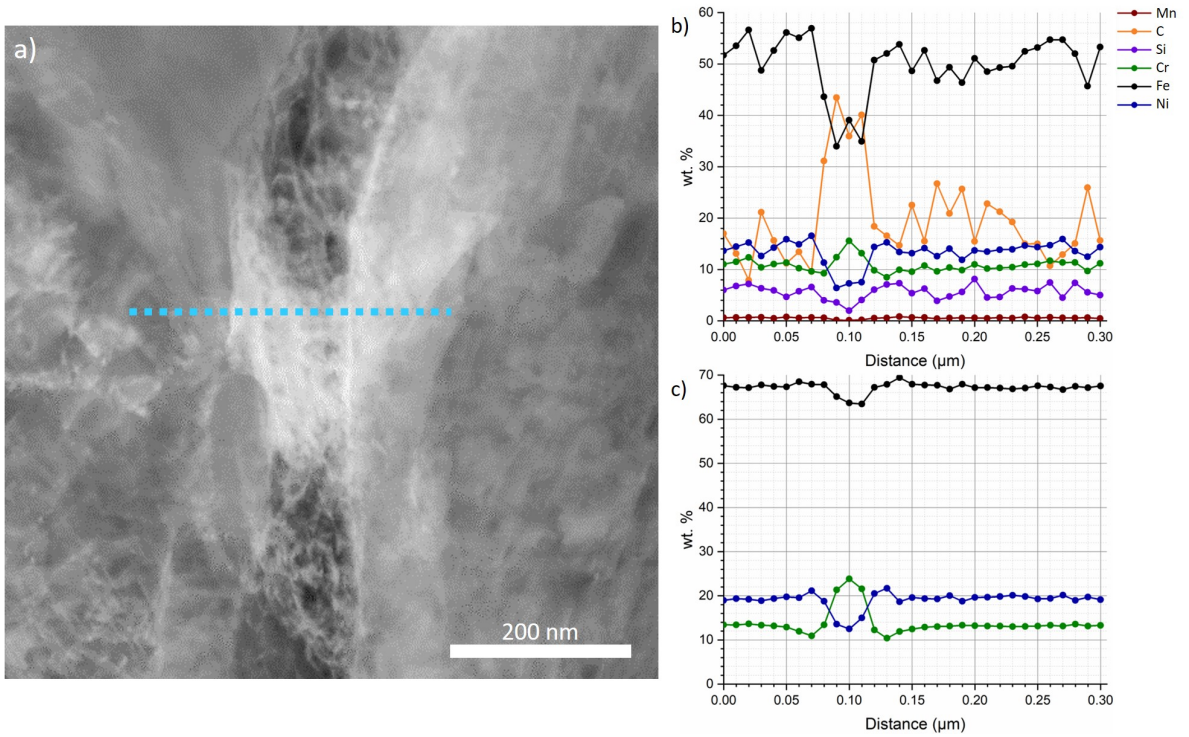

Figure 5.36: a) An STEM DF image of a GB in thermally treated AISI Type 304 stainless steel Lamella 1. Also, STEM EDX line scans collected across the blue dotted line shown in a): b) including manganese, carbon, silicon, chromium, iron and nickel, and c) only including chromium, iron, and nickel.

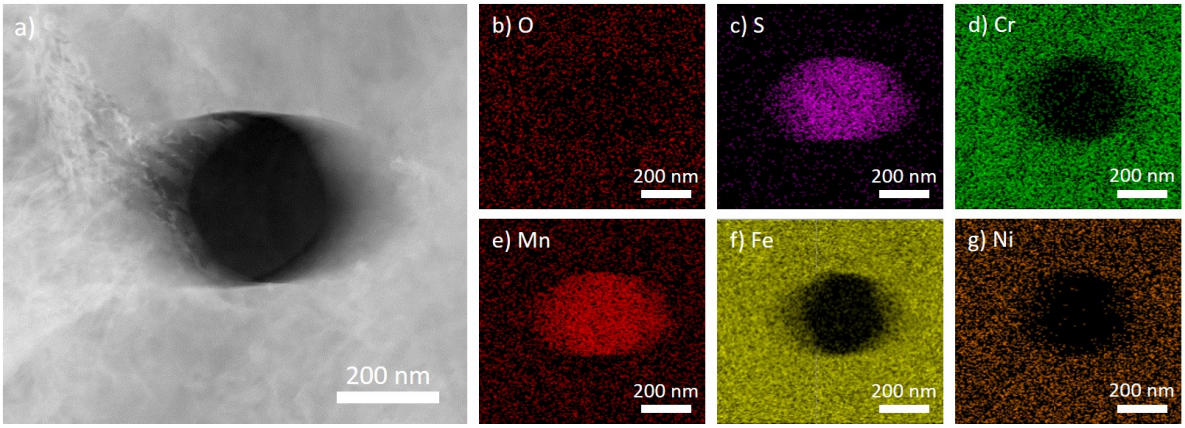

Figure 5.37: a) An STEM DF image showing an intragranular SPP in thermally treated AISI Type 304 stainless steel Lamella 1. Also, element specific STEM EDX maps showing: b) oxygen, c) sulfur, d) chromium, e) manganese, f) iron, and g) nickel.

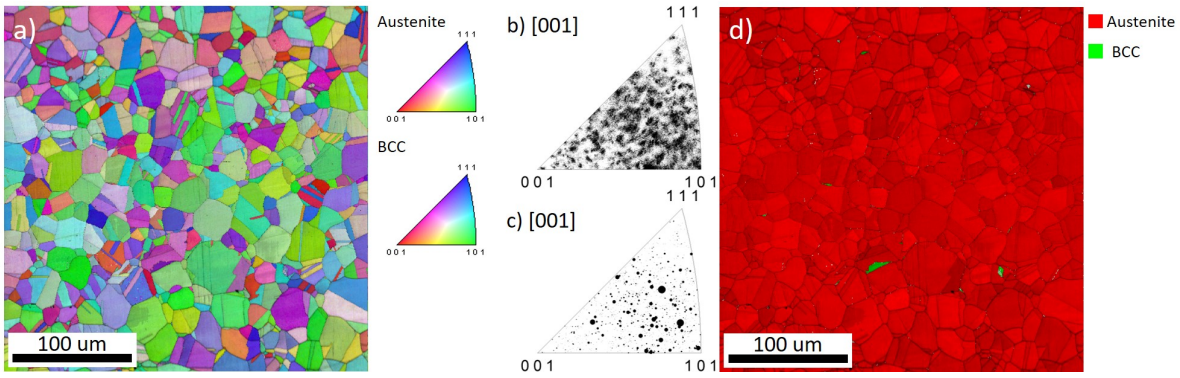

Figure 5.38: EBSD maps collected from a sample of thermally treated AISI Type 304 stainless steel: a) an IPF and IQ map with inset legend, b) a discrete IPF plot where each point represents each pixel collected in the Figure 5.38a, c) a discrete IPF plot where each point represents each grain in the Figure 5.38a weighted by size, and d) a phase and IQ map where red is austenite and green is BCC (likely ferrite).

5.4.1.1 Distribution of GB Misorientations

A GB misorientation map produced following EBSD analysis of the surface is shown in Figure 5.39. GBs are labelled as previously described in Section 5.2.1.1. Measured GB misorientation values were plotted as a histogram as shown in Figure 5.40. 24.6% of GBs were identified as HAGBs, 2.7% were LAGBs, and 19.2% were coherent twin GBs. The remaining GBs were sub-GBs. This corresponds to 52.9% HAGBs, 5.8% LAGBs, and 41.3% coherent twin GBs, if sub-GBs are negated from analysis.

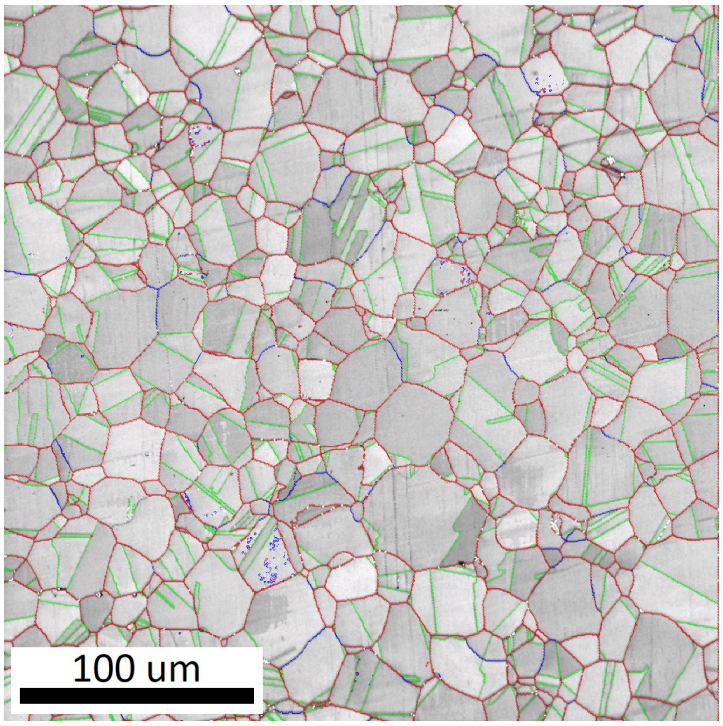

Figure 5.39: A map showing GB misorientations in a sample of thermally treated AISI Type 304 stainless steel in the same region shown in Figure 5.38a, where GB misorientation values in the range 5°-15° are indicated in blue, 15°-62.8° in red, and 60° (with misorientation axis < 111 >) in green.

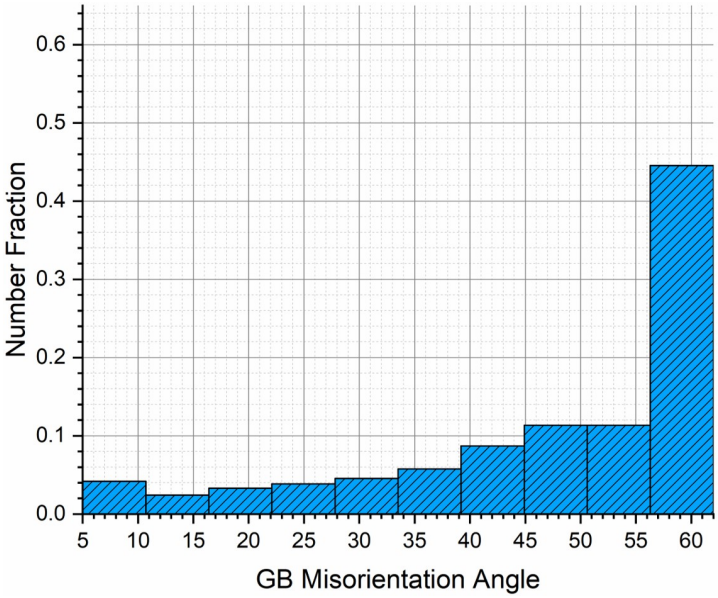

Figure 5.40: A histogram of all GB misorientations measured in Figure 5.39 from a sample of thermally treated AISI Type 304 stainless steel.

5.4.2 Measurements of GB Depletion Profiles for Thermally Sensitised GBs

Lamellae 1, 2, and 3 were collected from lift-out sites on the surface of a sample of thermally treated AISI Type 304 stainless steel as indicated in Figure 5.41. These lamellae each contained one GB. The misorientation of these GBs were measured from the surface by EBSD following the lift-out procedure. The GB present in Lamella 1 had a measured GB misorientation of 55.5°. Lamella 2 had a GB misorientation of approximately 50°, however the EBSD map contained some FIB damage. The misorientation of the GB in Lamella 4 could not be measured due to damage on the sample surface during the lift-out process. However, it is apparent from Figure 5.41c that this GB is expected to be a coherent twin GB.

STEM EDX line scans were collected across the GB in Lamella 1, a HAGB, at the positions indicated in Figure 5.42a. Multiple line scans were performed that intersected GB carbide precipitates, as observed within an STEM EDX map of the region showing chromium concentration, Figure 5.42b. It is also clear that this GB is tilted with respect to the electron beam. Resultant GB depletion profiles are shown in Figure 5.43. Positions of GB carbide precipitates are indicated by a peak in chromium concentration, accompanied by an asymmetric depletion of chromium in the regions directly adjacent. Also observed is an enrichment in nickel in the areas adjacent to GB carbide precipitates. Other elements showed little variation and have been omitted from this graph. Chromium depletion was detected down to 9.66 wt.% (Figure 5.43a), and nickel enrichment up to 22.50 wt.% (Figure 5.43b). The elemental profile width is approximately 140 nm; however, this is somewhat obscured by the presence of carbide precipitates.

Figure 5.44a shows the locations of STEM EDX line scans collected across the HAGB in

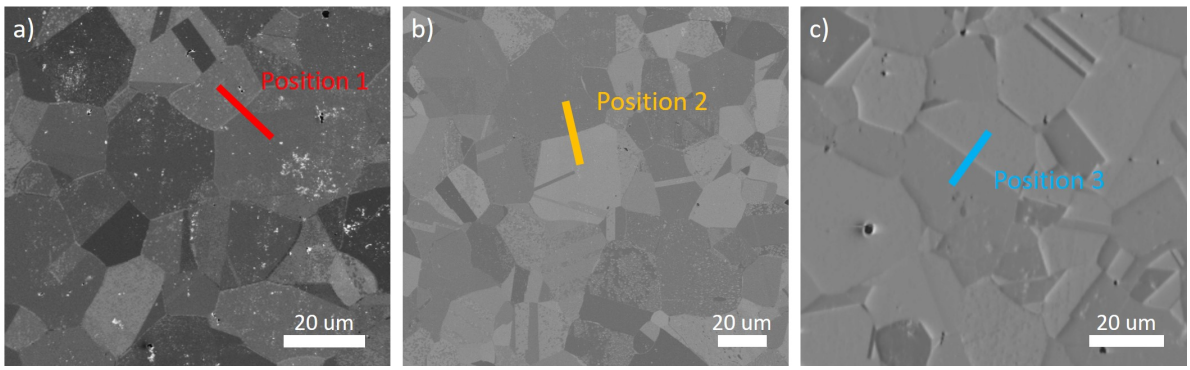

Figure 5.41: FIB images showing the surface of a sample of thermally treated AISI Type 304 stainless steel, with lift-out sites indicated for: a) Lamella 1 in red, b) Lamella 2 in yellow, and c) Lamella 3 in blue. Images in a), b), and c) collected at 30 kV and 0.92 nA, 27 pA, and 21 nA, respectively.

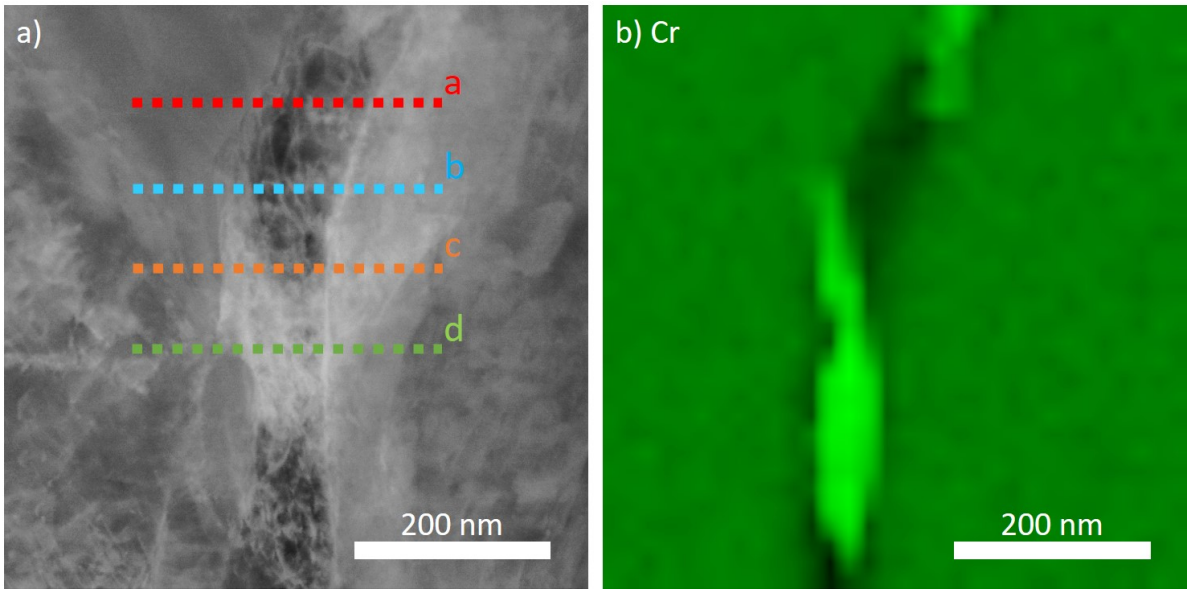

Figure 5.42: a) An STEM DF image of the HAGB in Lamella 1 (thermally treated AISI Type 304 stainless steel) analysed by STEM EDX, and b) an STEM EDX map of the same region shown in a) showing relative Cr concentrations.

Lamella 2. Multiple line scans were performed at varying distances from a GB carbide precipitate, as observed within a chromium STEM EDX map of the region, Figure 5.44b. Resultant GB depletion profiles are shown in Figure 5.45. Figure 5.45a contains a peak in chromium at the location of a carbide precipitate, Figures 5.45b-d do not include carbide precipitates. The minimum chromium concentration measured during these scans was 5.60 wt.% (Figure 5.45c), and nickel enrichment was detected up to a value of 25.32 wt.% (Figure 5.45f).

STEM EDX line scans performed across the twin GB in Lamella 3 are shown in Figure 5.46. This GB did not contain any carbide precipitates. Resultant GB profiles show little to no

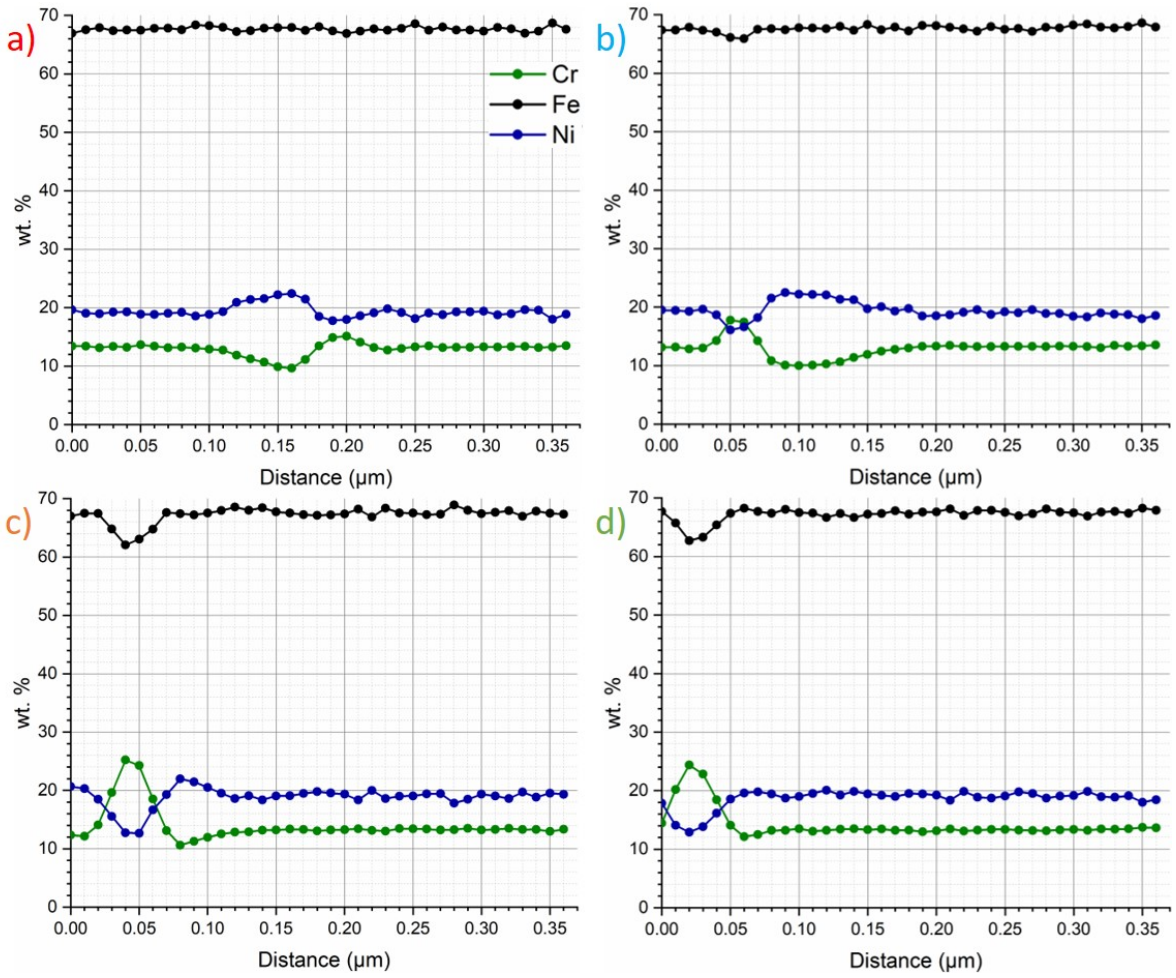

Figure 5.43: STEM EDX elemental line scans collected from Lamella 1 (thermally treated AISI Type 304 stainless steel) across 360 nm with 10 nm steps for the lines labelled in Figure 5.42: a) across the red line labelled a, b) across the blue line labelled b, c) across the orange line labelled c, and d) across the green line labelled d.

compositional variation.

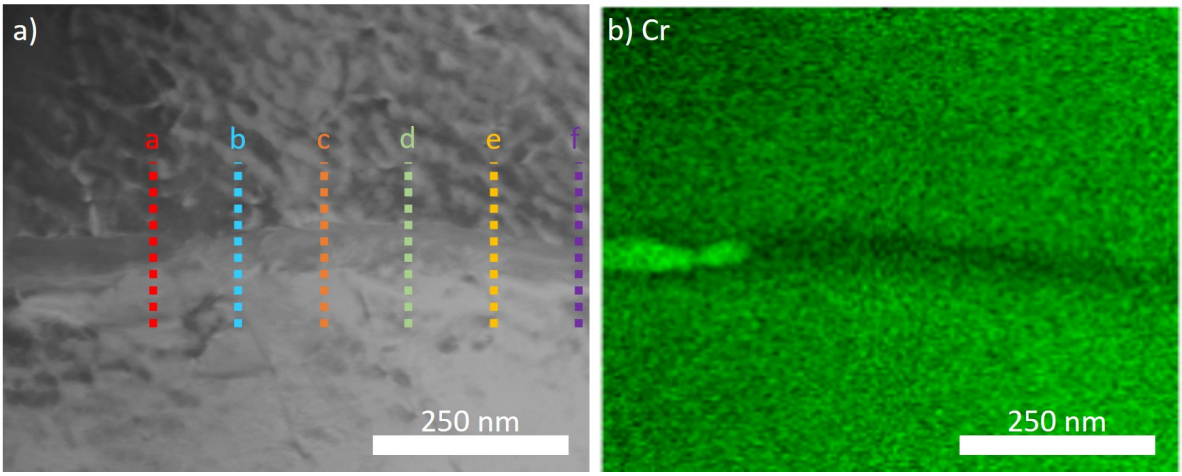

Figure 5.44: a) An STEM DF image of the HAGB in Lamella 2 (thermally treated AISI Type 304 stainless steel) analysed by STEM EDX, and b) an STEM EDX map of the same region shown in a) showing relative Cr concentrations.

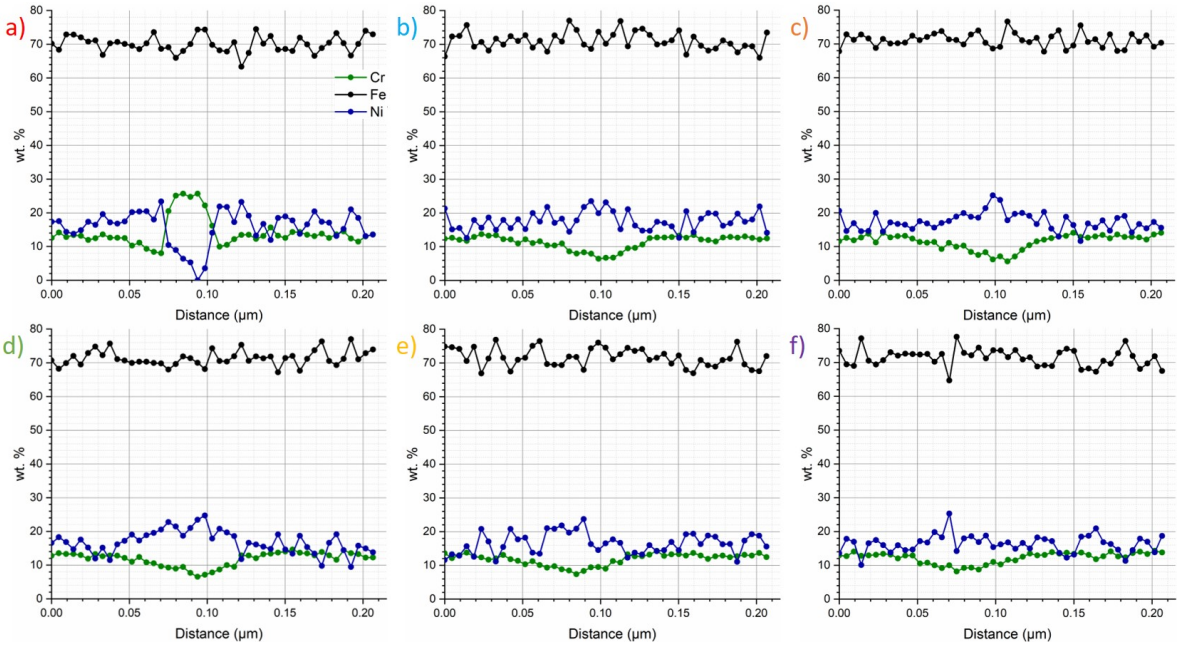

Figure 5.45: STEM EDX elemental line scans collected from Lamella 2 (thermally treated AISI Type 304 stainless steel) across 200 nm with 5 nm steps for the lines labelled in Figure 5.44: a) across the red line labelled a, b) across the blue line labelled b, c) across the orange line labelled c, d) across the green line labelled d, e) across the yellow line labelled e, and f) across the purple line labelled f.

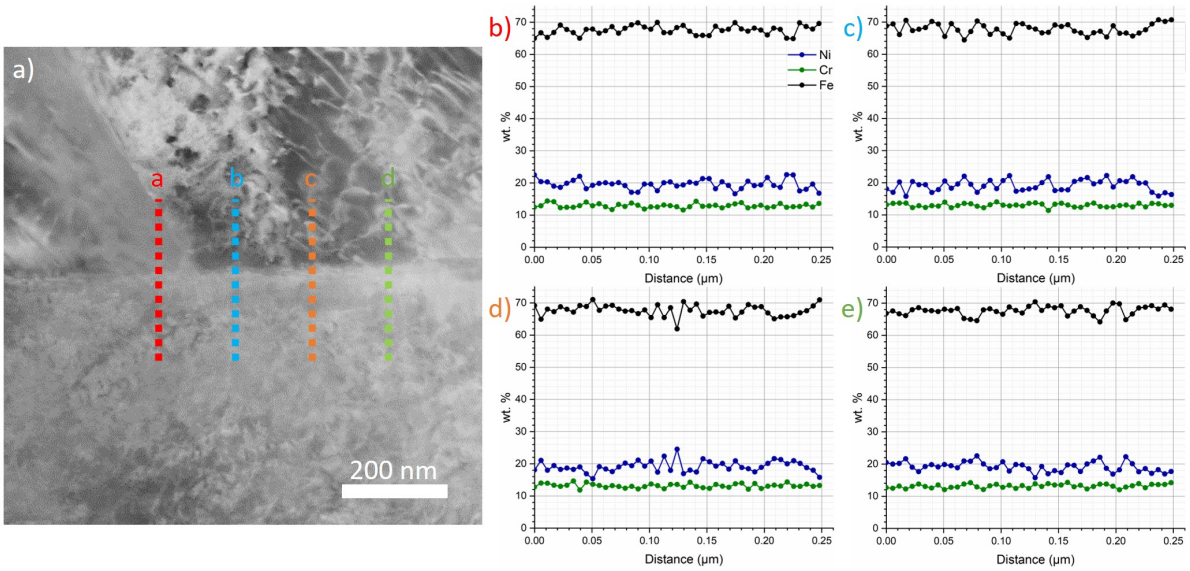

Figure 5.46: a) An STEM DF image of the GB in Lamella 3 (thermally treated AISI Type 304 stainless steel). Please note that no carbide precipitates were observed in this GB. Also, STEM EDX elemental line scans collected across 250 nm with 5 nm steps for: b) the red line labelled a in a), c) the blue line labelled b in a), d) the orange line labelled c in a), and e) the green line labelled d in a).

5.5 Discussion: Measurements of Irradiated and Thermally Sensitised Microstructures

A study of irradiated microstructure was performed using a variety of complementary techniques. This analysis built upon previous work performed at NNL described in Section 5.1.1.1. Analysis was performed on three samples of ex-service fuel cladding. Measurements performed on 1XA focussed on analysis of surface microstructures by HS-AFM and other correlative techniques including EBSD and EDX. This sample had been analysed previously at NNL. Analysis by HS-AFM has not been performed on ex-service AGR cladding previous to this work and so offers an opportunity for additional characterisation as well as possible future experimental work. Measurements performed on 2YB and 2YC focussed on GB depletion measurements and how this varied, if at all, with GB misorientation. These samples have also been analysed previously at NNL however previous TEM measurements have not considered GB misorientation.

A comparative study was performed on a thermally sensitised microstructure. Analysis was performed using the same suite of techniques for samples of thermally treated AISI Type 304 stainless steel. This material and the sensitisation conditions used within this work are relevant within a number of industries, as discussed in Section 2.1.5. In addition, the resultant microstructure is compared to ex-service AGR fuel cladding to evaluate suitability as a proxy material.

Samples were prepared in this chapter by two methods previously discussed in Chapter 4: mechanical and OPS polishing, and electropolishing. Specimens of AISI Type 304 stainless steel were prepared by mechanical and OPS polishing: the method highlighted as optimal for HS-AFM analysis in Chapter 4. HS-AFM measurements were of high quality, as expected. GBs and SPPs are clearly observed across the surface. Measurements performed by electron microscopy techniques were also of good quality. Cladding samples were prepared by electropolishing (in a perchloric acid and methanol solution) performed by NNL. This electropolish was a different recipe to that implemented in Chapter 4 (in an oxalic acid solution). The resultant HS-AFM images were of good quality, the flat surface allowed for clear observations of microstructural features and the surface was free of debris or residue. Subsequent analysis by SEM techniques were also of high quality. However, due to the large height of the SPPs across the surface HS-AFM images collected in the vicinity of SPPs exhibited imaging artefacts. This also affected EBSD images, where shadowing was observed. It is expected that this effect would be reduced if the samples were mechanically polished. The different chemical responses of the various SPPs on the surface to the chemical etch resulted in differing topographies, explored in Appendix B and discussed further in subsequent sections.

5.5.1 Analysis of Surface Microstructures

5.5.1.1 Ex-Service AGR Fuel Cladding

Large area analysis of the surface of Sample 1XA by HS-AFM and SEM techniques revealed large scale precipitation in the region analysed. HS-AFM analysis also revealed numerous voids across the surface. These features are discussed in greater detail in the following sections. Analysis of the microstructure by EBSD found the average grain size diameter was 1.4 μm, however the grain sizes measured varied considerably, from approximately 0.1 μm to 30.8 μm. The {101} surface grain orientation was found to be preferable, particularly for larger grains.

SPPs Non-irradiated 20Cr/25Ni-Nb is known to contain NbC precipitates, with other precipitates (such as sulphides and oxides) appearing less frequently [49, 88]. However, upon ageing and irradiation, additional phases form, some of which can be detrimental to the chemical and mechanical properties of the steel. Commonly seen are: $M_{23}C_6$ precipitates, sigma phase, and G phase [76, 88]. These SPPs were found to be present in the ex-service samples analysed.

Numerous SPPs with varying shape and size were observed across the surface of Sample 1XA during large area mapping (Figures 5.2, 5.3, 5.5, and 5.7). Larger SPPs were primarily intergranular, with some appearing on twin GBs. These SPPs were identified by cross analysing the large area maps shown in Section 5.2.1 (Figure 5.8), performing additional spot EDX analysis, and by comparing the results with those collected previously by NNL. The larger SPPs were identified as $M_{23}C_6$, sigma phase, NbC (with G phase shell), and G phase. Smaller SPPs could not be identified by EDX due to the resolution of the instrument. HS-AFM measurements of smaller SPPs were compared with previous work performed by NNL using TEM and literature [50] to allow for identification. This analysis led to the identification of small NbC present across the sample.

The majority of the larger SPPs were identified as G phase, as is clear from the silicon and nickel EDX maps in Figure 5.6. G phase precipitates were intergranular, as expected [88]. G phase is not expected to have a significant effect on the corrosion properties of the material, however nickel-rich SPPs such as G phase may result in local instabilities of the austenite [88].

In previous studies of thermally sensitised or proton irradiated 20Cr/25Ni-Nb, G phase has been found to form from NbC [88]. This was most prominent for intergranular NbC precipitates due to fast diffusion rates at GBs compared to the matrix [88]. Within this study, NbC precipitates were found to contain a shell of a phase identified as G phase. This suggests that G phase formation had occurred from the NbC precipitate, and that this evolution had initiated at the outer layers. This phenomenon has been reported in previous works using proton irradiated samples [50].

NbC observed within Sample 1XA varied in shape and size. Smaller NbC observed by HS-AFM were intragranular, circular in cross section and up to 1 μm in diameter. Large NbC was intergranular and irregular in shape, with some appearing globular, plate-like, or sometimes

elongated. Nb is added to 20Cr/25Ni-Nb as a stabiliser to deter chromium-rich carbide precipitate formation by preferentially forming NbC. It is therefore expected that the presence of NbC is somewhat beneficial for the corrosion properties of the material. However, recent works have found that NbC may act as an initiation site for localised corrosion processes such as pitting, as they are cathodically active leading to adjacent anodic dissolution [49].

A number of chromium-rich phases were also identified as $M_{23}C_6$ and sigma phase. $M_{23}C_6$ observed within Sample 1XA were located along GBs, with the largest precipitates appearing to replace grains (Figure 5.5). They varied in shape, with some appearing plate-like and others appearing more globular. Smaller SPPs also suspected to be $M_{23}C_6$ SPPs were observed by HS-AFM. $M_{23}C_6$ precipitates are known to form readily within austenitic stainless steels. In ex-service AGR cladding these SPPs form as a result of carbon pick-up from the reactor coolant [30]. These precipitates were often associated with G phase, as is expected from previous studies [88]. This is thought to be due to a local enhancement of carbon (and nitrogen) following the formation of G phase from NbC, discussed previously [88]. The presence of chromium-rich precipitates, such as $M_{23}C_6$, may adversely influence corrosion behaviour and lower resistance IGSCC [36, 74]. It has also been associated with loss of ductility and toughness [74].

Large sigma phase precipitates appeared plate-like in shape. Sigma phase is known to primarily form along GBs but can be found within the grain for samples at longer ageing times [74, 88]. Sigma phase is known to form preferentially at ferritic regions [86, 87]. Sigma phase formation is therefore promoted by the formation of G phase through destabilising the austenite, hence an association exists between the two phases, as observed within this work [88]. The presence of sigma phase can result in embrittlement of the metal [86, 87]. Whilst this would be an issue for in-service components, this is less of an issue for in-reactor fuel cladding due to the lower associated stress requirements. However, sigma phase precipitation can also result in chromium depleted regions in the adjacent matrix, leading to local corrosion susceptibility [74, 86, 87].

Additional HS-AFM analysis described in Appendix B details topographic measurements of various SPPs. It was found that the heights and surface textures varied with each type of SPP. $M_{23}C_6$ and sigma phase contained varying patterns of negative features across their surface, with differences in size and number density. On the other hand, NbC and G phase contained positive features, tentatively identified as atomic clusters. The similar appearance in NbC and G phase is likely the result of a G phase shell surrounding the NbC, as identified by EDX measurements. It is envisioned that measurements collected by HS-AFM of identified SPPs may allow for future analysis by HS-AFM to give an indication of the SPPs present, by topography and surface texture.

Voids Voids were present across the areas of Sample 1XA analysed by HS-AFM which may be identified as plastic voids, helium bubbles or cavities [90]. These voids were circular in cross section and varied in size and depth. Irradiation can result in the void formation through the

production of helium from neutron induced transmutation of nickel [98]. Helium then stabilises vacancy clusters, forming void cavities [92, 98], discussed further in Section 2.1.4.

The voids observed within this work were larger than those observed previously by NNL, with an average of 75 nm compared to 18.7 nm (Figure 5.11). This may be due to a number of different factors, including the method of data collection (i.e. TEM vs. HS-AFM), analysis, or selected sample area. It may also be the result of sample preparation, where electrolytic etching results in a dilation of the void. The small size of these microstructural features necessitated the use of HS-AFM.

Voids were found to concentrate along the GBs where they were wider (mean diameter 34 nm larger) and deeper (mean depth 3.9 nm larger), in some cases coalescing to form concentrated clusters (Figure 5.4). This may be explained as the GB acts as a defect sink and so voids formed as crystal defects (i.e. vacancies) may migrate towards GBs [50, 90, 92]. Differences in size and depth were observed when comparing HAGBs, LAGBs and twin GBs (Figures 5.13 - 5.18, and summarised in Table 5.4). Larger and deeper voids were often located along HAGBs. In some cases, the severity of this effect was such that the GB appeared almost perforated, as in Figure 5.13. In Figure 5.18 numerous voids were observed across one HAGB to another. This was found to be the result of a thin grain cross section at the surface. This is a rare insight into how the voids are distributed throughout a GB in 3D. In comparison, voids observed along coherent twin GBs or LAGBs were smaller and shallower, likely due to these GB types acting as less efficient sinks [29, 50, 66].

Large area analysis of the voids also revealed a possible association with SPPs (Figure 5.12). Such features are known to act as alternative defect sinks [50]. Voids were also observed to align along slip dislocations, therefore following the crystallographic planes in the material. To contrast this, however, some voids did not appear to follow any clear or obvious pattern.

The formation of inter- and intragranular voids can lead to adverse phenomena, such as embrittlement [90, 92]. Large agglomerations of bubbles/voids may also result in swelling and internal stresses [79]. As larger voids were located along GBs, this may have an adverse effect on IGSCC susceptibility [79, 92].

5.5.1.2 Thermally Treated AISI Type 304 Stainless Steel

Thermally treated AISI Type 304 stainless steel was found to contain many small intergranular SPPs and very few intragranular SPPs, discussed further in the following sections. Within HS-AFM analysis of the surface GBs were observed as topographically lower than the bulk grain and approximately 250 nm in width. Some GBs within the thermally treated sample were less obvious, however. Figure 5.30 shows instances where GBs appear to end abruptly or change direction as if at a GB triple point. It is posited that these features are due to the presence of an unsensitised GB that is not topographically visible, such as a coherent twin GB, as suggested by STEM EDX analysis (Figure 5.46). This interpretation would explain the disjoint between the

number of twin GBs observed within the EBSD analysis, and the lack of twin GBs (i.e. continuous straight lines) observed within HS-AFM analysis. HS-AFM measurements collected from the bulk of the thermally treated sample were largely featureless.

EBSD analysis revealed that the grain size diameter varied between approximately 1 μm and 43 μm, with an average diameter of 15 μm (Figure 5.38). The largest grains were in the {101} orientation. The majority of the surface was mapped to austenite, with approximately 0.1% identified as residual ferrite in the region analysed. This is a common occurrence within austenitic stainless steels as a result of the slow diffusion of chromium and nickel during cooling or insufficient hot working [87, 271]. These regions are preferential sites for sigma phase (if aged for a prolonged duration) and carbide formation, leading to local corrosion susceptibility [78, 87].

SPPs Numerous SPPs were observed within the GBs of this material by HS-AFM. These were identified as chromium-rich carbides by STEM EDX (Figures 5.35 and 5.36). STEM EDX was necessary in this case as these SPPs were too small (30 nm - 300 nm in diameter) for EDX analysis. Based on previous works for AISI Type 304 stainless steel heat treated at 700°C [30, 272], these precipitates are presumed to be predominantly $M_{23}C_6$, where M is principally chromium. Within HS-AFM images of the surface GB carbide precipitates are seen to stand in relief of the surface. This is illustrated by the line profile shown in Figure 5.31b. These precipitates are harder than the matrix, and as such topographic contrast is generated during polishing, they are also electrochemically noble and so resist dissolution by colloidal silica [150, 193]. The precipitation of these carbides is known to result in the depletion of chromium in the adjacent regions, as discussed previously. This process leads to thermal sensitisation leaving the material susceptible to IGA and IGSCC [33, 36, 57, 70, 74, 78, 81].

The varying distributions of carbide precipitates within the GB was highlighted in Figure 5.32. These differing precipitation distributions is expected to result in different GB Cr concentrations. In cases such as that observed in Figure 5.32c, near continuous chains of GB carbides were observed. This is expected to result in severe depletion of chromium in the adjacent areas [272, 273]. The differences in GB carbide precipitate distribution may be attributed to GB energy, i.e. high energy GBs such as HAGBs will precipitate carbides more readily than low energy GBs such as twins [74, 81, 105]. Notably, the carbide precipitates are often observed to sit towards one edge of the GB within topographic maps. This phenomenon has been observed in other works by TEM analysis [105]. Within this work, GB carbides were found to be semi-coherent with one of the austenite grains, and incoherent with the other [105]. A preferential growth is observed into the grain with which the carbide is incoherent [74, 81]. This has also been related to an asymmetry of Cr depletion in the regions adjacent to the GB carbide, where the high-energy incoherent carbide interface is more severely depleted [105]. This phenomenon may explain the asymmetries observed within this work, Figures 5.43 and 5.45, though this was not prominent within Figure 5.36.

Additional carbide precipitates with differing morphology were observed within this sample, as shown in Figure 5.32e. The carbide in Figure 5.32e was much larger than intergranular chromium-rich carbides (approximately 3 μm across) and square in shape. During EDX analysis, a possible core with differing composition is observed, Figure 5.33, however this is not conclusive due to the resolution of the instrument.

In addition to chromium-rich carbides, an MnS precipitate was observed within this sample during STEM EDX analysis (Figure 5.37). This precipitate occurred within the grain and was rounded in appearance. These SPPs form during fabrication and have been reported to be initiation sites for pitting corrosion in chloride containing solutions [56, 85, 89].

5.5.2 Effects of GB Misorientation

GB misorientation measurements performed on ex-service irradiated 20Cr/25Ni-Nb stainless steel, shown in Figure 5.10, followed a GB misorientation angle distribution expected for randomly oriented octahedral group crystals [59, 63], with the exception of the large number of twin GBs. Of the total (non-sub) GBs measured 51.78% were classified as coherent twin GBs. The high proportion of twin GBs is a result of the stabilising heat treatment performed prior to service, resulting in annealing twin GBs [50]. A similar distribution was observed for the thermally treated AISI Type 304 stainless steel sample, shown in Figure 5.40, with 41.29% of the measured (non-sub) GBs identified as coherent twin GBs.

Annealing twin GBs are common in face-centred cubic (FCC) metals with low stacking fault energy (SFE) [66]. An increased occurrence of twin GBs is beneficial to the material's mechanical strength [65, 134]. This may also improve material corrosion properties, as twin GBs have been found to be resistant to radiation induced segregation (RIS) and chromium-rich carbide formation, and therefore localised corrosion and IGSCC [50, 65, 66, 103, 132, 134].

5.5.2.1 GB Segregation

Previous works have considered severity of GB chromium depletion due to thermal treatments or RIS to be in part due to GB misorientation [29, 50, 64], as discussed in Section 2.1.5.2. Within this study the GB depletion profiles within an ex-service stainless steel and a thermally treated stainless steel are evaluated and discussed in the context of measured GB misorientation. This is an incomplete description of the GB type as coherent twin GBs could not be conclusively identified, this is considered within the analysis.

Ex-Service AGR Fuel Cladding STEM EDX line scans showed that Cr and Fe was depleted at the GBs, whilst nickel, and often silicon, was enriched. This was expected from literature [30, 50, 51, 79, 90–92, 94, 95], discussed in greater detail in Section 2.1.4.1.

Of all the GBs evaluated by TEM, sensitisation was limited to GBs classified as HAGBs, with four of the nine measured HAGBs containing <12 wt.% chromium. This is a result of the

high density of dislocations within this type of GB, acting as point-defect annihilation sites [50]. The resultant low concentration of point defects causes enhanced flux and further elemental segregation [50]. The lowest concentration of chromium was found to be 10.89 wt.%, on a GB with a misorientation of 42.10°. Given that 45.2% of the GBs analysed by EBSD were categorised as HAGBs, this has implications for the susceptibility of the material to localised corrosion events, such as IGSCC.

The width of the depletion profiles measured for HAGBs were between 40 nm and 50 nm. The shape of the compositional profiles collected from HAGBs were found to vary. With some appearing symmetric, such as that seen in Figure 5.20, and others appearing asymmetric such as those seen in Figures 5.21 and 5.22. Asymmetric composition profiles are indicative of GB migration [50]. GB migration is a result of differing chemical potentials either side of the GB and has previously been reported to be isolated to GBs categorised as HAGBs [50]. As the GB migrates, the front of the GB essentially 'drags' the chromium depletion across the bulk as segregation occurs at the moving GB position. The GB also annihilates radiation-induced dislocations as it migrates, the resultant compositional profile is therefore affected by the higher number of dislocations ahead of the GB, when compared to that behind the GB [50]. This results in a shallower depletion/enrichment on one side of the compositional profile, and a sharper depletion/enrichment on the other. This is clear within Figure 5.21b, where the right hand side of the compositional profile is steeper than that on the left. Within Figure 5.22b, this is seen to a greater extent, where the right hand side is so shallow that it is not recorded within the range of the EDX line scan. Further measurements over a larger distance would be required to observe the full extent of the depletion.

Only one GB within the samples analysed was identified as a LAGB (Figure 5.23). Elemental segregation at this GB was similar to that measured at twin GBs. The LAGB was not sensitised as the measured chromium concentration did not drop below 12 wt.%. The width of the segregation was much larger than that measured for the other GBs at approximately 130 nm. However, it was noted that within Figure 5.23a a shadow can be seen along the GB, this indicated that the TEM beam was not aligned. This can result in less severe segregation measurements across larger distances, as is the case for this data. Only one GB of this type was analysed and so more measurements would be required in order to establish significant conclusions.

Analysis of twin GBs by TEM showed that GBs within this category were generally less severely depleted in chromium, with no twin GBs classified as sensitised. This was as expected from previous studies of irradiated microstructure, and is often attributed to the fact that they are inefficient point-defect sinks [29, 50, 66]. The shape of the composition profiles for twin GBs were mostly symmetric, as seen in Figure 5.24, indicating that these GBs did not migrate. One of the measured twin GBs had a W-shaped composition profile, shown in Figure 5.25. The exact cause of this is unknown, however may be a result of compositional variations within the grain due to Ni and Si segregation to dislocation loops.

In 2019, Barcellini *et al.* performed measurements of local solute redistribution at defect sinks in proton irradiated (up to 0.8 dpa) 20Cr/25Ni-Nb at 420°C, 460°C and 500°C [50]. The shape of the compositional profiles differed with irradiation temperature, with primarily W-shaped and symmetric profiles at the lower temperature of 420°C, and asymmetric and double-peaked profiles at higher temperatures [50]. In the work presented here, samples were collected from the same region and so may be assumed to be at the same temperature. Differences in profile shape therefore may be related to GB energy.

A direct comparison of GB misorientation and GB segregation was given in Figure 5.26, where the identified anomalous data point should be negated. These graphs indicated that chromium depletion and nickel enrichment was more severe for GBs classified at HAGBs. GBs identified as sensitised (i.e. with chromium wt%<12%) were solely categorised HAGBs. This trend has been observed within previous studies [50]. Within the results presented here, no obvious relationship between maximum Si concentration and GB misorientation was identified.

Within Figure 5.26a, chromium depletion measured across varying HAGB misorientations did not differ exceptionally as GB misorientation increased. This agrees well with observations made by Barr *et al.* in 2015 for a Ni-5Cr alloy [29]. Barr noted that RIS measurements indicated only subtle differences in defect sink strength as GB misorientation varied, and that, overall, RIS was largely independent of exact GB misorientation angle for HAGBs [29]. Figure 5.26 also highlights a range in RIS severity for GBs identified at twin GBs. This may be the result of coherent and incoherent twin GBs both being grouped as twin GBs within this analysis. In the same work by Barr *et al.*, Barr also observed major differences between coherent and incoherent twin boundaries, and their response to irradiation [29]. Notably, incoherent twins were found to respond in a similar way to HAGBs and were not inefficient point-defect sinks [29]. This observation was linked to variations in atomic structure, resulting in substantial differences in GB energy [29].

Comprehensive knowledge of how GB character informs individual GB response to irradiation for ex-service specimens is key for the prediction of behaviour during wet storage, and for further development of predictive models.

Thermally Treated AISI Type 304 Stainless Steel STEM EDX measurements collected across HAGBs (Lamellae 1 and 2) in thermally treated AISI Type 304 stainless steel showed that chromium and iron were depleted at the GB and nickel was typically enriched, with depletion profiles between 100 nm and 140 nm wide. Measurements of silicon concentration showed little variation. These measurements were somewhat complicated by the presence of GB chromium-rich carbide precipitates, and so multiple line scans were performed across each GB.

Line scans collected in regions including GB carbide precipitates were typically asymmetric across the precipitate (Figures 5.43 and 5.45a). As discussed previously, this is likely due to a coherency between one carbide-GB interface, noted in other works [105]. The more severe

chromium depletion is expected to occur at the higher energy (i.e. incoherent) interface [105]. This phenomenon may also be due to, or amplified by, GB migration [105, 106].

The line scans shown in Figure 5.45 were collected at various distances from the carbide precipitate in the HAGB in Lamella 2. The first line scan was collected across the carbide precipitate, as indicated by a chromium peak. The second and third line scans (Figures 5.45b and c) were collected along the same GB immediately following the carbide precipitate. The chromium depletion measured across these line scans was severe, with concentrations down to 5.60 wt.%. At further points along the GB the chromium depletion improves somewhat up to a value of 8.18 wt.%, however the GB is still considered as severely sensitised. Previous studies have also reported significant variation dependent upon GB carbide distribution [103, 104].

Measurements were observed to vary substantially depending on GB type, as expected from literature [67, 81, 102, 103, 105, 107]. Whilst severe chromium depletion was measured across HAGBs, STEM EDX line scans collected from the coherent twin GB in Lamella 3 showed little or no variation in chromium concentration (Figure 5.46). This was also the case for iron and nickel concentrations. This is due to the lack of chromium-rich carbides formed along this GB. This has also been reported in other works, and is ascribed to lower boundary energy [67, 71, 81, 102, 103, 105].

5.5.3 Measurements of SCC in Ex-Service AGR Fuel Cladding

A crack formed due to irradiation-assisted SCC (IASCC) during post-irradiation storage in Sample 2YC was analysed, shown in Figure 5.27. This crack was intergranular and branched in morphology, this is typical for RIS-affected AGR cladding [30]. Presence of cracks indicates that GBs within the sample are sensitised (i.e. < 12% chromium wt.% [95]), and that sufficient stresses are present within the cladding. Within cladding there are many possible sources of stress, including: differential thermal expansion of the fuel and cladding, clad-fuel bonding, fuel pellet movement, swelling and fracture, internal gas pressures, and cold work during manufacture [30, 79].

Sample 2YC had been collected from the same stringer and element position as Sample 2YB but from a different pin position.

GB misorientation measurements were performed for GBs along the crack path and compared to those collected from adjacent GBs that had not undergone IASCC. Histograms of the data shown in Figure 5.29 highlighted that the crack path exclusively followed GBs categorised as HAGBs. From STEM EDX measurements on 2YB, this result was somewhat expected, as HAGBs were found to be most severely depleted in chromium, and therefore more susceptible to cracking. This observation is also in agreement with other reported works [95, 274].

In a study of IASCC by He *et al.*, a model austenitic alloy (Fe-13Cr-15Ni) was proton irradiated and strained in a high temperature water environment [130]. Within this study GB type was found to significantly affect cracking behaviour [130]. It was noted that specific random

HAGB underwent cracking [130], in agreement with work performed here. This observation was postulated to be due to GB composition [130]. Depletion of chromium and enrichment of nickel were both observed to be enhanced at the crack tip region, indicating that nickel content is also a key factor under the conditions studied [130].

Comparing crack path measurements with the GB misorientation measurements shown in Figure 5.10, it can be seen that, despite the high proportion of GBs with misorientations between 59° and 61° measured across the samples, no cracked GB was observed within this range. However, the shape of the profile for random HAGBs is similar, peaking around 40°.

Considering individual GB misorientation measurements given in Table 5.6 it was found that higher misorientation GBs cracked preferentially, with the exception of twin GBs which did not crack. This may be a direct result of twin GBs observed resistance to RIS, leading to a lack of sensitised twin GBs. The resistance of twin GBs to undergo cracking has been reported in other works [130, 134].

5.5.4 Thermally Treated Proxy Samples

IASCC is known to occur as a result of an amalgamation of factors, both chemical and mechanical. Improved understanding of IASCC mechanisms is important for the safe storage of ex-service AGR fuel and fuel cladding. Further experimental work is required. However, it is often impractical to perform such experiments on ex-service AGR cladding samples. It therefore is of interest to examine whether thermally sensitised samples may act a proxy samples to irradiation sensitised in order to improve ease of testing, as discussed in Section 2.1.5.3. The material and thermal treatment implemented within this study has been found to be a suitable proxy in previous corrosion studies regarding behaviour in storage pond conditions [30]. The work presented here aims to build upon this study.

Within the context of using thermally treated AISI Type 304 stainless steel samples as a proxy for ex-service AGR fuel cladding in order to characterise corrosion behaviours, key similarities and differences highlighted within the work performed are as follows (key quantities are compared in Table 5.8):

- **Sample compositions** - The samples contained differing chemical compositions, with AISI Type 304 stainless steel containing less chromium, nickel, and no niobium (Tables 5.1, 5.2, and 5.8). This key difference will result in differing precipitation behaviours and elemental compositions at GBs, as observed. However, it is not known whether this variation will result in significant differences in corrosion behaviours.

- **Precipitation** - The ex-service AGR cladding sample (Sample 1XA) contained a number of larger SPPs including $M_{23}C_6$, sigma phase, NbC, and G phase. The thermally sensitised AISI Type 304 stainless steel sample contained comparatively few large SPPs and many small GB carbide precipitates. These differences may result in an alteration of mechanical

properties, i.e. embrittlement. However, precipitation occurred primarily along GBs for both sample types, with the exception of NbC. Regions adjacent to SPPs may also act as preferential site for localised corrosion. This will likely affect cracking behaviour, though it is not known how behaviours will differ between the two materials.

- **Voids** - A large number of voids were observed across the surface of an ex-service AGR cladding sample (Sample 1XA), whilst none were present within the thermally sensitised samples. These voids can cause internal stress via swelling, as well as acting as micro stress raisers for external tensile stresses.

- **GB misorientation distribution** - the distributions within both sample types were similar, with the majority of GBs being HAGBs and a large fraction being identified as coherent twin GBs. This is a key similarity as GB type has been reported to affect propensity to IGSCC [130, 134].

- **GB depletion profiles - Elemental segregation** - the extent of elemental segregation varied between the two sample types analysed. This is expected from the differing mechanisms that give rise to GB segregation in irradiated samples (RIS) compared to thermally sensitised samples (GB carbide precipitation). However, the general observation that iron and chromium are depleted at the GB and nickel is enriched was found for both sample types. The extent of elemental segregation was found to be more severe for random HAGBs for both materials, with twin GBs being less affected (as summarised in Table 5.8). In the thermally sensitised sample, no elemental segregation was observed in the twin GB. This will lead to a resistance to localised corrosion processes at these GBs compared to HAGBs in both materials, but particularly for the thermally sensitised sample. Considering HAGBs for both sample types, chromium depletion was more severe within the thermally sensitised sample (5.60 wt.% vs. 10.89 wt.% for irradiated), however both samples contained GBs that were sufficiently depleted in chromium to be considered sensitised. Chromium is widely regarded as key in determining susceptibility to IGSCC [91]. Nickel enrichment was found to accompany chromium depletion for both sample types, this may have an effect on IGSCC susceptibility with varying reports [91, 130]. Silicon was found to be enriched within some of the HAGBs analysed in the ex-service sample, this was not observed within the thermally sensitised sample. This is not expected to affect susceptibility to IGSCC [91].

- **GB depletion profiles - Width** - measured depletion profiles at random HAGBs were wider in the thermally sensitised sample (approx. 140 nm for HAGBs) compared to the irradiated material (40-60 nm for HAGBs). This has been noted in other works [30, 49]. Shorter thermal treatments may result in narrower depletion profiles; however, this may also result in a discontinuous network of sensitised GBs. Though some works have noted that IGSCC has a stronger dependency on the depth of chromium depletion, rather than the widths [48].

- **Grain size** - AISI Type 304 stainless steel used in this work has a larger grain size (15 μm mean diameter) than that measured for ex-service AGR fuel cladding (1.4 μm mean diameter), inevitably affecting mechanical properties of the material. For example, yield/ultimate tensile stress values are larger for materials with smaller grain size, as per the Hall-Petch relationship [275]. This will result in differing fracture mechanics for the two materials.

- **Other factors** - other mechanical and chemical properties not analysed within this work should also be noted. Including other effects of irradiation such as hardening [91, 130]. However, it should be noted that IASCC is accelerated by irradiation effects rather than induced by them. It is likely therefore that differences in the underlying mechanisms of SCC within the irradiation sensitised samples compared to the thermally sensitised samples may be minimal.

In addition to these factors, it must also be noted that ex-service AGR fuel cladding as it is stored following removal from the reactor will not have a mirror finish surface such as the samples examined within this thesis. This will ultimately result in differing corrosion behaviours, for example scratches or machining marks on the surface can act as stress raisers resulting in initiation points for SCC.

In summary, the key differences between the ex-service AGR fuel cladding and the thermally sensitised AISI Type 304 stainless steel are expected to affect factors such as time to failure and crack velocity. High temperature irradiation changes the microstructure within AGR fuel cladding by a combination of thermal effects and neutron damage [30]. RIS is of particular significance as it results in GB chromium depletion [51]. Although RIS is accompanied by several different effects within the material, GB chromium depletion is the main concern due to the adverse effects in corrosion behaviour. In particular, GB segregation by RIS is considered to be a key factor in susceptibility to IASCC [91, 92]. As both sample types are sufficiently sensitised, with similar GB misorientation distributions, differences are not expected to result in fundamental difference in crack mode or mechanism when examined under similar cracking conditions, i.e. environment and stress. That is not to say, however that the differences highlighted between the two sample types should be negated. These factors should indeed be considered when drawing any conclusions following observation of corrosion behaviour in thermally sensitised proxy samples, as performed in subsequent chapters.

Table 5.8: Summary of key similarities and differences between ex-service AGR fuel cladding and thermally sensitised AISI Type 304 stainless steel highlighted within this study. *Compositions are given as comparative values where a plus sign indicates a higher compared concentration.

Factor	Ex-Service AGR Fuel Cladding	Thermally Treated Type 304
Composition*	+0.003 wt.% **C**, +0.24 wt.% **Si**, +0.014 wt.% **S**, +0.86 wt.% **Cr**, **Nb**, +16.12 wt.% **Ni**	+0.60 wt.% **Mn**, +0.008 wt.% **P**, **Mo**
SPPs	$M_{23}C_6$, sigma phase, NbC, G phase	Small intergranular $M_{23}C_6$, MnS
Void Size (Diameter)	75 nm mean void diameter, 66 nm mode diameter	n/a
Void Diameter Distribution	134 nm at GBs (143 nm at HAGBs, 108 nm at LAGBs, 113 nm at twin GBs), 100 nm in the grains	n/a
Void Depth Distribution	6.1 nm at GBs (7.2 nm at HAGBs, 2.9 nm at LAGBs, 3.4 nm at twin GBs), 2.2 nm in the grains	n/a
GB Misorientation Distribution	(negating sub-GBs) 45.2% HAGBs, 3.0% LAGBs, 51.8% twin GBs	(negating sub-GBs) 52.9% HAGBs, 5.8% LAGBs, 41.3% twin GBs
GB Depletion (HAGBs)	Lowest **Cr**: 10.89 wt.%, highest **Ni**: 42.61 wt.%, highest **Si**: 4.35 wt.%	Lowest **Cr**: 5.60 wt.%, highest **Ni**: 25.32 wt.%
GB Depletion (LAGBs)	Lowest **Cr**: 13.42 wt.%, highest **Ni**: 38.8 wt.%	n/a
GB Depletion (twin GBs)	Lowest **Cr**: 12.27 wt.%, highest **Ni**: 48.72 wt.%, highest **Si**: 5.34 wt.%	No clear variation
GB Depletion Width	HAGBs approx. 40 - 60 nm, LAGB approx. 130 nm, twin GBs 45 - 145 nm	HAGBs approx. 140 nm
Grain Size (diameter)	0.1 μm - 30.8 μm, 1.4 μm mean and 3.9 μm standard deviation	1 μm - 43 μm, 15 μm mean and 9 μm standard deviation

5.6 Conclusions

Large area analysis of ex-service AGR fuel cladding by HS-AFM, EBSD and EDX provided correlated topographic, crystallographic, and chemical information from the sample surface. This allowed for identification of SPPs and analysis of microstructure. Further analysis by STEM EDX was performed to assess GB segregation due to irradiation. The following conclusions are drawn from this work:

- Large area analysis of a sample of ex-service AGR fuel cladding revealed numerous large SPPs including: $M_{23}C_6$, sigma phase, NbC, and G phase. These precipitates were primarily intergranular. Numerous smaller NbC were found to be primarily intragranular.
- HS-AFM analysis of these precipitates revealed surface textures unique to each SPP, with the exception of NbC due to the presence of a G phase shell. This study introduced the potential of SPP identification by HS-AFM due to chemically induced topography. This may be extended to alternative electrolytic etch recipes for comparative studies with the potential to probe the chemical behaviours of the surface microstructural features by performing numerous subsequent etches.
- Numerous nm-scale voids were observed across the surface by HS-AFM, with intergranular voids appearing larger in size and depth. These voids had previously only been observed by TEM. The high throughput of HS-AFM allowed for large area analysis providing various surface statistics such as void size and variation. Voids were found to be larger and deeper at GBs, particularly HAGBs. An association was also noted between increased void frequency and SPPs.
- Samples of ex-service AGR cladding analysed by STEM EDX showed that HAGBs are more prone to sensitisation by RIS compared to LAGBs or twin GBs. Due to the frequency of HAGBs this may indicate susceptibility to localised corrosion during post-irradiation storage. Comprehensive measurements of how GB character affects individual GB response to irradiation for ex-service specimens is of considerable importance for prediction of behaviour during wet storage, as well as further development of accurate predictive models, and the simulation of RIS effects.
- Different GB type were also found to have distinct compositional profiles. The LAGB and twin GBs had symmetric profiles, with one twin GB producing a W-shaped profile. Some HAGBs were found to have asymmetric composition profiles, indicating that they had undergone GB migration.
- GB misorientation measurements performed along a crack in a sample that had suffered IGSCC revealed that higher misorientation GBs cracked preferentially, with the exception of twin GBs which did not crack.

- The observed twin GB resistance to RIS and subsequent cracking by IGSCC, may indicate that the high proportion of twin GBs observed within 20Cr/25Ni-Nb stainless steel may be of benefit for the macroscale physical and chemical properties of the material. This is the basis for GB engineered materials [66, 68, 69, 132, 133].

A comparative study of thermally sensitised microstructure was performed on thermally treated AISI Type 304 stainless steel samples. This material is used extensively within the subsequent chapters of this thesis. The following conclusions were made following this analysis:

- Large area surface analysis found numerous smaller SPPs identified as chromium-rich carbide precipitates in the majority of GBs, with the exception of twin GBs. These GBs were preferentially etched within topographic maps and GB carbide precipitates were seen to stand in relief of the surface. The length scale of these SPPs is such that they would be difficult to image at high resolution using other techniques [193]. Varying distributions of GB carbide precipitates are thought to be associated with GB misorientation value. Comparatively few larger SPPs were observed, these were identified as chromium-rich carbides and MnS precipitates.

- HAGBs were found to be severely sensitised with chromium depletion measured down to a value of 5.60 wt.%. Minimum chromium concentrations were measured near to GB carbide precipitates, values increased as the distance from the carbide precipitate increased.

- Twin GBs were found to be resistant to thermal sensitisation and were not observed within HS-AFM topographic analysis of the surface as a result.

Lastly, the following conclusion was drawn regarding the application of thermally sensitised AISI Type 304 stainless steel as a proxy for ex-service AGR cladding:

- The microstructural differences observed between the two materials within this study is expected to have an effect on SCC initiation times and propagation speeds. However, the fundamental mechanisms for failure of the thermally sensitised material are likely still relevant within studies of irradiated material within similar environmental and stress conditions.

In the following chapter (Chapter 6) samples of AISI Type 304 stainless steel (thermally sensitised under the same conditions as explored in this chapter) are exposed to various industrially relevant corrosive environments. These environments include a sodium chloride solution (known to induce pitting corrosion) and a sodium thiosulfate solution (known to induce IGSCC with sufficient tensile stress). Changes to the surface microstructures (as analysed in this chapter) are monitored both optically and by in-situ HS-AFM. The corroded surface is also analysed by ex-situ SEM and other correlative techniques allowing for detailed characterisation. The key aim of Chapter 6 is to identify features that corrode preferentially or act as initiation points.

In subsequent chapters, these features may then act as focal points for future SCC studies, increasing the likelihood that crack initiation may be observed.

CHAPTER 6

Studies into Localised Corrosion Events In the Absence of Stress: Pitting and Dissolution

In some cases it is pitting or intergranular attack
That when stress is applied can give rise to a crack
So next in this thesis we will try to assess
What happens to this material if it corrodes without stress

Detection methods of the early stages of localised corrosion events, such as pitting and intergranular attack (IGA), are of particular interest for further understanding of the initiation mechanisms occurring. These stages are poorly understood, as the small scale at which they occur presents a challenge for successful detection or measurement [150, 152]. Thus far, nucleation sites for localised corrosion events have not been conclusively identified, though they often occur at discontinuities on the surface, such as at grain boundaries (GBs) or inclusions [111, 149, 155]. By producing data of the early stages of localised corrosion, results and observations may be fed into computational models, allowing for a mathematical reconstruction of the electrochemical events occurring [149, 150].

In this chapter localised corrosion phenomena were investigated using contact mode high-speed atomic force microscopy (HS-AFM) in combination with other techniques including optical, electrochemical measurements, scanning electron microscopy (SEM) techniques, and energy-filtered photoelectron emission spectromicroscopy (EF-PEEM). Thermally sensitised American Iron and Steel Institute (AISI) Type 304 stainless steel, studied in Chapter 5, is exposed to two aqueous solutions of aggressive salts, both relevant within industrial applications. In the first part of this chapter, localised corrosion events were initiated by polarising the sample within a

sodium chloride solution. Chloride is an aggressive ion, known to cause pitting corrosion. Pitting sites can also act as precursors to stress corrosion cracking (SCC) if the sample is sufficiently stressed. This is a particular issue within nuclear applications, as described in Sections 2.2.2.3 and 2.5.1.

In later chapters of this thesis, SCC is initiated in a sample of thermally sensitised AISI Type 304 stainless steel exposed to a solution of sodium thiosulfate, such that SCC initiation and propagation may be studied. This is a well-known system for initiating intergranular SCC (IGSCC), as discussed in Section 2.5.2. The second part of this chapter explores the effect of sodium thiosulfate on AISI Type 304 stainless steel in the absence of stress. HS-AFM measurements are performed with the aim to better understand how the microstructure is affected by exposure to the solution, and how this may contribute to SCC.

EF-PEEM measurements shown within this chapter were collected by Mattia Cattelan on the NanoESCA instrument at the University of Bristol. This chapter includes figures and large sections of text taken directly from the following papers:

- **S. Moore**, R. Burrows, L. Picco, T. Martin, S. Greenwell, T. Scott, and O. Payton, 2018. A study of dynamic nanoscale corrosion initiation events by HS-AFM. Faraday Discussions, 2018, 210, 409 - 428.

- H. Alzahrani, C. Bentley, R. Burrows, C. Cao, Q. Cai, C. Chikere, R.M. Crooks, J. Dunevall, M. Edwards, A. Ewing, R. Gao, R. Hillman, M. Kahram, F. Kanoufi, C. Kranz, J.F. Lemineur, Y. Long, K. McKelvey, M. Mirkin, **S. Moore**, W. Nogala, H. Ren, W. Schuhmann, P. Unwin, A. Vezzoli, H. White, K. Willets, Z. Yang and Y. Ying, 2018. Dynamics of nanointerfaces: general discussion. Faraday discussions, 210, pp.451-479.

- **S. Moore**, R. Burrows, D. Kumar, M. B. Kloucek, A. D. Warren, P. E. J. Flewitt, L. Picco, O. D. Payton, and T. L. Martin, Observation of Stress Corrosion Cracking of Stainless Steel Using Real-Time In-Situ High-Speed Atomic Force Microscopy and Correlative Techniques. Npj Materials Degradation, 2021, 5(3).

6.1 Localised Corrosion of Thermally Sensitised AISI Type 304 Stainless Steel in a Sodium Chloride Solution

6.1.1 Electrochemical Measurements

6.1.1.1 Experimental Set-up

Pitting experiments were performed in-situ on the stage of the HS-AFM (shown in Figure 6.1). A standard three-electrode set-up was implemented for electrochemical tests, within an electrolyte of 1% (i.e. 10,000 mg L^{-1} or 0.17 M) aqueous sodium chloride (NaCl).

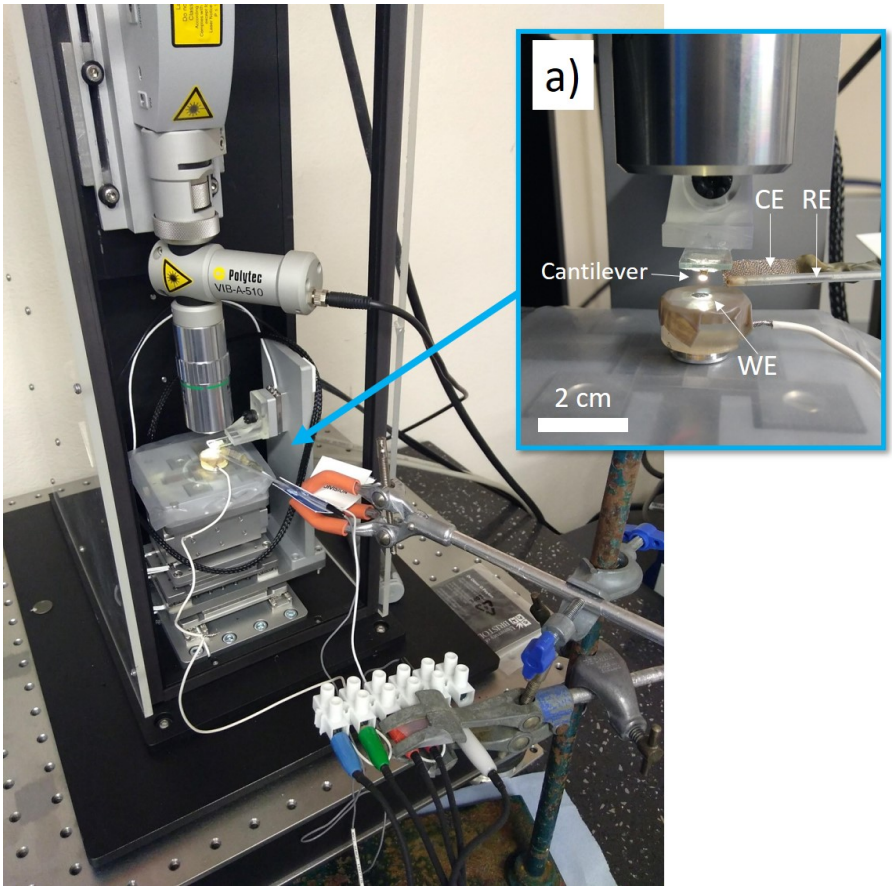

Figure 6.1: A photograph taken of the experimental set-up showing the HS-AFM and parallel electrochemical control. Inset: a) an additional photograph with scale bar showing a close-up of the three-electrode set-up, with labels for the working electrode (WE), counter electrode (CE) and reference electrode (RE). The cantilever is mounted onto the glass slide comprising the upper part of the liquid cell. No electrolyte was present in the set-up photographed.

Samples of thermally sensitised (as described in Section 5.1.2) AISI Type 304 stainless steel were cut into approximately 5×5 mm squares using an accutom. An electrical connection was made to the sample by attaching a wire to the back face of the sample using silver paint (Agar Scientific, UK), this wire was secured in place once samples were set in resin (cold set, Struers^{TM} Clarocit). Continuity tests of the connection between the wire and the sample surface were carried out using a multimeter. Subsequent surface preparation techniques were carried out by procedures described in Section 4.2.

A 4 mm diameter circular area (total area 0.13 cm^2) of the sample surface was exposed to the solution, acting as the working electrode (WE). The counter electrode (CE) consisted of a platinum wire mesh, and a silver/silver chloride (Ag/AgCl) micro-electrode with 2 mm diameter (World Precision Instruments Inc.) was used as the reference electrode (RE).

All experimental work was carried out at room temperature and humidity (20 ± 1°C, 45 ± 10%).

Post analysis of the current transients produced during the experiment was performed using Echem Analyst^{TM} software (Gamry Instruments).

6.1.1.2 Potentiodynamic Tests

The rates at which corrosion reactions take place are influenced by the potential difference across the metal/electrolyte interface [110]. These reactions can therefore be driven, or supressed, by the application of an overpotential, discussed in Section 2.2.1. Potentiodynamic tests were performed to characterise the corrosion behaviour of the system under investigation. Within these tests, a potential was applied between the WE and the RE by an Interface 1000 Potentiostat/Galvanostat/Zero Resistance Ammeter (ZRA) (Gamry Instruments), which then recorded the resultant net current (equivalent to the difference between anodic and cathodic reaction rates) between the WE and the CE, producing a polarisation curve.

Figure 6.2 shows polarisation curves for the sample before and after the sample surface had been damaged by localised corrosion events. The red line in Figure 6.2 shows the forward potentiodynamic scan for the undamaged surface. Within this scan peaks in current are observed, beginning at approximately 240 mV (vs. Ag/AgCl) and resulting in measured currents of approximately 100 nA (sample surface area of 0.13 cm^2). As the potential difference becomes more anodic, a considerable increase in the current is measured, up to a maximum of 0.3 mA. Currents are not quoted as current densities as, with localised corrosion studies, the active area of the surface is unknown.

The blue line in Figure 6.2 shows the forward and reverse potentiodynamic scan for the sample after localised corrosion events have taken place. The sample was allowed sufficient time for full repassivation of the surface before this test was performed. The forward scan (blue line starting at point A) has a similar shape to that observed for the red line, shifted to the right slightly, towards higher currents for the same voltage value. This scan had a lower measured open circuit potential (OCP), 131 mV (vs. Ag/AgCl) compared to 141 mV (Ag/AgCl) for the red line.

The return potentiodynamic scan (the second section starting at point B) of the blue line in Figure 6.2 reveals the effects measured immediately after localised corrosion events were initiated on the sample surface. The return scan is shifted considerably towards more cathodic potentials. In addition, the exchange current density has increased by orders of magnitude. The measured OCP had also shifted significantly between the forward and the reverse potentiodynamic scan, from 131 mV vs. Ag/AgCl to -339 mV vs. Ag/AgCl. A longer period of OCP measurement was taken directly after the reverse potentiodynamic scan returned a measured OCP of -352 mV (vs. Ag/AgCl).

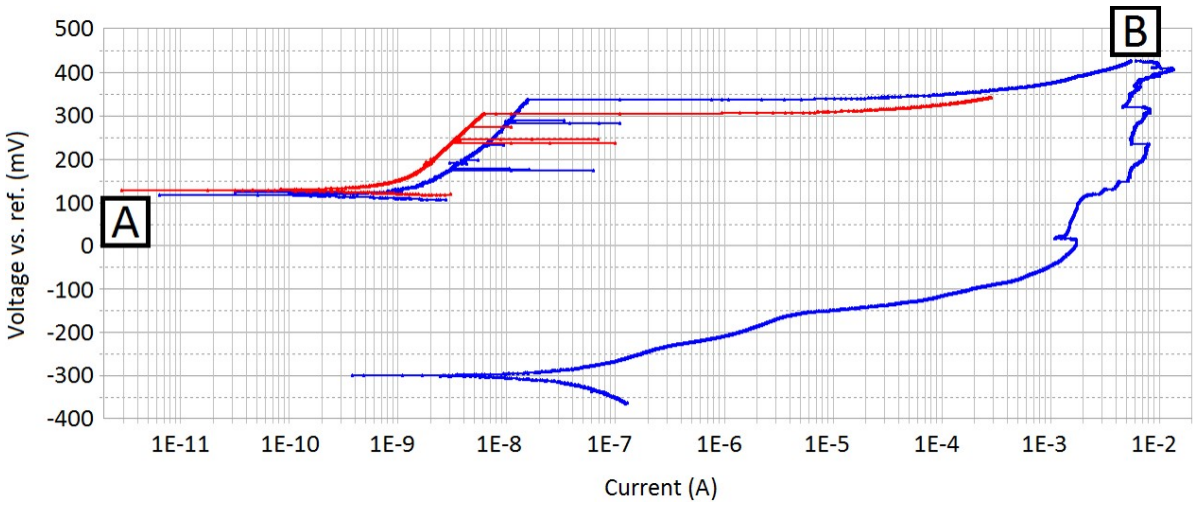

Figure 6.2: Polarisation curves showing a forward potentiodynamic scan (-25 to +200 mV vs. OCP) of a thermally sensitised AISI Type 304 stainless steel sample within 1% aqueous NaCl with a fresh surface, previous to corrosion events (red line, starting at point A). Also shown are forward (-25 to +300 mV vs. OCP) and reverse (+300 to -25 mV vs. OCP) potentiodynamic scans of a sample with a surface that had previously undergone localised corrosion events (blue line, starting at points A and B, respectively). Results are for a sample surface area of 0.13 cm^2.

6.1.1.3 Galvanostatic Tests

Following initial characterisation tests, galvanostatic experiments were performed. For these experiments, the potentiostat accurately controls the current flow between the WE and the CE though the application of a potential difference between the RE and WE required to maintain the chosen current. A galvanostatic scan was chosen over a potentiodynamic or a potentiostatic scan for the observation of stable pitting events as galvanostatic tests alter the potential such that the current stays constant, as a result, corrosion reactions are driven at a consistent rate. On the other hand, by ramping up the potential or maintaining a constant potential, corrosion reactions may be driven too aggressively. Once initiated, the rate of corrosion should by matched to the HS-AFM imaging rate such that in-situ HS-AFM measurements can be performed. During galvanostatic tests localised corrosion was driven at a reduced rate such that it could be observed over longer periods of time both optically and by HS-AFM. Appropriate current flow values were identified from the initial potentiodynamic tests.

Figure 6.3 shows a galvanostatic scan for a sample in which corrosion reactions are occurring on the surface. A current of 0.05 mA (sample surface area of 0.13 cm^2) was chosen for this test. This was chosen subsequent to measuring the polarisation curve for the undamaged surface (red line Figure 6.2). The polarisation curve illustrates that a current of 0.05 mA is sufficient to sustain localised corrosion events on the surface of the sample at a rate suitable for investigation by HS-AFM. Peaks and troughs in measured voltage are observed. As time increases, the overpotential

required to sustain a constant current decreases.

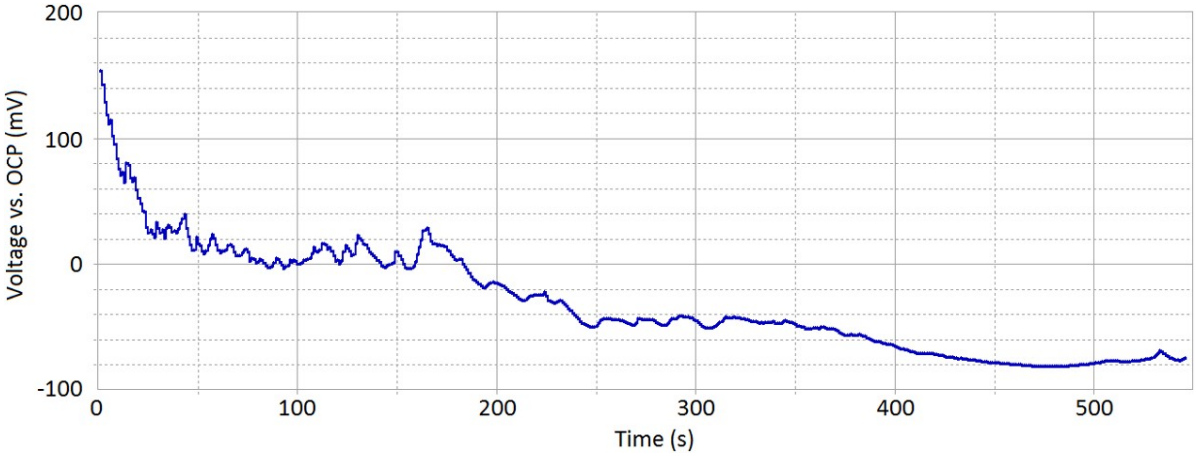

Figure 6.3: A galvanostatic scan of a thermally sensitised AISI Type 304 stainless steel sample within 1% aqueous NaCl taken at 0.05 mA. For a sample surface area of 0.13 cm^2.

6.1.2 Optical Observations

Samples were monitored by optical microscope during potentiodynamic tests in order to draw parallels between events visually occurring on the surface and the current transients being measured as potential is varied. It is important for subsequent HS-AFM measurements to identify optical triggers that indicate the onset of corrosion events. These areas may then be identified by the optical microscope of the HS-AFM and subsequently imaged.

Optical observations performed in-situ whilst the sample was polarised showed that multiple pitting sites propagate simultaneously on the sample surface. This is expected due to the large area of the exposed surface. Observations also revealed a number of characteristics for consideration when performing in-situ HS-AFM measurements. IGA was seen to progress across the sample surface steadily at timescales suitable for observations by HS-AFM. However, gas evolution reactions occurring on the CE surface, and, in some instances of high overpotential, on the sample surface, resulted in the production of gas bubbles. This may interfere with the cantilever during HS-AFM measurements. Additional interference may be caused due to corrosion products on the surface, seen as dark areas in Figure 6.4.

Post-corrosion optical observations of the samples were made using an optical microscope, shown in Figures 6.4 and 6.5. Large scale circular pits are observed across the surface. These images also revealed the intergranular nature of the localised corrosion events occurring on the surface, highlighted in Figure 6.5a.

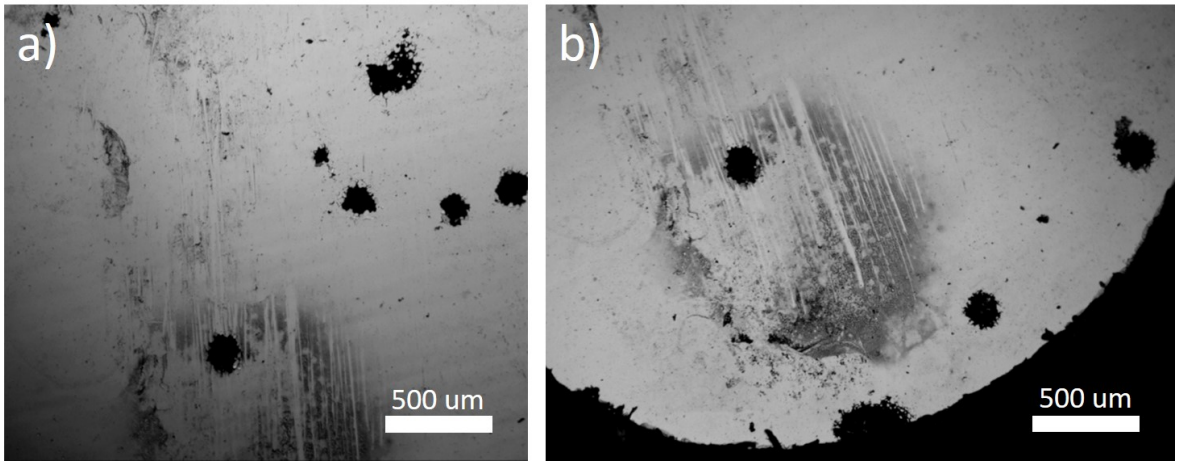

Figure 6.4: Optical images of a thermally sensitised AISI Type 304 stainless steel sample surface post-corrosion in 1% NaCl, taken by an Olympus BH2-UMA optical microscope demonstrating widespread pitting and corrosion products on the surface.

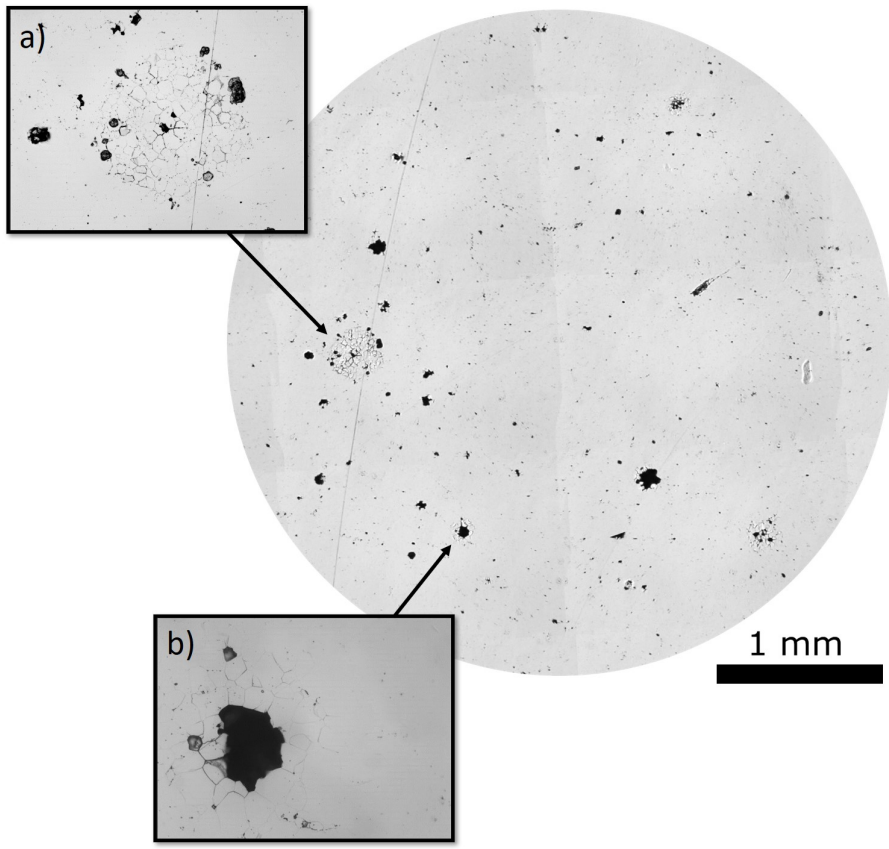

Figure 6.5: A mosaic photo of a thermally sensitised AISI Type 304 stainless steel sample surface post-corrosion in 1% NaCl, taken with a Leica optical microscope with a 5× optical objective, with additional photos of specific areas of interest taken by an Olympus BH2-UMA optical microscope at magnifications of: a) 20× and b) 50×.

6.1.3 Post-Corrosion HS-AFM Observations of Pitting and IGA

Ex-situ HS-AFM measurements performed post-corrosion were found to vary considerably, highlighting the localised nature of the corrosion processes. Corrosion product formed a film across some areas on the surface, such as that observed in Figure 6.6a, however most of the surface was largely unaffected and imaging quality was maintained. The majority of the GBs examined were similar in appearance to those measured previous to corrosion, example shown in Figure 6.6b. However, some GBs were found to contain debris, such as those imaged in Figures 6.6c and 6.6d.

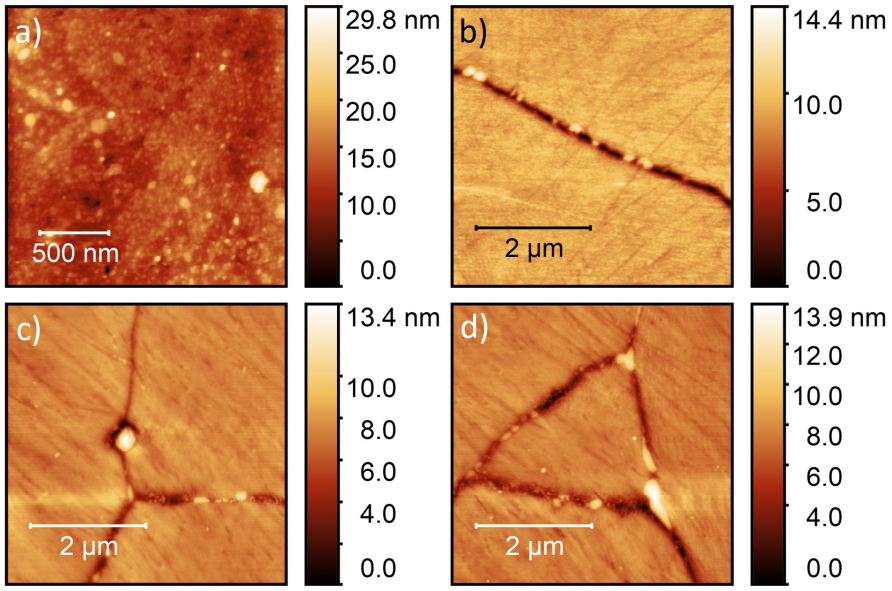

Figure 6.6: HS-AFM topographic maps from a thermally sensitised AISI Type 304 stainless steel sample surface post-corrosion in 1% NaCl showing: a) corrosion product on the sample surface, b) a GB with no apparent corrosion, c) a triple point GB with possible early stage IGA and dissolution of the areas adjacent to the carbide, and d) GBs with possible early stage IGA. All with inset colour scales.

Small pits were observed in isolated locations across the sample surface within the bulk of the grain, examples shown in Figure 6.7. These pits generally appeared rounded and varied in size. The pit shown in Figure 6.7a is observed to contain some debris. The pit in Figure 6.7c occurred within a large carbide precipitate.

A number of small intergranular pits were also measured by HS-AFM, shown in Figure 6.8. These were observed along GBs in the regions surrounding visibly pitted areas, as well as within isolated areas. Intergranular pits were elongated along the GB, and in some areas they occurred in chains along the GB, as seen in Figure 6.8c.

Measurements collected in regions that had visibly undergone localised corrosion were located using the HS-AFM's optical microscope. These regions are expected to be most severely affected by corrosion. Figure 6.9 shows a topographic map collected at the edge of a large pit. This map contains a triple point GB, where one grain is topographically lower than the other two.

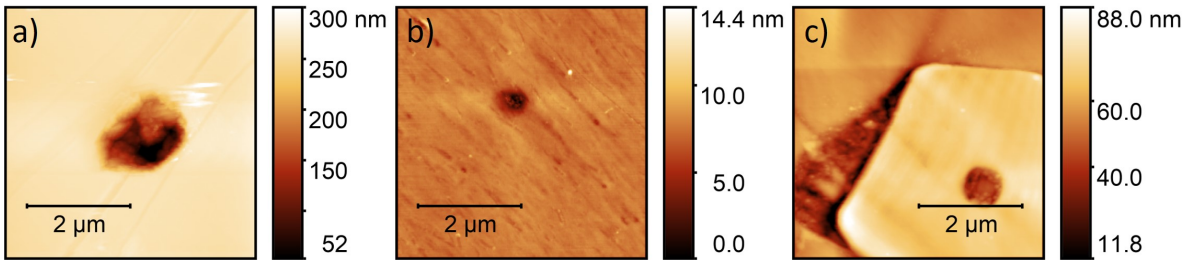

Figure 6.7: HS-AFM topographic maps of a thermally sensitised AISI Type 304 stainless steel sample surface post-corrosion in 1% NaCl. a) and b) show intragranular pits formed in the bulk metal, c) shows a pit formed within a large secondary phase precipitate (SPP). All with inset colour scales.

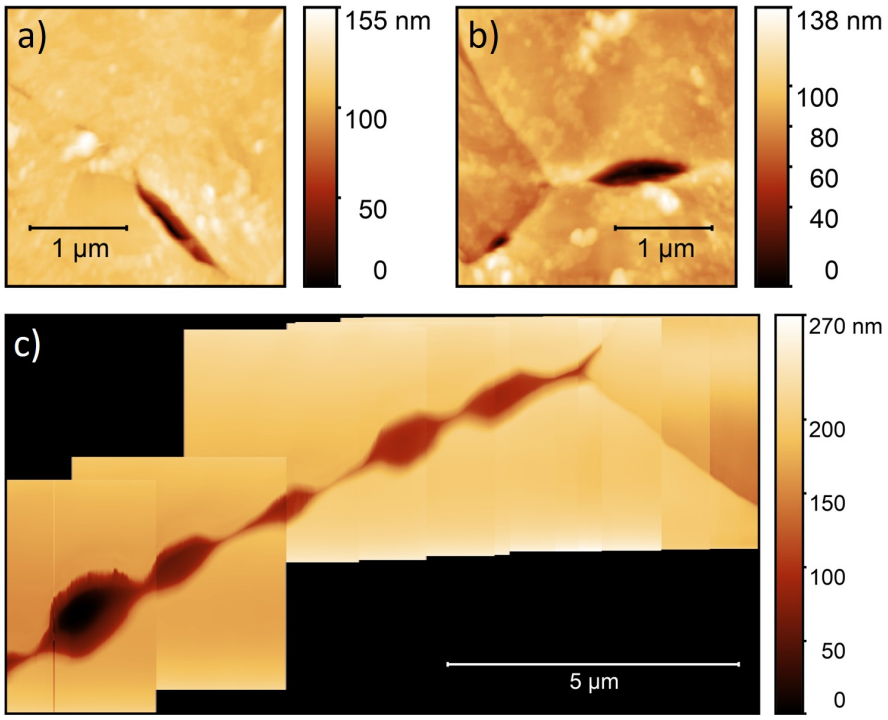

Figure 6.8: HS-AFM topographic maps of a thermally sensitised AISI Type 304 stainless steel sample surface post-corrosion in 1% NaCl showing: a) an isolated intergranular pit, b) intergranular pits on two GBs, and c) a chain of intergranular pits stitched together to form a composite image. All with inset colour scales.

Further measurements from areas adjacent to pitting are shown in Figure 6.10. These images exhibit slip banding, indicating high levels of local stress. Within Figure 6.10d a slip band appears to be pinned by a small intergranular pit.

HS-AFM measurements collected in regions of more severe IGA are shown in Figure 6.11. These images demonstrate significant corrosion at the GBs, with a formation of an oxide or corrosion product in the GB (Figures 6.11b-6.11d). Figure 6.11e contains an angular pit adjacent

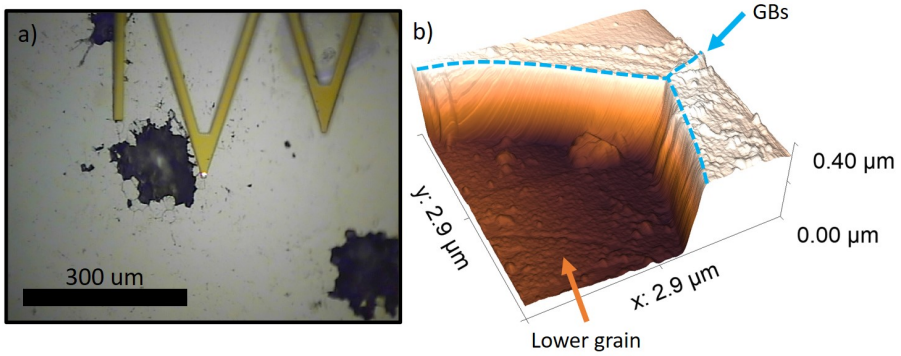

Figure 6.9: a) An optical image of a thermally sensitised AISI Type 304 stainless steel sample surface post-corrosion in 1% NaCl collected with the HS-AFM optical microscope, and b) the HS-AFM topographic map showing a triple point GB (indicated by a light blue dashed line) where one grain is topographically lower, collected at the position shown in a), with inset colour scale.

to the GB.

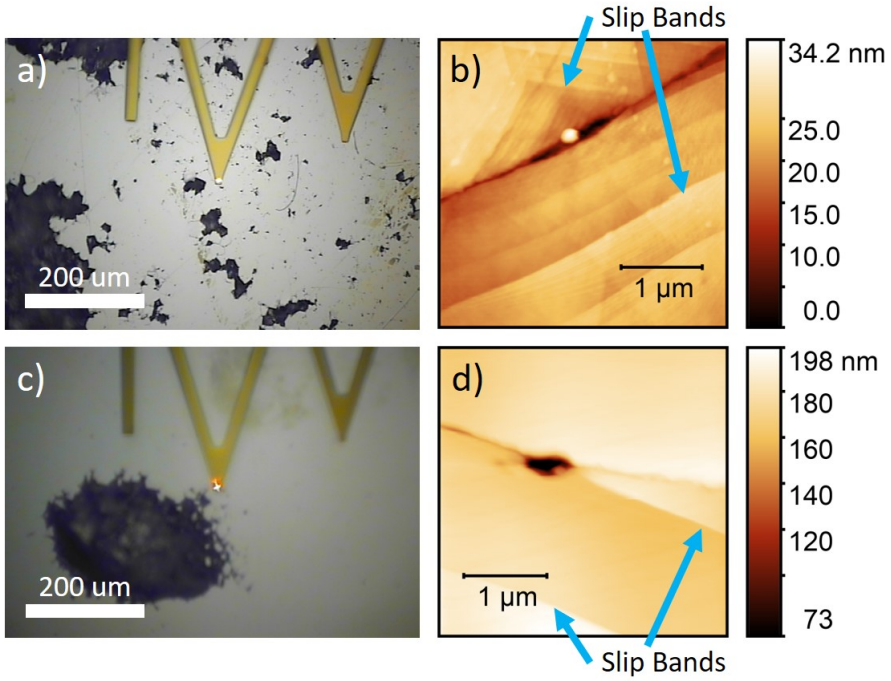

Figure 6.10: a) and c) show optical images of a thermally sensitised AISI Type 304 stainless steel sample surface post-corrosion in 1% NaCl collected with the HS-AFM optical microscope. b) and d) show HS-AFM topographic maps containing slip banding collected at the positions shown in a) and c), respectively. Both with inset colour scale.

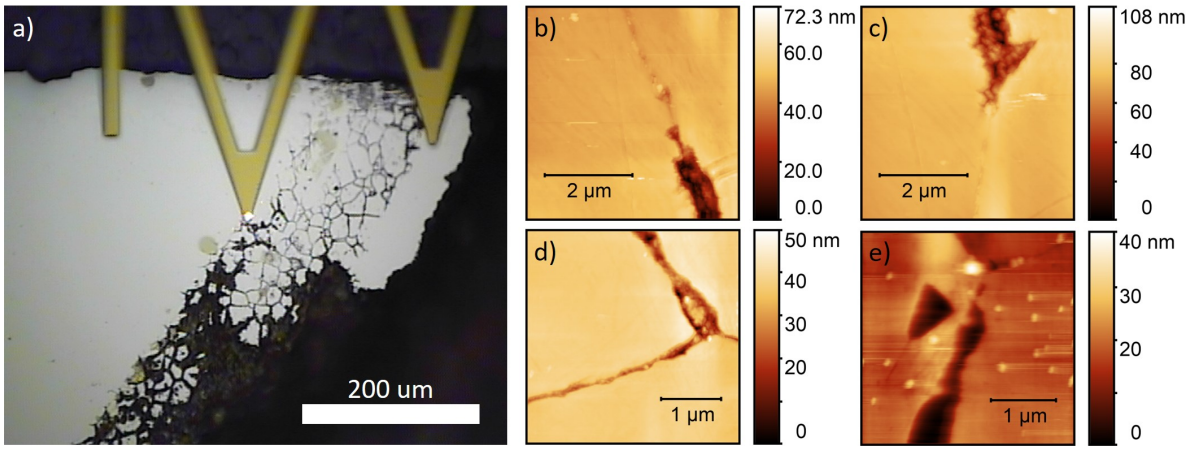

Figure 6.11: a) An optical image of a thermally sensitised AISI Type 304 stainless steel sample surface post-corrosion in 1% NaCl collected with the HS-AFM optical microscope, and b)-d) the HS-AFM topographic maps collected in the region shown in a), with inset colour scale.

6.1.4 Post-Corrosion Scanning Electron Microscopy (SEM) Analysis

The surface of the sample was imaged post-corrosion by scanning electron microscopy (SEM) techniques. High-resolution secondary electron (SE) images of the sample surface were taken at a potential of 5 kV and a current of 1.4 nA. Electron backscatter diffraction (EBSD) maps were also collected at a 70° tilt from the horizontal, using a constant beam voltage of 30 kV and an aperture of 120 μm. Maps were cleaned-up using confidence index standardisation (CIS) and points with a confidence index (CI) less than 0.1 were filtered out.

Low magnification SE images showing a number of large pits on the surface are shown in Figure 6.12. These vary in size and depth and contain etched GBs. An SE image collected at a tilt of 70° is shown in Figure 6.12b. The shallower pit on the left had formed earlier within the experiment and had repassivated. A low resolution (2 μm step size) inverse pole figure (IPF) and image quality (IQ) map was collected by EBSD, Figure 6.12c, showing the larger scale pits on the surface.

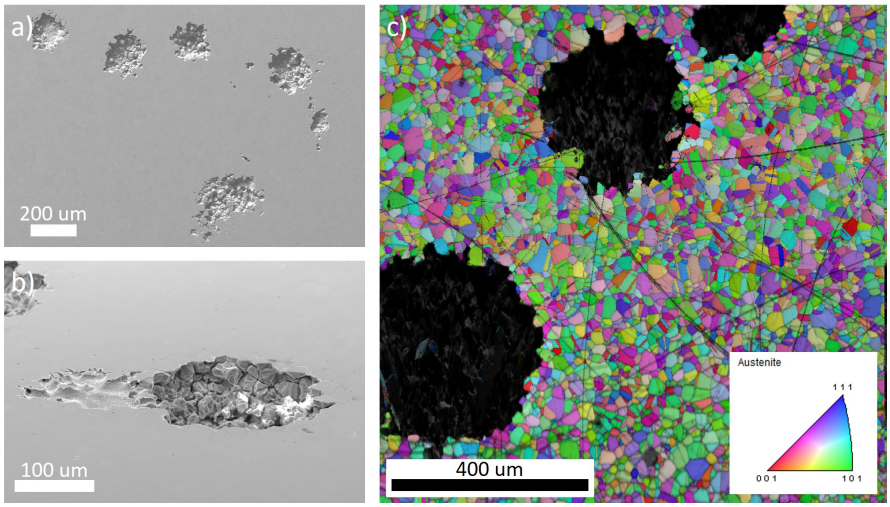

Figure 6.12: a) A low magnification SE image of a thermally sensitised AISI Type 304 stainless steel sample surface post-corrosion in 1% NaCl showing large pits, b) an SE image collected at a 70° tilt from the horizontal, and c) a low magnification IQ and IPF map with inset legend.

Figures 6.13a-f show higher magnification SE images of the corroded surface in the areas surrounding large pits. These images illustrate that larger pits form as an amalgamation of IGA and inter- and intragranular pitting. SE images collected at a tilt of 52° showed evidence of grain undercutting, Figures 6.13c and 6.13d. In some cases the grain was observed to hang into the pit, Figure 6.13f. Subsurface measurements are performed in later sections to evaluate the extent of this phenomenon.

As with previous HS-AFM measurements, chains of intergranular pits were observed along GBs, Figure 6.14. Again, these were observed in areas surrounding larger pits, as well as in

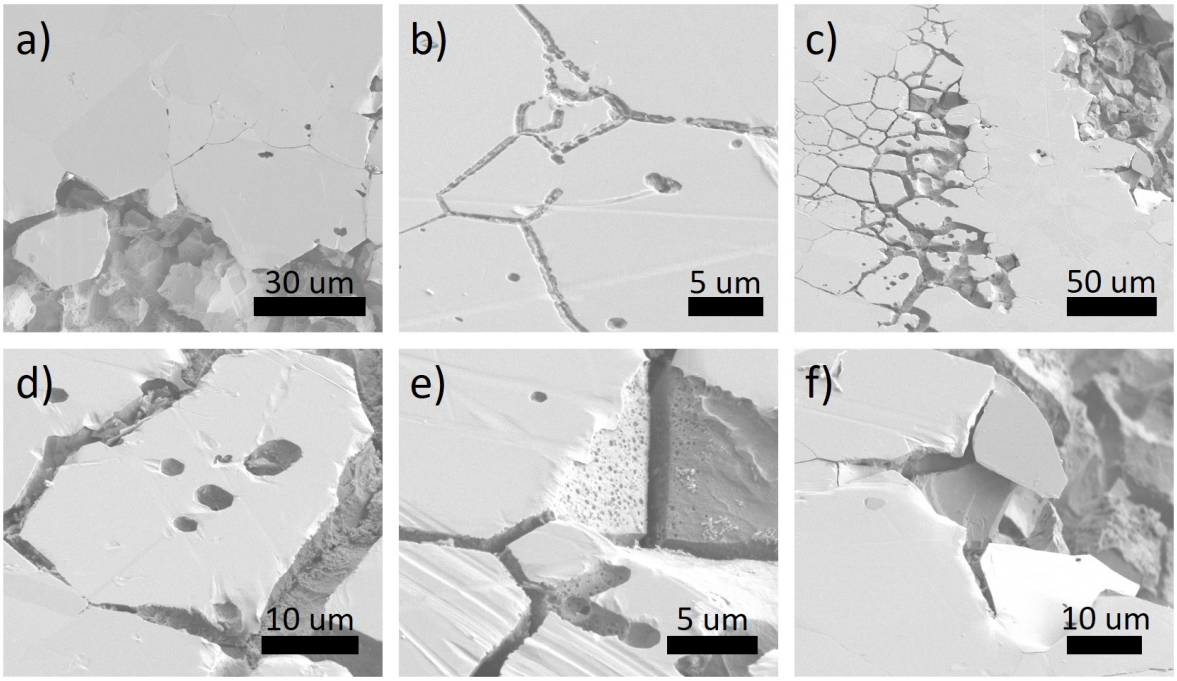

Figure 6.13: A series of SE images of different areas of a thermally sensitised AISI Type 304 stainless steel sample surface post-corrosion in 1% NaCl showing forms of localised corrosion. Image a) was taken at a tilt of 0°, images b)-f) were taken at a tilt of 52°.

isolation. Analysis of intergranular pitting by EBSD further supported the intergranular nature of the pitting, as shown in Figure 6.14c. The pits in this map formed exclusively along high-angle GBs (HAGBs).

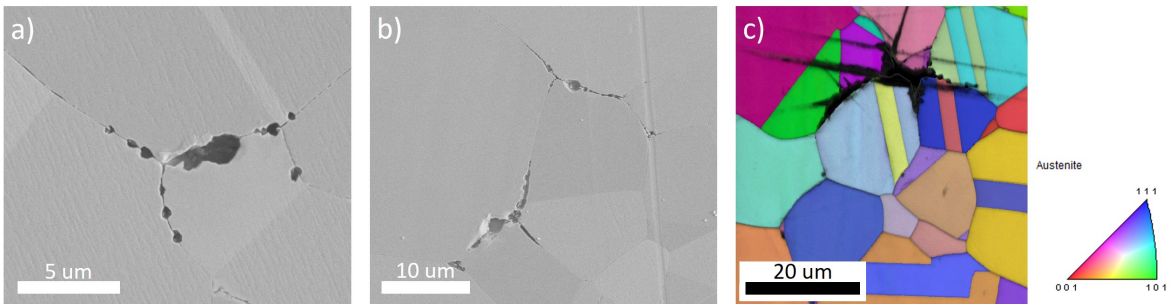

Figure 6.14: a) and b) are SE images of a thermally sensitised AISI Type 304 stainless steel sample surface post-corrosion in 1% NaCl showing intergranular pitting, and c) an IQ and IPF map of intergranular pitting collected with a step size of 0.1 μm, with inset legend.

6.1.5 Subsurface Analysis by Focussed Ion Beam (FIB) Milling

Areas of interest across the surface were selected for focussed ion beam (FIB) milling such that a better idea of the processes occurring beneath the surface could be obtained. FIB milling was performed at 30 kV and 2.8 nA.

6.1.5.1 Sectioning of an Intragranular Pit

FIB milling was performed in an area containing an intragranular pit, shown in Figure 6.15. Following initial FIB cutting of the surface some subsurface intergranular corrosion is observed, Figure 6.15a. Figure 6.15b demonstrates an undercutting of the grain directly below the intragranular pit as observed from the surface.

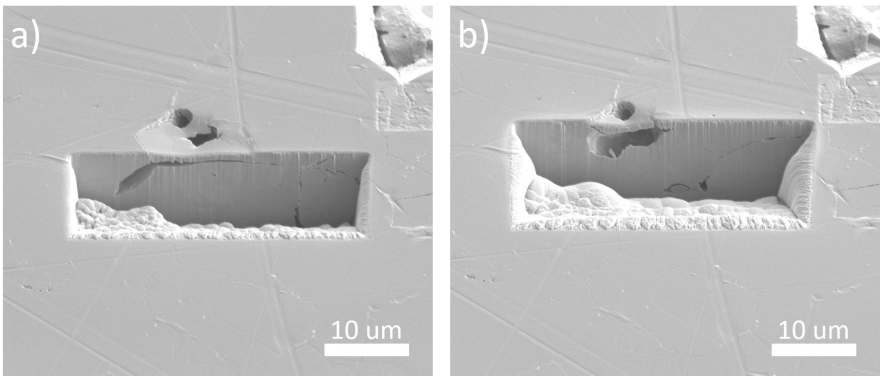

Figure 6.15: SE images taken as a part of a series of 2-5 μm thick slices into a region surrounding an intragranular pit in a thermally sensitised AISI Type 304 stainless steel sample surface post-corrosion in 1% NaCl using FIB, taken at a tilt of 52°.

6.1.5.2 Sectioning of an Intergranular Pit

Figure 6.16 shows SE images of an area adjacent to a large pit where an intergranular pit was studied by FIB milling. Figures 6.16a-6.16c were taken sequentially as the FIB milling process progressed. A large carbide precipitate is observed along the GB at the surface. Beneath the surface large voids are present where corrosion has taken place along the GB.

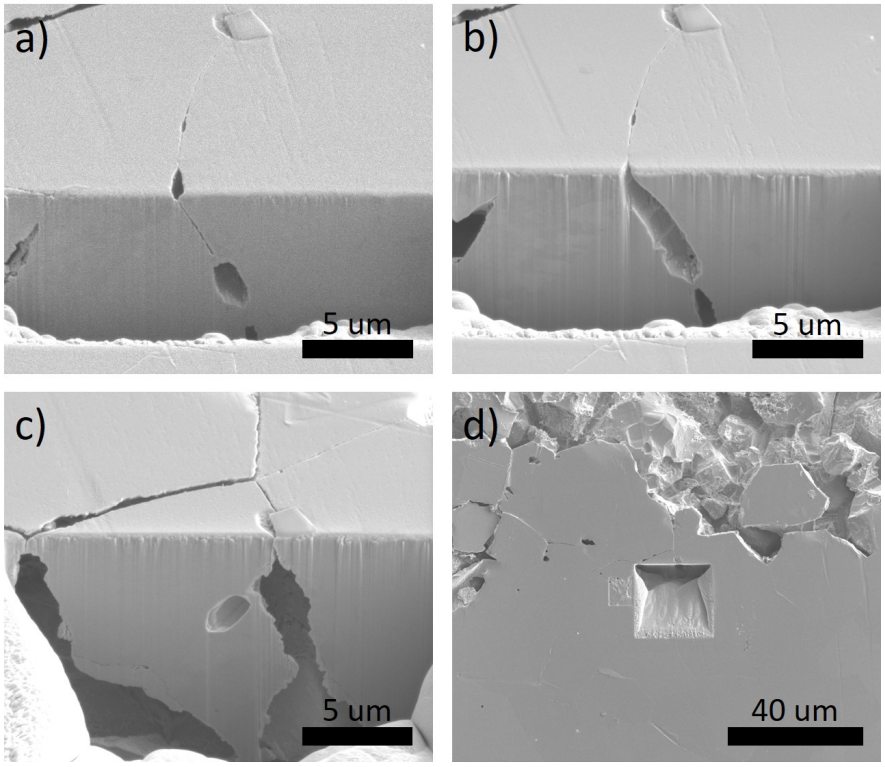

Figure 6.16: SE images taken as a part of a series of 2-5 μm thick slices into a region surrounding an intergranular pit in a thermally sensitised AISI Type 304 stainless steel sample surface post-corrosion in 1% NaCl using FIB. Images a), b) and c) were taken at a tilt of 52°, d) was taken at a tilt of 0°.

6.1.6 In-situ HS-AFM Observations of Pitting Corrosion and Dissolution in Aqueous Sodium Chloride

In-situ HS-AFM observations of localised corrosion events were performed using a custom-built liquid cell with a contact-mode MSNL cantilever (Bruker, USA) in the set-up shown in Figure 6.1. Samples of thermally sensitised AISI Type 304 stainless steel were imaged in a solution of 1% aqueous NaCl, with parallel potentiostatic control. The HS-AFM's optical microscope was used to identify features on the sample surface such that specific areas could be imaged, such as optically visible pitting events. Once pitting corrosion was optically visible, the cantilever tip was placed ahead of the corrosion front by approximately 20 μm such that initiation events may be imaged as the front passed through the frame, as illustrated in Figure 6.17. The large-scale pitting processes were observed to move at a variable rate, up to 5 μm/s for some of the potentiodynamic tests.

Measurements performed following the final frame shown in Figure 6.17d are shown in Figure 6.18. These images show the progression of pitting corrosion through a grain. Figures 6.18a-6.18c appear to show dissolution of a thin layer on the surface of the grain by nucleation

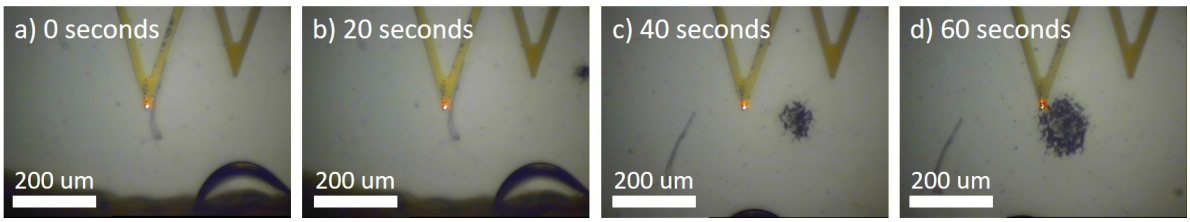

Figure 6.17: Sequential optical images showing the HS-AFM's optical view as a pitting event occurs on a thermally sensitised AISI Type 304 stainless steel sample surface in 1% NaCl.

of numerous small pits across the region imaged. Small pits in this thin layer were between 1 nm and 3 nm deep for Figure 6.18c. Figures 6.18d-6.18e show the corrosion front as it passes through the frame. Following the final collected frame, the image the cantilever lost contact with the surface as the pit had formed.

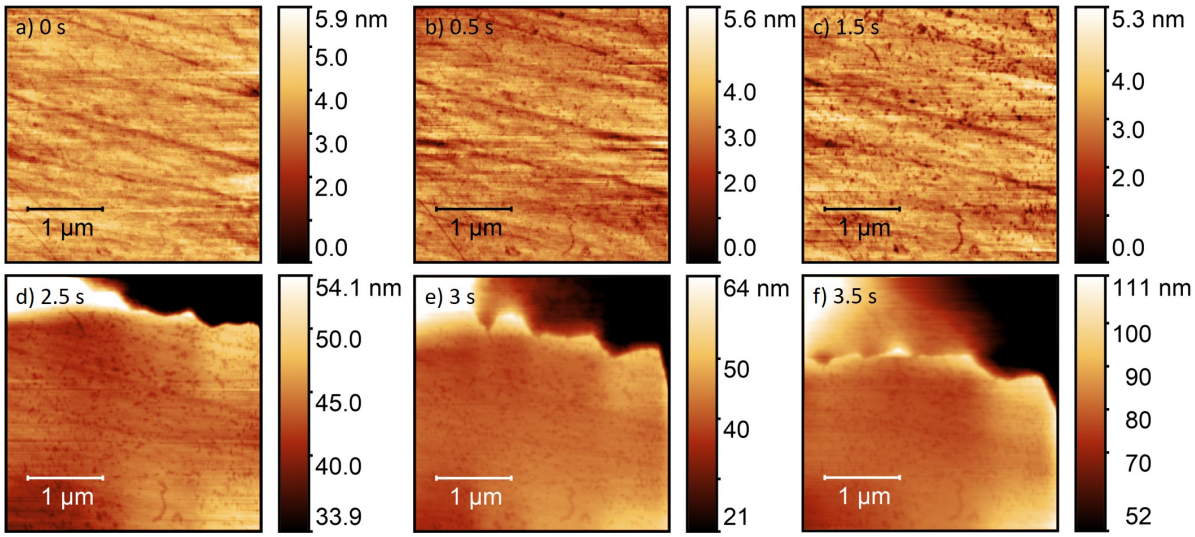

Figure 6.18: Sequential HS-AFM topographic maps showing large pit progression on a thermally sensitised AISI Type 304 stainless steel sample surface in 1% NaCl, with inset colour scales. Frames were collected at: a) 0 seconds, b) 0.5 seconds, c) 1.5 seconds, d) 2.5 seconds, e) 3 seconds, and f) 3.5 seconds.

6.1.6.1 Observation of Intergranular Pit Initiation and Growth

Figures 6.19a and 6.19b show before and after topographic maps of an intergranular pit forming at a GB during a galvanostatic scan. This pit formed between two subsequent HS-AFM frames. Given that the HS-AFM was collecting images at a rate of 2 s^{-1}, the timeframe at which this reaction occurred can be deduced as ≤ 0.5 s.

A map of the full intergranular pit was produced by stitching together two HS-AFM frames (Figure 6.19c). The sensitised GB is not clearly visible within this image as a result of the large

height scale range. Post processing of this topography produced approximate values for the volume of material dissolved. Using this data, the resultant ionic flux and current transients were calculated using Faraday's Law of Electrolysis:

$$Q = \frac{mFz}{M}$$

where Q is the total electric charge (C), m is the mass of metal corroded (g), F is the Faraday constant, z is the valency number of the metal ion, and M is the molar mass of the substance (g mole^{-1}) [178]. Calculated values are summarised in Table 6.1. Due to the high aspect ratio of the pit aperture to pit depth, topography of the imaged pit is influenced by the shape of the cantilever tip and the full extent of this pit may not have been measured [20]. Calculated volumes are therefore lower approximations.

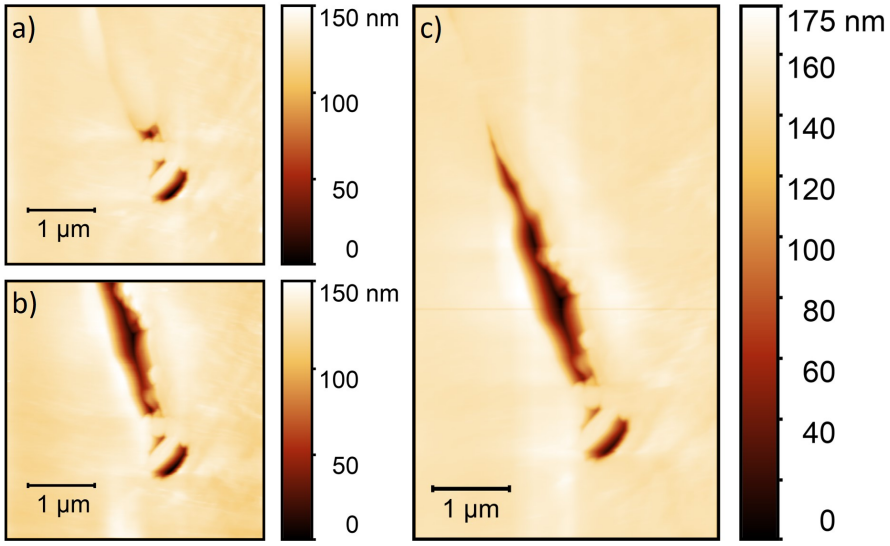

Figure 6.19: HS-AFM topographic maps showing a GB in a thermally sensitised AISI Type 304 stainless steel sample surface polarised in 1% NaCl: a) before formation of intergranular pit, b) after formation of intergranular pit, and c) the full intergranular pit formed. Image c) was produced by stitching two subsequent frames together.

Optical measurements of this area collected post-corrosion shown in Figure 6.5b revealed that the intergranular pit observed in Figure 6.19c had become part of a much larger pit following in-situ HS-AFM observations.

In addition to intergranular pit initiation, measurements of intergranular pit progression were also achieved, shown in Figure 6.20. This pit was observed to grow steadily over a duration of 10s of seconds. Following a 40 second period the pit had increased in diameter, the change in diameter as measured along the line scan shown in Figure 6.20d was approximately 0.3 μm. Between 20 seconds and 40 seconds the depth of the pit is observed to reduce. As the shape of the pit did not vary this is not thought to be the result of tip blunting. Figure 6.20e demonstrates the

Table 6.1: HS-AFM measurements and calculated values for the intergranular pit shown in Figure 6.19c.

Parameter	**Measured Value**	**Units**
Projected Area	1.054×10^{-12}	m^2
Depth	1.228×10^{-7}	m
Volume	5.03×10^{-20}	m^3
Parameter	**Calculated Value**	**Units**
Mass of Iron Dissolved	3.96×10^{-13}	g
Ionic Flux	1.35×10^{-2}	moles m^{-2} s^{-1}
Current Density	2.6×10^{3}	A m^{-2}

variation in pit depth and width with time over 5 second long intervals. It can be seen that width steadily increases, whilst depth changes at a variable rate.

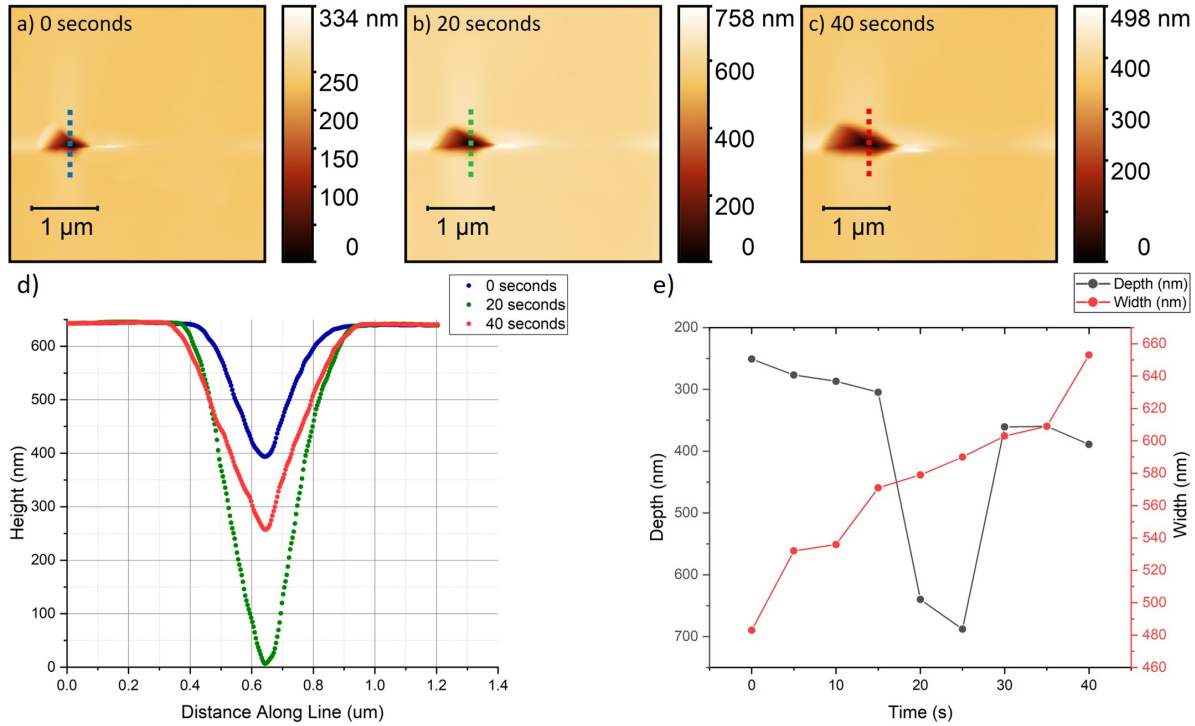

Figure 6.20: a)-c) Show sequential HS-AFM topographic maps showing intergranular pit progression on a thermally sensitised AISI Type 304 stainless steel sample surface polarised in 1% NaCl collected at: a) 0 seconds, b) 20 seconds, and c) 40 seconds, with inset colour scales. d) Shows height changes for line scans collected across the dotted line in a) in blue, the dotted line in b) in green, and the dotted line in c) in red. e) Shows the evolution of pit depth (note the inverted scale) in grey, and pit width in red.

6.1.6.2 Observations of Carbide Dissolution in the Absence of an Applied Potential

In-situ HS-AFM measurements of a specimen within a 1% aqueous NaCl solution in the absence of an applied potential showed little or no change across the surface. Measurements were performed over a duration of approximately an hour with no pitting or dissolution processes taking place.

However, similar measurements performed on a sample that had previously been polarised exhibited dissolution of GB carbide precipitates, as shown in Figure 6.21. At 0 seconds (Figure 6.21a), GB carbide precipitates are observed, these carbides dissolve gradually between each subsequent frame. This process took place over a 408 second period, a much longer duration than the intergranular pitting processes observed during the application of a potential.

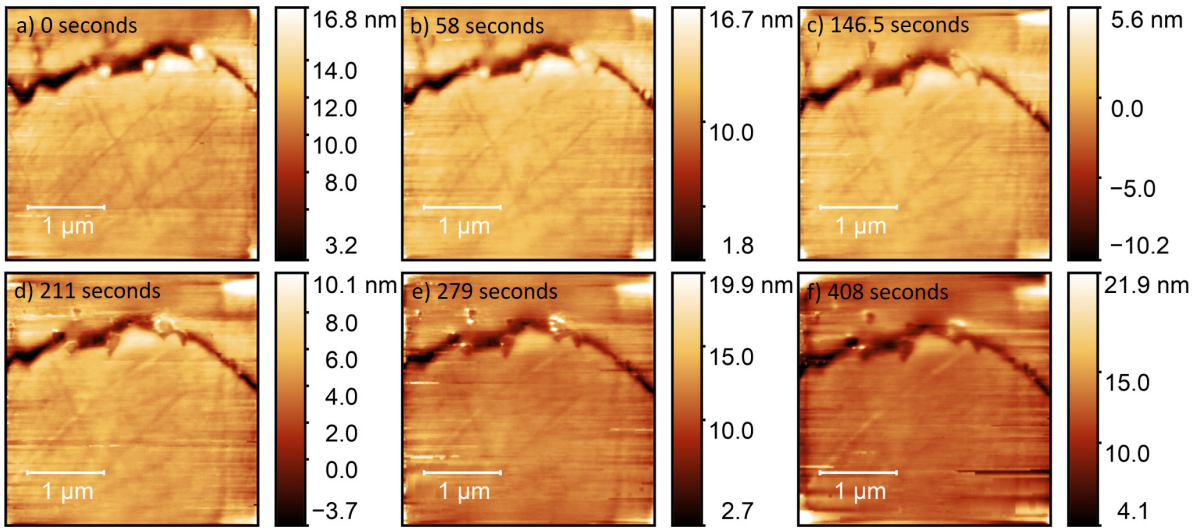

Figure 6.21: Sequential HS-AFM topographic maps showing GB carbide dissolution in a thermally sensitised AISI Type 304 stainless steel sample surface in 1% NaCl in the absence of an applied potential at: a) 0 seconds, b) 58 seconds, c) 146.5 seconds, d) 211 seconds, e) 279 seconds, and f) 408 seconds, with inset colour scales.

6.1.7 Computational Modelling

6.1.7.1 COMSOL Multiphysics

Post collection analysis of the topographic maps collected by HS-AFM of the sample surface was used to calculate the volume of metal reacting with respect to time, and so the current densities and ionic fluxes at work. Using this data, it was possible to produce a model of the system, allowing for a simulation of the events as they were observed.

A model of the system was produced in COMSOL Multiphysics 3.5a. A set of partial differential equations are compiled for the system being studied as a result of the user defining the physical attributes of the system, such as material properties, boundary constraints, initial conditions etc. [276]. A system may be modelled by the following steps:

1. Define parameters, variables, and functions.
2. Create a geometry sequence for the model component.
3. Specify materials and material properties.
4. Define the physics for domains and boundaries.
5. Create a mesh from the specified geometry.
6. Add a study to solve the model.
7. Evaluate results.

Modelling was performed using the Tertiary Current Distribution, Nernst-Planck interface. This is a pre-defined equation system for solving diffusion and migration for ionic transport under electroneutrality using the Nernst-Planck equations. For each species, i, the mass balance for the diluted species in an electrolyte is described by:

$$\frac{\partial c_i}{\partial t} + \nabla \cdot \mathbf{N}_i = R_{i,\,tot} \tag{6.1}$$

where c_i is the concentration of the ion i (mol m^{-3}), $R_{i,tot}$ is its rate of production/depletion (s^{-1}), and $\boldsymbol{N}_i$ is its flux (mol m^{-2} s^{-1}). Flux, $\boldsymbol{N}_i$, is defined by:

$$\mathbf{N}_i = -D_i \nabla c_i - z_i u_{m,i} F c_i \nabla \phi_l + c_i \mathbf{u} \tag{6.2}$$

where D_i is the diffusion coefficient of the ion i (m^2 s^{-1}), z_i is its valence, $u_{m,i}$ is its mobility (s mol kg^{-1}), F is the Faraday constant (96,487 C mol^{-1}), ϕ_l is the electrolyte potential (V) and $\boldsymbol{u}$ is the velocity vector (m s^{-1}) [112]. The velocity vector was set to zero, assuming zero convection.

The electroneutrality condition assumes that the model includes all significant current-carrying ions. It is satisfied by maintaining:

$$\sum z_i c_i = 0 \tag{6.3}$$

The model includes the water auto-ionisation equilibrium condition, and so:

$$\sum z_i c_i + c_H - c_{OH} = 0 \tag{6.4}$$

$$c_H c_{OH} = K_W \tag{6.5}$$

Where K_W is the water auto-ionisation constant ($10^{14.94}$ M^2).

A topographic map produced from HS-AFM data of the corroded area was manually imported into COMSOL to build-up the initial surface geometry. The surface features are interpreted as in-plane (flat) boundaries on a sub-domain surface with matching dimensions. The 3D sub-domain represents the volume of water adjacent to the surface. This geometry was used to set-up a mesh.

The ionic properties of the sub-domain were specified within the model. A simplified system of 5 species were considered in this model: Fe^{2+}, Cl^-, Na^+, H^+ and OH^- [112, 276, 277]. The mobility for each species was calculated using their respective diffusion coefficients [278, 279]. Boundary conditions were defined for the different features (representative ionic flux, bulk concentration, potential etc.), to give a specific representative set of reactions and behaviours at different boundaries.

The final step was to solve with a time dependent study, computing reaction kinetics and chemical composition of a system over a specified time interval. The results were then inspected and compared to measured results.

A series of assumptions were required for this study, which largely may be considered qualitatively. These included:

- This model did not consider speciation of the corrosion product.
- If a nucleation event occurred at the site of an inclusion, the dissolution products of the inclusion were not considered in the model.
- The rest of the surface in the imported geometry was considered to be inert.
- The action of the cantilever probe on the surface and its effect on local transport and pit initiation was not considered for this model.

6.1.7.2 Model of an Intergranular Pit

Topography data of the intergranular pit shown in Figure 6.19c was imported into COMSOL as geometry and used for subsequent simulations. Modelling was carried out following the assumption that this change in topography could be reasonably attributed to corrosion. The 3D geometry used in the model is shown in Figure 6.22a. This geometry was meshed by COMSOL, as seen in Figure 6.22b, the chosen mesh consisted of 239,226 domain elements, 17,514 boundary elements and 1,011 edge elements. A summary of the parameters used within this model are given in Table 6.2.

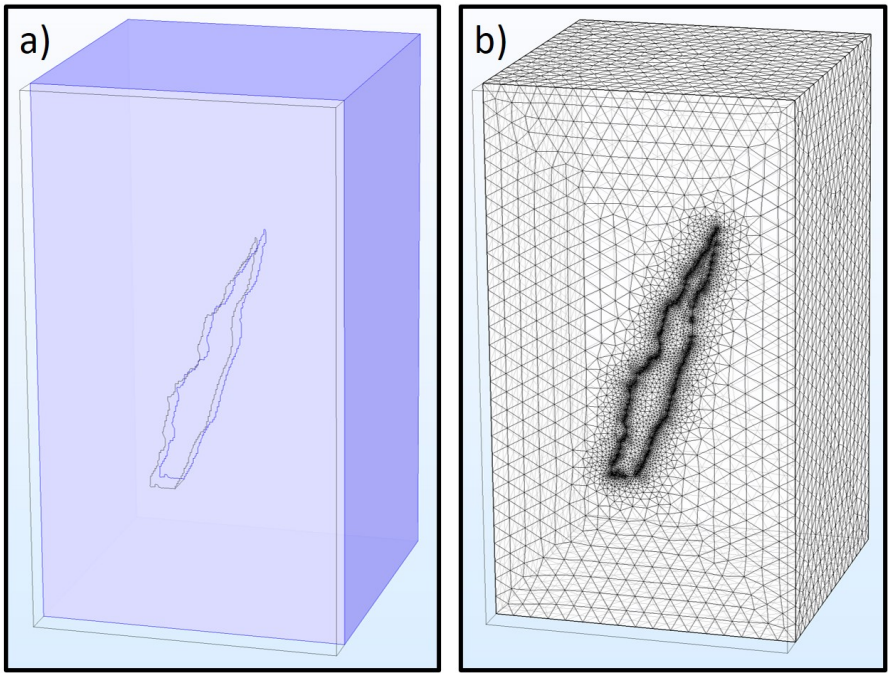

Figure 6.22: Images showing: a) the final 3D geometry created in COMSOL with the water sub-domain highlighted in blue, and b) the final meshed geometry created in COMSOL, the mesh was created over the water sub-domain.

Selected results from the time-dependent solution are shown in Figures 6.23 and 6.24. Figure 6.23a shows the final concentration of Fe^{2+} ions, the concentration is seen to diffuse radially

Table 6.2: User defined parameters and constants used in the model of an intergranular pit.

Parameter	**Value**	**Units**
Temperature, T	293.15	K
Velocity Field, $\boldsymbol{u}$	(0,0,0)	m s^{-1}
Diffusion Coefficients	**Value**	**Units**
$D_{c,Na}$	1.3E-9	m^2 s^{-1}
$D_{c,Cl}$	2.0E-9	m^2 s^{-1}
$D_{c,Fe2}$	7.19E-10	m^2 s^{-1}
$D_{c,H}$	9.3E-9	m^2 s^{-1}
$D_{c,OH}$	5.3E-9	m^2 s^{-1}
Charge Numbers	**Value**	**Units**
$Z_{c,Na}$	+1	-
$Z_{c,Cl}$	-1	-
$Z_{c,Fe}$	+2	-
Water Sub-Domain Initial Condition	**Value**	**Units**
c_{Na}	282.156	mol m^3
c_{Cl}	282.156	mol m^3
c_{Fe}	0	mol m^3
Electrolyte Potential	0	V
Electric Potential	0.3	V
Pit Initial Condition	**Value**	**Units**
Inward Flux of Fe^{2+}, $N_{0,c,Fe2}$	0.01346	mol m^{-2} s^{-1}
Inward Electrolyte Current Density, $i_{n,l}$	2.6E3	A m^{-2}

outwards from the intergranular pit site. Figure 6.23b shows a local accumulation of Cl^- ions in the areas immediately adjacent to the reaction area in a similar distribution as seen for the Fe^{2+} ions. The relative enhancement in Cl^- concentration reconstructed here is small as the pre-existing concentration within the bulk electrolyte is large. The Na^+ ions have the opposite distribution, with a local depletion in the region of the pit, Figure 6.23c. A plot illustrating the variation of pH (calculated from H^+ concentration) in the electrolyte was also produced by the time-dependent solution in COMSOL, shown in Figure 6.23d. It is observed that the areas surrounding the pit have become slightly acidic compared to the bulk solution.

The final electrolyte potential is shown in Figure 6.24. This solution has a similar distribution to Fe^{2+} and Cl^- ions. This is to be expected as it is the transfer of these ions that result in the flow of charge.

A line plot was produced illustrating the time taken to converge to the final concentration distribution of Fe^{2+} ions in the adjacent electrolyte, shown in Figure 6.25. This plot demonstrates that the system reaches a radial diffusion regime in under 0.01 s, as time steps beyond this have identical concentration profiles.

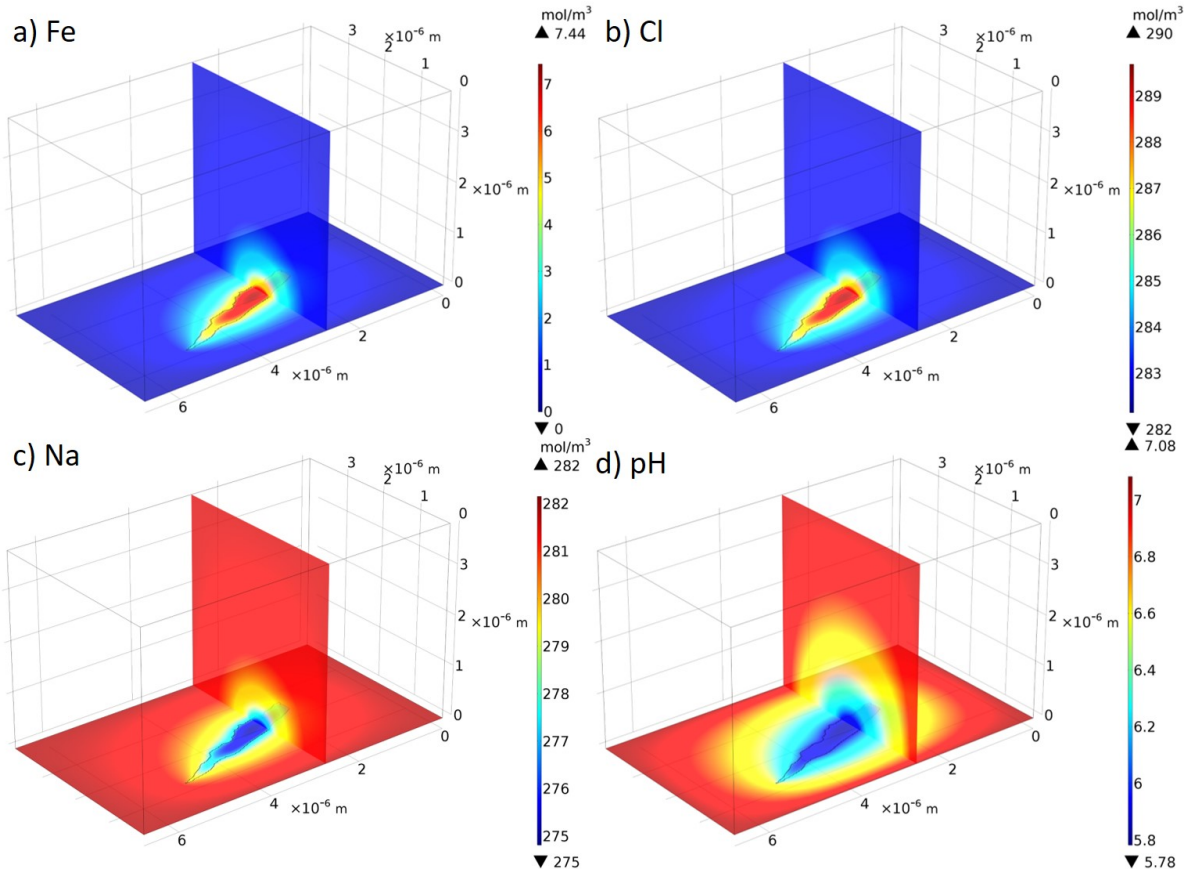

Figure 6.23: 3D multislice plots produced in COMSOL showing the final (at a time of 0.5 s): a) concentration of Fe^{2+} ions, b) concentration of Cl^{-} ions, c) concentration of Na^{+} ions, and d) pH.

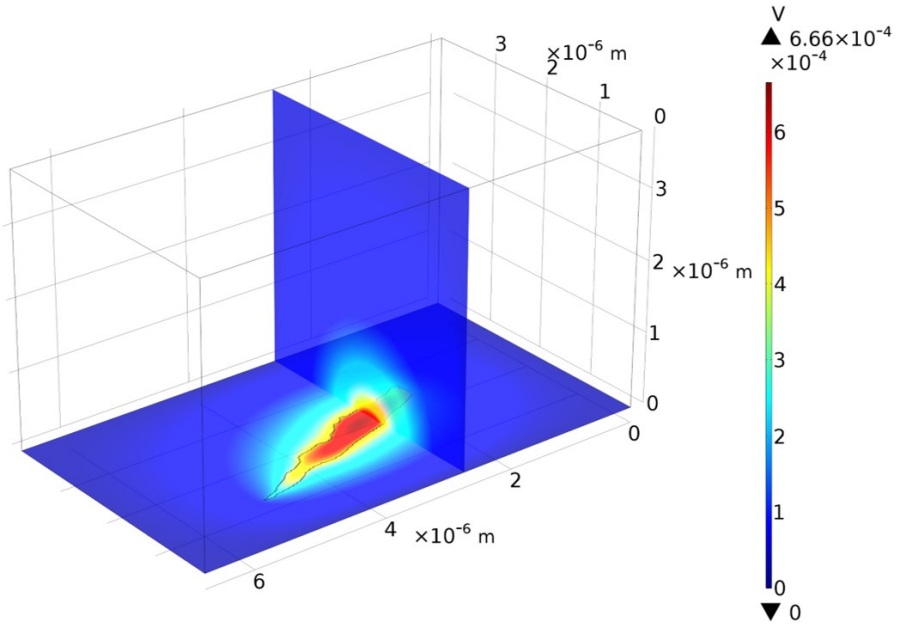

Figure 6.24: A 3D multislice plot produced in COMSOL showing the final (at a time of 0.5 s) electrolyte potential.

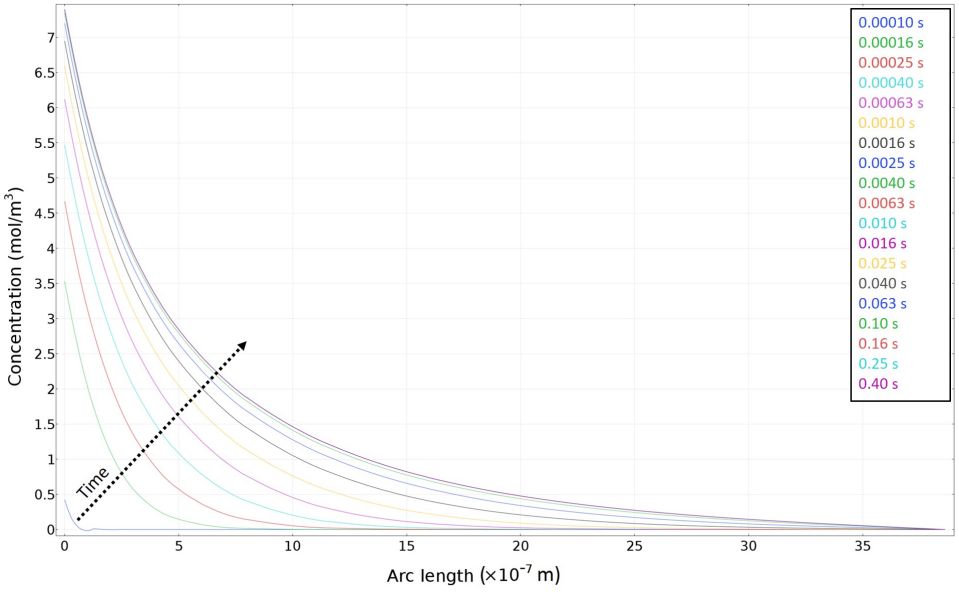

Figure 6.25: A line plot produced in COMSOL showing the concentration of Fe^{2+} ions along a line normal to the metal surface, starting from the centre of the pit extending out to the bulk solution, for different time steps.

6.2 Localised Dissolution of Thermally Sensitised AISI Type 304 Stainless Steel in a Sodium Thiosulfate Solution

6.2.1 Experimental Set-up

Samples of thermally sensitised AISI Type 304 stainless steel were freely corroded in a solution of 395 mg L^{-1} (2.5 mM) aqueous sodium thiosulfate ($Na_2S_2O_3$). These samples are the same material investigated previous in Section 5.1.2, and the surface was prepared following the steps described in Section 4.2.

The experimental set-up for in-situ HS-AFM measurements was similar to that shown in Figure 6.1, however the parallel electrochemical control was not required for these measurements. A freely corroding set-up was implemented as the purpose of study in this case was to establish understanding of the corrosion processes that may occur during future SCC tests.

6.2.2 In-Situ HS-AFM Observations

The surface of a specimen of thermally sensitised AISI Type 304 stainless steel was monitored in a solution of 395 mg L^{-1} $Na_2S_2O_3$ by HS-AFM for durations up to 10 minutes. Figure 6.26 shows two examples of the changes observed in the area imaged. Initial images of the surface (Figures 6.26a and 6.26d) showed GBs containing GB carbide precipitates. Over the duration of imaging, preferential dissolution of these carbides is evident (Figures 6.26c and 6.26f). Intergranular pits are located at the previous locations of carbide precipitates. During these measurements there were no visual changes, such as tarnishing or presence of a corrosion product, to the sample surface.

Line profiles collected before and after corrosion took place are shown in Figure 6.27. Figure 6.27b and 6.27c show the height profile of the GB with and without a carbide precipitate, respectively. Figure 6.27e, shows that GB carbide height was significantly reduced, though not removed completely.

Following monitoring experiments, HS-AFM imaging was performed in the regions directly adjacent to the area previously monitored. Figure 6.28 shows the topographic maps collected, with the area monitored outlined with a blue dashed line. Figure 6.28c shows two GB carbide precipitates outside of the area monitored. It is evident from the images collected that carbide dissolution was limited to the region being imaged. These images contain artefacts due to flattening. This is the result of height changes at the edge of the outlined areas. These height changes are likely due to debris swept to the edges of the frame by the tip during imaging.

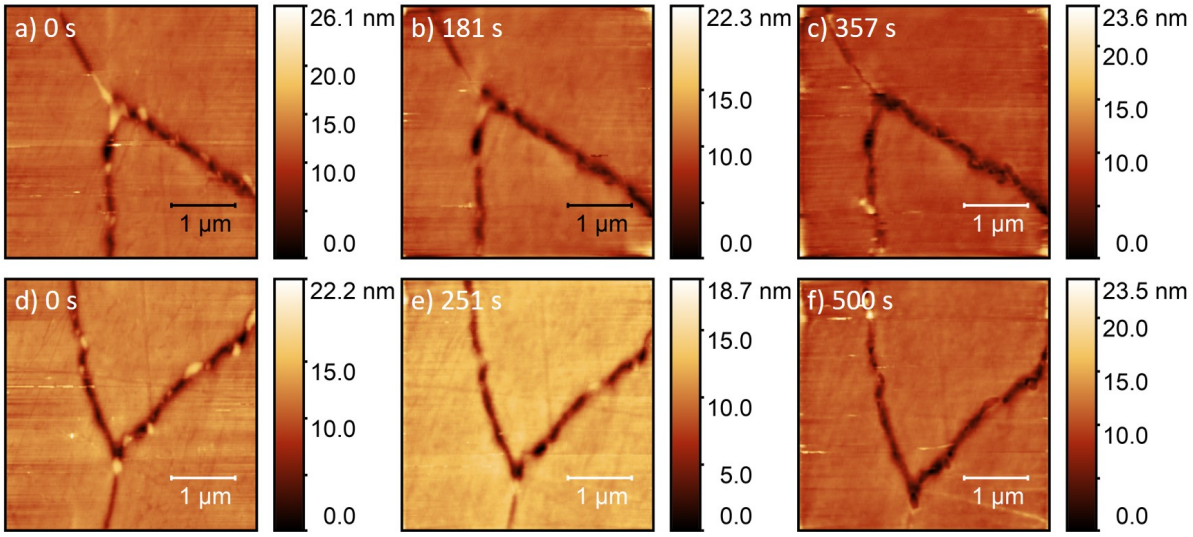

Figure 6.26: Sequential HS-AFM topographic maps showing GB carbide dissolution in thermally sensitised AISI Type 304 stainless steel in a solution of 395 mgL^{-1} $Na_2S_2O_3$, with inset colour scales. a)-c) were collected from a region on the surface at: a) 0 seconds, b) 181 seconds, and c) 357 seconds. d)-f) were collected from another region on the surface at: d) 0 seconds, e) 251 seconds, and f) 500 seconds.

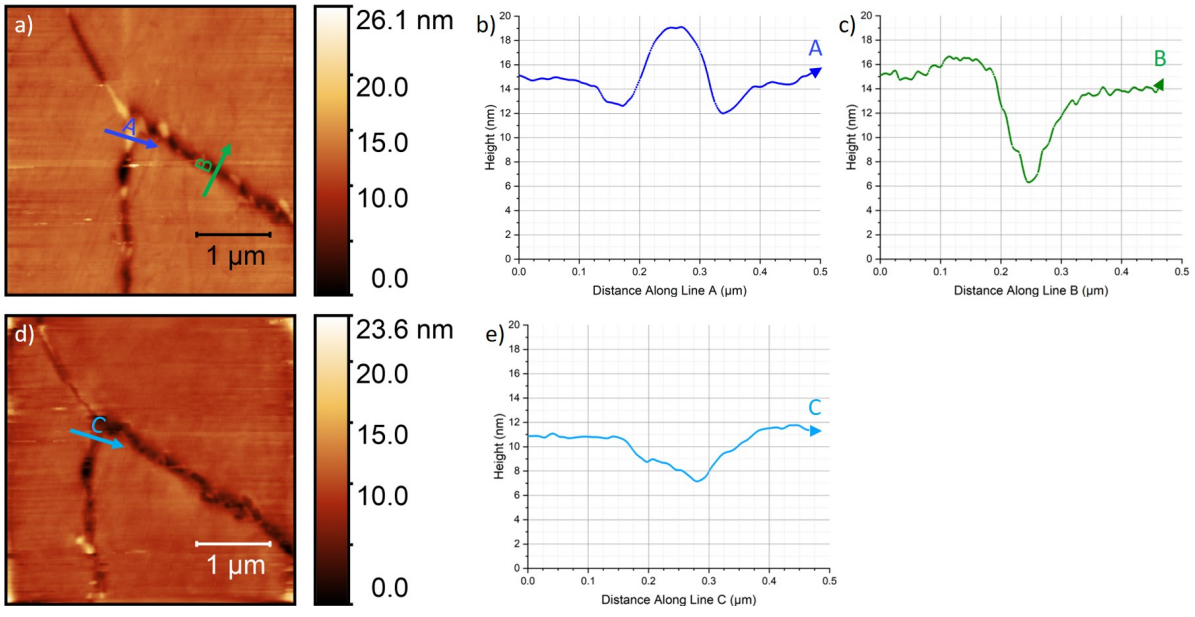

Figure 6.27: a) Shows the same region as 6.26a with arrows indicating the positions at which line profiles were collected, b) a line profile collected across the blue arrow labelled A in a), and c) a line profile collected across the green arrow labelled B in a). Also, d) shows the same region as 6.26c with arrows indicating the positions at which a line profile was collected, and e) a line profile collected across the light blue arrow labelled C in d).

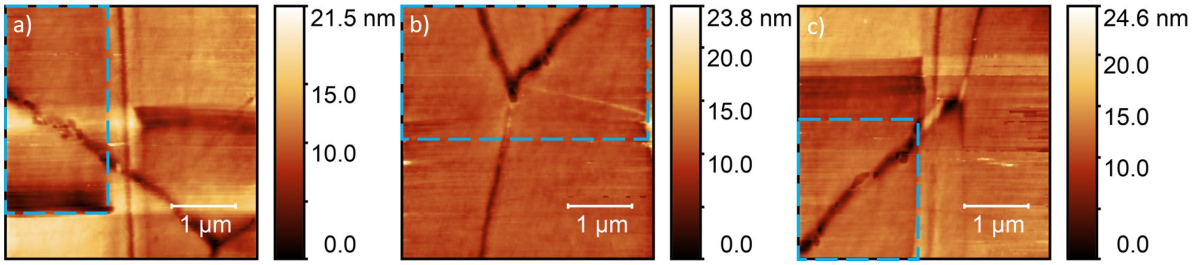

Figure 6.28: HS-AFM topographic maps showing regions adjacent to the imaging areas (outlined by a dashed blue box) following GB carbide dissolution in thermally sensitised AISI Type 304 stainless steel. a) shows the region adjacent to the area shown in Figure 6.26c, b) and c) show regions adjacent to the area shown in Figure 6.26f. All with inset colour scales.

6.2.2.1 Prolonged Exposure of Surface to Solution

In order to better understand the effect of the HS-AFM cantilever tip, a specimen was exposed to a solution of 395 mg L^{-1} $Na_2S_2O_3$ for a continuous period of ten days. With the aim of separating the effects of imaging and the effects of exposure to the solution. HS-AFM measurements were performed on days zero to six, and day ten. The sample was kept within the solution during imaging and the surface was not allowed to dry out at any point.

Figures 6.29a-6.29f show HS-AFM topographic images of the surface at increasing durations of exposure. Following one day of exposure (Figure 6.29a) some corrosion product or debris was present in some areas on the surface, otherwise no clear signs of corrosion were observed in the bulk or at the GBs. This was the case up to day six, as shown in Figures 6.29b-6.29e.

It should be noted that, whilst the microstructural features can vary considerably (as demonstrated during characterisation of the surface in Chapter 5) images were selected as representative of the surface. This was based on an average of 1 hour of imaging at a frame rate of 2 s^{-1} producing thousands of images of the surface.

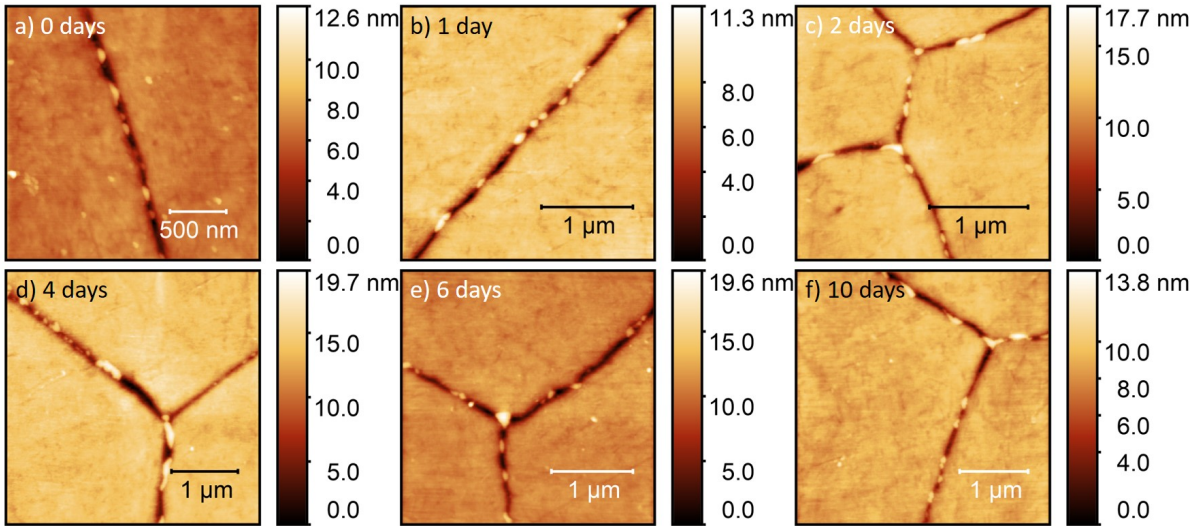

Figure 6.29: Representative HS-AFM topographic maps of a thermally sensitised AISI Type 304 stainless steel sample surface following prolonged exposure to a solution of 395 mg L^{-1} $Na_2S_2O_3$, with inset colour scales. a) 0 days, b) 1 day, c) 2 days, d) 4 days, e) 6 days, and f) 10 days.

Measurements performed after ten days of exposure to the corrosive solution found some variation across the surface. The majority of the surface was similar to that observed previously, as shown in Figure 6.29f. However, in some cases a possible oxide layer was observed at the GBs, Figure 6.30. Figure 6.30a shows a thin oxide layer at one edge of the GB. Figure 6.30b shows a thin oxide layer occurring on both sides of a GB in a discrete area between two GB carbides. It is possible that features such as this were present at earlier stages, however numerous measurements were performed across the surface where this was not observed.

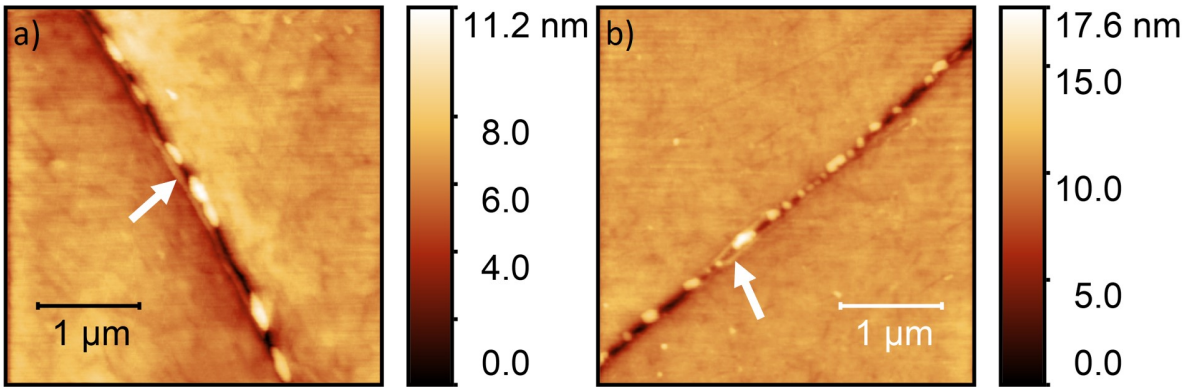

Figure 6.30: HS-AFM topographic maps showing a GB in thermally sensitised AISI Type 304 stainless steel containing a possible oxide (as indicated by a white arrow) after ten days of exposure to a solution of 395 mg L^{-1} $Na_2S_2O_3$, with inset colour scales.

6.3 Analysis of Work Function by EF-PEEM

In order to further understand the corrosion behaviour of the thermally sensitised AISI Type 304 stainless steel, analysis of the surface of a sample was performed by EF-PEEM. Sample was cut into a 10 mm by 10 mm square and fiducial marks were etched by FIB in order to consistently identify specific areas on the surface.

Photoemission intensity images and work function maps were produced from a sample following sputtering to remove the upper oxide layers. A photoemission intensity image and work function map of a 93.2 μm diameter area on the surface are shown in Figures 6.31a and 6.31b, respectively. In Figure 6.31a different grains appear bright or darker. In Figure 6.31b the lighter grains in Figure 6.31a are mapped to lower work function values, and the darker grains are mapped to higher work function values. The work function across the surface ranges between approximately 4.65 eV and 4.4 eV. The grains at the poles of the image appear to have much lower work functions, this banding effect is an image artefact and should be negated.

Figures 6.31c and 6.31d show a photoemission intensity image and work function map for a 35.4 μm diameter area located in the central region of the area shown in Figures 6.31a and 6.31b. It can be seen that the edges of the grains differ from the bulk of the grain however this effect is variable.

Following this, maps were produced for a sample that had not been sputtered and so the protective passive layer is still intact. In this case the work function maps produced had a much clearer banding effect that should be considered during data interpretation.

As previous, a larger area on the surface was analysed first, shown in Figures 6.32a and 6.32b, and a smaller area within the initial area was analysed, shown in Figure 6.32c and 6.32d. Within the photoemission intensity images (Figures 6.32a and 6.32c) the GBs are observed as darker when compared with the bulk of the grain. These images also show a small amount of variation from grain to grain. Figure 6.32b contains two bright points and a dark point. These features

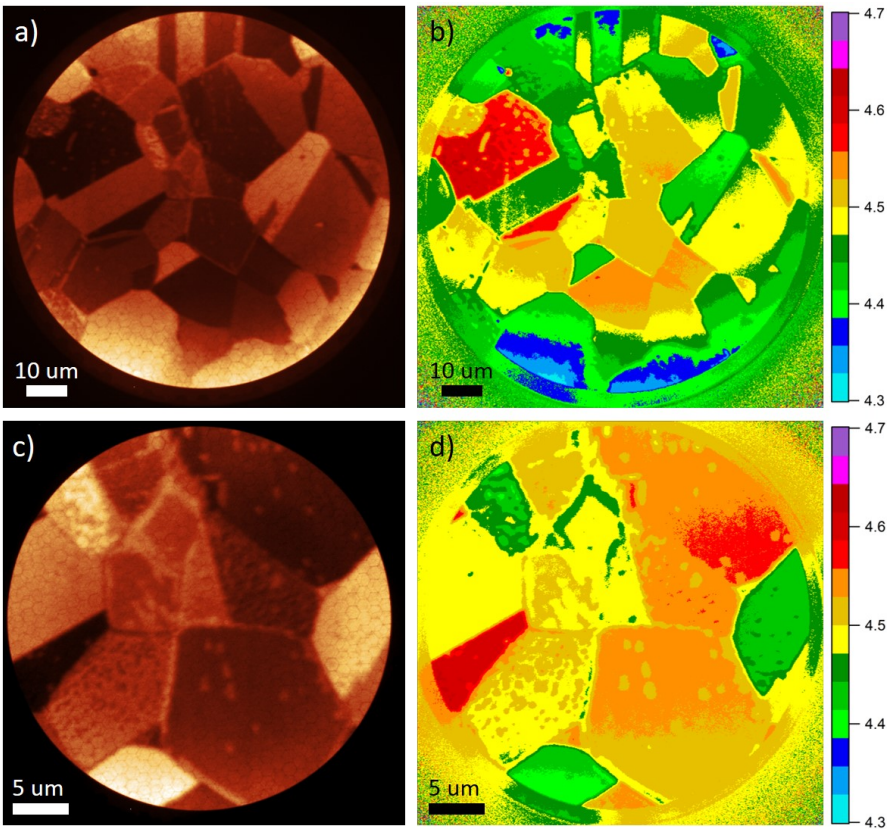

Figure 6.31: a) A photoemission intensity image and b) a work function map for a 93.2 μm diameter area on the sputtered surface of thermally sensitised AISI Type 304 stainless steel. Also, a) a photoemission intensity image and b) a work function map for a 35.4 μm diameter area in the central region of the area shown in a) and b). With inset scale measured indicating work function value in eV.

are also present in the work function map as points with lower and higher work functions, respectively.

In the 78.3 μm diameter work function map (Figure 6.32b) very little variation is observed. However, within the 37.5 μm diameter work function map (Figure 6.32d) the GBs are indicated by areas of a higher work function. The work function along the GBs is approximately 4.20 eV, this is 0.03 eV higher than that measured for the bulk grain. However, the higher work function along the GBs is not continuous.

Additional photoemission intensity and work function maps were produced from the surface of an unsensitised sample of AISI Type 304 stainless steel, shown in Figure 6.33. These images are largely featureless. In the larger 78.3 μm diameter maps shown in Figures 6.33a and 6.33b two points are observed with lower photoemission intensity and work function values. The photoemission intensity maps (Figures 6.33a and 6.33c) have a slight variation possibly coinciding with the different grains.

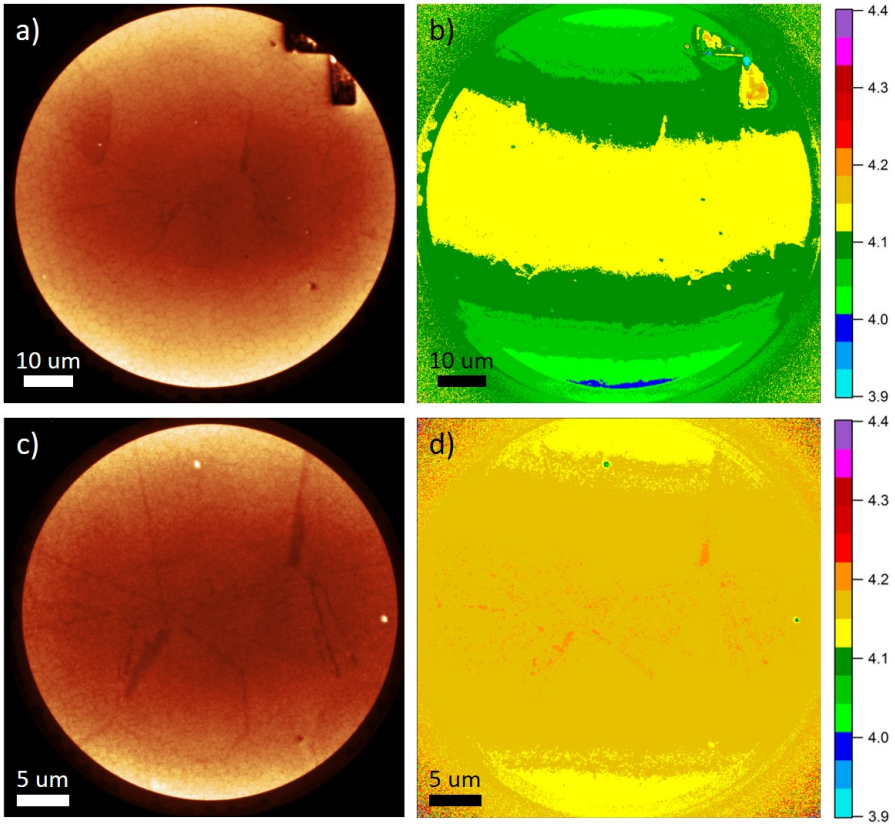

Figure 6.32: a) A photoemission intensity image and b) a work function map for a 78.3 μm diameter area on the non-sputtered surface of thermally sensitised AISI Type 304 stainless steel. Also, a) a photoemission intensity image and b) a work function map for a 37.5 μm diameter area in the central region of the area shown in a) and b). With inset scale measured indicating work function value in eV.

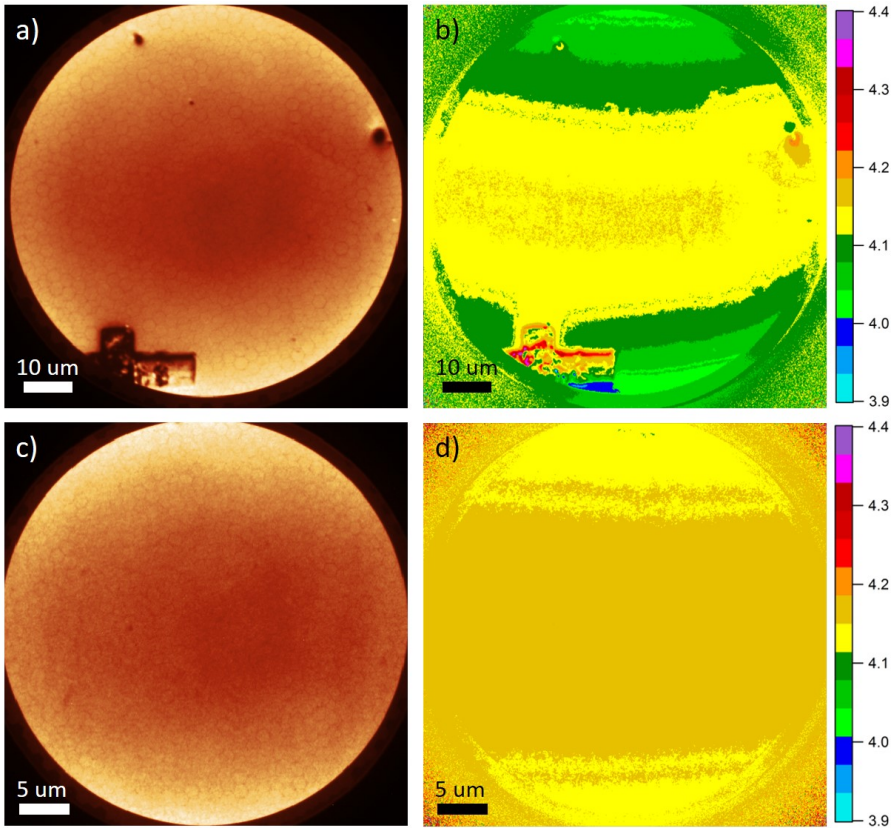

Figure 6.33: a) A photoemission intensity image and b) a work function map for a 78.3 μm diameter area on the non-sputtered surface of an unsensitised sample of AISI Type 304 stainless steel. Also, a) a photoemission intensity image and b) a work function map for a 37.5 μm diameter area in the central region of the area shown in a) and b). With inset scale measured indicating work function value in eV.

6.4 Discussion: Localised Corrosion Events In the Absence of Stress

6.4.1 Localised Corrosion of a Thermally Sensitised Stainless Steel in a Sodium Chloride Solution

In the first part of this chapter, localised corrosion of thermally sensitised AISI Type 304 stainless steel as a result of exposure to a 1% aqueous NaCl solution was studied using optical, HS-AFM and SEM imaging techniques. These techniques analyse different length-scales and therefore allow a more complete picture of the corrosion processes taking place.

HS-AFM measurements were collected across the sample surface revealing various morphologies of localised corrosion. As expected, large areas of the surface were unaffected, highlighting the localised nature of the processes occurring, as demonstrated in Figure 6.6. Large area measurements revealed that both inter- and intragranular pitting had occurred across the exposed surface, as well as larger scale pitting and IGA, discussed in greater detail in the following sections. Pitting occurs concurrently at various stages across the surface, as such different stages of corrosion can be measured by ex-situ techniques giving some insight into the corrosion process. However, this inevitably requires assumptions about the order of events when interpreting the data. In this section in-situ measurements of IGA and pitting corrosion events were performed giving unequivocal insight into the mechanisms of corrosion and order in which they occur.

6.4.1.1 Experimental Design

All samples within this section were prepared using the sample preparation method highlighted as optimal within Chapter 4. The flat surface allowed for easy identification of secondary phase precipitates (SPPs) and GBs, i.e. the sites at which localised corrosion events typically occur. The clear topographic images produced also allowed for identification of pits. In some works, it has been reported that a smooth surface finish affects the corrosion behaviour of the surface [122, 155]. In work performed by Burstein *et al.* a smoother surface was found to result in a higher frequency of pit nucleation events and a lower frequency of metastable pitting [122]. Mechanical polishing has also been reported to have an effect on the local electrochemical properties [155]. Indeed, this may be the case for this sample and additional sample preparation methods are considered, however any sample preparation method must produce a surface also suitable for HS-AFM analysis, highlighted in Chapter 4.

The experimental set-up used within this work implemented a three-electrode set-up alongside HS-AFM measurements. The set-up allowed for electrochemical measurements to be performed in synchronisation with topographic imaging within a liquid environment. Resultant topographic images were unaffected by the presence of the wire connected to the sample.

By using parallel potentiostatic control, the reactions occurring on the surface could be monitored alongside optical monitoring of the surface. Pitting corrosion on stainless steels is

characterised by multiple sharp peaks in the measured current [111, 114, 122, 149, 152, 155]. These occur as a result of the breakdown of the passive layer in the localised areas affected [112]. Figure 6.2 shows a potentiodynamic scan where characteristic peaks in current that may be attributed to pitting events can be seen. Near the end of the potentiodynamic scan, a continuous increase in the current is measured, indicating that corrosion reactions are occurring on the surface at an increased rate. By monitoring the electrical activity, these characteristic features alert the user that corrosion events are occurring. This is also true during galvanostatic scans, such as shown in Figure 6.3. The peaks and troughs present in the scan suggest that corrosion kinetics across the sample surface are varying. Additionally, as time increased, the overpotential required to sustain a constant current decreased. This indicates that corrosion events became more self-sustaining as the extent of corrosion progressed.

The HS-AFM's optical microscope allowed for quick identification of regions of interest. Once a region can be seen that is undergoing pitting corrosion within the imaging window, it typically takes the user around 10-40 seconds to adjust the position of the cantilever tip. An example is shown in Figure 6.17. The corrosion front surrounding a pit moved at a variable rate, up to 5 μm/s for some of the potentiodynamic tests. The imaging window can be adjusted at velocities far exceeding the lateral growth rate of the pit, enabling the user to adjust sufficiently to keep up with the rate of pit growth.

During in-situ measurements it was found that too high an overpotential can result in the formation of bubbles. This can disrupt imaging. In some cases, bubbles were observed to nucleate at the cantilever tip, as demonstrated in Figure 6.34.

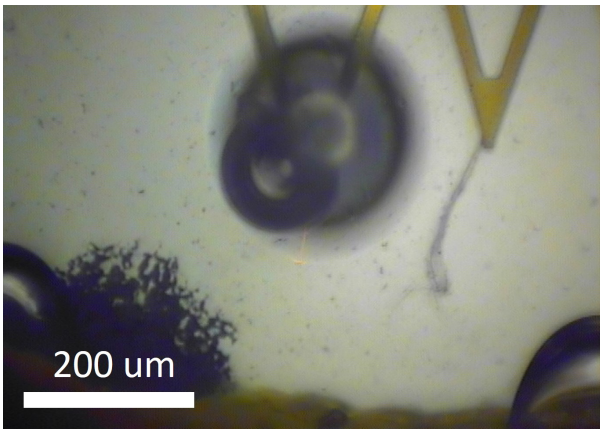

Figure 6.34: An optical image of a thermally sensitised AISI Type 304 stainless steel sample surface during in-situ HS-AFM polarisation measurements in 1% NaCl following nucleation of bubbles at the cantilever.

Later stages of pit propagation were found to be generally unsuitable for observation by HS-AFM due to the large associated height changes. In some cases, it was found that pit images were affected by tip convolution due to the high aspect ratio of the pit aperture to pit depth. This highlights the advantages of using additional techniques at different length scale to complement

HS-AFM observations. HS-AFM is best suited to measurements of the very early stages of localised corrosion processes. It is these stages that are of the most interest in order to better understand nucleation events.

Overall, HS-AFM was found to be a suitable technique for the in-situ observation of pitting events occurring on the surface, and the implemented set-up was generally successful. However, the following alterations to the methodology are considered:

- Build-up of corrosion products on the sample surface resulted in loss of resolution within some frames whilst performing in-situ HS-AFM. A custom-built flow-through cell is currently being designed with the aim of minimising this. This modification will also result in the maintenance of the concentration of Cl^- ions, which may influence the rate at which corrosion events take place.

- An intergranular pit initiation event was observed to occur within a time interval shorter than that measured by HS-AFM. The contact mode HS-AFM has the capability to reach much higher frame rates than those used within this study. Application of this capability will be implemented in future observations. However, at increasing frame rates, the resolution of the topographic map will be reduced. Alternatively, the corrosion rate may be slowed by altering the voltage or reducing the concentration of the NaCl solution.

- In order to draw parallels between measured current transients and initiation events observed by HS-AFM, it is required that the active area of sample be reduced considerably in size, as in other works [34, 114, 152]. This, however, introduces a number of challenges, such as crevice corrosion events.

6.4.1.2 Large-Scale Pitting and IGA

Optically visible pits were present at discrete sites across the sample surface, Figures 6.4 and 6.5. These pits differed in morphology to lacy pits observed for unsensitised stainless steels [120, 148]. The pits observed in this work had appeared to form as a result of an amalgamation of inter- and intragranular pitting, however the severity of IGA appeared to be the leading factor in producing the pits on this scale. This was clear during SEM imaging of the surface post-corrosion, Figures 6.12 and 6.13, where the GBs appear etched and intragranular pits are much less prominent. The prominence of IGA is a consequence of the severity of thermal sensitisation leading to a reduction in the GBs local resistance to corrosion, as measured in Chapter 5, and observed in other works [82, 99, 120]. Pits of a similar morphology were observed by Cheng *et al.* for thermally sensitised (700°C for 24 hrs) Type 304 stainless steel in 1 M $MgCl_2$ droplets [99]. Cheng found that sensitised samples had an irregular morphology compared to unsensitised samples, where preferential corrosion had occurred along the GBs [99]. Sensitisation also resulted in higher pitting probability, larger average pit size and decreased pitting potential [99].

An IPF and IQ map showing the large scale pits was shown in Figure 6.12c. The edge of the pit is observed to follow the grain structure, indicating the severity of IGA. It is possible that at later stages of pitting the GBs were sufficiently etched to result in grain fall out. HS-AFM measurements performed in the regions adjacent to large scale pits indicated possible grain movement, Figure 6.9. This map contained a grain that was topographically lower than the adjacent grains, indicating that the grains closest to the pit are sinking into the pit itself. It is likely that this grain had been undercut. It is also possible that this observation is due to preferential dissolution of specific grain orientations, though if this were the case it would be expected that this would be observed for other grains of similar orientations across the surface. Further measurements collected adjacent to large pits were shown in Figure 6.10. These images contained slip bands. These are the result of plastic deformation due to stress, as discussed in Section 2.3.3.2. This stress likely originates from an undercutting of the grains in the regions adjacent to larger pits, as speculated previously, and demonstrated in Figure 6.13f. Previous works have considered pitting as early stage SCC, where the pit acts as a stress accumulator as tensile stress is applied to the sample. These observations indicate that large pit formation may result in additional local stresses.

In-situ observations of large scale pit growth were performed by HS-AFM, shown in Figure 6.18. Initial images showed dissolution of a thin surface layer, Figures 6.18a-6.18c. This may be an observation of passive film breakdown. The chromium-rich oxide film formed on stainless steel is known to be <5 nm thick [53, 54], this is a similar scale to the pit depths measured in Figure 6.18c (between 1 nm and 3 nm). The later stages of pit propagation were less suited for in-situ measurements by HS-AFM due to the large associated height changes. Despite this, Figures 6.18d-6.18f show apparent grain dissolution progressing across the bulk grain at approximately 1.5 μm over a 1 second duration.

Regions on the surface that exhibited large scale IGA, such as shown in Figure 6.13c, were also analysed by HS-AFM, Figure 6.11. The GBs in these regions contained an oxide layer or corrosion product following oxidation of the GB region. Figure 6.11d contains a GB triple point where two GBs are significantly less corroded, this may be the result of differing GB chromium depletion as a result of GB misorientation as investigated in Chapter 5. In Figure 6.11e an angular pit is observed, this is thought to be due to the removal of a chromium-rich carbide such as those observed in Figure 5.32d in Chapter 5. GBs in Figures 6.6c and 6.6d contained features that appeared as debris. From pre-corrosion measurements of the surface, these features can be confidently identified as features formed as a result of corrosion processes, such as corrosion product or oxidation indicating early stage IGA. It was also observed that at this stage GB carbides are still intact, though some evidence of IGA in the areas surrounding the GB carbide is occasionally apparent.

In Section 2.5.1.1 the SCC behaviour of stainless steels in chloride solutions was described. For this system it has been reported that SCC can be intergranular or transgranular. It is

expected that, upon the application of stress, this sample would fail largely by IGSCC due to the severity of IGA observed, as well as the GB chromium depletion measured in Chapter 5.

6.4.1.3 Intragranular Pitting

Intragranular pits were present across the sample surface in isolated areas as well as surrounding larger pits, as observed in Figures 6.13a, b, d, and e. These pits were round in appearance rather than the elongated shape observed for intergranular pits. Some intragranular pits appeared to have a similar morphology to that of a "satellite" pit, observed by Street *et al.* [151]. "Satellite" pits occurred adjacent to larger pits [151]. The pit shown in Figure 6.7a appeared to contain debris, possibly following initiation at an MnS precipitate, as reported within other works [54, 121, 122, 155–157, 194], or possibly the remnants of a pit cap, as described for "satellite" pits [151].

In an isolated event, a pit was observed within a large SPP, previously identified as a chromium-rich carbide, Figure 6.7c. It is possible that this is an instance of a "cored" SPP observed in other works [193]. These features are SPPs with a different composition in the inner region of the SPP, resulting in different hardness and corrosion properties in that region. In a study by Liu *et al.*, a carbide precipitate was identified with a core with an increased hardness, resulting in a topographic difference during polishing [193]. The opposite is true here, where the inner core has been preferentially corroded [193]. It is possible that this feature was formed following polishing steps, as in Liu's work, however no such feature was observed prior to corrosion experiments.

FIB milling was performed in an area containing an intragranular pit, Figure 6.15. This study revealed undercutting of the material beneath the surface, Figure 6.15b. Here, the pit has acted as an entryway. Corrosion reactions have attacked the bulk of the grain first, propagating outwards from the pit opening. In occluded regions such as this, an aggressive chemistry can develop [112]. Following computational model results (Figure 6.23b), it can be assumed that the concentration of Cl^- ions will increase within these cavities, as reported in other studies [120]. This then leads to further corrosion processes. This is evident from the initial FIB cut shown in Figure 6.15a where deeper corrosion along the GB is seen. The synergy of intragranular pitting and IGA has also been reported in other works [120].

Initiation of an intragranular pit were not seen during in-situ HS-AFM measurements or optical monitoring of the sample surface. Pitting events are known to often initiate at discontinuities in the passive film on the surface, such as at SPPs [56, 82, 99, 111, 121, 122, 155–157]. These events have also been reported to be influenced by grain orientation [55, 123, 280], this is explored further in later sections (Section 6.4.3). Further investigation is required to identify the intragranular sites at which these pits initiated.

6.4.1.4 Intergranular Pitting

Optical images (Figure 6.5) in combination with SEM images (Figure 6.13) revealed on a larger scale that intergranular pits were a common feature in the areas surrounding larger pits, just ahead of the corrosion front. However, intergranular pits also occurred in isolated areas on the surface, such as in Figure 6.8 and 6.14.

The intergranular pits encountered within this work are similar in morphology to those observed by electrochemical atomic force microscopy (ECAFM) by Martin *et al.* in 2007 [155]. However, within Martin's work, investigations were carried out on a sample of unsensitised Type 304L stainless steel [155]. This type of material does not contain sensitised GBs, and so pit initiation events will likely differ from the work presented here [155].

SEM and HS-AFM measurements showed that intergranular pits form as chains along the GB (Figures 6.8c and 6.14). These pits were observed to form at HAGBs. It is expected that this relates to the dependence of GB type on GB chromium depletion observed in Chapter 5 and associated GB energy (as found in other works [86, 120]). However, additional measurements are required to draw stronger conclusions. By comparing these pit chains to the GB carbide precipitates observed previously (for example, Figure 6.6b), it is apparent that there are similarities in their distributions, indicating a possible mechanistic link.

Investigation by FIB milling (Figure 6.16) demonstrated that intergranular pits are small surface entryways to much larger voids produced by IGA beneath the surface. It is unclear, however, whether this undercutting is a result of the intergranular pit acting as an initiation site leading to GB dissolution, or that this is a result of corrosion progressing along GBs from the larger pit nearby (as seen in Figure 6.16d). Regardless, this observation further confirms the propensity for subsurface propagation of corrosion processes as discussed previously.

The formation of an intergranular pit was observed in-situ by HS-AFM, as seen in Figures 6.19a and 6.19b taken before and after the pitting event, respectively. This data was collected ahead of the corrosion front. Intergranular pit formation occurred between two sequential frames whilst the system was imaging at a rate of 2 frames per second, and therefore occurred within a time frame ≤ 0.5 s. Optical data collected post-corrosion of the area in which this pitting event occurred (Figure 6.5b) revealed that the intergranular pit studied in Figure 6.19c was no longer present on the surface as the corrosion front had progressed across the site to form a larger pit. This highlights the importance of in-situ observation techniques, such as HS-AFM, as these measurements would not have been possible using ex-situ methods.

In-situ observation of intergranular pit propagation was also achieved, shown in Figure 6.20. An intergranular pit was monitored for a duration of 40 seconds. During this time the pit steadily grew in diameter by approximately 0.2 μm as measured along the line scan (Figures 6.20d and 6.20e). The time taken for this change to occur (40 seconds) was considerably longer than for observations of intergranular pit formation (≤ 0.5 seconds). Between 20 seconds and 40 seconds the pit depth was observed to reduce, Figure 6.20d, this is likely the result of deposited debris

such as corrosion products. This is corroborated by depth measurements collected at 5 second intervals, shown in Figure 6.20e. Between 0 s and 15 s a steady increase in depth is observed, at 20 s a sudden increase in depth is observed, followed by a sudden decrease in depth at 25 s, indicating that debris produced at 20 s becomes trapped in the pit.

In-situ observation of pit formation combined with SEM observations of intergranular pits in areas at a distance from larger pits suggest that intergranular pits may act as initiation events that lead to larger scale IGA. This is particularly evident in Figure 6.13b where IGA appears to consist of continuous intergranular pit formation. A suggested sequence of events is discussed in a later section.

Intergranular Pit Formation Model By modelling the system using HS-AFM and electrochemical data, it was found that the system reached a radial diffusion regime in under 0.01 s (Figure 6.25), resulting in fast dissolution of material and rapid diffusion of corrosion products away from the pit site. In this model corrosion product speciation was not simulated, this simplification was supported by this result, in combination with observations that the event transient was very short lived, and the fact that little corrosion product was apparent from the HS-AFM measurements.

3D multislice plots showed an increase in Fe^{2+} ions in the region adjacent to the pit (Figure 6.23a). These ions are produced from dissolution of the metal during pit formation. Cl^- ion concentration is also observed to be enhanced in this region (Figure 6.23b). This is a consequence of the concentration of Fe^{2+} cations in that area [34, 114, 152]. As the pit is anodic with respect to the cathodic surface surrounding it, electroneutrality of the pit electrolyte requires an increased abundance of Cl^- counter-ions [34, 114, 152]. Figure 6.23d shows a reduction in pH (calculated by H^+ concentration) in the areas surrounding the pit site. Enhanced local acidification is known to be a result of hydrolysis of the Fe^{2+} ions dissolving [34, 112, 114, 119, 152]. Local accumulation of Cl^- ions in combination with pH reduction is a key factor in the propagation of pitting corrosion, preventing repassivation [34, 114].

The current density (averaged over the assumed time interval) produced by this event was calculated to be considerable (2.6×10^3 A m^{-2}), translating to a very sudden and rapid dissolution event. However, as a result of the extremely small scale at which it occurred, the pitting current during the event was very small (approximately 2.7×10^{-9} A), as was the total charge transfer (1.37×10^{-9} C). Multiple pitting sites were observed to propagate simultaneously on the sample surface. As such, the current transient signals produced by events such as the one observed, are dwarfed by the current from other much larger stable pitting sites. The calculated current transient is similar to those measured in other works where single transients for pitting events were successfully measured [122, 152]. Burstein *et al.* measured current transients for isolated metastable pitting events reaching nA values, these measurements were taken for an unsensitised sample of Type 304 stainless steel [122, 152].

Without An Applied Potential When monitoring GBs for periods up to 10 minutes in a 1% aqueous NaCl solution in the absence of an applied potential, no changes were observed. However, following a period of polarisation, instances of GB carbide dissolution were observed over the course of approximately 7 minutes, shown in Figure 6.21.

Potentiodynamic scans were performed for a sample with an undamaged surface, as well as for a surface that has already been polarised and undergone corrosion events, Figure 6.2. It can be seen that the kinetic behaviour is not dissimilar from the undamaged surface (red line in Figure 6.2). However, the forward scan for the damaged surface has a slightly higher corrosion current density than that measured for the undamaged surface. This indicates that, despite the surface being free of any active corrosion sites, the surface has a decreased passivity. This was also reflected by a slight decrease in the measured OCP, 131 mV (vs. Ag/AgCl) compared to 141 mV (Ag/AgCl). The return scan (the second section of the blue line starting at point B in Figure 6.2) was collected immediately after polarisation, this line was shifted considerably towards more cathodic potentials. In addition, the exchange current density had increased by orders of magnitude. This indicates that the sample surface contained active corrosion sites, demonstrating that the corrosion processes occurring on the surface are self-sustaining. Furthermore, the measured OCP immediately after the forward potentiodynamic scan (-339 mV vs. Ag/AgCl) was considerably more cathodic than immediately before (131 mV vs. Ag/AgCl), indicating a more active surface. The active sites on the surface are likely the pitted regions where trapped corrosion products and electrolyte create an enhanced chloride environment.

It is possible that carbide precipitate dissolution observed in Figure 6.21 occurred as a result of decreased passivity of the surface. Though it may be affected by other factors such as GB misorientation or GB chromium depletion and so is not consistently observed across the surface. The same phenomenon may have occurred during the application of a potential but was not observed due to the long monitoring times required. It is possible that carbide precipitate dissolution is the mechanism by which intergranular pits form but may be observed at a slower rate in the absence of a potential.

A similar effect was observed by Laferrere *et al.* [84]. Laferrere performed HS-AFM measurements of a sample of thermally sensitised 20Cr/25Ni-Nb stabilised stainless steel in a 5 mg L^{-1} chloride solution [84]. Laferrere applied a potential of +500 mV vs. reference to drive corrosion reactions, resulting in the dissolution of GB precipitates across the sample within a few seconds [84].

Further considerations such as the nobility of these carbide precipitates and the effect of the cantilever tip are discussed in Section 6.4.2.

Suggested Sequence of Events Considering all the information ascertained from this study the following mechanisms for intergranular pitting are suggested (illustrated in Figure 6.35):

- Intergranular pits appeared in isolated areas; therefore, they are likely an earlier form of

the more severe IGA observed later in the experiment (Figure 6.35a-b).

- Chains of intergranular pits had comparable distributions to that observed for GB carbide precipitates. In the absence of an applied potential, a slow dissolution process was observed to occur affecting GB carbides. It is therefore considered that the applied potential resulted in rapid dissolution of carbide precipitates leading to the phenomenon of intergranular pits (Figure 6.35c-d).
- These initial pits then act as penetration points for the corrosive solution, resulting in substantial subsurface IGA and accelerating formation of large scale pits (Figure 6.35e-f).

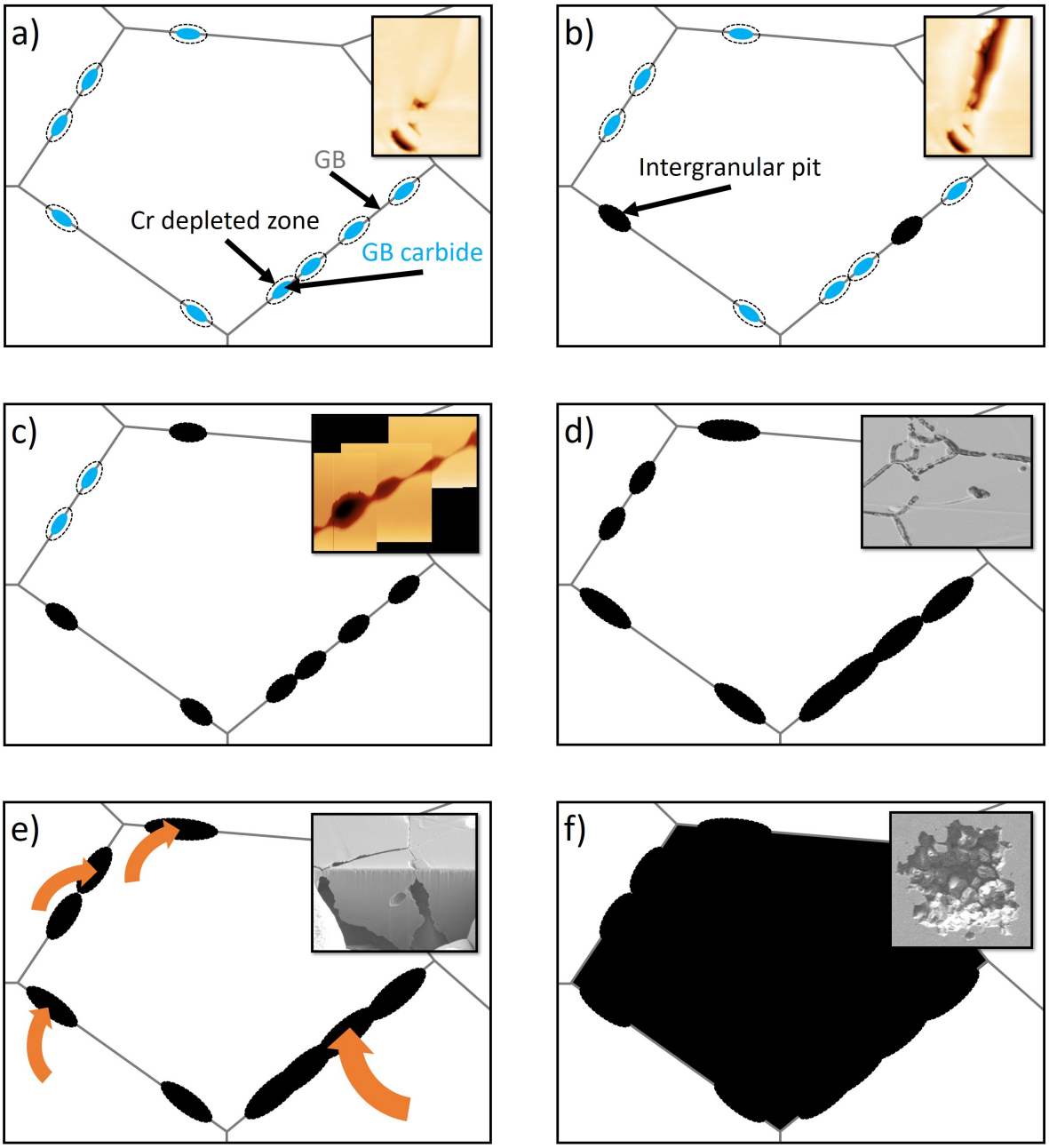

Figure 6.35: A schematic diagram demonstrating a possible sequence of events leading to large scale pitting and IGA: a) the initial grain structure with GB carbide precipitates, b) dissolution of a select number of carbide precipitates and/or the associated chromium depleted adjacent regions, c) further carbide precipitate dissolution leading to chains of intergranular pits, d) intergranular pit growth leading to larger scale IGA and an etched GB appearance, e) ingress of corrosive solution through intergranular pits leading to subsurface corrosion and undercutting of the grain (note that part e could take place immediately following part b), and f) grain falls out of the microstructure due to loss of material leading to larger scale pitting.

6.4.2 Localised Corrosion of a Thermally Sensitised Stainless Steel in a Sodium Thiosulfate Solution

In the second part of this chapter, the corrosion behaviour of thermally sensitised AISI Type 304 stainless steel in a solution of 395 mg L^{-1} $Na_2S_2O_3$ was investigated using HS-AFM. It was found that GB carbide precipitates preferentially corroded, as discussed in greater detail in the following sections. During these experiments, no optical changes to the surface were observed.

In later chapters within this thesis, SCC experiments are performed using the same material and corrosive solution. The key aim within this chapter was to analyse the effects of exposure to this solution in the absence of stress, in order to deconvolute the individual factors that lead to SCC. It is considered that this dissolution process may occur at the crack tip during SCC, resulting in stress accumulation at the resultant micro-pit structures. However, due to the synergistic nature of the individual factors leading to SCC this may not be the case.

6.4.2.1 Carbide Precipitate Dissolution

During HS-AFM measurements of the surface in 395 mg L^{-1} $Na_2S_2O_3$ carbide precipitates at the GB were seen to undergo gradual dissolution, leaving behind small intergranular pits. This can be seen in Figure 6.26c (or 6.26f), where dark spots are lower areas within the GB, located at the same positions as carbides were observed previously in Figure 6.26a (or 6.26d). This is similar to the phenomenon observed in 1% NaCl following polarisation of the surface, Figure 6.21. However, dissolution in the thiosulfate solution did not require activation of the surface.

The dissolution of carbide precipitates is not as expected as they are typically more noble with respect to the bulk [81, 150]. It could be argued that the regions adjacent to the carbide precipitate were corroded resulting in the carbide being lost, however the gradual reduction of carbide precipitate size and the final line scan collected (Figure 6.27e) suggests that this is not the case.

Studies of thermally sensitised Type 304 stainless steel in thiosulfate solutions without applied stress have been performed in other works with varying reports [161, 166]. Some works state that thiosulfate does not result in anodic activity or localised corrosion in the absence of stress [103, 160, 161, 164]. However, in other works thiosulfate was found to initiate and propagate localised corrosion processes in such a way that the role of stress was considered to be secondary [166]. However, these experiments were performed by reaction sensing techniques and precise reaction sites were not reported. The observations made in this study show that thiosulfate does indeed have a corrosive effect on the sample surface, and this occurs at the GB carbide precipitates positioned on sensitised GBs.

GB voids or pits (as seen in Figure 6.26c) formed following GB precipitate removal and dissolution have been observed in other works [84]. Laferrere *et al.* performed HS-AFM measurements of a sample of thermally sensitised 20Cr/25Ni-Nb stabilised stainless steel in a 5 mg L^{-1} chloride solution [84], as discussed previously. Laferrere observed dissolution of GB precipitates

widespread across the sample surface, whereas in this work, carbide dissolution was limited to individual areas as they were imaged [84]. However, this may be explained by the lack of applied potential in this work. Dissolution reactions in Laferrere's work will have been accelerated by the overpotential [84].

Effect of the HS-AFM Probe Due to the slower dissolution rates and longer resultant imaging times, the effect of the HS-AFM cantilever tip should be considered within these measurements.

It was noted during measurements that GB carbide precipitate dissolution was localised to area being imaged, whereas the surrounding areas did not obviously exhibit dissolution. This was demonstrated by imaging the regions adjacent to the previous imaging area (Figure 6.28).

The HS-AFM probe mechanically interacts with the surface of the sample, and so may affect the rate at which corrosion occurs, such as by influencing diffusion, or by 'sweeping away' debris on the surface (as evidenced in Figure 6.28) and maintaining the local solution concentration [281]. This must be noted when considering the timescales of observed reactions. However, it should be emphasised that when the same material is imaged within non-corrosive conditions, such as within deionised water, no such reactions are observed. It can be concluded, therefore, that these observations are not a result of the action of the HS-AFM probe alone. The effect of the tip on mass transfer has been explored in other works. In a study by Burt *et al.* it was found that cantilever beams similar to those used within the presented study hindered diffusion processes [281]. This may result in the build-up of an aggressive solution and so promotion of corrosion processes, as observed here. However, in the study conducted by Burt, experiments were performed at slower imaging rates (0.1-0.25 Hz) which may impact the degree to which diffusion processes are affected [281].

To better understand the effect of the HS-AFM probe the material was exposed to the $Na_2S_2O_3$ solution for an extended period in order to observe the longer term changes to microstructure in the absence of imaging. Following exposure to the solution for a period of six days, little or no changes were observed across the sample surface and GB carbide precipitates were still present, Figure 6.29. By day ten, the majority of the surface remained unchanged (Figure 6.29f), however some GBs were found to contain a possible oxide layer, Figure 6.30. It is possible that this oxide layer could lead to brittle failure of these GBs following the application of stress. These measurements further support the notion that the probe effects the observed corrosion behaviour. Further study is required to quantify this effect.

6.4.3 Work Function Analysis

The work function is the minimum energy required to remove an electron from the surface, discussed in greater detail in Section 3.6. Therefore, work function maps may be used to predict the likelihood that specific areas on the surface will preferentially corrode. The areas with lowest

work function require less energy to release surface electrons, and therefore are expected to be energetically favourable to oxidise or corrode.

A work function map collected following sputtering of the sample surface is shown in Figure 6.31. Sputtering was performed in a vacuum so the passive layer could not reform. This map highlighted the differences in work function between each grain. This may be related to the differing orientations present on the sample surface. This is particularly valid within studies of general corrosion, where the protective chromia layer is broken down allowing for uniform corrosion across the surface. In work performed by Lindell *et al.*, the corrosion rate of Type 316L (austenitic) stainless steel in 30 vol.% sulfuric acid was observed to vary with crystal orientation [55]. Corrosion rate increased as {111}<{110}$\lessapprox${100}, with a ratio between the slowest and fastest corrosion rates of approximately 3 [55]. This map may also indicate orientations that preferentially pit. In other works, it has been found that pitting corrosion is dependent upon crystallographic orientation [55, 123, 280]. It was found by Shahryari *et al.* for a sample of Type 316 stainless steel that {111} and {100} planes, i.e. planes with higher atomic density, exhibit the highest resistance to pit nucleation in a chloride solution [280]. The same phenomenon was also observed by Lindell *et al.* for a sample of Type 316L [55].

Figure 6.31 also shows that the edges of the grains have a differing work function compared to the bulk grain. Sometimes the measured work function is lower, however in some cases it is higher. Higher values are not expected from the observations of IGA seen within this work, as well as the lower chromium concentrations measured at the GB.

Measurements performed without sputtering of the passive layer (Figure 6.32) showed less variation from grain to grain, though some variation was apparent, particularly within the photoemission intensity image (Figure 6.32a). Again, this indicates a variation with grain orientation, possibly due to variations in the thickness of the passive layer. A key feature observed in Figure 6.32d is the differing work function values at the GBs. The work function along the GBs is approximately 0.03 eV higher than that measured for the bulk grain. This is not as expected as the GBs have been observed to preferentially corrode (such as observed in Figure 6.13). As this work function variation is discontinuous it may align with GB carbide precipitates, or the spaces between the carbide precipitates. Indeed, carbide precipitates are more noble and so would be expected to have a higher work function, however this disagrees with previous observations of carbide precipitate dissolution (for example Figure 6.26). Additional experimental work is suggested to reconcile this. Discrete points with higher work function seen in Figure 6.32d may coincide with passive features such as certain SPPs. Points with lower work function measured in the same map may be due to a pit on the surface from casting, or less noble SPPs.

Additional photoemission intensity and work function maps collected from a sample of unsensitised AISI Type 304 stainless steel (without sputtering), showed markedly less variation than observed on sensitised samples, Figure 6.33. No variation at the GBs is observed, likely coinciding with the lack of GB segregation and precipitation caused by thermal treatments. The

photoemission intensity maps (Figures 6.33a and 6.33c) do show a variation for certain grains, again indicating a variation with orientation, however this effect is very slight. Two discrete points with lower work function values are observed in Figure 6.33b. It is expected that these features are at pits or SPPs (i.e. MnS) from casting.

Measurements of the work function have highlighted opportunities for further work, this is discussed in greater detail in Section 9.2.5.

6.4.4 Further Context of Observations

The experiments performed within this chapter highlighted the corrosion behaviour changes that occur as a result of precipitation and sensitisation explored previously in Chapter 5. AISI Type 304 stainless steel is a versatile material that is used widely in a large number of industrial applications. The corrosive conditions explored within this work are also relevant within numerous applications including nuclear, oil and gas, pulp and paper, medical, and marine, to name a few [99, 151, 158–160, 280]. In addition to these directly relevant applications, this material may also be considered a proxy for AGR fuel cladding (20Cr/25Ni-Nb), as discussed within Chapter 5.

In previous work performed by Whillock *et al.* Type 304 stainless steel thermally treated at 600°C for 72 hours acted as an accurate proxy for AGR fuel cladding corrosion behaviour in pond storage conditions [30]. Within this chapter, the GBs in thermally sensitised AISI Type 304 stainless steel were particularly susceptible to IGA. Furthermore, chains of intergranular pits were purported to be the result of GB carbide dissolution. Whilst GB carbide precipitates were not as prominent within ex-service AGR fuel cladding, observed GB chromium depletion may result in higher susceptibility to IGA in chloride or thiosulfate environments. Additionally, NbC precipitates have been reported to play a role in pitting corrosion, possibly leading to a similar phenomenon as observed in this work [49, 282]. In a study by Clark *et al.*, thermally sensitised 20Cr/25Ni-Nb was exposed to various concentrations of chloride solution. Clarke found that NbC precipitates acted as initiation points for IGA, resulting in dissolution of the adjacent regions whilst these precipitates remained intact [49]. However, in another study by Clark *et al.*, when the same material was exposed to a high pH sodium hydroxide solution, these precipitates were observed to undergo dissolution [282].

Historically, IGA has occurred in AGR fuel cladding chloride solutions typically around 1.0 mg L^{-1} concentrations [30]. Though current IGA events are prevented by dosing storage pond water to a pH around 11.4 [30]. The conditions explored in this chapter were chosen as they accelerate pit initiation times and therefore may be implemented to establish new methodologies for pitting corrosion studies. These conditions do not simulate pond storage conditions, though the observations achieved in this chapter are still pertinent to such applications. Notably, the chloride concentration within pits is known to increase in concentration, so while the bulk solution may differ, the small scale conditions are still relevant. Additionally, the corrosion behaviours under the conditions studied in this chapter are applicable following future disposal. In particular, long

term storage in a geological disposal facility (GDF) where chloride within groundwater can reach concentrations of 5 M [46, 47].

6.5 Conclusions

Within the first part of this chapter, localised corrosion events were investigated for samples of thermally sensitised AISI Type 304 stainless steel in an aqueous solution of 1% NaCl. The sample surface was polarised by performing potentiodynamic and galvanostatic scans. A number of large pits were observed to form across the sample surface. Post-corrosion analysis of the surface revealed that these pits were a result of severe IGA in combination with intragranular pitting events. Within this study HS-AFM was combined with optical, SEM, FIB milling, and modelling to produce a multifaceted picture of localised corrosion events. The following conclusions may be drawn from this work:

- Results from this work demonstrated the potential of detailed in-situ surface techniques, such as HS-AFM, working in combination with ex-situ techniques such as FIB milling and SEM that allow for subsurface investigation.
- HS-AFM measurements were performed in-situ by imaging within a custom built liquid cell with parallel electrochemical control. The developed methodology is suitable for additional studies using different conditions.
- The high resolution of the HS-AFM allowed for measurements to be performed at individual reaction sites, i.e. at specific GB carbide surfaces, this allowed for accurate measurements of the dimensions of pits formed. Using these measurements, it was possible to calculate, and subsequently model, the volumes of metal reacting with respect to time, and so the current densities and ionic fluxes at work. Thus, demonstrating that the measurements yielded from such experiments may be directly fed into predictive models.
- In-situ HS-AFM observation of intergranular pit formation occurred in ≤ 0.5 seconds. The actual measured geometry during this event in combination with electrochemical data was fed into a computational model using COMSOL MP software. The model calculated that that the system reached a radial diffusion regime in under 0.01 s. Results were used to generate 3D plots that illustrated local acidification and a build-up of chloride ions in the areas adjacent to the pitting site.
- Intergranular pits were observed to occur in chains along GBs, purported to be the result of GB carbide precipitate dissolution. These chains were found to be an early form of IGA.
- Intergranular pitting was found to be much more severe than intragranular pitting, leading to an observed dominance of IGA.

- Severity of IGA is linked to thermal sensitisation of the GBs leading to lower resistance to corrosion.
- Investigation by FIB milling revealed that in some areas intergranular pits are small surface entryways to much larger subsurface voids produced by IGA.
- FIB milling performed in an area containing an intragranular pit revealed subsurface corrosion that appeared to progress outwards from the pit through the bulk of the grain. Further progression of deeper corrosion by IGA was also observed, demonstrating an interplay between the two mechanisms.
- In-situ HS-AFM measurements performed in the absence of an applied potential showed GB carbide precipitate dissolution over a duration of 408 seconds. This phenomenon only occurred after previous polarisation of the surface.

In the second part of this chapter, similar HS-AFM measurements were performed for the same material exposed to 395 mg L^{-1} aqueous $Na_2S_2O_3$, without an applied potential. The following conclusions were made:

- Preferential dissolution of GB carbide precipitates was observed.
- The HS-AFM probe was found to interact with the surface in such a way that accelerated corrosion of carbide precipitates when the surface is exposed to a corrosive environment.
- Prolonged exposure to the thiosulfate solution resulted in a possible oxide layer forming at specific GBs.

Measurements of photoemission intensity and work function highlighted interesting possibilities for future correlated microscopy studies, as discussed in Further Work (Section 9.2.5). The following concluding statements from this work are:

- Measurements of work function by EF-PEEM showed variation that may be related to grain orientation, possibly influencing general corrosion rate and pitting corrosion nucleation.
- A differing work function was also measured at the GBs in sensitised samples that was not observed for unsensitised samples as a result of the thermal treatment causing GB segregation and precipitation.

In the next Chapter (Chapter 7) the corrosion conditions explored in the second part of this chapter are explored in the presence of applied tensile stress. Samples of thermally sensitised AISI Type 304 stainless steel are exposed to 395 mg L^{-1} aqueous $Na_2S_2O_3$ and deflected on a three-point strain rig, resulting in failure by IGSCC (as discussed in Section 2.5.2). Various factors that may affect the propensity of specific GBs to undergo SCC are explored using a suite of ex-situ analytical methods, including GB misorientation (EBSD), oxide formation and GB SPPs

(HS-AFM), oxide composition and GB element segregation (atom probe tomography (APT)), and sub-surface contributions (FIB tomography).

CHAPTER 7

EX-SITU ANALYSIS OF SCC CRACK PROPAGATION PATH AND CHARACTERISATION OF THE CRACK TIP

When the factors are separate is it still realistic?
As when these factors come together they are synergistic
Thus far, it is stress that this thesis has been lacking
So without further ado, let's get cracking

A multitude of factors are known to affect the path of stress corrosion cracking (SCC) through a material, such as grain boundary (GB) misorientation, precipitation, composition, depletion profile, or local stress field [36, 68, 69, 108, 134, 232], as discussed in Section 2.3. The key aim of this chapter is to explore some of the key factors that determine why certain GBs crack.

Within this chapter, a number of different methods are combined for the ex-situ study of SCC. A sample of thermally sensitised American Iron and Steel Institute (AISI) Type 304 stainless steel, as studied in Chapter 5, was exposed to a solution of sodium thiosulfate, as studied in Chapter 6, whilst under tensile stress to induce SCC. Pre- and post-SCC measurements are performed by high-speed atomic force microscopy (HS-AFM), atom probe tomography (APT) and scanning electron microscopy (SEM) techniques, and correlated in order to better understand the microstructural changes occurring and their associated mechanisms.

APT measurements in this chapter were performed by Tomas Martin. This chapter includes figures and large sections of text taken directly from the following papers:

- **S. Moore**, R. Burrows, D. Kumar, M. B. Kloucek, A. D. Warren, P. E. J. Flewitt, L. Picco, O. D. Payton, and T. L. Martin, Observation of Stress Corrosion Cracking of Stainless Steel

Using Real-Time In-Situ High-Speed Atomic Force Microscopy and Correlative Techniques. Npj Materials Degradation, 2021, 5(3).

- **S. Moore**, R. Burrows, L. Picco, T. Scott, A. Laferrere and O. Payton, Investigating Corrosion Using High-Speed AFM, EUROCORR 2017 PROCEEDINGS.

7.1 Conditions For SCC Tests

All experimental work within this chapter was performed using thermally sensitised AISI Type 304 stainless steel detailed in 5.1.2. Samples were cut from this sheet by waterjet into test specimens. The dimensions of the specimen shapes used within this work are described in Section 8.2.1. Samples were then polished following the steps detailed in Section 4.2.

Samples were pre-exposed to a solution of 395 mg L^{-1} (2.5 mM) aqueous sodium thiosulfate ($Na_2S_2O_3$) for a duration of 6 days prior to application of stress, discussed in Chapter 8. Sodium thiosulfate is an aggressive salt solution known to cause intergranular SCC (IGSCC) in sensitised austenitic stainless steels [101, 103, 126, 147, 158, 160, 161, 163–169], as discussed in Section 2.5.2.1. Stress was applied by deflection on a three-point strain rig. The strain rig design is discussed in greater in detail in Section 8.2.1.

7.2 Analysis of SCC Crack Path

7.2.1 Analysis of Crack Mode

Optical images of specimens which had failed by SCC in a solution of 395 mg L^{-1} aqueous $Na_2S_2O_3$ are shown in Figure 7.1. SCC was observed to initiate at a number of sites along the apex of the bend, in areas of maximum deflection. Cracks were observed to propagate from these initiation points, causing an alteration of the stress state of the sample. These cracks joined to form a crack extending over the width of the sample resulting in the curved crack shape observed. A discolouration of the surface is observed in the areas surrounding the crack.

Cracked samples were removed from the strain rig and polished to a mirror finish as described in Section 4.2 such that the crack path could be analysed by SEM techniques including electron backscatter diffraction (EBSD). Secondary electron (SE) images of the sample surface are shown in Figure 7.2. Figure 7.2a shows a sample that has been polished at 90° (along the edge of the sample) to produce a cross section. As with previous optical images this shows multiple crack propagation sites with one dominant crack. Figure 7.2b shows an SE image collected from the surface of a different specimen showing the intergranular nature of the crack path, as well as numerous branches leading off the dominant crack. By tilting the same sample at 52° to the primary electron beam the granular structure of the crack face is further revealed, as shown in Figure 7.2c.

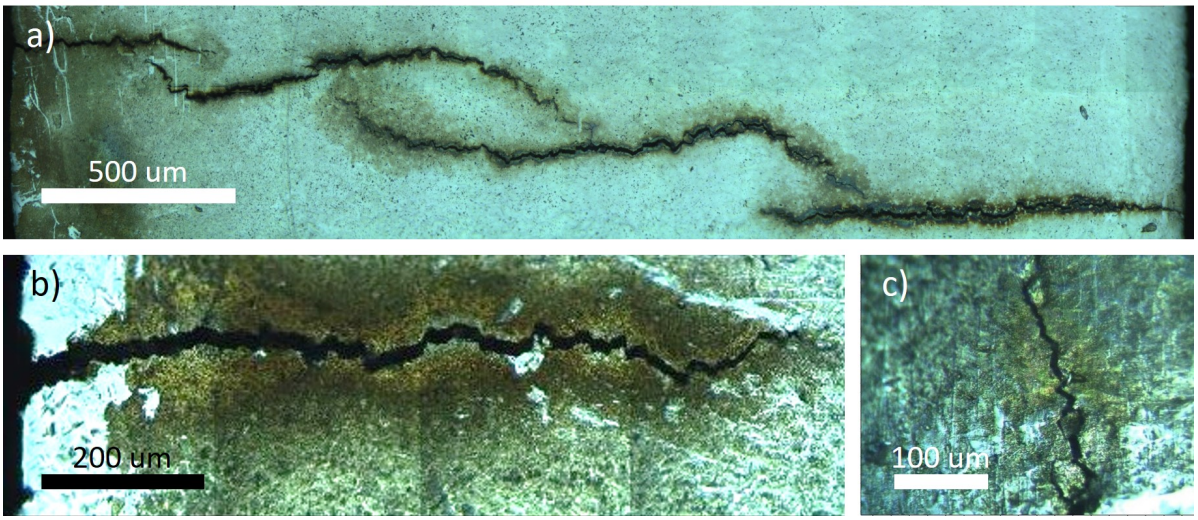

Figure 7.1: Optical images collected following failure by SCC: a) across the whole width of the sample, and b) and c) at specific regions on the surface showing the crack pathway.

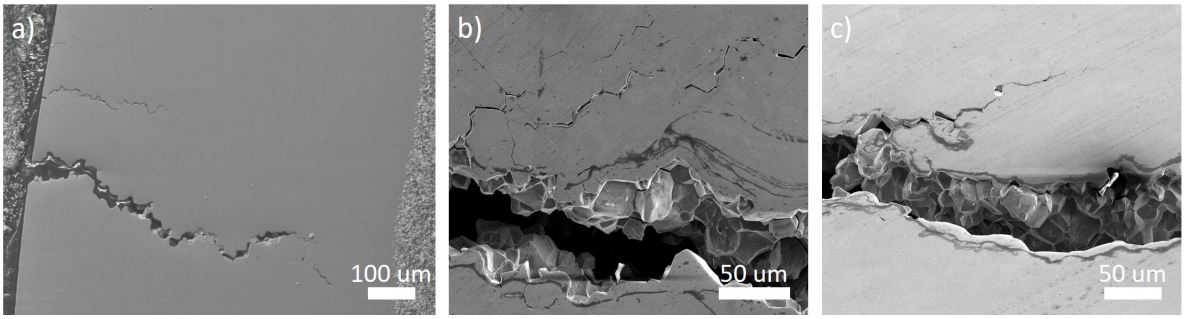

Figure 7.2: SE images showing: a) a polished cross section of a cracked sample with a dominant crack penetrating through most of the sample width, b) a crack in a sample with smaller cracks leading off the dominant crack, c) a crack in a sample collected at 52°.

EBSD analysis was performed using a constant beam voltage of 30 kV with an aperture of 120 μm. Inverse pole figure (IPF) and image quality (IQ) maps of the surface are shown in Figure 7.3. Figure 7.3c shows an IPF and IQ map collected at the edge of the crack where a cluster of grains are falling away from the crack edge. These images confirm the intergranular nature of the crack as it propagated through the sample.

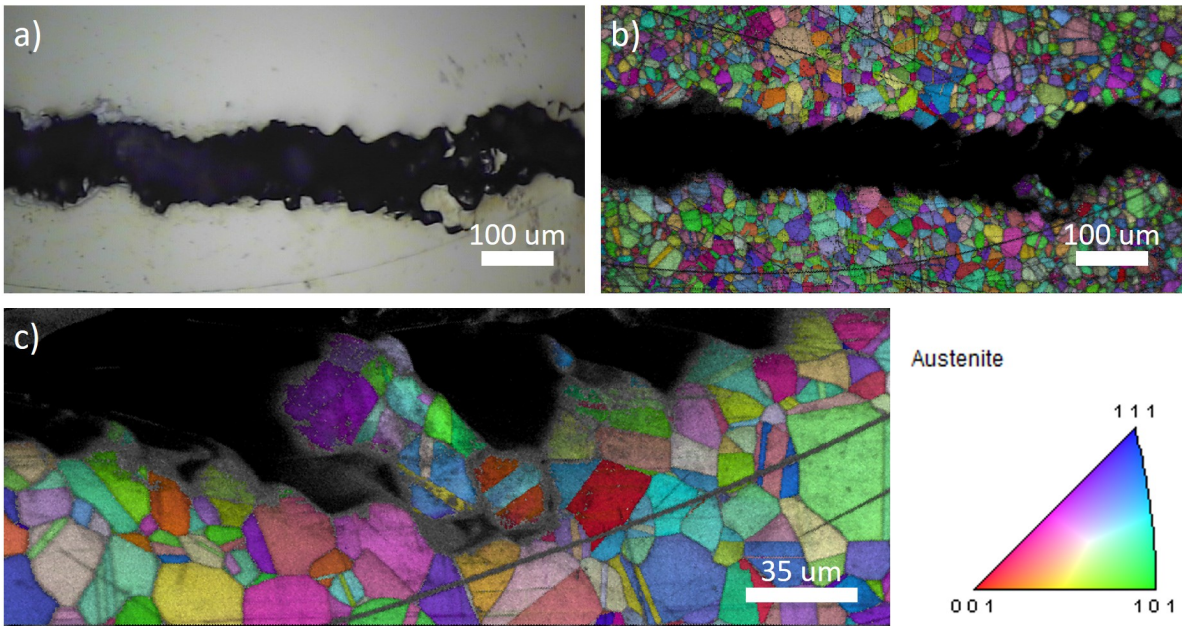

Figure 7.3: a) An optical image of the cracked sample surface, b) an IPF and IQ map showing the crack collected using a step size of 2 μm. Also, c) an IPF and IQ map showing the edge of the crack collected with a step size 0.5 μm. EBSD maps have been rotated 90° clockwise. Raw data was cleaned up using a confidence index standardisation (CIS) algorithm [28] and a confidence index (CI) > 0.1 partition was applied before analysis. Inset IPF colour key.

7.2.2 GB Misorientation Measurements Along The Crack Path

Figure 7.4a shows an SE image of the sample prior to failure, and Figure 7.4b shows the same sample following failure. Two dominant cracks are observed, one leading upwards and the other downwards. Figure 7.4c and 7.4d show EBSD maps collected from the region outlined in blue in Figure 7.4a. With the GB misorientation map shown in Figure 7.4d, GBs are labelled using the same convention established in Section 5.2.1.1.

Figure 7.5a shows an SE image of the two dominant cracks in the failed specimen, one crack that propagated upwards (left) and one downwards (right). Figure 7.6b and show an IPF and IQ map collected prior to cracking with the crack path indicated in white. The labels are discontinuous as some areas did not have a clearly defined path. Figure 7.6c shows the same path indicated on a GB misorientation map. The measured GB misorientations are listed in Tables C.1-C.4 in Appendix C.

Figure 7.6a shows an SE image of a smaller crack to the right of the dominant cracks leading upwards and passivating. As previous, the crack path is indicated on an IPF and IQ map shown in Figure 7.6b, and a GB misorientation map shown in Figure 7.6c. This path is discontinuous in areas where the path was unclear. Tables C.5-C.7 in Appendix C lists the GB misorientations of the cracked GBs and the adjacent non-cracked GB misorientations.

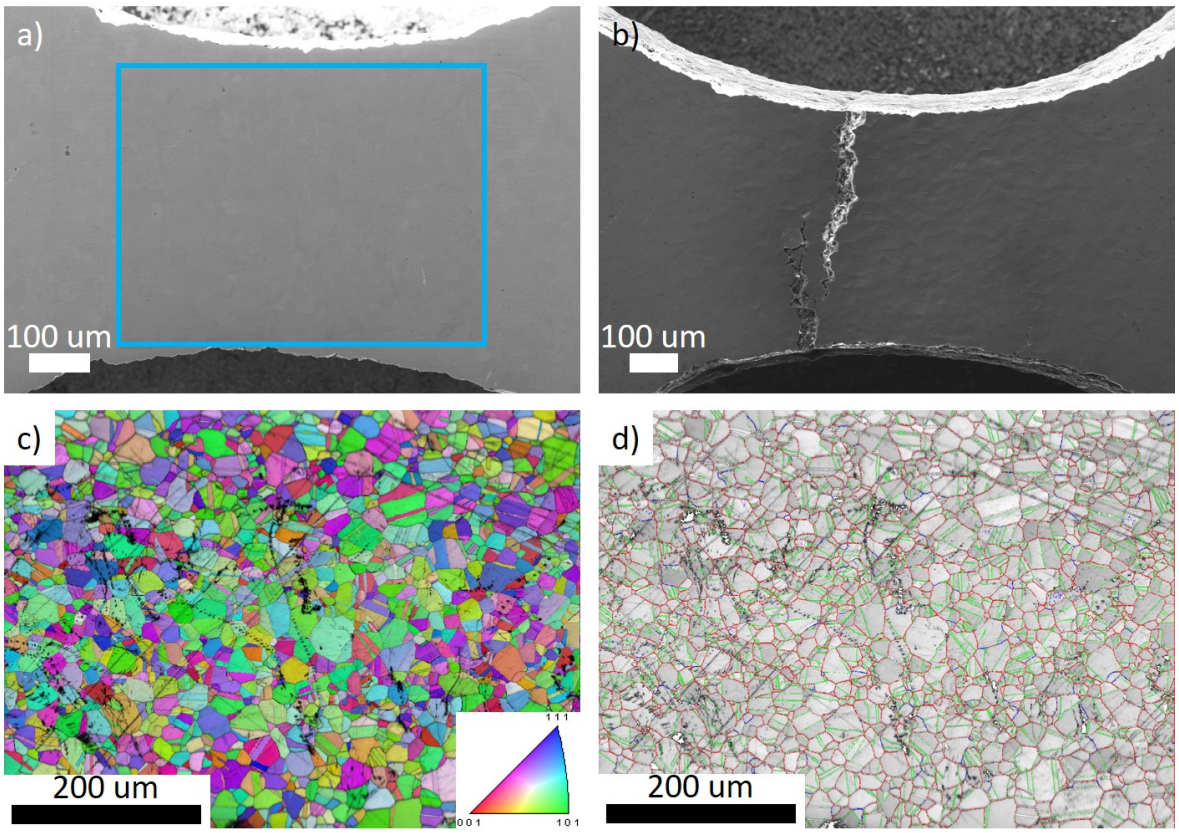

Figure 7.4: a) and b) show SE images collected of the sample surface before and after SCC, respectively. c) and d) show EBSD maps collected from the region outlined in blue in a). c) is an IPF and IQ map collected using a step size was 0.5 μm, and d) is a GB misorientation map where low-angle GBs (LAGBs) (with misorientation value in the range 5°-15°) are labelled in blue, high-angle GBs (HAGBs) (with misorientation value 15°-62.8°) in red, and coherent twin GBs (with misorientation value 60° and misorientation axis < 111 > [29]) in green. The sample surface was mapped to austenite. Raw data was cleaned up using a CIS algorithm [28] and a CI> 0.1 partition was applied before analysis.

Figure 7.7 shows histograms of the cracked and non-cracked GBs, produced using the values listed in Tables C.1-C.7 in Appendix C.

Figure 7.8 shows an area where the crack shown in Figure 7.6a is discontinuous on the surface. This crack tip differs from those previously observed as it appears jagged. An IPF and IQ map of the area is shown in Figure 7.6d. Due to the resolution of the EBSD maps collected, the GB type is unclear. A secondary phase precipitate (SPP) is observed to the right of the crack,

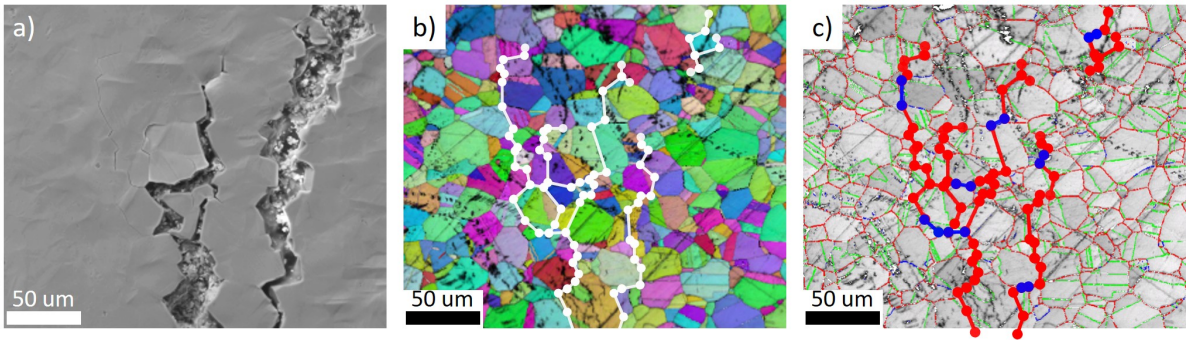

Figure 7.5: a) An SE image showing the end sections of the two dominant cracks shown in Figure 7.4, b) shows an IPF and IQ map for the region shown in a) cropped from Figure 7.4c with the cracked GBs indicated in white, c) shows a GB misorientation map for the region shown in a) cropped from Figure 7.4d with cracked LAGBs (with misorientation value in the range 5°-15°) labelled in blue and cracked HAGBs (with misorientation value 15°-62.8°) in red.

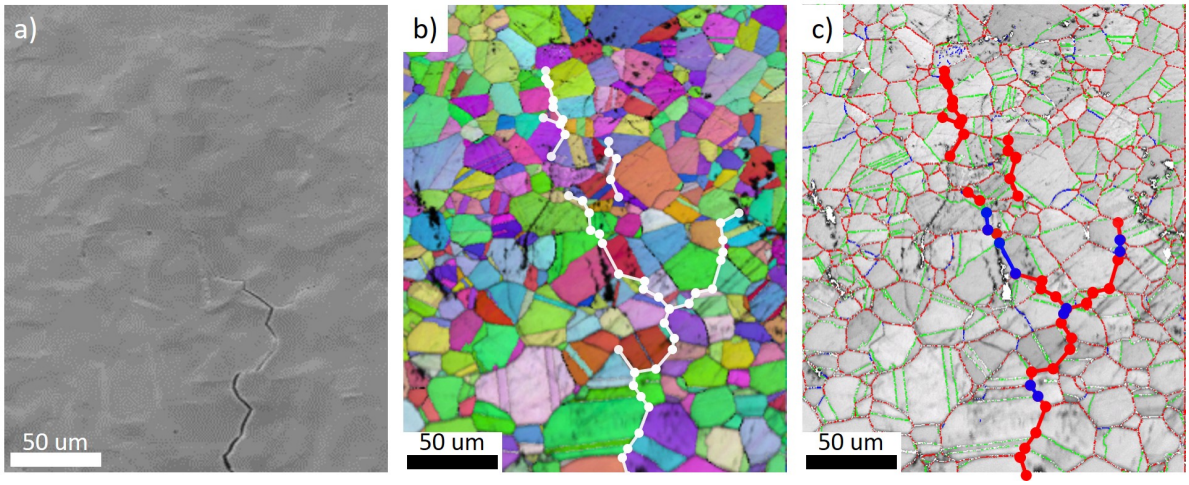

Figure 7.6: a) An SE image showing the end section of the smaller crack to the right of the dominant cracks shown in Figure 7.4, b) shows an IPF and IQ map for the region shown in a) cropped from Figure 7.4c with the cracked GBs indicated in white, c) shows a GB misorientation map for the region shown in a) cropped from Figure 7.4d with cracked LAGBs (with misorientation value in the range 5°-15°) labelled in blue and cracked HAGBs (with misorientation value 15°-62.8°) in red.

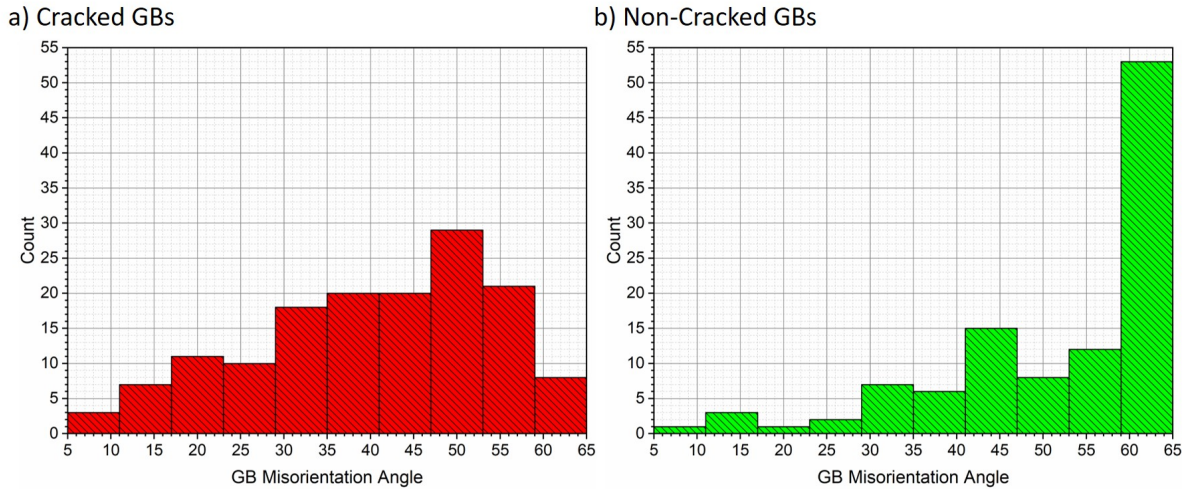

Figure 7.7: a) A histogram of GB misorientation values measured along the crack path, b) a histogram of GB misorientation values measured across the non-cracked GBs adjacent to the cracked GBs.

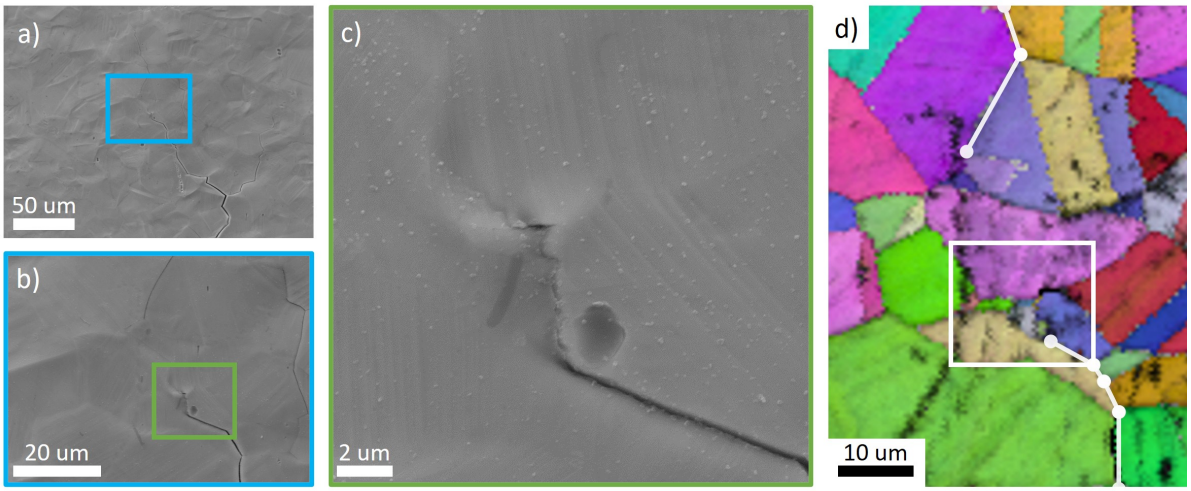

Figure 7.8: SE images showing: a) the end section of the crack shown in Figure 7.6, b) a higher magnification of the region outlined in blue in a), c) a higher magnification of the region outlined in green in b). Also, d) shows an IPF and IQ map for the central area of the region shown in b) cropped from Figure 7.4c with the cracked GBs indicated in white. The white box indicates the same region shown in c).

7.3 Arrested Microcracks and Crack Tip HS-AFM Measurements

Samples that had failed by SCC were mounted and polished following the steps described in Section 4.2 for analysis by HS-AFM. HS-AFM topographic maps of cracked GBs are shown in Figures 7.9a-7.9d. These images were collected by tracing a deflected crack that branched away from the dominant crack. Figures 7.9a-7.9c contain GB triple points in which certain GBs have widened as a result of IGSCC, whereas others remain relatively unchanged, as labelled in Figure 7.9e. This is highlighted by comparing the line scans shown in Figure 7.10. The line scan collected across the GB that has started to crack is approximately twice the width of the non-cracked GB.

Topographic maps shown in Figure 7.9 also revealed that carbide precipitates are present within non-cracked and cracked GBs. Additionally, the cracked GBs contain an oxide layer, as labelled in Figure 7.9e. This oxide does not uniformly fill the GB.

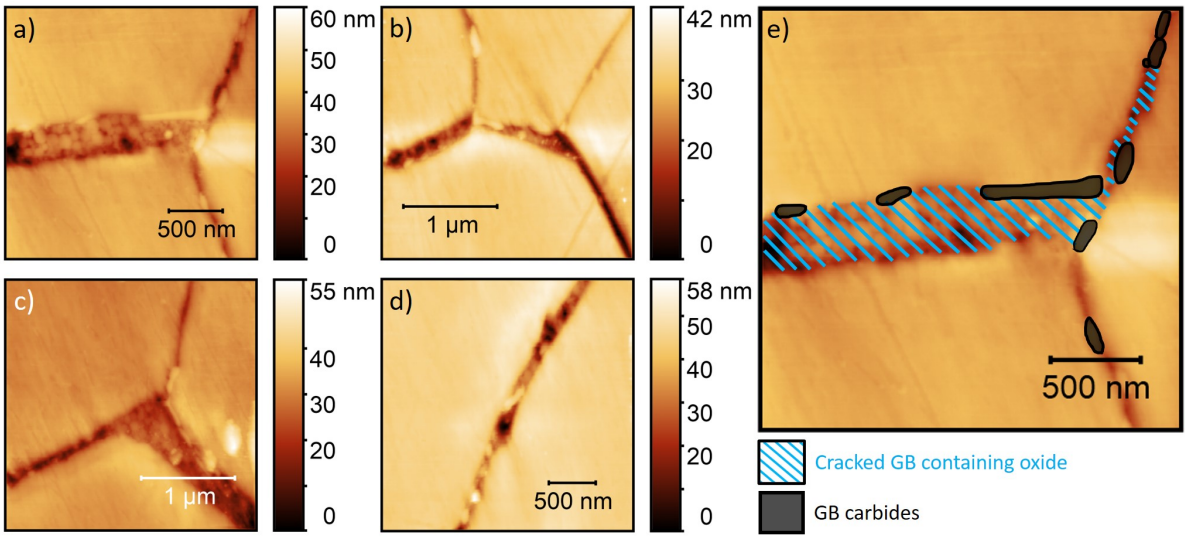

Figure 7.9: a)-d) are images showing HS-AFM topographic maps of microcracks measured in a polished cracked sample, with height colour map, imaged within deionised water. e) is a labelled version of the image shown in a).

Figure 7.11 shows instances where surface crack tips were measured by HS-AFM. Within Figures 7.11a and 7.11b the crack propagated part way down a GB then stopped. In both cases the crack stopped at a GB carbide precipitate. In the case of Figure 7.11c the crack tip appears to extend into the bulk grain. However, it is likely that the crack encountered an unsensitised GB. In this instance, a GB carbide is observed to bridge the crack.

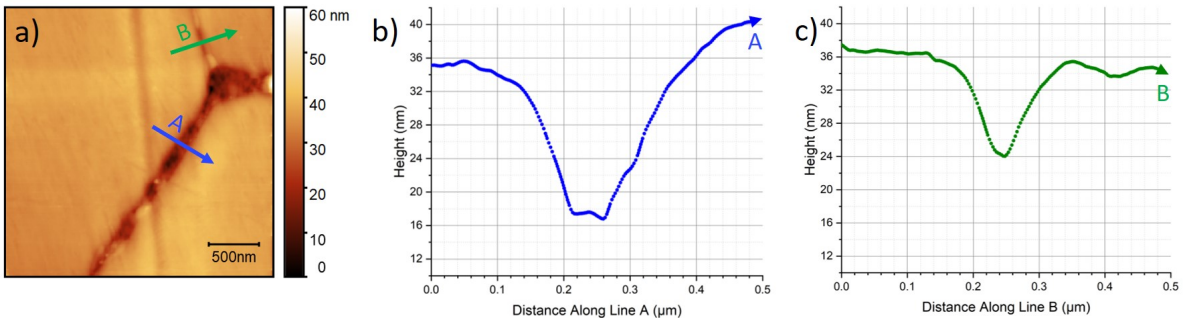

Figure 7.10: a) An HS-AFM topographic image showing the path of a microcrack through a triple point, and line profiles collected for: b) the line labelled A shown in Figure 7.10a as a dark blue line, and c) the line labelled B shown in Figure 7.10a as a green line, showing the difference between cracked GBs and non-cracked GBs.

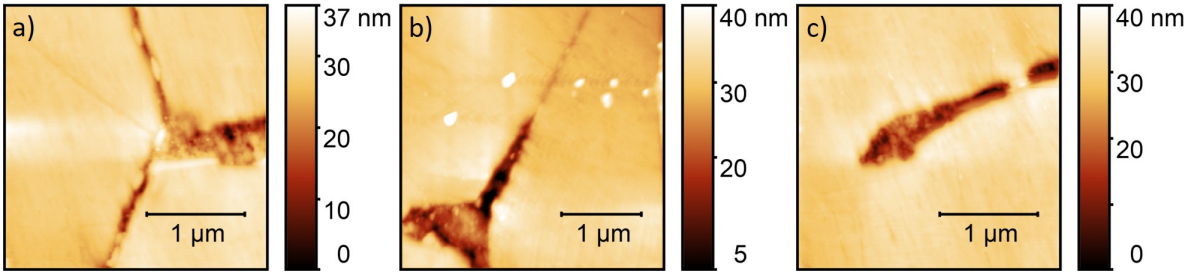

Figure 7.11: HS-AFM topographic maps showing: a)-b) crack tips part way down a GB, and c) a crack tip extending into the grain.

7.4 Tip Chemistry Measurements by APT

Chemical analysis of the oxide layer observed by HS-AFM was performed by APT. Samples evaluated by APT were extracted using a site-specific focussed ion beam (FIB) lift-out preparation method adapted from Lotharukpong *et al.* [237] from a region containing an arrested crack tip, described in greater detail in Section 3.5.3.

APT analysis was performed on a needle containing part of the oxide-filled crack and part of the bulk metal, allowing for analysis of the oxide-metal interface. Figure 7.12 shows SE images collected during the thinning process of the needle specimen. The crack is observed to run diagonally through the specimen, this crack is filled with an oxide. The final tip analysed is shown in Figure 7.12c.

Figure 7.13a shows a 3D APT atom map of the needle selectively showing chromium and iron ions, as well as CrO_x and FeO_x ions. The needle contains two distinct regions: a region of oxide, and a region of bulk metal. Within this figure, these two regions are separated by a 37.7 at.% oxygen iso-concentration surface, i.e. further into the oxide the oxygen concentration increases, into the bulk the oxygen concentration decreases. Figure 7.13b shows the same needle containing only the oxygen iso-concentration surface and (2× size) sodium ions. Once again, two distinct

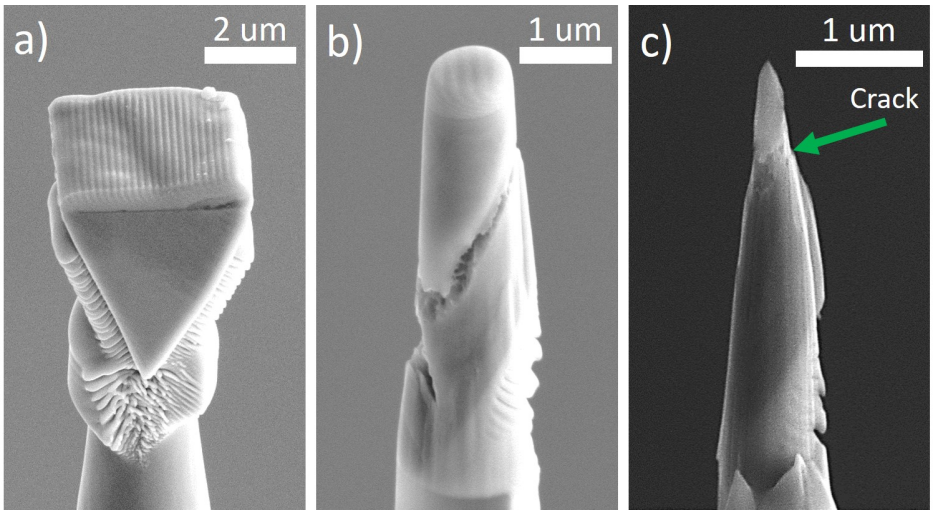

Figure 7.12: SE images showing: a) a segment of the area outlined in yellow in Figure 3.13 mounted onto an APT grid, b) an intermediate needle following FIB thinning, and c) the final APT needle seen to contain a section of the crack, as indicated.

regions are observed, the oxide and the bulk metal.

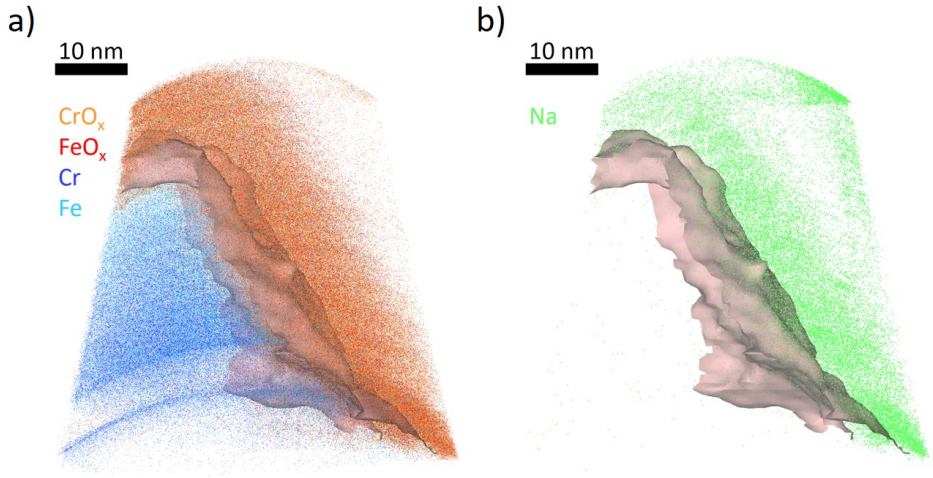

Figure 7.13: 3D APT reconstructions containing a 37.7 at.% oxygen iso-concentration surface with: a) CrO_x, FeO_x, chromium and iron ions, and b) (2× size) sodium ions.

Figure 7.14 contains a deconvoluted proximity histogram for the 37.7 at.% oxygen iso-concentration surface showing the variation of relative element concentrations from the bulk metal to the oxide. The histogram shows variations in chromium, iron, sodium, nickel, and oxygen. Other elements were detected at significantly lower at.% and so have been negated from this graph. Four distinct sections can be interpreted from this graph: the bulk metal (up to -10 nm), the oxide interface or GB (-10 nm to 0 nm), the oxide (0 nm to 19 nm), and outside the oxide (19 nm onwards). The oxide has a varying composition indicating a layered structure. An inner

chromium-rich oxide is indicated by a small peak in chromium up to 17 at.% at 0.5 nm. Chromium is observed to be depleted at the oxide interface, i.e. the GB, down to a value of 6.5 at.%. This corresponds to approximately 7 wt.%. Outside of the oxide the metallic contributions are observed to rapidly reduce towards 0 at.%, and sodium concentration increases significantly.

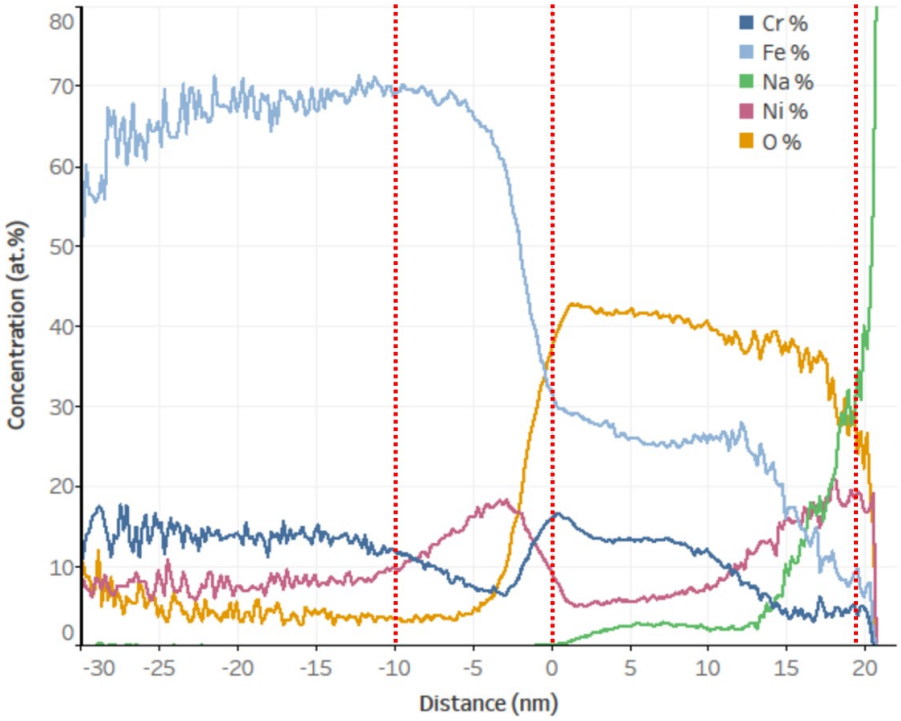

Figure 7.14: A deconvoluted proximity histogram showing the concentration profile either side of the 37.7 at.% oxygen iso-concentration surface shown in Figures 7.13a and 7.13b, red dotted lines indicate boundaries between compositionally differing regions.

APT results for sulfur were not conclusive as it is a challenge to accurately deconvolute the overlap between the sulfur peak from the O_2 peak within the mass spectrum, as shown in Figure 7.15a. Within Figure 7.15a the overlapping peaks were coarsely separated into O_2 (in orange) and sulfur (in grey). Using this approximation the ions may be tentatively labelled as shown in Figure 7.15b. This needle shows a higher concentration of O_2 in the oxide layer, and occasional sulfur present within the bulk metal.

A deconvoluted histogram corresponding to the analysis shown in Figure 7.15 is given in Figure 7.16. This histogram shows a concentration of sulfur across the oxide boundary into the bulk metal. The start of the oxide region is observed as a peak in O_2. However, it should be noted that this evaluation would be altered by any changes made to the separation of the peaks previously shown in Figure 7.15a.

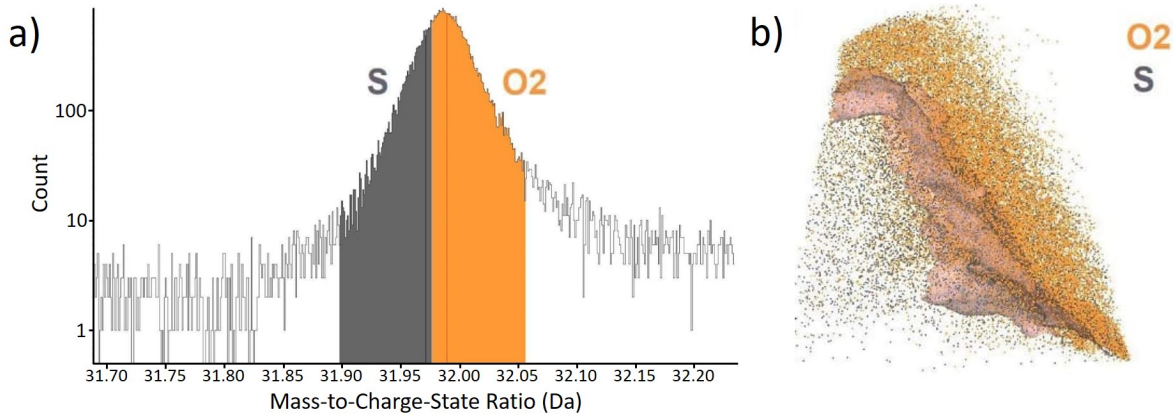

Figure 7.15: a) A section of the mass spectrum containing the overlapping peaks of O_2 (in orange) and sulfur (in grey), and b) a 3D APT reconstruction containing a 37.7 at.% oxygen iso-concentration surface with O_2 and sulfur ions.

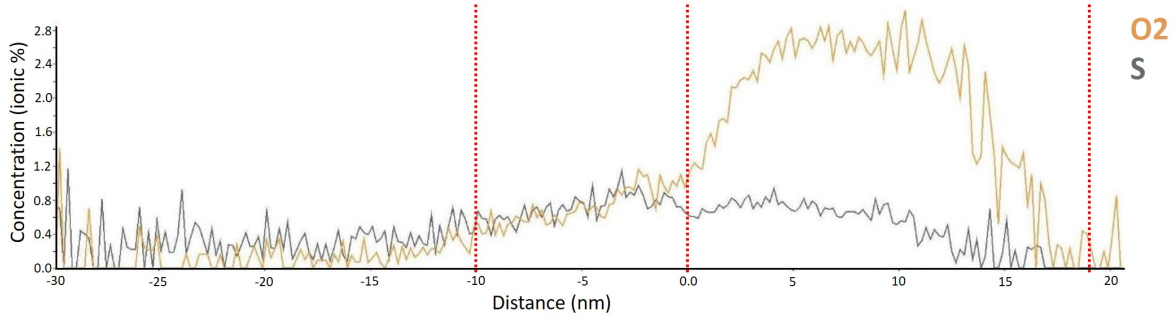

Figure 7.16: A deconvoluted proximity histogram showing the concentration profiles for O_2 and sulfur either side of the 37.7 at.% oxygen iso-concentration surface shown in Figure 7.15b. Red dotted lines indicate boundaries shown in Figure 7.14 indicating compositionally differing regions.

7.5 Sub-Surface Crack Propagation

Within surface images of the cracked sample, the crack tip was discontinuous in some cases, as seen in Figure 7.17. In Figure 7.17a grains are observed to bridge the crack tip. In Figure 7.17c a grain appears to have been undercut, resulting in collapse. These features indicate that the crack had propagated subsurface. In order to investigate this, FIB milling and SEM imaging were used in tandem for 3D analysis of a volume beneath the sample surface.

FIB cuts were performed at 30 kV and 6.5-20 nA, and SE images were collected at regular intervals using the SEM at 10 kV and 0.34 nA. FIB milling was performed ahead of a crack tip, shown in Figures 7.18a-7.18b. These images demonstrated that subsurface GBs ahead of the surface crack tip had been corroded. A series of SE images were collected as the serial sectioning progressed closer to the crack tip on the surface, shown in Figures 7.18c-7.18f. These images

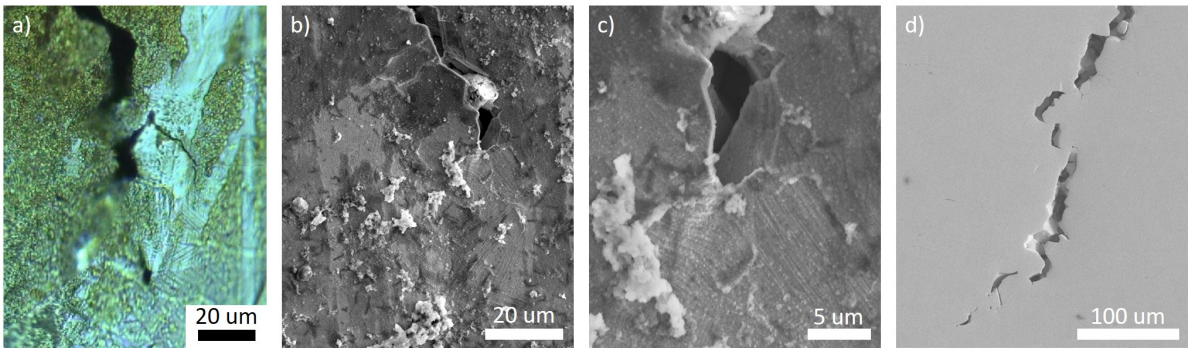

Figure 7.17: a) An optical image showing a discontinuous crack tip, also SE images showing: b) a crack tip, c) a higher magnification image of the crack in b) showing an opening leading to possible subsurface crack propagation, and d) a discontinuous crack tip in a polished sample.

reveal a network of subsurface intergranular cracks.

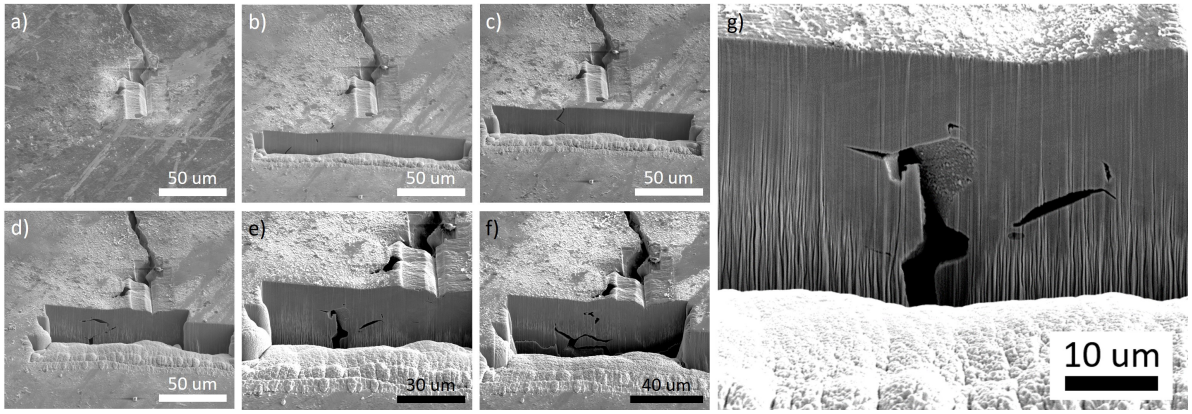

Figure 7.18: a)-f) show SE images collected as a part of a series of FIB slices into the area ahead of a crack tip, in the same region as that analysed by APT. g) Shows a higher magnification SE image of the subsurface crack shown in Figures 7.18e. All images were collected at a tilt of 52° with respect to the primary electron beam.

Within Figures 7.18g and 7.19a an oxide layer is observed along the walls of the corroded GB. This was supported by energy dispersive X-ray spectroscopy (EDX) measurements showing increased oxygen and sodium, shown in Figures 7.19b and 7.19c, respectively. The oxide thickness varied from 10s to 100s of nanometres. Notably, the oxide does not fill the cracked GB.

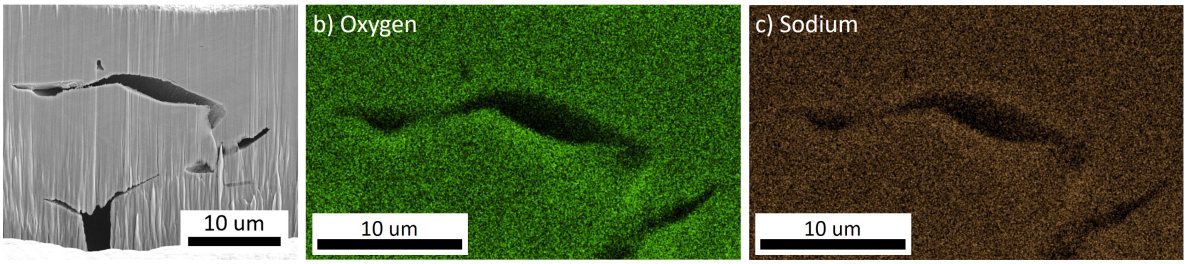

Figure 7.19: a) A higher magnification SE image of the subsurface crack shown in Figure 7.18d. b) and c) show EDX element maps collected for the region shown in a) for oxygen and sodium, respectively. All images were collected at a tilt of 52° with respect to the primary electron beam.

7.6 Discussion: SCC in Thermally Sensitised AISI Type 304 Stainless Steel in a Sodium Thiosulfate Solution

Within this chapter, SCC was studied for a thermally sensitised AISI Type 304 stainless steel in a solution of 395 mg L^{-1} $Na_2S_2O_3$. This chapter utilised a number of different methods at different length scales with the aim of characterising the system. Imaging techniques including optical microscopy, HS-AFM, and SE imaging allowed for inspection of the resultant surface. EBSD analysis gave insight into the path the crack had taken through the surface microstructure. The composition of the crack oxide was evaluated by APT and EDX. Lastly, FIB milling of the surface allowed for consideration of the sub-surface processes occurring. The results from each technique are discussed in the following sections. The results from this chapter will aid understanding during in-situ analysis performed in Chapter 8.

7.6.1 Surface Analysis of the Crack Path

7.6.1.1 Optical and SEM Observations

For the conditions used in this study, SCC was observed to be intergranular (Figures 7.1-7.3), this is as expected from literature [101, 103, 126, 147, 158, 160, 161, 163–169]. By tilting the sample, the upper region of the fracture surface was observed in Figures 7.2a and 7.2b. The fracture surface has a 'rock candy' appearance, characteristic of IGSCC in materials with equiaxed grain structures [131].

Optical images of the surface (Figure 7.1) showed that cracking initiated at a number of points in areas of maximum deflection and therefore maximum strain. These initial cracks joined up with one another as cracking progressed to form a dominant crack across the surface. The discolouration that surrounds the crack is likely to be oxidation that originated at the crack tip.

In some cases crack paths isolated 'islands' of grains, as seen in Figure 7.1c. In literature, these 'islands' are referred to as crack bridges or bridging ligaments and are formed as the result of the crack interacting with crack-resistant unsensitised GBs, such as coherent twins (as measured in

Chapter 5) [68–70, 100, 125, 133, 135]. This is illustrated in Figure 7.20. Observations performed at the crack tip showed instances where these bridges are still intact, forming a barrier across the crack (Figure 7.17a). Crack bridges have been reported to shield the crack tip from applied stress thereby reducing the rate of short crack propagation [69, 70, 100, 125, 133, 283]. In these instances, the crack appears to propagate subsurface (Figure 7.17).

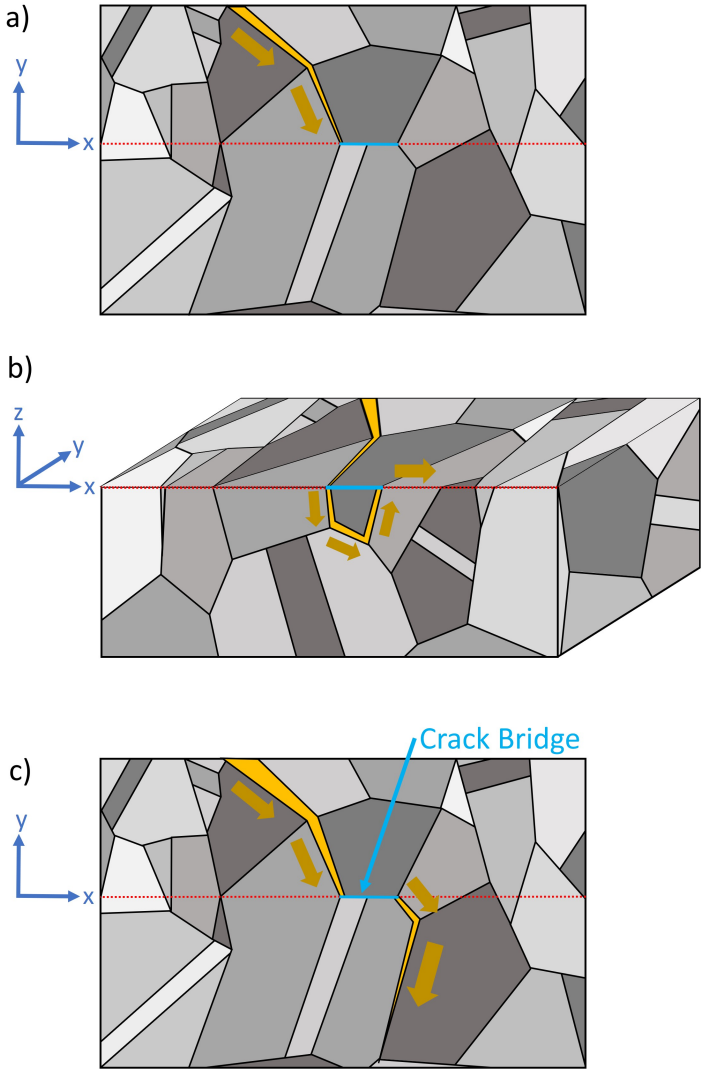

Figure 7.20: A series of schematic diagrams showing: a) an intergranular crack (highlighted in yellow) propagating through a sample microstructure approaching an non-susceptible GB (highlighted in blue), b) a cross-section along the red dotted line shown in a) showing sub-surface crack propagation (in yellow), and c) the continuation of the crack shown in a) with the non-susceptible GB forming a crack bridge.

Some cracks on the surface were passivated (as observed in Figure 7.2), this is expected to be due to a change in stress state as the dominant crack propagated across the surface. Alternatively, this may have been the result of the crack tip encountering unsensitised GBs that are resistant

to cracking (such as twin GBs), or GB carbide precipitates. In order for cracks to extend across the entire sample a continuous network of susceptible GBs is required [72].

7.6.1.2 HS-AFM Analysis

HS-AFM measurements were performed on a sample that had failed by SCC and was subsequently mounted and polished. Analysis of the crack path by HS-AFM further corroborated the intergranular nature of the cracking process. It was observed that certain GBs had widened as a result of IGSCC, whereas others were relatively unchanged (Figure 7.9), highlighting the localised nature of IGSCC. This was illustrated by comparing line scans collected across cracked and adjacent non-cracked GBs in Figure 7.10. The cracked GB also contained an oxide, possibly as a result of GB oxidation at, or ahead of, the crack tip (discussed further in Section 7.6.2).

By comparing the results attained in this chapter to measurements performed prior to any SCC processes in Chapter 5, changes to the microstructure are emphasised. The line profile collected across a GB prior to any corrosion processes in Figure 5.31 may be compared to that collected from the non-cracked GB in Figure 7.10c. It can be seen that these GBs are similar in size and shape, indicating that the uncracked GBs are relatively unaffected by corrosion processes.

GB carbide precipitates were still present within the GBs that had suffered IGSCC (as labelled in Figure 7.9e). This indicates that the carbide dissolution observed in Chapter 6 was not prominent during IGSCC. This is not to say, however, that the GB carbides did not play a role in the cracking process. It is possible that dissolution or modification of a limited number of GB carbide precipitates could have resulted in a stress accumulation event leading to crack initiation or propagation.

The carbide precipitates in the cracked GB are along one edge of the GB, indicating the GB had parted during IGSCC following dissolution of the chromium depleted areas adjacent to the carbide precipitates. The asymmetry of dissolution along the crack is likely the result of the different orientations of the grains either side of the crack, and the relative crystallographic coherence of the carbide precipitate with either grain [105]. This also relates to an asymmetry of the GB chromium depletion, resulting in preferential dissolution of the higher energy carbide-GB interface [105]. An additional factor may be GB migration during thermal sensitisation [105, 284].

Instances of crack passivation were also observed within HS-AFM analysis. Different morphologies of crack tip were encountered within this work, as shown in Figure 7.11. However, it should be considered that all instances of apparent crack tips on the surface may be the result of subsurface crack propagation, explored further in Section 7.6.3.

In Figure 7.11a the crack passivated shortly after a GB triple point. The energy required to crack either GB may have exceeded that required to crack the leading GB. This may be due to both GBs being resistant to cracking or orientated unfavourably with respect to the stress axis [72]. Additionally, the tip of this crack occurred at a GB carbide, again indicating that additional

energy may be required to pass the carbide. A similar phenomenon was observed in Figure 7.11b, where the crack propagated part way down a GB before stopping. This may be due to passivation, a change in stress state or crack propagation along a subsurface GB. As before, the crack tip is coincident with a GB carbide. In the case of Figure 7.11c the crack tip appears to passivate within the bulk grain. In this case it is likely that the crack encountered a twin GB and either passivated or propagated subsurface.

Another key feature of Figure 7.11c is the presence of a GB carbide within the cracked GB that appears to bridge the crack. This has been observed previously in a study by Williford *et al.* for a sample of thermally sensitised (625°C for 24 hours) Type 304 stainless steel following etching in 1% oxalic acid [150]. Such features may act similarly to crack bridges, resulting in a reduction of the rate of short crack propagation [69, 70, 100, 125, 133, 283].

Measurements by HS-AFM provided a better understanding of the microstructural features present within a cracked sample in preparation for in-situ HS-AFM experiments performed in Chapter 8.

7.6.1.3 The Effect of GB Misorientation

GB character has been reported to affect the path a crack takes through a material by affecting GB chromium depletion and precipitation. This is discussed in greater detail in Sections 2.1.5.2 and 2.3.1.1.

EBSD measurements were performed following SCC as shown in Figure 7.3. However, as this map was collected post-failure, the GBs on the surface (particularly for the dominant crack) were completely severed. This made measurements of GB misorientation difficult as it is not always clear which grains were adjacent to one another, and it could not be ruled out that some grains may have been lost during the cracking process. Additionally, in order to collect this map, the surface required re-preparation, producing a cross section of the sample. Therefore, the grains within the EBSD map may have originated from different depths into the material. Analysis of the GB misorientations along the crack path was therefore performed in the reverse order: EBSD maps were collected, the sample failed by SCC, and the crack path was determined by comparing pre- and post-failure SE images (Figure 7.4). By implementing this method, higher quality EBSD maps may be collected. This allowed for a unique opportunity to follow the whole length of the crack path in some instances.

GB misorientation measurements were performed along the two dominant cracks shown in Figures 7.4b and 7.5, as well as a smaller crack shown in Figure 7.6. The GB misorientation values measured along the cracks were listed in Appendix C. These values were used to produce a histogram for the cracked and non-cracked GBs, shown in Figure 7.7.

It was observed that the crack path predominantly followed high-angle GBs (HAGBs) over low-angle GBs (LAGBs) or twin GBs. However, the GB misorientation distribution should be considered within this analysis. It was found in Chapter 5 that this material contains markedly

less LAGBs, and so it is likely that less will suffer IGSCC. By comparing the histogram shown in Figure 7.7 to the GB misorientation distribution graph in Figure 5.40, it can be seen that there exists a clear preference for HAGBs or LAGBs to suffer IGSCC over twin GBs. No cracked coherent twin GBs were observed within this work. This pattern is not surprising following measurements of GB chromium depletion performed in Chapter 5. These measurements found that the HAGBs were severely depleted in chromium, whereas the measured twin GB was not.

Individual GB triple points are listed in Appendix C, where the crack progresses along one GB or the other. Excluding instances where one GB is facing in an unfavourable direction with respect to the cracking direction, in cases where both GBs are HAGBs (not including twin GBs) or both are LAGBs, it was observed that the GB with higher GB misorientation angle cracked in 50 % of instances. It is expected that higher angle GBs have higher GB energies and therefore higher propensity to suffer sensitisation and SCC [131]. However, no such preference has been observed within this work, in agreement with findings by Olmsted *et al.* [62]. Olmsted reported that GB misorientation angle alone is insufficient to determine GB energy (though at low angles it does tend towards zero) [62]. GB energy can vary between GBs with similar misorientation angles due to the differing boundary planes [62].

In cases where one GB was an LAGB, and one was an HAGB, the HAGB cracked in 33 % of cases. Cracking of LAGBs is not as expected, with some studies reporting that such GBs are very resistant, 'if not immune' [60]. Though some studies have reported cracking of LAGBs [71]. In a study by Gertsman *et al.* LAGBs in sensitised Type 304 were found to crack in high temperature water environments, though a confident conclusion could not be drawn due to the infrequency of LAGBs [71]. In this study, 10 LAGBs had cracked, out of 147 cracked GBs (with measured GB misorientations, as listed in Tables C.1-C.7 in Appendix C).

In instances where one GB was an HAGB and one was a twin GB, the HAGB cracked in 93 % of cases. In none of these cases was the cracked GB a coherent twin GB. In the single case where one GB was an LAGB and one was a twin GB, the LAGB cracked. Incoherent twin GBs that had cracked were found along the dominant crack path (Figure 7.5), rather than the smaller crack (Figure 7.6). It is possible, if these GBs are more resistant to cracking, that these boundaries cracked due to the increased local stress experienced by the GBs in the dominant crack path. The local stress values experienced at these GBs are likely higher than those experience by GBs along the smaller crack path.

Previous studies have reported that twin GBs (coincident-site lattice (CSL) $\Sigma 3$ GBs) are resistant to IGSCC [71]. It is often specified that this resistance is limited to coherent twin GBs [100]. Incoherent twin GBs (i.e. GBs with the same GB misorientation angle but a different boundary plane) have been found to have higher GB energy [62] and are susceptible to localised corrosion and cracking [60, 100]. It should be noted that this analysis does not consider higher order CSL GBs, which in some studies have been reported to have special properties [68–70]. These may influence the crack path.

During analysis of the smaller crack path, a crack tip was observed that appeared jagged, as seen in Figure 7.8. This jagged appearance suggests that cracking occurred in a stepwise fashion, i.e. that cracking initiated and passivated multiple times, rather than a smooth process. The crack path continues further up the sample indicating that the crack propagated subsurface. Due to the resolution of the EBSD maps collected the GB misorientation values in this area are not clear. An intragranular SPP is observed to the right of the crack. This SPP appears similar to an MnS precipitate observed in Chapter 5. It is possible that this SPP acted as a stress raiser, overcoming the threshold energy required to crack the adjacent GB, though not sufficient to allow for a continuous cracking process.

There are a number of parameters that may affect the propensity of a GB to suffer IGSCC, such as GB misorientation, composition, depletion profile, or local stress field [36, 68, 69, 71, 108, 134, 232]. Within this system degree of sensitisation and local stress field are considered to be key factors [103, 160, 167, 168]. The analysis presented in this section has only considered surface measurements of GB misorientation, it must be noted therefore that other factors are significant in determining the path IGSCC takes through a material, including the various parameters of subsurface GBs.

7.6.2 Crack Oxide

Within HS-AFM images and subsurface analysis the cracked GBs were observed to contain a corrosion product or an oxide layer (Figures 7.9 and 7.19). This oxide layer has not been reported previously for this SCC system (Type 304 in thiosulfate). This oxide does not uniformly fill the GB, indicating that it is porous. A porous structure is consistent with a deposited corrosion product and not a passivating oxide as observed in some high temperature systems [175, 219, 228, 229].

Chemical analysis was performed by APT on samples produced from a crack tip. An APT reconstruction of a sample that contained a section of the oxide-filled crack was produced (Figure 7.13). This reconstruction contained two distinct regions separated by a 37.7 at.% oxygen iso-concentration surface: a region of lower oxygen concentration (the bulk) and a region of higher oxygen concentration (the oxide). The oxide region of the needle appeared to contain a lower density of ions than the metallic region. This is expected to be partly due to the apparent porous structure of the oxide, and partly due to the metal and the oxide having differing evaporation fields resulting in aberrations [285].

The oxide was found to have a varying composition indicating a layered structure (Figure 7.14). The inner oxide was found to contain more chromium than the outer oxide, as indicated by a small peak in the chromium concentration profile. Layered oxides have been observed in other works, however these oxides occurred during SCC tests performed at high temperatures in simulated PWR environments [175, 223, 228, 229, 286]. Under these conditions a chromium-rich inner layer has been noted, though for chromium concentrations much higher than observed here [175, 223].

The oxide/metal interface occurs between -10 nm and 0 nm in Figure 7.14, this may be considered as the edge of the cracked GB. At this interface chromium concentration is calculated to be approximately 7 wt.%, indicating that the GB is severely sensitised. There is a nickel enrichment up to 18 at.% at the GB, which can occur during thermal sensitisation [284]. In previous works it has been suggested that sulfur can enhance dissolution of iron and nickel [147, 158, 160, 164]. As iron is more electrochemically active than nickel, it is possible that selective dissolution has amplified this nickel enrichment. However, comparing these measurements to scanning transmission electron microscopy EDX (STEM EDX) analysis performed across sensitised GBs in Chapter 5, nickel enrichment values as high as 25.32% were measured due to thermal sensitisation (Figure 5.45f).

Previous works have reported that accumulation of adsorbed sulfur at the crack tip is an important mechanism for IGSCC for this system [147, 158, 160, 164–166]. However, APT results for sulfur were not conclusive due to difficulties deconvoluting the overlap between the sulfur peak from the O_2 peak within the mass spectrum (Figure 7.15a). This has been encountered in other works [287]. Notably, 32 Da ions were identified below the apparent surface of the metal (Figures 7.15b and 7.16) which could indicate the presence of adsorbed sulfur or oxygen.

Outside of the oxide the metallic contributions are observed to rapidly reduce towards 0 at.%, and sodium concentration increases significantly. It is likely that this sodium originates from retained solution in the crack tip post-testing. This solution then evaporates leaving the high concentration observed outside of the oxide.

7.6.3 Sub-Surface Crack Propagation

Post IGSCC analysis performed by FIB milling revealed crack propagation beneath the sample surface. A network of intergranular cracks was observed ahead of the apparent crack tip seen on the surface. The extent of subsurface corrosion is likely the result of limited diffusion, this allows for a build-up of aggressive electrolyte chemistry and subsequent acceleration of corrosion processes.

An oxide layer was present on the walls of the subsurface cracks (Figure 7.19). As discussed previously in Section 7.6.2. This oxide appeared limited to the cracked GBs, rather than extending along deformation bands (as observed in some cold worked stainless steels in high temperature water conditions [219, 223, 286]).

This oxide was very thin compared to the large void left following the cracking process. In this regard, these measurements are comparable to subsurface measurements of cracking by Terachi *et al.* for a Type 316 stainless steel in PWR conditions [228]. Though SCC conditions were markedly different.

Cracks with a comparatively thin layer of oxide such as these are consistent with the propagation of the crack being stress driven. This suggests a possible mechanism where oxidation occurs ahead of the crack before being ruptured by stress. This is supported by previous HS-AFM

measurements shown in Figure 7.9, where the oxide was observed to fill the majority of the crack. These images were collected along GBs that branched away from the visible crack, and so may demonstrate a pre-oxidation phenomenon that weakens the GB allowing for a fracture to occur.

These observations illustrate the 3D nature of SCC, this should be considered during analysis by 2D surface techniques. As highlighted in previous FIB studies of SCC [124, 217, 219].

7.6.4 Comparison to Cracking In AGR Fuel Cladding

In Chapter 5, analysis was performed on a sample of ex-service advanced gas-cooled reactor (AGR) fuel cladding that had suffered SCC (Figure 5.27). The morphology of the cracks in AGR cladding is comparable to those observed in this chapter. Both systems crack along GBs with multiple branches. As with the AGR cladding sample, these cracks primarily occurred along HAGBs. However, in the AGR cladding sample, no twin GBs (coherent or incoherent) were found to have cracked. Though, due to the comparative ease of performing experimental work using non-active specimens, more cracked GBs were measured within this chapter. Thus, allowing for more significant conclusions.

In contrast to AGR cladding, IGSCC in the AISI Type 304 sample had one dominant crack. It was noted that this dominant crack likely caused the passivation of the other smaller cracks due to a change in stress state. It is reasonable to assume that without a change in stress state the smaller cracks would continue to propagate. This may be the case for systems with a more uniform constant load.

In Chapter 5, the key differences between the two materials were discussed. This included the possible differences in cracking behaviour as a result of differing SPP distributions. In the thermally sensitised sample, the GBs were decorated with GB carbide precipitates. However, irradiated samples are sensitised largely due to RIS. In this chapter, GB carbide precipitates were observed within both cracked and uncracked GBs indicating that the carbide dissolution observed in Chapter 6 was not a key mechanism for crack propagation, though a few dissolution events may have led to initiation events. As such a mechanistic link between the cracking processes in the thermally sensitised sample and the irradiated sample may be established.

7.7 Conclusions

Within this chapter, a number of complementary ex-situ techniques were combined, including: HS-AFM, APT, FIB and SEM methods. It was demonstrated that by combining these techniques, a more comprehensive analysis of the IGSCC processes occurring was achieved across a range of length-scales. The following conclusions may be drawn from this work:

- Failure by IGSCC indicated the presence of continuous networks of susceptible GBs within this material.

- Cracking initiated in the central region of the sample, where stress and strain are localised. These regions also showed a discolouration in the regions surrounding the crack due to oxidation processes.
- GB carbide precipitates were present in cracked GBs, indicating that dissolution of these features was not a prominent process during IGSCC. It is possible that dissolution or modification of a few GB carbide precipitates may have led to sufficient stress accumulation resulting in crack initiation or propagation.
- Crack bridges were observed, both intact at the crack tip and ruptured following sufficient crack propagation. Such features are known to reduce crack velocity.
- Cracking was found to passivate at GB triple points or GB carbide precipitates, as additional energy is required to rupture certain GBs or precipitates.
- GB misorientations measured along the crack path showed the following behaviours: Firstly, HAGBs cracked preferentially, however no preference was observed between HAGBs with higher GB misorientation angle. Secondly, no coherent twin GBs were cracked during IGSCC, indicating a resistance of coherent twin GBs to cracking. Conversely, incoherent twin GBs were susceptible to cracking, though this may be limited to the dominant crack path where stress is localised. Lastly, LAGBs were measured along the crack path, demonstrating that these boundaries were not immune to cracking.
- Sub-surface crack propagation is evident at the crack tip, where limited diffusion leads to a build-up of aggressive chemistry within the occluded crack interior.
- An oxide layer was present along the cracked GBs. This oxide had a layered structure. The outer oxide layers appeared porous, resulting in retained solution following experimental work.
- Possible sulfur or O_2 signals were detected below the crack wall surface, possibly indicating sulfur adsorption, though additional work is required to deconvolute the overlapping signals.
- The subsurface oxide layer was thin compared to the crack volume, indicating that crack propagation was stress driven.
- A possible mechanism was proposed where oxidation occurs ahead of the crack before being ruptured by stress.
- Cracks formed in thermally sensitised AISI Type 304 stainless steel were compared to cracking in ex-service irradiated AGR fuel cladding. Similarities were found in their morphologies and cracking modes.

In Chapter 8 the SCC system analysed in this chapter (thermally sensitised AISI Type 304 stainless steel in aqueous sodium thiosulfate) using various ex-situ methods, is observed by in-situ HS-AFM. The requires the development of a methodology such that SCC can be initiated in a predictable and reproducible manner. An experimental set-up is also designed that is compatible with in-situ HS-AFM measurements. This set-up and methodology is then applied for in-situ measurements of the effects of applied tensile stress, crack initiation, and crack propagation, with the aim of better understanding the nanoscale mechanisms of SCC.

CHAPTER 8

IN-SITU OBSERVATIONS OF IGSCC BY HIGH-SPEED AFM

So which factor decided where the crack led?
Was it the oxidised grain boundary that ruptured ahead?
So many of the details you are left to infer
Surely the solution is to watch it occur

Stress corrosion cracking (SCC) is known to occur in combinations of three conditions: a susceptible material, a corrosive environment, and sufficient tensile stress. By combining these factors, tests can be designed for the investigation of SCC. Methods in which SCC can be imaged non-destructively and in-situ are of particular importance for the understanding of the physical mechanisms occurring [40]. However, SCC is a stochastic process, so the time taken for initiation to occur can vary considerably, adding difficulty to in-situ observation. For this reason, work aimed to produce a recipe such that SCC could be induced more reliably for ease of data collection. In the first part of this chapter, methodology for reproducible in-situ SCC measurements by high-speed atomic force microscopy (HS-AFM) is developed. This includes optimisation of the experimental set-up. The second part of this chapter implements the developed methodology in order to measure microstructural changes to the surface that occur during intergranular SCC (IGSCC).

This chapter includes figures and large sections of text taken directly from the following papers:

- **S. Moore**, R. Burrows, D. Kumar, M. B. Kloucek, A. D. Warren, P. E. J. Flewitt, L. Picco, O. D. Payton, and T. L. Martin, Observation of Stress Corrosion Cracking of Stainless Steel Using Real-Time In-Situ High-Speed Atomic Force Microscopy and Correlative Techniques.

Npj Materials Degradation, 2021, 5(3).

- **S. Moore**, R. Burrows, L. Picco, T. Scott, A. Laferrere and O. Payton, Investigating Corrosion Using High-Speed AFM, EUROCORR 2017 PROCEEDINGS.

8.1 Materials

All samples described within this Chapter were cut from a sheet of thermally sensitised American Iron and Steel Institute (AISI) Type 304 stainless steel as described in Section 5.1.2 and prepared as described in Section 4.2.

8.2 Experimental Design For The Study of SCC By HS-AFM

8.2.1 HS-AFM Strain Rig Design

Sustained tensile stress can be imparted to a material in various different loading modes. The implemented test method is typically determined by the application of the material under investigation, as well as the property being measured; methods include [40, 288]:

- Bent-beam (two-, three- or four-point loaded, or welded double-beam)
- U-bend
- C-ring
- Double cantilever beam
- Compact tension specimens
- Slow strain rate

The HS-AFM uses a stage scanning design, as such the weight and size of the sample should be minimised in order to prevent imaging artefacts or loss of resolution. The set-up should also keep the sample secured as loose or moving parts may interfere with imaging. Considering this, for optimal imaging quality the final strain rig design should be physically small, lightweight, and rigid. Additionally, the sample should be held securely and in such an orientation that measurements may be made by cantilever from above. Following these criteria, micro three-point strain rigs were designed such that samples could be imaged under tensile stress, such as the cylinder three-point strain rig shown in Figure 8.1 and the triangle-edge three-point strain rig shown in Figure 8.2. Multiple similar designs were developed to accommodate for different sample sizes and shapes. An advantage of the three-point bend design is that the strain is localised, and the area of peak stress is small. Consequently, the area expected to suffer SCC is minimised, compared to other designs such as slow strain rate, outlined in Figure 8.2b.

An additional design consideration for in-situ SCC experiments is the environment in which measurements are performed. Within this work a liquid environment is required, this may be achieved by imaging the sample within a liquid meniscus, as with localised corrosion measurements performed in Chapter 6. Liquid imaging is performed using a liquid cell with a contact-mode MSNL cantilever (Bruker, USA), shown in Figure 8.1d and 8.2c-e. The triangle-edge rig incorporates a liquid bath for ease of liquid imaging (Figure 8.2).

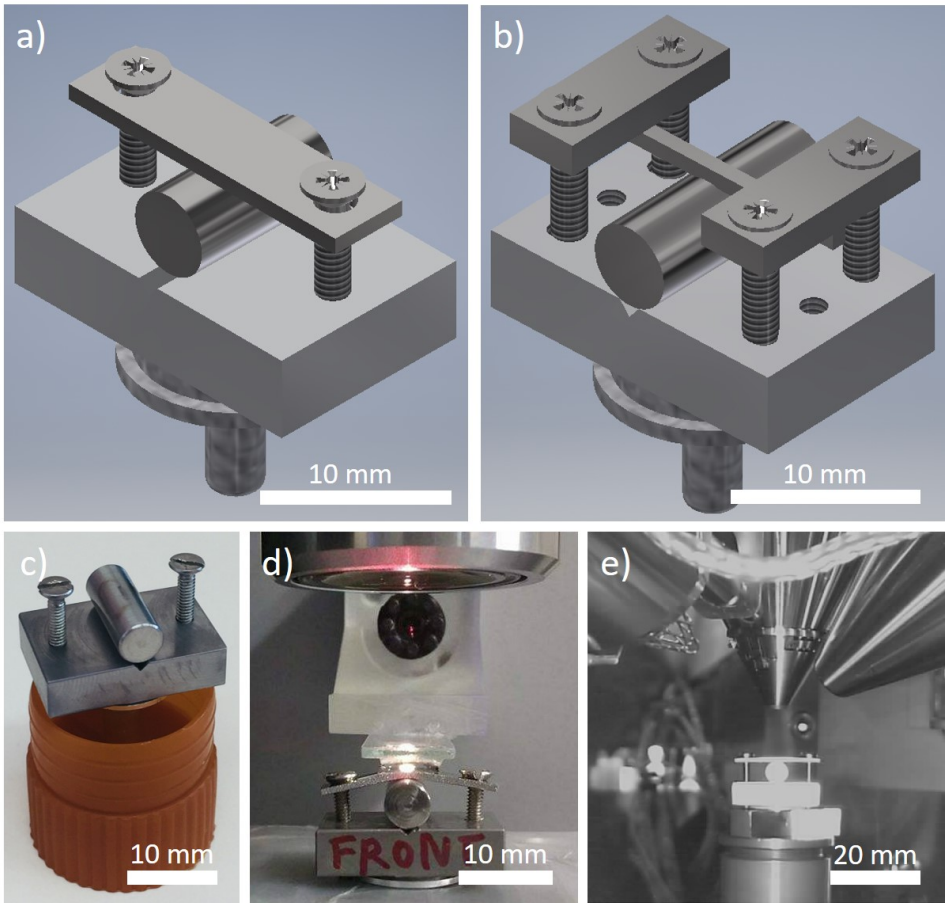

Figure 8.1: The cylinder three-point strain rig. Schematics created using Autodesk Inventor 2019 showing: a) the three-point strain rig design, and b) the three-point strain rig altered to hold thinner samples. Also, optical images showing: c) the rig without a sample, d) the HS-AFM set-up in an aqueous environment, and e) the scanning electron microscope (SEM) set-up.

Figure 8.3 shows the various sample shapes used within this study and their dimensions. Smaller samples were chosen to reduce the total weight, as well as the area in which failure could occur making in-situ measurements easier. Smaller samples are ideal for SCC testing as they initiate and fail by SCC more rapidly. A notch in the surface of the material acts as a stress accumulator, such as for Type E and F sample shapes (Figure 8.3).

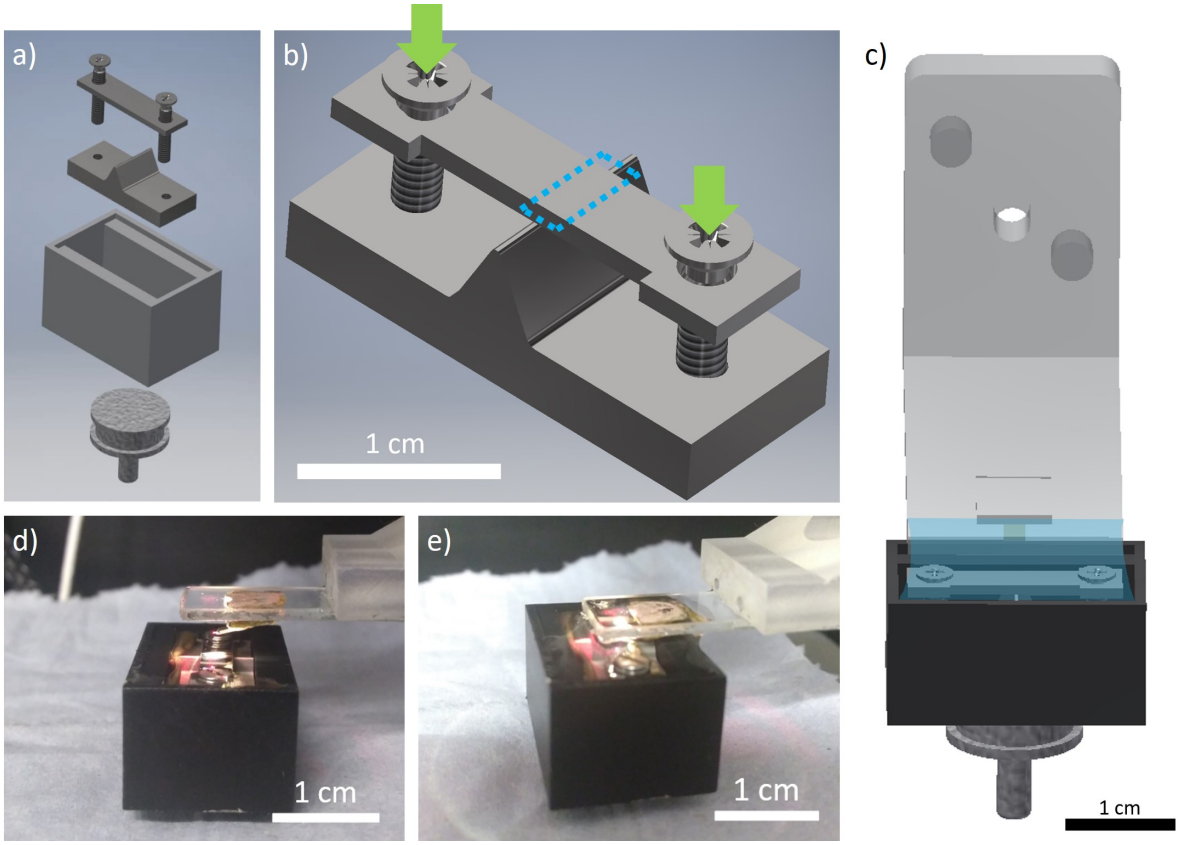

Figure 8.2: The triangle-edge three-point strain rig. Schematics showing: a) an exploded view showing the sample, rig, and bath set-up, b) the three-point strain rig design with the typical area imaged outlined with a dotted blue box, and c) the HS-AFM SCC set-up with strain rig, bath, and liquid cell where the liquid is represented in blue created using Autodesk Inventor 2019. Also shown are optical images of the HS-AFM set-up: d) without an aqueous environment, and e) with an aqueous environment.

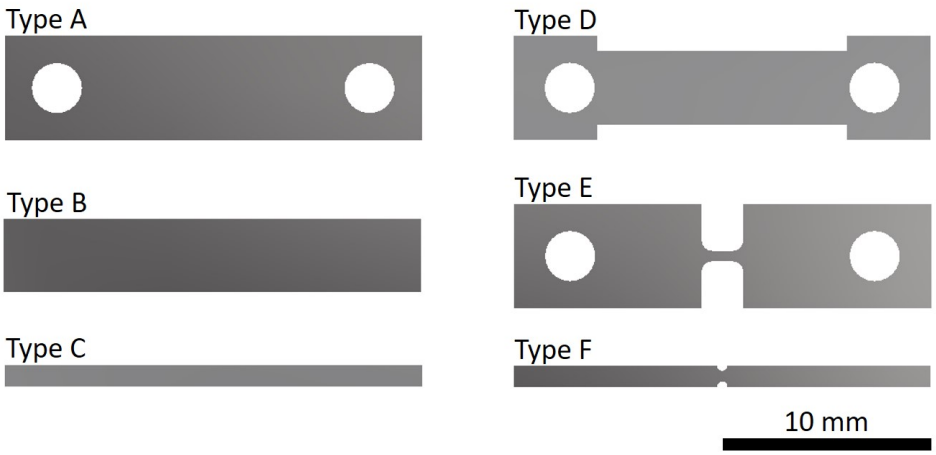

Figure 8.3: A schematic showing the dimensions of the different sample shapes used within this work. Type A, B and C are rectangular samples. Type D, E and F are dog-bone type samples. All samples are cut from a 1 mm metal sheet.

8.2.2 Modelling Stress

Applied load on the specimen can be altered by tightening or loosening the bolts on the three-point strain rig, resulting in a change in the vertical deflection of the specimen [288]. Elastic stress at the midpoint, σ, can then be calculated using the following equation:

$$\sigma = \frac{6EtY}{L^2} \tag{8.1}$$

Where E is the elastic modulus of the material, t is the sample thickness, Y is the maximum sample deflection, and L is the distance between outer contacts, as shown in Figure 8.4 [288–290].

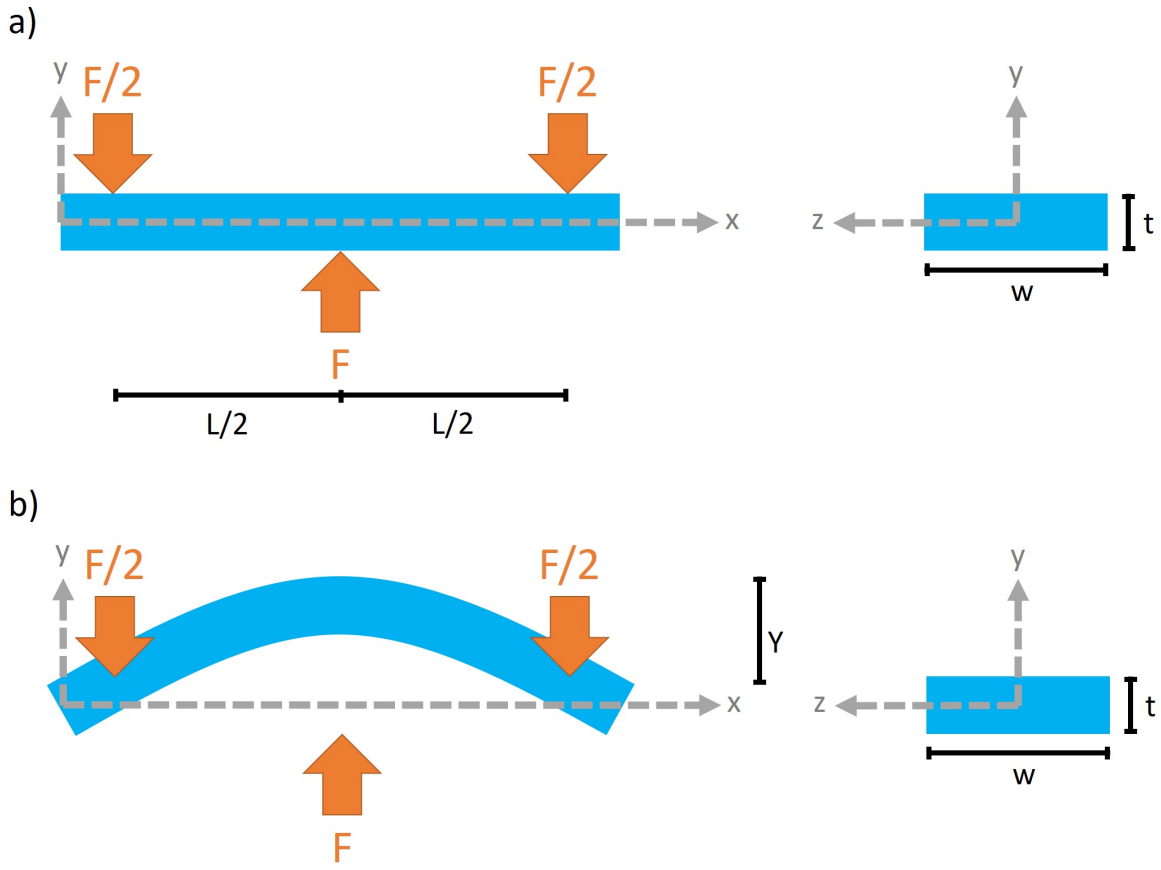

Figure 8.4: Schematics of a specimen with forces applied when stressed on a three-point strain rig: a) before deflection, and b) after deflection where F is the applied load. Labels indicate specimen thickness, t, specimen width, w, distance between outer contacts, L, and maximum deflection, Y. Axes x, y and z are also shown.

Within SCC tests, the material is deflected sufficiently past the yield stress of the material, such that the sample is plastically deformed. In this case the maximum stress is equivalent to the yield stress of the material and equation 8.1 is no longer relevant. However, strain will continue to increase as the sample is further deformed. This may be calculated simply by measuring the

extension; however, this strain will be localised in the central region of the sample as the specimen is not uniformly deformed. In order to estimate the maximum strain, the system was modelled using Autodesk Inventor Professional 2019 in the static stress environment. This environment uses the following assumptions:

- The deflection and resultant stress are linearly proportional to the applied load.
- The material does not yield.
- Loading is static and slowly applied.
- Temperature is not considered.

All models were constrained by a tangent relationship with the cylinder/bend edge of the strain rig. The sample material within these models was specified as an austenitic stainless steel, with specifications listed in Table 8.1.

Table 8.1: Mechanical properties of built in austenitic stainless steel used in the Autodesk Inventor Professional 2019 models and the same quantities specified for AISI Type 304 stainless steel.

	Model	AISI Type 304 Specifications	Units
Young's Modulus	190.30	190.00	GPa
Poisson's Ratio	0.3	0.29	-
Shear Modulus	85.98	86.18	Gpa
Density	8.03	8.03	g cm^{-3}
Yield Strength	0.23	0.22	GPa
Tensile Strength	0.54	0.50	GPa

Figure 8.5 shows a model for the Type A sample shape placed on the cylinder three-point strain rig shown in Figure 8.1 deflected by 1 mm. It can be seen that stress and strain are localised in the central 5-10 mm region of the specimen. It is also observed that there are two regions either side of the centre of the specimen where stress and strain are greatest.

The maximum deflection achievable within this rig design is approximately 3.9 mm, as the distance from the top of the cylinder to the base of the rig is 4.9 mm and the sample is approximately 1 mm thick. Stress and strain at 1 mm deflection and 3.9 mm deflection (maximum) are summarised in Table 8.2.

Figure 8.6 shows a model for the Type A sample shape placed on the triangle-edge three-point strain rig shown in Figure 8.2. The area of maximum stress and strain is more localised for this strain rig as the sample is bent over an edge with radius 0.25 mm, rather than a 5 mm diameter cylinder. The maximum deflection possible within this rig design is approximately 2.69 mm, as the distance from the top edge to the base of the rig is 3.69 mm. Stress and strain values are summarised in Table 8.2.

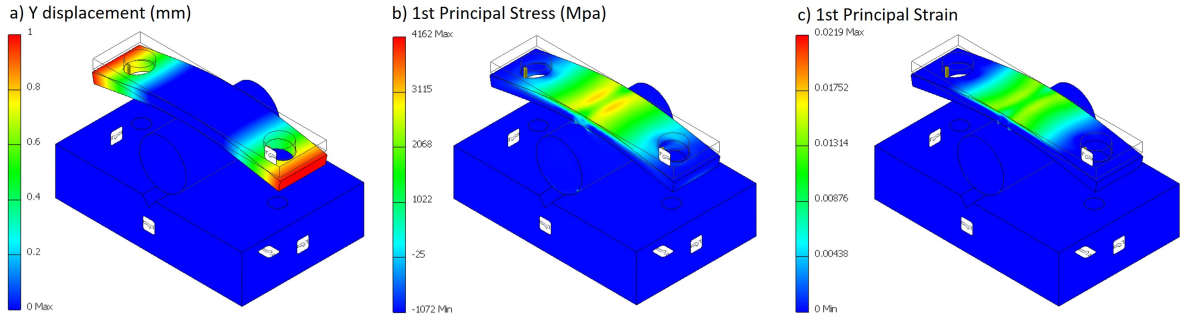

Figure 8.5: Model results for a Type A sample shape deflected by 1 mm in the cylinder three-point strain rig showing: a) Y displacement in mm, b) 1st principal stress in MPa, and c) 1st principal strain.

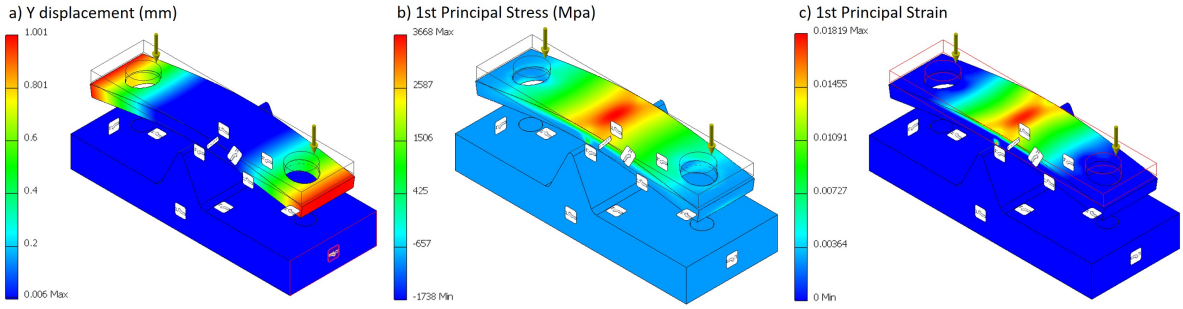

Figure 8.6: Model results for a Type A sample shape deflected by 1 mm in the triangle-edge three-point strain rig showing: a) Y displacement in mm, b) 1st principal stress in MPa, and c) 1st principal strain.

Table 8.2: Maximum 1st principal stress and strain values for the models shown in Figures 8.5 and 8.6.

	1 mm Deflection		Max Deflection	
	Stress (GPa)	Strain	Stress (GPa)	Strain
Cylinder three-point strain rig	4.162	0.0219	16.226	0.08539
Triangle-edge three-point strain rig	3.668	0.01819	9.860	0.04888

8.2.2.1 Effect of Sample Shape

The dimensions of the sample must be considered when applying SCC tests as results are influenced by cross-section [288]. In the same manner as previous, models were produced for each sample type (as described in Figure 8.3) by Autodesk Inventor Professional 2019 using the static stress environment.

Figure 8.7 shows models produced for each sample shape (as in Figure 8.3) deflected by 1 mm on the triangle-edge strain rig. Maximum 1st equivalent stress and strain values are given in Table 8.3. It can be seen that the maximum 1st principal strain is more localised in the Type D-F

samples compared to the Type A-C samples.

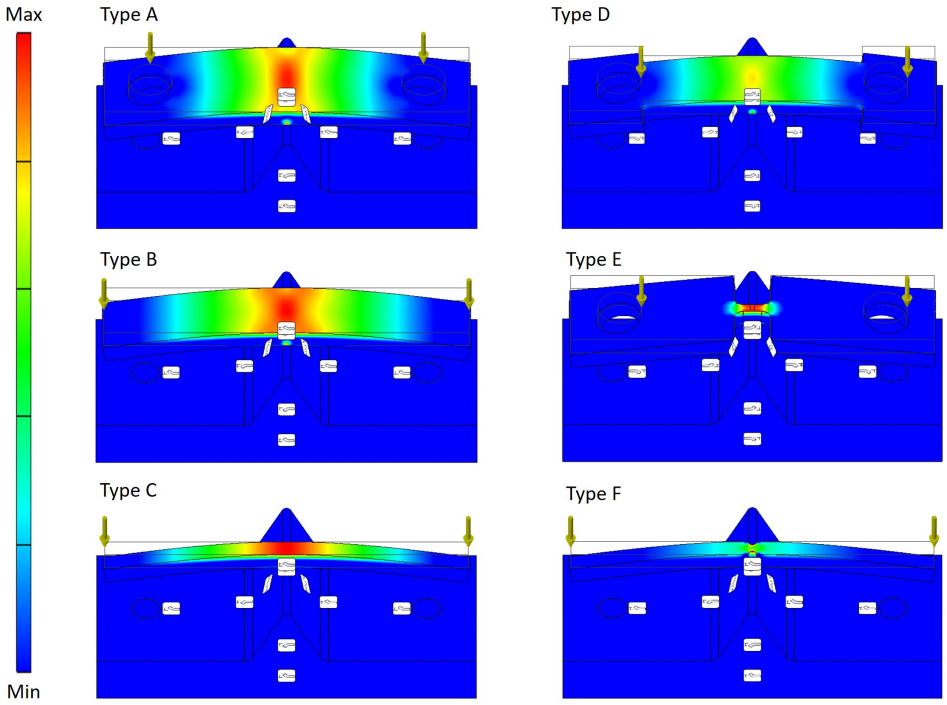

Figure 8.7: Model results showing 1st principal strain for each sample shape (as in Figure 8.3) deflected by 1 mm in the triangle-edge three-point strain rig. The minimum equivalent strain values for all sample shapes was 0 and max values are indicated in Table 8.3.

Table 8.3: Maximum 1st equivalent stress and strain values for the models shown in Figure 8.7.

	Stress (GPa)	Strain
Sample Type A	3.668	0.01819
Sample Type B	3.051	0.01518
Sample Type C	2.808	0.01472
Sample Type D	4.406	0.02147
Sample Type E	8.256	0.04263
Sample Type F	5.819	0.02880

Figure 8.8 shows optical images of a Type E sample following deflection on the triangle-edge three-point strain rig. Numerous slip bands are observed on the surface as a rough surface texture, Figure 8.8. The transition from rough to smooth surface texture (Figure 8.8b) demonstrates that this effect is limited to the central region of the sample, in agreement with the model results.

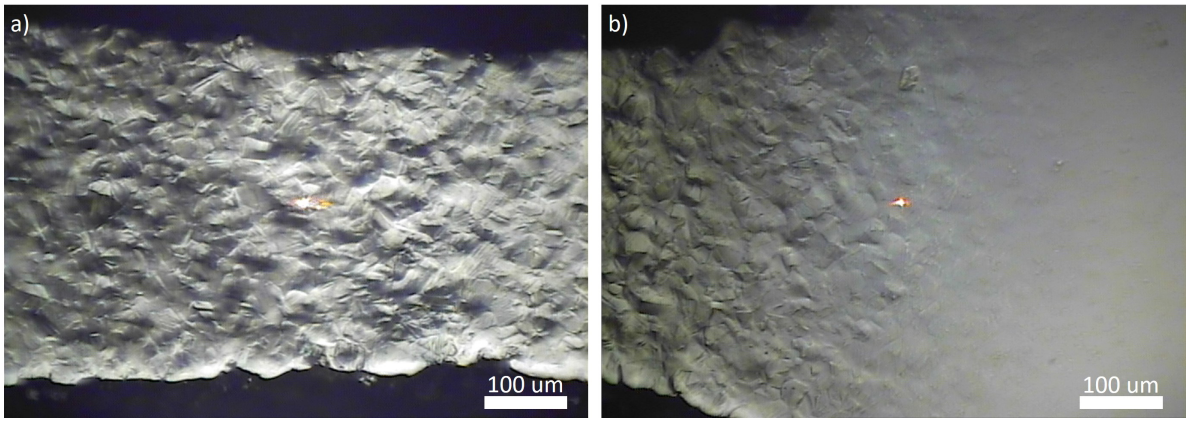

Figure 8.8: Optical images showing a rough surface texture on the sample surface of a Type E sample: a) in the centre of the sample where deflection is greatest, and b) at the edge of the sample where stress and strain decrease rapidly.

8.2.3 Optical Monitoring and the Effects of Pre-Exposure

Optical techniques can be used to yield visual information about what changes are taking place on the surface of a material during SCC tests. The data gained from this is useful within HS-AFM monitoring experiments, providing information about which areas to monitor on the sample surface and what optical events indicate the onset of SCC.

Samples of thermally sensitised AISI Type 304 stainless steel were pre-exposed to a solution of 395 mg L^{-1} $Na_2S_2O_3$ prior to deflection on a three-point strain rig. Samples were then monitored optically, as shown in Figure 8.9.

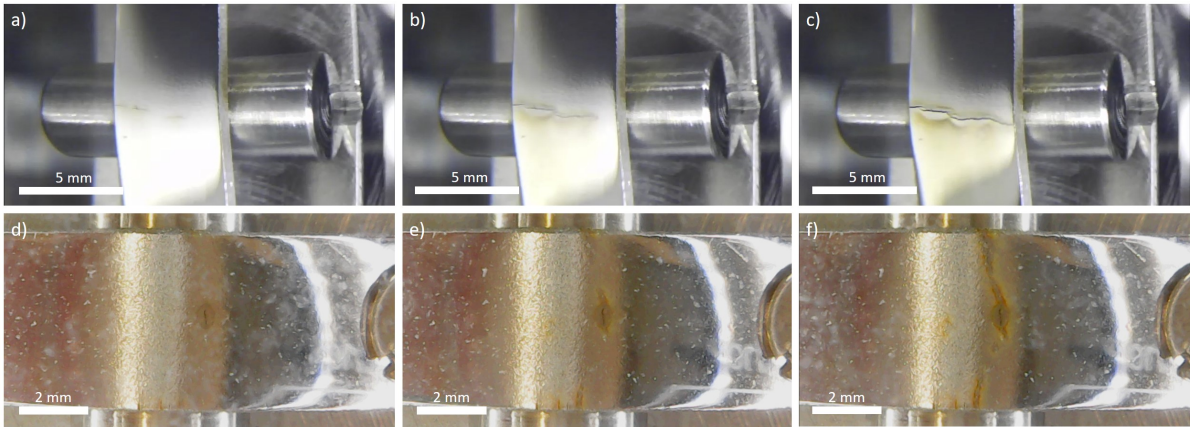

Figure 8.9: Optical images showing Type A samples of thermally sensitised AISI Type 304 stainless steel failing by SCC in a solution of 395 mg L^{-1} $Na_2S_2O_3$. a)-c) show one sample over a duration of approximately 2 days, and d)-f) show another sample over a duration of approximately 1 day.

The time to initiate was found to vary significantly with pre-exposure to 395 mg L^{-1} aqueous

$Na_2S_2O_3$. A series of experiments were performed where samples of thermally sensitised AISI Type 304 stainless steel were pre-exposed to a solution of 395 mg L^{-1} aqueous $Na_2S_2O_3$ for various durations prior to the application of stress. The results of these tests are summarised in Figure 8.10.

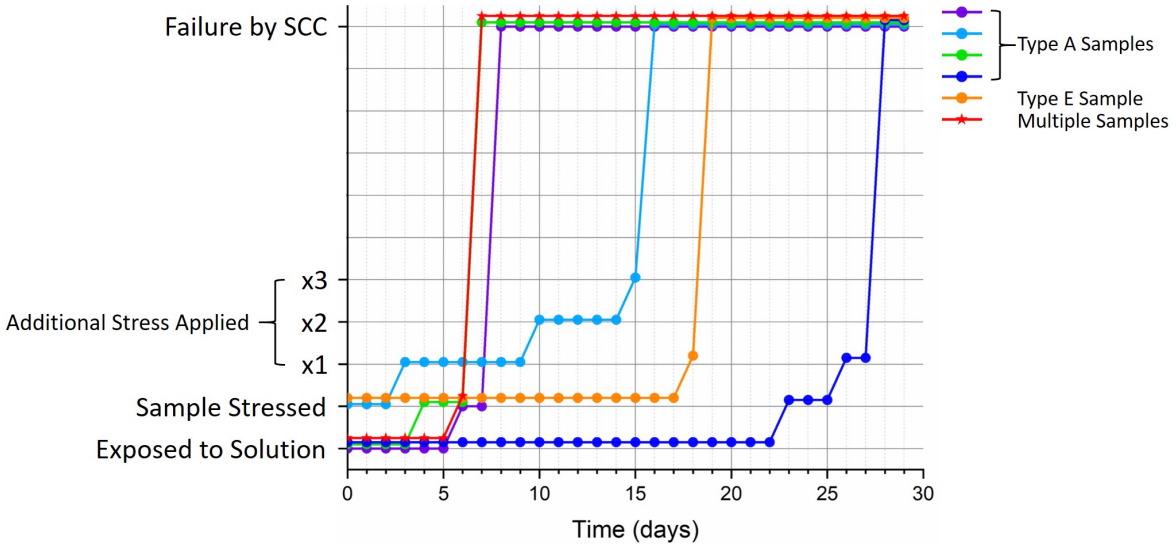

Figure 8.10: A graph showing the time to failure by SCC for various conditions explored. The y axis begins at the initial exposure to 395 mg L^{-1} aqueous $Na_2S_2O_3$, the next step refers to initial deflection of the sample, with additional steps referring to further deflection of the specimen, and the final step showing failure by SCC. Different line colours refer to different conditions. Red indicates a method trialled multiple times on different samples including: two Type D samples, two Type E samples and one Type F sample.

8.2.4 Ex-Situ HS-AFM Measurements

A cracked sample was imaged in air by HS-AFM immediately following failure by SCC whilst still within the strain rig, as seen in Figure 8.11. Figure 8.12 shows HS-AFM topographic images collected from the sample surface. A crack is observed in Figure 8.12a extending from the top to the bottom of the frame. Figure 8.12b appears to contain a crack tip at the top of the frame. A topographic image collected from a region away from the crack is shown in Figure 8.12c.

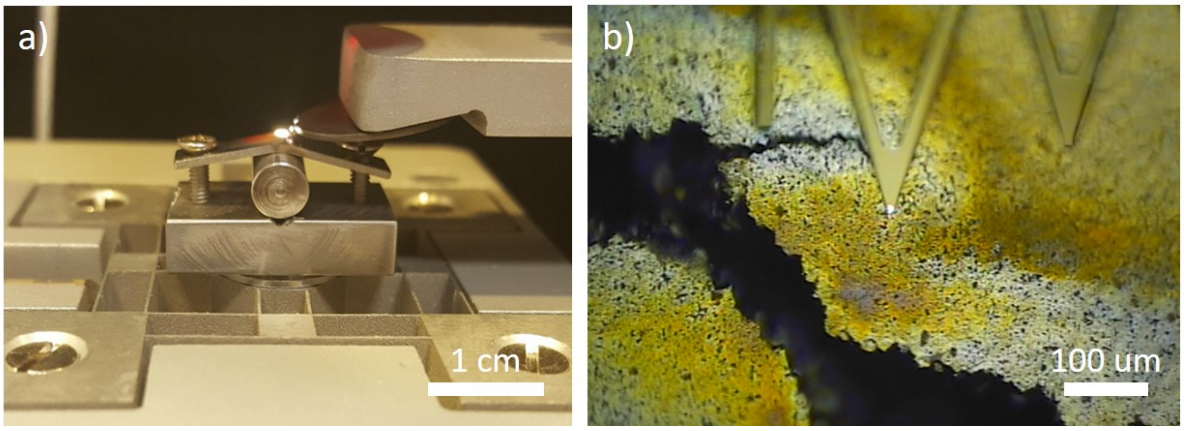

Figure 8.11: Optical images showing: a) a cracked sample on the cylinder three-point strain rig on the HS-AFM stage, and b) the sample surface as it is imaged by HS-AFM.

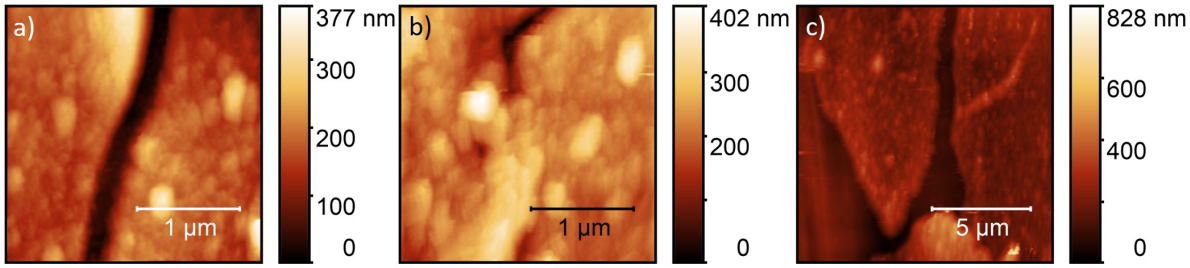

Figure 8.12: HS-AFM topographic images showing: a) a crack, b) an arrested crack tip, c) cracks in the surface oxide layer.

8.3 Discussion: Experimental Design

8.3.1 Strain Rig Design

Two strain rig designs were developed for in-situ SCC studies that fulfilled the criteria for optimal HS-AFM analysis, shown in Figures 8.1 and 8.2. In circumstances where a liquid environment is required for an extended duration, i.e. hours or days, the triangle-edge three-point strain rig shown in Figure 8.2 is preferred as the bath design allows for easy transfer between the HS-AFM stage and a beaker of solution.

Modelling of the different strain rigs highlighted differences in their design. The triangle-edge strain rig created a localised stress and strain along the central area. The cylinder three-point strain rig (Figure 8.1) also created a localised stress and strain, however two areas of maximum stress and strain were highlighted by modelling (Figure 8.5). These areas occurred either side of the centre of the specimen. This is due to the deflection of the sample not following the curve of the cylinder surface, essentially creating a four-point bend.

The values listed in Table 8.2 demonstrate that as deflection is increased the maximum strain increases. The modelling assumed linear stress. In cases where the modelled value for

stress exceeds the yield stress (0.22 GPa), the material no longer behaves linearly. For this reason, the models should only be considered as indicative of the areas of maximum stress and not an accurate value. Even at a relatively small deflection of 1 mm, the central areas of the specimen were plastically stressed. Values of strain are expected to be more accurate. Within tests performed by Kloucek and Kumar these modelled results were compared to experimental values measured using a strain gauge [291]. Results demonstrated that measured values for strain were in good agreement with the values yielded from modelling [291].

8.3.2 Sample Shape

Different sample shapes were explored, shown in Figure 8.3. Models of the sample shapes were shown in Figure 8.7. The areas of highest stress and strain were limited to the central regions of the samples. This was supported by optical images of the surface following the application of stress (Figure 8.8).

It can be seen in Figure 8.7 that the maximum 1st principal strain is more localised in the Type D-F Samples compared to the Type A-C samples. This is especially evident in the model for the Type E samples, where maximum 1st equivalent strain was considerably higher than the other sample shapes for the same deflection (Table 8.3). This reduces the area in which SCC is expected to initiate. It is often the case that cracking initiates at the base of the notch where the stress in highest [33, 41, 113, 288]. However, it must be noted that by notching the surface, tri-axial stresses are introduced into the system [288]. Tri-axial stresses are not as simply modelled as uni-axial stresses and as such are difficult to accurately estimate [288].

8.3.3 Optical Identifiers of SCC

IGSCC was observed to initiate at multiple sites, before joining up or passivating resulting in one dominant crack that extends across the sample, Figure 8.9. Initiation typically occurred in the central regions of the sample where stress and strain are localised. Crack initiation caused an alteration of the stress conditions resulting in the deviation of the crack from the centre of the sample, this is typical for three-point bend set-ups [290]. A clear optical identifier of IGSCC is a discolouration surrounding the area of the crack, due to the release of corrosion products from reactions occurring at the crack tip. These features were also noted during previous optical studies in Chapter 7.

8.3.4 HS-AFM Measurements Following IGSCC

HS-AFM measurements were performed following failure by IGSCC, without re-preparation of the sample surface, Figures 8.11 and 8.12. A region containing a crack was shown in Figure 8.12a. The surface either side of the crack appeared to be covered in an oxide layer or corrosion product, visible in optical images of the surface (Figure 8.11). The crack did not appear to contain any

grain boundary (GB) carbide precipitates. A crack tip was observed in Figure 8.12b, where the crack had passivated or deflected. However, it is possible that this is not a crack tip but instead a crack with oxide obscuring the actual tip.

Figure 8.12c was collected away from the crack. This region contains a discontinuous oxide layer. Breaks in the oxide layer appear similar to IGSCC cracks and so may cause doubt during analysis, it is therefore important to consider the optical image showing the imaging region (and therefore crack location) alongside the topographic images collected.

These results should be considered during in-situ imaging of SCC. However, these images were collected following drying of the surface, the oxide/corrosion product layer may not pose a problem during in-situ imaging of the surface.

8.3.5 Sample Pre-Exposure

The time to initiate was found to vary significantly with time exposed to 395 mg L^{-1} aqueous $Na_2S_2O_3$ before the application of tensile stress. Sample pre-exposure durations were varied between 0 and 22 days in order to identify a duration that resulted in fast failure by SCC, Figure 8.10. It was found that by pre-exposing the sample to the solution for a duration of 6 days prior to plastically stressing the sample, SCC could be reproducibly initiated within 1 day of the application of stress. Subsequent failure by SCC, defined here as the time for the crack to extend across the width of the sample, occurred over the course of a few hours. Such timescales are suited for in-situ imaging by HS-AFM.

In Chapter 6, signs of possible GB oxidation were observed along selected GBs following 10 days of exposure to the solution. It is postulated that 6 days of pre-exposure is sufficient for the oxidation of a few GBs on the surface. These GBs may act as crack initiation points upon the application of tensile stress.

8.3.6 Suggested Methodology

Following this study, and with consideration to previous analysis performed within this thesis of the SCC system under investigation, the methodology for performing in-situ HS-AFM SCC tests for this particular system was developed:

- **Experimental set-up:** The triangle-edge three-point strain rig shown in Figure 8.2 is preferred as the sharper bend edge localises stress and strain. Additionally, the bath surrounding the strain rig allows for extended measurements in a liquid environment and easy transition between environments (without the sample surface drying out).

- **Sample shape:** The dog-bone type samples are optimal for localisation of strain. Samples should be cut by waterjet to avoid unnecessary stressing of the cut face. Sample surface should be prepared in such a way that stress-raising features are avoided, and HS-AFM images are clear, steps described in Section 4.2 are recommended for stainless steels.

- **Pre-exposure:** Pre-expose thermally sensitised AISI Type 304 stainless steel to 395 mg L^{-1} aqueous $Na_2S_2O_3$ for a duration of 6 days (Figure 8.13a).
- **Tensile stress:** After 6 days of exposure, apply tensile stress to the sample via three-point strain rig such that the sample is plastically stressed (1 mm deflection), and place the rig onto the HS-AFM stage whilst maintaining the liquid environment via meniscus or bath (Figure 8.13b-c).
- **Optical identifiers:** Using the HS-AFM's optical microscope, monitor the sample for discolouration or crack initiation, primarily in the central areas where stress and strain are localised.
- **Imaging locations:** Following SCC initiation lower the cantilever such that it is ahead of the tip of the crack and allow the crack to propagate through the area being imaged. Given the intergranular nature of the localised corrosion events, HS-AFM measurements should focus primarily along GBs (Figure 8.13d).

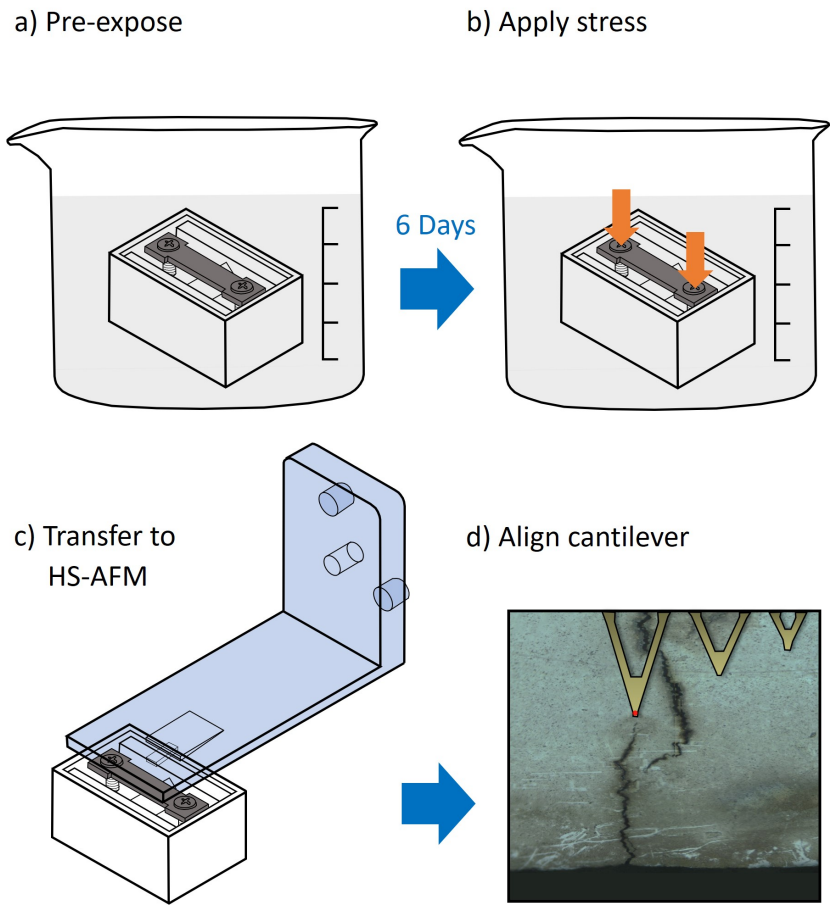

Figure 8.13: A schematic diagram demonstrating the suggested steps for in-situ SCC analysis by HS-AFM: a) pre-expose for 6 days, b) apply tensile stress, c) transfer to HS-AFM stage and optically monitor, and d) position cantilever ahead of crack tip.

8.4 In-Situ HS-AFM Measurements of Stress and IGSCC

8.4.1 HS-AFM Measurements of a Stressed Sample

To isolate the effects of stress in the absence of corrosion, a test specimen with an A Type sample shape was deflected using the cylinder three-point strain rig and imaged by HS-AFM. The specimen was stressed sufficiently to cause plastic deformation, this was achieved by deflecting the sample by 1 ± 0.01 mm, as measured with a calliper. The resultant stress was therefore equal to the material's yield stress and maximum equivalent strain was approximately 0.02.

HS-AFM measurements were collected along the midsection of the bend, in areas of maximum stress, shown in Figure 8.14. These topographic maps contain slip bands at regular intervals, with differing directions in each grain either side of the GB. In some areas the slip bands have two directions within a single grain, due to the activation of a second slip system, as observed in Figure 8.14a.

In some instances, slip band direction was observed to change in the middle of a grain due to an unsensitised GB, seen in Figure 8.14b. This is accompanied with a change in slope, topographically forming an inverted 'v' shape.

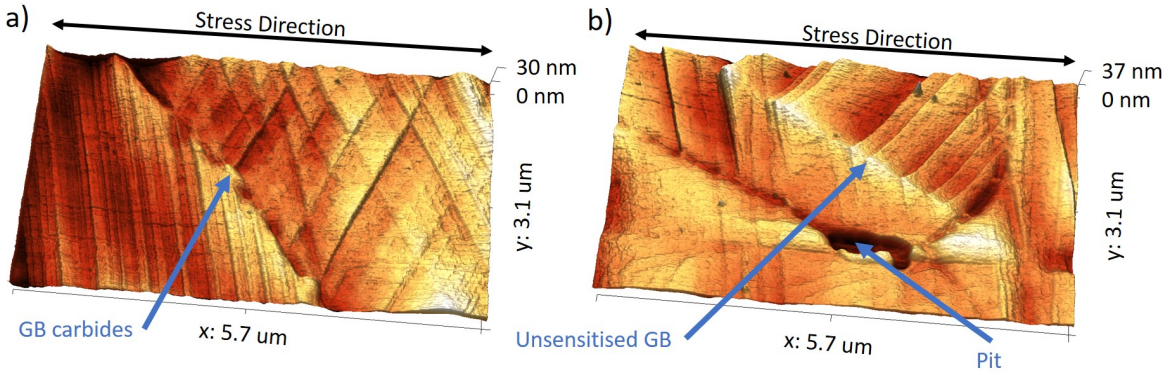

Figure 8.14: 3D HS-AFM topographic images showing: a) slip bands across a GB with GB carbide precipitates, and b) slip bands across two GB triple points, one containing a pit and one containing an unsensitised GB. Direction of tensile stress is indicated.

Line profiles showing height changes across slip bands are shown in Figure 8.15. Numerous small steps are observed with each slip band. Another periodicity is observed within some of the line profiles collected. It can be seen in Figure 8.15b that there are larger repeating peaks over length scales of approximately 300 nm, and even larger repeating peaks over 1,800 nm. The same can be observed within Figure 8.15c, where two repeating peaks are seen over approximately 600 nm.

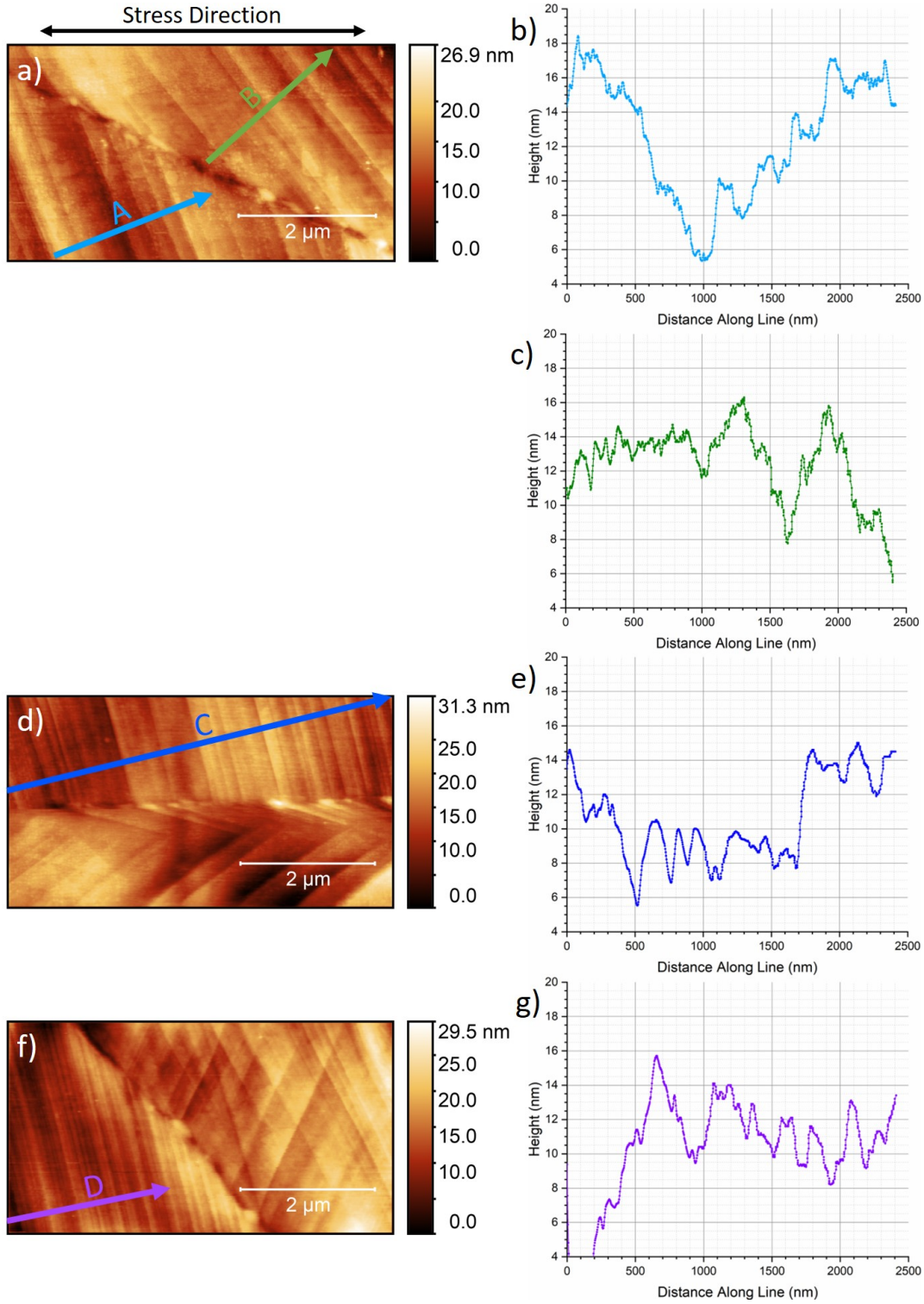

Figure 8.15: a), d) and f) show HS-AFM topographic maps collected in the central regions of a stressed specimen, also shown are line profiles showing height changes across: b) the light blue line labelled A in a), c) the green line labelled B in a), e) the dark blue line labelled C in d), and g) the purple line labelled D in f). Line profiles were collected perpendicular to the slip planes.

8.4.2 HS-AFM Measurements of IGSCC Processes

Following steps described in Section 8.3.6, IGSCC was initiated in a sample of thermally sensitised AISI Type 304 stainless steel whilst being monitored by HS-AFM. Areas undergoing cracking were identified using the HS-AFM's optical microscope and measurements were performed at, and ahead of, the crack tip.

8.4.2.1 GB Uplift

Measurements performed ahead of the crack tip revealed a phenomenon where the GB appeared uplifted in comparison to other GBs or the bulk grain, shown in Figure 8.16. Figure 8.16b contains a GB triple point where two of the GBs are uplifted and one is not.

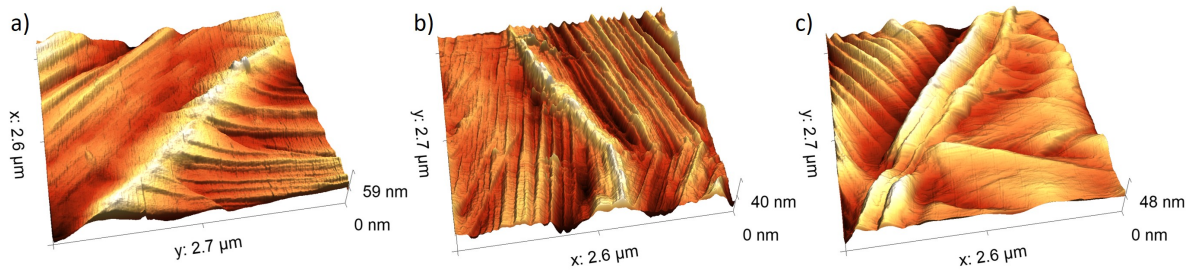

Figure 8.16: a)-c) 3D HS-AFM topographic images showing uplift effect ahead of the crack tip.

Figure 8.17 shows a GB observed ahead of the crack tip, where one section of the GB (right-hand side) is uplifted and the other section is not. Figure 8.17a shows an optical image of the surface at the time uplift measurements were performed, and Figure 8.17b shows the same area following failure by IGSCC. It can be seen that the GB sections that later fail by IGSCC are uplifted compared to those that do not.

The uplifted section of the GB in Figure 8.17c is also shown in Figure 8.18a. Two grains are observed, separated by a GB. The grain to the right of the GB contains slips bands arising from two slip systems. The grain to the left of the GB contains single slip and is uplifted at the GB compared with the grain on the right, as emphasised by the line profile shown in Figure 8.18b.

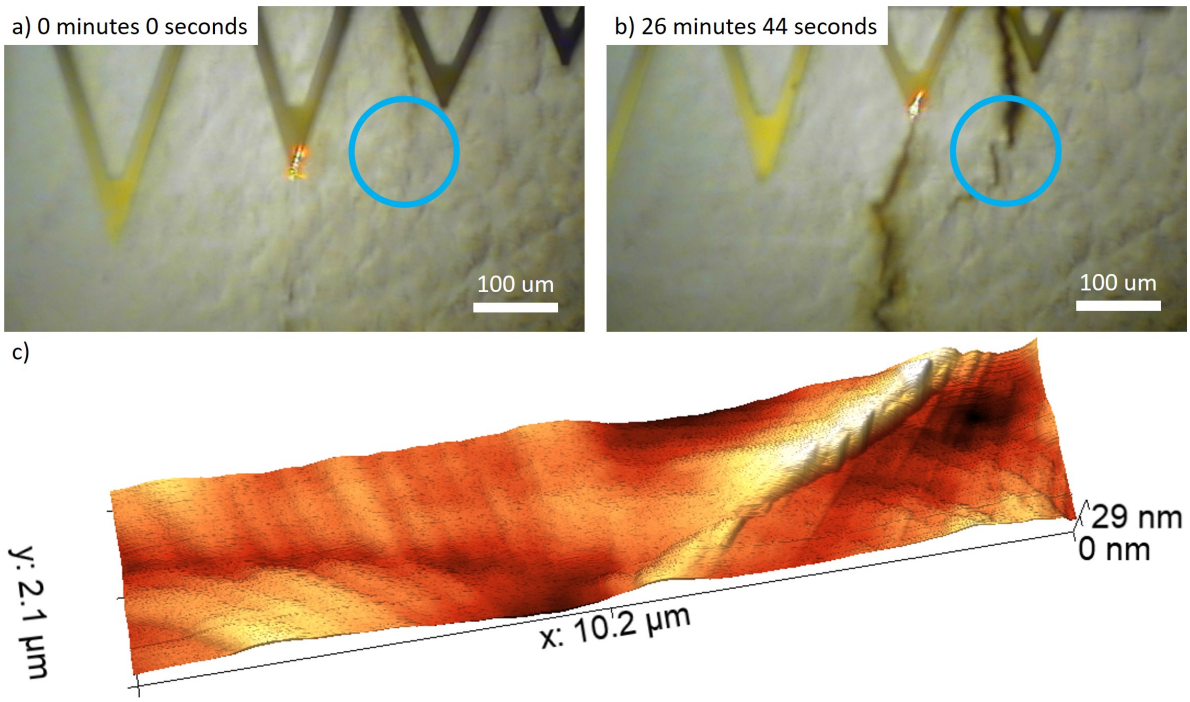

Figure 8.17: Optical images showing: a) the sample surface at 0 seconds, and b) the sample surface at 26 minutes 44 seconds, with the imaged region circled in blue. Also, a 3D HS-AFM topographic image collected at 0 seconds showing a GB that is partially uplifted. Time periods are relative to the initial frame collected.

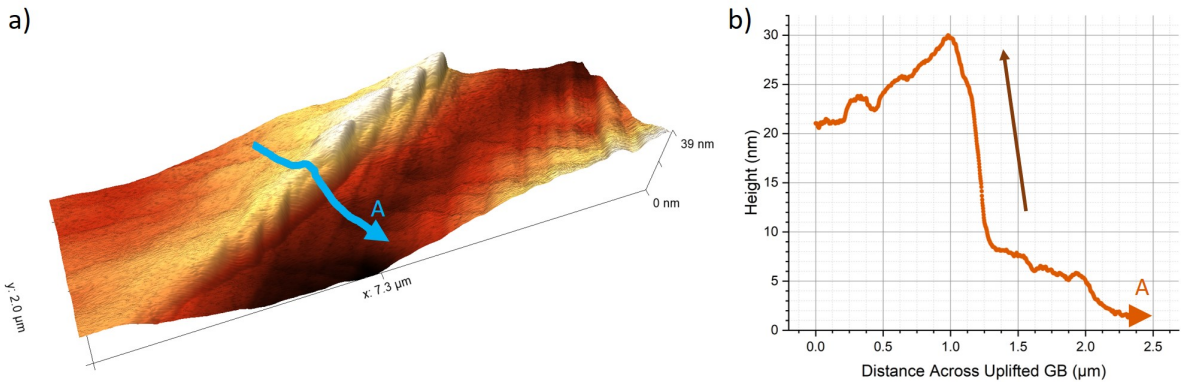

Figure 8.18: a) A 3D HS-AFM topographic map showing uplifting of a GB prior to IGSCC occurring, and b) a line profile collected across the line labelled A shown in Figure 8.18a as a light blue line demonstrating the asymmetry of the uplift effect.

8.4.2.2 Crack Propagation

Initial measurements performed near to the crack tip did not show crack propagation, examples of these measurements are shown in Figures 8.19-8.21. Figures 8.19 and 8.20 show topographic images collected across cracked GBs. Within Figure 8.19b some debris is present on the surface resulting in a loss of image quality. The crack within this image is deep and narrow resulting in tip convolution. The crack observed in Figure 8.20b is clearer than that shown in Figure 8.19b and the edges of the crack are much more defined. Figures 8.19 and 8.20 were collected from different Type E samples under the same conditions.

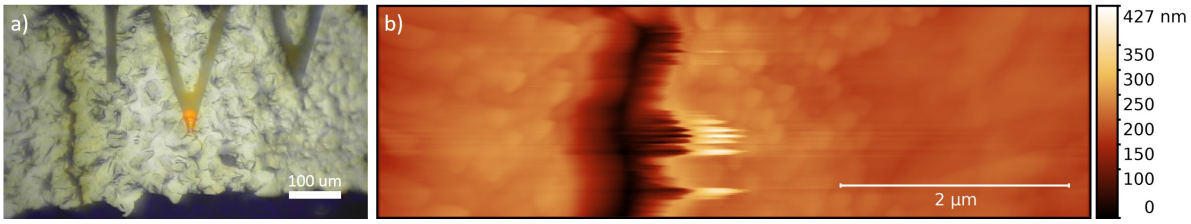

Figure 8.19: a) An optical image of the surface during HS-AFM imaging showing the position of the cantilever, b) an HS-AFM topographic image showing a crack.

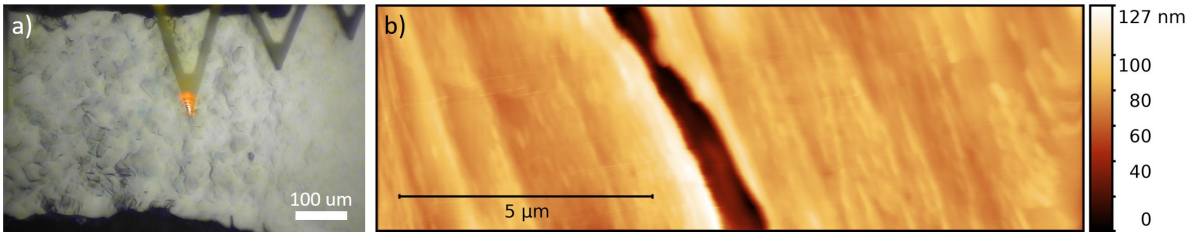

Figure 8.20: a) An optical image of the surface during HS-AFM imaging showing the position of the cantilever, b) an HS-AFM topographic image showing a crack with GB carbide precipitate.

Figure 8.21 shows a crack tip. Figure 8.21b shows the cracked GB as it reaches a GB triple point. During collection of this image, as with previous images shown in Figures 8.19 and 8.20, no crack progression was observed. Figure 8.21 was collected from the same sample as shown in Figure 8.20.

Changes to the sample surface in the stages prior to crack passivation were observed for another sample shown in Figure 8.22. Figures 8.22a-8.22g were collected over a duration of 478 seconds at a frame rate of 2 s^{-1}. During these measurements, the cantilever was positioned immediately ahead of the optically visible crack tip, shown in Figure 8.23. As the cracking process progresses a crack is observed to initiate and progressively deepen in the top edge of the frame from approximately 122 seconds. Between 406 seconds and 478 seconds (Figures 8.22f and 8.22g, respectively) no crack progression was observed, indicating that the crack passivated or deflected.

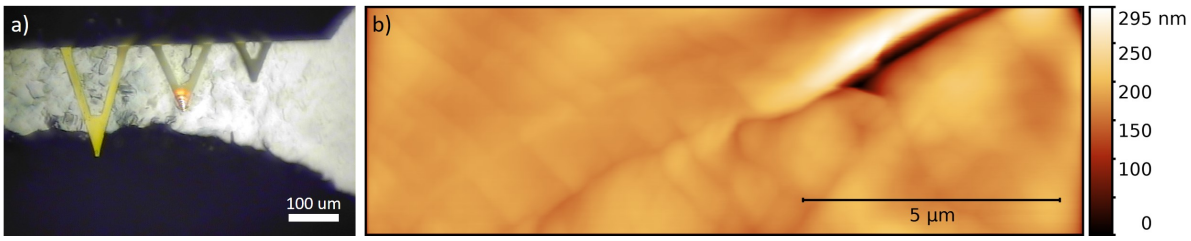

Figure 8.21: a) An optical image of the surface during HS-AFM imaging showing the position of the cantilever, b) an HS-AFM topographic image showing a crack tip.

Following the collection of the final frame shown in Figure 8.22g, HS-AFM measurements were collected moving closer to the visible crack. Topographic maps collected along this path were stitched together to form a composite image shown in Figure 8.24. In order for the cracking observed in Figure 8.22 to be the continuation of the main crack observed in Figure 8.24 subsurface crack propagation must have occurred.

HS-AFM measurements successfully showing crack propagation as it occurred are shown in Figure 8.25. The optical view of the surface during these measurements is shown in Figure 8.26. The tip of the crack is observed at the top of the frame in Figure 8.25a, leading down into a GB. This is contrary to optical images of crack propagation (Figure 8.26), where the crack is progressing upwards.

Comparing Figures 8.25b and 8.25c, the crack is observed to propagate downwards through the frame at approximately 23 nm s^{-1}. Figure 8.25d shows the crack 280 seconds after Figure 8.25a. At this point the crack extends across the whole frame. As the cracking progresses further in Figures 8.25e-g, a steady increase in crack width is observed.

In Figure 8.25 cracking has been observed as a clear crack passing through the GB. This was not always the case. In other similar measurements of crack propagation, the GB was observed to gradually come apart, as shown in Figure 8.27. Again, these images were collected ahead of the visible crack tip.

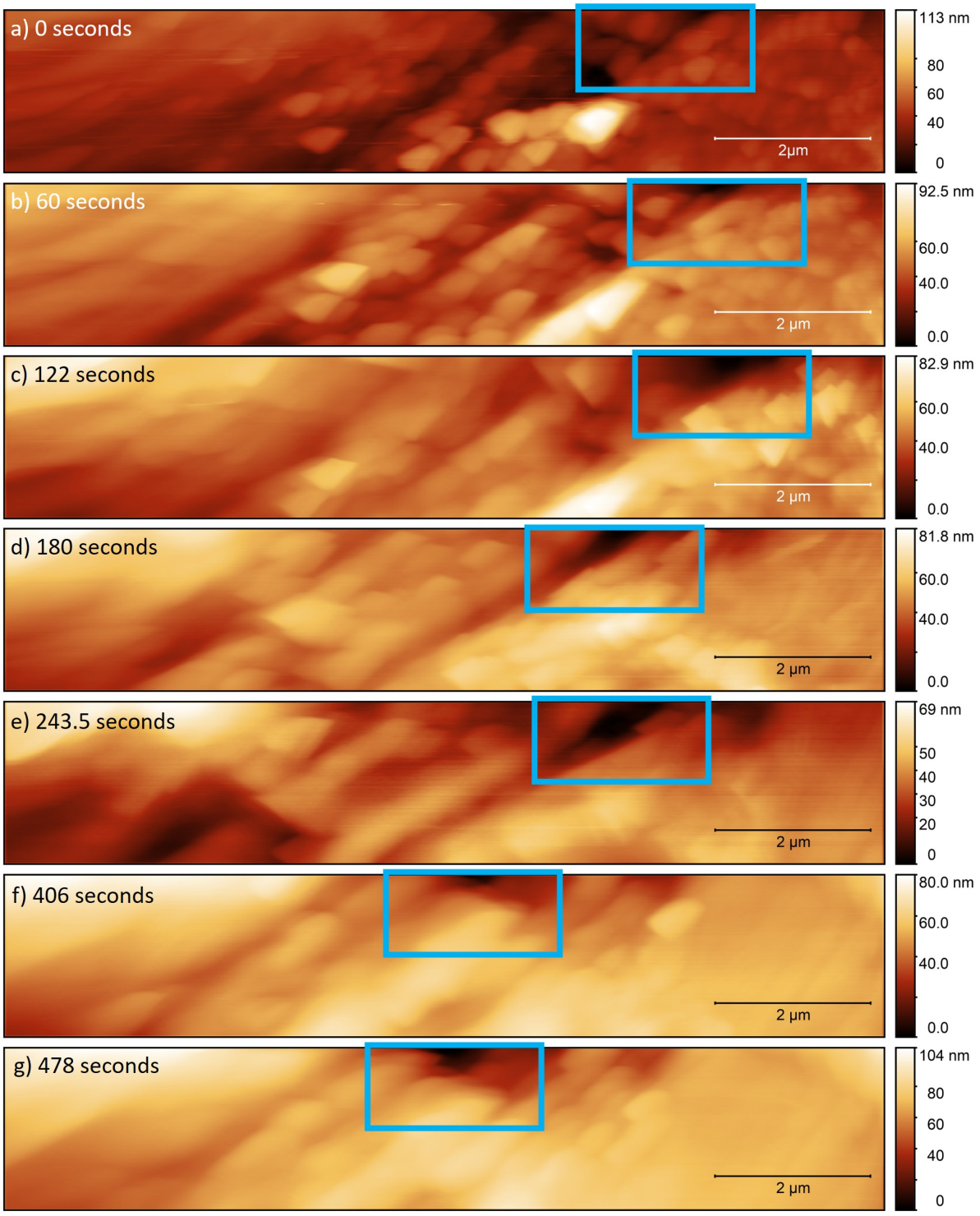

Figure 8.22: Sequential HS-AFM topographic maps showing crack propagation (crack area outlined in blue) as IGSCC occurs at: a) 0 seconds, b) 60 seconds, c) 122 seconds, d) 180 seconds, e) 243.5 seconds, f) 406 seconds, and g) 478 seconds. Time periods are relative to the initial frame collected. Each topographic map took 0.5 s to collect.

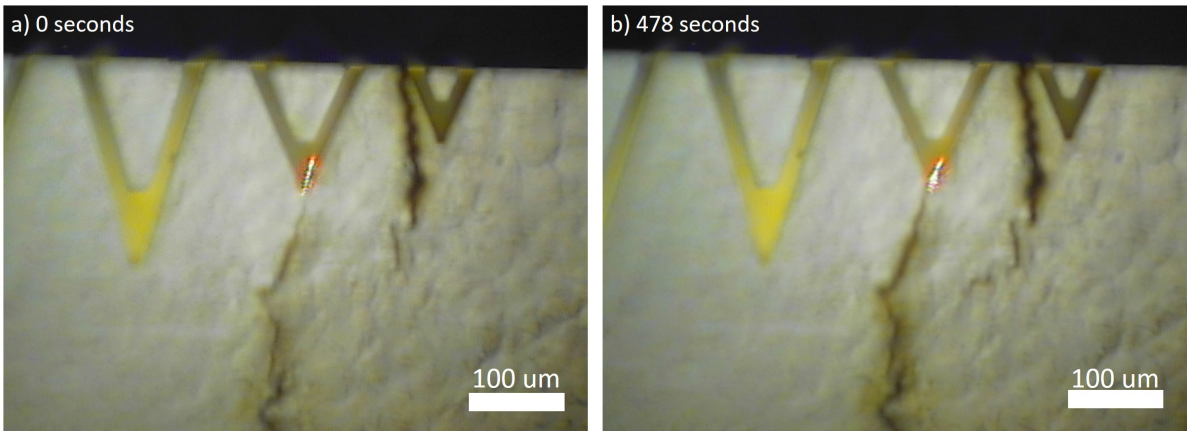

Figure 8.23: Sequential optical images of the surface during HS-AFM imaging showing the position of the cantilever at: a) 0 seconds, and b) 478 seconds, corresponding to Figures 8.22a and 8.22g, respectively.

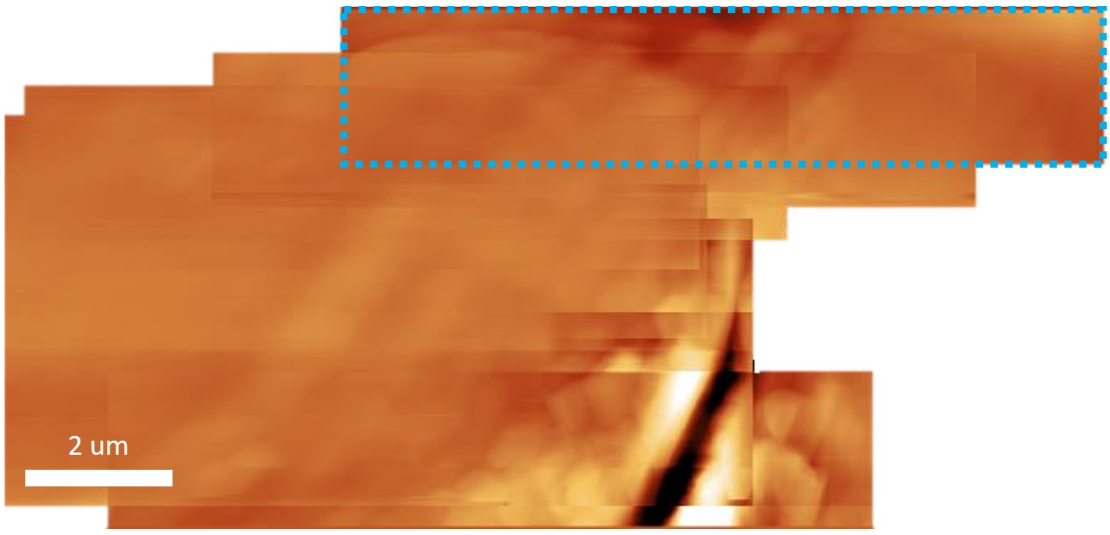

Figure 8.24: A stitched HS-AFM topographic image of the region adjacent to the region monitored in Figure 8.22, the area shown in Figure 8.22g is outlined by a dotted blue box.

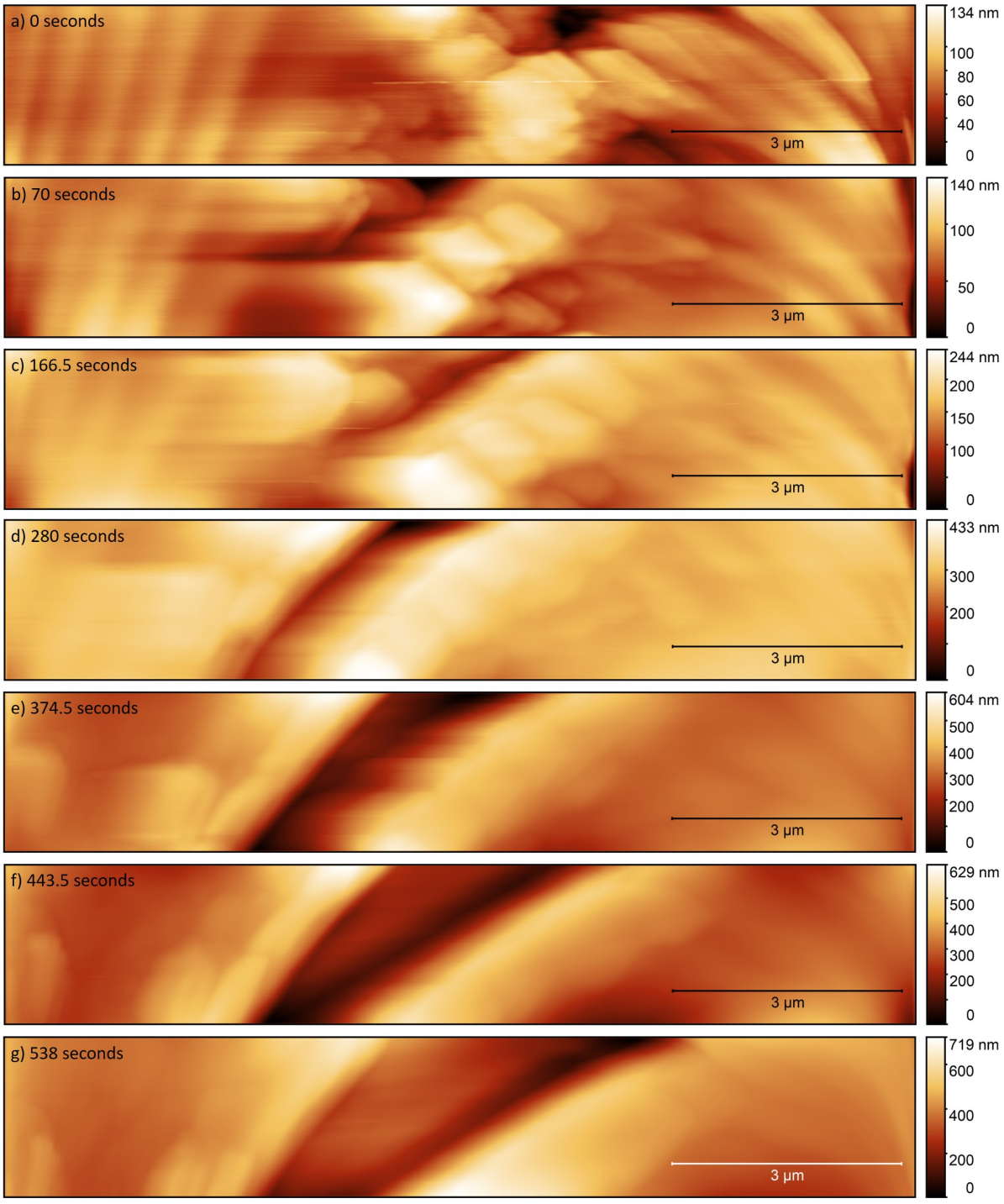

Figure 8.25: Sequential HS-AFM topographic maps showing crack propagation as IGSCC occurs at: a) 0 seconds, b) 70 seconds, c) 166.5 seconds, d) 280 seconds, e) 374.5 seconds, f) 443.5 seconds, and g) 538 seconds. Time periods are relative to the initial frame collected.

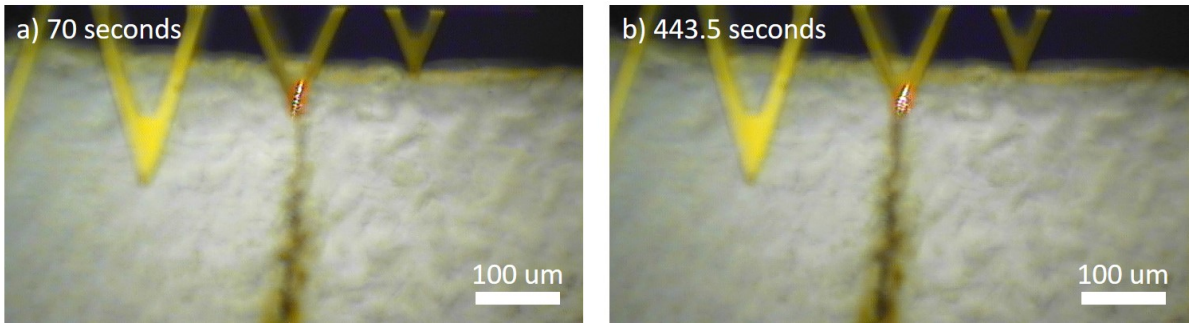

Figure 8.26: Sequential optical images of the surface during HS-AFM imaging showing the position of the cantilever at: a) 70 seconds, and b) 443.5 seconds, corresponding to Figures 8.25b and 8.25f, respectively.

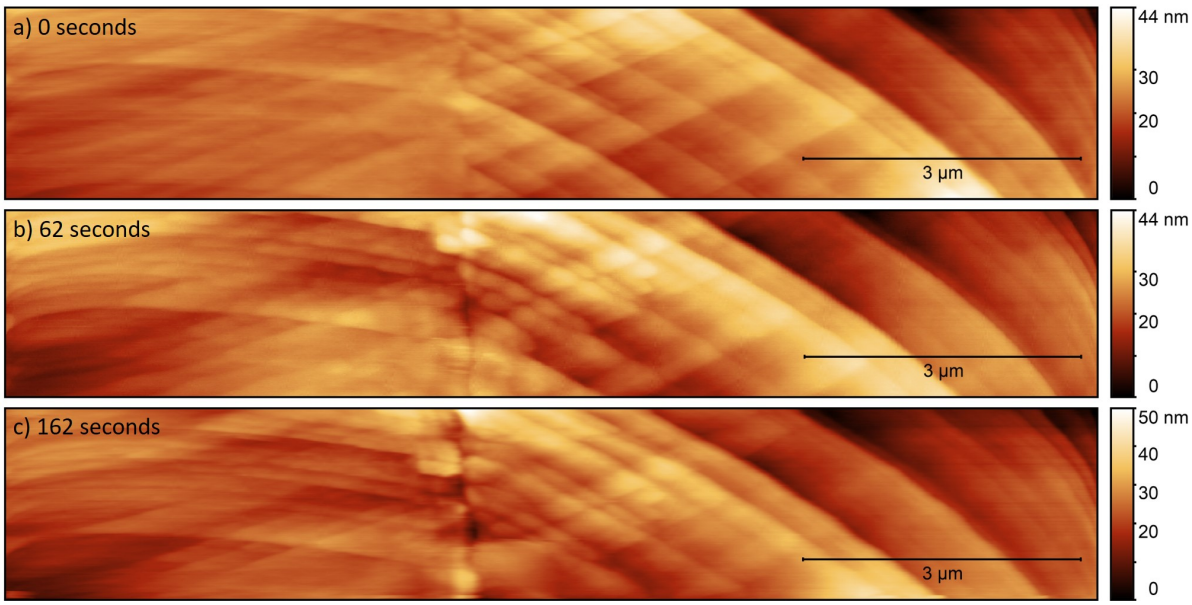

Figure 8.27: Sequential HS-AFM topographic maps showing a crack propagation as IGSCC occurs at: a) 0 seconds, b) 62 seconds, and c) 162 seconds. Time periods are relative to the initial frame collected. Each topographic map took 0.5 s to collect.

8.5 Discussion: Measurements of Stress and IGSCC by HS-AFM

8.5.1 Experimental Design

In the first part of this chapter, the considerations for the experimental design were addressed and a suggested methodology was described. The HS-AFM has some restrictions due to the nature of its operation. These restrictions were addressed, and a successful design was developed. Both three-point strain rig designs (Figures 8.1 and 8.2) were stable allowing for high quality measurements of the surface. The three-point strain rig design localised stress and strain to the central regions of the sample. This area was easily located using the HS-AFM's optical microscope and could be traversed within a matter of seconds in order to determine specific locations of interest on the surface. Utilising the method developed in Section 8.3.6, in-situ observation of IGSCC crack propagation by HS-AFM was successfully performed. These measurements were seldom obscured by an oxide or corrosion layer, as with ex-situ measurements collected following removal from the corrosive aqueous environment.

Each sample shape satisfied different criteria. The smaller sample shapes have the advantage of being fabricated with very little material, which is sometimes desirable in studies with limited material or hazardous material. Additionally, it can be easier to observe crack initiation in a specimen with a minimal area in which cracking can occur. However, the larger sample shapes result in larger distances for the crack to traverse prior to specimen failure, thereby offering more opportunity to observe crack propagation in-situ. Of all the sample shapes explored in this work Type D was found to be optimal, offering a Goldilocks type solution. In future experiments variations of the Type D sample shape should be considered, such as altering the notch dimensions.

As with previous chapters, the sample preparation method highlighted as optimal in Chapter 4 was suitable for in-situ SCC measurements. High-resolution, clear images were produced with no debris or residue from preparation. This allowed conclusions to be made without the caveat of improper sample preparation.

During in-situ HS-AFM measurements, it was noted that the image was extended in the direction of the fast scan. This letterbox effect was the result of the height and weight of the strain rig, specimen, and bath set-up. The easiest way to address this issue is to reduce the set-up weight. This may be achieved by using a different material for the strain rig. However, it is important that this material is strong enough to bend the specimen and remain stable whilst on the stage of the HS-AFM. It must also be resistant to corrosion in the environment being investigated.

8.5.2 HS-AFM Measurements of Stress

HS-AFM measurements were performed of a specimen following deflection of 1 mm on a three-point strain rig. These measurements were performed with the intention of isolating the mi-

crostructural changes that occur as a result of stress, much in the same way as that explored for the other factors that lead to SCC: susceptible microstructure in Chapter 5 and corrosive environment in Chapter 6.

Following the application of stress, measurements were performed near the apex of the bend. Slip bands forming at regular intervals were observed clearly within the grains in this region of the specimen, seen in Figure 8.14. Austenitic stainless steels are known to produce slip in the most closely packed {111} planes [138, 139] (Section 2.3.3.2). Slip bands in the same slip system were observed to change direction either side of GBs as each grain has a different crystallographic orientation. This phenomenon has been observed within other atomic force microscopy (AFM) studies of deformed austenitic stainless steels [138–140].

In some cases, slip bands were observed to form in two directions within a single grain, indicating that a second slip system had been activated, such as in Figure 8.14a. This is indicative of high levels of strain, or a slip direction with a similar Schmid factor [138, 140]. Also observed in Figure 8.14a is a possible accumulation of dislocations in regions adjacent to GB carbide precipitates. It may be the case that, as precipitates can impede the movement of dislocations, the presence of carbide precipitates has resulted in dislocation pile-up. Dislocation pile-up can lead to stress accumulation and so can act as an initiation site for SCC [137, 292]. Alternatively, due to the common occurrence of GB carbide precipitates within this material and the existing periodicity of slip bands, it is possible that this apparent interaction is coincidental.

It was found that following the application of stress, unsensitised GBs could be observed as there is a change in slip direction either side of the GB, as seen in Figure 8.14b. It is expected that this is a coherent twin GB. The slip dislocations either side of the coherent twin GB line up with one another indicating that transmission has occurred through the GB [292, 293]. Numerous twin boundaries were identified within this material previous to deformation during large area analysis by electron backscatter diffraction (EBSD) described in Chapter 5. However, coherent twin GBs were not observed by HS-AFM prior to the application of stress as they are resistant to sensitisation, and so are not topographically visible after mechanical polishing as with other GBs [102, 103].

Line profiles were produced showing the height changes across slip bands (Figure 8.15). Single dislocations in this material are known to have a magnitude of 2.58×10^{-10} m, i.e. the magnitude of one Bürgers vector [141]. Figure 8.15 shows repeating steps with height changes down to approximately 5×10^{-10} m, corresponding to two slip dislocations. Larger height changes are also seen, corresponding to movement of multiple dislocations, owing to the high level of local strain induced in the sample.

In some cases, a larger scale periodicity of slip dislocations was noted (Figure 8.15). A similar phenomenon was observed by Frechard *et al.* in a study combining AFM and EBSD to analyse the slip systems in a duplex stainless steel [140]. Frechard measured a maximum step height around 10 nm that did not increase following further deformation [140]. This phenomenon was

attributed to a saturation of dislocations [140]. The maximum step height observed in this work was approximately 12 nm in height (Figure 8.15b), comparable to the maximum height observed by Frechard [140].

8.5.3 GB Uplift

HS-AFM measurements of GBs prior to failure by IGSCC were observed to be uplifted compared to other GBs or the bulk (Figures 8.16 and 8.17). GB uplift has not been reported in other works. As with observations of IGSCC, GB uplift was a localised phenomenon, as illustrated in Figure 8.16b where two GBs are uplifted at a GB triple point and one GB is not.

The tip of an uplifted GB was observed in Figure 8.17. The uplifted section was also shown in Figure 8.18a. The highest features present along the uplifted GB may be identified as GB carbide precipitates, slip bands, or an oxide layer distributed along the GB. It was noted that the grain to the right of the GB contained slip bands arising from two slip systems, as observed previously in Figure 8.14a. The grain to the left of the GB contained single slip and was uplifted at the GB, as illustrated by the line profile collected across the GB (Figure 8.18b). GB uplift is likely influenced by the orientations of the grain either side of the GB, as indicated by the frequent asymmetry of the phenomenon.

The uplift effect occurs ahead of the crack tip and was not observed elsewhere on the surface. Hence it is an effect local to the crack tip. It is possible that GB uplift is the result of concentrated strain ahead of the crack tip in combination with crack tip corrosion processes. Uplifted GBs are topographically raised by 10s of nanometres compared to stressed GBs (Figure 8.18b), indicating that this phenomenon is not solely due to the effects of sample deformation.

Subsurface crack propagation must also be considered, as explored in Chapter 7 by focussed ion beam (FIB) sectioning. It was postulated that oxidation occurring ahead of the crack leads to a weakening of the GB, allowing for rupture by stress. Notably, the oxide thickness is of a similar order of magnitude to GB uplift observed during in-situ IGSCC measurements. By considering these datasets together, oxidation of subsurface GBs may be observed on the surface as an uplifting of the GB prior to cracking.

8.5.4 Crack Propagation

Initial attempts to measure crack propagation were unsuccessful due to crack passivation or deflection. In Figures 8.19-8.21 no propagation occurred. Notably, GB carbides were only seldom evident in the cracked GBs. The crack shown in Figure 8.20 a feature that may be identified as a GB carbide precipitate remains attached to the right hand side grain. This contrasts ex-situ HS-AFM measurements of IGSCC in Chapter 7, where carbide precipitates were present within the cracked GBs, along with an oxide layer. These differences are due to re-preparation of the sample surface, resulting in a cross section of the sample. In-situ measurements are made of the

very top surface. GB carbide precipitates may undergo dissolution as observed in Chapter 6 or drop out as cracking progresses.

Topographic changes occurring on the surface during crack progression were shown in Figure 8.22. Figure 8.22a shows two grains either side of a GB. The GB is not clearly defined as the result of a surface oxide or debris. The region ahead of a crack tip experiences high local stress and strain resulting in further distortion of microstructure. A crack was observed to initiate in the top of the frame. This crack became deeper as cracking progressed but did not propagate through the frame. Optically the crack was observed to progress from the bottom of the sample towards the top (Figure 8.23) indicating subsurface crack propagation. Traversing the surface following the final frame (Figure 8.24) further supported that subsurface propagation had occurred. The monitored grains formed a crack bridge such as observed in Chapter 7.

Figure 8.25 shows HS-AFM measurements of crack propagation. Initial frames are similar to those shown in Figure 8.22. Two grains are observed, separated by a distorted GB. The region shown in Figure 8.25 also shares similarities with the uplifted GB in Figure 8.18a. The GB appears uplifted with respect to the bulk. Angular features are observed along the GB, previously identified as GB carbide precipitates, slip bands or an oxide layer formed along the GB. The deformed region at the crack tip may contain strain-induced martensite, as measured in other works [105, 143, 144], however, in this study this behaviour was not clearly observed.

The large height range and increased presence of corrosion product results in inevitable loss of resolution making the data somewhat difficult to interpret. Despite this, crack propagation is evident as the crack has grown in length and width. The crack was observed to propagate downwards through the frame at approximately 23 nm s^{-1}. The crack velocity observed here is orders of magnitude slower than the 8 μm s^{-1} observed in other studies [164]. However, the value given here is calculated from two consecutive images and so may not be representative of the system. Furthermore, previous studies used differing sensitisation conditions and solution concentration, and typically implemented a constant extension rate test [164].

IGSCC was observed to occur as a smooth, continuous process rather than a stepwise process. This contrasts with previous studies where cracks were found to grow as discrete microcracks, considered to be indicative of a hydrogen fracture mechanism [160, 165]. However, it must be noted that the observations were performed at the surface, and it is possible that any sub-surface cracking progressed in a stepwise fashion.

As the crack became wider and deeper, the resultant topographic maps began to exhibit imaging artefacts due to the nature of AFM. In particular, as the crack deepens, measurements are affected by tip convolution. For this reason, HS-AFM is most suited for the dynamic in-situ measurement of crack initiation and the very early stages of SCC, rather than the later stages.

In Figure 8.25, the crack appeared to propagate downwards through the frame. This was contrary to optical images of the surface, where the crack propagated upwards. This indicates that the crack had propagated upwards below the surface, before appearing to crack downwards

in the HS-AFM data, this further highlights the apparent prominence of subsurface effects. In previous reports, degree of sensitisation and local stress field are considered to be key factors within this system [103, 160, 167, 168]. However, subsurface crack propagation indicates that local stress intensity is not the critical parameter of GB cracking, but other factors such as GB misorientation should be considered. Subsurface cracking then leads to the development of a network of subsurface cracks as observed in Chapter 7 by FIB.

Different forms of crack propagation were observed in this study. Within Figure 8.25, the crack propagated through the frame as the crack tip progressed. However, in Figure 8.27 the two grains appeared to pull apart. It is possible that these different forms are due to the processes occurring subsurface.

Summary The observations made within this chapter alongside previous analysis discussed in Chapters 6 and 7 may be summarised into a possible sequence of events (illustrated in Figure 8.28):

- Following thermal treatments, samples of AISI Type 304 stainless steel are thermally sensitised. As a result, GBs contain numerous GB carbide precipitates with adjacent chromium depleted regions, Figure 8.28a.
- After 6 days of pre-exposure to aqueous sodium thiosulfate, a small number of select GBs/carbide precipitates become oxidised (Figure 8.28b). Most GBs appear unchanged.
- Following the application of stress via three-point strain rig, slip bands are formed across the plastically stressed regions of the sample. It is possible that regions that had previously oxidised may fracture soon after the application of stress, as these regions are more brittle than the bulk material (Figure 8.28c). GB carbide dissolution may also occur at a small number of carbides across the surface, forming intergranular pits (Figure 8.28d).
- Fractured regions/intergranular pits act as stress accumulators and SCC will preferentially initiate at these features as a result (Figure 8.28e). Localised corrosion processes will also occur sub-surface as cracks, fractured regions, and intergranular pits can act as surface entryways leading to sub-surface dissolution and crack propagation (Figure 8.28f).
- Sub-surface crack propagation and sub-surface oxide formation is theorised to result in GB uplift at the surface (Figure 8.28g).
- Cracking progresses along GBs, leading to large-scale crack propagation, and ultimately to the failure of the specimen (Figure 8.28h).

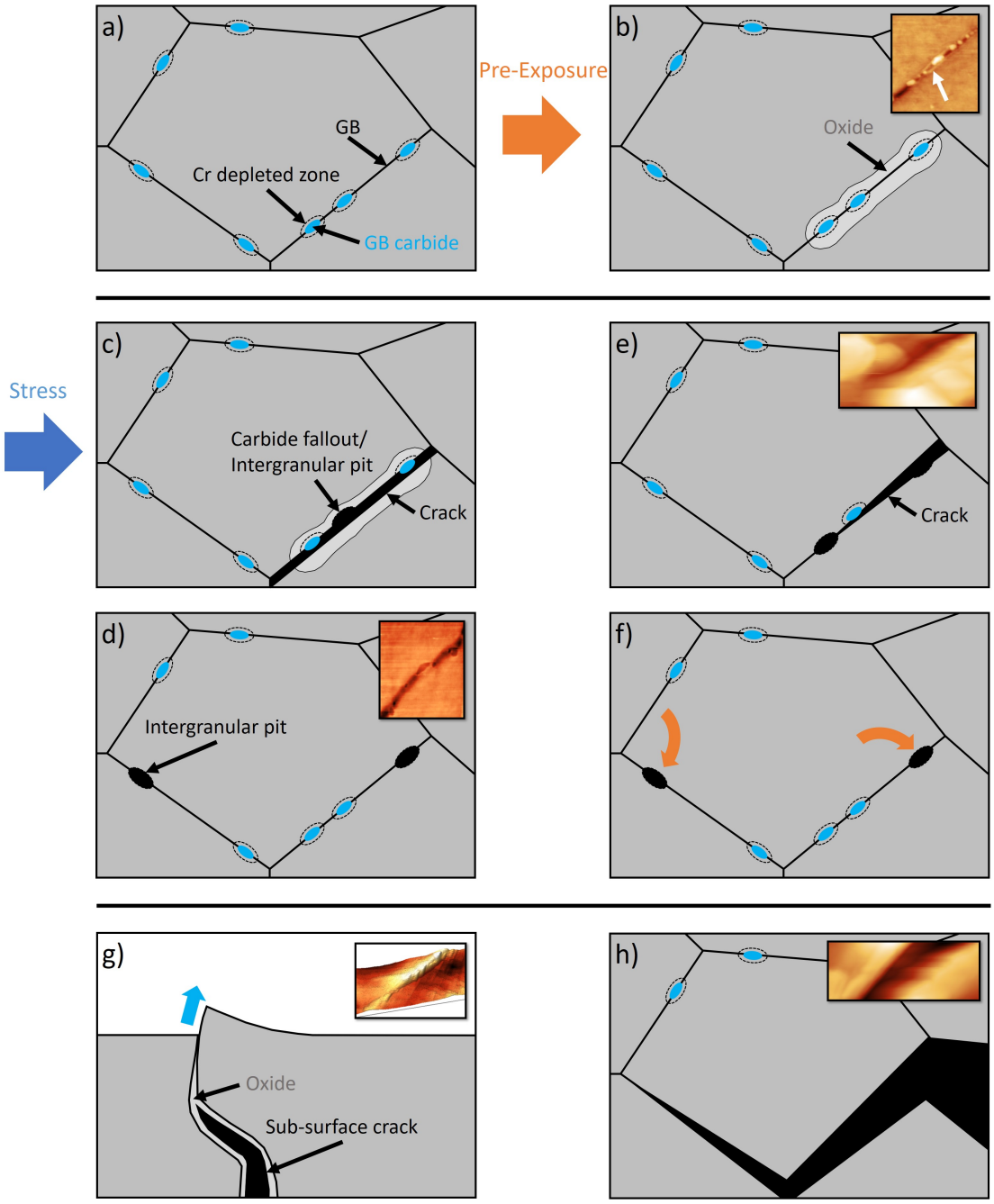

Figure 8.28: A schematic diagram showing a possible sequence of events leading to IGSCC: a) initial sample microstructure with GB carbide precipitates, b) oxidation of a few select GB carbides following sample pre-exposure, c) fracture of oxide regions following the application of stress, d) dissolution of a small number of GB carbides resulting in intergranular pits, e) stress accumulation at intergranular pits/pre-cracks leading to an SCC initiation event, f) ingress of corrosive solution through surface entryways lead to sub-surface dissolution, g) sub-surface oxidation and sub-surface crack propagation lead to GB uplift, and h) crack propagation leads to large-scale cracking.

8.6 Conclusions

In the first part of this chapter, a methodology was developed for in-situ studies of IGSCC by HS-AFM. The following conclusions are drawn from this work:

- A system for imparting stress to the sample during in-situ HS-AFM analysis was designed, modelled, and constructed. This design localised stress and strain such that SCC may be limited to a specific area.

- The effect of sample shape was modelled. By utilising different sample shapes, stress and strain could be localised further. The set-up implemented reduced specimen sizes in order to reduce the area of interest, this is also advantageous for radioactive samples as activity is reduced.

- The time to initiate was found to vary significantly with time exposed to 395 mg L^{-1} aqueous $Na_2S_2O_3$ prior to the application of tensile stress. It was found that by pre-exposing the sample to the solution for a duration of 6 days, SCC could be reproducibly initiated within 1 day following stressing. This duration was postulated to be sufficient for the oxidation of a few GBs on the surface. These GBs may act as crack initiation points upon the application of tensile stress.

- A suggested methodology for the in-situ study of IGSCC by HS-AFM was developed, detailing experimental set-up, sample shape and preparation, pre-exposure duration, optical identifiers, and imaging locations.

The second part of this chapter focussed on in-situ observations of SCC by HS-AFM, utilising the methodology developed in the first part of this chapter. In-situ observations of real-time quantitative morphology evolution such as those performed here allow for further understanding of the cracking mechanisms. Such measurements provide quantitative data from a dynamic system essential for model development and validation. Furthermore, this study may be extended to different SCC systems in the future for comparative results. These observations yielded the following conclusions:

- The application of tensile stress resulted in the formation of repeating slip dislocations on the surface with differing directions in each grain either side of the GB. In some areas the slip bands have two directions within a single grain, due to the activation of a second slip system, indicative of high levels of strain, or a slip direction with a similar Schmid factor.

- A coherent twin GB was observed following the application of stress. Slip transmission through the coherent twin GB was evident.

- Line profiles collected across stressed grains measured height changes down to approximately 5×10^{-10} m, corresponding to two slip dislocations. The largest steps observed were around 12 nm indicating that plastic deformation had led to a saturation of dislocations.
- In-situ HS-AFM measurements revealed that GBs local to the crack tip were uplifted. It is thought that this phenomenon occurs prior to rupture by IGSCC. GB uplift was speculated to be the result of sub-surface oxidation as the oxide layer occurred on a similar length scale to the observed GB uplift effect. It is expected that GB uplift is likely influenced by the orientations of the grain either side of the GB.
- In-situ observation of IGSCC crack propagation by HS-AFM was successfully performed, allowing for measurements of crack growth. The crack was observed to propagate downwards through the frame at approximately 23 nm s^{-1}.
- In-situ measurements showed a smooth crack propagation process, contrasting previous studies where cracks were found to grow as discrete microcracks [158, 165, 166].
- As cracks became wider and deeper, the resultant topographic maps exhibited imaging artefacts such as tip convolution. For this reason, HS-AFM is most suited for the dynamic in-situ measurement of crack initiation and the very early stages of SCC, rather than the later stages. These are the stages that other techniques struggle to image due to environmental requirements and both spatial and temporal resolution limitations. Thus, highlighting that by combining the strengths of multiple techniques, a more complete picture of the SCC process can be achieved.
- Propensity of sub-surface crack propagation was evident within this study indicating that local stress intensity is not the critical parameter of GB cracking.

CHAPTER 9

CONCLUSIONS AND FURTHER WORK

The mechanisms of SCC may continue to elude
But the time has now come for me to conclude
I'll be sure to cover the important outcomes as it is no illusion
That many who come to read this thesis will skip to the conclusion

Stress corrosion cracking (SCC) is an important failure mode in many metal systems but has a complicated mechanism that makes failure difficult to predict. Techniques that can measure SCC in-situ as it occurs may give important insight into the mechanisms that give rise to macroscale cracking, and the sequence in which they occur.

A key aim of this thesis was to implement contact mode high-speed atomic force microscopy (HS-AFM) to measure SCC as it progresses in-situ and in real-time with nanometre resolution. A plethora of techniques have been implemented in previous studies. These include surface and volume measurements such as optical microscopy, electron microscopy techniques and atom probe tomography (APT), and reaction sensing techniques such as electrochemical noise (EN) and the scanning vibrating electrode technique (SVET) [19, 108, 174–176, 294]. These techniques operate over a range of length- and time-scales, however, techniques that offer the highest resolution seldom facilitate the conditions necessary for in-situ measurements. The work presented in this thesis implemented HS-AFM to obtain the high temporal and spatial resolution necessary for such measurements. Previous experiments have been conducted using conventional atomic force microscopy (AFM) to measure crack propagation [196–198], however with the limited imaging rate capabilities of traditional AFM a vast amount of information is lost.

In this thesis SCC was induced in thermally sensitised American Iron and Steel Institute (AISI) Type 304 stainless steel under tensile stress in an aggressive thiosulfate solution. This is

a well-studied system known to induce intergranular SCC (IGSCC). However, despite numerous studies, crack initiation and propagation mechanisms in sensitised stainless steels in thiosulfate solutions are yet to be conclusively identified. This thesis aimed to apply in-situ HS-AFM in combination with other complementary techniques to give insight into the mechanisms that give rise to IGSCC initiation and propagation.

9.1 Conclusions

9.1.1 Chapter by Chapter Conclusions

Chapter 4: Sample Preparation Methods for Optimal HS-AFM Analysis At the beginning of this thesis, a study of sample preparation methods was undertaken. The quality of the surface analysis obtained by HS-AFM is highly dependent upon the resultant final surface finish. This work aimed to identify a sample preparation method for stainless steels that was optimal for analysis by HS-AFM. Four sample preparation methods were compared: mechanical and oxide polishing suspension (OPS) polishing, acid etching in Carpenter's reagent, electrolytic etching in an oxalic acid solution, and focussed ion beam (FIB) etching. These methods were performed on samples of Sandvik Austenite Ferrite (SAF) 2205 stainless steel: a duplex stainless steel with an approximate 1:1 ratio of austenite to δ-ferrite. This material was chosen in order to compare the behaviours of different phases. The key conclusions from this work include:

- Mechanical and OPS polishing provided a gentle etch that allowed for high quality topographic measurements to be collected.
- Acid etching and electrolytic etching recipes performed in this work were less suited for analysis by high resolution HS-AFM, due to the large height changes across the surface which can distort or hide finer microstructures.
- FIB etching revealed grain structure, however a distorted microstructure was observed by HS-AFM, possibly due to Ga^+ ion implantation.

Following the conclusions of Chapter 4, samples in later chapters were prepared by mechanical and OPS polishing. Following this preparation method, HS-AFM measurements of thermally sensitised AISI Type 304 stainless steel were of high quality. Measurements performed by electron microscopy techniques including electron backscatter diffraction (EBSD) were also of good quality. This is advantageous as the surface did not require repreparation for different analytical techniques. Grain boundaries (GBs) and secondary phase precipitates (SPPs) were clearly observed across the surface. This was particular important during localised corrosion studies, as these sites were preferentially attacked. During in-situ pitting, dissolution and SCC studies high-resolution, clear images were produced with no debris or residue from preparation.

This allowed for interpretation of the data without the caveat of improper sample preparation, leading to stronger conclusions.

Cladding samples in Chapter 5 were prepared by electropolishing performed by the National Nuclear Laboratory (NNL). This electropolish was a different recipe to that implemented in Chapter 4. The resultant HS-AFM images were of good quality, the flat surface allowed for clear observations of microstructural features and the surface was free of debris or residue. However, due to the large height of the SPPs across the surface HS-AFM images collected in the vicinity of SPPs exhibited imaging artefacts. The different chemical responses of the various SPPs on the surface to the chemical etch resulted in differing topographies, explored in Appendix B. This study introduced the potential of SPP identification by HS-AFM due to chemically induced topography. This may be extended to alternative electrolytic etch recipes for comparative studies with the potential to probe the chemical behaviours of the surface microstructural features by performing numerous subsequent etches.

Chapter 5: Characterisation of Sensitised Microstructure Prior to IGSCC experiments, sensitised microstructure and its response to corrosive environments and tensile stress were independently studied by HS-AFM and complementary techniques in Chapters 5, 6, and 8, respectively. These three factors were studied separately to deconvolute their individual contributions to IGSCC. It is well recognised that these factors act synergistically and that their behaviours will differ when isolated. A key aim of this work is to highlight that synergy.

Analysis was performed on ex-service advanced gas-cooled reactor (AGR) cladding samples in order to evaluate the microstructural changes caused by irradiation and heating. This analysis included large area measurements of topography by HS-AFM, with correlated microstructural and elemental analysis by EBSD and energy dispersive X-ray spectroscopy (EDX), as well as scanning transmission electron microscopy EDX (STEM EDX) measurements of GB elemental segregation. The following key conclusions were drawn:

- Numerous large SPPs were present across the surface, including: $M_{23}C_6$, sigma phase, NbC, and G phase. These precipitates were primarily intergranular, though smaller NbC were found to be primarily intragranular.

- Nanometre-scale voids were observed across the surface by HS-AFM. Voids were found to be larger and deeper at GBs, particularly high-angle GBs (HAGBs). An association was also noted between void frequency and SPPs.

- HAGBs were found to be more prone to sensitisation by radiation induced segregation (RIS) compared to low-angle GBs (LAGBs) or twin GBs. Different GB types were also found to have distinct compositional profiles. The LAGB and twin GBs had symmetric profiles, with one twin GB producing a W-shaped profile. Some HAGBs were found to have asymmetric composition profiles, indicating that they had undergone GB migration.

A comparative study of thermally sensitised microstructure was performed on thermally treated AISI Type 304 stainless steel samples. The key conclusions from this work are as follows:

- SPPs identified as chromium-rich carbide precipitates were observed in the majority of GBs. These GBs were preferentially etched within topographic maps and GB carbide precipitates were seen to stand in relief of the surface. Comparatively few larger SPPs were observed, these were identified as chromium-rich carbides and MnS precipitates.

- HAGBs were found to be severely sensitised with chromium depletion measured down to a value of 5.60 wt.%. Minimum chromium concentrations were measured near to GB carbide precipitates, values increased as the distance from the carbide precipitate increased. Twin GBs were found to be resistant to thermal sensitisation.

In this chapter, analysis of irradiation assisted SCC (IASCC) in ex-service AGR cladding by EBSD was performed. Analysis revealed that higher misorientation GBs cracked preferentially, with the exception of twin GBs which were not observed along the crack path. Limited analysis was possible due to the sample surface condition. The mechanisms that lead to IASCC is an area of ongoing research. However, limited lab work is possible with irradiated samples as it is technically challenging and expensive. For this reason, conditions were selected such that the thermally treated material (AISI Type 304 stainless steel) may act as an analogue to irradiated samples. It was concluded that:

- The microstructural differences observed between thermally sensitised AISI Type 304 stainless steel and ex-service AGR fuel cladding are expected to have an effect on SCC initiation times and propagation speeds. However, the fundamental mechanisms for failure of the thermally sensitised material are expected to still be relevant within studies of irradiated material within similar environmental and stress conditions.

Chapter 6: Studies into Localised Corrosion Events In the Absence of Stress: Pitting and Dissolution Following analysis of the sensitised microstructure, the effect of exposure to a corrosive environment was explored. Two aqueous solutions of aggressive salts were studied, both relevant within industrial applications. In the first part of this chapter, pitting corrosion and intergranular attack (IGA) were initiated by polarising samples of thermally sensitised AISI Type 304 stainless steel within a 1% sodium chloride solution. Pitting sites are known to act as precursors to SCC upon the application of stress, however the exact sites of pit nucleation are yet to be conclusively identified. The aim of this chapter was to implement in-situ HS-AFM alongside complementary FIB, optical, and electron microscopy techniques in order to observe and measure pitting corrosion. By using in-situ techniques it is hoped that further understanding of the nanoscale mechanisms and the order in which they occur is achieved. The following key conclusions were made:

- HS-AFM measurements were performed in-situ by imaging within a custom built liquid cell with parallel electrochemical control. The high resolution of the HS-AFM allowed for accurate measurements of the dimensions of pits formed.

- In-situ observation of intergranular pit formation occurred in ≤ 0.5 seconds. The actual measured geometry during this event in combination with electrochemical data was fed into a computational model using COMSOL Multiphysics software. Results were used to generate 3D plots that illustrated local acidification and a build-up of chloride ions in the areas adjacent to the pitting site, demonstrating that the measurements yielded from such experiments may be directly fed into predictive models.

- Intergranular pits were observed to occur in chains along GBs, purported to be the result of GB carbide precipitate dissolution. These chains were found to be an early form of IGA. Severity of IGA is linked to thermal sensitisation of the GBs leading to lower resistance to corrosion.

- FIB milling revealed that in some areas intergranular pits are small surface entryways to much larger subsurface voids produced by IGA. FIB milling performed in an area containing an intragranular pit revealed subsurface corrosion that appeared to progress outwards from the pit through the bulk of the grain. Further progression of deeper corrosion by IGA was also observed, demonstrating an interplay between the two mechanisms.

- In-situ HS-AFM measurements performed in the absence of an applied potential showed GB carbide precipitate dissolution over a duration of 408 seconds. This phenomenon only occurred after previous polarisation of the surface, supporting the notion that surface passivity was reduced.

The second part of this chapter explored the effect of 395 mg L^{-1} aqueous sodium thiosulfate. Relatively few previous studies have explored the effect of this corrosive medium. The findings of these studies vary considerably. Some works state that thiosulfate does not result in anodic activity or localised corrosion in the absence of stress [103, 160, 161, 164]. However, in other works thiosulfate was found to initiate and propagate localised corrosion processes in such a way that the role of stress was considered to be secondary [166]. However, these experiments were performed by reaction sensing techniques and precise reaction sites were not reported. In this chapter it was concluded that:

- Preferential dissolution of GB carbide precipitates by sodium thiosulfate in the absence of stress was observed.

- The HS-AFM probe was found to interact with the surface in such a way that accelerated corrosion of carbide precipitates when the surface is exposed to a corrosive environment.

- Prolonged exposure to the thiosulfate solution resulted in a possible oxide layer forming at specific GBs.

Following these conclusions, in Chapter 8 it was found that time to initiation of IGSCC in thermally sensitised AISI Type 304 stainless steel varied with time pre-exposed to aqueous sodium thiosulfate prior to the application of tensile stress. It was found that by pre-exposing the sample to the solution for a duration of 6 days, SCC could be reproducibly initiated within 1 day following stressing. This duration was postulated to be sufficient for the oxidation of a few GBs on the surface. These GBs may act as crack initiation points upon the application of tensile stress.

Chapter 7: Ex-Situ Analysis of SCC Crack Propagation Path and Characterisation of the Crack Tip In Chapter 7 pre- and post-failure analysis was performed by various complementary ex-situ methods. The resultant topography, changes to the microstructure, crack tip chemistry and sub-surface contributions were evaluated. The following key conclusions concerning the SCC system under investigation were drawn:

- GB carbide precipitates were present in cracked GBs, indicating that dissolution of these features was not a prominent process during IGSCC. It is possible that dissolution or modification of a few GB carbide precipitates may have led to sufficient stress accumulation resulting in crack initiation or propagation.

- Crack bridges were observed, both intact at the crack tip and ruptured following sufficient crack propagation. Such features are known to reduce crack velocity.

- Cracking was found to passivate at GB triple points or GB carbide precipitates, as additional energy is required to rupture certain GBs or precipitates.

- GB misorientations measured along the crack path showed the following behaviours: Firstly, HAGBs cracked preferentially, however no preference was observed between HAGBs with higher GB misorientation angle. Secondly, no coherent twin GBs were cracked during IGSCC, indicating a resistance of coherent twin GBs to cracking. Conversely, incoherent twin GBs were susceptible to cracking, though this may be limited to the dominant crack path, where stress is localised. Lastly, LAGBs were measured along the crack path demonstrating that these boundaries were not immune to cracking.

- FIB milling revealed a network of intergranular cracks below the surface lined with a thin oxide. The oxide layer did not fill the cracks, suggesting that the SCC process was stress-driven. However, within measurements performed closer to the crack tip the oxide was observed to fill the crack, indicating a possible pre-oxidation phenomenon that may lead to oxide-weakened GBs.

- APT analysis of the oxide found a layered structure where the inner oxide was found to contain more chromium than the outer oxide. The outer oxide layers appeared porous, resulting in retained solution following experimental work.

Chapter 8: In-Situ Observations of IGSCC by High-Speed AFM In-situ HS-AFM measurements of IGSCC were performed in Chapter 8. In order to achieve such measurements a methodology was developed such that SCC could be induced more reliably for ease of data collection. The following steps were suggested for this SCC system:

- **Experimental set-up:** The triangle-edge three-point strain rig is preferred as the sharper bend edge localises stress and strain. Additionally, the bath surrounding the strain rig allows for extended measurements in a liquid environment and easy transition between environments (without the sample surface drying out).
- **Sample shape:** Dog-bone type samples are optimal for localisation of strain. Samples should be cut by waterjet to avoid unnecessary stressing of the cut face. The sample surface should be prepared in such a way that stress-raising features are avoided, and HS-AFM images are clear, steps described in Section 4.2 are recommended for stainless steels.
- **Pre-exposure:** Samples of thermally sensitised AISI Type 304 stainless steel should be pre-exposed to 395 mg L^{-1} aqueous sodium thiosulfate for a duration of 6 days.
- **Tensile stress:** After 6 days of exposure, tensile stress should be applied to the sample via three-point strain rig such that the sample is plastically stressed (1 mm deflection). The sample/rig set-up can then be transferred to the HS-AFM stage.
- **Optical identifiers:** Using the HS-AFM's optical microscope, the sample should be monitored for discolouration or crack initiation, primarily in the central areas where stress and strain are localised.
- **Imaging locations:** Following SCC initiation, the cantilever should be positioned ahead of the tip of the crack such that the crack may propagate through the area being imaged. Given the intergranular nature of the localised corrosion events, HS-AFM measurements should focus primarily along GBs.

Utilising this methodology, in-situ HS-AFM observations of topographic changes due to IGSCC were successfully performed. These observations lead to the following key conclusions:

- The application of tensile stress resulted in the formation of repeating slip dislocations on the surface with differing directions in each grain either side of the GB. Line profiles collected across stressed grains measured height changes down to approximately 5×10^{-10}m, corresponding to two slip dislocations. The largest steps observed were around 12 nm indicating that plastic deformation had led to a saturation of dislocations [140].

- In-situ HS-AFM measurements revealed that GBs local to the crack tip were uplifted. It is thought that this phenomenon occurs prior to rupture by IGSCC. GB uplift was speculated to be mechanistically linked to sub-surface oxidation as the oxide layer occurred on a similar length scale to the observed GB uplift effect.
- In-situ observation of IGSCC crack propagation showed a smooth crack propagation process, contrasting previous studies where cracks were found to grow as discrete microcracks. The crack was observed to propagate downwards through the frame at approximately 23 nm s^{-1}.
- Sub-surface crack propagation was found to be a key phenomenon within this system, where limited diffusion allows for a build-up of aggressive electrolyte chemistry within the occluded crack interior. The observed propensity of sub-surface crack propagation indicates that local stress intensity is not the critical parameter of GB cracking.

The current literature may be coarsely summarised into two main theories: film rupture and anodic dissolution [126, 158, 159, 163, 164, 168], and hydrogen induced fracture [158, 165, 166]. Whilst the oxide observations may support a film rupture mechanism similar to that proposed in previous works, inherent contributions from other mechanisms such as hydrogen induced fracture cannot be ruled out. However, it is clear from the measurements performed that the crack growth process is highly localised and combines both chemical and mechanical processes.

Whilst the presented study does not explicitly favour a particular model for cracking, some key mechanisms have been observed that are previously unreported, including GB uplift, the role of an oxide layer and the precedence of sub-surface crack propagation. It is also notable that, prior to the present study, visualisation of the mechanisms occurring had been performed using only optical microscopy or post-corrosion scanning electron microscopy (SEM) analysis.

9.1.2 General Concluding Remarks

High-resolution measurements have provided important insights into the SCC system studied and may be applied to other systems in future. In-situ observations of surface crack propagation performed by HS-AFM allows for better understanding of the evolution of the cracking process as it happens, rather than only characterising the failed specimen after cracking has finished. Combining these observations of real-time quantitative morphology evolution with chemical composition and structural information using other cutting-edge techniques such as APT is essential to inform models of SCC and provide evidence for SCC mitigation methodologies.

The work presented here demonstrates how HS-AFM complements currently established techniques in materials science. The SCC system studied in this thesis (thermally sensitised AISI Type 304 stainless steel in aqueous sodium thiosulfate) is considered as a model system. Aspects of this system may be related to the behaviour of AGR cladding in in aqueous storage and repositories, acting as a key motivation within this thesis. However, ambient temperature SCC

is a life-limiting degradation mechanism for numerous other industrial applications, including light water reactor (LWR) spent fuel storage, waste packages, and various plant and pipework. This work acts as an excellent basis for further experimentation both by HS-AFM as well as other complementary techniques and highlights the opportunity for further study of corrosion processes by HS-AFM. The methodology developed within this work may be applied to other SCC systems, further extending the applicability of this research.

9.2 Suggestions for Further Work

This thesis has highlighted a number of areas where additional study by HS-AFM may be performed, including SPP texture analysis, void distribution analysis, and analysis of other SCC systems such as chloride cracking. In addition, further correlated studies of localised corrosion may be performed by combining HS-AFM with complementary techniques. This section outlines options for further work that have become apparent following the work described in this thesis.

9.2.1 Possible Modifications to the Existing Experimental Set-Up

Modifications to the existing set-up implemented for corrosion studies described in Chapter 6 within this work are considered. Whilst the set-up allows for corrosion processes to be controlled by application of a potential, the subsequent electrochemical measurements are global. Implementing a method that allows for local measurements could be a powerful combination. This information could be compared to real-time measurements of change in topography, allowing for improved characterisation of the processes occurring on the surface. In other works, scanning electrochemical microscopy AFM (SECM-AFM) has produced very promising results. The experimental set-ups described by Kranz [295] or Macpherson [296] suggest that SECM-AFM may be compatible with the contact mode HS-AFM system. Such a set-up would require a potentiostat with a sufficient bandwidth, as well as suitable SECM-AFM tips. From literature, sputter-coated silicon nitride cantilever tips are likely the most appropriate way to achieve this [295, 296].

9.2.2 In-Situ HS-AFM Measurements of Pitting in Unsensitised Stainless Steel and Other Localised Corrosion Systems

Following work performed in Chapter 6 studying localised corrosion events on thermally sensitised austenitic stainless steel, it would be of interest to perform similar experiments on samples of unsensitised samples. Preliminary experiments have been performed with ex-situ analysis by SEM, shown in Figure 9.1. Differences are observed in morphology between the resultant pits compared to those observed in Chapter 6. This study could extend to in-situ measurements of chloride cracking with the application of tensile stress.

The study of different SCC systems, such as chloride cracking, by HS-AFM may reveal similarities with the SCC system studied in this thesis, such as GB uplift or oxide formation.

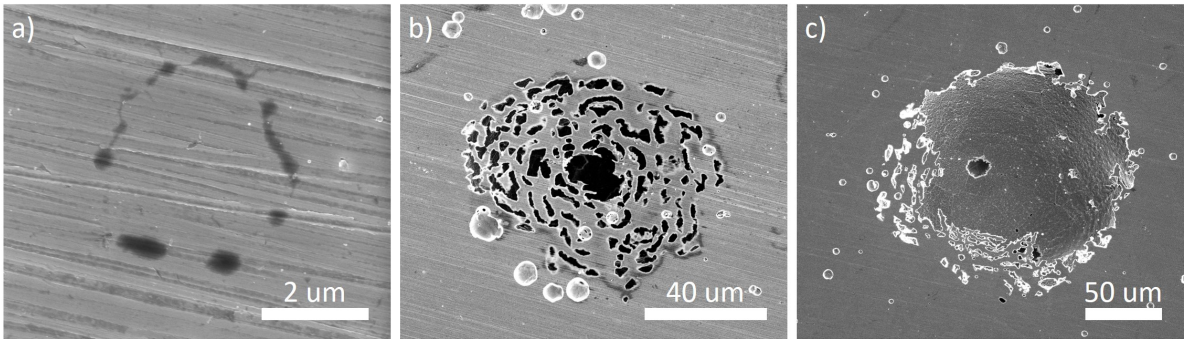

Figure 9.1: SE images showing: a) early stage pitting, b) a lacy pit cover, c) a pit following the collapse of the lacy pit cover, on a sample of unsensitised AISI Type 304 stainless steel in 1% aqueous sodium chloride solution, collected at 10 kV and 0.34 nA.

Different SCC systems could also include tests on irradiated materials as the HS-AFM is capable of high-resolution imaging of small-scale samples, thus reducing the overall activity. This may include ex-service neutron irradiated samples, as well as ion-irradiated specimens.

Currently, in-situ HS-AFM SCC tests are performed in ambient conditions; however, this may be extended to different gaseous or higher temperature environments in the future, leading to additional opportunities for studying other SCC systems.

9.2.3 Self-Loaded Microcantilever SCC Tests by HS-AFM

With recent advances in microscale techniques, micromechanical methods have been implemented within studies of material properties and SCC [19, 297–299]. These SCC tests are performed on microcantilevers fabricated from the material under investigation by FIB [19, 297]. Microcantilevers take a number of similar forms (Figure 9.2) and may be displaced by a micromanipulator in order to measure mechanical properties on the nanoscale, including fatigue strength [298], critical intensity factor [45], and fracture toughness [297, 300, 301].

By fabricating the self-loaded microcantilever shown in Figure 9.2e, HS-AFM measurements can be made along the isolated GB, as the beams are orientated in such a way that allows for measurements to be performed from above. Additionally, as the beams are loaded against one another, a micromanipulator is not required to maintain the stress state of the beams. This approach would require preliminary tests to produce a suitable methodology, however in-situ HS-AFM micromechanical SCC tests would have a number of advantages over SCC studies using a three-point strain rig including:

- **Reduced Material:** By reducing the material required to perform SCC tests, ex-service irradiated materials could be studied due to the reduced associated activity. Additionally, the weight of the experimental set-up is reduced, resulting in higher quality imaging.

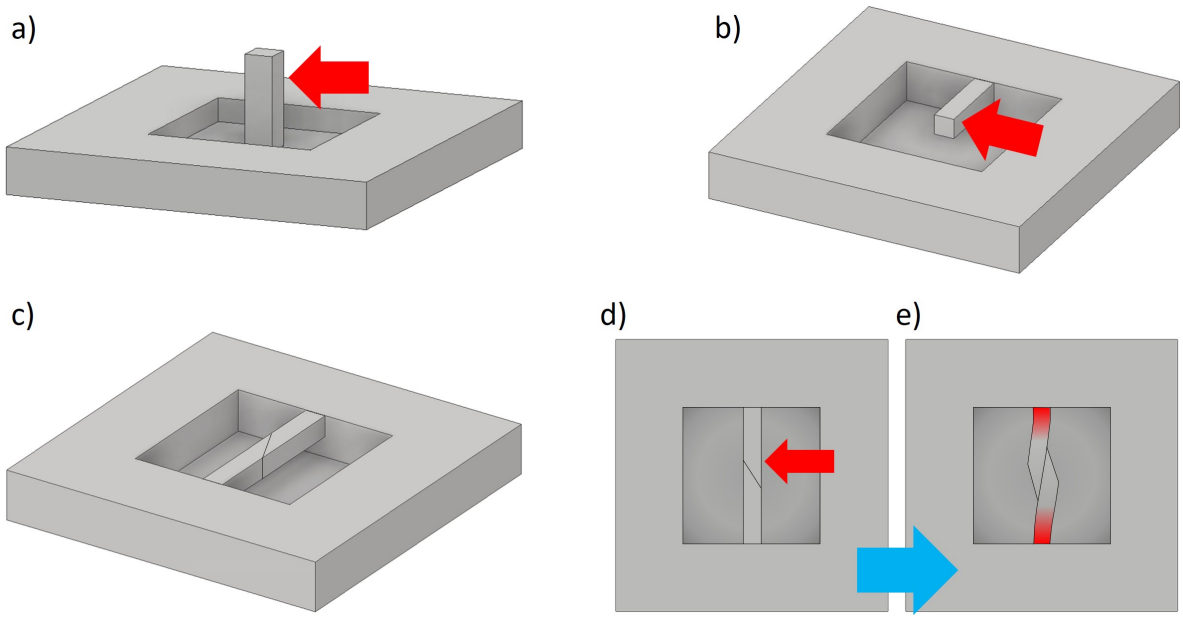

Figure 9.2: Schematic diagrams demonstrating three forms of microcantilever for micromechanical tests: a) a pillar where stress is applied via a micromanipulator as indicated by a red arrow, b) a one-ended beam where stress is applied via a micromanipulator as indicated by a red arrow, and c)-e) demonstrate the method in which self-loaded beams are produced: c) two beams formed by a single beam that has been cut diagonally in the centre, d) the micromanipulator pushes one beam (as indicated by a red arrow) until the diagonal cut reaches the other side of the second beam, and e) the final self-loaded microcantilever with stress concentration indicated in red.

- **Reduced Area:** As this technique reduces the region in which SCC can take place down to a single GB, observations of SCC initiation and propagation are considerably easier.

9.2.4 In-Situ Measurements of Dislocation Formation by HS-AFM

Measurements of slip dislocations were performed in Chapter 8. In-situ deformation of a sample of thermally sensitised stainless steel may reveal how the slip dislocations evolve, as well as how they interact at random GBs, twin GBs and SPPs. Measurements of these microstructural features, such as height, width and spacing, may also be valuable in quantifying the degree of localised deformation. This may be extended to in-situ stressing during SCC tests with the aim of imaging crack initiation sites. Tests may also be performed on unsensitised specimens such that the effects of etched GBs and GB carbide precipitates may be isolated.

In order to deform a sample in-situ, a different strain rig design is required. A suggested design is shown in Figure 9.3. This design implements a three-point bend with motor-driven deflection mechanism such that a pre-defined deflection distance may be applied. This experimental set-up would also be suitable for in-situ SCC initiation studies.

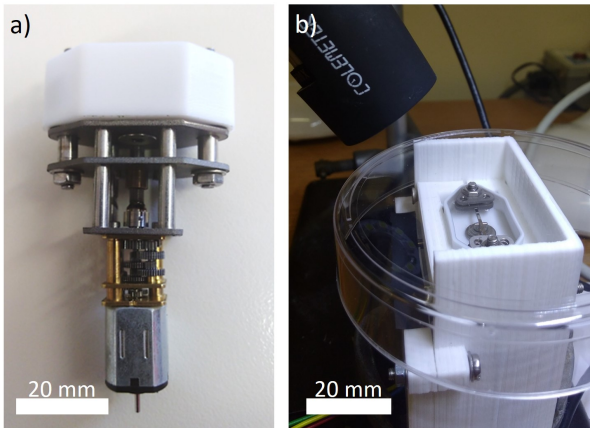

Figure 9.3: Optical images showing a prototype design for an in-situ strain rig: a) a side view showing the bath at the top and the motor beneath, and b) a view showing the three-point strain rig (with sample) inside of the bath.

9.2.5 Further Correlated Studies

Whilst many of the experiments performed in this thesis implemented multiple complementary techniques, these techniques were not always correlated with one another. Further correlated experiments could lead to enhanced characterisation of corrosion processes, leading to stronger conclusions.

For example, in Chapter 6 it was found that work function varied with grain orientation, possibly influencing general corrosion rate and pitting corrosion nucleation. By combining these measurements with correlated corrosion studies, this relationship may be corroborated. This could also lead to enhanced modelling of corrosion [123]. Furthermore, work function was found to vary at the GBs in thermally sensitised samples but not for unsensitised samples. By combining energy-filtered photoelectron emission spectromicroscopy (EF-PEEM) measurements with large area HS-AFM measurements, the precise sites of higher work function (i.e. GBs or GB carbide precipitates) may be identified.

APPENDIX A

IDENTIFICATION OF SPPS IN EX-SERVICE AGR FUEL CLADDING

Now you know what this work is all about
You may find yourself considering the details left out
Within this section key clues are described
To explain how each precipitate was identified

Numerous secondary phase precipitates (SPPs) were observed across the surface of Sample 1XA. A number of SPPs previously identified within the same material as Sample 1XA are described in Section 5.1.1.1. These SPPs are compositionally very different and so may be tentatively identified using energy dispersive X-ray spectroscopy (EDX) and electron backscatter diffraction (EBSD) maps collected previously (Figures 5.5, 5.6 and 5.7). Within this appendix these maps are supplemented with EDX spot analysis and each SPP is identified. Whilst EDX analysis is not at a high enough resolution to allow for accurate identification of precipitates, it may instead be used as an indication of chemical composition and distributions allowing for sufficient confidence when identifying SPPs known to be present within this material.

A.1 Identification of SPPs

EDX spot analysis was performed at the positions shown in Figure A.1. Results are given in Table A.1.

The SPPs coloured orange in Figure 5.5b were large, angular in shape, and intergranular. Spot EDX for this SPP type is labelled as Spot 1 in Figure A.1. An EDX line scan collected across one of these SPPs is shown in Figure A.2. Moving from the bulk to SPP, chromium concentration is observed to increase considerably. Iron and nickel are seen to decrease in concentration, with

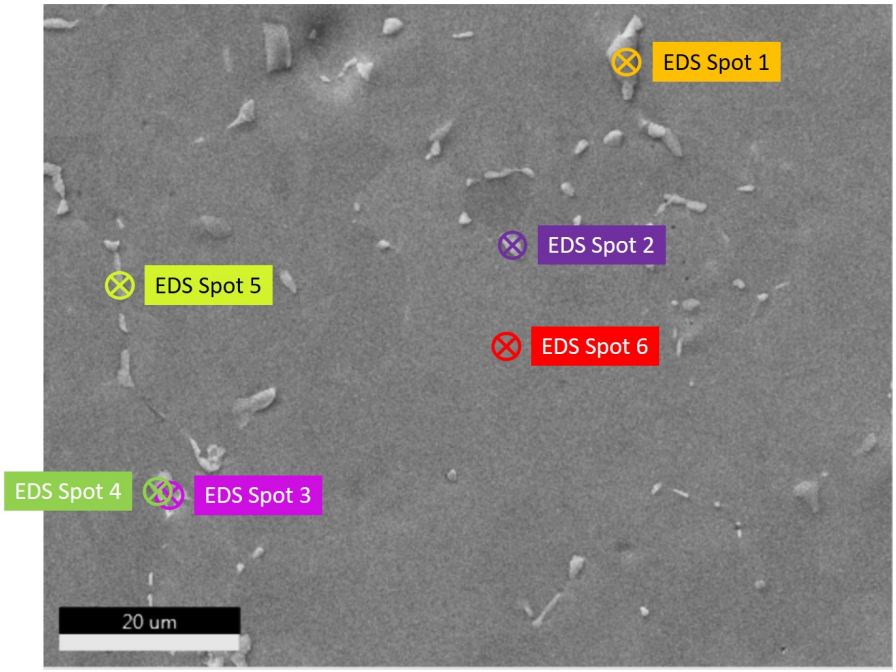

Figure A.1: A reference map showing the locations of EDX spot analysis on the surface of Sample 1XA for the values given in Table A.1.

Table A.1: A table of weight % as measured by spot EDX for the positions shown in Figure A.1 on Sample 1XA.

	Si	Cr	Fe	Ni	Nb
Spot 1	0.02	70.95	20.21	8.04	0.77
Spot 2	9.79	8.20	21.45	40.32	20.24
Spot 3	3.55	5.31	12.07	26.30	52.77
Spot 4	8.13	7.80	20.17	34.58	29.32
Spot 5	4.99	15.67	42.22	28.84	8.29
Spot 6	0.39	20.35	55.92	22.77	0.56

respect to the surrounding bulk. Niobium and silicon are unchanged. This SPP is therefore identified as the chromium rich carbide, $M_{23}C_6$. It must be noted that this SPP was mapped to a body-centred cubic (BCC) crystallography during EBSD measurements, as shown in Figure 5.7. This is not as expected for $M_{23}C_6$.

Unlike the EDX 'phase' map shown in Figure 5.5b, the EDX line scan shown in Figure A.2 shows no indication of a 'shell'. Referring to the compositions listed in Table A.1, the surrounding blue 'shell' is enriched in chromium, but to a lesser degree than that measured for $M_{23}C_6$ and contains a larger proportion of iron and nickel. For this reason, the blue 'shell' is considered to be the result of subsurface $M_{23}C_6$ in the areas immediately adjacent.

In the case of entirely blue 'phase' SPPs in Figure 5.5b, these may be the result of measuring

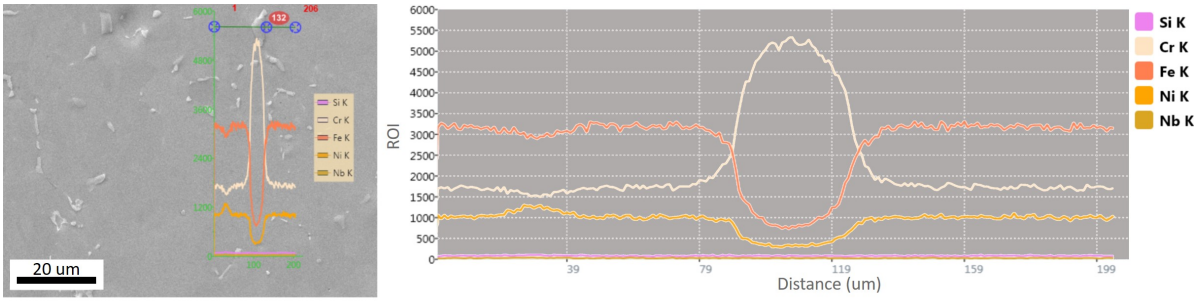

Figure A.2: An EDX line scan of $M_{23}C_6$ on the surface of Sample 1XA. Collected with a dwell time of 200 ms.

a very thin cross section of $M_{23}C_6$, present as a result of surface preparation steps, or these may be a different chromium-rich SPP such as sigma phase. Within EBSD maps of the same area, blue 'phase' is, in some cases, mapped to sigma phase (5.7b). As such, these SPPs are considered to be sigma phase.

The SPPs coloured purple in Figure 5.5b contain considerably more niobium than bulk measurements, as well as increased concentrations of silicon and nickel. This indicates that this SPP may be NbC or G phase. In this case G phase was ruled out due to the high ratio of niobium. Spot EDX analysis performed at the positions labelled Spots 2 and 3 in Figure A.1 were collected in an area identified as NbC. Spot 2 was measured to contain a higher concentration of niobium, nickel, and silicon, suggesting that this may be NbC or G phase. Results from Spot 3 contain a large proportion of niobium indicating that the SPP is likely NbC. In general, SPPs mapped to purple 'phase' were considered to likely be NbC.

The green/yellow 'phase' in Figure 5.5b is observed to occur in areas surrounding NbC as well as in standalone SPPs. The green/yellow 'phase' is enriched in silicon, niobium and, to some extent, nickel. Spot EDX results for the positions labelled Spot 4 and Spot 5 in Figure A.1 were found to be enriched in niobium, nickel and silicon. Consequently, this SPP was identified as G phase.

An EDX line scan was performed across a SPP identified as NbC with a G phase shell, shown in Figure A.3. The G phase shell was enriched in nickel, silicon, and niobium, and depleted in iron and chromium, with respect to bulk measurements. The NbC was found to contain an increased concentration of niobium as expected, as well as silicon to some extent, and was depleted in iron and chromium, again, with respect to bulk measurements. Increased silicon is likely due to an overlap in the measurements of NbC and the surrounding G phase shell.

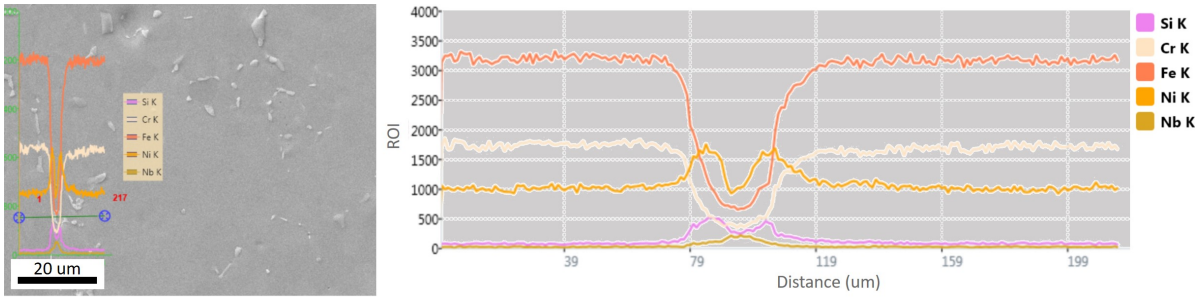

Figure A.3: An EDX line scan of NbC with a G phase shell on the surface of Sample 1XA. Collected with a dwell time of 200 ms.

APPENDIX B

HS-AFM MEASUREMENTS OF SPPS IN EX-SERVICE AGR FUEL CLADDING

Different precipitates were found to have a different texture
Could this lead to identification or is this just conjecture?
Indeed, this may be another way to use the high-speed AFM
Particularly if you don't have access to EDX or STEM

Following identification of secondary phase precipitates (SPPs) present in Sample 1XA, high-speed atomic force microscopy (HS-AFM) measurements of each type of SPP were compared in order to ascertain whether HS-AFM analysis of the surface alone would be sufficient for SPP identification under the conditions explored.

B.1 HS-AFM Measurements of SPPs

Figure B.1 shows examples of topographic maps containing $M_{23}C_6$ and sigma phase for Sample 1XA. Key identifiers from each subfigure were observed as follows:

- Figure B.1a: The $M_{23}C_6$ is around 260 nm in height and has a speckle pattern of negative features on the surface (shown in Figure B.3a), G phase is around 200 nm in height and has a dotted texture of positive features on the surface (shown in Figure B.3d).
- Figure B.1b: The $M_{23}C_6$ is around 250 nm in height and has a speckle pattern of negative features on the surface. G phase is around 300 nm in height (however this may be due to the $M_{23}C_6$ propping the G phase up) and has a dotted texture of positive features on the surface.

- Figure B.1c: The $M_{23}C_6$ is around 270 nm in height and is largely smooth on the surface dotted with negative features varying in size.

- Figure B.1d: Sigma phase is around 120 nm in height and is largely smooth on the surface with a single negative feature similar to a void (shown in Figure B.3b). NbC is around 200 nm in height and has a dotted texture of positive features on the surface similar to G phase. G phase is around 200 nm in height and has some dots of positive features on the surface.

- Figure B.1e: Sigma phase is around 110 nm in height and has some negative features similar to voids on the surface.

This analysis suggests that there are different textures present on the surface when comparing $M_{23}C_6$ or sigma phase and NbC or G phase. However, it is worth noting that any feature observed within these maps are the result of sample preparation techniques and any resultant preferential etching of the surface. When comparing $M_{23}C_6$ and sigma phase a difference in height is observed, as well as differences in texture.

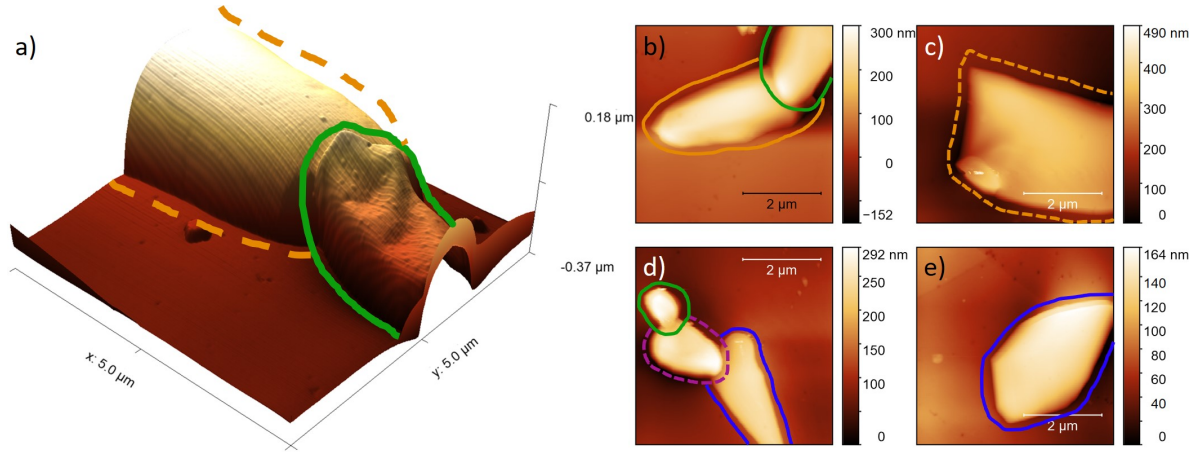

Figure B.1: Images showing HS-AFM topographic maps of regions on the surface of Sample 1XA containing SPPs where an orange line denotes an $M_{23}C_6$, a dotted orange line denotes an $M_{23}C_6$ with a possible shell, a blue line denotes sigma phase, a dotted purple line denotes NbC with a G phase shell and a green line denotes G phase. Within these images: a) and b) show an $M_{23}C_6$ with G phase resting on one edge, c) shows an $M_{23}C_6$, d) shows sigma phase with a NbC with a G phase shell resting on one edge with a further G phase, and e) shows sigma phase. Parallel horizontal lines are the result of the method of data collection.

HS-AFM observations of NbC and G phase collected on Sample 1XA are shown in Figure B.2. Key identifiers from each subfigure were observed as follows (for the following list NbC with a G phase shell is referred to only as NbC as all NbC observed by energy dispersive X-ray spectroscopy (EDX) had a G phase shell):

- Figure B.2a: NbC is around 200 nm in height and has a dotted texture of positive features on the surface(shown in Figure B.3c). G phase is around 220 nm and has a similar texture.
- Figure B.2b: NbC is around 260 nm in height and has a dotted texture of positive features on the surface. G phase is around 310 nm and has a similar texture.
- Figure B.2c: NbC is around 270 nm in height and has a dotted texture of positive features on the surface.
- Figure B.2d: NbC is around 210 nm in height and has a dotted texture of positive features on the surface. G phase is around 180 nm, the texture was difficult to analyse due to debris on the surface.

From these observations it was found that there was little topographic difference between G phase and NbC with a G phase shell. This may be explained by the G phase shell fully encasing the NbC precipitate such that it is not observable on the surface. This is not expected to be the case if the sample were mechanically polished to produce a genuine cross section, however this surface was electrolytically etched and will differ as a result.

Figure B.2 was considered separately as the precipitate is irregular in shape, appearing to border a dipped area. This SPP is the same as that analysed within Figure A.3. Within Figure 5.5b this SPP is labelled as purple 'phase' with a green/yellow 'phase' shell, comparing this to 5.5a shows a ring enriched in nickel, silicon, and niobium, with a centre enriched in niobium, phosphorus, and sulfur. It is therefore concluded that this image shows a cross section through an NbC with a G phase shell. Unfortunately, due to debris on the surface the textures were difficult to compare.

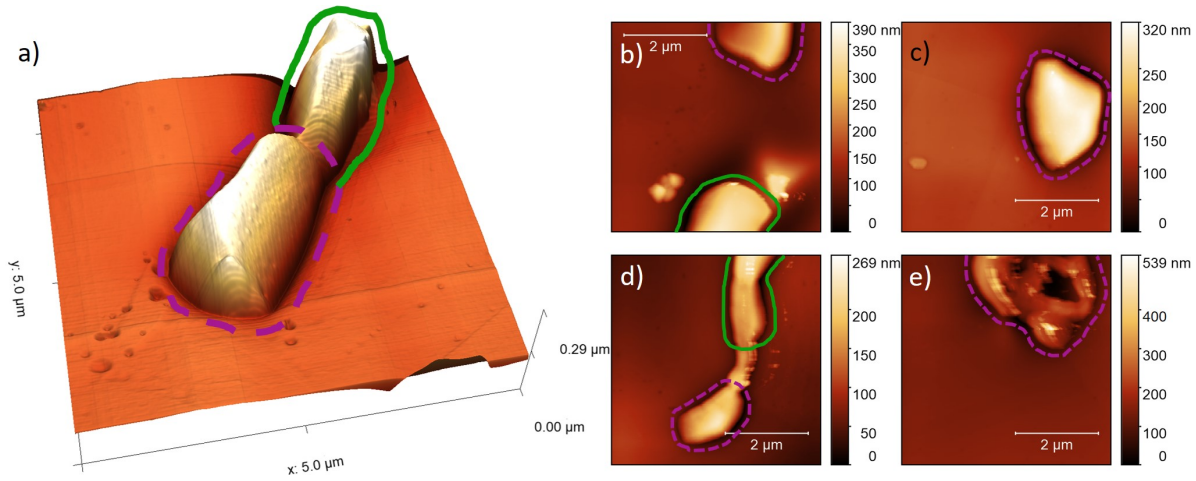

Figure B.2: Images showing HS-AFM topographic maps of regions on the surface of Sample 1XA containing SPPs where a dotted purple line denotes NbC with a G phase shell and a green line denotes G phase. Within these images: a), b) and d) show NbC with a G phase shell and G phase, and c) and e) show NbC with a G phase shell.

Figure B.3 shows a selection of topographic maps collected containing various SPPs that have been cropped such that only the surface textures are within the frame, additional detail was attained by altering the z-scale. The same effect can be achieved by using a repeating scale, this is shown for a selection of images in Figure B.4. However, it is important to keep in mind that lower/higher features no longer map to darker/lighter features, as was the case for single gradient scales such as those in Figure B.3.

Firstly, comparing $M_{23}C_6$ and sigma phase, both phases have negative features on their surface. Generally, the features present on $M_{23}C_6$ are much smaller and more frequent than those observed on sigma phase, almost appearing 'speckled'. The negative features observed on the sigma phase are similar to the voids observed across the bulk of the sample. The lines following the contours of the sigma phase are due to a slight misalignment of the laser dot on the cantilever beam during HS-AFM measurements, resulting in a ringing effect, and are not real topographic features. As stated previously, the negative features present on both $M_{23}C_6$ and sigma phase contrast the positive features present on NbC and G phase. This may be due to the processes of formation, or due to different composition resulting in different responses to the electrolytic etch.

The dotted texture of positive features may be the result of atomic clustering on the surface of the SPP. Positive features present on NbC with a G phase shell is more densely patterned than that observed on the surface of G phase. This may give insight into the method of formation and growth as the G phase shell evolves.

A number of smaller SPPs were observed by HS-AFM that were not resolved by EDX analysis. Some of these SPPs are shown in Figure B.5. Figures B.5a-c show small round SPPs, that bow in the centre. By comparing this analysis to previous work by NNL outlined in Section 5.1.1.1, these were identified as NbC. In contrast with larger NbC precipitates, these smaller NbC were intragranular. The bowed structure may be the result of variation in composition across the SPP, thereby reacting slightly differently within the electrolytic etch solution.

Figure B.5d is a cropped image of a grain boundary (GB) collected between two larger SPPs. This SPP is similar in appearance to $M_{23}C_6$ observed in thermally aged austenitic stainless steels. Figure B.5e shows an area with a number of small white dots that were suspected to be dirt or debris on the surface. Also present within this image is a large void or pit. This pit is similar in size to some SPPs identified on the surface, as such it was likely formed as a result of the removal of an SPP during mechanical polishing or electrolytic etching.

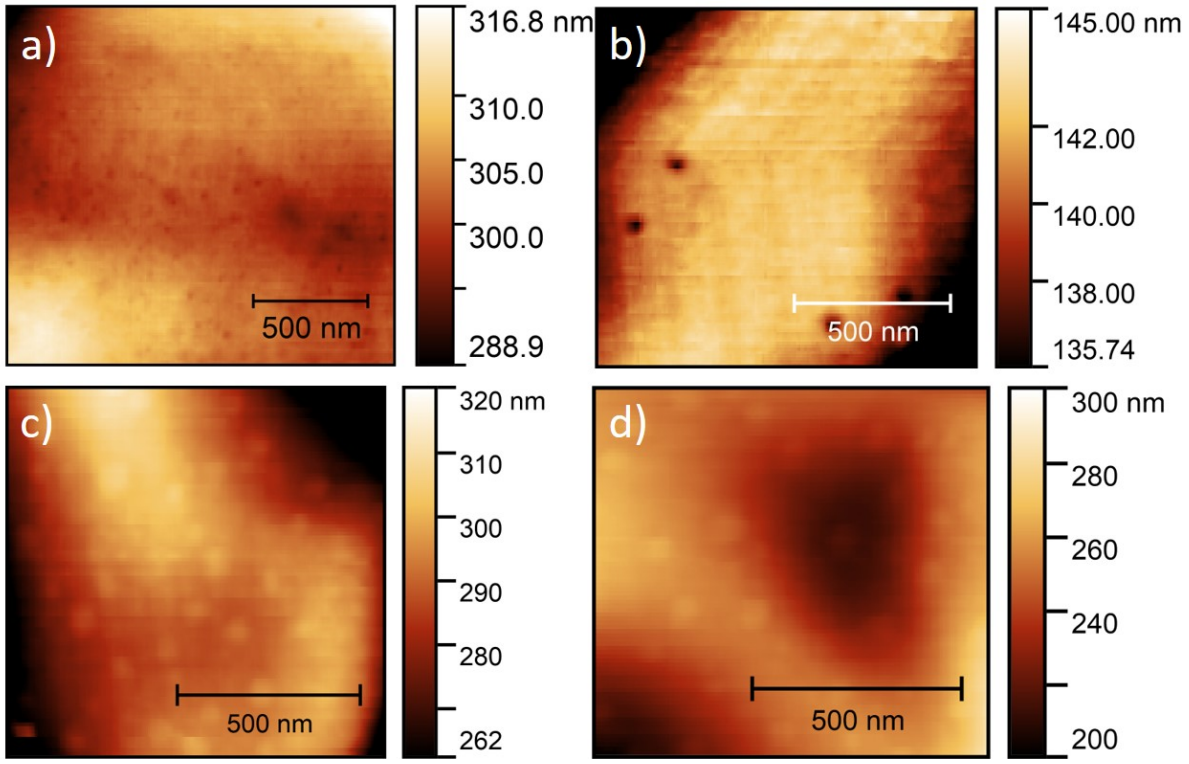

Figure B.3: Images showing cropped HS-AFM topographic maps of the textures observed on the surface of various precipitates on Sample 1XA as a result of electrolytic etching conditions. a) The carbide shown in Figure B.1a, b) the sigma phase shown in Figure B.1e, c) the NbC shown in Figure B.2c, d) the G phase shown in Figure B.1a.

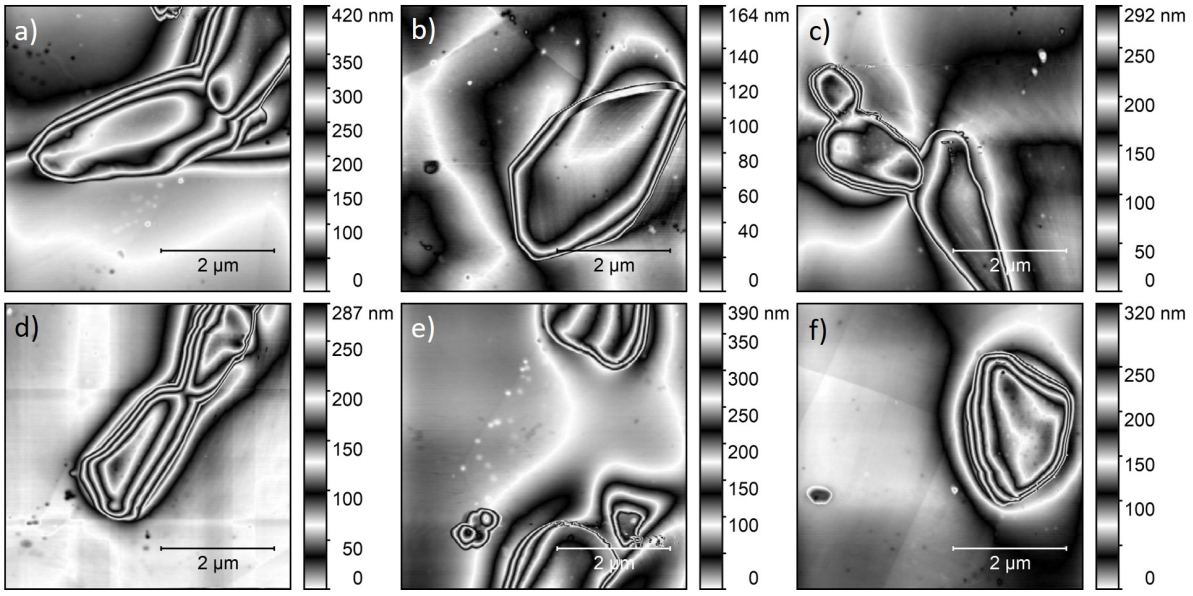

Figure B.4: Images showing HS-AFM topographic maps of regions on the surface of Sample 1XA containing SPPs presented previously with a repeating gradient scale. a) Figure B.1b, b) Figure B.1e, c) Figure B.1d, d) Figure B.2a, e) Figure B.2a, and f) Figure B.2c.

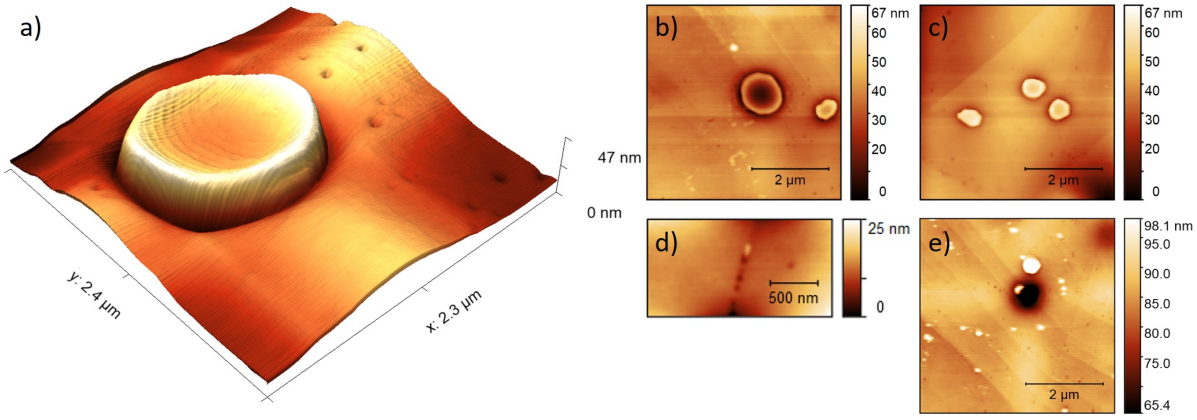

Figure B.5: Images showing HS-AFM topographic maps of unidentified SPPs on Sample 1XA. a) is a 3D topographic map and d) is a cropped image showing a GB located between two larger SPPs (not in frame) with a small intergranular SPP.

APPENDIX C

MISORIENTATION MEASUREMENTS ALONG THE CRACK PATH

In this appendix we seek out a correlation
Between the path of the crack and misorientation
Though we must be careful to remember the other factors
Such as those explored in the previous chapters

Within this Appendix, the measured grain boundary (GB) misorientations along crack paths studied in Chapter 7 are listed in Tables C.1-C.7. This analysis was performed during post-processing of electron backscatter diffraction (EBSD) maps shown in Figures 7.5 and 7.6 within Section 7.2.2. GB misorientation angles were measured by point-to-point misorientation.

Also listed within Tables C.1-C.7 are the misorientations measured for the adjacent uncracked GBs, that is, the uncracked GB that forms a triple point with the other two crack GBs. Asterisks are used to denote adjacent GBs that led away from the proposed direction of propagation. For example, if the main crack appeared to propagate upwards, and the uncracked GB was directed towards the bottom half of the sample, that GB misorientation is labelled with an asterisk. In cases where all adjacent GBs had also cracked, n/a has been inserted into the table, and in cases where the uncracked GB misorientation was unclear or could not be measured, a dash has been inserted into the table.

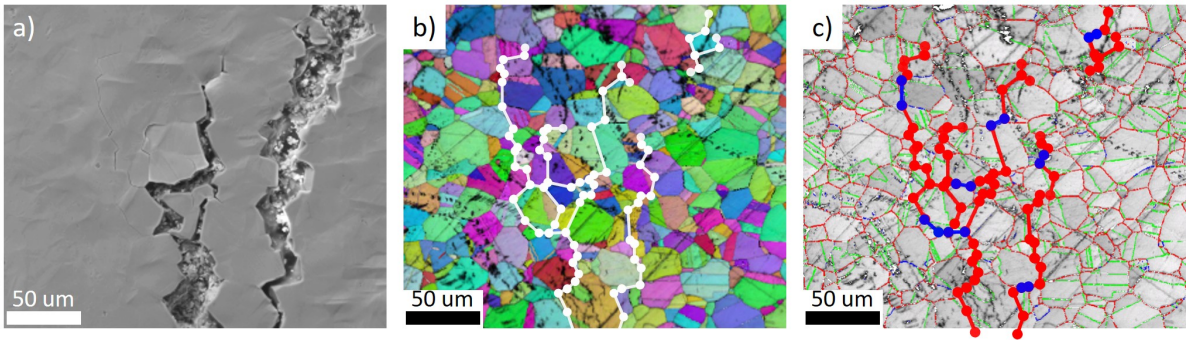

Figure C.1: Duplication of Figure 7.5 included for reference. a) An SE image showing the end sections of the two dominant cracks shown in Figure 7.4, b) shows an IPF and IQ map for the region shown in a) cropped from Figure 7.4c with the cracked GBs indicated in white, c) shows a GB misorientation map for the region shown in a) cropped from Figure 7.4d with cracked LAGBs (with misorientation value in the range 5°-15°) labelled in blue and cracked HAGBs (with misorientation value 15°-62.8°) in red.

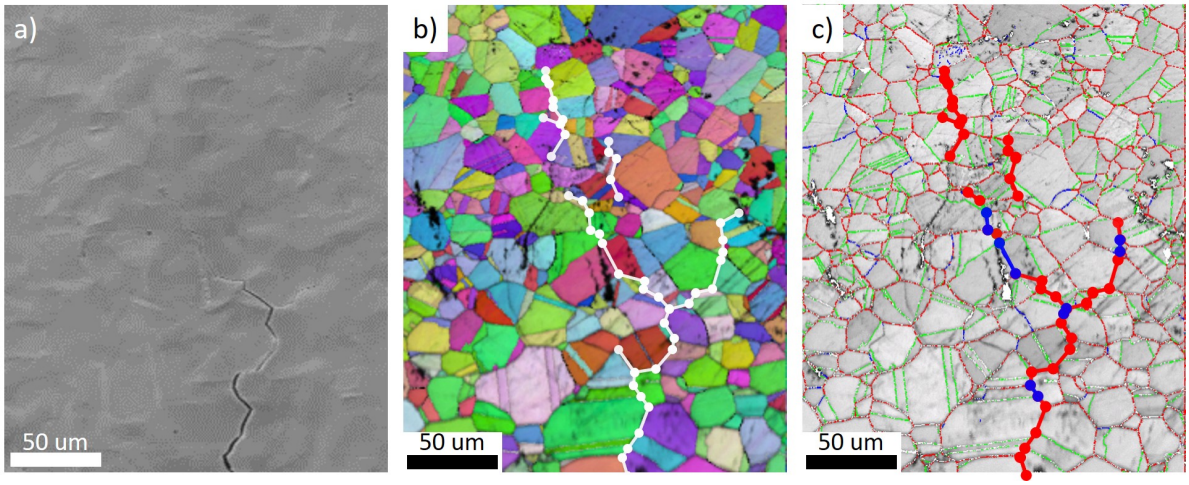

Figure C.2: Duplication of Figure 7.6 included for reference. a) An SE image showing the end section of the smaller crack to the right of the dominant cracks shown in Figure 7.4, b) shows an IPF and IQ map for the region shown in a) cropped from Figure 7.4c with the cracked GBs indicated in white, c) shows a GB misorientation map for the region shown in a) cropped from Figure 7.4d with cracked LAGBs (with misorientation value in the range 5°-15°) labelled in blue and cracked HAGBs (with misorientation value 15°-62.8°) in red.

Table C.1: Measured GB misorientations along the left hand crack path for the crack leading upwards shown in Figure C.1 (Figure 7.5).

Misorientation	**Adjacent Uncracked GB Misorientations**
37.4665	-
58.8477	59.8232*
31.7162	-
54.2239	56.3686*
27.3606	53.2501
49. 8030	59.2467*
26.9697	57.3743*
33.9713	-
31.1280	-
58.8717	59.8308
32.5524	39.5012*
46.7733	36.1716
60.5282	n/a
9.89567	59.7113*
55.0555	-
13.4767	42.8808*
58.3764	-
29.5174	59.7873*
34.6522	59.5189
50.9371	59.423*
58.5827	57.9406
53.2599	45.5946
41.813	59.3055*
42.1655	59.3946
47.399	n/a
48.9233	58.904
60.3745	30.076
19.1626	46.1967*
54.7617	59.6637
30.417	-
48.9002	52.8633*
47.7345	38.8144
55.6439	-
59.7683	42.3917*
18.361	56.1752
56.1083	58.9979
18.6853	59.2292
55.8646	59.3307
50.9347	17.6833*

Table C.2: Measured GB misorientations along the middle crack path for the crack leading upwards shown in Figure C.1 (Figure 7.5).

Misorientation	**Adjacent Uncracked GB Misorientations**
46.7647	n/a
44.3942	-
43.5117	46.1654
46.9479	n/a
36.0267	n/a
38.486	59.2565*
35.6516	59.9906
52.3632	28.9778
26.6042	43.5225*
40.3764	47.0975*
28.1432	36.6075
38.2101	59.6654
43.5546	-

Table C.3: Measured GB misorientations along the right hand crack path for the crack leading upwards shown in Figure C.1 (Figure 7.5).

Misorientation	**Adjacent Uncracked GB Misorientations**
21.9947	-
49.6389	n/a
26.2248	36.1396
51.5396	47.982*
19.4718	50.09*
52.2872	59.4865
19.2973	58.9394
11.8619	30.2353
43.2281	-
22.8732	n/a

Table C.4: Measured GB misorientations along the crack path for the crack leading downwards shown in Figure C.1 (Figure 7.5).

Misorientation	**Adjacent Uncracked GB Misorientations**
33.2058	-
58.0326	45.1513
11.1589	59.4599*
51.5864	42.0607*
23.2518	59.9772
52.2088	59.5586
40.7697	n/a
30.0553	41.7620
48.9352	-
44.7154	29.3643
56.7767	-
28.8865	59.7696*
56.9530	59.5234*
51.5413	48.101
20.3072	59.9198
11.9491	10.0135
9.5713	51.7326
56.2173	58.4591
45.3595	59.9959
56.3124	59.6686
57.7258	25.8277*
21.3022	58.8044
58.4919	59.6686
19.8425	58.4831
28.6238	54.1073*
25.3636	59.6072
60.2717	58.9612
53.388	11.9698
31.2517	-
38.5473	-
43.503	12.7518*
43.8067	-
34.1558	-
56.1534	-
10.5067	52.0112
34.7264	49.7121*
42.8495	59.9947*
46.6694	43.5007*
36.4816	59.3622*

Table C.5: Measured GB misorientations along the left hand crack path for the crack leading upwards shown in Figure C.2 (Figure 7.6).

Misorientation	**Adjacent Uncracked GB Misorientations**
43.9117	-
46.6534	27.6069
42.0845	59.8637*
32.9148	59.8641*
41.9388	59.9958*
46.6016	59.9076*
52.8159	37.0663
12.2757	59.5036
38.9752	45.7054
22.6422	59.9708
28.8573	-
50.4123	59.8397
22.2076	59.953
36.7424	32.4349*
49.6605	56.6357*
29.5751	-
10.4865	45.2748*
51.3342	-
45.828	57.2176
14.8108	50.2922
58.6886	59.4216
41.5152	29.1804
43.9197	59.8783
30.5877	45.9213
56.4223	-
52.546	-
37.1187	n/a
52.1511	42.4021
36.8399	34.2647*
45.5166	59.4497
48.1432	59.828
23.1925	59.439*
20.5684	10.8124

Table C.6: Measured GB misorientations along the middle isolated crack path for the crack leading upwards shown in Figure C.2 (Figure 7.6).

Misorientation	**Adjacent Uncracked GB Misorientations**
35.5122	-
41.8254	59.6665*
33.6168	-
38.0635	59.6868
33.7684	59.6087
48.9401	58.6143
36.0549	59.5522*
49.3327	59.854*

Table C.7: Measured GB misorientations along the right hand crack path for the crack leading upwards shown in Figure C.2 (Figure 7.6).

Misorientation	**Adjacent Uncracked GB Misorientations**
37.2312	-
52.3498	55.017*
39.0545	-
35.4797	59.2909
56.9029	43.7552

BIBLIOGRAPHY

[1] E. Nonbel, "Description of the advanced gas cooled type of reactor," *Risø National Laboratory, NKS/RAK2 (96) TR-C2*, 1996.

[2] J. B. Goode, D. Harbottle, and B. C. Hanson, "Vacuum drying of advanced gas reactor fuel," *Progress in Nuclear Energy*, vol. 109, pp. 145–158, 2018.

[3] J. R. Greer, "It's all about imperfections," *Nature materials*, vol. 12, no. 8, pp. 689–690, 2013.

[4] J. Bystrzycki, W. Przetakiewicz, and K. Kurzydłowski, "Study of annealing twins and island grains in FCC alloy," *Acta metallurgica et materialia*, vol. 41, no. 9, pp. 2639–2649, 1993.

[5] P. Guiraldenq and O. H. Duparc, "The genesis of the Schaeffler diagram in the history of stainless steel," *Metallurgical Research & Technology*, vol. 114, no. 6, p. 613, 2017.

[6] S. Rahmi, *Behaviour of short intergranular stress corrosion crack in Type 304 austenitic stainless steel*.
The University of Manchester (United Kingdom), 2009.

[7] R. L. Plaut, C. Herrera, D. M. Escriba, P. R. Rios, and A. F. Padilha, "A short review on wrought austenitic stainless steels at high temperatures: processing, microstructure, properties and performance," *Materials Research*, vol. 10, no. 4, pp. 453–460, 2007.

[8] A. F. Padilha, R. L. Plaut, and P. R. Rios, "Annealing of cold-worked austenitic stainless steels," *ISIJ international*, vol. 43, no. 2, pp. 135–143, 2003.

[9] J. Knaster, A. Moeslang, and T. Muroga, "Materials research for fusion," *Nature Physics*, vol. 12, no. 5, pp. 424–434, 2016.

[10] D. Kiselev, R. Bergmann, R. Sobbia, V. Talanov, and M. Wohlmuther, "Radiation damage of components in the environment of high-power proton accelerators.," in *Proc. 21st Int. Conf. on Cyclotrons and Their Applications (Cyclotrons'16), Zurich, Switzerland, Sep. 2016, paper MOC01, pp. 24-29, ISBN: 978-3-95450-167-0, doi:10.18429/JACoW-Cyclotrons2016-MOC01, http://jacow.org/cyclotrons2016/papers/moc01.pdf.*, 2017.

[11] P. C. Wu, “Sensitization, intergranular attack, stress corrosion cracking, and irradiation effects on the corrosion of iron–chromium–nickel alloys,” tech. rep., Westinghouse Electric Corp., Madison, PA (USA). Advanced Reactors Div., 1978.

[12] T. Sourmail, C. Too, and H. Bhadeshia, “Sensitisation and evolution of chromium-depleted zones in Fe-Cr-Ni-C systems,” *ISIJ international*, vol. 43, no. 11, pp. 1814–1820, 2003.

[13] D. Enos and L. Scribner, “The potentiodynamic polarisation scan–technical report 33,” *Solartron Instruments*, 1997.

[14] M. F. Ashby and D. R. H. Jones, *Engineering Materials: An Introduction to Their Properties and Applications*.
Butterworth-Heinemann, 1996.

[15] R. Jones, *Stress Corrosion Cracking-Material Performance and Evaluation*.
ASM International, 2017.

[16] A. U. Rao, V. Vasu, M. Govindaraju, and K. S. Srinadh, “Stress corrosion cracking behaviour of 7xxx aluminum alloys: A literature review,” *Transactions of Nonferrous Metals Society of China*, vol. 26, no. 6, pp. 1447–1471, 2016.

[17] R. A. Vadlamani, S. T. Revankar, and J. R. Riznic, “Stress corrosion cracking models and mechanisms for Inconel 600, part 2: Crack growth”,” *Int. J. Adv. Eng. Appl*, vol. 5, no. 6, pp. 1–17, 2012.

[18] S. Schilling, *Liquid in situ analytical TEM: Technique development and applications to austenitic stainless steel*.
PhD thesis, The University of Manchester (United Kingdom), 2017.

[19] R. N. Clark, R. Burrows, R. Patel, S. Moore, K. R. Hallam, and P. E. Flewitt, “Nanometre to micrometre length-scale techniques for characterising environmentally-assisted cracking: An appraisal,” *Heliyon*, vol. 6, no. 3, p. e03448, 2020.

[20] D. Ricci and P. C. Braga, “Recognizing and avoiding artifacts in AFM imaging,” in *Atomic Force Microscopy*, pp. 25–37, Springer, 2004.

[21] P. West and N. Starostina, “A guide to AFM image artifacts,” *Pacific Nanotechnology training manual*, 2002.

[22] R. R. Erdman N., Bell D.C., *Scanning Electron Microscopy. In: Hawkes P.W., Spence J.C.H. (eds) Springer Handbook of Microscopy. Springer Handbooks.*
Springer, Cham, 2019.

[23] J. I. Goldstein, D. E. Newbury, J. R. Michael, N. W. Ritchie, J. H. J. Scott, and D. C. Joy, *Scanning electron microscopy and X-ray microanalysis*.
Springer, 2017.

[24] M. Ezzahmouly, A. Elmoutaouakkil, M. Ed-Dhahraouy, H. Khallok, A. Elouahli, A. Mazurier, A. ElAlbani, and Z. Hatim, "Micro-computed tomographic and SEM study of porous bioceramics using an adaptive method based on the mathematical morphological operations," *Heliyon*, vol. 5, no. 12, p. e02557, 2019.

[25] F. Archie, *Damage nucleation in DP-steels: experimental characterization of the contributing microstructural parameters*.
PhD thesis, RWTH Aachen University, 2018.

[26] K. Kaja, *Development of nano-probe techniques for work function assessment and application to materials for microelectronics*.
PhD thesis, Joseph Fourier University Grenoble, 2010.

[27] M. Escher, N. Weber, M. Merkel, C. Ziethen, P. Bernhard, G. Schönhense, S. Schmidt, F. Forster, F. Reinert, B. Krömker, *et al.*, "NanoESCA: a novel energy filter for imaging X-ray photoemission spectroscopy," *Journal of Physics: Condensed Matter*, vol. 17, no. 16, p. S1329, 2005.

[28] EDAX, *OIM ANALYSIS 5.3 Manual*, 1997-2007 TexSEM Laboratories, Incorporated.

[29] C. M. Barr, L. Barnard, J. E. Nathaniel, K. Hattar, K. A. Unocic, I. Szlurfarska, D. Morgan, and M. L. Taheri, "Grain boundary character dependence of radiation-induced segregation in a model Ni-Cr alloy," *Journal of Materials Research*, vol. 30, no. 9, p. 1290, 2015.

[30] G. O. Whillock, B. J. Hands, T. P. Majchrowski, and D. I. Hambley, "Investigation of thermally sensitised stainless steels as analogues for spent AGR fuel cladding to test a corrosion inhibitor for intergranular stress corrosion cracking," *Journal of Nuclear Materials*, vol. 498, pp. 187–198, 2018.

[31] "AISI 304 stainless steel, TSA Manufacturing." `https://www.tsamfg.com/304/`.
Accessed: 2021-01-20.

[32] G. Du, J. Li, W. Wang, C. Jiang, and S. Song, "Detection and characterization of stress-corrosion cracking on 304 stainless steel by electrochemical noise and acoustic emission techniques," *Corrosion Science*, vol. 53, no. 9, pp. 2918–2926, 2011.

[33] R. Cottis, "Guides to good practice in corrosion control—stress corrosion cracking," *National Physical Laboratory, Teddington*, 2000.

[34] W. Tian, S. Li, N. Du, S. Chen, and Q. Wu, "Effects of applied potential on stable pitting of 304 stainless steel," *Corrosion Science*, vol. 93, pp. 242–255, 2015.

[35] R. Cottis *et al.*, *Shreir's Corrosion*.
Elsevier Science, 2009.

[36] V. Raja and T. Shoji, *Stress corrosion cracking: theory and practice*.
Elsevier, 2011.

[37] B. Fang, A. Atrens, J. Wang, E.-H. Han, Z. Zhu, and W. Ke, "Review of stress corrosion cracking of pipeline steels in "low" and "high" pH solutions," *Journal of materials science*, vol. 38, no. 1, pp. 127–132, 2003.

[38] E. McCafferty, *Introduction to corrosion science*.
Springer Science & Business Media, 2010.

[39] D. Kalderon, "Steam turbine failure at Hinkley Point 'A'," *Proceedings of the Institution of Mechanical Engineers*, vol. 186, no. 1, pp. 341–377, 1972.

[40] L. Calabrese, L. Bonaccorsi, M. Galeano, E. Proverbio, D. Di Pietro, and F. Cappuccini, "Identification of damage evolution during SCC on 17-4 PH stainless steel by combining electrochemical noise and acoustic emission techniques," *Corrosion Science*, vol. 98, pp. 573–584, 2015.

[41] T. Wong, "Stress corrosion cracking in a high strength steel," Master's thesis, University of Canterbury. Engineering, 1986.

[42] M. Faller and P. Richner, "Material selection of safety-relevant components in indoor swimming pools," *Materials and Corrosion*, vol. 54, no. 5, pp. 331–338, 2003.

[43] S. MacKenzie, "Overview of the mechanisms of failure in heat treated steel components," *Failure Analysis of Heat Treated Steel Components, ASM International*, pp. 43–86, 2008.

[44] J. Kovač, A. Legat, B. Zajec, T. Kosec, and E. Govekar, "Detection and characterization of stainless steel SCC by the analysis of crack related acoustic emission," *Ultrasonics*, vol. 62, pp. 312–322, 2015.

[45] A. Stratulat, D. E. Armstrong, and S. G. Roberts, "Micro-mechanical measurement of fracture behaviour of individual grain boundaries in Ni Alloy 600 exposed to a pressurized water reactor environment," *Corrosion Science*, vol. 104, pp. 9–16, 2016.

[46] E. Howett, C. Boxall, and D. Hambley, "AGR cladding corrosion: Investigation of the effect of temperature on unsensitized stainless steel," *MRS Advances*, vol. 2, no. 11, pp. 615–620, 2017.

[47] C. Anwyl, C. Boxall, R. Wilbraham, D. Hambley, and C. Padovani, "Corrosion of AGR fuel pin steel under conditions relevant to permanent disposal," *Procedia Chemistry*, vol. 21, pp. 247–254, 2016.

[48] A. Al-Shater, D. Engelberg, S. Lyon, C. Donohoe, S. Walters, G. Whillock, and A. Sherry, "Characterization of the stress corrosion cracking behavior of thermally sensitized 20Cr-25Ni stainless steel in a simulated cooling pond environment," *Journal of Nuclear Science and Technology*, vol. 54, no. 7, pp. 742–751, 2017.

[49] R. N. Clark, J. Searle, T. L. Martin, W. Walters, and G. Williams, "The role of niobium carbides in the localised corrosion initiation of 20Cr-25Ni-Nb advanced gas-cooled reactor fuel cladding," *Corrosion Science*, vol. 165, p. 108365, 2020.

[50] C. Barcellini, R. Harrison, S. Dumbill, S. Donnelly, and E. Jimenez-Melero, "Local chemical instabilities in 20Cr25Ni Nb-stabilised austenitic stainless steel induced by proton irradiation," *Journal of Nuclear Materials*, vol. 518, pp. 95–107, 2019.

[51] M. Ashworth, D. Norris, and I. Jones, "Radiation-induced segregation in Fe-20Cr-25Ni-Nb based austenitic stainless steels," *Journal of nuclear materials*, vol. 189, no. 3, pp. 289–302, 1992.

[52] A. D. Warren, *The role of secondary phases in the long term degradation of stainless steels at high temperatures*.
PhD thesis, University of Bristol, 2015.

[53] L. Vitos, H. Zhang, S. Lu, N. Al-Zoubi, B. Johansson, E. Nurmi, M. Ropo, M. Punkkinen, and K. Kokko, *Alloy Steel: Properties and Use First-Principles Quantum Mechanical Approach to Stainless Steel Alloys*.
Intech, 2016.

[54] T. Souier, F. Martin, C. Bataillon, and J. Cousty, "Local electrical characteristics of passive films formed on stainless steel surfaces by current sensing atomic force microscopy," *Applied surface science*, vol. 256, no. 8, pp. 2434–2439, 2010.

[55] D. Lindell and R. Pettersson, "Crystallographic effects in corrosion of austenitic stainless steel 316L," *Materials and Corrosion*, vol. 66, no. 8, pp. 727–732, 2015.

[56] J. H. Park and Y. Kang, "Inclusions in stainless steels- a review," *steel research international*, vol. 88, no. 12, p. 1700130, 2017.

[57] M. Breimesser, S. Ritter, H.-P. Seifert, S. Virtanen, and T. Suter, "Application of the electrochemical microcapillary technique to study intergranular stress corrosion cracking of austenitic stainless steel on the micrometre scale," *Corrosion Science*, vol. 55, pp. 126–132, 2012.

[58] P. Lejček, "Grain boundaries: description, structure and thermodynamics," in *Grain boundary segregation in metals*, pp. 5–24, Springer, 2010.

[59] A. Morawiec, "Misorientation-angle distribution of randomly oriented symmetric objects," *Journal of applied crystallography*, vol. 28, no. 3, pp. 289–293, 1995.

[60] A.-F. Gourgues, "Electron backscatter diffraction and cracking," *Materials Science and technology*, vol. 18, no. 2, pp. 119–133, 2002.

[61] V. Randle, H. Davies, and I. Cross, "Grain boundary misorientation distributions," *Current Opinion in Solid State and Materials Science*, vol. 5, no. 1, pp. 3–8, 2001.

[62] D. L. Olmsted, S. M. Foiles, and E. A. Holm, "Survey of computed grain boundary properties in face-centered cubic metals: I. grain boundary energy," *Acta Materialia*, vol. 57, no. 13, pp. 3694–3703, 2009.

[63] J. Mackenzie, "Second paper on statistics associated with the random disorientation of cubes," *Biometrika*, vol. 45, no. 1-2, pp. 229–240, 1958.

[64] D. Brandon, "The structure of high-angle grain boundaries," *Acta metallurgica*, vol. 14, no. 11, pp. 1479–1484, 1966.

[65] M. D. Sangid, H. J. Maier, and H. Sehitoglu, "The role of grain boundaries on fatigue crack initiation–an energy approach," *International Journal of Plasticity*, vol. 27, no. 5, pp. 801–821, 2011.

[66] A. H. King and S. Shekhar, "What does it mean to be special? the significance and application of the Brandon criterion," *Journal of materials science*, vol. 41, no. 23, pp. 7675–7682, 2006.

[67] H. Kokawa, M. Shimada, and Y. S. Sato, "Grain-boundary structure and precipitation in sensitized austenitic stainless steel," *Jom*, vol. 52, no. 7, pp. 34–37, 2000.

[68] T. Liu, S. Xia, Q. Bai, B. Zhou, L. Zhang, Y. Lu, and T. Shoji, "Three-dimensional study of grain boundary engineering effects on intergranular stress corrosion cracking of 316 stainless steel in high temperature water," *Journal of Nuclear Materials*, vol. 498, pp. 290–299, 2018.

[69] S. Rahimi, D. Engelberg, J. Duff, and T. Marrow, "In situ observation of intergranular crack nucleation in a grain boundary controlled austenitic stainless steel," *Journal of Microscopy*, vol. 233, no. 3, pp. 423–431, 2009.

[70] A. King, G. Johnson, D. Engelberg, W. Ludwig, and J. Marrow, "Observations of intergranular stress corrosion cracking in a grain-mapped polycrystal," *Science*, vol. 321, no. 5887, pp. 382–385, 2008.

[71] V. Gertsman and S. M. Bruemmer, "Study of grain boundary character along intergranular stress corrosion crack paths in austenitic alloys," *Acta Materialia*, vol. 49, no. 9, pp. 1589–1598, 2001.

[72] V. Gertsman, M. Janecek, and K. Tangri, "Grain boundary ensembles in polycrystals," *Acta materialia*, vol. 44, no. 7, pp. 2869–2882, 1996.

[73] R. Boehler, "The phase diagram of iron to 430 kbar," *Geophysical Research Letters*, vol. 13, no. 11, pp. 1153–1156, 1986.

[74] A. Padilha and P. Rios, "Decomposition of austenite in austenitic stainless steels," *ISIJ international*, vol. 42, no. 4, pp. 325–327, 2002.

[75] A. Handbook, "Metallography and microstructures," *Edited by GF Vander Voort, ASM Intenational*, vol. 9, 2004.

[76] T. Sourmail, "Precipitation in creep resistant austenitic stainless steels," *Materials science and technology*, vol. 17, no. 1, pp. 1–14, 2001.

[77] P.-J. Cunat, "Alloying elements in stainless steel and other chromium-containing alloys," *ICDA, Paris*, 2004.

[78] B. Miller, "Precipitation behavior of M23C6 carbides in Type 304 stainless steel containing delta ferrite," *Microscopy and Microanalysis*, vol. 18, no. S2, pp. 1352–1353, 2012.

[79] S. J. Zinkle and G. Was, "Materials challenges in nuclear energy," *Acta Materialia*, vol. 61, no. 3, pp. 735–758, 2013.

[80] T. Allen, K. Sridharan, L. Tan, W. Windes, J. Cole, D. Crawford, and G. S. Was, "Materials challenges for generation IV nuclear energy systems," *Nuclear Technology*, vol. 162, no. 3, pp. 342–357, 2008.

[81] S. M. Bruemmer and G. S. Was, "Microstructural and microchemical mechanisms controlling intergranular stress corrosion cracking in light-water-reactor systems," *Journal of Nuclear Materials*, vol. 216, pp. 348–363, 1994.

[82] M. W. Abd Rashid, M. Gakim, Z. M. Rosli, and M. A. Azam, "Formation of Cr23C6 during the sensitization of AISI 304 stainless steel and its effect to pitting corrosion," *Int. J. Electrochem. Sci*, vol. 7, pp. 9465–9477, 2012.

[83] C. Moss and J. Sykes, "Thermal sensitisation of 20Cr/25Ni/Nb stainless steel," 1986.

[84] A. Laferrere, R. Burrows, C. Glover, R. N. Clark, O. Payton, L. Picco, S. Moore, and G. Williams, "In situ imaging of corrosion processes in nuclear fuel cladding," *Corrosion Engineering, Science and Technology*, vol. 52, no. 8, pp. 596–604, 2017.

[85] E. Lee, P. Maziasz, and A. Rowcliffe, "Structure and composition of phases occurring in austenitic stainless steels in thermal and irradiation environments," tech. rep., Oak Ridge National Lab., 1980.

[86] C.-C. Hsieh and W. Wu, "Overview of intermetallic sigma phase precipitation in stainless steels," *Isrn Metallurgy*, vol. 2012, 2012.

[87] C. Tseng, Y. Shen, S. Thompson, M. Mataya, and G. Krauss, "Fracture and the formation of sigma phase, M23C6, and austenite from delta-ferrite in an AlSl 304L stainless steel," *Metallurgical and Materials Transactions A*, vol. 25, no. 6, pp. 1147–1158, 1994.

[88] D. Powell, R. Pilkington, and D. Miller, "The precipitation characteristics of 20% Cr/25% Ni-Nb stabilised stainless steel," *Acta metallurgica*, vol. 36, no. 3, pp. 713–724, 1988.

[89] M. Baker and J. Castle, "The initiation of pitting corrosion at MnS inclusions," *Corrosion Science*, vol. 34, no. 4, pp. 667–682, 1993.

[90] O. Chopra and A. Rao, "A review of irradiation effects on LWR core internal materials–IASCC susceptibility and crack growth rates of austenitic stainless steels," *Journal of Nuclear Materials*, vol. 409, no. 3, pp. 235–256, 2011.

[91] G. S. Was and S. M. Bruemmer, "Effects of irradiation on intergranular stress corrosion cracking," *Journal of nuclear materials*, vol. 216, pp. 326–347, 1994.

[92] P. Scott, "A review of irradiation assisted stress corrosion cracking," *Journal of nuclear materials*, vol. 211, no. 2, pp. 101–122, 1994.

[93] Z. Lu, R. Faulkner, G. Was, and B. Wirth, "Irradiation-induced grain boundary chromium microchemistry in high alloy ferritic steels," *Scripta Materialia*, vol. 58, no. 10, pp. 878–881, 2008.

[94] H.-H. Jin, S. S. Hwang, M. J. Choi, G.-G. Lee, and J. Kwon, "Proton irradiation for radiation-induced changes in microstructures and mechanical properties of austenitic stainless steel," *Journal of Nuclear Materials*, vol. 513, pp. 271–281, 2019.

[95] Z. Jiao and G. Was, "Impact of localized deformation on IASCC in austenitic stainless steels," *Journal of nuclear materials*, vol. 408, no. 3, pp. 246–256, 2011.

[96] J. Gupta, J. Hure, B. Tanguy, L. Laffont, M.-C. Lafont, and E. Andrieu, "Characterization of ion irradiation effects on the microstructure, hardness, deformation and crack initiation behavior of austenitic stainless steel: Heavy ions vs protons," *Journal of Nuclear Materials*, vol. 501, pp. 45–58, 2018.

[97] R. E. Stoller, S. I. Golubov, and A. V. Barashev, "Low-temperature swelling in lwr internal components: a computational assessment," tech. rep., Oak Ridge National Lab.(ORNL), 2015.

[98] C. Barcellini, R. Harrison, S. Dumbill, S. Donnelly, and E. Jimenez-Melero, "Evolution of radiation-induced lattice defects in 20/25 Nb-stabilised austenitic stainless steel during in-situ proton irradiation," *Journal of Nuclear Materials*, vol. 514, pp. 90–100, 2019.

[99] C.-Q. Cheng, L.-I. Klinkenberg, Y. Ise, J. Zhao, E. Tada, and A. Nishikata, "Pitting corrosion of sensitised Type 304 stainless steel under wet–dry cycling condition," *Corrosion Science*, vol. 118, pp. 217–226, 2017.

[100] S. Rahimi and T. Marrow, "A new method for predicting susceptibility of austenitic stainless steels to intergranular stress corrosion cracking," *Materials & Design*, vol. 187, p. 108368, 2020.

[101] R. Zhao, D.-H. Xia, S.-Z. Song, and W. Hu, "Detection of SCC on 304 stainless steel in neutral thiosulfate solutions using electrochemical noise based on chaos theory," *Anti-Corrosion Methods and Materials*, 2017.

[102] E. Trillo and L. Murr, "A TEM investigation of M23C6 carbide precipitation behaviour on varying grain boundary misorientations in 304 stainless steels," *Journal of materials science*, vol. 33, no. 5, pp. 1263–1271, 1998.

[103] H. Isaacs, "Initiation of stress corrosion cracking of sensitized Type 304 stainless steel in dilute thiosulfate solution," *Journal of the Electrochemical Society*, vol. 135, no. 9, p. 2180, 1988.

[104] M. Gaudett and J. Scully, "Distributions of Cr depletion levels in sensitized AISI 304 stainless steel and its implications concerning intergranular corrosion phenomena," *Journal of the Electrochemical Society*, vol. 140, no. 12, p. 3425, 1993.

[105] E. Butler and M. Burke, "Chromium depletion and martensite formation at grain boundaries in sensitised austenitic stainless steel," *Acta Metallurgica*, vol. 34, no. 3, pp. 557–570, 1986.

[106] T. Devine, "The mechanism of sensitization of austenitic stainless steel," *Corrosion science*, vol. 30, no. 2-3, pp. 135–151, 1990.

[107] M. Laws and P. Goodhew, "Grain boundary structure and chromium segregation in a 316 stainless steel," *Acta metallurgica et materialia*, vol. 39, no. 7, pp. 1525–1533, 1991.

[108] A. Stratulat, J. A. Duff, and T. J. Marrow, "Grain boundary structure and intergranular stress corrosion crack initiation in high temperature water of a thermally sensitised

austenitic stainless steel, observed in situ," *Corrosion science*, vol. 85, pp. 428–435, 2014.

[109] A. Alshater, D. Engelberg, C. Donohoe, S. Lyon, and A. Sherry, "Proton irradiation damage in cold worked Nb-stabilized 20Cr-25Ni stainless steel," *Applied Surface Science*, vol. 454, pp. 130–137, 2018.

[110] S. Pondichery, *A study on the effect of magnetic field on the corrosion behavior of materials*. PhD thesis, The University of Texas at Arlington, 2014.

[111] A. Yagati, J. Min, and J. Choi, "Electrochemical scanning tunneling microscopy (ECSTM)–from theory to future applications," *Mod. Electrochem. Methods Nano Surf. Corros. Sci., Mahmood Aliofkhazraei*, 2014.

[112] G. Frankel, "Fundamentals of corrosion kinetics," in *Active Protective Coatings*, pp. 17–32, Springer, 2016.

[113] B. Nimmo and G. Hinds, "Beginners guide to corrosion," *NPL, Teddington*, 2003.

[114] W. Tian, N. Du, S. Li, S. Chen, and Q. Wu, "Metastable pitting corrosion of 304 stainless steel in 3.5% NaCl solution," *Corrosion Science*, vol. 85, pp. 372–379, 2014.

[115] S. P. Kounaves, "Voltammetric techniques," *Handbook of instrumental techniques for analytical chemistry*, pp. 709–726, 1997.

[116] F. P. Ford, P. M. Scott, P. Combrade, and C. Amzallag, "Environmentally-assisted degradation of structural materials in water cooled nuclear reactors–an introduction," 2015.

[117] S. Cramer and B. Covino Jr, "Corrosion: Fundamentals, testing, and protection, volume 13a, ASM handbook," *Journal of Thermal Spray Technology*, vol. 12, no. 4, p. 459, 2003.

[118] N. Sridhar, "Local corrosion chemistry—a review," *Corrosion*, vol. 73, no. 1, pp. 18–30, 2017.

[119] J. Galvele, "Tafel's law in pitting corrosion and crevice corrosion susceptibility," *Corrosion science*, vol. 47, no. 12, pp. 3053–3067, 2005.

[120] T. Burnett, S. McDonald, A. Gholinia, R. Geurts, M. Janus, T. Slater, S. Haigh, C. Ornek, F. Almuaili, D. Engelberg, *et al.*, "Correlative tomography," *Scientific reports*, vol. 4, p. 4711, 2014.

[121] J. Park, M. Verhoff, and R. Alkire, "Microscopic behavior of single corrosion pits: the effect of thiosulfate on corrosion of stainless steel in NaCl," *Electrochimica acta*, vol. 42, no. 20-22, pp. 3281–3291, 1997.

[122] G. Burstein and S. Vines, "Repetitive nucleation of corrosion pits on stainless steel and the effects of surface roughness," *Journal of The Electrochemical Society*, vol. 148, no. 12, p. B504, 2001.

[123] P. T. Brewick, N. Kota, A. C. Lewis, V. G. DeGiorgi, A. B. Geltmacher, and S. M. Qidwai, "Microstructure-sensitive modeling of pitting corrosion: Effect of the crystallographic orientation," *Corrosion Science*, vol. 129, pp. 54–69, 2017.

[124] A. Turnbull, "Characterising the early stages of crack development in environment-assisted cracking," *Corrosion Engineering, Science and Technology*, vol. 52, no. 7, pp. 533–540, 2017.

[125] J. Marrow, D. Engelberg, A. Jivkov, L. Babout, N. Stevens, P. Wood, L. Li, M. Preuss, M. Kuroda, J. Duff, *et al.*, "Microstructure engineering for improved intergranular stress corrosion cracking resistance of stainless steels," in *Global, Tsukuba, Japan (2005)*, 2005.

[126] J. Kovac, C. Alaux, T. J. Marrow, E. Govekar, and A. Legat, "Correlations of electrochemical noise, acoustic emission and complementary monitoring techniques during intergranular stress-corrosion cracking of austenitic stainless steel," *Corrosion Science*, vol. 52, no. 6, pp. 2015–2025, 2010.

[127] J. Scully, *The Fundamentals of Corrosion*.
Pergamon Press, third ed., 1990.

[128] E. Meletis and R. Hochman, "A review of the crystallography of stress corrosion cracking," *Corrosion science*, vol. 26, no. 1, pp. 63–90, 1986.

[129] G. S. Was and P. L. Andresen, "Irradiation-assisted stress-corrosion cracking in austenitic alloys," *JOM*, vol. 44, no. 4, pp. 8–13, 1992.

[130] M.-R. He, D. C. Johnson, G. S. Was, and I. M. Robertson, "The role of grain boundary microchemistry in irradiation-assisted stress corrosion cracking of a Fe-13Cr-15Ni alloy," *Acta Materialia*, vol. 138, pp. 61–71, 2017.

[131] W. Becker and S. Lampman, "Fracture appearance and mechanisms of deformation and fracture.," *Materials Park, OH: ASM International, 2002.*, pp. 559–586, 2002.

[132] K. Wang, A. Wei, X. Tong, J. Lin, L. Jin, X. Zhong, and D. Wang, "Improvement of the anti-corrosion property of twinning-induced plasticity steel by twin-induced grain boundary engineering," *Materials Letters*, vol. 211, pp. 118–121, 2018.

[133] T. Marrow, A. Jivkov, P. Wood, D. Engelberg, L. Babout, N. Anyachor, N. Stevens, P. Withers, and R. Newman, "Intergranular stress corrosion crack propagation in sensitised

austenitic stainless steel (microstructure modelling and experimental observation)," in *16th European Conference on Fracture (ECF16), Alexandropolis, Greece*, 2006.

[134] M. Seita, J. P. Hanson, S. Gradečak, and M. J. Demkowicz, "The dual role of coherent twin boundaries in hydrogen embrittlement," *Nature communications*, vol. 6, p. 6164, 2015.

[135] A. Jivkov, N. Stevens, and T. Marrow, "A two-dimensional mesoscale model for intergranular stress corrosion crack propagation," *Acta materialia*, vol. 54, no. 13, pp. 3493–3501, 2006.

[136] P. Ferreira, J. Vander Sande, M. A. Fortes, and A. Kyrolainen, "Microstructure development during high-velocity deformation," *Metallurgical and Materials Transactions A*, vol. 35, no. 10, pp. 3091–3101, 2004.

[137] Z. Shen, R. Wagoner, and W. Clark, "Dislocation pile-up and grain boundary interactions in 304 stainless steel," *Scripta metallurgica*, vol. 20, no. 6, pp. 921–926, 1986.

[138] F. Martin, J. Cousty, J. Masson, and B. Bataillon, "In situ AFM study of pitting corrosion and corrosion under strain on a 304L stainless steel," in *Congress Proceedings EUROCORR 2004, 12*, vol. 16, pp. 1–10, 2004.

[139] A. F. Payam, O. Payton, L. Picco, S. Moore, T. Martin, A. Warren, M. Mostafavi, and D. Knowles, "Development of fatigue testing system for in-situ observation of stainless steel 316 by HS-AFM & SEM," *International Journal of Fatigue*, vol. 127, pp. 1–9, 2019.

[140] S. Fréchard, F. Martin, C. Clément, and J. Cousty, "AFM and EBSD combined studies of plastic deformation in a duplex stainless steel," *Materials Science and Engineering: A*, vol. 418, no. 1-2, pp. 312–319, 2006.

[141] L. Li, S. Liu, B. Ye, S. Hu, and Z. Zhou, "Quantitative analysis of strength and plasticity of a 304 stainless steel based on the stress-strain curve," *Metals and Materials International*, vol. 22, no. 3, pp. 391–396, 2016.

[142] A. Boeuf, S. Crico, R. Caciuffo, F. Rustichelli, I. Pomot, and G. Uny, "Effects of M23C6 precipitation on the lattice parameter of AISI 304 stainless steel," *Materials Letters*, vol. 3, no. 3, pp. 115–118, 1985.

[143] H. F. G. d. Abreu, S. S. d. Carvalho, P. d. Lima Neto, R. P. d. Santos, V. N. Freire, P. M. d. O. Silva, and S. S. M. Tavares, "Deformation induced martensite in an AISI 301LN stainless steel: characterization and influence on pitting corrosion resistance," *Materials Research*, vol. 10, no. 4, pp. 359–366, 2007.

[144] L. Zhang, Z. Li, J. Zheng, Y. Zhao, P. Xu, C. Zhou, and X. Li, "Effect of strain-induced martensite on hydrogen embrittlement of austenitic stainless steels investigated by

combined tension and hydrogen release methods," *International journal of hydrogen energy*, vol. 38, no. 19, pp. 8208–8214, 2013.

[145] M. Kamaya and T. Haruna, "Influence of local stress on initiation behavior of stress corrosion cracking for sensitized 304 stainless steel," *Corrosion science*, vol. 49, no. 8, pp. 3303–3324, 2007.

[146] D. R. Jones and M. F. Ashby, *Engineering materials 1: An introduction to properties, applications and design*.
Elsevier, 2011.

[147] M. S. Breimesser, *Microelectrochemical approach towards the analysis of electrochemical noise signals related to intergranular stress corrosion cracking of austenitic stainless steel*.
PhD thesis, Universitat Erlangen-Nurnberg, Germany, 2012.

[148] M. Ghahari, D. Krouse, N. Laycock, T. Rayment, C. Padovani, M. Stampanoni, F. Marone, R. Mokso, and A. J. Davenport, "Synchrotron X-ray radiography studies of pitting corrosion of stainless steel: Extraction of pit propagation parameters," *Corrosion Science*, vol. 100, pp. 23–35, 2015.

[149] N. Laycock and S. White, "Computer simulation of single pit propagation in stainless steel under potentiostatic control," *Journal of the Electrochemical Society*, vol. 148, no. 7, pp. B264–B275, 2001.

[150] R. E. Williford, C. Windisch Jr, and R. H. Jones, "In situ observations of the early stages of localized corrosion in Type 304 SS using the electrochemical atomic force microscope," *Materials Science and Engineering: A*, vol. 288, no. 1, pp. 54–60, 2000.

[151] S. R. Street, N. Mi, A. J. Cook, H. B. Mohammed-Ali, L. Guo, T. Rayment, and A. J. Davenport, "Atmospheric pitting corrosion of 304L stainless steel: the role of highly concentrated chloride solutions," *Faraday discussions*, vol. 180, pp. 251–265, 2015.

[152] G. Burstein and S. Mattin, "Nucleation of corrosion pits on stainless steel," *Philosophical magazine letters*, vol. 66, no. 3, pp. 127–131, 1992.

[153] L. Liu, Y. Li, and F. Wang, "Pitting mechanism on an austenite stainless steel nanocrystalline coating investigated by electrochemical noise and in-situ AFM analysis," *Electrochimica Acta*, vol. 54, no. 2, pp. 768–780, 2008.

[154] J.-y. Jiang, Y. Liu, H.-y. Chu, D. Wang, H. Ma, and W. Sun, "Pitting corrosion behaviour of new corrosion-resistant reinforcement bars in chloride-containing concrete pore solution," *Materials*, vol. 10, no. 8, p. 903, 2017.

[155] F. Martin, C. Bataillon, and J. Cousty, "In situ AFM detection of pit onset location on a 304L stainless steel," *Corrosion Science*, vol. 50, no. 1, pp. 84–92, 2008.

[156] R. M. Rynders, C.-H. Paik, R. Ke, and R. C. Alkire, "Use of in situ atomic force microscopy to image corrosion at inclusions," *Journal of The Electrochemical Society*, vol. 141, no. 6, p. 1439, 1994.

[157] B. Vuillemin, X. Philippe, R. Oltra, V. Vignal, L. Coudreuse, L. Dufour, and E. Finot, "SVET, AFM and AES study of pitting corrosion initiated on MnS inclusions by microinjection," *Corrosion science*, vol. 45, no. 6, pp. 1143–1159, 2003.

[158] L. Choudhary, D. D. Macdonald, and A. Alfantazi, "Role of thiosulfate in the corrosion of steels: a review," *Corrosion*, vol. 71, no. 9, pp. 1147–1168, 2015.

[159] K. Sieradzki, H. S. Isaacs, and R. C. Newman, "Ambient temperature stress-corrosion cracking of sensitized stainless steels," tech. rep., Brookhaven National Lab., 1982.

[160] D. Wells, J. Stewart, R. Davidson, P. Scott, and D. Williams, "The mechanism of intergranular stress corrosion cracking of sensitised austenitic stainless steel in dilute thiosulphate solution," *Corrosion science*, vol. 33, no. 1, pp. 39–71, 1992.

[161] L. Choudhary, W. Wang, and A. Alfantazi, "Electrochemical corrosion of stainless steel in thiosulfate solutions relevant to gold leaching," *Metallurgical and Materials Transactions A*, vol. 47, no. 1, pp. 314–325, 2016.

[162] M. Mohammadi, L. Choudhary, I. M. Gadala, and A. Alfantazi, "Electrochemical and passive layer characterizations of 304L, 316L, and duplex 2205 stainless steels in thiosulfate gold leaching solutions," *Journal of The Electrochemical Society*, vol. 163, no. 14, p. C883, 2016.

[163] H. Isaacs, B. Vyas, and M. Kendig, "Stress-corrosion cracking of sensitized stainless steel by sulfur-containing compounds," tech. rep., Brookhaven National Lab., 1981.

[164] R. Newman, K. Sieradzki, and H. Isaacs, "Stress-corrosion cracking of sensitized Type 304 stainless steel in thiosulfate solutions," *Metallurgical Transactions A*, vol. 13, no. 11, pp. 2015–2026, 1982.

[165] M. Gomez-Duran and D. D. Macdonald, "Stress corrosion cracking of sensitized Type 304 stainless steel in thiosulfate solution: I. fate of the coupling current," *Corrosion science*, vol. 45, no. 7, pp. 1455–1471, 2003.

[166] M. Gomez-Duran and D. D. Macdonald, "Stress corrosion cracking of sensitized Type 304 stainless steel in thiosulphate solution. II. dynamics of fracture," *Corrosion Science*, vol. 48, no. 7, pp. 1608–1622, 2006.

[167] A. Aballe, R. A. Cottis, R. C. Newman, *et al.*, "Electrochemical noise study of stress corrosion cracking of sensitized 304SS in thiosulfate," in *CORROSION 2003*, NACE International, 2003.

[168] S. Roychowdhury, S. Ghosal, and P. De, "Role of environmental variables on the stress corrosion cracking of sensitized AISI Type 304 stainless steel (SS304) in thiosulfate solutions," *Journal of materials engineering and performance*, vol. 13, no. 5, pp. 575–582, 2004.

[169] Y. Sato, T. Atsumi, and T. Shoji, "Continuous monitoring of back wall stress corrosion cracking growth in sensitized Type 304 stainless steel weldment by means of potential drop techniques," *International journal of pressure vessels and piping*, vol. 84, no. 5, pp. 274–283, 2007.

[170] S. Wu, J. Wang, S. Song, D.-H. Xia, Z. Zhang, Z. Gao, J. Wang, W. Jin, and W. Hu, "Factors influencing passivity breakdown on UNS N08800 in neutral chloride and thiosulfate solutions," *Journal of The Electrochemical Society*, vol. 164, no. 4, p. C94, 2017.

[171] C. Duret-Thual, D. Costa, W. Yang, and P. Marcus, "The role of thiosulfates in the pitting corrosion of Fe-17Cr alloys in neutral chloride solution: electrochemical and XPS study," *Corrosion Science*, vol. 39, no. 5, pp. 913–933, 1997.

[172] R. Zhao, Z. Zhang, J.-b. Shi, L. Tao, and S.-z. Song, "Characterization of stress corrosion crack growth of 304 stainless steel by electrochemical noise and scanning Kelvin probe," *Journal of Central South University of Technology*, vol. 17, no. 1, pp. 13–18, 2010.

[173] J. A. Duff and T. J. Marrow, "In-situ observations of intergranular stress corrosion cracking," in *ASME Pressure Vessels and Piping Conference*, vol. 48296, pp. 847–854, 2008.

[174] J. Li, W. Chu, Y. Wang, and L. Qiao, "In situ TEM study of stress corrosion cracking of austenitic stainless steel," *Corrosion science*, vol. 45, no. 7, pp. 1355–1365, 2003.

[175] M. Meisnar, M. Moody, and S. Lozano-Perez, "Atom probe tomography of stress corrosion crack tips in SUS316 stainless steels," *Corrosion Science*, vol. 98, pp. 661–671, 2015.

[176] H. Uchida, M. Yamashita, S. Inoue, and K. Koterazawa, "In-situ observations of crack nucleation and growth during stress corrosion by scanning vibrating electrode technique," *Materials Science and Engineering: A*, vol. 319, pp. 496–500, 2001.

[177] S. Rossi, M. Fedel, F. Deflorian, and M. del Carmen Vadillo, "Localized electrochemical techniques: Theory and practical examples in corrosion studies," *Comptes Rendus Chimie*, vol. 11, no. 9, pp. 984–994, 2008.

[178] C. D. Fernández-Solis, A. Vimalanandan, A. Altin, J. S. Mondragón-Ochoa, K. Kreth, P. Keil, and A. Erbe, "Fundamentals of electrochemistry, corrosion and corrosion protection," in *Soft Matter at Aqueous Interfaces*, pp. 29–70, Springer, 2016.

[179] R. M. Asmussen, W. J. Binns, P. Jakupi, P. Dauphin-Ducharme, U. M. Tefashe, J. Mauzeroll, and D. Shoesmith, "Reducing the corrosion rate of magnesium alloys using ethylene glycol for advanced electrochemical imaging," *Corrosion Science*, vol. 93, pp. 70–79, 2015.

[180] E. Fayyad, M. Almaadeed, A. Jones, and A. Abdullah, "Evaluation techniques for the corrosion resistance of self-healing coatings," *Int. J. Electrochem. Sci.*, vol. 9, pp. 4989–5011, 2014.

[181] O. Payton, L. Picco, and T. Scott, "High-speed atomic force microscopy for materials science," *International Materials Reviews*, vol. 61, no. 8, pp. 473–494, 2016.

[182] G. Binnig, C. F. Quate, and C. Gerber, "Atomic force microscope," *Physical review letters*, vol. 56, no. 9, p. 930, 1986.

[183] O. D. Payton, *High-speed atomic force microscopy under the microscope*. PhD thesis, University of Bristol, 2012.

[184] A. Humphris, M. Miles, and J. Hobbs, "A mechanical microscope: high-speed atomic force microscopy," *Applied physics letters*, vol. 86, no. 3, pp. 34106–34106, 2005.

[185] G. Schitter, K. J. Astrom, B. E. DeMartini, P. J. Thurner, K. L. Turner, and P. K. Hansma, "Design and modeling of a high-speed AFM-scanner," *IEEE Transactions on Control Systems Technology*, vol. 15, no. 5, pp. 906–915, 2007.

[186] F. Eghiaian, F. Rico, A. Colom, I. Casuso, and S. Scheuring, "High-speed atomic force microscopy: Imaging and force spectroscopy," *FEBS letters*, vol. 588, no. 19, pp. 3631–3638, 2014.

[187] T. Ando, T. Uchihashi, and N. Kodera, "High-speed atomic force microscopy," *Japanese journal of applied physics*, vol. 51, no. 8S3, p. 08KA02, 2012.

[188] A. J. Katan and C. Dekker, "High-speed AFM reveals the dynamics of single biomolecules at the nanometer scale," *Cell*, vol. 147, no. 5, pp. 979–982, 2011.

[189] O. Payton, L. Picco, D. Robert, A. Raman, M. Homer, A. Champneys, and M. Miles, "High-speed atomic force microscopy in slow motion—understanding cantilever behaviour at high scan velocities," *Nanotechnology*, vol. 23, no. 20, p. 205704, 2012.

[190] H.-S. Liao, K.-Y. Huang, I.-S. Hwang, T.-J. Chang, W. W. Hsiao, H.-H. Lin, E.-T. Hwu, and C.-S. Chang, "Operation of astigmatic-detection atomic force microscopy in liquid environments," *Review of Scientific Instruments*, vol. 84, no. 10, p. 103709, 2013.

[191] C. A. Putman, B. G. De Grooth, N. F. Van Hulst, and J. Greve, "A detailed analysis of the optical beam deflection technique for use in atomic force microscopy," *Journal of Applied Physics*, vol. 72, no. 1, pp. 6–12, 1992.

[192] T. Uchihashi, H. Watanabe, S. Fukuda, M. Shibata, and T. Ando, "Functional extension of high-speed AFM for wider biological applications," *Ultramicroscopy*, vol. 160, pp. 182–196, 2016.

[193] C. Liu, P. Heard, O. Payton, L. Picco, and P. Flewitt, "A comparison of two high spatial resolution imaging techniques for determining carbide precipitate type and size in ferritic 9Cr-1Mo steel," *Ultramicroscopy*, vol. 205, pp. 13–19, 2019.

[194] H. Chen, Z. Qin, M. He, Y. Liu, and Z. Wu, "Application of electrochemical atomic force microscopy (EC-AFM) in the corrosion study of metallic materials," *Materials*, vol. 13, no. 3, p. 668, 2020.

[195] P. Bai, H. Zhao, S. Zheng, and C. Chen, "Initiation and developmental stages of steel corrosion in wet H2S environments," *Corrosion Science*, vol. 93, pp. 109–119, 2015.

[196] K. Minoshima, Y. Oie, and K. Komai, "In situ AFM imaging system for the environmentally induced damage under dynamic loads in a controlled environment," *ISIJ international*, vol. 43, no. 4, pp. 579–588, 2003.

[197] Y. Nakai, T. Kusukawa, and N. Hayashi, "Grain-size effect on fatigue crack initiation condition observed by using atomic-force microscopy," *ASTM STP*, vol. 1406, pp. 122–135, 2001.

[198] K. Komai, K. Minoshima, and T. Miyawaki, "In situ observation of stress corrosion cracking of high-strength aluminum alloy by scanning atomic force microscopy and influence of vacuum," *JSME International Journal Series A Solid Mechanics and Material Engineering*, vol. 41, no. 1, pp. 49–56, 1998.

[199] T. Ando, "High-speed atomic force microscopy," *Microscopy*, vol. 62, no. 1, pp. 81–93, 2013.

[200] A. Koorikkat, O. Payton, L. Picco, and W. Schwarzacher, "Imaging the surface of a polycrystalline electrodeposited Cu film in real time using in situ high-speed AFM," *Journal of the Electrochemical Society*, vol. 167, no. 16, p. 162510, 2020.

[201] A. Pyne, W. Marks, L. M. Picco, P. G. Dunton, A. Ulcinas, M. E. Barbour, S. B. Jones, J. Gimzewski, and M. J. Miles, "High-speed atomic force microscopy of dental enamel

dissolution in citric acid," *Archives of histology and cytology*, vol. 72, no. 4+ 5, pp. 209–215, 2009.

[202] D. Nečas and P. Klapetek, "Gwyddion: an open-source software for SPM data analysis," *Open Physics*, vol. 10, no. 1, pp. 181–188, 2012.

[203] P. Klapetek, D. Necas, and C. Anderson, "Gwyddion user guide," *Czech Metrology Institute*, vol. 2007, p. 2009, 2004.

[204] R. Navarro and A. Tabernero, "Gaussian wavelet transform: two alternative fast implementations for images," *Multidimensional Systems and Signal Processing*, vol. 2, no. 4, pp. 421–436, 1991.

[205] D. Nečas and P. Klapetek, "Study of user influence in routine SPM data processing," *Measurement Science and Technology*, vol. 28, no. 3, p. 034014, 2017.

[206] M. A. Sutton, N. Li, D. Joy, A. P. Reynolds, and X. Li, "Scanning electron microscopy for quantitative small and large deformation measurements part I: SEM imaging at magnifications from 200 to 10,000," *Experimental mechanics*, vol. 47, no. 6, pp. 775–787, 2007.

[207] R. Borrajo-Pelaez and P. Hedström, "Recent developments of crystallographic analysis methods in the scanning electron microscope for applications in metallurgy," *Critical Reviews in Solid State and Materials Sciences*, vol. 43, no. 6, pp. 455–474, 2018.

[208] T. Maitland and S. Sitzman, *Electron backscatter diffraction (EBSD) technique and materials characterization examples*, vol. 14.
Springer Berlin, 2007.

[209] F. Humphreys, "Characterisation of fine-scale microstructures by electron backscatter diffraction (EBSD)," *Scripta materialia*, vol. 51, no. 8, pp. 771–776, 2004.

[210] R. Gauvin, P. Hovongton, D. Drouin, P. Horny, H. Demers, and A. Real Couture, *3D CASINO Version 3.2*.
Universite de Sherbrooke, Quebec, Canada, aug 2011.
URL Download at: http://www.gel.usherbrooke.ca/casino/download.html.

[211] K. Mingard, B. Roebuck, E. Bennett, M. Gee, H. Nordenstrom, G. Sweetman, and P. Chan, "Comparison of EBSD and conventional methods of grain size measurement of hardmetals," *International Journal of Refractory Metals and Hard Materials*, vol. 27, no. 2, pp. 213–223, 2009.

[212] L. Koll, P. Tsipouridis, and E. Werner, "Preparation of metallic samples for electron backscatter diffraction and its influence on measured misorientation," *Journal of microscopy*, vol. 243, no. 2, pp. 206–219, 2011.

[213] H. Jazaeri and F. Humphreys, "Quantifying recrystallization by electron backscatter diffraction," *Journal of microscopy*, vol. 213, no. 3, pp. 241–246, 2004.

[214] M. Othon and M. Morra, "EBSD characterization of SCC in Alloy 182 weld metal," *Microscopy and Microanalysis*, vol. 12, no. S02, pp. 928–929, 2006.

[215] D. J. Dingley, G. Meaden, D. J. Dingley, and A. P. Day, "A review of EBSD: from rudimentary on line orientation measurements to high resolution elastic strain measurements over the past 30 years.," in *IOP conference series: materials science and engineering, vol. 375*, p. 012003, 2018.

[216] J. Li, M. Elboujdaini, M. Gao, and R. Revie, "Investigation of plastic zones near SCC tips in a pipeline after hydrostatic testing," *Materials Science and Engineering: A*, vol. 486, no. 1, pp. 496–502, 2008.

[217] Y.-Z. Wang, R. Revie, M. Phaneuf, and J. Li, "Application of focused ion beam (FIB) microscopy to the study of crack profiles," *Fatigue & fracture of engineering materials & structures (Print)*, vol. 22, no. 3, pp. 251–256, 1999.

[218] L. A. Giannuzzi and F. A. Stevie, "A review of focused ion beam milling techniques for TEM specimen preparation," *Micron*, vol. 30, no. 3, pp. 197–204, 1999.

[219] S. Lozano-Perez, P. Rodrigo, and L. C. Gontard, "Three-dimensional characterization of stress corrosion cracks," *Journal of nuclear materials*, vol. 408, no. 3, pp. 289–295, 2011.

[220] A. Basa, C. Thaulow, and A. Barnoush, "Chemically induced phase transformation in austenite by focused ion beam," *Metallurgical and Materials Transactions A*, vol. 45, no. 3, pp. 1189–1198, 2014.

[221] K. Knipling, D. Rowenhorst, R. Fonda, and G. Spanos, "Effects of focused ion beam milling on austenite stability in ferrous alloys," *Materials Characterization*, vol. 61, no. 1, pp. 1–6, 2010.

[222] S. Reyntjens and R. Puers, "A review of focused ion beam applications in microsystem technology," *Journal of micromechanics and microengineering*, vol. 11, no. 4, p. 287, 2001.

[223] S. Lozano-Perez, J. Dohr, M. Meisnar, and K. Kruska, "SCC in PWRs: learning from a bottom-up approach," *Metallurgical and Materials Transactions E*, vol. 1, no. 2, pp. 194–210, 2014.

[224] T. Since, "TEM: an introduction," *III-Vs Review*, vol. 13, no. 6, 2000.

[225] G. Iriarte, A. Méndez-Vilas, and J. Díaz, "Using transmission electron microscopy (TEM) for chemical analysis of semiconductors," *Microscopy: Science, Technology, Applications and Education, Book Chapter*, pp. 1888–1896, 2010.

[226] M. Dománková, E. Kocsisová, I. Slatkovskỳ, and P. Pinke, "The microstructure evolution and its effect on corrosion properties of 18Cr-12Ni-2, 5Mo steel annealed at 500-900 C," *Acta Polytechnica Hungarica*, vol. 11, no. 3, pp. 125–137, 2014.

[227] T. Slater, R. Bradley, G. Bertali, R. Geurts, S. Northover, M. Burke, S. Haigh, T. Burnett, and P. Withers, "Multiscale correlative tomography: an investigation of creep cavitation in 316 stainless steel," *Scientific reports*, vol. 7, no. 1, pp. 1–10, 2017.

[228] T. Terachi, K. Fujii, and K. Arioka, "Microstructural characterization of SCC crack tip and oxide film for SUS 316 stainless steel in simulated PWR primary water at 320 C," *Journal of nuclear science and technology*, vol. 42, no. 2, pp. 225–232, 2005.

[229] Y. Huang and J. Titchmarsh, "TEM investigation of intergranular stress corrosion cracking for 316 stainless steel in PWR environment," *Acta materialia*, vol. 54, no. 3, pp. 635–641, 2006.

[230] Z. Song and Z.-H. Xie, "A literature review of in situ transmission electron microscopy technique in corrosion studies," *Micron*, vol. 112, pp. 69–83, 2018.

[231] Z. Wang, "Transmission electron microscopy of shape-controlled nanocrystals and their assemblies," *J. Phys. Chem. B*, vol. 104, no. 6, pp. 1153–1175, 2000.

[232] M. Meisnar, A. Vilalta-Clemente, A. Gholinia, M. Moody, A. J. Wilkinson, N. Huin, and S. Lozano-Perez, "Using transmission Kikuchi diffraction to study intergranular stress corrosion cracking in Type 316 stainless steels," *Micron*, vol. 75, pp. 1–10, 2015.

[233] A. Devaraj, D. E. Perea, J. Liu, L. M. Gordon, T. J. Prosa, P. Parikh, D. R. Diercks, S. Meher, R. P. Kolli, Y. S. Meng, *et al.*, "Three-dimensional nanoscale characterisation of materials by atom probe tomography," *International Materials Reviews*, vol. 63, no. 2, pp. 68–101, 2018.

[234] T. F. Kelly and M. K. Miller, "Atom probe tomography," *Review of Scientific Instruments*, vol. 78, no. 3, p. 031101, 2007.

[235] B. Gault and D. J. Larson, "Atom probe tomography: Looking forward," *Scripta Materialia*, vol. 148, pp. 73–74, 2018.

[236] Z. Shen, D. Tweddle, H. Yu, G. He, A. Varambhia, P. Karamched, F. Hofmann, A. J. Wilkinson, M. P. Moody, L. Zhang, *et al.*, "Microstructural understanding of the oxidation of

an austenitic stainless steel in high-temperature steam through advanced characterization," *Acta Materialia*, 2020.

[237] C. Lotharukpong, D. Tweddle, T. Martin, M. Wu, C. Grovenor, M. Moody, and P. Wilshaw, "Specimen preparation methods for elemental characterisation of grain boundaries and isolated dislocations in multicrystalline silicon using atom probe tomography," *Materials Characterization*, vol. 131, pp. 472–479, 2017.

[238] M. K. Miller, K. F. Russell, K. Thompson, R. Alvis, D. J. Larson, R. Anderson, S. Klepeis, J. Cairney, D. Saxey, D. Mcgrouther, *et al.*, "Review of atom probe FIB-based specimen preparation methods," *Microscopy and Microanalysis*, vol. 13, no. 6, pp. 428–436, 2007.

[239] S. Lozano-Perez, "A guide on FIB preparation of samples containing stress corrosion crack tips for TEM and atom-probe analysis," *Micron*, vol. 39, no. 3, pp. 320–328, 2008.

[240] M. Escher, N. Weber, M. Merkel, B. Krömker, D. Funnemann, S. Schmidt, F. Reinert, F. Forster, S. Hüfner, P. Bernhard, *et al.*, "NanoESCA: imaging UPS and XPS with high energy resolution," *Journal of electron spectroscopy and related phenomena*, vol. 144, pp. 1179–1182, 2005.

[241] A. Szczepanska, G. Wan, M. Cattelan, N. A. Fox, and N. Vasiljevic, "Surface investigation on electrochemically deposited lead on gold," *Surfaces*, vol. 2, no. 1, pp. 56–68, 2019.

[242] A. D. Warren, A. I. Martinez-Ubeda, O. D. Payton, L. Picco, and T. B. Scott, "Preparation of stainless steel surfaces for scanning probe microscopy," *Microscopy Today*, vol. 24, no. 03, pp. 52–55, 2016.

[243] Struers, "Metallographic preparation of stainless steel - Struers Application Notes," Struers A/S Pederstrupvej 84 DK-2750 Ballerup, Denmark, Feb 2006.
Accessed online on 24/04/17 at: www.struers.com.

[244] P. Martínek and P. Podaný, "Etching techniques for duplex steels," *Journal of Achievements in Materials and Manufacturing Engineering*, vol. 68, no. 1, pp. 11–16, 2015.

[245] D. Zipperian, "Chemical etching," *PACE Technologies*, vol. 2, p. 5, 2003.

[246] "Standard practice for microetching metals and alloys," 1999.
ASTM Standard E407, 1999, ASTM International, West Conshohocken, PA, www.astm.org.

[247] G. Vander Voort and E. Manilova, "Hints for imaging phases in steels," *Advanced Materials & Processes*, vol. 163, no. 02, pp. –, 2005.

[248] G. F. Vander Voort, *Metallography, principles and practice*.
ASM international, 1999.

[249] B. Varbai, T. Pickle, and K. Májlinger, "Development and comparison of quantitative phase analysis for duplex stainless steel weld," *Periodica Polytechnica Mechanical Engineering*, vol. 62, no. 3, pp. 247–253, 2018.

[250] B. Varbai and K. Májlinger, "Optimal etching sequence for austenite to ferrite ratio evaluation of two lean duplex stainless steel weldments," *Measurement*, vol. 147, p. 106832, 2019.

[251] F. Cardarelli, *Materials handbook: a concise desktop reference*.
Springer Science & Business Media, 2008.

[252] K. B. Hensel, "Electropolishing," *Metal Finishing*, vol. 97, no. 1, pp. 447–455, 1999.

[253] A. Kosmac, *Electropolishing Stainless Steels*, vol. 11.
Materials and Applications Series, first ed., 2010.
Euro Inox.

[254] J. Swain, "The "then and now" of electropolishing," *Surface World, Anopol Ltd*, 2010.

[255] J. R. Davis *et al.*, *Stainless steels*.
ASM international, 1994.

[256] B. L. Bramfitt and A. O. Benscoter, *Metallographer's guide: practice and procedures for irons and steels*.
Asm International, 2001.

[257] P. West and N. Starostina, "How to recognize and avoid AFM image artifacts," *Microscopy Today*, vol. 11, no. 3, pp. 20–27, 2003.

[258] B. N. Inc., "MSNL-10 - Bruker AFM probes," Bruker, USA, 2020.
Accessed online on 24/03/2020 at: https://www.brukerafmprobes.com/p-3710-msnl-10.aspx.

[259] R. W. Bruce, *Handbook of lubrication and tribology, volume II: Theory and design*.
CRC press, 2012.

[260] Š. Mikmeková, K. Matsuda, K. Watanabe, S. Ikeno, I. Müllerová, and L. Frank, "FIB induced damage examined with the low energy SEM," *Materials Transactions*, vol. 52, no. 3, pp. 292–296, 2011.

[261] A. Warren, R. Harniman, Z. Guo, C. Younes, P. Flewitt, and T. Scott, "Quantification of sigma-phase evolution in thermally aged 2205 duplex stainless steel," *Journal of Materials Science*, vol. 51, no. 2, pp. 694–707, 2016.

[262] J. N. Al-Khamis and H. Pickering, "IR mechanism of crevice corrosion for alloy T-2205 duplex stainless steel in acidic-chloride media," *Journal of The Electrochemical Society*, vol. 148, no. 8, pp. B314–B321, 2001.

[263] Y. Guo, T. Sun, J. Hu, Y. Jiang, L. Jiang, and J. Li, "Microstructure evolution and pitting corrosion resistance of the Gleeble-simulated heat-affected zone of a newly developed lean duplex stainless steel 2002," *Journal of Alloys and Compounds*, vol. 658, pp. 1031–1040, 2016.

[264] C. Örnek and D. L. Engelberg, "An experimental investigation into strain and stress partitioning of duplex stainless steel using digital image correlation, X-ray diffraction and scanning Kelvin probe force microscopy," *The Journal of Strain Analysis for Engineering Design*, vol. 51, no. 3, pp. 207–219, 2016.

[265] L. Guo, M. Lin, L. Qiao, and A. A. Volinsky, "Ferrite and austenite phase identification in duplex stainless steel using SPM techniques," *Applied Surface Science*, vol. 287, pp. 499–501, 2013.

[266] J. W. Edington and K. T. Russell, *Practical electron microscopy in materials science*. Macmillan International Higher Education, 1977.

[267] N. Peighambardoust and F. Nasirpouri, "Electropolishing behaviour of pure titanium in perchloric acid–methanol–ethylene glycol mixed solution," *Transactions of the IMF*, vol. 92, no. 3, pp. 132–139, 2014.

[268] D. Gabe, "Toward a universal electropolishing solution," *Metallography*, vol. 5, no. 5, pp. 415–421, 1972.

[269] D. Gabe, "Electropolishing of mild steel in phosphoric and perchloric acid containing electrolytes," *Corrosion Science*, vol. 13, no. 3, pp. 175–185, 1973.

[270] Ö. Çelík, *Surface and thin film studies of the etching of molybdenum by xenon difluoride*. PhD thesis, Rutgers University-Graduate School-New Brunswick, 2010.

[271] A. Warren, I. Griffiths, R. Harniman, P. Flewitt, and T. Scott, "The role of ferrite in Type 316H austenitic stainless steels on the susceptibility to creep cavitation," *Materials Science and Engineering: A*, vol. 635, pp. 59–69, 2015.

[272] H. Yanliang, B. Kinsella, and T. Becker, "Sensitisation identification of stainless steel to intergranular stress corrosion cracking by atomic force microscopy," *Materials Letters*, vol. 62, no. 12-13, pp. 1863–1866, 2008.

[273] B. Kinsella and T. Becker, "The use of atomic force microscopy in corrosion research," *Corrosion and Materials*, vol. 34, pp. 31–39, 2009.

[274] Y. Nemoto, Y. Miwa, T. Tsukada, and H. Tsuji, "AFM evaluation of grain boundary corrosion behavior on ion irradiated stainless steel," tech. rep., 2003.

[275] R. W. Armstrong, "60 years of Hall-Petch: past to present nano-scale connections," *Materials Transactions*, vol. 55, no. 1, pp. 2–12, 2014.

[276] S. Salleh, *Modelling pitting corrosion in carbon steel materials*.
PhD thesis, University of Manchester, 2012.

[277] D. Macdonald and G. Engelhardt, "2.39 predictive modeling of corrosion," *Shreir's Corrosion, Elsevier BV*, 2010.

[278] R. Burrows, *Passive and Localised Corrosion Behaviour of a High Magnesium Alloy (Magnox Al80)*.
PhD thesis, University of Manchester, 2013.

[279] J. Buffle, Z. Zhang, and K. Startchev, "Supplementary information for the paper: Metal flux and dynamic speciation at (bio) interfaces. part i: Critical evaluation and compilation of physicochemical parameters for complexes with simple ligands and fulvic/humic substances," *Environmental science & technology*, vol. 41, no. 22, pp. 7609–7620, 2007.

[280] A. Shahryari, J. A. Szpunar, and S. Omanovic, "The influence of crystallographic orientation distribution on 316LVM stainless steel pitting behavior," *Corrosion Science*, vol. 51, no. 3, pp. 677–682, 2009.

[281] D. P. Burt, N. R. Wilson, U. Janus, J. V. Macpherson, and P. R. Unwin, "In-situ atomic force microscopy (AFM) imaging: influence of AFM probe geometry on diffusion to microscopic surfaces," *Langmuir*, vol. 24, no. 22, pp. 12867–12876, 2008.

[282] R. N. Clark, C. M. Chan, T. L. Martin, W. Walters, D. Engelberg, R. Burrows, and G. Williams, "The effect of sodium hydroxide on niobium carbide precipitates in thermally sensitised 20Cr-25Ni-Nb austenitic stainless steel," *Corrosion Science*, p. 108596, 2020.

[283] R. O. Ritchie, "Mechanisms of fatigue-crack propagation in ductile and brittle solids," *International journal of Fracture*, vol. 100, no. 1, pp. 55–83, 1999.

[284] S. Ortner, "A STEM study of the effect of precipitation on grain boundary chemistry in AISI 304 steel," *Acta metallurgica et materialia*, vol. 39, no. 3, pp. 341–350, 1991.

[285] B. Gault, M. P. Moody, J. M. Cairney, and S. P. Ringer, *Atom probe microscopy*, vol. 160.
Springer Science & Business Media, 2012.

[286] S. Lozano-Perez, T. Yamada, T. Terachi, M. Schröder, C. English, G. Smith, C. Grovenor, and B. Eyre, "Multi-scale characterization of stress corrosion cracking of cold-worked stainless steels and the influence of Cr content," *Acta Materialia*, vol. 57, no. 18, pp. 5361–5381, 2009.

[287] T. Meiners, Z. Peng, B. Gault, C. H. Liebscher, and G. Dehm, "Sulfur–induced embrittlement in high-purity, polycrystalline copper," *Acta Materialia*, vol. 156, pp. 64–75, 2018.

[288] J. R. Davis, *Corrosion of aluminum and aluminum alloys*.
Asm International, 1999.

[289] B. N. Popov, *Corrosion engineering: principles and solved problems*.
Elsevier, 2015.

[290] G. H. Koch, "Tests for stress-corrosion," *Advanced materials & processes*, vol. 159, no. 8, pp. 36–38, 2001.

[291] D. Kumar, "The journey towards in-situ measurements of SCC using HS-AFM," Master's thesis, The University of Bristol, 2018.

[292] J. Kacher, B. Eftink, B. Cui, and I. Robertson, "Dislocation interactions with grain boundaries," *Current Opinion in Solid State and Materials Science*, vol. 18, no. 4, pp. 227–243, 2014.

[293] J. Kacher and I. Robertson, "Quasi-four-dimensional analysis of dislocation interactions with grain boundaries in 304 stainless steel," *Acta Materialia*, vol. 60, no. 19, pp. 6657–6672, 2012.

[294] N. Badwe, X. Chen, D. K. Schreiber, M. J. Olszta, N. R. Overman, E. Karasz, A. Tse, S. M. Bruemmer, and K. Sieradzki, "Decoupling the role of stress and corrosion in the intergranular cracking of noble-metal alloys," *Nature materials*, vol. 17, no. 10, pp. 887–893, 2018.

[295] C. Kranz, G. Friedbacher, B. Mizaikoff, A. Lugstein, J. Smoliner, and E. Bertagnolli, "Integrating an ultramicroelectrode in an AFM cantilever: combined technology for enhanced information," *Analytical chemistry*, vol. 73, no. 11, pp. 2491–2500, 2001.

[296] J. V. Macpherson and P. R. Unwin, "Combined scanning electrochemical- atomic force microscopy," *Analytical Chemistry*, vol. 72, no. 2, pp. 276–285, 2000.

[297] D. Armstrong, A. Haseeb, S. Roberts, A. Wilkinson, and K. Bade, "Nanoindentation and micro-mechanical fracture toughness of electrodeposited nanocrystalline Ni–W alloy films," *Thin Solid Films*, vol. 520, no. 13, pp. 4369–4372, 2012.

[298] Y. Yan, T. Sumigawa, and T. Kitamura, "Effect of environment on fatigue strength of Cu/Si interface in nanoscale components," *Materials Science and Engineering: A*, vol. 556, pp. 147–154, 2012.

[299] H. Dugdale, D. E. Armstrong, E. Tarleton, S. G. Roberts, and S. Lozano-Perez, "How oxidized grain boundaries fail," *acta materialia*, vol. 61, no. 13, pp. 4707–4713, 2013.

[300] D. Di Maio and S. Roberts, "Measuring fracture toughness of coatings using focused-ion-beam-machined microbeams," *Journal of materials research*, vol. 20, no. 02, pp. 299–302, 2005.

[301] S. Wurster, C. Motz, and R. Pippan, "Characterization of the fracture toughness of micro-sized tungsten single crystal notched specimens," *Philosophical Magazine*, vol. 92, no. 14, pp. 1803–1825, 2012.